Bernd Schmidt · Klaus Wetzig

Ion Beams in Materials Processing and Analysis

Springer

Ion Beams in Materials Processing and Analysis

Bernd Schmidt · Klaus Wetzig

Ion Beams in Materials Processing and Analysis

Springer

Bernd Schmidt
Helmholtz-Zentrum Dresden-Rossendorf
Dresden
Germany

Klaus Wetzig
Leibniz-Institut für Festkörper- und
Werkstoffforschung
Dresden
Germany

ISBN 978-3-211-99355-2 ISBN 978-3-211-99356-9 (eBook)
ISBN (Mycopy): 978-3-211-99357-6
DOI 10.1007/978-3-211-99356-9
Springer Wien Heidelberg New York Dordrecht London

Library of Congress Control Number: 2012952142

Printed on acid-free paper

Springer-Verlag is a part of Springer Science+Business Media (www.springer.com)

Preface

Ion beam technologies have been established as indispensable tools in modern materials research, development, and production, being employed for both the modification and the characterization of surfaces and thin films of solids. At present, the ion beam is one of the most fascinating and leading tools for materials processing, surface and thin film preparation, and also for materials analysis. Ions have been successfully applied in particular in micro- and nanoelectronics since close to half a century, and they are in current use in numerous additional areas of high socioeconomic importance. Examples are investigations for materials optimization and waste disposal in nuclear fission and fusion research, the treatment of prosthetic components and radiation cancer therapy in the health area, and ion-based analytics both in environmental studies and for the characterization and preservation of cultural heritage. Fast ions also play an increasing role in emerging technologies which operate at the nanometer scale, such as for mechanical and chemical sensors and new photovoltaic materials, for nanopatterning, and, more general, for the creation and analysis of surfaces and thin films with tailored electrical, optical, or magnetic properties.

The above applications of ion beam technologies rely on fundamental knowledge of ion–surface interaction which has been mainly established during the past 50 years. Consequently, the methodology of ion beam application is no longer a broad topic of forefront research, so that the academic training can no longer be considered as a sufficient source of expertise and educational material. In this context, the aim of the present book is to provide a compact one-volume overview of the fundamentals of ion beam technologies and the most prominent areas of application. It shall address a broad audience of readers such as researchers, developers, and operators of both the public and the private sector, who are active in solid-state and atomic physics, electronics, and materials research and engineering, or in the field of modern functional materials and their processing. In particular, it may serve as a compendium for newcomers and interdisciplinary scientists and engineers. In this way, we hope to fill a gap on the international scientific book market and to promote the application of ion beams as a modern essential and sensitive microtool in materials research and technology.

This book is a result of long-lasting professional experience of the authors. Most recently, Klaus Wetzig worked as Director of the Institute of Solid State Analytics and Structural Research at Leibniz-Institut für Festkörper- und Werkstoffforschung

Dresden. Bernd Schmidt acts as head of the Process Technology Division at Helmholtz-Zentrum Dresden-Rossendorf. Naturally, numerous specific results from their research groups enter the present volume.

The fruitful interaction with numerous colleagues has been essential for the compilation of this book. Only a few of them can be particularly mentioned here. The authors are grateful to a number of people from the Helmholtz-Zentrum Dresden-Rossendorf who have contributed to this book by their experimental and theoretical works. These people include Prof. Wolfhard Möller, Dr. Johannes von Borany, Dr. Wolfgang Skorupa, Dr. Viton Heera, Dr. Lothar Bischoff, Prof. Andreas Kolitsch, Dr. Chavket Akhmadaliev, Dr. Rainer Grötzschel, Dr. Michael Zier, and Dr. Christian Neelmeijer as well as Mrs. Dr. Fine Fiedler, Dr. Karl-Heinz Heinig, and Dr. Mathias Posselt. These colleagues are gratefully acknowledged for cooperation and numerous discussions. Furthermore, the authors are indebted to Prof. Wolfgang Hauffe (Dresden) for fruitful discussions and the transfer of micrographs on ion beam slope cutting. Also thanks to Dr. Steffen Oswald, Dr. Siegfried Menzel, and Dr. Jürgen Thomas (all Leibniz Institut IFW Dresden) for experimental cooperation. K.W. in particular expresses his gratitude to Mrs. Anne Job (Dresden) for her qualified and great engagement in preparing a lot of illustrations for this book, such as schematic views, section drawings, and diagrams. B.S. is grateful to Maria Schmidt for her technical help to compile Chaps. 3 and 4.

Finally, the authors are grateful for the help and support provided by Dr. Alois Sillaber, BSc. Stephen Soehnlen, and Mrs. Mag. Eva-Maria Oberhauser from Springer-Verlag GmbH Wien during this project.

Dresden, April 2012 Bernd Schmidt and Klaus Wetzig

Contents

Introduction 1

The main purpose of this book is twofold. On the one hand, it is meant as a compendium for the physical fundamentals of ion–solid interactions, which are important not only for the understanding of ion implantation, ion beam sputtering, ion channeling, ion-induced damage formation, and ion beam mixing, but also for the comprehension of ion beam synthesis, ion-induced phase transformation, and nanopatterning. Therefore, the book addresses both scientists and research engineers. The principles of ion–solid interactions are not only of fundamental importance, but ion beam irradiation of solids is becoming an increasingly important technique for modifying surface and thin film properties. Therefore, this book is also intended to bridge the gap between fundamental phenomena and their technological applications in modern materials research, development, and analysis.

The book demonstrates the possibilities for optimization of solid state properties related to modern functional materials such as doped semiconductors and metal-based layers for micro- and nanoelectronics, to metal alloys, to nanopatterned surfaces, and to new ion beam synthesized materials. A thematic rounding of the book is realized by special ion beam applications in selected materials fields. To these belong the use of ion beam analysis in magnetoelectronic layers, in art and archeometry, and also in life sciences.

The present book is organized into several chapters ranging from principal aspects and phenomena over actual technological and device concepts to contemporary challenges in materials science. We thereby mainly concentrate on the relevant fields of semiconductors, nanomaterials, metals and polymers, interfaces, and thin layers.

In Chap. 2 the most important fundamental processes of ion–solid interactions will be compiled as a prerequisite for the understanding of ion-induced materials modifications and of ion beam-induced materials preparation and analytical techniques. These fundamental interactions include binary elastic particle collisions, ion stopping, and recoil processes and also ion channeling as a special case of ion transport in crystalline solids. The understanding of the ion channeling process allows the application of this phenomenon for wanted high ion penetration depth. On the other hand, problems of ion channeling such as uncontrolled ion stopping,

B. Schmidt and K. Wetzig, *Ion Beams in Materials Processing and Analysis*,
DOI 10.1007/978-3-211-99356-9_1,

deep ion penetration, and backscattering yield can be overcome by the knowledge of the physical process. For this purpose ion range and range distributions will be discussed in some detail.

Ion–solid interactions may also cause different ion-induced target modifications. To these belong ion implantation profiles, ion mixing processes, and ion-induced sputtering. Ion implantation modifies many material properties. Actually, it is the most important doping technique in the semiconductor technology. Special advantages of ion implantation are short process times, doping of small device structures, excellent lateral homogeneity, and adjustable doping profiles. Yet there are also disadvantages such as disturbing influence of diffusion and channeling and also ion irradiation-induced crystal damage up to amorphization. To overcome these difficulties the ion implantation process has to be well understood.

Another ion irradiation-related process is ion mixing. In an inhomogeneous multicomponent target, the relocation of atoms due to ion collision cascades results in a "mixing" of target atoms. This can be an intermixing or also alloying, and it results in a concentration profile broadening of a species A in a matrix B. Finally, ion sputtering is an important process of target surface modification under ion bombardment. In this process surface atoms are removed by collisions between incoming ions and the atoms in near-surface regions of a solid. If the energy transferred to a near-surface atom is sufficiently high to overcome its binding energy to the surface, then it will be ejected from the surface as a sputtered ion or neutral atom. This sputter process is characterized by the sputtering yield, and it depends on a lot of physical parameters in a complicated manner. Some relations will be discussed in Chap. 2 and also in Chap. 5.

The subject of Chap. 3 is the description of typical equipment for different ion accelerators developed for different purposes in a broad ion energy range between some 100 eV and some tens of MeV. From the technical point of view ion accelerators can be roughly divided into two groups: (1) ion accelerators in the low- and medium-energy range, which are usually called ion implanters, and (2) ion accelerators in the MeV ion energy range, which are usually called electrostatic ion accelerators. Nearly all ion beam accelerators include main building blocks, which are individually presented in this chapter. In particular, accelerated ion beams are treated from the viewpoints of ion sources, ion beam formation and acceleration, ion mass separation, ion optics and beam focusing, ion beam deflection and scanning, as well as ion beam current measurement and ion detection. The special designs of different ion beam tools are related to their main application fields of ion beam-assisted materials processing (e.g., broad beam or scanned beam ion implantation) and ion beam-based materials analysis, where usually stationary, low size beams of high energetic ions are required. Finally, ion beam techniques using scanned focused ion beams with spot sizes in the sub-μm range are shortly described with respect to their application in micro- and nanotechnologies and analysis.

Chapter 4 covers at first ion beam-based materials processing with respect to ion irradiation effects in crystalline materials, mainly in crystalline semiconductors, including formation of implanted impurity depth profiles, ion-induced crystal damage

formation and its annealing during different subsequent thermal treatments. The description of ion implantation into semiconductors focuses on the most important materials of silicon, germanium, III–IV compound semiconductors (GaAs, InP), group III-nitride materials (GaN, AlN, InN), and wide bandgap semiconductors (SiC). For these semiconductor materials the selection of appropriate doping ions, the implantation, and subsequent annealing conditions are summarized. More specialized applications of ion implantation and ion irradiation of silicon-based devices are discussed in relation with ion-implanted silicon sensors and radiation detectors, and with ion-assisted defect engineering in silicon power devices.

Ion beams have been increasingly applied for synthesis and exploration of new materials properties, for example, of metallic or semiconductor alloys and composites outside of thermodynamic equilibrium. The usual equilibrium solubility limits of implanted impurities in the solid host can be largely overcome, achieving depth-controlled local atom concentrations inaccessible by conventional synthesis routes (e.g., thermal diffusion). Ion beam synthesis of new phases, ion beam mixing, and ion beam slicing have been investigated progressively in the last 20 odd years. Consequently, the chapter takes ion beam synthesis of silicides and buried oxide in silicon as well as of metallic and semiconductor nanocrystals embedded in a solid host as examples to discuss the control of materials synthesis and evolution using ion implantation or irradiation. The self-organized formation of nanoscale surface ripples and dots on solid surfaces driven by continuous low- and medium-energy ion irradiation emerged as a further intense research field of ion beam materials processing. Examples of nanocrystal (and nanowire) synthesis, nanovoid formation, and shaping of nanoparticles under high-energy ion irradiation as a part of ion beam processing in the field of nanomaterials are also discussed in this chapter.

Finally, in Chap. 4 ion implantation techniques into metals, polymers, and insulating optical materials, such as amorphous glasses and nonlinear optical crystals, with the aim to improve or to achieve new materials properties are described, and summaries of the main process parameters for ion beam treatment of these materials are given.

Chapter 5 is devoted to the ion beam-assisted preparation of materials by the removal of target atoms as a result of ion sputtering. A permanent surface ion bombardment causes different sputter effects, such as selective sputtering, atomic mixing, ion channeling, crater bottom roughening, as well as charging effects for insulators. The dependence of the sputtering yield on different parameters appears complicated and will be discussed in detail. To these parameters belong ion energy and ion mass, ion incidence direction, and the atomic number of target materials.

In the case of polycrystalline and/or heterogeneous targets the phenomenon of selective sputtering can be used for surface preparation because it reveals the internal grain structure. Because of different binding energies and energy transfers for the different atomic species in multicomponent target materials preferential sputtering of certain species will take place, leading to a change of target composition in the near-surface region. Only after a material removal up to depths of about 10 nm, the steady state with real bulk element concentration will be reached.

Furthermore, several kinds of target modifications induced by ion beam irradiation will be described, for example, surface cleaning and etching, depth profiling, materials deposition, as well as ion beam-induced target cutting and thinning. All these ion beam techniques can be used for the targeted and high-precision manufacturing of materials, especially for the preparation of samples for different techniques of micro- and nanoanalytics.

An ion beam preparation technique of increasing importance is sample thinning, e.g., for the production of thin material lamellas, which can be penetrated by fast electrons as in the transmission electron microscope. Sample thinning with ions can be realized by two different techniques: by a conventional oblique bombardment with ions in the keV range (the so-called ion beam milling) or by focused ion beam (FIB) technique. Over the past few years the FIB technique has become more and more important because it combines a fast material removal with low damage generation in the sample. FIB preparation is now well established in materials research for microelectronics, especially for electron microscopic imaging, cross-section failure analysis, and device modification in the semiconductor industry.

The Chap. 6 gives an overview of analytical techniques using accelerated charged ions for material bombardment. The interaction between primary ions and the bombarded material leads to the emission of different particles or photon radiations from the surface. The energy of secondary particles and photons is characteristic for the elements constituting the sample material, and therefore they are mediator for analytical information. Ion beam-based analytical techniques allow the detection of specific elements and the determination of their concentration in near-surface regions of solids. Furthermore, they permit to determine the thickness, position, and concentration of individual layers in multilayer targets. Ion beam-based analytical techniques are characterized by some advantages: they are generally nondestructive (except for SIMS) and typically multielement methods, and they allow a simple and quick sample preparation with only small quantities (mg) and detection ranges (μm).

The analytical ion beam methods which are described in Chap. 6 are based on different ion–solid state interactions. Elastically scattered ions can be analyzed with different techniques, depending on their energy. Low-energy ion scattering (LEIS) and medium-energy ion scattering (MEIS) represent surface-sensitive methods with atomic layer depth resolution. High-energy ions scattered in backward direction are used in Rutherford Backscattering (RBS) analysis, whereas recoiled target atoms are detected at Elastic Recoil Detection Analysis (ERDA). High-energy ion beam-induced X-rays or γ-radiation emitted from the electron clouds or the nuclei of target atoms, respectively, allows the nondestructive identification of elements and the determination of their concentration in the investigated sample. The corresponding methods are referred to particle-induced X-ray emission (PIXE) and particle-induced gamma emission (PIGE). Furthermore, low-Z target elements can be analyzed by carrying out nuclear reactions with accelerated ions, giving secondary particles and γ-rays. The nuclear reaction analysis (NRA) and PIGE are nuclear techniques because they are governed by rules of nuclear reactions and kinematics.

Besides the particle and photon radiations mentioned above also secondary ions are emitted from low-energy ion-bombarded surfaces and can be used for analytical aims. For this purpose the emitted ions are analyzed in a mass spectrometer and the method is known as secondary ion mass spectrometry (SIMS). Ion beam imaging techniques such as field ion microscopy (FIM) and scanning ion microscopy (SIM) complete the content of Chap. 6.

The final Chap. 7 of the book gives some examples for ion beam applications in different materials analysis problems. These examples of use range from nano-analytical investigations of functional thin layers over ion beam analysis in art and archeometry to special applications in life sciences. For the study of functional thin films and layers the ion beam plays an important role. On the one hand, such layers can be produced by ion sputter deposition, prepared by FIB techniques and ion beam sputter material removal for cross sectioning. On the other hand, ions are a useful tool for the near-surface and cross-section analysis of these layers. Two typical examples are discussed in Sect. 7.1, namely, direct study of diffusion processes in amorphous thin layer systems and nanoanalytical investigations of tunnel magnetoresistance layers.

Ion beam analysis plays also an important role in art and archeometry with demands for a quantitative, multielement, and nondestructive analysis with detection limits down to trace elements. Such investigations allow an indirect dating and the authentification of artworks. Furthermore, in many cases ion beam analysis methods—preferentially by PIXE or PIGE—lay the foundations for a compatible and reversible restoration technique. In Sect. 7.2 the ion beam analysis of medieval paintings and of historical glass objects, ceramics, and porcelain will be discussed in some detail.

In recent years ion beams were increasingly applied in life sciences. On the one hand, this is related to the nondestructive element analysis of tissues, as by ion beam-induced X-ray emission (PIXE). Furthermore, ion beams are used more and more for medical diagnostics and therapy, especially for the discreation of cancer cells. These applications will be demonstrated by some examples of tissue investigations. Heavy ions and also protons are applied increasingly for tumor tissue irradiation. This so-called particle therapy is used when conventional radiotherapy reaches its limits, either for tumors that are nearly insensitive to photons or for tumors located next to high sensitive healthy tissues. This is the consequence of some physical and biological advantages of proton and heavy ion irradiation in comparison with photon irradiation. The most important physical advantage is a higher local precision allowing the administration of a higher irradiation dosage. Furthermore, heavy ion or proton radiation is biologically more effective. Here new promising developments are just in progress.

Ion–Solid Interactions

2

2.1 Fundamental Principles

Any ion beam modification of materials is the result of interactions between energetic ions and the solid by inter atomic potentials. These interactions manipulate ion ranges and range distributions in the solid, ion stopping processes and anisotropic ion distributions by channeling and collision cascades. On the other hand, these interactions are the basis for ion damage in solids by implantation, sputtering, and mixing processes. The effects caused by interactions between energetic ions and solids are not only the basis for understanding of ion beam materials processing but can also be exploited by a lot of micro- and nano-analytical techniques. Therefore, some important fundamentals of ion–solid interactions will be discussed in this chapter.

Particle scattering in matter was first described by Rutherford [1], where he enunciated his famous scattering formula (2.14). Early theoretical concepts were given by Thomson [2], Bohr [3], Born [4], and Bethe [5]. On the basis of Bohr's papers [6, 7] the theoretical understanding was promoted by computer simulation studies of Gibson [8] and later on of Eckstein [9].

First investigations of ion implantation [10], radiation damage [11], and sputtering erosion [12] were published in the 1960s of last century. Outstanding new results were given by Sigmund. This concerns ion ranges, radiation damage, and sputtering [13], and more recent books review energy loss theory [14, 15]. Sputtering and related phenomena are extensively covered in a series of books edited by Behrisch [16–19]. A broad overview on both ion–solid interaction phenomena and their applications in materials research was presented by Nastasi et al. [20, 21]. Modern aspects of ion–surface interactions involving high-energetic ions and ion-induced nanostructure formation and control are discussed in two recently collected editions by Sigmund [22, 23]. Furthermore, a modern overview on materials science with ion beams was edited by Bernas [24].

Because of the broad scale of existing publications it cannot be the purpose of the present chapter to give a description of the fundamentals of ion–solid

B. Schmidt and K. Wetzig, *Ion Beams in Materials Processing and Analysis*,
DOI 10.1007/978-3-211-99356-9_2,

interactions in detail or to derive the theoretical relationships or formulas ab initio. Rather, the task of this chapter is to compile the most important fundamentals of ion–solid interactions as assumption for the understanding of ion-induced materials modifications and of ion beam-induced materials preparation as well as of ion beam-assisted analytical techniques. These fundamental interactions include binary elastic particle collisions, ion stopping and recoil processes, ion range and range distributions, ion implantation, channeling and sputtering processes, and specimen modifications such as radiation damage, preferential sputtering, and ion mixing. The content will restrict to short-time phenomena during the slowing down phase of incident ions, whereas thermal and long-time effects, such as ion-induced diffusion and phase formation, are not the subject of this chapter.

2.2 Binary Elastic Collisions

Fast ions, bombarding a solid, will have collisions with both the electrons of the solid and also with atomic nuclei. Ion interactions with an atomic electron are purely governed by Coulomb's law. These interactions are inelastic, because they result in

- Ionization, where the electron is ejected from its atomic orbit
- Atomic excitation, where the electron is raised to an outer orbit

In both cases, the ionized/excited atom may return to its ground state, accompanied by the emission of one or more X-rays or photons, respectively.

Ion collisions with the atomic nuclei are often called "elastic," although they can be accompanied by an energy loss by generating bremsstrahlung. In the case of pure elastic scattering the ion–nucleus interaction is governed by Coulomb's force, and it results in a change of direction but no reduction of energy. Ion–nucleus collisions may also be inelastic, leading to an energy loss by generation of the mentioned bremsstrahlung or by a nucleus excitation. The possible effects of ion–solid interactions at Coulomb interaction force are summarized in Table 2.1.

To describe a nuclear or electronic ion collision under simplified assumptions one can treat it as a binary elastic interaction of two point charges, as illustrated in Fig. 2.1.

In an idealized laboratory system (LS) (Fig. 2.1a) the starting velocity of target particle 2 is assumed as zero. After the collision, the bombarding ion 1 and the target particle 2 are ejected under scattering angles Θ and Φ, respectively. As the collision does not affect the total system momentum, the kinematics can be demonstrated by a center of mass-system (CMS in Fig. 2.1b), where the two-body system is described by the kinematics of a single particle with the reduced mass μ:

$$\mu = \frac{m_1 \cdot m_2}{m_1 + m_2}, \tag{2.1}$$

Table 2.1 Effects of Coulomb ion–solid interactions

Collision partners	Interaction force	Interaction type
Ion–atomic electron	Coulomb	Ionization
Ion–atomic electron	Coulomb	Atomic excitation
Ion–atomic nucleus	Coulomb	Elastic scattering
Ion–atomic nucleus	Coulomb	Inelastic collision
Ion–atomic nucleus	Coulomb	Nucleus excitation

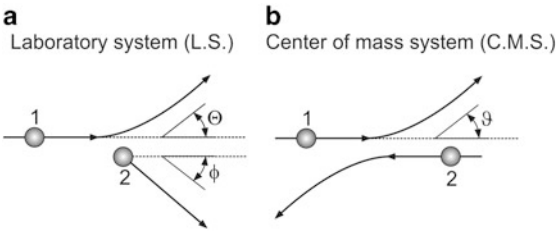

Fig. 2.1 Elastic ion-target scattering (bombarding ion 1, bombarded target particle 2). (**a**) Laboratory system (LS) and (**b**) center of mass-system (CMS)

where m_1 the mass of the bombarding ion and m_2 the mass of the bombarded target particle.

The correlation between the scattering angles Θ and Φ in the laboratory system (Fig. 2.1a) and ϑ in the CMS (Fig. 2.1b) is given by the transformation formulas:

$$\tan\Theta = \frac{\sin\vartheta}{\frac{m_1}{m_2} + \cos\vartheta}, \quad \Phi = \frac{\pi - \vartheta}{2}. \tag{2.2}$$

From these equations the scattering angle ϑ in the center of mass-system follows a reverse transformation:

$$\vartheta = \Theta + \arcsin\left(\frac{m_1}{m_2} \cdot \sin\Theta\right). \tag{2.3}$$

The energy transfer E_T from the bombarding ion (m_1, initial energy E_0) to the bombarded target particle m_2 can be described as

$$E_T = \gamma \cdot E_0 \cdot \sin^2\left(\frac{\vartheta}{2}\right) \tag{2.4}$$

with the energy transfer factor

$$\gamma = \frac{4m_1 \cdot m_2}{(m_1 + m_2)^2}. \tag{2.5}$$

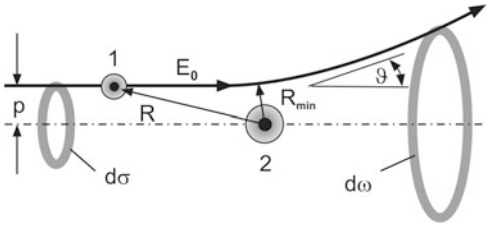

Fig. 2.2 Classical ion scattering trajectory, as for the definition of the differential scattering cross section $d\sigma/d\omega$ (after [25])

The kinetic energy E_c that remains in the CMS system follows as

$$E_c = \frac{m_2}{m_1 + m_2} \cdot E_0. \tag{2.6}$$

The residual energy E' of the bombarding ion after collision results as

$$E' = E_0 - E_T = E_0 \cdot \left(1 - \gamma \sin^2\left(\frac{\vartheta}{2}\right)\right). \tag{2.7}$$

Substituting the scattering angle ϑ by those of the laboratory system (LS) (Fig. 2.1a) one can also write

$$E' = \left(\frac{m_1}{m_1 + m_2}\right)^2 \cdot E_0 \left(\cos\Theta \pm \sqrt{\left(\frac{m_2}{m_1}\right)^2 - \sin^2\Theta}\right). \tag{2.8}$$

As follows from (2.8) for $m_1 \geq m_2$ a maximum scattering angle will exist, which cannot be exceeded.

In order to derive a formula for the differential scattering cross section $d\sigma/d\omega$, Fig. 2.2 shows the course of a classical ion scattering trajectory in the CMS system. The decrease of scattering angle with increasing impact parameter p is represented by the so-called classical trajectory integral:

$$\vartheta = \pi - 2p \int_0^{R_{min}^{-1}} \frac{d\left(\frac{1}{R}\right)}{\sqrt{1 - \frac{V(R)}{E_c} - \frac{p^2}{R^2}}} \tag{2.9}$$

for any spherically symmetric interaction potential $V(R)$ which depends on the distance R of the collision partners 1, 2. The root of the denominator determines the minimum distance of approach, R_{min}. Projectiles which enter an annulus of differential area $d\sigma$ are scattered into a differential solid angle $d\omega$, from which, at known $\vartheta(p)$ relation, the differential cross section of the scattering process is given by

$$\frac{d\sigma}{d\varpi} = \left|\frac{2\pi \cdot p \cdot dp}{2\pi \cdot \sin\vartheta \cdot d\vartheta}\right| = \frac{p}{\sin\vartheta} \cdot \frac{dp}{d\vartheta}. \tag{2.10}$$

From (2.9) and (2.10) the so-called Rutherford scattering cross section [1] can be derived under well-defined conditions. For the potential $V(R)$ we choose the Coulomb interaction potential between two charged particles (charge numbers Q_1, Q_2 and e—elementary charge):

$$V(R) = \frac{Q_1 \cdot Q_2 \cdot e^2}{4\pi \cdot \varepsilon_0 \cdot R}. \tag{2.11}$$

The evaluation of the trajectory integral (2.9) gives

$$\tan\left(\frac{\vartheta}{2}\right) = \frac{b}{2 \cdot p} \tag{2.12}$$

with the so-called collision diameter

$$b = \frac{Q_1 \cdot Q_2 \cdot e^2}{4\pi \cdot \varepsilon_0 \cdot E_c}. \tag{2.13}$$

By the combination of (2.10), (2.12), and (2.13) one yields the famous Rutherford cross-section formula [1]:

$$\left(\frac{d\sigma}{d\omega}\right)_R = \frac{1}{16} \cdot \left(\frac{Q_1 \cdot Q_2 \cdot e^2}{4\pi \cdot \varepsilon_0}\right)^2 \cdot \frac{1}{E_c^2} \cdot \frac{1}{\sin^4 \frac{\vartheta}{2}}. \tag{2.14}$$

The possibilities to increase the differential cross section can be immediately concluded from (2.14). These are

- Using projectiles of larger Z_1 and m_1
- Decreasing the initial energy E_0 of the probing particles
- Decreasing the scattering angle ϑ

The sensitivity of ion scattering experiments can be increased by different steps. As will be described in Chap. 6 especially for RBS, but also for other scattering techniques such procedures are:

- Increasing the differential cross section $d\sigma/d\omega$
- Increasing the number of bombarding particles
- Increasing the detector's solid angle
- Increasing the detector's efficiency

2.3 Ion Stopping

The interaction of impinging ions with the bombarded target consists of a series of collisions with the target atoms until ions stop as depicted in Fig. 2.3, which illustrates the Monte Carlo calculation of ion trajectories for 50 keV boron ions implanted into a Si target [26].

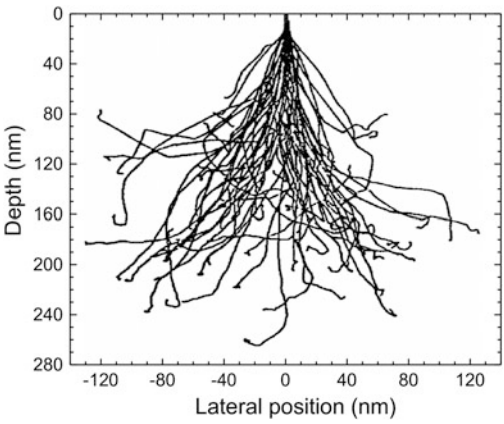

Fig. 2.3 Monte Carlo calculation of 128 trajectories for 50 keV B ions implanted into Si [26]

During ion stopping two different collision processes take place. Since the energy of the impinging ion is much higher than lattice binding energies, the latter can be neglected at simulated elastic collisions between pairs of nuclei. The energy loss by these collisions is the so-called nuclear stopping component. Furthermore, a second component of scattering comes from inelastic collisions with electrons in the target. This energy loss is called electronic stopping. The total stopping power S_{total} which is defined by the energy loss per unit length $\mathrm{d}E/\mathrm{d}x$ of the impinging ion can be written as sum of the two energy loss components:

$$S_{\text{total}} = \left(\frac{\mathrm{d}E}{\mathrm{d}x}\right)_{\text{nuclear}} + \left(\frac{\mathrm{d}E}{\mathrm{d}x}\right)_{\text{electronic}}. \tag{2.15}$$

The relative share of both terms in (2.15) for the total stopping power S_{total} can be seen in Fig. 2.4 as a function of ion velocity (proportional to the ion energy) over a wide energy range [27]. Low ion energies in the range of up to few 100 keV, typically for conventional ion implantation, are characterized by a remarkable rate of nuclear stopping. This is evident from its maximum in the left corner of region I in Fig. 2.4.

The nuclear stopping process can be described by classical kinematics. Because electrons screen the nuclear charges of the colliding atoms, the Coulomb interaction potential $V(R)$ between them [see (2.11)] must be corrected by a screening function $f_{\text{S}}(R)$:

$$V_{corr}(R) = V(R) \cdot f_{\text{S}}(R). \tag{2.16}$$

This corrected interaction potential V_{corr} allows to calculate the scattering angle ϑ for any incident ion trajectory. In the center of mass-system the connection between the energy transfer E_{T} and the scattering angle is given by (2.4), using (2.5):

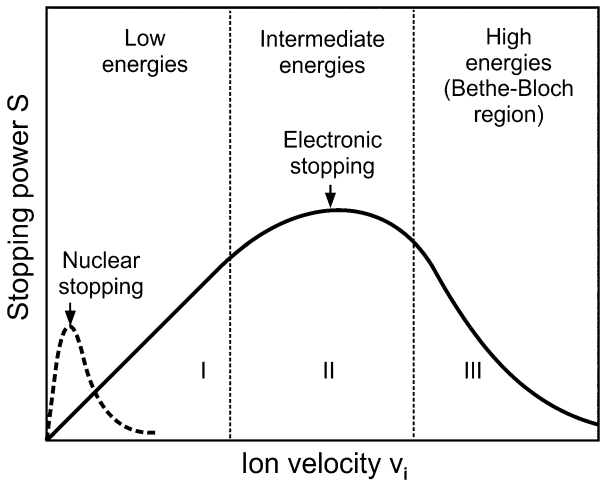

Fig. 2.4 Nuclear and electronic components of the ion stopping power S as a function of ion velocity [27]

$$\mathrm{E_T} = \frac{4m_1 \cdot m_2}{(m_1 + m_2)^2} \cdot E_0 \cdot \sin^2 \frac{\vartheta}{2}. \tag{2.17}$$

The rate of energy transfer to nuclear collisions per unit path length can be calculated. For this purpose the energy transfers multiplied by the collision probability must be added. For the known maximum possible energy transfer $E_{\mathrm{T,\,max}}$ the nuclear stopping power S_n follows immediately:

$$S_\mathrm{n} = \left(\frac{\mathrm{d}E}{\mathrm{d}x}\right)_{nuclear} = N \cdot \int_0^{E_{\mathrm{T,max}}} E_\mathrm{T} \mathrm{d}\sigma \tag{2.18}$$

with N the number of target atoms per unit volume, and $\mathrm{d}\sigma$ the differential cross section.

By the energy transfer from the bombarding ion to the target atom the latter one may be displaced from its atomic place, creating a damage or defect site (e.g., interstitial atom in crystalline lattice).

Electronic stopping is caused by the interaction between the incoming ion and the electrons in the target. The theoretical models are quite complex, but in the low energy regime, the stopping is similar to a viscous drag force and is proportional to the ion velocity. Electronic stopping is inelastic. The energy loss by incident ions is dissipated through the electron cloud into thermal vibrations of the target atoms.

At higher ion velocities (or intermediate ion energies, region II in Fig. 2.4) the charge state of the ion increases, and it becomes, for example, fully stripped of all its electrons at velocities $v \geq v_\mathrm{o} \cdot {Z_1}^{2/3}$. There, the ion is moving with a velocity exceeding the mean orbital velocity of electron in the target atom shells. Thus, the ion–target interaction results in electronic stopping and it can be described by

Bohr's theory of stopping power, based on classical considerations [3]. The energy loss of incoming ions was given by Nastasi et al. [20] in 1996:

$$S_e = \left(\frac{dE}{dx}\right)_{\text{electronic}} = \frac{2\pi \cdot Z_1^2 \cdot e^4}{E_0} \cdot N \cdot Z_2 \cdot \left(\frac{m_1}{m_2}\right) \cdot \ln\frac{2m_e \cdot v_2}{I} \tag{2.19}$$

with m_1—ion mass, m_2—target atom mass, m_e—mass of a target-atom electron, Z_1—atomic number of the ion, Z_2—atomic number of the stopping target atom, and I—average excitation energy. For most elements, the average excitation energy (in eV) can be roughly approximated by $I \approx 10{\cdot}Z_2$. The calculation of S_e using (2.19) gives values to within 10 % of the experimental values.

A well-known model of electronic stopping in the velocity-proportional region is given by the so-called LSS-theory, which is named after Lindhard, Scharff, and Schiott [28] and can be obtained from the earlier model of Firsov [29]. The primary difference between the two models exists in different interatomic potentials [30]. The LSS theory describes the interaction of ions with amorphous solids, where no channeling effects, no diffusion, and no defect interactions are considered. Thus, the interaction is mainly based on elastic collisions with nuclei and inelastic collisions with electrons.

For calculations, the LSS electronic stopping power S_e can be expressed by the following equation:

$$S_e(E) = 3.83 \cdot \frac{Z_1^{7/6} \cdot Z_2}{\left(Z_1^{2/3} + Z_2^{2/3}\right)^{3/2}} \cdot \left(\frac{E_0}{m_1}\right)^{1/2} = K_L \cdot {E_0}^{1/2}, \tag{2.20}$$

where

$$K_L = 3.83 \cdot \frac{Z_1^{7/6} \cdot Z_2}{m_1^{1/2}\left(Z_1^{2/3} + Z_2^{2/3}\right)^{3/2}}. \tag{2.21}$$

$S_e(E)$ will be given in units of 10^{-15} eV cm^2 atom^{-1} for ion energies E_0 given in keV and m_1 given in atomic mass units. Both, nuclear and electronic stoppings are statistically independent processes and the total stopping power S_{total} is the sum of both terms [see (2.15)].

As an example Fig. 2.5 shows both the electronic and nuclear stoppings for As, P, and B ions, impinging in a Si substrate with different energies E_0 [31]. The critical energy E_C when the nuclear and the electronic stopping powers are equal differs from one element to another: E_C(B) $\approx$ 17 keV, E_C(P) $\approx$ 150 keV, E_C(As) $>$ 500 keV. In general, the portion of electronic stopping grows with increasing ion energy.

At extremely high ion velocities (or ion energies) in region III (Bethe-Bloch region) of Fig. 2.4, the electronic stopping power decreases again with increasing ion velocity because of shorter ion interaction time in the vicinity of the target

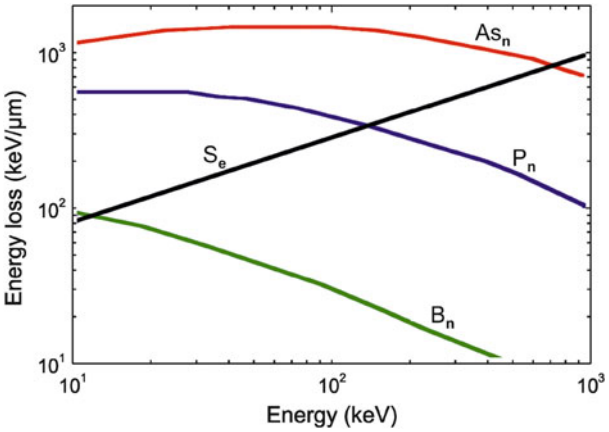

Fig. 2.5 Electronic stopping power S_e and nuclear stopping powers S_n for As ions (As_n), P ions (P_n) and B ions (B_n), impinging in a Si target [31]

atoms. In the case of As ions impinging in Si this is valid for energies $>10^5$ keV [28]. In this high energy range, the so-called fast collision regime, the values of S_e are proportional to $(Z_1/v)^2$.

2.4 Ion Channeling

Ion stopping phenomena were discussed in the previous section under the assumption of an amorphous target, where atoms are randomly arranged in the target material. However, in many cases targets possess a crystalline structure. In this case, long-range open spaces exist through which the ions can fly without significant scattering. Ions can be steered to these open channels by glancing collisions with the atom rows or planes, hereby extending the final ion distribution deeper into the target. This effect is called ion channeling and was predicted by Stark [32]. After first corresponding experimental evidence in the early 1960s [33, 34], Lindhard [35] and Morgan [36] formulated a theoretical basis of ion channeling. A good overview is also given in the book of Feldman et al. [37] and, more recently, in the famous book of Nastasi [38].

As an example Fig. 2.6 shows range distributions for channeled 100 keV As ions implanted along the <100> axis of crystalline Si target [38]. The dashed line shows the Gaussian distributions for incident ions aligned away from any channeling direction. As evident from the figure, the channeled implantation along crystal axes leads to a much deeper ion penetration, several times the projected range R_P.

The channeling effect can be demonstrated by a computer simulation of ion trajectories, given by Robinson (Fig. 2.7) [39]. An ion (atomic number Z_1) which is directed at a small angle Ψ to close-packed rows or planes of atoms in a crystal

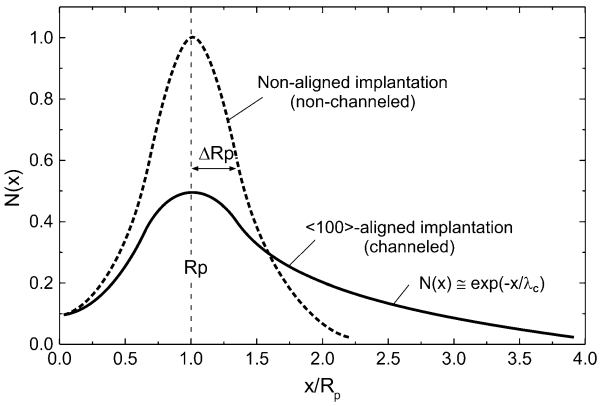

Fig. 2.6 Range distributions for channeled As (100 keV) ions implanted along the <100> Si axis (*dashed line*: non-channeled ions) [38]

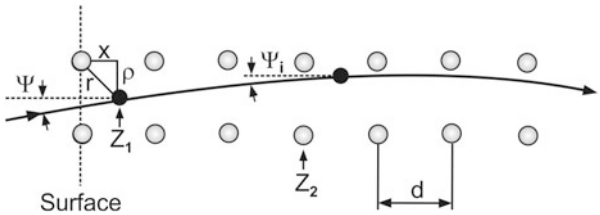

Fig. 2.7 Schematic presentation of channeled ion trajectories [39]

(atomic number Z_2) is steered by a series of gentle collisions with the atoms so that it is channeled into the regions between these rows or planes. The channeling effect is easily understood as a correlated series of elastic two-body collisions. This classical collision model is only valid under the following assumptions:

- Small scattering angles
- Strongly correlated collisions
- Elastic two-body collisions
- Perfect crystal

After Lindhard [30, 35] the ions move in a transverse potential:

$$V_{\mathrm{T}}(\rho) = \frac{1}{d} \cdot \int V[(\rho^2 + x^2)^{1/2}]\mathrm{d}x \tag{2.22}$$

with ρ the distance ion-string of atoms, x the distance traveled along the string, and d the atom distance.

The two-body potential $V(r)$ is generally taken to have the Thomas–Fermi form:

$$V(r) = \left(\frac{Z_1 \cdot Z_2 \cdot e^2}{r}\right) \cdot \varphi\left(\frac{r}{a}\right), \tag{2.23}$$

where Z_1 and Z_2 are the atomic numbers of the ion and the target atom in the string, respectively, e is the electronic charge, r is the nuclear separation distance, φ is the Thomas–Fermi screening function, and a is the screening distance.

The condition for ion channeling is fulfilled, if the ion incidence angle ψ relative to the crystal orientation is smaller than a critical angle ψ_{crit}, which is defined as the maximum angle of incident ions to a channel between rows of atoms (axial channeling) or planes of atoms (planar channeling) so that the ion remains in a channel trajectory. For axial channeling the critical angle ψ_{crit} is expressed by the following equation [35]:

$$\psi_{\text{crit}} = k \cdot \sqrt{\frac{Z_1 \cdot Z_2 \cdot e^2}{E_0 \cdot d}} = 9.71 \cdot \sqrt{\frac{Z_1 \cdot Z_2}{E_0 \cdot d}}, \tag{2.24}$$

where Z_1 and Z_2 are the atomic numbers of incident ions and the target atoms, respectively. E_0 is the energy for the incident ion and d is the distance between successive atoms along the channel wall. The approximate constant k amounts to 9.71 of the ion energy, given in keV, and the distance d, given in Å [40]. The critical angle ψ_{crit} is in the order of 7° and can be used to estimate roughly whether the implanted ion is preferentially channeled or not. Equation (2.24) reveals that channeling is more likely for heavier ions (higher Z_1) and lower energies E_0.

Planar channeling means that energetic ions, moving in a solid are steered by planes of lattice atoms. For planar channeling the critical angle is expressed by

$$\Psi_{\text{p}} = \sqrt{\frac{\pi \cdot Z_i \cdot Z_t \cdot e^2 \cdot N \cdot d_{\text{p}} \cdot C \cdot a_{\text{TF}}}{E_0}}, \tag{2.25}$$

where N is the atomic number density, d_{p} the planar spacing, a_{TF} the Thomas–Fermi screening parameter, and $C \approx (3)^{0.5}$ the Lindhard constant [35, 41, 42].

The most widely adopted procedure for minimizing channeling, for example in silicon, is the tilt of the crystal surface relative to the incident ion beam direction commonly by 7° so that the lattice appears as a dense orientation of the Si crystal. Nevertheless, at 7° tilt the Si atoms aligned in a highly symmetric array of planes and the planar channeling can still produce channeling effects. Therefore, the crystals must also be oriented with an appropriate azimuthal (or rotation) direction, in addition to the selected tilt angle. As shown in Fig. 2.8, for example for <100>-oriented Si, the tilt of crystal around the <110>-axis by 7° prevents only the axial channeling component (Fig. 2.8b) and planar channels are still open for incident ions. Only an additional azimuthal rotation of the tilted crystal around the <100>-axis by 20–30° (Fig. 2.8c) closes the planar channels and the channeling of ions will be effectively suppressed.

Selected examples of as-implanted depth distributions in dependence on the tilt angle and the rotation degree are shown in Fig. 2.9 for the implantation of 35 keV B^+ ions with a fluence of 5×10^{14} cm^{-2} into <100>-oriented silicon. Figure 2.9a

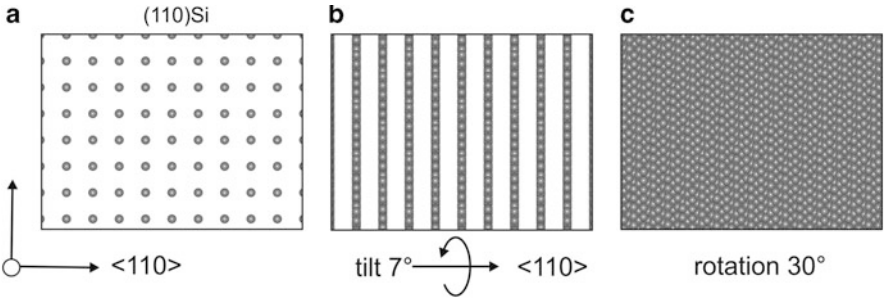

Fig. 2.8 Perpendicular and parallel view onto the (100)-surface of a silicon crystal in ion beam direction (**a**), the crystal tilted by 7° (**b**) and additionally rotated by 30° around the surface normal (**c**)

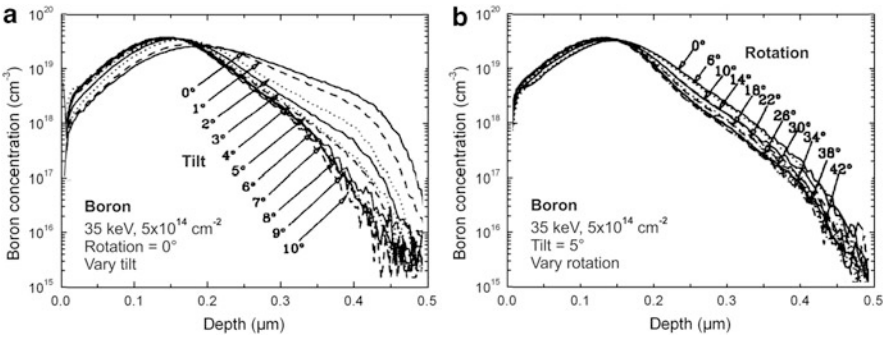

Fig. 2.9 As-implanted boron depth distribution implanted with 35 keV, 5×10^{14} cm^{-2} into <100>-oriented silicon measured by SIMS: (**a**) varying tilt angles and fixed rotation angle at 0°, (**b**) varying rotation angles and fixed tilt angle at 5° [43]

demonstrates that the axial channeling of boron is minimized at tilt angles of (7–10)° and further increase of the angle does not change the profile. The dependence of the planar channeling on the rotation angle at a given tilt angle is less pronounced compared to the axial channeling as shown in Fig. 2.9b, and rotation angles above 30° do not change the channeled part of the profile [43].

Channeling effects are successfully simulated in a highly accurate manner by using, for example, the dual Pearson model [44] and the Crystal-TRIM code [45].

Figure 2.10 shows the ion back-scattering yield around a channeling direction. The yield is minimum when the ion beam is well aligned with a channel ($\psi_{ion} < \psi_{crit}$). In order to preclude disturbing channeling, the wafers in semiconductor processing are normally tilted by about 7° to avoid the major crystal channels. But in practice this is only of restricted viability. The channeled impurity profile is sensitive to changes in the order of 1° of the wafer tilt and beam divergence, and ions are scattered by amorphous surface films and residual damage from previous processing steps.

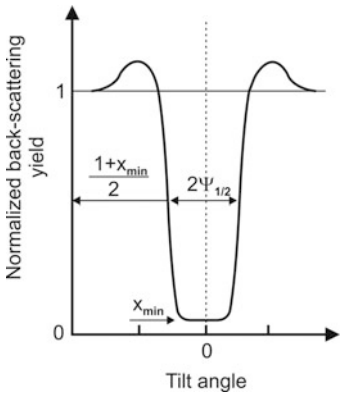

Fig. 2.10 Ion back-scattering yield around a channeling direction [26]

As an example for another silicon crystal orientation, Fig. 2.11 shows electrically active 300 keV As depth distributions in Si as a function of the beam angle, tilted against [111] direction of the (111)-oriented Si crystal. The usual 7° tilt, here named "random equivalent," still shows again significant differences from a Gaussian profile.

For perfect crystals at low temperatures the ratio χ of the back-scattering yield for ions incident with $\psi_{\text{ion}} < \psi_{\text{crit}}$ to that for a randomly oriented crystal is in the order of 0.01. Thermal vibrations and impurity atoms can lead to a degradation process. If 50 % of the impurity atoms are placed in the channel, χ will grow up to ≈ 0.5, and if the impurity atoms are placed near the center of the channel even a peak of χ may exist at $\psi_{\text{ion}} = 0°$. The influence of crystal defects on ion scattering in a crystal is schematically illustrated in Fig. 2.12. There χ is the measure for the backscattering yield. For a nearly perfect crystal (A) χ is very low. In the case of dechanneling by point defects (B) the change of χ with the depth is proportional to the concentration of displaced host atoms. If a near-surface layer of the crystal is completely disordered (amorphized), χ becomes equal to unity. Since ions lose energy as they penetrate into the crystal, the energy increment over which $\chi = 1$ corresponds to the thickness of the amorphous region.

Ion channeling includes different problems when using ions for materials processing and analytics. The most important problems are:

(a) Deviation from normal implanted profiles
(b) Quantification of target damage
(c) Determination of depth of analysis
(d) Determination of scattering cross sections

To overcome these problems, for example during ion beam analysis, following actions can be implemented:

(a) Minimizing of target damage can be realized by
- Increasing the detector solid angle
- Analyzing only near channeling directions
- Moving the analyzing spot

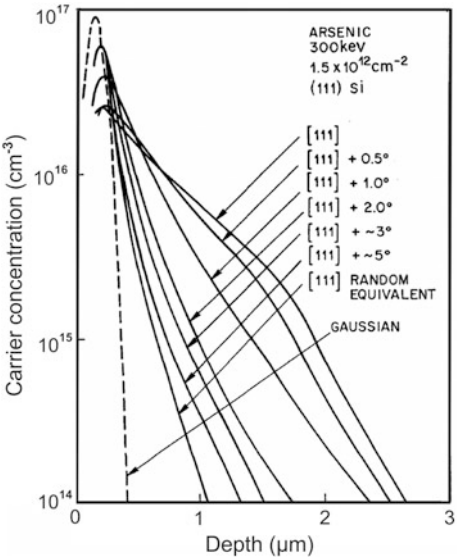

Fig. 2.11 Electrically active As depth distributions in Si as a function of beam angle relative to the wafer surface normal [26]. The "random equivalent" case is the usual 7° tilt to avoid channeling, but still shows significant differences from a Gaussian profile

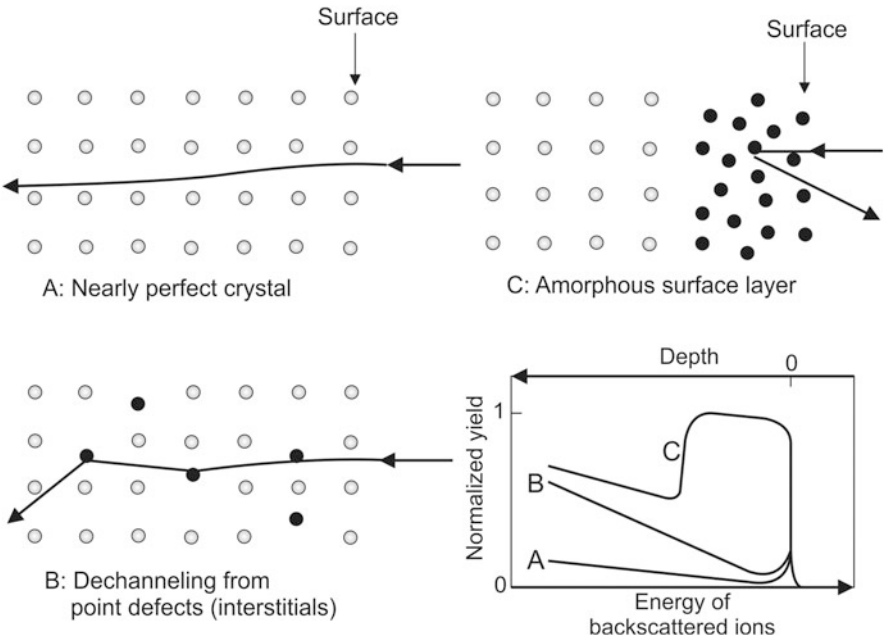

Fig. 2.12 The influence of crystal defects on ion scattering

- Using high energy and low mass ions
  Because ion channeling is a relatively well-established method to measure lattice damage of the target (minimum detectable impurity atomic fraction 10^{-3}–10^{-4}) it must be compared with other analytical methods, e.g., transmission electron microscopy. That is why we must take into consideration the following facts:

(b) Depth of analysis:
- The stopping powers of a channeling and a randomly directed ion beam are assumed to be equal (so-called Aarhus convention)
- For lattice location of impurities the channeling yields of both host and impurity atoms are compared

(c) Determination of scattering cross sections:
- Frequently only normalized yields rather than absolute yields can be used
- For heavier ions standards are required

As a rule, these procedures allow a quantitative or at least semiquantitative valuation of ion channeling effects.

2.5 Ion Induced Target Modifications

2.5.1 Ion Implantation

Ion implantation is a low-temperature technique for the introduction of dopants into targets, especially into semiconductors. Actually, it is the most important doping process in Si planar technology because it offers more flexibility than atomic diffusion. For instance in MOS transistors ion implantation allows to adjust precisely the threshold voltage. Further advantages are short process times, excellent fluence homogeneity over large waver areas, the fabrication of very small device structures, dopant mass separation during implantation and adjustable doping profile by multiple implantation. This is not possible by diffusion techniques.

In ion implantation, dopant atoms are volatilized, ionized, accelerated, separated by mass-to-charge ratios, and directed at a target that is typically a Si substrate or another semiconductor. The atoms collide with the host atoms, lose energy, and rest at a penetration depth, determined by the dopant, the substrate material, and the ion energy. The implantation parameters vary in a wide range:

- Energy ranges from 100 eV to some MeV
- Penetration depth from <10 nm to 10 μm
- Fluence range from 10^{11} to 10^{18} cm^{-2}

The ion implantation technique bases essentially on a patent of Shockley and Noice pended in 1957 [46] and on theoretical investigations of Lindhard et al. [28]. For the last 40 years ion implantation became the key technology for the production of ultra-large-scale integrated (ULSI) circuits as Si processors and memory devices. Present activities for further technical development in semiconductor integrated circuit technology concern new annealing techniques after ion implantation for

removing of ion-induced crystal damage and implanted dopant activation [47, 48] as well as the application of laser doping.

In the frame of this chapter only some important fundamentals shall be compiled. Each implanted ion traverses a random path as it penetrates the target, losing energy by nuclear and electronic stopping, $S_n(E)$ and $S_e(E)$, respectively, as discussed in Sect. 2.3. Since implantation fluences are usually higher than 10^{11} cm^{-2} ion trajectories are predicted employing statistical means.

The range R of an ion with the initial energy E_o in the target material can be determined from the stopping powers $S_n(E)$ and $S_e(E)$:

$$R = \frac{1}{N} \int_0^{E_0} \frac{\mathrm{d}E}{S_n(E) + S_e(E)} \tag{2.26}$$

with N the concentration of the implanted ions.

The average depth of the implanted ions is called the projected range R_p (projection of R on direction of ion incidence) and the distribution of the implanted ions about the depth x can be approximated by a Gaussian profile with a standard deviation ΔR_p roughly determining the thickness of the implanted layer. For a given ion implantation fluence Φ the Gaussian profile describing the range distribution of the implanted ions $N(x)$, also called dopant concentration profile, can be written as

$$N(x) = N_{max} \cdot \exp - \left[\frac{(x - R_p)^2}{2 \cdot \Delta R_p^2} \right], \tag{2.27}$$

where the maximum of the concentration profile at $x = R_p$ is given by

$$N_{max} = \frac{\Phi}{\sqrt{2\pi} \cdot \Delta R_p} = \frac{0.4 \cdot \Phi}{\Delta R_p}. \tag{2.28}$$

The projected ion straggling ΔR_p can be approximated in terms of the projected range R_p and the masses of implanted ions m_1 and target atoms m_2 by the following expression after Lindhard and Scharff [49]:

$$\Delta R_p \cong \frac{2 \cdot R_p}{3} \cdot \left[\frac{\sqrt{m_1 \cdot m_2}}{m_1 + m_2} \right]. \tag{2.29}$$

Typical depth concentration profiles for B and As ion implantations in Si with 10^{15} cm^{-2} fluences and different initial energies are depicted as examples in Fig. 2.13 [50]. These profiles can be well described by a Gaussian distribution.

In spite of the advantages discussed above ion implantation is also connected with some disadvantages. To these belong:

- Deviation from Gaussian profile by additional disturbing effects (defect-enhanced diffusion, channeling)

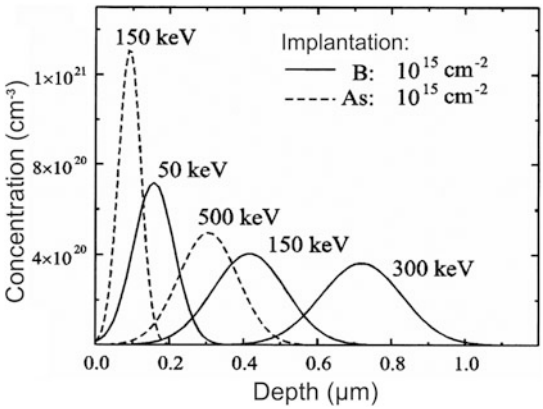

Fig. 2.13 Theoretical Gaussian depth-concentration profiles for B and As ion implantation in Si with fluences of 10^{15} cm^{-2} (see e.g. [50])

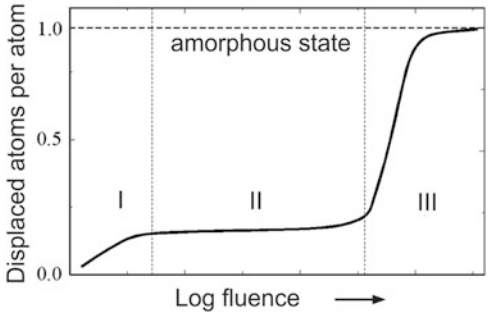

Fig. 2.14 Number of displaced atoms per target atom in dependence on the ion fluence [51, 52]

- Formation of irradiation damage up to amorphization
- Subsequent annealing necessary for ion induced crystal damage removal
- Ion implantation only possible for near-surface regions

The reason for irradiation damage buildup is the development of crystal defects by target atoms displaced from their lattice sites leading to interstitial atoms and vacancies in the crystal lattice. This is illustrated in Fig. 2.14, which shows the number of displaced atoms per target atom in dependence on the ion fluence [51, 52]. There is a coexistence of crystalline and amorphous phases, the relative fraction of which changes with the implantation fluence. In the weak damage range I the defect density increases continuously with growing implantation fluence. In the medium damage range II the implantation temperature-dependent plateau exists, characterized by an equilibrium between defect generation and annihilation. At low implantation temperature (e.g., for cooled samples) the defect recombination only plays a minor role. Further increasing of the implantation fluence causes an enhanced defect accumulation and a collapse-like target amorphization will take place (region III).

Table 2.2 Surface-sensitive material properties influenced by ion implantation

Mechanical	Chemical	Optical/electronic
Adhesion, lubrication, friction	Electrochemistry	Refractive index
Hardening, wear fatigue	Catalysis, oxidation resistance	Magnetic properties, reflectance

Ion implantation also modifies surface-sensitive material properties introducing impurities and structural changes in the host matrix. This can induce disturbing effect, but in most cases ion implantation or irradiation is used as means of beneficially modifying the mechanical, chemical, or also the optical, magnetic, and electronic properties of materials. Table 2.2 summarizes some research fields for the application of ion beam modified material surfaces (after [20]).

2.5.2 Ion Mixing

In an inhomogeneous multicomponent substrate, the relocation of atoms due to ion knock-on and ion collision cascades results in "mixing" of the atoms. This can be an intermixing or also alloying of its sample constituents. Prototypes of such inhomogeneous materials are thin marker layers of atoms A in an otherwise homogeneous material B, which is broadened under ion irradiation, or a stack of two homogeneous layers of different materials A and B, the interface of which becomes blurred under ion irradiation. Ion mixing was first investigated by Van der Weg et al. [53]. More recently some review articles were published by Cheng [54], Nastasi and Mayer [55], and Bolse [56].

The relocation of the marker is characterized by the relocation cross section $\mathrm{d}\sigma(x, y)$ describing the displacement z of a marker atom (at original depth x) along the depth axis. Under ion irradiation with a fluence Φ ion mixing can be described as a multiple relocation process with mean displacement $\overline{\Delta z}$:

$$\overline{\Delta z} = \Phi \int_z z \cdot \mathrm{d}\sigma(x, z). \tag{2.30}$$

This is valid for small relocations where the cross section $\mathrm{d}\sigma(x, z)$ remains constant. The variance of the relocation distribution can be expressed by the standard deviation Ω_m:

$$\Omega_m^2 = (\Delta z - \overline{\Delta z})^2 = \Phi \int_z z^2 \mathrm{d}\sigma(x, z). \tag{2.31}$$

With (2.30) and (2.31) a Gaussian marker distribution around Δz with a standard deviation Ω_m can be described in first order.

Collisional ion mixing is a more complicated process which can be described by three mechanisms in a marker system (Fig. 2.15):

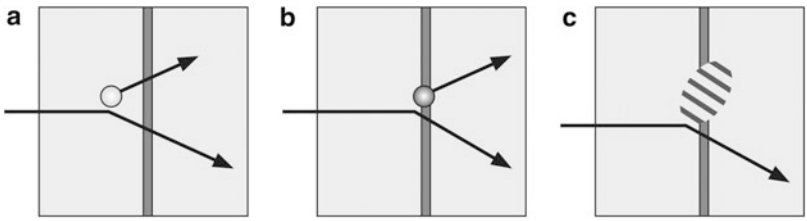

Fig. 2.15 Mechanisms of ion mixing in a marker system: (**a**) matrix relocation, (**b**) marker relocation, (**c**) cascade mixing of the marker

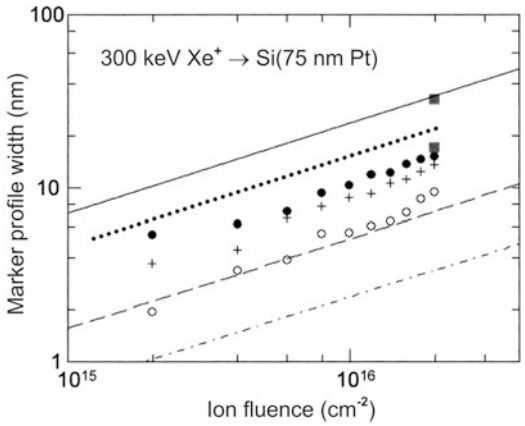

Fig. 2.16 Theoretical predictions, computer simulation data and experimental results for ion mixing of a thin Pt marker in Si by 300 keV Xe^+ irradiation [25, 57, 58]

(a) Matrix relocation by ion collision with matrix atoms into or beyond the marker, resulting in marker broadening and a shift towards the surface
(b) Marker relocation by ion collision with marker atoms, contributing to profile broadening and a shift towards the bulk
(c) Cascade mixing, where collision cascades generate by large energy transfers to marker atoms and the marker is broadened

These mechanisms occur simultaneously, interacting in a complicated way.

Figure 2.16 shows an example of ion mixing of a thin Pt marker in Si by 300 keV Xe^+ ions. Theoretical predictions, computer simulations, and experimental results are reproduced. The thin lines display results from linear cascade theory [57] for multiple matrix relocation (solid line), multiple marker relocation (dashed line), and cascade mixing (dashed-dotted line, half-width-at-half-maximum (HWHM) data).

For the latter, a relocation threshold energy of 7.83 eV and an associated mean projected range of 0.3 nm have been assumed. The small symbols show HWHM results from a TRIDYN computer simulation with relocation threshold energies of 4 eV (full dots), 8 eV (crosses), and 25 eV (open dots). Squares are from different

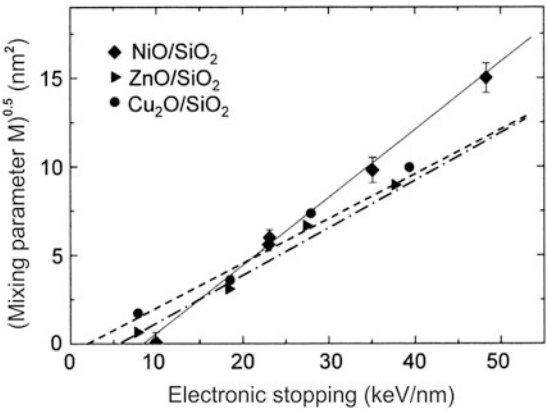

Fig. 2.17 Mixing parameter M in dependence on the electronic stopping S_e in three different top oxide layers on SiO_2 (linear fits with the corresponding threshold values of S_e) [62]

experimental HWHM data. The dotted line represents a fit through experimental data obtained at a marker depth of 50 nm [58]. The experimental data give best accordance with the course of the solid line. That means the linear cascade theory for multiple matrix relocation reflects the reality with good approximation.

Ion mixing of bilayer systems with different atomic masses will show additional effect (especially in the case of very high energy ions of tens or hundreds of MeV energy, see region III in Fig. 2.4), attributed to chemical atom interactions in the collision cascade [54, 55]. This interaction can be described by the enthalpy of mixing ΔH_{mix}, which is a measure for compound formation from its constituents. The cohesive energy ΔH_{coh} of the compound represents the average sublimation energy of the compound. The mixing parameter in a bilayer system is given by a semi-empirical formula of Johnson et al. [59]:

$$M = K_1 \cdot n^{-5/3} \cdot \left(\frac{S_n(\bar{E})}{\Delta H_{coh}} \right)^2 \cdot \left(1 + K_2 \cdot \frac{\Delta H_{mix}}{\Delta H_{coh}} \right), \tag{2.32}$$

where n is the average atomic density of the bilayer system and K_1, K_2 are universally valid constants ($K_1 = 0.0037$ nm, $K_2 = 27$).

Ion mixing in bilayer or trilayer systems can lead to so-called low-energy elastic thermal spikes in which transient diffusion results in atomic transport. This allows the formation of molten tracks in a multilayer system, and the effect was investigated in detail by Leguay et al. [60] and Wang et al. [61].

The formation of molten tracks as a result of ion mixing was also found for covalent and ionic compounds [62]. As an example Fig. 2.17 shows the critical determination of the mixing process by electronic stopping power S_e. Stopping takes place in the different top oxide layers on the SiO_2 backing which is more easily liquified. As expected, the mixing parameter M scales quadratically with the stopping power S_e above a characteristic threshold associated with the formation of molten tracks [25, 62].

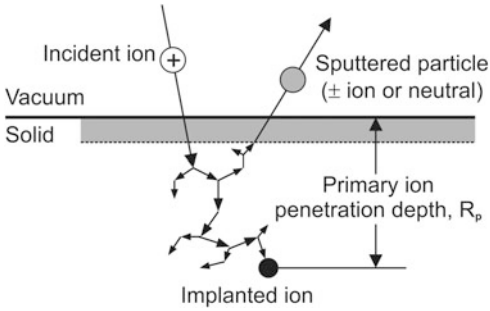

Fig. 2.18 Schematic presentation of ion sputtering process in the linear cascade regime

2.5.3 Ion Sputtering

Ion sputtering is the erosion of a sample surface under energetic ion bombardment. In this process surface atoms are removed either by primary or by secondary collisions of the incoming ions or the recoiled atoms with the target atoms in near-surface regions of a solid, respectively. If a collision cascade of primary ions intersects the surface, sufficient energy can be transferred to a near-surface atom to overcome its binding energy to the surface. So it can be ejected from the surface as a sputtered ion or neutral. A schematic presentation of this sputter process in the linear cascade regime is given in Fig. 2.18.

As the ion sputtering process will be detailed discussed in Chap. 5, here only the most important facts shall be briefly mentioned. The sputtering yield Y is defined as the mean number of emitted target atoms per incident ion:

$$Y = \frac{j_{\mathrm{sp}}}{j_{\mathrm{i}}}, \tag{2.33}$$

where j_{i}, j_{sp} are the fluxes of incident and sputtered particles, respectively. The sputtering yield typically lies in the range between 1 and 10, and it depends upon a lot of physical parameters, such as

- Ion mass number
- Ion energy
- Ion beam direction
- Target atom mass number
- Chemical reactivity between primary ions and target atoms

For more details the reader is referred to Chap. 5. An extensive list of sputtering yields was published by Matsunami et al. [63] and later on by Nastasi and Mayer [20, 21]. Yields can also be calculated using SRIM Monte Carlo Simulations [64]. For single-element materials the energy dependence of sputtering yield $Y(E)$ can be predicted by theory. As an example Fig. 2.19 shows the ion energy dependence of the sputter yield $Y(E)$ for Ar sputtering of Si. The solid line representing

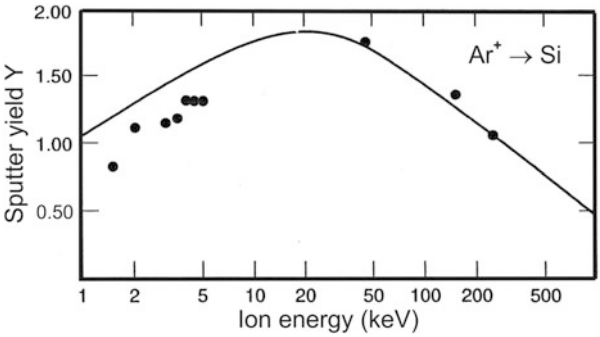

Fig. 2.19 Energy dependence of the Ar^+ ion induced sputtering yield of Si. *Solid line* represents calculations of Sigmund [57], data points are experimental results [65]

calculations of Sigmund and Gras–Marti [57] and the data points after experiments of Andersen and Bay [65] are in good agreement.

The course of $Y(E)$ can be understood under the assumption that the yield is proportional to the number of displaced or recoil atoms. Furthermore, for medium mass ions as Ar—the number of recoils is proportional to the energy deposited per unit depth by the nuclear energy loss:

$$Y = \Lambda \cdot F_D(E) \tag{2.34}$$

with Λ the materials factor, $F_D(E)$ the energy deposited per unit length at the surface. $F_D(E)$ can be expressed as

$$F_D(E) = \alpha \cdot N \cdot S_n(E) \tag{2.35}$$

with N the atomic density of target atoms, $S_n(E)$ the nuclear stopping cross section and α the correction factor.

From (2.34) and (2.35) follows a proportionality between yield and nuclear stopping cross section: $Y \sim S_n(E)$. Furthermore, $S_n(E)$ is proportional to the screening function $S_n(\varepsilon)$ after Ziegler et al. [64] showing the same typical energy dependence as $Y(E)$ does in Fig. 2.19.

More complicated ion sputtering conditions exist for polycrystalline and/or multi component target systems where phenomena as selective sputtering and preferential sputtering may occur. These effects rely on different sputtering yields for different incidence angles and for different atomic species in the target. These effects will be discussed in more detail in Chap. 5.

References

1. Rutherford E (1911) The scattering of alpha and beta particles by matter and the structure of the atom. Philos Mag 21:669–688
2. Thomson JJ (1912) Ionisation by moving electrified particles. Philos Mag 23:449–457

3. Bohr N (1913) On the theory of the decrease of velocity of moving electrified particles on passing through matter. Philos Mag 25:10–31
4. Born M (1926) Quantum mechanics in impact processes. Z Phys 38:803–840
5. Bethe H (1930) The theory of the passage of rapid neutron radiation through matter. Ann Phys 5:325–400
6. Bohr N (1941) Velocity-range relation for fission fragments. Phys Rev 59:270–275
7. Bohr N (1948) The penetration of atomic particles through matter. Mat Fys Medd 18:8f
8. Gibson JB et al (1960) Dynamics of radiation damage. Phys Rev 120:1229–1253
9. Eckstein W (1991) Computer simulation of ion-solid interactions, vol 10, Springer series in materials science. Springer, Berlin
10. Carter G, Grant WA (1976) Ion implantation of semiconductors. Arnold, London
11. Thompson MW (1969) Defects and radiation damage in metals. Cambridge University Press, Cambridge
12. Sigmund P (1969) Theory of sputtering, part I. Phys Rev 184:383–416
13. Sigmund P (1972) Collision theory of displacement damage, ion ranges and sputtering I, II, III. Rev Roum Phys 17:823–870, 969–1000, 1079–1106
14. Sigmund P (2004) Stopping of heavy ions: a theoretical approach, vol 204, Springer tracts in modern physics. Springer, Berlin
15. Sigmund P (2006) Particle penetration and radiation effects, vol 151, Springer series in solid-state sciences. Springer, Berlin
16. Behrisch R (ed) (1981) Physical sputtering of single-element solids, vol 1, Sputtering by particle bombardment. Springer, Berlin
17. Behrisch R (ed) (1983) Sputtering of alloys and compounds, electron and neutron sputtering, surface topography, vol 2, Sputtering by particle bombardment. Springer, Berlin
18. Behrisch R (ed) (1991) Characteristics of sputtered particles, technical applications, vol 3, Sputtering by particle bombardment. Springer, Berlin
19. Behrisch R, Eckstein W (eds) (2007) Sputtering by particle bombardment, vol 110, Topics in applied physics. Springer, Berlin
20. Nastasi M, Mayer JW, Hirvonen JK (2004) Ion solid interactions: fundamentals and applications, Cambridge solid state science series. Cambridge University Press, Cambridge
21. Nastasi M, Mayer JW (2007) Ion implantation and synthesis of materials. Springer, Berlin
22. Sigmund P (2006) Ion beam science: solved and unsolved problems, part 1. Mat Fys Medd 52:1–755
23. Sigmund P (2006) Ion beam science: solved and unsolved problems, part 2. Mat Fys Medd 52:756f
24. Bernas H (ed) (2010) Materials science with ion beams, vol 116, Topics in applied physics. Springer, Berlin
25. Moeller W (2004) Fundamentals of ion-surface interaction. Lecture Script, TU Dresden
26. Zeng X (1998) Ion implantation. City University of Hong Kong, Kowloon
27. Götz K, Gärtner K (1988) High energy ion beam analysis of solids. Akademie Verlag, Berlin
28. Lindhard J, Scharff M, Schiott HE (1963) Range concepts and heavy ion ranges. Mat Fys Medd 33(14):1–42
29. Firsov OB (1959) A qualitative interpretation of the mean electron excitation energy in atomic collisions. Sov Phys JETP 36:1076–1080
30. Lindhard J, Nielsen V, Scharff M (1968) Approximation method in classical scattering by screened Coulomb fields. Mat Fys Medd 36:1–32
31. Proceedings of Conference EE 212 (2000) Ion implantation. Dunham, Washington
32. Stark J (1912) Prinzipien der Atomdynamik. S. Hirzel, Leipzig
33. Piercy GR et al (1963) Experimental evidence for increase of heavy ion ranges. Phys Rev Lett 10:399–400
34. Lutz H, Sizmann R (1963) Super ranges of fast ions in copper single crystals. Phys Lett 5:113–114

35. Lindhard J (1965) Influence of crystal lattice on motion of energetic charged particles. Mat Fys Medd 34:1f
36. Morgan DV (1973) Channeling: theory, observation and applications. Wiley, London
37. Feldman LC, Mayer JW, Picraux ST (1982) Materials analysis by ion channeling. Academic, New York
38. Nastasi M (2012) Ion beam analysis: fundamentals and applications. Tailor & Francis, London
39. Robinson MT, Oen OS (1963) The channeling of energetic atoms in crystal lattices. Appl Phys Lett 2:30–32
40. Ziegler JF, Biersack JP, Littmark U (1985) The stopping and range of ions in solids. Pergamon, New York
41. Picraux ST, Andersen JU (1969) Measurements and calculations of critical angles for planar channeling. Phys Rev 186:267–272
42. Roosendaal HE, Kool WH, van der Weg WF et al (1974) Critical angles and minimum yields for planar channelling. Radiat Eff 22:89–99
43. Park C, Klein KM, Tasch AF et al (1991) Critical angles for channeling of boron ions implanted into single-crystal silicon. J Electrochem Soc 138:2107–2215
44. Klein KM, Park C, Tasch AF et al (1991) Analysis of the tilt and rotation angle dependence of boron distributions implanted into <100> silicon. J Electrochem Soc 138:2102–2107
45. Posselt M, Schmidt B, Murthy CS et al (1997) Modeling of damage accumulation during ion implantation into single-crystalline silicon. J Electrochem Soc 144:1495–1504
46. Shockley W, Noice R (1957) Forming semiconductive devices by ionic bombardment. U.S. Patent # 2967985
47. Gelpey JC et al. (2004) Integrating diffusionless anneals into advanced CMOC technologies. Proceedings of International Conference on Solid State Devices, Leuven, p. 180f
48. Durgun Ö et al (2011) Rare earth scandate/TiN gate stacks in POI MOSFETs fabricated with a full replacement gate process. IEEE Trans 58:617–622
49. Lindhard J, Scharff M (1961) Energy dissipation by ions in the keV region. Phys Rev 124:128–130
50. Ryssel H, Ruge I (1978) Ionenimplantation. Akademische Verlagsgesellschaft, Leipzig
51. Wendler E et al (1995) Defect investigation in boron implanted Si. Nucl Instrum Methods 106:303–307
52. Hecking N, Te Kaat E, Heidemann KF (1986) Defects in semiconductors. Nucl Instrum Meth Phys Res B 15:760f
53. Van der Weg WF, Sigurd D, Mayer JW (1974) Ion beam induced intermixing in the Pd/Si system. In: Picraux ST et al (eds) Applications of Ion Beams to Metals. Plenum, New York, p 209f
54. Cheng YT (1990) Thermodynamic and fractal geometric aspects of ion-solid interaction. Mater Sci Rep 5:45–97
55. Nastasi M, Mayer JW (1994) Ion beam mixing in metallic and semiconductor materials. Mat Sci Eng R 12:1–52
56. Bolse W (1998) Mechanisms of ion beam induced atomic mixing in solids. Mat Sci Eng A Struct 253:194–201
57. Sigmund P, Gras-Marti A (1981) Theoretical aspects of atomic mixing by ion beams. Nucl Instrum Methods 182:25–41
58. Möller W, Eckstein W (1985) Ion mixing and recoil implantation simulation by means of TRIDYN. Nucl Instrum Methods Phys Res B 7–8:645–649
59. Johnson WL et al (1985) When is thermodynamics relevant to ion-induced atomic rearrangements in metals. Nucl Instrum Methods Phys Res B 7–8:657–665
60. Leguay R et al (1997) Evidence for atomic mixing induced in metallic bilayers. Nucl Instrum Methods Phys Res B 122:481–502
61. Wang ZG et al (2003) Electronic thermal spike effects in intermixing of bi-layers induced by swift heavy ions. Nucl Instrum Methods Phys Res B 209:194–199
62. Bolse W (2003) Interface modification by swift heavy ions. Radiat Meas 36:597–603

63. Matsunami N et al (1984) Energy dependence of the ion-induced sputtering yields of monatomic solids. At Data Nucl Data Tables 31:1–84
64. Ziegler JF, Biersack JP, Ziegler D (2008) SRIM – The stopping and range of ions in matter. SRIM Co., Chester, MD
65. Andersen HH, Bay HL (2007) Sputtering yield measurements. In: Behrisch R, Eckstein W (eds) Sputtering by particle bombardment. Springer, Berlin

Ion Beam Technology

3

Energetic ion beams and related tools are powerful instruments for research and a wide area of fabrication and materials characterization techniques. They were basically developed to probe and to understand the nuclear structure, but later on, in the past few decades, they have given rise to many key techniques for materials engineering and analysis. For example, ion implantation has become the main technique for semiconductor doping in modern microelectronic technology while Rutherford backscattering (RBS), channeling (c-RBS), medium energy ion scattering (MEIS), ERDA, proton-induced X- and γ-ray emission (PIXE and PIGE), and nuclear reaction analysis (NRA) have emerged as powerful and unique tools for surface and interface analysis. For processing and analysis of many materials a wide range of ion species, ion energies, and ion currents have been explored. To demonstrate the universal nature of ion beams in materials processing and analysis, Fig. 3.1 shows the different applications of ion beam techniques in a map of ion energies versus ion beam currents.

Ion beams in microelectronic technology for doping of semiconductors have replaced the classical diffusion doping techniques for introducing different dopants mainly into silicon, but also into germanium and compound semiconductors. Nowadays, in the advanced CMOS technologies routine medium energy implantation (5–200 keV), low energy implantation (0.5–10 keV), and high energy implantation (0.2–3 MeV) are established [1]. Among the application of ion implantation in microelectronic device and integrated circuit technologies, ion beams became a valuable and innovative tool for advanced materials processing with novel electrical, optical, and magnetic properties, e.g., for surface modification (hardness, texture, corrosion), formation of metastable phases (surface patterning, ripples, plastic flow), and for ion beam-induced slicing. Other ion beam applications such as plasma immersion implantation, ion etching and milling, and ion beam-assisted deposition (IBAD) using low ion energies in the range of some eV up to some 100 keV emerged in the last 20 years [2]. Due to technological and economic demands for all these techniques often high ion currents above 1 μA until some hundreds of mA are used.

B. Schmidt and K. Wetzig, *Ion Beams in Materials Processing and Analysis*,
DOI 10.1007/978-3-211-99356-9_3,

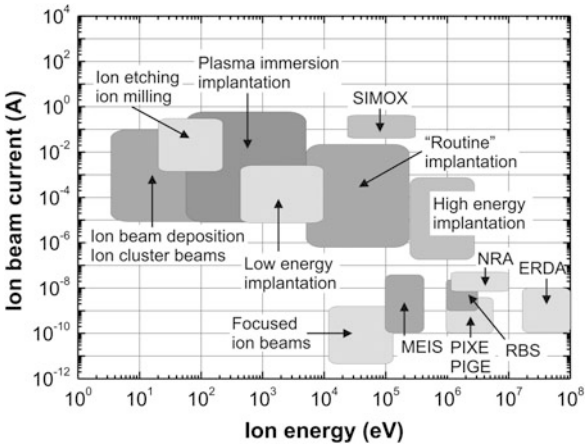

Fig. 3.1 Fluence-energy map of ion beam techniques for materials processing and analysis

In ion beam analysis techniques, ion energies above 0.1 up to 100 MeV with rather low ion beam currents are required. Focused ion beams (FIB) are used to machine away and to deposit solid-state material on nanometer scale. Focused MeV proton and other ion beams were more recently developed to fabricate three-dimensional nanostructures with extremely high aspect ratios.

The reasons for current efforts in ion beam processing of advanced materials are the highly developed level of ion implantation techniques: (1) the concentration of introduced atoms (impurities) is precisely controlled by electrical ion current measurement in the fluence range 10^9–10^{18} ions cm^{-2}; (2) the penetration depth of ions in the range of 1 nm–100 μm can be precisely adjusted by choosing the ion energy in the range of 10–10^8 eV; (3) isotope clean impurity implantation using ion mass separation; and (4) wide variability between ion species and substrates to be implanted. Additionally, the ion–solid interactions are well understood and there exist a variety of physical models describing the ion–solid interaction in general as well as ion range and straggling of implanted ions, recoil cascades and sputtering of target atoms, the formation and annealing of defects, and processes of phase separation. Existing simulation tools are:

- TRIM [3], CrystalTRIM [4], and TRIDYN [5] to calculate depth profiles of ion-implanted impurities and defect depth distributions
- 3DKLMC [6] for simulation of phase separation
- Classical MD (e.g., [7]) for calculation of defect formation
- Ab initio calculations (e.g., [8]) for describing defect structures and their electronic states

3.1 Principles of Ion Acceleration

Ion accelerators, in general, have a long history and their basic design is based on the development of Thomson in the nineteenth century [9]. The accelerators used in ion implantation are more similar to Thomson's design compared to modern

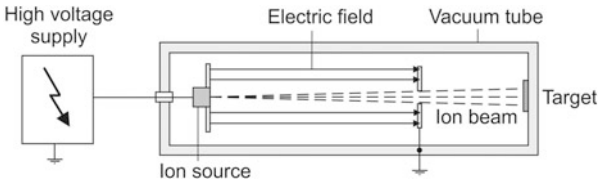

Fig. 3.2 Principal scheme of ion beam formation

accelerators used for ion beam analysis with MeV ion energies and in high energy particle physics where recently GeV and even TeV machines are used to accelerate electrons, protons, and heavy ions to probe elementary particles.

In the most simple case, as shown in Fig. 3.2, an ion accelerator includes basic elements of high-voltage supply, an ion source, an accelerating electrostatic field between the ion source and a grounded electrode, and a vacuum tube in which the ions move to the target with an energy of $E = q \cdot e \cdot U$ where q is the charge state of the ion ($q = 1, 2, 3, \ldots$), e the elemental charge unit, and U the voltage between the ion source and the grounded electrode. The charge state q is initially determined by the degree of ionization attained in the ion source, a device that typically contains a plasma from which charged particles are extracted. The extraction process forms the original beam and sets certain properties of it, such as emittance, brightness, and maximum ion current. Beyond this starting phase of ion beam formation, the charge state at various stages of acceleration requires careful consideration. It can be increased by electron stripping from the ion usually reducing the beam current intensity. Charge exchange processes with the residual gas in most situations mean loss of the ions with initial charge state. The major characteristics of an ion beam are ion species, ion charge state, kinetic energy, and energy spread. Also of great importance are the ion beam intensity (ion current density), emittance, and the related concept of brightness. For many applications in nuclear physics, the energy per nucleon E_n, rather than total energy E, is the decisive quantity; this is given by $E_n = E/M_i$, where M_i is the mass number of the ion. Hence an ion falling through a potential U will get the energy per nucleon $E_n = (q/M_i) \cdot e \cdot U$. Consequently, the charge to mass ratio of an ion is an important quantity. The lower the value of q/M_i, the greater the voltage U required to reach a given E_n. Another consideration is that the deflection of ions by magnetic fields—important for bending and focusing—is proportional to the ion beam rigidity R, which is given by momentum divided by charge: $R = B \cdot \rho = p/q$, where B is the magnetic field, ρ is the gyroradius of the ion due to this field, p is the particle momentum, and q is its charge. It is frequently referred to as simply "$B\rho$." If two particles having the same energy per atomic mass unit (amu) but different q/M_i, the ion with the lower q/M_i will have a higher rigidity, requiring stronger magnetic fields for beam handling.

For the development of accelerators for research and industrial applications, additional technical parts are necessary to place the ions of choice at the desired target position or to distribute them uniformly over the target area. For this purpose different kinds of ion sources, acceleration tools, ion optical elements for beam shaping, ion mass analyzers for isotope separation, beam scanning, and target

manipulation facilities have been designed. Since the 1960s different design concepts concerning the arrangement of the acceleration electrode relative to the mass separation and to the ground potential have been developed. Postacceleration mass analysis (mass separation) has the advantage that only the ion source and the ion extraction voltage have to be controlled on high voltage; all other ion beam elements are connected to ground potential. The disadvantage here is that the magnet for ion mass separation has to be quite large due to the high energy of the accelerated ions. In the case of ion mass separation before ion acceleration significant smaller analyzing magnets can be used and the change of the acceleration voltage can be done during ion beam operation. The operation of the analyzing magnet takes place together with the ion source and ion extraction on high potential. There are some books in which technical details of accelerator and implanter developments are described [10–13] more in detail. Therefore, only the principles of low and high energy ion accelerators will be shortly described.

3.1.1 Low Energy Ion Accelerators (Ion Implanters)

All ion implanter designs utilize subsystems that are basically similar. These basic building blocks are: (1) the ion source, (2) the accelerator stage, (3) the mass analyzer or separator, (4) the beam scan system, and (5) the target chamber or end station. These subsystems can be used in different configurations as shown in Fig. 3.3.

Early implanter designs usually consist of a single acceleration stage and a magnetic analyzer (Fig. 3.3a). The ions travel in a straight line through the analyzer. The acceleration stage was usually placed before the ion mass analyzer. This arrangement was mostly used as atomic research tools to accelerate light ions such as hydrogen and helium. Therefore, the mass analyzer was small with minimum resolving power. The mass separation of heavier ions used in ion implantation requires very large magnetic fields. These very large electromagnets—sometimes weighing as much as a ton—also consumed very large amounts of electric power for water cooling. For this reason, later on in the design the acceleration was split into two parts, preacceleration and postacceleration, as shown in Fig. 3.3b, c. The preacceleration typically accelerates the ions to 10–30 keV. After mass separation, the selected ions are again accelerated to their finally energy of, typically, 80–500 keV. This accelerator design has the further advantage of accelerating only the required ion species to high energy. Furthermore, this design reduces the power consumption and more importantly the X-ray generation level resulting from removing the unwanted ions from the beam before acceleration. The majority of modern ion implanters are based on the concept shown in Fig. 3.3b. This design optimizes the trade-offs between power consumption, floor space, and other technical and vacuum requirements. By placing the beam scanning system before the postacceleration stage (Fig. 3.3c) the voltage for beam deflection can be reduced to lower levels which can be important at higher ion energies. The principal technical

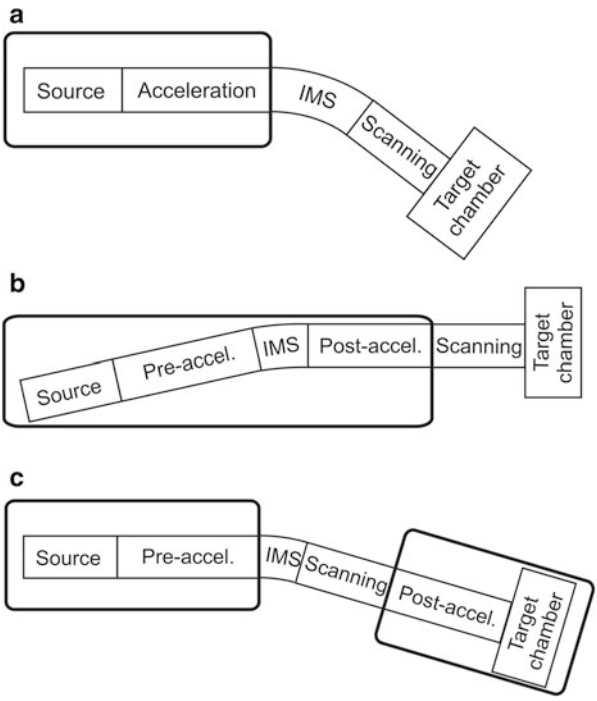

Fig. 3.3 Three basic implanter configurations

buildup of ion accelerators with mass separation before ion acceleration providing ions in the "low" energy range is shown in Fig. 3.4.

From the ion source which is at high positive potential of 0–500 kV the ions are extracted by an additional voltage of 10–30 kV and are formed to a beam entering the entrance slit of the mass separation magnet selecting the ions (isotopes) of choice. The separated ion beam passes through the exit slit at the focus of the analyzing magnet into the entrance side of the acceleration tube. In the most simple case at low energies ($\leq$50 keV) a single accelerating electrode and for higher energies an accelerating tube with some ring electrodes (up to 20) are used (see insert in Fig. 3.4). Now the ions are accelerated to the desired energy. The isotope clean ion beam is focused by the acceleration tube itself and by following appropriate ion optical elements (e.g., quadrupole lens) and can be directed to the target chamber in an un-scanned or *xy*-scanned manner. Usually, before the electrostatic *xy*-scanning system the ion beam is electrostatically deflected by the neutral trap and beam gate unit to select neutralized ions from the ion beam and to collect them in the beam trap. The *x*, *y*-scanning system is used to distribute the ions uniformly over the target area. At the target stage (or around it) the incident ion current is measured by Faraday cups connected to current integrators which measure directly the ion fluence Φ (ions cm^{-2}) by collecting the beam current and integration of it over the irradiation time. Different modern designs of low energy ion accelerators

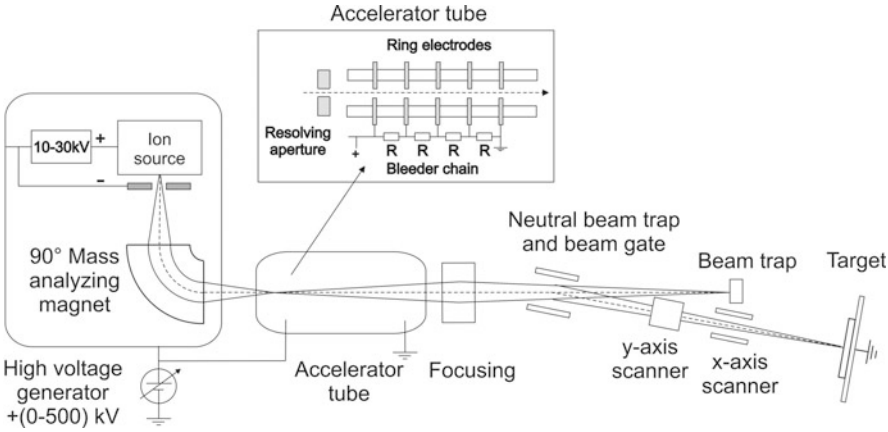

Fig. 3.4 Principal technical buildup of low energy ion accelerators (ion implanter)

(ion implanters) accelerating ions in the energy range 0.5–500 keV will be described in more detail in Sect. 3.5.

3.1.2 High Energy Ion Accelerators

High energy ion accelerators in the ion energy range of 0.5–100 MeV for materials modification and analysis are mostly designed as single-stage accelerators (e.g., Van de Graaff accelerator) and two-stage accelerators (or Tandem accelerators) [14]. They differ from low energy accelerators in the use of high-voltage generators which are able to provide voltages of several MV and the design of the postacceleration stage sustaining such high voltages. Figure 3.5 shows the principal technical buildup of a single-stage Van de Graaff accelerator able to provide ions in the "high" energy range of 1–10 MeV.

In the Van de Graaff generator (Fig. 3.5) [15], an insulated belt is used to carry up the charge to a terminal that is maintained at a high potential. Positively charged ions from the ion source located in the terminal are accelerated through the potential difference between terminal and ground to an ion energy of $E = q{\cdot}e{\cdot}U$, where q is the charge state ($q = +1, +2$), e is the elementary charge, and U is the terminal voltage. Van de Graaff accelerators are able to achieve high voltages of 7–10 MV at relatively low ion currents. An alternative high-voltage generator is the Cockcroft–Walton generator [16]. The high-voltage unit consists of a multiplying rectifier–condenser chain providing high voltages up to 4 MV but with much higher ion currents of many mA compared to Van de Graaff generators. Van de Graaff accelerators provide mainly H^+ and He^+ ions without a mass separating magnet after the ion source.

With the development of negative ion sources in the 1950s it became possible to build two-stage (or Tandem) accelerators (Fig. 3.6) [17] in which negatively

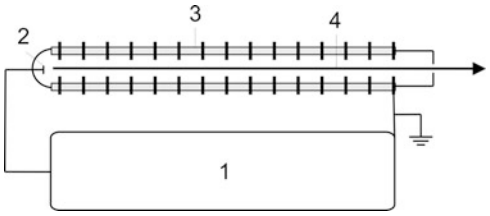

Fig. 3.5 Principal technical buildup of a single-stage Van de Graaff accelerator with (1) high-voltage generator, (2) ion source on high potential, (3) accelerating system, and (4) ion beam

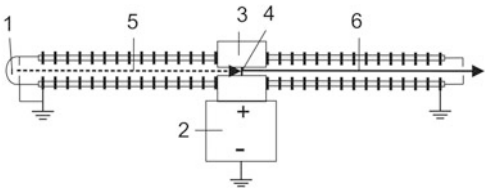

Fig. 3.6 Principal technical buildup of a two-stage (or Tandem) accelerator with (1) negative-ion source, (2) high-voltage generator, (3) high-voltage electrode, (4) stripper for ion charge exchange, (5) negative-ion beam, (6) positive-ion beam

charged ions are extracted from the ion source at ground potential and injected into the first stage of the acceleration tube, where they are accelerated up to the positive high-voltage terminal with an energy of $E = e{\cdot}U$, where e is the elementary charge and U is the terminal voltage. In the stripper system, a few electrons are stripped off from the negative ions converting them to positive ions (single or multiple charged). Now in the second stage, the positively charged ions are accelerated back to the ground potential. The final ion energy is equal to $E = (q + 1){\cdot}e{\cdot}U$, where U is the terminal high voltage and q is the charge state of the positively charged ions after stripping ($q = +1, +2, +3, +4, +5, \ldots$). Using appropriate ion sources together with a mass separating magnet after the ion source tandem accelerators are able to provide H^+, He^+ ions and a wide variety of heavy ions. For heavy ions and high terminal voltages the charge state q can be quite high, and therefore ion energies of hundreds of MeV can be achieved. The big advantage, the achievement of higher energies than those achieved with single-stage accelerators, is reduced in some cases by the fact that not from all elements of the periodic table negatively charged ions can be produced.

For all electrostatic accelerators above about 1 MV, pressurized vessels are used to contain the high-voltage components. This allows working with much higher electric fields and thus reduces the physical size of the apparatus, which is limited by breakdown and corona phenomena. In modern accelerators sulfur hexafluoride (SF_6) is used as insulating gas with pressures up to 12 bar inside the acceleration vessel. The accelerating tube must have a high vacuum of $<10^{-6}$ bar to avoid unwanted charge exchange for heavy ions with residual gas molecules in the residual vacuum. With electric field gradients in the accelerating tubes of

(2–3) MV/m, a conditioning process is often necessary for steady and reliable operation. The fundamental objective in conditioning is to eliminate by controlled discharges small (often microscopic) irregularities on the high-voltage surfaces in the accelerating tube. Quadrupole lenses are appropriately located in the beam line for beam control; with beam profile monitors and steering elements, beam transmission from source to target is straightforward. A change in ion energy or in charge state can be easily and quickly accomplished.

3.2 Ion Sources

Many ion sources have been developed during introduction and operation of accelerators in materials processing and ion beam analysis [18–22]. Concerning the physical principle they can be divided into three groups: electron bombardment sources, radio frequency (RF) sources, and microwave sources. In low energy accelerators (<500 keV) electron bombardment sources are mostly used and different designs have been highly developed for ion implanters in microelectronic industry. Not only design considerations but also general performances, for example, the lifetime directly influencing the economic use of the ion source, are included in their figure of merit. Sources with hot filaments have a lifetime of some tens of hours, whereas cold cathode sources can operate some hundred of hours.

The most commonly used types of ion sources in ion accelerators are:

- Hot cathode ion source (Sidenius source/Danfysik, Freeman source, Bernas ion source)
- Cold cathode ion source (Penning ion source)
- Indirectly heated cathode source (IHC)
- High frequency ion source
- Hollow cathode ion source
- Duoplasmatron ion source
- Sputter ion source

The choice of the ion source depends on different demands, e.g., high current sources for ion implanters in semiconductor manufacturing, low current sources with high lifetime, or sources with low ion energy spread and much more. In principle, ion sources can be divided in sources operating with gases or solid substances and in high and low current ion sources. Ion sources for large area ion implantation provide ions with energies in the range 0.2–500 keV and relative high fluences corresponding to ion currents in the μA to mA range. Ion implanters in microelectronic industry for semiconductor (silicon) doping mostly use gas ion sources, because a fast change of the feed gas becomes possible, if the change of the dopant element is required during wafer processing.

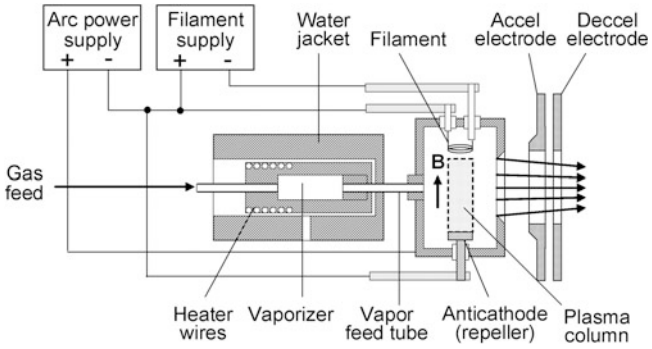

Fig. 3.7 Principal buildup of a Bernas ion source

3.2.1 Hot Filament (Hot Cathode) Ion Sources

The *Bernas ion source* [23] consists of a discharge chamber with an isolated thermionic filament (or cathode) providing a source of primary electrons which cause ionization of the atoms introduced into the arc chamber by gas feed or by vapor feed from a heated oven (Fig. 3.7).

As shown in Fig. 3.7 the primary electrons revolve around the magnetic field lines towards to the so-called repeller (anticathode) negatively biased relative to the arc chamber. Electrons arriving in the vicinity of the repeller are turned around and spiral back to the filament leading to a prolonged electron path length and therefore giving an efficient ionization of the atoms. In the case of nonbiased repeller charging up to a certain negative floating potential relative to the plasma potential takes place and the repeller will function in the same way. As shown in Fig. 3.7 the ion source operates at high potential relative to ground. Together with the extraction electrode with negative potential, a second grounded electrode is placed at the source exit. The aim of the grounded electrode is to suppress backstreaming electrons which could pass through the extraction slit and strike the source, generating intense X-rays and adding to the extraction current. The faces of the source and the hole or slit in the extraction electrode are shaped to help focusing and therefore to achieve high transmission of the extracted ion beam through the full beamline. Bernas-type ion sources are widely used in modern ion implantation machines and achieve high ion currents up to 30 mA (for dopant ions of As^+ and P^+). To generate also high currents for boron ions and to get multiply charged ions a second filament (anticathode or repeller) is added [24].

The second type of highly developed ion sources applied in ion implanters is a hot filament ion *source introduced by Freeman* [25], shown Fig. 3.8, from which the ions are extracted through a wedge-shaped (slit) opening because the ions are extracted in a direction perpendicular to the plasma axis. The source consists of a discharge chamber (discharge voltage 40–700 V, typically 60–70 V) with a hot filament. The ion beam current is controlled by the discharge current of 1–2 A from

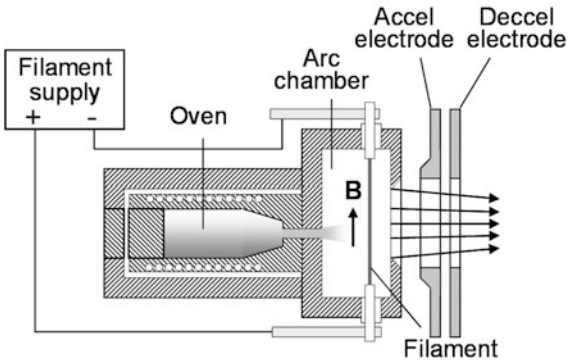

Fig. 3.8 Principal buildup of a Freeman ion source

the directly heated filament (cathode) to the body of the source chamber (anode). In some modification of the Freeman ion source indirectly heated cathodes are used.

A magnetic field applied parallel to the filament spirals the emitted electrons around the filament leading to long path length of the electrons and therefore to increased ionization of the atoms. The Freeman-type ion source can either operate with gas feeding or vapor feeding from heated oven (up to 1,100 °C). In semiconductor implanters mainly gases that contain the desired doping species are used, namely BF_3, AsH_3, and PH_3 for silicon and SiH_4 and H_2 for gallium arsenide. At high gas pressures, the electron current is often sufficient to maintain a glow discharge in the chamber which breaks up the gas molecules into atomic and molecular species, some of which will be ionized, for example, BF_3 into B, B^+, BF_2, BF_2^+, F^+, and other ones. The positive ions exit the source chamber which is on large negative bias (1–5 kV) with respect to the filament through a slit. The resulting ion beam has rectangular form of a few millimeters by 1–2 cm and an ion current of typically a few mA. The Freemann gas source has a more simple design compared to the source with an oven for evaporation of elements or compounds into the ion source chamber. To provide a wide range of elements with sufficient vapor pressure for stable operation, a well-controlled oven temperature is required, and special oven designs have been developed to address problems such as condensation of the evaporated material or positive thermal feedback from the discharge chamber.

The *Sidenius (or Scandinavian) ion source* [26] shown in Fig. 3.9 is a hollow cathode source and has been designed for lower ion currents. The source has relatively compact size and requires low power supply (<500 W). The source consists in most cases of a boron nitride oven which allows direct vaporization of many solid materials at high temperatures up to 2,000 °C. The hot helical filament cathode and the anode are arranged on-axis in the direction of the ion beam. The inhomogeneous magnetic field concentrates the magnetic field and therefore the plasma towards the extraction aperture with a diameter of ~0.5 mm. The plasma discharge is controlled by the electric power applied to the helical tungsten

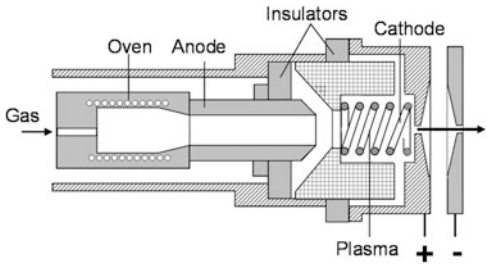

Fig. 3.9 Sidenius (or Scandinavian, Danfysik) ion source

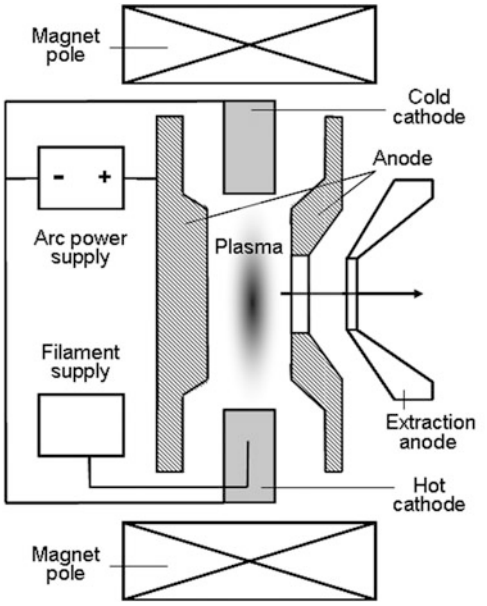

Fig. 3.10 Penning ion source

filament. Ion beams extracted from this source type have a circular form because the ions are extracted parallel to plasma axis.

3.2.2 Cold Cathode Ion Source (Penning Ion Source)

A *Penning ion source* [27] shown in Fig. 3.10 consists of cold or heated electrodes to establish a high-voltage, low-pressure plasma discharge. In a typical configuration, an anode ring is placed between two cathode electrodes. An axial magnetic field is used to confine the electrons so that they oscillate between the cathodes and inside the ring. Further, the magnetic field increases the path length of ionizing electrons, making plasma production more efficient. This type of device was

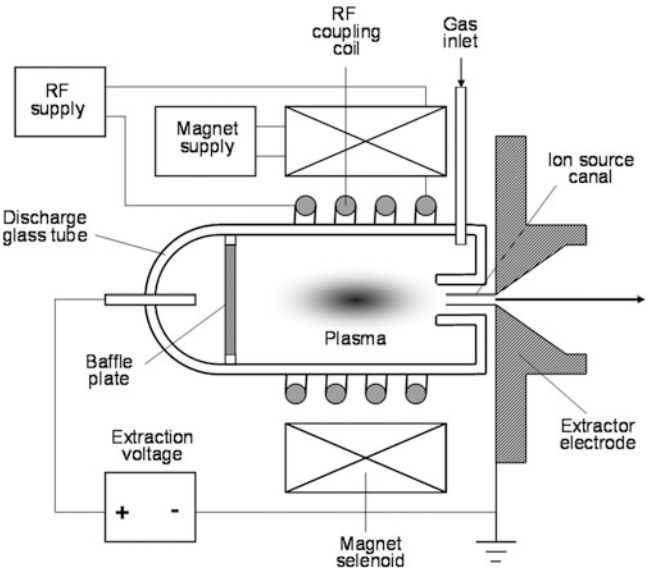

Fig. 3.11 Principal buildup of a radio-frequency ion source

originally proposed by Penning as a low-pressure manometer (i.e., cold cathode or Penning gauge [28]) and was later adapted to also function as an ion source.

Penning ion sources have been used for a variety of applications, such as sputtering and evaporation of surfaces, accelerator, and fusion applications.

3.2.3 High Frequency (RF) Ion Source

Radio frequency (10–100 MHz) ion sources [29] shown in Fig. 3.11 are widely used in single-stage accelerators to provide ion beams in the low energy range of 20–200 keV as well as in high energy electrostatic accelerators (>500 keV) for the production of ions from gaseous source feeds, e.g., from high purity gases of H, He, N, Ar, etc.

The body of the source is made from a quartz tube with some cm of diameter used as the discharge chamber in which the gas at a typical pressure of 10^{-2}–10^{-3}mbar is ionized by collisions produced by RF power of some 100 W supplied to the source. Modern RF ion sources use capacitive rather than inductive coupling and a magnetic field to concentrate the discharge in the region of the extractor. The glass tube is closed at one end with a fused metal extraction pin. A silica baffle plate (with holes around the perimeter) in front of the extraction pin prevents arcing of the extraction voltage through the plasma. At the other end the quartz tube is bonded to the metal source mounting plate containing in the center a silica sheathed metal extraction canal (1–2 mm diameter). The high frequency is applied to the chamber either via a coiled antenna around the glass body or by a pair of coupling rings mounted onto it.

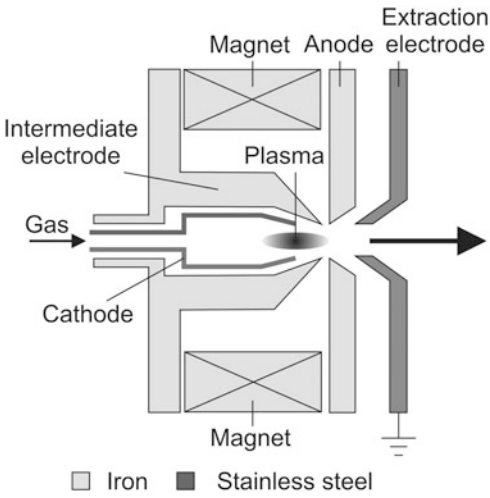

Fig. 3.12 Schematic diagram of the Duoplasmatron ion source

A solenoid coil (magnetic field) around the base causes an increased plasma density in the region of the ion source canal. The ion beam current is controlled by changing the extraction voltage in combination with the adjustment of the gas pressure. The gas pressure in the glass chamber is about 0.1 Pa. The ion beam current produced by RF ion sources is in the range of some mA for light ions where electron bombardment sources are not giving efficiently high ion currents.

3.2.4 Duoplasmatron Ion Source

The Duoplasmatron ion source was developed by von Ardenne [30] and, based on his principle, different designs have been developed for application of this ion source type mainly as a proton source for high energy accelerators but also for the production of multiply charged heavy ions [31, 32].

Concerning the source principle shown in Fig. 3.12 the ions are axially extracted from the plasma of the low pressure plasma discharge between a hot cathode and an anode (Fig. 3.12). The emission aperture ($d \approx 0.3$–0.6 mm) in the anode on the discharge axis provides the extraction of positive ions. In order to obtain an enhanced plasma density and a high ionization degree in front of the anode aperture, the discharge is strongly concentrated successively by the focusing action of an intermediate electrode and the effect of a strong axial magnetic field set up by the lens, the poles of which are the anode and intermediate electrode. In the case of positive ion extraction ion currents of 1 mA for hydrogen can be achieved.

Positive ion source operation is required for helium, for which only He^+ can be created with a good efficiency inside the Duoplasmatron ion source. In the case of ion source application in high energy ion accelerators, He^+ ions after extraction pass through the so-called *charge exchange channel*, in which vapor of lithium is

present. The result is that about 1 % of the incoming He beam turns negative and can be thus further accelerated in a tandem accelerator. Obviously, this limits the maximum current available for He ions to a few μA. To operate the source in a negative ion mode, it is necessary to offset the intermediate electrode from the anode aperture. This results in the extraction of ions from the periphery of the arc discharge which is enriched with negative ions with a simultaneous reduction in electrons due to differences in their diffusion and recombination coefficients. Negative ion currents (H^-, D^-, T^-) of 50–150 mA are possible to be extracted from the source.

3.2.5 Ion Sources for Electrostatic Accelerators

The purpose of ion sources in high energy accelerators [20] is to produce either positive or negative ions from neutral atoms. Positive ion sources are placed inside the tank of a single-stage accelerator (Van de Graaff accelerator); negative ion sources inject the ion beam into the tank of a two-stage accelerator (Tandem accelerator). In single-stage accelerators (Van de Graaff accelerator), mostly RF- and Duoplasmatron ion sources giving positively charged ions are used. For the injection of negative ions into two-stage accelerators different positive source types can be connected to a charge exchange channel, in which the transfer from positively to negatively charged ions takes place. For ions from gases (H, D, T, He, etc.) again RF and Duoplasmatron ion sources and for ions from vaporized solids Cs sputtering ion sources are applied. Different negative ions can be formed by adding an extra electron which is possible for most of elements and many molecules, where the negative ion state is characterized by the binding energy of the additionally attached electron or by the electron affinity. The electron affinity for about 80 % of the elements has positive value and only a few have a negative electron affinity (e.g., Be, Mg, N, Mn, and noble gases). For the formation of negatively charged ions the following different physical processes are known:

- Collision between ions, atoms, and molecules
- Nonthermodynamic equilibrium surface ionization

In practice, among different designs mainly RF- and Duoplasmatron ion sources combined with charge exchange channels have been introduced to provide indirectly H^- and He^- ions. At the charge exchange mechanism collisional processes of positive ions with atoms take place and electrons are transferred from one particle to the other one. Therefore, each positive ion has to undergo two collisions, first to become neutral, and second to become negative. The electron transfer from one particle to the other one depends on the collision energy, the ionization potential, and the electron affinity of the colliding particles. Mainly vapors of alkaline elements, e.g., Li and Rb, are used because the only one electron in the outer atom shell of these elements has a low binding energy (low ionization potential) compared to other nonalkali elements. The exchange canal is usually designed as a tube about 0.75 cm in diameter and about 10 cm in length to which an oven for

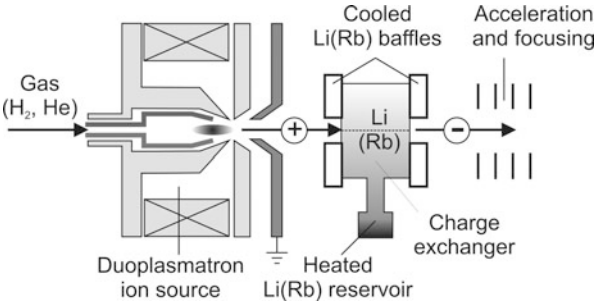

Fig. 3.13 Close-coupled Duoplasmatron ion source with charge exchange cell for production of negative ions

introduction of the vapor from alkaline elements is attached. Charge exchange efficiencies up to 90 % have been achieved for these elements.

For example, Fig. 3.13 shows a negative ion source in which a closed-coupled *Duoplasmatron* is combined with the charge exchange cell. The Duoplasmatron ion source produces firstly positive ions of H^+ or He^+. To provide a negative H^- or He^- ion beam, the positive beam is extracted from the source and immediately injected into a lithium (or rubidium) charge exchange cell. This type of negative ion source is often applied to two-stage accelerators. In the case of a RF ion source instead of the Duoplasmatron a gas or gas mixture is bled into a quartz bottle; the RF oscillator connected to the quartz bottle causes the plasma inside the quartz chamber which dissociates the neutral gas molecules (H_2) or atoms (He) into positively charged ions H^+ and He^+. A voltage difference (usually about 2-6 kV) is used to push the ions out of the chamber through the exit aperture into the charge exchange cell to get a negative H^- or He^- ion beam. Negative RF ion sources are less effective compared to Duoplasmatron sources and are more often used without charge exchange cell for H^+ and He^+ ions in single-stage accelerators.

3.2.6 Cesium Sputtering Ion Source

The direct formation of negatively charged ions is based on the nonthermodynamic equilibrium surface ionization process where a surface covered with a thin layer of highly electropositive material, for example Cs, is sputtered (nonequilibrium process) by a primary beam of positive ions formed by surface ionization of group IV elements (e.g., also Cs). The primary positive ion beam is accelerated to the cathode to sputter the element of interest from the sample in the cathode. A few sputtered target atoms are negatively charged by taking away an electron from the thin layer of the electropositive Cs material. Different negative ion sources based on direct surface ionization of Cs vapor have been described and reviewed (see for example [32]). The sources differ mainly in the geometry of the ionizer, the spacing relative to negatively biased target (source sample), the spacing of the sample relative to the ion exit aperture, and the aperture size.

The mostly used ion source providing a wide variety of negative ion beams for the injection into Tandem accelerators is the Cesium Sputtering source with spherical

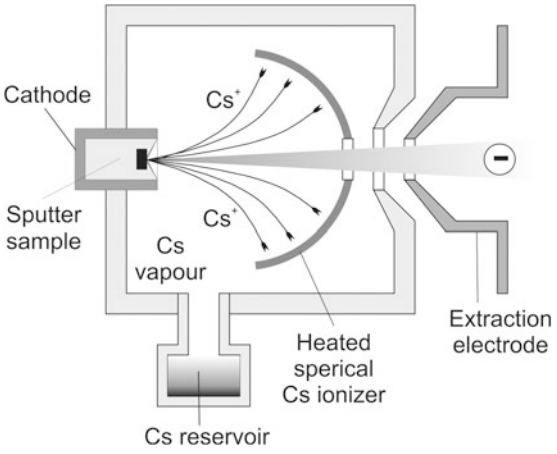

Fig. 3.14 Schematic buildup of a Cs-sputtering ion source with spherical ionizer geometry

[33] or ellipsoidal [34] geometry of the ionizer. Figure 3.14 shows the principal scheme of a Cs sputter ion source with spherical geometry of the Cs ionizer.

Cesium vapor comes from the cesium oven into an enclosed area between the cooled cathode and the heated ionizing surface. Some part of the cesium condenses on the front of the cathode and some cesium is ionized by the hot surface. The ionized cesium accelerates towards the cathode consisting in the middle the source material, sputtering particles from the cathode through the thin condensed cesium layer. Some materials will preferentially sputter neutral or positive particles which pick up electrons as they pass through the condensed cesium layer, producing negative ions. The Cs^+ ion beam is usually focused to a beam spot of about 0.5–0.6 mm diameter when the sample is positioned in the focal point of the spherical (or ellipsoidal) ionizer. Therefore, the high-density beam spot on the negatively biased sample serves as the source region from which the negative ion beam is generated within the ion source.

As an example, Table 3.1 gives an overview about used positive and negative ion beam currents, ion sources, and source feed materials used for accelerators in the Ion Beam Center of the Helmholtz-Zentrum Dresden-Rossendorf (HZDR) [35].

A comprehensive collection of known source feed materials to provide in overall 89 different kinds of negatively charged ions was published by Middleton in his "Negative Ion Cookbook" [36].

3.2.7 Field Evaporation or Liquid Metal Ion Sources

Liquid metal (or metal alloy) ion sources have found their wide application in Focused Ion Beam (FIB) tools due to their characteristic high brightness through the use of the liquid metal field-evaporation process. The Liquid Metal Ion Sources (LMIS) have the advantage of high beam intensities and relative long lifetimes.

Table 3.1 List of ions used at the HZDR Ion Beam Center [35]

Isotope	Emitted ion	Ion current (μA)	Source material	Source type
Van de Graaff accelerator (2 MV)				
^{1}H	H^{+}	0.1–2.0	H_2 gas	RF-IS
^{4}He	He^{+}	0.1–1.0	He gas	RF-IS
Tandem accelerators (3, 5, 6 MV)				
^{1}H	H^{-}	10–40	TiH_2	Cs-SIS
^{2}H	D^{-}	20–40	TiD_2	Cs-SIS
^{4}He	He^{-}	2–3	He gas	DP-IS (Li-ch.)
^{7}Li	Li^{-}	1.7–2.4	LiO_2 + W	
^{11}B	B^{-}	2.0–4.0	B + W	Cs-SIS
^{12}C	C^{-}	40–80	Graphite	Cs-SIS
^{14}N	$(CN)^{-}$	1–15	BN + C	Cs-SIS
^{15}N	$(CN)^{-}$	2–2.5	$Na^{15}N_3$ + C	Cs-SIS
^{15}N	$(NH_2)^{-}$	2–2.7	80%H_2 + 20%N_2	Cs-SIS
^{16}O	O^{-}	40–140	Fe_2O_3	DP-IS
^{19}F	F^{-}	20–35	LiF + W	Cs-SIS
^{27}Al	Al^{-}	0.6–2.0	Al	Cs-SIS
^{28}Si	Si^{-}	50–130	Si-monocryst.	Cs-SIS
^{31}P	P^{-}	10–45	GaP	Cs-SIS
^{35}Cl	Cl^{-}	8–33	CsCl + W	Cs-SIS
^{39}K	K^{-}	0.2	$KHCO_3$ + Ag	Cs-SIS
^{48}Ti	Ti^{-}	5–10	TiH_2	Cs-SIS
^{52}Cr	$(CrH)^{-}$	2–8	Cr + TiH_2	Cs-SIS
^{58}Fe	Fe^{-}	2–4	Fe_2O_3	Cs-SIS
^{58}Ni	Ni^{-}	20–35	Pure Ni	Cs-SIS
^{63}Cu	Cu^{-}	5–25	Cu	Cs-SIS
^{64}Zn	$(ZnO)^{-}$	0.5–1.0	ZnO + W	Cs-SIS
^{74}Ge	Ge^{-}	5–13	Ge-monocryst.	Cs-SIS
^{75}As	As^{-}	9–20	GaAs	Cs-SIS
^{80}Se	Se^{-}	5–20	CdSe	Cs-SIS
^{79}Br, ^{81}Br	Br^{-}	10–30	CsBr + W	Cs-SIS
^{93}Nb	$(NbC)^{-}$	1.2–1.5	Nb + C	Cs-SIS
^{105}Pd, ^{106}Pd	Pd^{-}	0.6–0.9	Pure Pd	Cs-SIS
^{107}Ag	Ag^{-}	4–6	Pure Ag	Cs-SIS
^{112}Cd, ^{113}Cd, ^{114}Cd	Cd^{-}	0.1–0.2	Cd + W	Cs-SIS
^{115}In	In^{-}	0.3–0.5	InO_2 + W	Cs-SIS
^{120}Sn	Sn^{-}	2.0–7.0	Sn, Sn + W	Cs-SIS
^{121}Sb, ^{123}Sb	Sb^{-}	0.8–1.4	Sb + Pb	Cs-SIS
^{127}I	I^{-}	20–50	CsI + W	Cs-SIS
^{166}Er, ^{167}Er, ^{168}Er	$(ErO)^{-}$	0.9	ErO + W	Cs-SIS
^{195}Pt, ^{196}Pt	Pt^{v}	25–30	Pt	Cs-SIS
^{197}Au	Au^{-}	60–75	Au	Cs-SIS

Remark: Cs-CIS—Cs sputter ion source, RF-IS—RF ion source, DP-IS—Duoplasmatron ion source

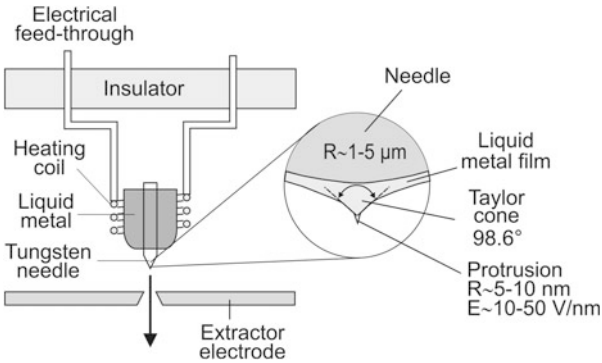

Fig. 3.15 Schematic diagram of a liquid metal ion source (LMIS).

Furthermore, they have a simple design and are easy to operate. Micro- and nano-focused ion beams have nowadays a wide field of applications, for example in micro- and nano-fabrication, materials characterization and analysis, and space propulsion. Consequently, this type of ion source has been studied by many groups and there exist many review articles [37, 38] and books [39–41] giving an overview about the development and the technology as well as about the physics and application of LMIS.

In order to focus an ion beam into a spot size of a diameter smaller than 1 µm a source is needed which emits the ions from a very small area into a limited solid angle. To meet this demand several types of LMIS such as needle-type LMIS and capillary-type LMIS have been proposed. The needle-type ionizer [42, 43] is most commonly used and shown in Fig. 3.15.

The needle-type liquid-metal ion sources usually consist of a tip (usually tungsten with a radius of a few microns). The reservoir of liquid metal is maintained below at the other end of the tip. The tip is located close to the extraction aperture which is negatively biased typically to 2–10 kV relative to the tip. By heating the reservoir to a suitable temperature, the metal flows down and wets the tip. The strong electric field applied to the tip displaces the molten metal in such a way that at a critical field strength of about some 10 V nm^{-1} on the tip a liquid cone with a half angle of 49.31°, the so-called Taylor-cone [44], is formed. The ion emission occurs from a liquid jet based on this cone, mainly due to a field evaporation process [45] from the apex of the cone which has a typical radius of 1.5–3 nm. Applying these unique point-like sources with a virtual spot size of ~20 nm and a brightness in the order of 10^6 A cm^{-2} sr^{-1} focused ion beams with a diameter less than 10 nm can be formed. Current densities of more than 10 A cm^{-2} are achieved.

Demands to metals or metal alloys used in LMIS are a relative low melting point, high surface tension, low vapor pressure in its molten state, and no corrosion of the tip itself. Therefore, gallium with a melting point of $T_m = 29.8$ °C is considered most suitable and is mostly used in FIB tools. Additionally, compared to other suitable low melting elements Ga has the advantage that the emitted ion mass spectrum contains about 99 % singly charged ions. Therefore, no mass filter is

Table 3.2 Elemental and eutectic alloy materials for LMIS

Selected ions	Liquid element or alloy	T_m (°C)	References
Without mass separator			
Ga^+	Ga	29.6	[46]
In^+	In	157	[47]
Bi^+	Bi	271	[48, 49]
Rb^+	Rb	39	[50]
Cs^+	Cs	26	[51]
With mass separator			
In^+, (Ga^+)	$In_{14}Ga_{86}$	14.2	[52]
Sn^+, Pb^+	$Sn_{74}Pb_{26}$	183	[53]
Bi^+, (Ga^+)	$Ga_{38}Bi_{62}$	222	[54]
Bi^+, Li^+, (Ga^+)	$Ga_{35}Bi_{60}Li_5$	250	[49]
Au^+, Ge^+	$Au_{73}Ge_{27}$	365	[55]
Au^+, Ge^+, Si^+	$Au_{77}Ge_{14}Si_9$	365	[56]
Au^+, Si^+	$Au_{82}Si_{18}$	365	[57]
Co^+, Nd^+	$Co_{36}Nd_{64}$	566	[58]
Mn^+, Ge^+, Si^+	$Mn_{45}Ge_{54}Si_1$	720	[59]
Pr^+, Si^+	$Pr_{89}Si_{11}$	732	[60]
Er^+, Ni^+	$Er_{69}Ni_{31}$	765	[61]
Co^+, Ge^+	$Co_{27}Ge_{73}$	817	[62]
Er^+, Fe^+, Ni^+, Cr^+	$Er_{70}Fe_{22}Ni_5Cr_3$	862	[63]
Al^+, Ce^+, C^+	$Al_{10}Ce_{70}C_{20}$	660	[64]

needed and the ion column design becomes more easy and the majority of FIB systems operating worldwide are suited only for gallium ions. Possible other elemental metals are listed in Table 3.2. With the development of modern FIB columns with mass separation (ExB filter) it became possible to provide several kinds of other ions from metal alloys used in LMIS which are successfully used for research and development in micro- and nanofabrication [40, 41, 65]. The versatility of the LMIS ion source in terms of extracted ions is partially listed in Table 3.2 which refers to a number of sources that generate ion beams from both elemental and eutectic alloy materials.

The vapor pressure of all alloy materials is less than 10^{-8} torr at source operation temperature, except Mn. Actually, among monomer ions often cluster ions (dimers, trimers, etc.) and multiple charged ions are emitted from LMIS. As an example Fig. 3.16 shows the mass spectrum of a pure Bi LMIS containing besides the dominating Bi^+ ions single-charged Bi_n^+ ($n = 2, 3, 4$) and double-charged Bi_m^{++} ($m = 1, 3, 5$) cluster ions [49].

Recent developments of other types of ion sources are mainly related to microwave or electron cyclotron resonance (ECR) ion sources [66, 67], single- and multicusp ion sources [68, 69], and electron beam ion trap (EBIT) sources [70].

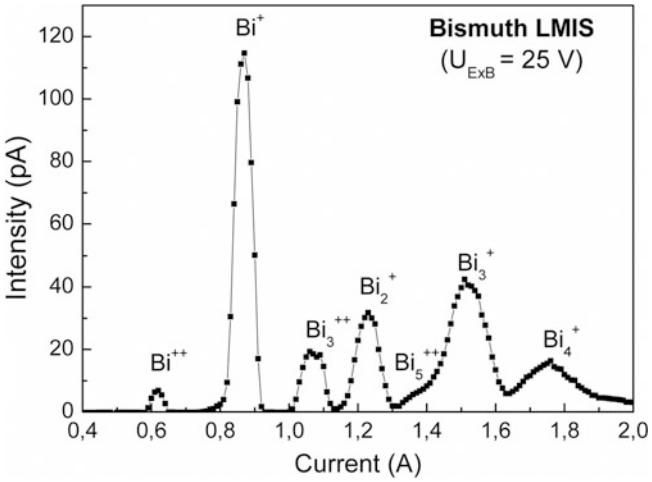

Fig. 3.16 Ion mass spectrum of a Bi LMIS, measured within a CANION 31Mplus FIB column (Orsay Physics) at an acceleration voltage of 30 kV. The applied voltage to the ExB mass filter was 25 V

3.2.8 Beam Extraction from Ion Sources

The extraction of an ion beam current from an ion source in general is limited by either the emission capability or by space charge forces. In the latter case the maximum ion current density j_{sc} is given by the Child–Langmuir formula [71, 72]:

$$j_{sc} = \frac{4 \cdot \varepsilon_0}{9} \sqrt{\frac{2 \cdot n \cdot q}{M \cdot m_a}} \cdot \frac{\Phi^{3/2}}{d^2} \tag{3.1}$$

with the absolute permittivity ε_0, the electric charge q, the charge state n, the mass in atomic units M, the atomic mass unit m_a, and Φ the potential drop across the extraction gap d. Equation (3.1) can be rewritten in more practical units as

$$j_{sc}\left[\mathrm{mA \cdot cm^{-2}}\right] = 1.72 \cdot \sqrt{\frac{n}{M}} \cdot \frac{\Phi[\mathrm{kV}]^{3/2}}{d[\mathrm{mm}]^2}. \tag{3.2}$$

As can be concluded from (3.1, 3.2) the space charge limited ion current is proportional to $\Phi^{3/2}$. The proportionality factor is called perveance and describes the beam broadening due to repulsive forces in the space charge region [73]. The emission limited ion current density j_p extracted from a plasma ion source is given by formula (3.3):

$$j_p = 1.57 \times 10^{-10} \cdot n_i \sqrt{\frac{z \cdot T_i}{M_i}}, \tag{3.3}$$

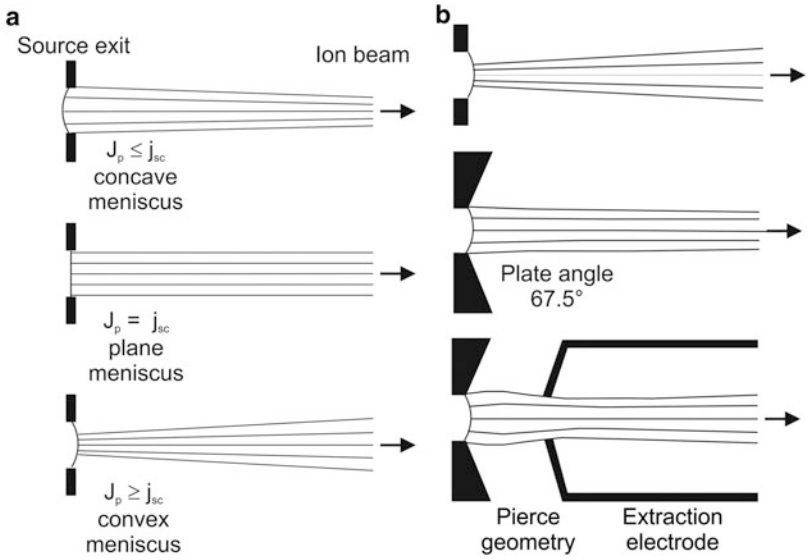

Fig. 3.17 Influence of the plasma boundary surface on the ion beam divergence

where n_i is the ion density in the plasma, z is the charge state of the ion, T_i is the ion temperature, and M_i is the ion mass. The geometric form of the plasma boundary, from which the ions are extracted, depends on the ratio of the space charge limited current density j_{sc} to the saturation current density of the plasma j_p. Therefore, the form of the plasma boundary mainly depends on the extraction (acceleration) voltage and on the ratio of the source opening to the distance of the extraction electrode from the source. The plasma boundary at the source exit acts as an electrostatic lens and has itself an important influence on the divergence during formation of the ion beam, which is schematically shown in Fig. 3.17a.

Undesirable effects as the space charge influence on beam formation are minimized by appropriate geometry of the extraction aperture and a following second (pulling) electrode (axial diode arrangement), which is on ground potential. Figure 3.17b shows the ion beam formation for different geometries of the extraction aperture and the geometries with a second electrode (Pierce geometry). By analytical calculations it was found that a parallel ion beam can be achieved if the surface of a circular extraction electrode is tilted relative to the beam axis by an angle of 67.5° (see Fig. 3.17b) [74, 75]. For the second electrode an optimal electrode angle can be also calculated and the arrangement of such extraction and second (pulling) electrodes with their optimized geometric design is often called the Pierce geometry of the ion beam extraction system. In the case of small ion currents, the potential $\Phi(z)$ along ion beam direction z between the extraction electrode at Φ_0 and the second electrode at ground potential decreases linearly. For high ion current densities j_{sc} in (3.2), space charge forces cause a $\Phi(z) \sim z^{4/3}$ dependence of the potential over the gap between the two electrodes as shown in

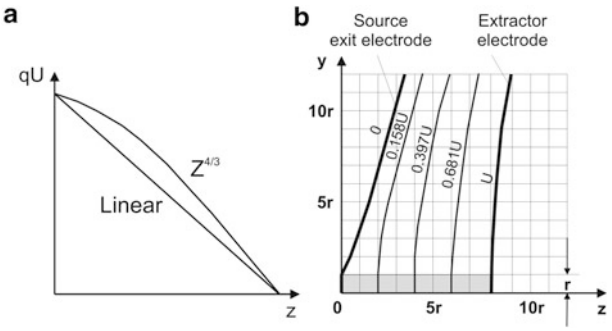

Fig. 3.18 Pierce geometry of the ion beam extraction system from the source

Fig. 3.18a. At ion currents smaller than j_{sc} in (3.2) the curve of the potential energy will be in between the two dependencies.

In the case of an ion beam of spatially limited circular cross-section in x, y-direction with the radius r corresponding boundary conditions must be taken into account: the potential inside the beam must linearly depend only on z, at the beam boundary $\Phi(r) = \Phi(z)$ and $d\Phi(r)/dx = d\Phi(r)/dy = 0$. With these conditions the Laplace equation $\Delta\Phi = 0$ can be solved for some simple geometric configurations of the two electrodes of the extraction system, for example, for the Pierce geometry shown in Fig. 3.18b. Supposing that the electrodes are extended into the beam the potential distribution in the presence of the ion beam with a current density j_{sc} gives the same conditions in the beam as in the case of an infinite beam. By introducing an exit hole into the right electrode the boundary conditions are not fulfilled furthermore and deviations from the ideal case arise. Ion beams extracted by electrodes with Pierce geometry have two important properties: the potential and the ion velocity across the beam diameter are constant, and the ion beam current is not limited although the ion current density j_{sc} is limited by space charge effects.

For further ion beam handling (manipulation) not only the extracted ion beam current density is important but also the ion source emittance ε is of great importance, which describes the ion distribution in the phase space (in spatial coordinates x, y, z and in velocity components $\dot{x}, \dot{y}, \dot{z}$). Usually, the longitudinal phase space is given by the ion energy E and energy spread ΔE and the longitudinal emittance (ε_z or ε_L) and the transverse emittances (ε_x, ε_y) are given separately. In the case of cylinder-symmetric ion beams, the transverse emittances are equal and $\varepsilon_x = \varepsilon_y = \varepsilon$. For comparison of beams with different ion energies and ion masses often the normalized emittance ε_n is introduced:

$$\varepsilon_n = \beta \cdot \gamma \cdot \varepsilon \quad \text{with} \quad \beta = \frac{v}{c} = \frac{1}{c}\sqrt{\frac{2qeU}{M_i}} \text{ and } \gamma = \frac{1}{\sqrt{(1-\beta^2)}}. \tag{3.4}$$

The measure for the ion current density per unit solid angle is the brightness B of the ion beam:

$$B\left[A \cdot (mrad)^{-2}\right] = \frac{I[A]}{\pi^2 \cdot \varepsilon_x[mrad] \cdot \varepsilon_y[mrad]} \tag{3.5}$$

In general, a high ion beam quality means low emittance and high brightness values. For the characterization of the ion beam, the emittance has to be measured at different positions along the forward direction of the ion beam. In most cases, the emittance increases with increasing distance from the ion source due to space charge effects, collisions of ions with residual gas molecules, etc. Nowadays the emittance and brilliance of ion beams extracted from different ion sources can be calculated using different computer codes (http://www.integratedsoft.com, http://www.cobham.com/home.aspx, and http://www.fieldp.com/omnitrak.html), but these calculations are often extensive and parasitic electric and/or magnetic field cannot be taken into account.

In summary, the quality of an ion source is governed by maximum extracted ion beam density, the ion charge state, and the characteristic ion beam parameters of energy spread, normalized emittance, and brightness. For different types of ion sources these performance parameters can be found, for example in [20–22, 39, 40].

3.3 Ion Acceleration

After the magnetic analyzer the ion mass separated beam is electrostatically accelerated to the desired ion energy. Usually the two components ion source and mass analyzer are at high potential whereas the ion source extraction voltage U_{ex} has to be added to the acceleration voltage U_{ac}. The ion acceleration takes place in an electrostatic acceleration tube. The tube consists of a series of cylindrical intermediate electrodes, which are connected together by high resistivity resistors leading to a linearization of the voltage drop over the tube (see Fig. 3.19). The potential distribution between the cylinders and their beam focusing behavior are determined by the design of the cylinder chain, namely by the diameter, length, the cylinder inter-distance, and the applied voltage. The velocity of an ion v ($m \cdot s^{-1}$) after passing through the potential difference U_{ac} is given by

$$v = v_0 + v_{ac} = \sqrt{\frac{2 \cdot q \cdot U_{ex}}{m}} + \sqrt{\frac{2 \cdot q \cdot U_{ac}}{m}}, \tag{3.6}$$

where v_0 is the initial ion velocity after extraction from the ion source, $q = n \cdot e$ is the net ion charge with n the charge state of the ion, and e is the elemental charge; m is the ion mass which can be expressed by the atomic mass number M as $m = 1.67 \times 10^{-27} M$. Taking into account these expressions we get

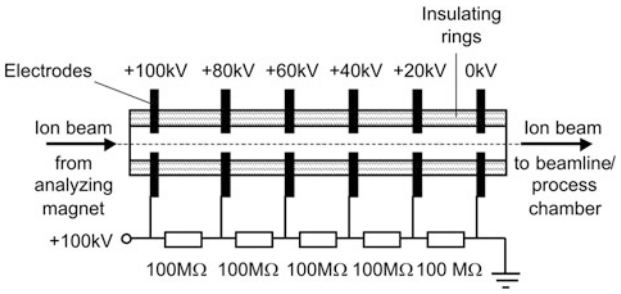

Fig. 3.19 Principal construction of accelerator columns for ion acceleration. The voltage divider distributes the potential drop equally across each of the gaps between the plates

$$v = 1.39 \times 10^4 \left(\sqrt{\frac{n \cdot U_{\mathrm{ex}}}{M}} + \sqrt{\frac{n \cdot U_{\mathrm{ac}}}{M}} \right)$$
$$= 1.39 \times 10^4 \cdot \sqrt{\frac{n}{M}} \left(\sqrt{U_{\mathrm{ex}}} + \sqrt{U_{\mathrm{ac}}} \right). \tag{3.7}$$

If ions of equal mass M but different initial velocity v_0 are accelerated the difference of their kinetic energies before and after the acceleration stage is equal and $\Delta E = \Delta E_0$ which means that the absolute energy difference of the initial state maintains after ion acceleration. Ions with different masses M_1 and M_2 have the same kinetic energy after traveling through the potential difference U_{ac}; they move in the electrostatic field with different velocities and we get

$$\frac{v_1}{v_2} = \sqrt{\frac{M_2}{M_1}} \quad \text{if} \quad E_1 = E_2 = \text{const.} \tag{3.8}$$

The energy difference ΔE is additionally increased, if the ions with the initial velocity v_0 enter the acceleration tube under a certain angle β and is given by

$$\Delta E = \Delta E_0 \cdot \sin^2 \beta. \tag{3.9}$$

Accelerator columns are usually assembled from many simple nut-shaped metallic plates insulated from one another by a short length (1–2 cm) of glass or ceramic tubes (Fig. 3.19).

The vacuum integrity is maintained by O-rings placed between each plate and tube section. In modern acceleration tubes now special epoxies are used to glue metal plates to the insulators. The insulators themselves may also be made of the same epoxy material. Each plate is electrically connected in series to the next plate resistor of 50–100 MΩ, forming a voltage divider. The total accelerating potential is supplied across this series of gaps. In modern accelerator tubes individual plates have special shapes to allow self-focusing of the ion beam. Very high vacuum inside the

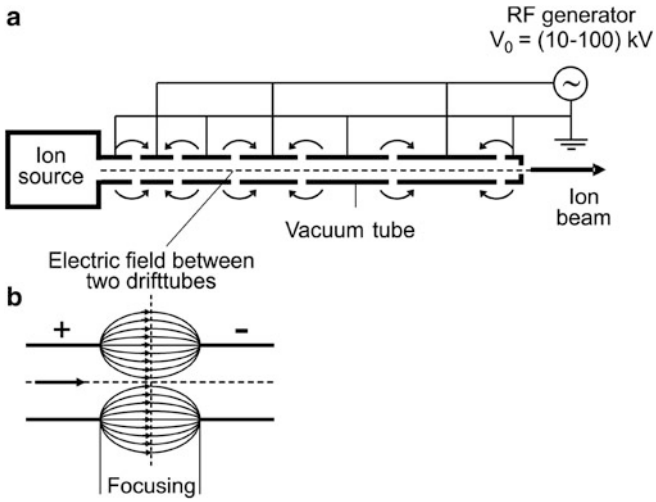

Fig. 3.20 Principle of an RF-LINAC

acceleration tube allows larger voltage drops across each gap. This results in the need of fewer gaps and can significantly reduce the overall size of the acceleration system.

The radio frequency linear acceleration (RF-LINAC) technique which was originally developed for accelerators in nuclear physics research is an alternative method to accelerate ions to relative high energies of >500 keV [76]. Recently, this technique has found application in high energy ion implanters in microelectronic industry. The principal scheme of a RF-LINAC is shown in Fig. 3.20a. The ions travel through a chain of tubes (cavities) to which a high frequency voltage ($f \sim 13$ MHz–3 GHz, $U \sim 100$–500 V) is applied in such a way that the particles meet always an accelerating potential between two tubes. In the inner part of the drift tubes, there is no electric field which exists only in the gap between the neighboring tubes on which the potential has an opposite polarity (see Fig. 3.20b).

If the ion moves through the next following tube the polarity of the electric field in the next gap has to be changed to ensure the next acceleration step. The high voltage $U = U_0 \cdot \cos(\omega_{RF} \cdot t)$ with a constant high frequency ω_{RF} applied to the tubes causes an increasing tube length in the direction of ion traveling to match the increasing particle velocity. The final ion energy is $E = n \cdot q \cdot U_0$ where n is the number of accelerating tubes. The advantage of RF-LINACS compared to electrostatic accelerators is the relative low RF voltage of 100–400 kV.

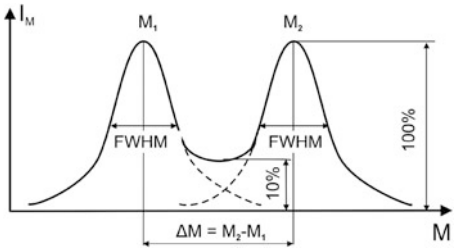

Fig. 3.21 Definition of ion mass resolution

3.4 Ion Beam Handling

3.4.1 Ion Mass Separation

The ion mass analyzing device performs the selection of the ion species of interest according to their mass and rejecting all others. The ion beam extracted from the ion source must be spatially separated into several beams according to their mass and charge state because the initial beam is a mixture of different types of ionized atoms and molecules from the source feed material. The ion mass resolution R is defined as the ratio of the ion mass M_i and the mass difference ΔM with $R = M_i/\Delta M$, where ΔM gives the smallest mass difference at which in the mass spectrum lines of equal intensity seem to be resolved. Two masses are resolved if the intensity valley between the neighboring masses is not higher than 10 % of the intensity of the mass lines (see Fig. 3.21). This means, that at a given full width half maximum (FWHM) of the lines the distance between the two maxima amounts approximately to $\Delta M \approx 2{\cdot}\text{FWHM}$, two times the FWHM of the line for the mass M_i.

The ion mass separation is usually done with an *analyzing sector magnet* (Fig. 3.22) before the acceleration stage (tube). Sector magnets have a constant mass resolution R over the full nominal mass range and are mainly determined by the focus of the ion beam at the entrance, by the width of the analyzing exit slit and the distance L between the magnet exit plane and the slit. With ion optics (e.g., by an einzel lens) before the magnet with the radius r the ion beam is usually focused to the exit slit D at the distance L and the slit width is selected in such a way that D is approximately equal to FWHM of the focused ion beam. Neighboring masses should have a minimum distance of 2D from the slit center. In this case, the mass resolution R is given by the following approximation:

$$R = \frac{M}{\Delta M} \approx \frac{L + r}{4 \cdot D}. \tag{3.10}$$

The 90° sector magnet deflects the collimated ion beam of mass M incident and leaving the magnet normal to the pole faces at the angle φ where the position of the object and the image is not important. Through an entrance slit (object in Fig. 3.22a) the ion beam enters the vacuum chamber within a magnet where the magnetic field

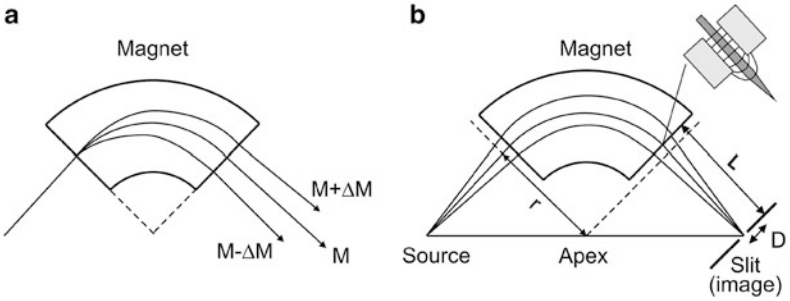

Fig. 3.22 Scheme of the basic sector magnet for mass analyzing (**a**). The higher masses are less deflected and the lower masses more. Co-linearity (Barber's rule) of sector magnet object (source), image, and magnet apex (**b**). Due to the extended magnetic field the pole faces can be shifted relative to the *dotted line* by a distance in the order of gap width of the exit slit

is perpendicular to the beam direction. The ions entering the magnet are moving now on a circular path with the radius R:

$$r = \frac{M \cdot v}{q \cdot B} = \frac{1}{B}\sqrt{\frac{2 \cdot M}{q} \cdot U_{\text{ext}}}, \tag{3.11}$$

where q and M are the charge and mass of the ion, respectively, U_{ext} is the extraction voltage, and B is the magnetic field intensity (induction). From (3.11) it can be seen that ions with different masses and equal energy are deflected to different paths. By placing a slit at the image plane of the magnet only one mass to charge ratio M/q will have the correct radius of curvature to exit the mass separator. Usually, the magnetic field is everywhere homogeneous and perpendicular to the beam direction and the entrance slit (object) and the exit slit (image) are symmetric. In the case of the symmetric arrangement where the ion beam enters and leaves perpendicular a 90° magnet (see Fig. 3.22) the separation D for a mass difference $\pm\ \Delta M$ is given by [10, 11]:

$$D = \pm\frac{r \cdot \Delta M}{2M}\left(1 - \cos\varphi + \frac{L}{r} \cdot \sin\varphi\right), \tag{3.12}$$

where r is the radius of the analyzing magnet, L is the length from the magnet to the image plane (exit slit), and φ is the angle between magnet entrance plane and exit plane (see Fig. 3.22b). Two masses are resolved when the distance D is larger than the width of ion beam (entrance slit) plus the width of the exit slit. The best resolution is achieved if the radius r is large and the mass M small. Additionally, the sector magnets have focusing properties as shown in the inset of Fig. 3.22b for usually divergent beams and objects (sources) of finite size in the image plane. Special geometric design of the pole faces is sometimes done to improve the focusing. Concerning Barber's rule [77] the object (source), its focused image,

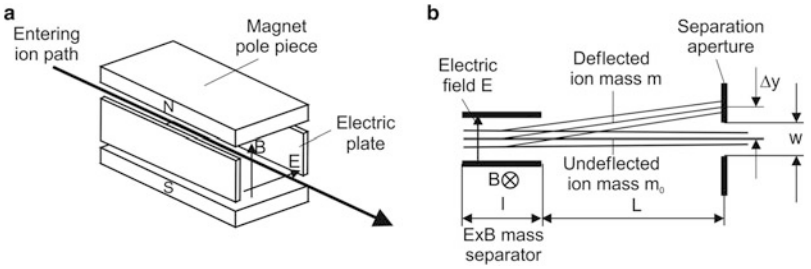

Fig. 3.23 ExB velocity analyzing mass separator. (**a**) Principal buildup, (**b**) ion deflection by an ExB filter

and the apex of the magnet lie in a straight line. For example, the dotted line in Fig. 3.22b illustrating Barber's rule corresponds to an apex which is larger than the actual magnet. The real magnet field extends outside the magnet gap as shown in the inset of Fig. 3.22b allowing the outward displacement of actual pole faces parallel to themselves by an amount which can be readily calculated for the given magnet using Barber's rule.

Most ion mass filters applied in ion implanters and accelerators have a radius r of a meter or less, an angle of $\varphi = 90°$, and a distance L of a meter or more. Neutral particles from the ion source are not deflected and therefore separated by sector analyzing magnets. Generally smaller magnets used in ion implanters have a resolving power $M/\Delta M$ of about 70.

The second type of ion mass analyzers is the so-called *Wien- or ExB-filter* [78, 79], which is mainly used for low current ion beams (<100 μA), for example in focused ion beam (FIB) tools equipped with LMIS ion sources. As shown in Fig. 3.23a in a Wien filter electric and magnetic fields are perpendicularly arranged.

If the forces of both fields acting on a charged particle are equal, which means $q{\cdot}E = q{\cdot}v{\cdot}B$, where E is the electric field strength, v is the particle velocity, and B is the magnetic field strength, it will be un-deflected and therefore separated by the exit slit. Ions with masses $M \pm \Delta M$ will be deflected up- or downwards, respectively (see Fig. 3.23b). At small angle deflections in uniform E and B fields the displacement of ions with the mass M in y-direction can be described by the following analytical expressions [79]:

$$\text{electrical deflection: } y_e = -\frac{E}{2U_{accel}} \cdot l\left(\frac{l}{2} + L\right), \tag{3.13}$$

$$\text{magnetic deflection: } y_m = \sqrt{\frac{q}{2M}} \cdot \frac{B}{\sqrt{U_{accel}}} \cdot l\left(\frac{l}{2} + L\right), \tag{3.14}$$

with q the charge state of the ion, l the length of the deflection system, L the distance from the system exit to the slit, and U_{accel} the ion acceleration voltage from the ion source, as shown in Fig. 3.23b. From (3.13) and (3.14) it can be deduced that the ion

with an energy of $E_0 = q{\cdot}U_{\text{accel}}$ will be not deflected and passes through the system if the fields satisfy the following equation:

$$\frac{E}{B} = \sqrt{\frac{2q \cdot U_{\text{accel}}}{M}}. \tag{3.15}$$

Small deviations of the ion mass $M \pm \Delta M$ and of the ion energy $E \pm \Delta E = q(U_{\text{accel}} \pm \Delta U_{\text{accel}})$ result in the deviations of the ion trajectories from their undeflected path, which are:

$$\text{for mass dispersion: } D_{\text{M}} = \frac{E}{2U_{\text{accel}}} l\left(\frac{l}{2} + L\right)\frac{\Delta M}{M}, \tag{3.16}$$

$$\text{for energy dispersion: } D_{\text{e}} = \frac{E}{2U_{\text{accel}}} l\left(\frac{l}{2} + L\right)\frac{\Delta U_{\text{accel}}}{U_{\text{accel}}}. \tag{3.17}$$

The mass separation and resolution of the ExB filter can be changed by changing the electric field E and the magnetic field B. In modern FIB tools usually the magnetic field is first fixed in a certain range and the isotope masses of a given element are selected by tuning the electric field. In existing FIB systems parallel plate configurations are used which are designed using uniform electric and magnetic field approximations of (3.16) and (3.17). Other filter types are described and numerically simulated in [79]. It was found that the optimum geometry is achieved by slightly curved inner surfaces of the electric field electrodes and the magnetic pole pieces. Nevertheless, estimations of small deflections, mass and energy dispersions for ExB mass filters of square geometry can be easily done by using (3.13)–(3.17).

A disadvantage of the ExB filter is that neutral particles in the ion beam are not selected and travel unhindered through the filter to the target. For avoiding neutral particles an additional electrostatic beam deflection (neutral trap) is necessary to be built into the system.

3.4.2 Ion Beam Focusing

Thermal velocity distribution, convex plasma sheets at the source exit, and repulsion between ions cause divergent ion beams extracted from the ion source. In many applications ion beam focusing is carried out by electrostatic focusing with the extraction electrodes (so-called extraction assembly) close to ion source exit and before the acceleration stage. If necessary, further ion beam focusing elements are introduced also after mass separating elements. As focusing ion optical elements mainly electrostatic lenses are used which can be designed as single lenses (einzel lenses), quadrupole lenses, or multiple arrangements of them (doublets, triplets, etc.). Detailed description of different lens types with their ion-optical properties

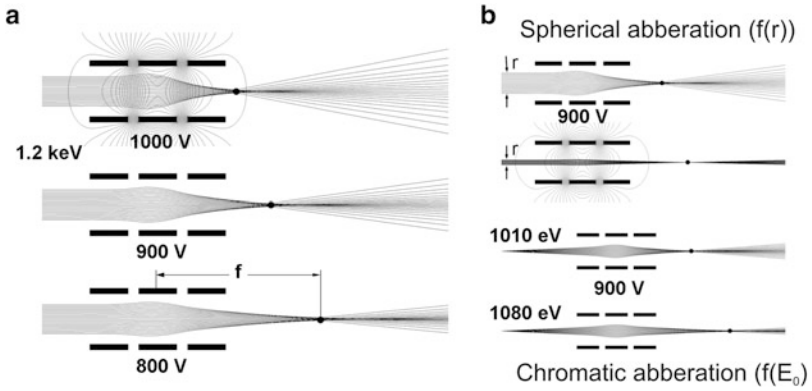

Fig. 3.24 Principal buildup of an electrostatic einzel lens and manipulation of the focus length f by the potential (voltage) applied to the middle electrode (**a**). Spherical and chromatic aberrations of an electrostatic einzel lens (**b**)

can be found in [77, 80]. Furthermore, the focusing behavior of electrostatic fringe fields at plates with central holes has been applied to certain ion beam focusing.

The *electrostatic single lens (einzel lens)* usually consists of three symmetric tube electrodes where the middle electrode is at high positive lens potential and the left and right electrodes are grounded (Fig. 3.24a). The resulting electric field distribution between the electrodes focuses the ion beam without changing the ion energy. The focusing is accomplished through the manipulation of the electric field by changing the potential (voltage) applied to the middle electrode (Fig. 3.24a). Because the lens elements are symmetric the ions will regain their initial energy on exiting the lens although the velocity of the outer particles will be altered so that they converge on to the axis. This causes the outer particles to arrive at the focus intersection slightly later than the ones that travel along a straight path as they have to travel an extra distance. The change of the radial velocity of the ion passing between any pair of cylinders of the lens can be described by (3.18):

$$\Delta v_{\mathrm{r}} = \int \frac{q \cdot E_{\mathrm{r}}(r,z)}{M \cdot v_{\mathrm{z}}} \mathrm{d}z, \tag{3.18}$$

where z is the central lens axis in ion beam direction and r is the radial direction normal to z. If the lens is constructed with cylindrical plates, the field is symmetrical around z. $E_{\mathrm{r}}(r, z)$ is the magnitude of the electric field in the radial direction for an ion at a particular radial distance and distance across the lens gap, M is the ion mass, v_{z} is the velocity, and q is the charge of the ion. The integral occurs over the gap between the plates. This is also the interval where the lensing occurs. The pair of plates is also called an electrostatic immersion lens, thus an einzel lens can be described as two or more electrostatic immersion lenses. Solving the equation above twice to find the change in radial velocity for each pair of plates can be used to calculate the focal length of the lens. As shown in Fig. 3.24b the focus

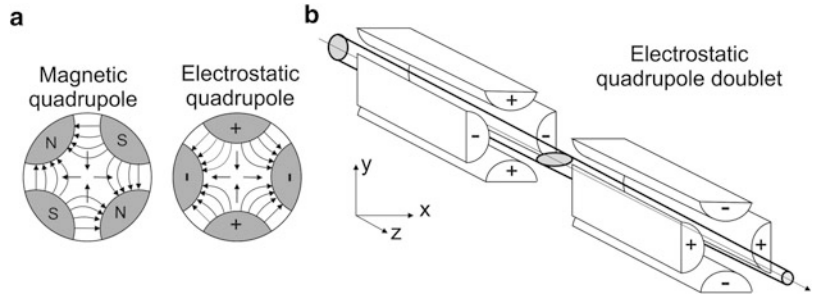

Fig. 3.25 (**a**) Principal buildup of electrostatic and magnetic quadrupole lenses. (**b**) Arrangement of two singlet quadrupole lenses rotated around beam direction z by 90° forming a quadrupole doublet

length f of the beam depends on the radius r of the incoming ion beam [$F = f(r)$, spherical aberration] and on the ion energy E_0 [$F = f(E_0)$, chromatic aberration] at the entrance of the lens.

The electrostatic and magnetic *quadrupole lenses* consist of four identical poles with length dimensions in the order of the distance between the poles (Fig. 3.25a). The opposite pole pairs have the same polarity which means that quadrupole lenses focus the incoming ion beam only in one direction (x) perpendicular to the ion beam direction z (Fig.3.25b). In direction y the beam will be defocused. By arranging a second singlet quadrupole in such a way that the x–y directions are rotated by 90° relative to the first quadrupole focusing in both x- and y-directions takes place and a point-like focusing will be achieved (see Fig. 3.24b). In magnetic quadrupole lenses mostly four electromagnets are used enabling the manipulation magnetic field strength for focusing.

3.4.3 Ion Beam Scanning

The scanning of the ion beam with a usual diameter of some mm to cm in two directions (xy-direction) mainly in ion implantation tools is necessary to distribute the ion fluence homogeneously over large sample areas at the final target chamber. The most simple method for xy-scanning is the electrostatic deflection of the ion beam in these two directions, which is applied to low and medium ion currents ($I < 1$ mA). The deflection of the ion beam by a pair of electrostatic plates is illustrated in Fig. 3.26.

For the periodic transverse electric field a linear and symmetric sawtooth voltage U_d is applied to the two plates having a length of L and a plate distance of d. The scan width x of the ions accelerated by the voltage U_a at the sample distance l from the center of the plate pair is given by

$$x = 2 \cdot l \cdot \tan\alpha \approx \frac{l \cdot L \cdot U_\mathrm{d}}{2 \cdot d \cdot U_\mathrm{a}} \tag{3.19}$$

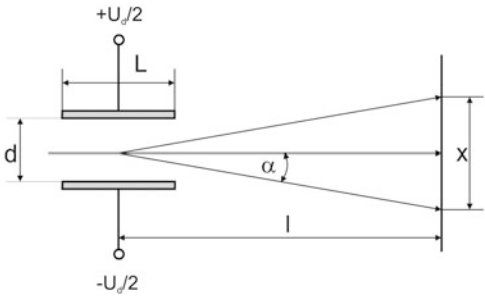

Fig. 3.26 Illustration of the ion beam deflection by single electrostatic plates (plate capacitor)

For two-dimensional electrostatic scanning using two crossed pairs of plates, the *x*- and *y*-frequencies in a usual rage of 1 Hz–10 kHz must have an irrational ratio to avoid Lissajous images leading to inhomogeneous ion fluence distribution over scanned target area. Large frequency differences (e.g., 10 Hz and 1 kHz), as well as very small differences (e.g., 999 Hz and 1 kHz) ensure satisfying homogeneous fluence distribution over large target areas. In every case the scan process must secure that a high number of scan lines in close distance to each other covers the target surface. Homogeneous ion implantation of silicon wafers needs a certain over-scan behind the wafer boundary of about $3 \times R$, where R is the beam diameter. At these conditions the turn-back point of the scanned beam, where the ion fluence is significantly increased is located sufficiently outside of the irradiated sample surface. The distance between two scan lines must be in the order of $\sqrt{\sigma}$, where σ is the standard deviation of the Gaussian ion profile. With increasing deflection angles the ion incidence angle on the target surface at a given distance l also increases. Because for ion irradiation of crystalline samples this angle often has to be smaller than a critical angle of about 1° for ion channeling in the crystal (see Sects. 3.3 and 4.1), electrostatic beam scanning systems using two sequential pairs of plates for each scan direction have been applied. In this case the ion beam is scanned parallel to normal beam incidence over the full sample surface in both *x*, *y*-directions.

An additional demand for low deflection angles arises from tilting of crystalline samples relative to the surface normal to avoid ion beam channeling. Both tilt angle of usually ~7° and deflection angle cause an inhomogeneous areal ion density (fluence) over the target area. Figure 3.27 shows an example of the fluence inhomogeneity over a target (silicon wafer) of 100 mm diameter tilted by 7° to the surface normal and located in a distance of 1 m from the center of the last pair of deflection plates [81].

The vacuum conditions before and over the length of the electrostatic *x*, *y*-scanning system have additional influence on the areal ion density (fluence) distribution on the target surface due to charge exchange and neutralization during collision of ions with atoms and molecules of the rest gas in the vacuum. The neutralized particles must be selected from the ion beam, otherwise inhomogeneities and

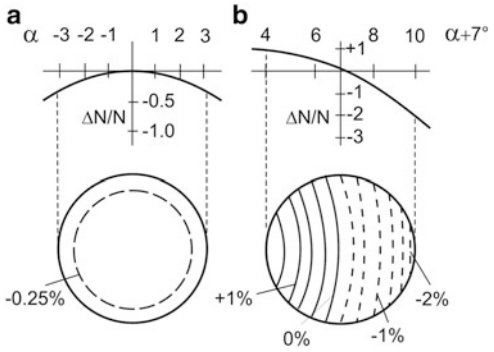

Fig. 3.27 Fluence inhomogeneity at electrostatic ion beam x, y-scanning. (**a**) Target surface perpendicular to beam incidence, (**b**) target tilted by 7° relative to normal beam incidence

nonacceptable errors of the absolute ion fluence will arise. The ratio between the fluence of neutrals ΔN^0 and single-charged ions N^+ is given by [82]:

$$\frac{\Delta N^0}{N^+} = 2.48 \times 10^{14} pL\sigma_{10}, \tag{3.20}$$

with p the vacuum pressure, L the ion path length, and σ_{10} the cross-section for neutralization of single charge ions, which is in the order of 10^{-16} cm^2 and depends on the ion velocity and therefore on the ion mass and acceleration voltage. As can be seen from (3.20) the amount of neutral particles can be reduced by lowering the pressure in the vacuum to $p < 10^{-5}$ Pa and by implementation of a so-called neutral beam trap, which additionally deflects only the ionized particles as shown schematically in Fig. 3.28.

The value of cross-section σ_{12} for the formation of double-charged ions is in the same order as σ_{10} and has to be taken into account only in the case of high vacuum pressure ($p > 10^{-3}$ Pa) due to increasing errors in the ion current measurement.

Magnetic deflection systems increasingly are used only in modern ion implantation equipment with ion currents of high current density and large beam scan areas up to 400 × 400 mm^2 [83]. In the latter case, hybrid scan systems combining a beam scan only in one direction and a one axis mechanical wafer scan are applied. In this case, the ion beam is scanned and collimated in one plane using either electrostatic or magnetic fields to produce a parallel beam. The wafer is then mechanically scanned in an orthogonal direction to achieve the uniform doping over the wafer. Different scan system in modern ion implanters will be described in Sect. 3.5.

3.4.4 Ion Beam Current Measurement

The most common way to measure the ion current is by using Faraday cups collecting the ions of an ion beam in an electrically insulated cup, and the charge

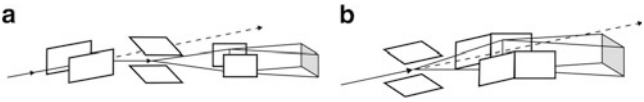

Fig.3.28 Gating of the neutral beam by electrostatic deflection of charged particle beam using separate deflection plates (**a**) or an superimposed constant potential at one plate pair (**b**)

is measured by a calibrated resistor of 10^{10}–10^{12} Ω in an appropriate electronic circuit (current integrator). When an ion beam hits an electrically insulated metal collector it gains a small net charge while the ions are neutralized. The metal can then be discharged to measure a small current equivalent to the number of impinging ions. Essentially the Faraday cup is part of a circuit where ions are the charge carriers in vacuum and the Faraday cup is the interface to the solid metal where electrons act as the charge carriers (as in most circuits). By measuring the electrical current (the number of electrons flowing through the circuit per second) in the metal part of the circuit, the number of charges being carried by the ions in the vacuum part of the circuit can be determined. For a continuous beam of ions with an ion current I and a given measuring area A, the number of ions per unit area (areal density or fluence) in a time t is given by

$$N = \frac{1}{A}\int_0^t \frac{I}{q}dt = \frac{t \cdot I}{q \cdot A} \tag{3.21}$$

where $q = n{\cdot}e$ is the charge carried by the ion with n the charge state and e the elementary charge. Thus, for single charge ions a measured current of 1×10^{-9} A corresponds to about one billion ions striking the Faraday cup with an area of 1 cm^2 each second.

The error of ion current measurement with Faraday cups and therefore of the absolute ion fluence determination is mainly influenced by secondary electrons and secondary ions of both polarities which are created when the ions impinge the surface. The measured net current is therefore

$$I_m = I_i^+ + I_{se}^- + I_{si}^- - I_{si}^+. \tag{3.22}$$

For suppression of secondary electron current I_{se}, the Faraday cup consists of a negatively biased electrostatic SE suppression electrode, cylinder suppressors (Fig. 3.29a), or a magnetic SE suppressor (Fig. 3.29b). By using cylinder suppressor both the secondary electron current I_{se}^- and the current of negatively charged secondary ions I_{si}^- are suppressed. To minimize the current of positively charged secondary ions, I_{se}^+ cup materials with low sputtering coefficients have to be selected. The voltage for negative biasing of the suppressor electrode depends on the geometric design of the Faraday cup and must be measured experimentally. Usual values are −(60–200) V. For magnetic SE suppression magnetic fields in the order of ~10^{-2} T are used. Modern Faraday cups with magnetic shielding at the

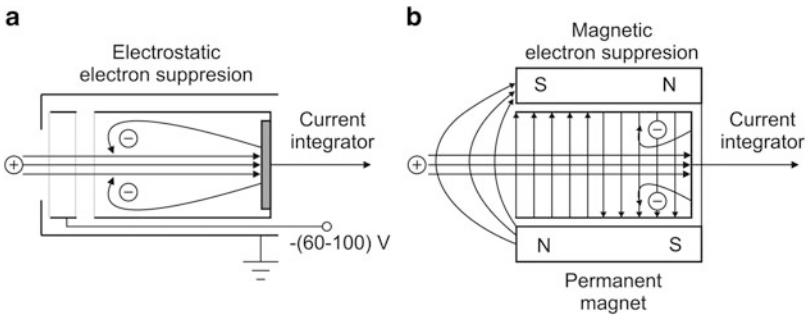

Fig. 3.29 Faraday cups with electrostatic (**a**) and magnetic (**b**) suppression of electrons

entrance of the collection cup provide accurate measures of the net current flux. However, they do not measure the charge state of individual ions and do not count atoms which arrive as neutrals at the Faraday cup and the target surface. As mentioned the charge state of ions can be changed as a result of collisions with residual gas atoms and molecules in the beam line and the target chamber. Whether an ion picks up an electron and becomes neutral or losses an electron and becomes more positively charged depends mainly on the ion energy. For ion energies less than ≈500 keV (slow ion velocity), neutralization is more likely, whereas for fast ions with energy >500 keV up to several MeV collisions with gas atoms are more likely to result in the loss of an electron from the ion (known as charge stripping). In the latter case, ions with higher positive charge state are created. Both effects cause ions with altered charge states striking the Faraday cup collector, and this leads to errors in the measured ion fluence because the fluence is inferred by the charge collected by the Faraday cup assuming that each ion has the specific charge state +1. Therefore, neutralization of ion leads to a lower ion fluence and electron stripping to a higher ion fluence measured by the Faraday cup compared to the real ion fluence on the target surface. The influence of other disturbing effects on the accuracy of ion current measurement, for example heating up of the cups by high beam power, leakage currents due to deterioration of insulating parts inside the cup by sputtering or high temperatures, etc. as well as other methods of direct ion beam current measurements can be found in [22].

The ion beam measurement in analogous mode using Faraday cups is related to the characterization of primary ion beams mainly in ion implantation but also in high energy accelerators. Mostly used Faraday cups are limited in their sensitivity of ion current measurement ($I \sim 10^{-12}$ A) and in their dynamic range of ~10^5, which depends mainly on the electronics used for charge, current, or voltage measurements.

3.4.5 Ion Detection (Detectors, Spectrometers)

Ion detection measures the rate of ions directly, i.e., the direct counting of the number of ions appearing at the detector over a certain period of time. Two categories of ion detection systems can be distinguished: ion detectors and ion spectrometers. Ion detectors provide information, such as time or position and ion energy, often with high efficiency and resolution, without preselection of the incident particles. Spectrometers disperse or select the incident ion beam according to ion mass or energy by using electrostatic and/or magnetic separation before detection by different kinds of ion detectors or multifunctional detection systems that can carry out high resolution measurements of several properties of the incident ions.

In all ion detector types the ions are detected based on their interaction with detector material. Penetrating of the ion into the detector material causes it to give away its energy through electronic and nuclear energy deposition.

Solid state detectors are most often based on the semiconductor materials of silicon and germanium. The advantage of semiconductor radiation detectors is that they can be built much smaller compared, for example, to gas ionization chambers or szintillator counters. The density of silicon and germanium is by a factor of ~10^3 higher as that for gases, and therefore the particle energy deposition in these materials is much more concentrated in a small detector volume. For ion detection mostly silicon detectors are used whereas germanium detectors are more favored for photon detection (X- and γ-rays).

The basic principle of a semiconductor detector is a reverse-biased pin-diode. The pin-diode represents a pn-junction with an intrinsic (very low doped) interlayer. The reverse bias voltage applied to the pin-diode, causes in the intrinsic region a zone free of charge carriers (depletion layer), representing the active detector volume. The principal structure of a silicon particle detector is illustrated in Fig. 3.30a. A high resistivity silicon substrate of *n*-type conductivity, usually phosphorous doped with a low concentration of about $N_D \approx 10^{12}$ cm^{-3}, has a highly p^+-doped thin layer on one side and a highly n^+-doped layer on the other side (both ion implanted). The surface boundary of the pn-junction is passivated by silicon dioxide (SiO_2). Both layers are electrically contacted by evaporated aluminum layers.

As shown in Fig. 3.30b the particles penetrating the active detector volume generate electron–hole pairs, which number is proportional to the energy E_0 of the particle. The number of electron–hole pairs N is given by $N = E_0/\varepsilon$, where $\varepsilon = 3.62$ eV is the necessary average electronic energy deposition for the creation of an electron–hole pair in silicon with a statistical distribution of $\Delta N = \sqrt{F \cdot N}$ with $F \approx 0.1$ the Fano factor for silicon. For semiconductors, ε is essentially independent of the ion energy. For example, an α-particle (He^+ ion) with an energy of 3.6 MeV generates ≈10^6 electron–hole pairs along its penetration path in the silicon material. The electric field of about 4–5 kV cm^{-1} in the depletion region separates the electrons and holes which afterwards drift to the corresponding collecting electrodes. The depth of the depletion layer is given by

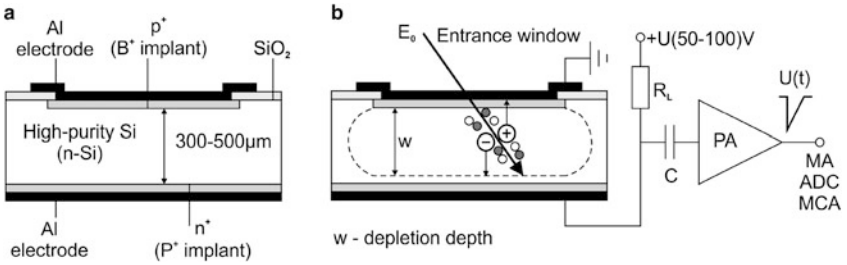

Fig. 3.30 Principal structure and operation of a silicon particle detector (**a**) and charge generation and collection (**b**)

$$w = \sqrt{\frac{2 \cdot \varepsilon_0 \cdot \varepsilon_{Si}}{q \cdot N_D}(U + U_{bi})} \approx \sqrt{\frac{2 \cdot \varepsilon_0 \cdot \varepsilon_{Si}}{q \cdot N_D} \cdot U}, \tag{3.23}$$

where ε_0 and ε_{Si} are the absolute and relative dielectric constants, respectively, q is the elemental charge, N_D is the donor (phosphorous) concentration of the silicon substrate, and U reverse bias voltage applied to the detector. The so-called built-in voltage U_{bi} is very small compared to the detector voltage U and can be neglected. For the extension of the depletion layer over a 300 µm thick detector substrate (full depletion) with a doping concentration of $N_D = 10^{12}$ cm^{-3} a detector reverse bias of 70 V will be necessary.

As shown in Fig. 3.30b the resulting charge pulse is coupled through a capacitor into a preamplifier transforming it into a voltage pulse both of which are proportional to the energy E_0 of the detected ion. Silicon particle detectors are mainly used in spectroscopic methods where light ions (H^+, He^+) with energies of several MeV have to be detected. The energy resolution for these particles $\Delta E/E_0$ with ΔE the full width at half maximum (FWHM) is for modern silicon particle detectors very high and in the order of (0.2–0.3) % (e.g., $\Delta E \approx$ 10–15 keV for α-particles with an energy of 5.5 MeV). The given detector energy resolution ΔE is the square root over the sum of different contributions:

$$\Delta E = \sqrt{\Delta E_{stat}^2 + \Delta E_{nc}^2 + \Delta E_w^2 + \Delta E_{el}^2 + \ldots}, \tag{3.24}$$

where ΔE_{stat}^2—statistics of charge carrier generation, ΔE_{nc}^2—energy straggling due to nuclear stopping, ΔE_w^2—influence of the detector window (p^+-doped dead layer), and ΔE_{el}^2—electronic noise (of detector and preamplifier).

Silicon particle detectors are limited in their counting rate of $<10^5$ particles/s and to light ions. With increasing ion mass ($M_i > 12$, carbon) the rate of defect generation in the Si crystal active detector volume increases leading to increased detector reverse current and noise and finally to a decreased detector energy resolution [84].

The highly developed standard silicon planar technology permits the fabrication of monolithically integrated multiple detector devices, such as strip detectors and

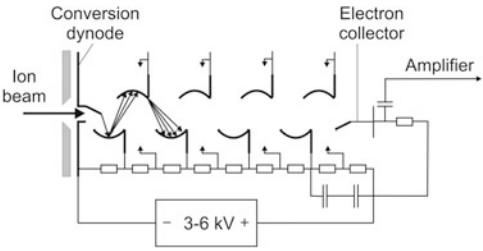

Fig. 3.31 Operation principle of an electron multiplier tube (EMT)

charge-coupled devices (CCDs), providing high spatial resolution of 5–10 μm [85]. Silicon particle detectors have been also designed as continuous position sensitive detectors (PSDs) which are often used in high resolution particle spectrometers [86]. PSDs are then located in the focal plane of a magnetic or electrostatic ion analyzer where they measure the ion energy and the incidence position of the ion with a position resolution of about 0.3 mm. This allows the determination of both the ion energy and the ion mass as well as the energy and the charge state of the detected ions in magnetic and electrostatic spectrometers, respectively. The combination of an ultrathin ion transmitting ΔE silicon detector (thickness of 10–30 μm) together with a common silicon particle detector in a $\Delta E-E$ telescope allows the determination of the ion mass M_i (or atomic number Z) together with the ion energy E.

All kinds of *electron multiplier tubes (EMT)* first use the ions to generate electrons which are then amplified. The electron multiplier tube consists of a series of dynodes maintained at increasingly positive potentials of up to several 10^3 V (Fig. 3.31). The impact of the incoming ion generates secondary electrons in the first dynode. The number of secondary electrons depends on different factors (ion energy and mass, surface material of the first dynode, etc.). As dynode surface layers mostly oxides, such as MgO, BeO, and Al_2O_3 are used. The electric field between the dynodes accelerates the emitted electrons to the second dynode where each accelerated electron generates about 2–4 lower energy electrons. Finally, over all dynodes one gets an electron emission with a high gain up to ~10^6 resulting in a high sensitivity of these detectors.

In EMTs each ion produces short electron pulses which are detected by the electron collector and subsequently amplified and counted. The number of electrons after the final dynode is proportional to efficiency of electron generation at the first dynode. The gain can be varied by adjusting the voltage applied to the EMT. At high gains and count rates the EMP response often becomes nonlinear. The first dynode can be damaged by ions and tends to degrade over time. Another disadvantage of EMPs is the need of shielding against magnetic and electric fields.

The *single channel electron multiplier or channeltron* shown in Fig. 3.32 exhibits a small horn-shaped, continuous electron multiplication tube, which can be small enough to substitute Faraday cups [87]. To the entrance of the channeltron

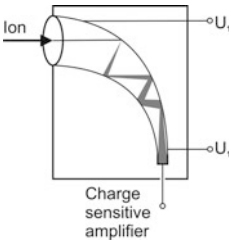

Fig. 3.32 Schematic buildup of a single channel electron multiplier or channeltron

a high voltage of −(1–3) kV is applied to the inner continuous resistive surface layer which acts as an electron emissive material (thermally treated lead glass).

Ions striking the channeltron create secondary electrons, which are gained by an Avalanche effect up to a typical factor of ~10^6 to form the final current pulse of 10^7–10^8 electrons for the following charge sensitive amplifier which is sufficient enough for single ion counting. The gain is, in general, a function of the secondary emission coefficient (k_{se}) of the glass, the applied voltage (V), and the length-to-diameter ratio (l/d) of the tube [88]. Counting rates up to 10 MHz can be achieved with a time resolution of a few ns. The detection efficiency is a function of both ion energy, more properly, ion velocity at the point of impact on the secondary emitting surface, and ion mass to charge ratio (m/q). Channeltrons have relative high ion detection efficiencies of up to 80 % for ions with energies >3 keV. They are the premier detectors used in quadrupole mass spectrometers. The channeltron suffers many of the same problems as EMTs.

The *multichannel plate (MCP)* consists of an array of 10^4–10^7 miniature electron multiplying channels arranged each parallel to one another and embedded in a glass substrate (Fig. 3.33). The diameter of each channel and the channel length (channeltron thickness) are in the order of 5–25 μm and 0.5–1.0 mm, respectively, with an overall diameter of the channeltron between 18 and 100 mm [87]. The matrix of the glass channel surfaces is specially treated to optimize the secondary electron emission characteristics.

The glass material (lead glass) has a high resistance and a large secondary electron yield. During heat treatment of this glass at 400 °C in hydrogen atmosphere the lead is reduced. Some part of lead evaporates and the rest forms lead nanoclusters in the near-surface region, which are assumed as reason for the high secondary electron yield. To the channel matrix a high voltage U_0 is applied between the front (entrance) and the back (output) side both covered with electrical metal contacts to form a continuous electric field $E = U_0/l$ inside the channels with the length l for accelerating the generated secondary electrons. For optimal particle detection all channels are tilted by ~8° relative to the channeltron entrance surface normal. In ion detection system single channeltrons with a gain of 10^4 or for increasing the gain up to 10^8 a stack of two (Chevron assembly) or three channeltrons (z-stack assembly) can be arranged [89]. Channeltrons can achieve very fast response times in the sub-ns region. Advantages of microchannel plates are: (1) fast response, because of short distance travel of the electrons (1–2 mm) and

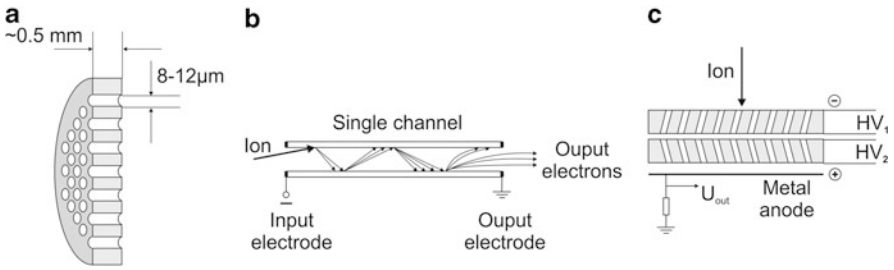

Fig. 3.33 Structure and dimensions of a multichannel plate (**a**), detector principle (**b**), and Chevron assembly of two MCPs (**c**)

the high electric field (1–20 kV cm^{-1}), the transit time is extremely short (pulse duration $\approx$ 0.2 ns, response time $<$ 200 ps); (2) insensitivity to magnetic fields, because of the short travel, high electric field, and the constraint imposed by the microchannels; (3) spatial resolution of ~10 µm due to honeycomb structure of the MCP conversion of the ion impact position on the cathode into a corresponding electron image on the anode. Spatial information can be recovered by using patterned pixel anodes [90] or CCD imaging devices [91] or anodes with charge integrated read-out structures (e.g., resistive anode encoder, wedge, and strip) [92]. However, MCPs also have limitations in application to ion beam detection: (1) limitations on count rate and linearity in the pulse mode due to the inherent limitation on the average current density at the output to a few µA cm^{-2} and the long recovery time per channel; (2) limitations of useful life, because of large total surface (hygroscopic!) which makes it difficult to outgas completely; internal electron bombardment therefore generates ions that bombard the cathode and quickly reduce sensitivity.

Gas ionization chambers are one of the oldest and most versatile types of ion detectors [93]. The absorbed energy deposited in a gas by ions is proportional to the charge Q produced in the gas by ionization of the gas atoms or molecules. In any practical case the charge Q' that is collected and measured by an electrometer circuit is less than Q, because of recombination of some positive ions and negative electrons within the gas. The detector assembly consists of a power supply to two electrodes in a chamber filled with gas. Depending on the geometry of the ionization chamber the ionization track can be perpendicular or parallel to the electric field (Fig. 3.34a).

The chamber has a very thin entrance window which can be easily penetrated by high energy ions with only a small energy loss. The window can be made from a mylar foil [thickness (0.3–1.0) µm] or from a very thin silicon nitride foil [thickness (30–100) nm] [94]. As ions pass through the gas that fills the chamber, they cause ionization and the formation of electron–ion pairs formed along the incident ion's

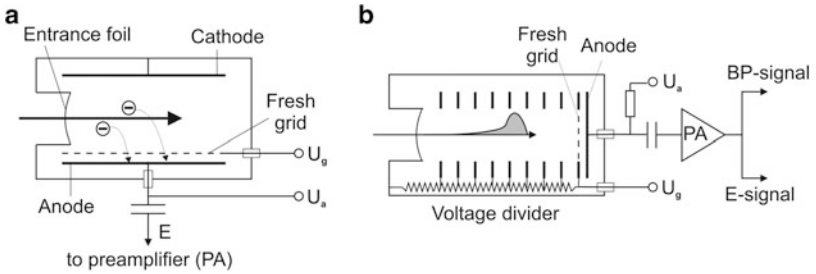

Fig. 3.34 Principle of gas ionization chamber. (**a**) Conventional gas ionization chamber and (**b**) Bragg ionization chamber (BIC)

path. The electrons and ions drift apart in the electric field inducing corresponding charges at the electrodes. The electric field strength is chosen to be low enough in order to exclude secondary ionization in the gas. Most often only the charge induced by electrons at the anode is used for ion energy determination. It is important to screen the anode from positive ions by the so-called Frisch-grid making the electron induced charge signal independent of the track position. The number of electron–ion pairs created in a given volume of the gas depends on the type of gas as well as on the kind and energy of ions. For example, the number of charges created by a He^+ ion with the energy $E_0 = 5.5$ MeV is given by $N = E_0/\varepsilon$ where ε for mostly used gases (noble gases Ar, Kr, Xe, methane, propane, isobutane) is in the order of (20–40) eV and amounts to (1–3) $\times$ 10^5 charges. Most commonly, gas chambers used for ion detection are operated in the "ionization" or "saturation" mode [95] where the number of electrons generated by ionization is proportional to the amount of electronic energy deposited by the ion. The generated electrons drift towards the anode creating a measurable charge pulse or electrical current. Ionization chambers can be built with large solid angles, their energy resolution for heavy ions is better than that of solid state detectors, and particle identification (atomic number Z or ion mass M) can easily be deduced from the measured electrical signal.

A special kind of the gas ionization chamber is the so-called Bragg ionization chamber (BIC) [96, 97] allowing simultaneous measurement of the ion energy E and determination of the ion species (atomic number Z or ion mass) by only one detector.

The BIC detector shown in Fig. 3.34b has an additional applied electric field parallel to the incident particle direction and a sufficient gas pressure to stop it. This last property allows the determination of the range of particles in the detection medium and its total energy E. The nuclear charge Z of the particle can be obtained by determining the portion of the energy that the particle has lost over a given path length and the spatial distribution of the specific ionization dQ/dx produced along the path x of the particles in the gas (the so-called Bragg curve). dQ/dx can be transformed into a time depending charge dQ/dt collected at the anode. The total charge is related to the particle energy E and the maximum value of dQ/dx, i.e., the

Bragg maximum, to the atomic number Z. Projectiles with different nuclear charges Z have different specific ionization at their Bragg maxima E_B. For isobars, the ratio of their range is equal to their Z^2 ratio.

3.5 Ion Implantation Systems

Ion implantation is a low-temperature technique for the introduction of impurities into a solid material and offers more flexibility than thermal diffusion. For example, in contrast to thermal diffusion the concentration of introduced impurities can be easily increased over the solubility limit of the impurity in the host target matrix, which opens new application fields of ion implantation. In ion implantation, impurity atoms are volatilized, ionized, accelerated, separated by the mass to charge ratios, and directed at a target. The atoms enter the solid target, collide with the host atoms, lose energy, and finally come to rest at some depth within the solid. The average penetration depth is determined by the impurity, the substrate material, and acceleration energy. Ion implantation energies range from several hundred to several million electron volts, resulting in ion distributions with average depths from 1 nm to 100 μm. The fluence can range from 10^9 to 10^{18} ions cm^{-2}. Concerning the wide energy and fluence ranges different kinds of ion implantation tools have been developed: low energy and high energy ion implanters and low current and high current ion implanters. This development in the last 50 years was and is furthermore mainly driven by the microelectronic industry. When ion implanters began to be widely used in the fabrication of integrated circuits in the early 1980s two distinct types were commercially offered:

- *Medium-current implanters* with ion currents from a few μA up to ~1 mA, which operate over an ion energy range of 10–200 keV
- *High-current implanters* with ion currents from a few 100 μA up to 30 mA, which can operate at maximum ion energies from 80 to 200 keV

With moving of integrated circuit technology toward deep submicrometer feature sizes the implanter architectures were driven to divide the functionality in the following way according to their useful energy range:

- *Low energy implanters* providing high ion currents between 1 and 20 mA in the energy range 0.2–80 keV
- *High energy implanters* with ion currents from 10 μA up to 1 mA in the energy range of 0.5–3.0 MeV

There exist several books [13, 98, 99] and review articles reflecting this development and describing the main application of ion implantation for semiconductor doping [83, 100–103]. The advantages of ion implantation for application in ion beam processing of advanced materials are:

- Very precise control of the concentration of implanted ions by electrical ion current measurement (I_i)
- Precise adjustment of mean ion penetration depth R_p by choosing the ion energy E
- Independent control of impurity depth and ion fluence
- Very clean process—vacuum, isotope clean impurity implantation

- Very shallow (10 nm) and very deep buried (10 μm) impurity concentration profiles are achieved
- Fast (seconds, minutes) irradiation of large targets with areas up to ~100 × 100 cm^2
- Complex depth profiles can be achieved by multienergy implants
- Wide variability between ion species and target material to be implanted

3.5.1 Common Low Energy Beam Line Implanters

Ion implanter tools consist of the following main modules: (1) the ion source with the extraction- and focusing electrodes, (2) the ion mass analyzing magnet, (3) the acceleration column with mostly used electrostatic ring electrodes and focusing anode, (4) ion beam scanning and out-blanking of the neutral beam, and (5) the process chamber with target manipulation and ion current measurement. Different arrangement possibilities of these modules are governed by the application of ion implanters with high productivity in industry or with high flexibility in research and development. Demands for high productivity mean high sample (or wafer) throughput with short cycle times. The cycle time t_c is defined as the sum of the pure implantation time t_i, the time for pump-down and flooding of target chamber t_v, the time for sample/wafer exchange t_w and, sometimes, the time for cooling or heating of the samples t_t. The cycle times t_v, t_w, and t_t can be optimized by appropriate technical solutions, e.g., multiple chambers, load-lock systems, wafer handling systems, etc. The implantation time t_i is given by

$$t_i = \frac{q \cdot A \cdot \boldsymbol{\Phi}}{I \cdot m}, \tag{3.25}$$

where A is the implanted sample/wafer area, I the ion current, m the number of atoms in the ion (molecule), and $q = n{\cdot}e$ the ionization degree of the ion. For a given ion fluence Φ to achieve a certain impurity concentration in the target the implantation time is directly proportional to the area A to be irradiated and reciprocal to the ion current I. Therefore, for large area implantation, for example, for silicon wafers of 300 mm diameter, high current implantation tools are needed.

The main principal designs of ion implantation tools are shown in Fig. 3.35. Many early implanters were based on the megavolt accelerators that had been built for nuclear research. A typical system is shown schematically in Fig. 3.35a. These systems had often been developed for proton and helium beams and the magnet was used more to calibrate the energy of the beam rather than as a mass filter. For the heavy ions there is a number of drawbacks to use this type of implanter architecture. An ion source running on ionized vapor or gases produces a range of ionized components and the ions being of interest are a small fraction of the total beam that must be accelerated.

The ions are selected from the other accelerated ions by an analyzing magnet. The length of the beam line in this type of accelerator geometry hinders compact

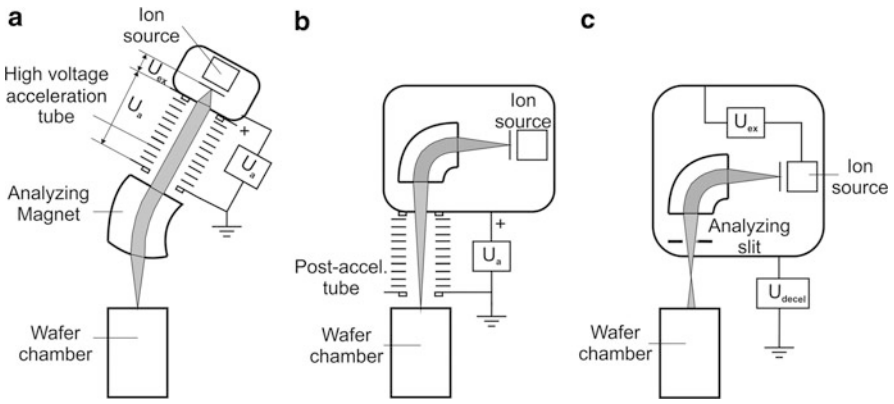

Fig. 3.35 The three basic design concepts from which almost all designs have evolved. (**a**) Postacceleration analysis. (**b**) Analysis before acceleration. (**c**) Extraction energy only with the option of postanalysis deceleration

packaging of the implanter. In consequence implanters of this type for the most part were used only for research. The first implanters to be successfully introduced into semiconductor processing were designed for modest energies allowing atmospheric pressure high-voltage insulation. Consequently, it was comparatively easy to provide a high-voltage terminal large enough to contain both the ion source and the analyzing magnet with adequate pumping as shown schematically in Fig. 3.35b. The analyzed beam leaving the terminal is accelerated to ground potential. In this way the implanter takes advantage of the best features of the accelerator and the isotope separator and was able to provide ion currents of 250 μA or more and ion energies between 20 and 500 keV. Figure 3.35c illustrates a variation of the "preacceleration" configuration shown in Fig. 3.35a. For high current implanters a high current ion source is required for many applications in modern semiconductor integrated circuit fabrication. For most high current applications the terminal enclosure is at ground potential and the beam acceleration is provided by the extraction power supply alone. To obtain higher beam currents at very low ion energies <2 keV, the terminal is raised to a negative potential to decelerate the beam before entering the following beam line. For the most commonly used ion implanters (medium current implanter) the necessary components have been described before.

The choice of the ion sources for most implanters in semiconductor industry has narrowed to two types of source developed by Freeman [25] and by Bernas [23]. Both sources are capable of producing high current and low emittance beams. The replacement of the directly heated filament in the Bernas source by an indirectly heated cathode improved the performance especially the lifetime enough for it to become the source of choice for almost all the implanters built today [104]. For doping of silicon with boron, phosphorous, and arsenic gases of BF_3, PH_3, PH_5, AsH_3, and AsF_5 (most corrosive and toxic) and for doping of GaAs with silicon and hydrogen gases of SiH_4 and H_2 are supplied to these ion sources. Most implanters set up for gaseous sources will allow any of several gasses to be selected by opening

Table 3.3 Comparison of gas ion sources with their typical ion currents

Source type	Ions	Typical (max) ion current (mA) scanned over the sample			
		$^{11}B^+$	$^{31}P^+$	$^{75}As^+$	$^{121}Sb^+$
Bernas (slit)	B, P, As, Sb, Ar	1.0 (30)	1.25	1.5	1.5
Arc (slit)	B, P, As, Sb	4.0	10.0	10.0	4.0
Penning (cold cathode)	B, P, As	0.2	0.15	0.15	–
Penning (hot cathode)	B, P, As	0.3	0.6	0.6	–
Hollow cathode	B, P, As, Sb	0.05	0.07		–
Electron ionization	B, P, As	0.03	0.04	0.06	–

the corresponding valve. The gas flow to the ion source can be regulated by mass-flow controllers (MFCs). If the desired implant species is not available in gaseous form a solid feed material can be heated and the vapor is used as the source (see, for example [13]). The mainly used gas ion sources with their typical ion currents are summarized in Table 3.3.

Alternative ion sources have been developed. For example, the microwave source has been developed to produce beams of the common dopants and nonmetallic species. The ion implanter developed by Tokiguchi et al. [105] for the fabrication of buried oxide layers in silicon (SIMOX) requires 100 mA oxygen beams and the microwave source was found to be capable to meet this objective.

The beam extracted from an ion source usually contains unwanted ion species and to select the beam of dopant ions the extracted beam is filtered by some form of sector analyzing magnet. Except for better materials and cooling, magnetic mass analyzers have not undergone big changes in their basic design. One significant development has been the use of the entrance and exit edges of the magnet to cause focusing by "fringe fields" and the use of shim angles at the entrance and exit to provide vertical and horizontal focusings [106, 107]. The drift distance from the source to the magnet and from the magnet to the analyzing slits is a radius length or more and space charge blow up limits the transmitted ion beam. Consequently, in recent implanters analyzing magnets often have indexed magnetic fields that produce stronger quadrupole focusing and other quadrupole elements that enable the ion source to be located close to the magnet are used [108].

Every dopant ion has potential contaminants close to it in momentum that must be considered when designing an analyzing magnet. For example, $^{10}B^+$ and $^{12}C^+$ must be separated cleanly from ^{11}B at the analyzing slits. In the case of phosphorus $^{31}P^+$ must be separated from PH^+ and $O_2{}^+$. There are contaminants that cannot be separated by the analyzer due to their equivalent momentum, e.g., Mo^{++} and $BF_2{}^+$ and CF^+ and P^+. Heavier dopants have similar problems. Sb has two stable isotopes, ^{121}Sb and ^{123}Sb requiring a resolving power greater than 100 to be separated cleanly. Generally, smaller magnets are used having a resolving power $M/\Delta M$ of about 70 and the ion source construction and operating materials are selected

carefully to eliminate or reduce the contamination of adjacent masses to an acceptable level. After passing through the analyzing slits the beam is either accelerated to higher energy, as in the medium current or high energy implanters, or immediately enters a scanning system in low energy implanters.

Careful considerations have to be done to avoid neutral particles from the ion beam. The neutrals entering the wafer are not detected by the ion current Faraday cups and will disturb the determined absolute ion fluence and the doping uniformity. Usually, before the electrostatic *xy*-scanning system the ion beam is electrostatically deflected by the neutral trap and beam gate unit to select neutralized ions from the ion beam and to collect them in the beam trap (see Fig. 3.4). The ability to irradiate the wafer under the same conditions, independent of the beam position on the wafer and on the angle of beam incidence, has been a vital feature of all industrial implantation equipment. This implant uniformity requirement has evolved from variations of a few percents over the 2″ wafers used in the early 1970s to total variations of less than ±0.25 % (1 sigma) over the 300 mm wafers used today. This requirement cannot be fulfilled with the simple electrostatic scanning system shown in Fig. 3.4 which can be applied only to scanned ion beams with small incidence angles relative to the wafer surface normal ($\alpha < 1°$). Different approaches to achieve uniform lateral and depth distributions of dopants have been developed:

- Two-axis electrostatic beam scanning over a stationary wafer
- One-axis electrostatic beam scanning and a one-axis mechanical wafer scan
- Scanning combining a uniform ribbon beam and a one axis mechanical wafer scan
- Two-dimensional mechanical wafer scanning

The two-axis *electrostatic beam scan* technique described in Sect. 3.4.3 has been used extensively in production implanters, and in this configuration a fixed dc field is superimposed on the scanning field of the second deflector so as to minimize the length of the beam line region from where charge neutralized particles can reach the wafer. This particular approach became the preferred technique and was the basis for most of the implanters shipped in the 1970s and 1980s. It can be seen, however, that with this particular beam scan approach, the angle at which the ions impinge on the wafer varies as a function of the position on the wafer. Furthermore, this type of the scanning system requires a small ion beam size (cross-sectional area) as it strikes the sample. This is in conflict with demands on high ion beam currents in production implanters for two reasons: (1) strong focusing of high current beams increase space charge effect in the beam, and, (2) high intensity small beam spots can lead to tremendous local heating or even to melting of the wafer. For example, the total instantaneous power in a beam spot is given by $P = I{\cdot}U$. If we assume a beam current of 1 mA, an ion energy of 100 keV and a spot size of 3 mm diameter one gets $P = 100$ W, or 14.3 kW cm^{-2}! Averaging this power density over large wafers of 200 or 300 mm diameter and using efficient water cooling wafer surface damage is difficult to avoid. Therefore, pure electrostatic beam scanning is used only in low and medium current ion implanters and is effective only up to few 100 μA. A typical example of a medium current ion implanter is shown in Fig. 3.36. High current ion implanters use hybrid scanning to overcome these difficulties.

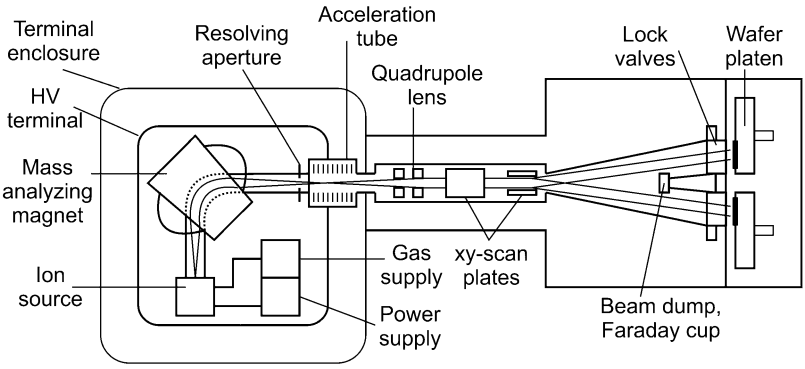

Fig. 3.36 Medium ion current implanter VARIAN 350D MCI with wafer cassette adapter (single wafer implantation) [109].

The implanter type VARIAN-350D shown in Fig. 3.36 has been used for ion implantation of 100 and 150 mm single wafers in the energy range 10–200 keV with ion currents in the range of 0.3–1.5 mA depending on ion energy and ion species ($^{11}B^+$, $^{31}P^+$, $^{75}As^+$). The twin end station (two wafer cassette adapters) has been introduced to enhance throughput but still single wafer load in atmosphere.

In the case of one-axis electrostatic beam scan (line scan) and a one-axis mechanical wafer scan, the ion beam is scanned and collimated in one plane using either electrostatic or magnetic fields to produce a parallel beam. The wafer is then mechanically scanned in an orthogonal direction to achieve uniform doping over the wafer. The first step in both methods is to apply a periodic saw-tooth field to deflect the beam about its mean direction. This scanned beam drifts until the scan is large enough to cover a wafer and is then made parallel either by an electrostatic lens (Fig. 3.37a) or by a tapered dipole magnet (Fig. 3.37b).

An electrostatic parallelizing lens used for electrostatic scan of the ion beam consists of two electrodes spaced apart along the direction of the ion movement. The first electrode decelerates the ions and the second lens accelerate them to exit the lens structure with ion trajectories parallel to the ion beam direction.

In the second case the scanning of parallel beams is achieved by the combination of the entire electrostatic deflector and a rectangular dipole magnet with a varying pole gap. The field of the magnet varies in the direction perpendicular to the beam direction (see Fig. 3.37b) in order to convert the first electrostatic angular scan into a one-dimensional parallel scan. The wafer moves now perpendicular through line-scanned ion beam. Using this technique the beam spot can be much larger, thus lowering the energy density introduced in the wafer. As described in Sect. 3.2 high current ion sources provide rectangular shaped ion beams which are maintained through the ion mass separation and acceleration stages. The rectangular beam is then scanned in the direction perpendicular to its long dimension. By moving a certain amount of wafers (e.g., 25 wafers of a batch) through this scanned beam, the ion beam power is dissipated over all wafers and the average energy density

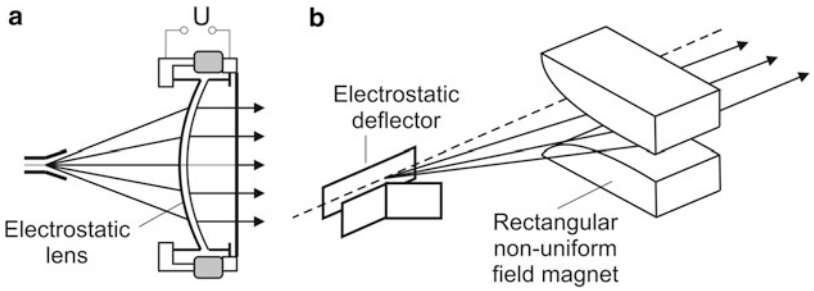

Fig. 3.37 Schematic of two common hybrid scan systems combining an electrostatic scan with (**a**) a collimating electrostatic lens [110] or (**b**) a tapered dipole magnet [111]

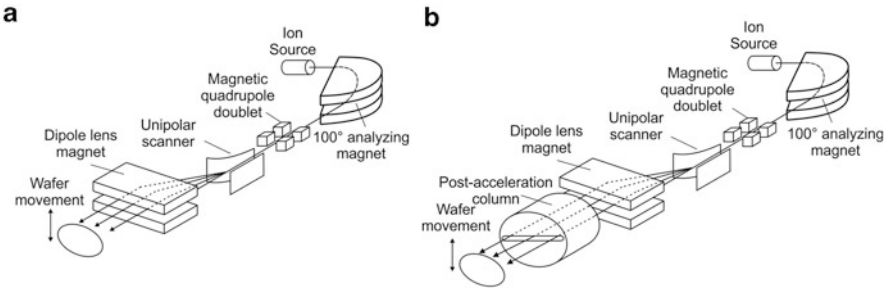

Fig. 3.38 Principal layouts of an Extrion 220 medium current ion implanters [112].

amounts to a few watts even for beam currents of 10 mA. A typical implanter architecture using ion beam line scan and orthogonal mechanical scan is shown in Fig. 3.38.

This implanter type was designed for the magnetic parallel scan over 200 mm wafers (Fig. 3.38a) for implantation with medium ion currents (50–500 μA for 5 keV $^{11}B^{+}$). A significant gain in the low ion energy range was achieved by introducing a postacceleration stage between the dipole lens magnet and endstation (Fig. 3.38b). The technical description of the implanter and its performance can be found in [112]. Later on in 1993 Eaton introduced his medium current implanter model NV8250 which has nearly the same layout but including electrostatic parallel beam scanning and orthogonal mechanical wafer scanning with higher productivity, yield, and better performance [113]. This was achieved by an additional electrostatic scan angle correction leading to a beam parallelism better than $\pm 0.2^{\circ}$ over a 200 mm wafer at ion energies in the range of 3–750 keV and fluence range between 1×10^{11} and 1×10^{16} cm^{-2}. Depending on ion species and energy the ion beam current is in the same range compared to the Extrion 220 machine. The design of the Eaton MC3 medium current ion implanter meeting the requirements of high precision and homogeneous ion implantation into 300 mm wafers is based on that of the model NV8250. This machine delivers ion beam

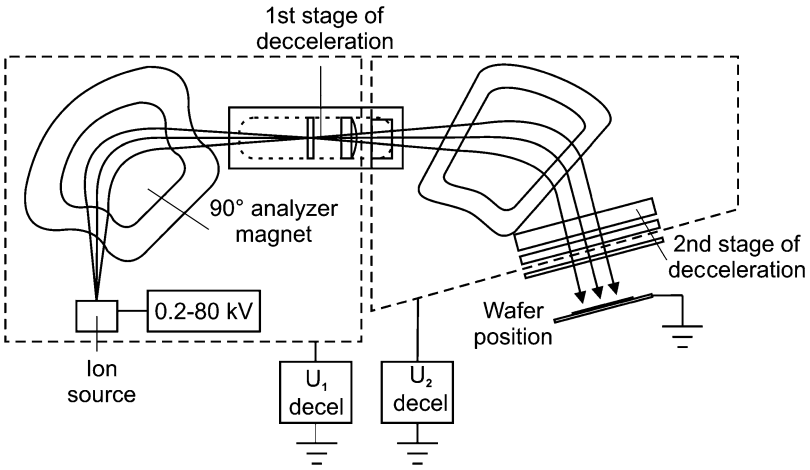

Fig. 3.39 Arrangement of optical elements producing a uniform ribbon beam across a wafer. The source slit lies in the plane of the analyzer poles

currents in the range 2 μA–3.5 mA in the energy range 3–250 keV (B^+, P^+, As^+), 250–500 keV (B^{++}, P^{++}, As^{++}), and 500–750 keV (triple-charged ions) [114].

The ion beam scanning combining a *uniform ribbon beam* and a *one axis mechanical wafer scan* uses a ribbon-shaped ion beam in conjunction with mechanical scan of the wafer along an axis orthogonal to the long axis of the ribbon [115]. This requires the formation of a long ribbon beam (up to 500 mm length) with a low uniformity error of <1 %. Modern ion sources of the Bernas type with source slits (see Sect. 3.2) itself are able to provide rectangular-shaped ion beams with high currents, which are further extended in the long direction by the following ion optical stages as shown in Fig. 3.39. The feature of this beam line architecture is the fact that the long axis of the ion source aperture is located orthogonal to the direction of the field in the magnetic analyzers. After ion mass analysis in the 90° magnet and focusing the beam onto the mass resolving aperture the beam is allowed to diverge to an appropriate size before entering a second sector magnet which collimates the beam as shown and deflects the ribbon beam toward the wafer. Uniform intensity along the length of the ribbon beam is achieved by manipulation of a series of small correcting lenses.

The ion beam can be decelerated to low ion energies up to 1 keV or even below by applying appropriate voltages $U_1 < -30$ kV and $U_2 < -5$ kV to the two terminals (dashed lines). For high energy implantation requirements, the drift mode for beam production is used, in which the ions are extracted from the ion source at final ion implantation energy. The potential of the ion source corresponds always to the same final implantation energy. The terminal with the beam line and the 90° magnet can be raised to a negative potential of max. −30 kV, providing an effective extraction and energy transportation of 30 keV plus the ion implantation energy. The first deceleration after the mass resolving aperture and before the

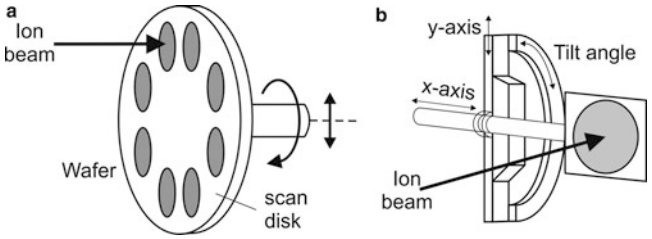

Fig. 3.40 Main principles of mechanical wafer scanning systems: (**a**) rotating wafer disk or "spinning disk," (**b**) two-dimensional single wafer scan

entrance to the 70° magnet provides low ion energy and high beam current. Furthermore, the following 70° magnet acts as a filter for charge exchanged high energy ion contaminants. The first deceleration stage produces a virtual source of low energy ions immediately after the mass resolving aperture which effectively shortens the beam line length for transportation of low energy ions. The second stage of deceleration immediately in front of the wafer can be used for ultralow ion energies, down to 0.2 keV.

Several approaches of *two-dimensional mechanical wafer scanning* also providing the opportunity to distribute the beam power over larger areas and so reducing wafer heating problems associated with high powers are reviewed in [116]. In the technique preferred in the early 1980s, the wafers are mounted on the face and toward the perimeter of a disk that can rotate with a rotation speed up to 900 min^{-1} (Fig. 3.40a). The rotating disk moves then across the incoming ion beam with an appropriate velocity inversely proportional to the radius to achieve a uniform implanted fluence across the wafer.

Nearly all high current (high fluence) implanter used for semiconductor fabrication between 1980 and 2002 employed this "spinning disk" approach.

In recent years significant changes in the ion implantation requirements in semiconducter technology took place: (1) increased wafer size up to 300 mm diameter, (2) systematically shrinking of device geometries, and (3) expansion of the precise control of the implantation angle from the traditional "normal" range of (0–10)° to large angles of incidence up to 60° (halo implant, see Sect. 4.2.1). To fulfill these requirements there is now a strong preference to process one wafer. In response to this, implanter manufacturers have developed mechanical scan systems scanning a single wafer in two dimensions through the stationary ion beam. One solution illustrated in Fig. 3.40b is to use two orthogonal linear stages employing vacuum compatible air bearings to eliminate the friction of a vacuum seal [117]. In this design the wafer can be scanned in a raster pattern in the plane of the wafer and inclined at the desired angle to the incoming ion beam. This architecture ensures that in every point on the wafer surface will be identical implantation conditions in terms of fluence and implantation angle. In this situation, the total length of the beam line from the source to the wafer can be made very compact which maximizes the transmission efficiency of the beam. This

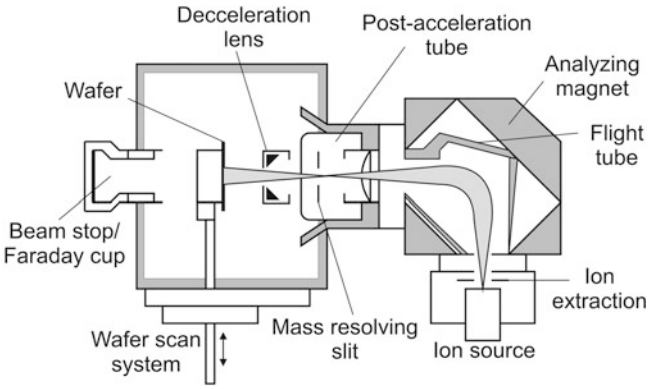

Fig. 3.41 Schematic of a high current and low energy ion implanter, model xRLEAP from Eaton

example exploits the use of air bearings with differential pumping to transmit the high speed scan motions of the single wafer into the vacuum system. An example of a high current ion implanter with two-dimensional wafer scan and single wafer ion processing is shown in Fig. 3.41.

For ion implantations with high fluences of 10^{16} cm^{-2} to be used, for example, for source/drain implantation in MOS field-effect transistors (see Sect. 4.2.1.1) high current implanters became important providing ion beam currents greater than 10 mA. For this purpose, first, more efficient ion sources with larger slit gap were developed, and second, the ion acceleration across the extraction gap provides enough energy for these implants and usually no postacceleration is necessary in high current and low energy ion implanters. For low energy ion implantation the initial ion energy given by the extraction voltage can be additionally lowered by the deceleration lens immediately after the ion mass analyzing aperture. As mentioned earlier, the major problem of wafer heating by high ion beam currents was initially solved by processing 7–25 wafers at the same time (depending on the wafer size) on a spinning disk. This solution was applied in the Eaton/Sumitomo Eaton Nova high current implantation system NV-GSD-HC3 for processing of 300 mm wafers [118]. With improving of wafer cooling techniques and increased wafers diameter, single wafer processing became more attractive and has become the preferred method of high fluence implantation, especially as it also allows wafers to be tilted to the beam direction controlling the angle of implant.

Nevertheless, for high current implanters with ion energies below a few keV it is difficult to obtain an ion beam current high enough for economic operation. The standard high current implanter can only achieve fractions of mA at this low energy. To improve the capture and transport of the ion beam at low energy, the use of postanalysis deceleration has become mainstream even though the deceleration lens can introduce undesirable angular spread of the ions in the beam and ion charge exchange creates fast neutrals in the lens, which influence the shallowness of the implanted dopant profile. The high current beam line demonstrated in Fig. 3.39 reduces the influence of space charge by spreading the beam in the plane of the

magnet and reducing the positive charge density. As in other designs deceleration is employed for low energy performance and a decelerating lens is located just after the analyzing slits of the first magnet. This location is advantageous because fast neutrals cannot reach the wafer.

The continuous scaling of transistor devices towards geometries in the nm-range imposes requirements on increasing ion beam currents at decreasing ion energies well below 10 keV. The Eaton ULE2 ultralow energy ion implanter has been developed to satisfy these requirements [119]. The implanter can provide high beam currents in the range of ~1 mA at ion energies of 1–2 keV in the ion drift mode without the use of deceleration techniques. The main difference to high current and low energy implanters using deceleration stages is the incorporation of RF excited ion source, a 135° window frame ion mass analyzer with distributed variable beam focusing and a RF plasma cell for charge control of the beam before entering the chamber with the wafer spinning disk. The final ion energy is always set by the potential applied to the ion source. The mass analyzing magnet incorporates three electromagnetic quadrupole elements distributed through the magnet creating the equivalent to a triplet design in conventional magnets.

3.5.2 Specialized Low Energy Beam Line Implanters

Different implanters have been developed for applications requiring customized performance. For example, *high current oxygen implanter for SIMOX wafer production* is capable of beam current exceeding 100 mA and implants of 300 mm silicon wafers. SIMOX (separation by implanted oxygen) is a technology that enables the creation of a buried silicon oxide (BOX) layer and a silicon on insulator (SOI) device layer by implanting oxygen ions in a silicon substrate. This requires very high ion fluences in the order of (1–5) $\times$ 10^{17} cm^{-2} to form the buried, stoichiometric silicon dioxide layer during subsequent high temperature annealing. This high fluence is 2 or 3 orders of magnitude larger than conventional implantation for impurity doping in semiconductors.

Through the precise control of the ion energy and O^+ ion fluence, this method has a significant advantage in that the depth, thickness, and uniformity of the SOI and BOX layers can be freely controlled. The typical SIMOX implanter [120, 121] consists of a microwave ion source that generates high-current oxygen beams, a mass separator to select atomic oxygen ions (O^+) from the beam extracted from the ion source, a postacceleration tube to accelerate the ions to the desired energy level, magnetic quadrupole lenses (doublet or triplet system) to control the cross-sectional shape of the ion beam, a 30° deflecting magnet to eliminate neutral oxygen atoms from the ion beam, and an implantation chamber with a mechanically scanned (fast rotation and slow horizontal movement) spinning wafer disk carrying silicon wafers with a diameter up to 200 or even 300 mm. To avoid amorphization of the crystalline silicon above the buried implanted layer the wafers are heated to 500–650 °C during implantation using a combination of lamp and ion beam

radiation power heating. Corresponding to the variation of the ion beam power, the heater power is varied to control so that the wafer temperature is maintained at a certain level with an accuracy of below ±10 K. The most important part of these high current implanters is the ion source providing high-current beam extraction of oxygen ions. A microwave ion source is well suited for the use in high-current oxygen implanters, because it does not have parts that deteriorate, such as filaments, and it has a long life, even if used for chemically active ions such as oxygen. By adjusting the voltage of the postacceleration tube, the oxygen ion implanter allows implantation at various ion energies in the range of 50–250 keV. The shape of the ion beam on the wafer is adjusted to about 40 cm in width and 10 cm in height by controlling the magnetic quadrupole lens at any energy in the given range. Oxygen implantation at 100 mA can be performed in the energy range of 180–210 keV. When implanting a standard ion fluence of 4×10^{17} cm^{-2} at 100 mA, the SIMOX implantation requires of about 3 h for one wafer batch of twelve 300 mm wafers on the spinning disk. For example, on 300 mm SIMOX wafers with an oxygen implantation at 180 keV/80 mA and 3.7×10^{17} cm^{-2}, and then thermally treated at high temperature, a SOI device layer thickness of (50–200) nm with a thickness deviation of ±0.6 % and a thickness variation of a 100 nm thick buried SiO_2-layer of ±1 % or less have been demonstrated. Alternatively to pure mechanical wafer scan ion beam scanning in one direction and wafer scan in orthogonal direction using magnetic beam scanning systems has been also developed [122, 123]. The performance of these high current oxygen implanters is comparable with those described earlier.

Eighty to ninety percent of SOI wafers are manufactured with either an oxygen or hydrogen implantation step for vertical isolation. Separation by IMplantation of OXygen (SIMOX) SOI wafers are manufactured by high dose (10^{17}–10^{18} cm^{-2}) oxygen implantation and this was first reported 30 years ago by researchers from the Nippon Telegraph and Telephone Corporation (NTT). In this technique oxygen is implanted directly into the silicon wafer and a buried oxide layer is formed by a high temperature anneal/oxidation process at 1,350 °C for 6 h [124]. IBIS Technology, Nippon Steel, and Komatsu Materials are examples of SIMOX SOI wafer manufacturers.

The *Smart-cut/UNIBOND wafer production* as the second SOI manufacturing method uses hydrogen implantation (~10^{16} cm^{-2}) to form a splitting buried layer in the SOI wafer bonding manufacturing method. SOITEC [125] and SHE America [126] are examples of companies using this smart cut/UNIBOND SOI bonded wafer manufacturing method. High fluence hydrogen implants cause lattice disruption below the surface of the silicon substrate, leading to cleaving of the surface layers at the implant depth ("Layer Separation") [127]. This is an established production process in the manufacture of Silicon-On-Insulator substrates by SOITEC and others supplying microelectronic-grade SOI wafers. Recently, the technique has entered the photovoltaic market being addressed, for example, by SiGen [128] and others. Hydrogen ion implantation is performed on large area wafers (300 mm) and substrates for solar cells at a fluence range from

3×10^{16}–1×10^{17} cm^{-2} while keeping the substrate temperature in the range from 225 to ~300 °C.

Large area ion-implantation system for doping of poly-Si thin-film-transistors (TFT) was developed to meet various requirements for fabrication of high-quality liquid-crystal-displays (LCD) and organic-light-emitting-displays (OLED) [129, 130]. Ion implanters for these applications have been used for the doping from low fluence to high fluence implantation of the TFTs integrated in LCDS on 100 × 120 cm^2 glass panel through a 100 cm wide ion beam. Implanters of this kind do not have an ion mass analyzer and are usually equipped with a hot-cathode-type ion source with a number of filaments and slits to extract a ribbon-shaped ion beam of 30 cm length. This type of ion source has the difficulty in establishing stability in a low dose condition and in keeping overall uniformity of a substrate, especially for a long operation period, because of the unequal erosion between source filaments. Later on an inductively coupled plasma ion source with a multislit ion extraction system and a beam shutter system in order to handle both high- and low-dose implantation conditions was introduced providing implantation of impurities with excellent stability and uniformity. The beam shutter system reduces the number of slits from seven slits for high-fluence implantation to one slit for low-fluence implantation. The large glass panels are mechanically scanned over the ribbon-shaped to achieve uniform implantation over an area of ~1 m^2. An uniformity error for large area doping of less than 3 % (1σ) has been demonstrated.

These last two examples of ion implantation activities are characteristic of the commercial ion implantation industry where development occurs when radically new processes outside the range of available tools are required.

3.5.3 High Energy Beam Line Implanters

The use of ion implantation of ions with energies in the region (0.2–200) keV was considered in the early 1970s and by the early 1980s it became well established in the semiconductor industry [100]. On the other hand, ever shrinking device sizes created a need for MeV ion implantation systems. These needed to be complete turn key systems that would work well in the production environment. Today, MeV ion implantation is a common place [131], and research implanters in the MeV energy region continue to be built in a wide variety of configurations. In semiconductor industry different acceleration technologies have been adapted for MeV ion implantation: the tandem ion acceleration principle and the radio-frequency linear acceleration (RF-LINAC) technique, both originally used for nuclear physics research. The area that industry has adopted most readily has been the use of high energy beams to directly fabricate deep retrograde wells, buried doping layers and deeply implanted crystal defects in integrated MOS circuits, sensor devices, and high power devices, respectively. The reason for this application of MeV ion implantation is to replace epitaxial layers or deep thermal diffusion processes in many device structures. Both types of high energy implanters are relative compact tools compared to electrostatic accelerators used in ion beam analysis of materials and

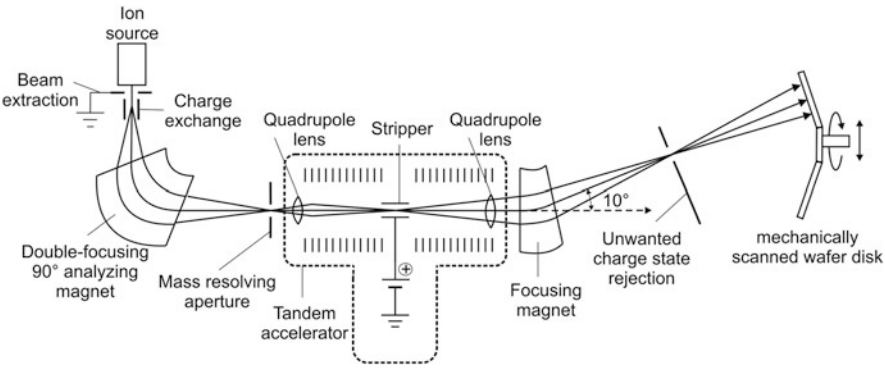

Fig. 3.42 Schematic of a tandem implanter with a spinning wafer disc [132]

are designed for high output ion beam currents and a high wafer throughput as well as for continuous variation of the final ion energy over a broad range. Additionally, the high energy ion implanters must be capable to accelerate a complete range of the ion species available from a proven, reliable ion source and must have an architecture where both the ion source and the wafer end station are at "ground" potential. The first systems were based on 650–750 kV tandem accelerators completed with a spinning wafer disk [132, 133].

The principal buildup of the tandem implanter is shown in Fig. 3.42. In contrast to sputter ion sources used mostly in electrostatic accelerators (see Sect. 3.2.6), here an axial hot-cathode Penning ion source was introduced which uses either solid sources or gases for boron, phosphorous, and arsenic beam generation. After being extracted from the ion source accelerated to an energy of 35 keV the ions pass through a charge exchange region and are converted from positive polarity to negative. In conjunction with the high current positive ion source several 100 μA of $^{11}B^-$ and more than 1 mA of P^- and As^- are available for acceleration by the tandem accelerator. The negative ions are mass analyzed by passage through a 30 cm radius uniform-field magnetic dipole. After analysis the negative ions are accelerated to a higher energy of 200 keV before injection into the first tandem accelerator section. This high injection energy ensures efficient tandem transmission over a broad energy range. In the first tandem acceleration section the injected negative ions are focused by a quadrupole lens and accelerated towards a positive polarity high-voltage terminal maintained at a potential between $U_T = 0$–750 kV. At the terminal in the middle of the tandem accelerator, in a gas stripper tube, the negatively charged ions are stripped into singly, doubly, and triply charged positive ions. The implanter provides therefore a final ion energy of $E = E_i + U_T \cdot e \cdot (1 + q)$, where E_i is the energy of the injected negative ions, U_T is the terminal potential at the stripper, and q is the charge state of the stripped negative ion. After that, positive ions are repelled from the positive terminal and are accelerated in the second tandem acceleration section back to ground. After final acceleration of positive ions from the tandem, they are focused again and pass through a 10° filter

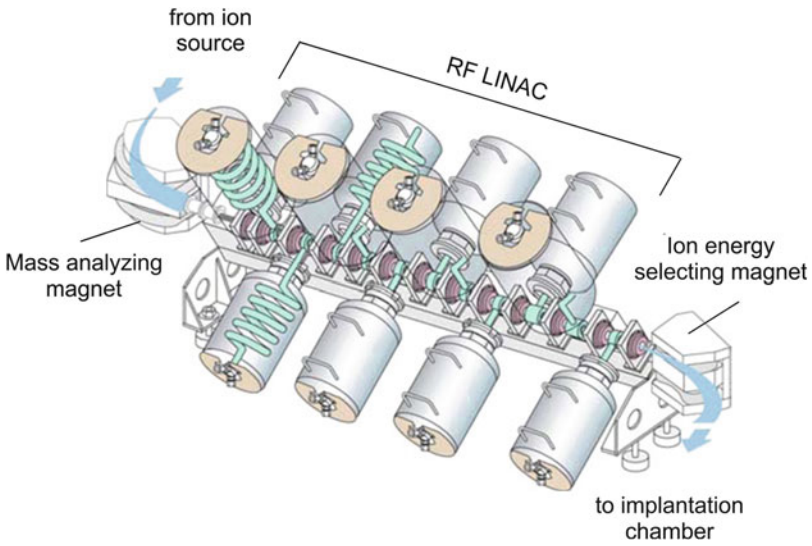

Fig. 3.43 Beam line for a RF-LINAC high energy implanter [136]

magnet which, with its resolving aperture, acts as a beam filter and neutral trap. Since during charge exchange in the tandem single, double, and triple charged ions are created, the beam filter magnet is used to select from different energies and charge state beams the desired charge state and therefore the desired ion energy E. The non-scanned ion beam with a spot diameter in the order of 1–2 cm enters the chamber with a mechanically scanned (fast rotation and slow vertical movement) spinning wafer disk.

A high energy tandem-based implanter with an alternative scan system is described in [134, 135]. In this case a hybrid scan system—beam scanning in horizontal direction wide enough (up to 300 mm) to cover the wafer and mechanical vertical scanning of a single wafer—has been applied. This design requires the introduction of an electrostatic scanner together with a corrector magnet after the analyzing magnet at the exit of tandem accelerator to create the parallel ion beam scan over the wafer moving slowly in vertical direction.

As an alternative to the tandem accelerator a positive ion RF-LINAC shown in Fig. 3.43 was developed especially for high energy ion implantation. The principles of this implanter type are described in [136]. The use of independent phase and amplitude control provides the ability to accelerate a wide range of different mass particles, for example, boron or arsenic, over a continuous energy range.

An analyzed ion beam from a conventional ion source is injected into the linear accelerator and beam currents in the mA range can be obtained from 50 to 170 keV ion energies. The LINAC consists of a series of double accelerating gap resonators operating at 13.56 MHz. Each resonator is capable of providing a voltage of 70 kV across each of its acceleration gaps and is individually controlled, both in amplitude and phase. Electrostatic quadrupole lenses are used in the beam line between the

acceleration tubes to provide periodic focusing of the ion beam. Positive ions are generated by an indirectly heated cathode ion source. The specific ion of interest is then selected by a 70° triple indexed analyzer magnet and injected into the LINAC. A 40° final energy magnet is used to filter the output ion energy of the LINAC. The output energy of this implanter can continually be varied from 10 keV to 1.7 MeV, for single-charged ions like B^+. However, the beam current is limited to about 1 mA. For multiple charge ions the ion current is below 1 mA, e.g., 300 μA B^{2+} at 3 MeV and 200 μA P^{3+} at 5 MeV ion energies. The LINAC implanter GSD/HE from Eaton is equipped in the wafer chamber with a spinning disk which, additionally to rotation and linear moving, can be tilted by ±10° in two planes to perform high energy implantation at different tilt angles. The reason for doing this is to avoid shadowing of the ion beam by thick implantation masks (e.g., photoresist).

For the last decade high current and high energy implanters were designed with a large disk capable of handling up to eighteen 200 mm wafers per batch/load. Only medium current implanters were single wafer tools. With the transition to 300 mm wafers and the concern with batch processing, so single wafer high current and high energy implanters are now available commercially (high energy single wafer: VIISta-810 & 3000 and SWIFT; high current single wafer: VIISta-80 and VIISta-10 P2LAD). A alternative implantation method called plasma implantation is also now available for very low energy implantation down to 20 eV of various species for ultra-shallow junction dopant profiles and the new higher k gate material modification application in microelectronics. This single wafer chamber design could lead to clustering implantation to other processing steps and this could dramatically change implanter designs in the future.

3.5.4 Plasma-Based Ion Implanters

Plasma-based ion implantation (PBII), also called plasma immersion ion implantation (PIII or PI^3), has been developed to introduce impurities with high concentrations into samples with complex three-dimensional geometries, which is too complicated and time consuming using conventional beam-line implantation [2]. In contrast to conventional ion implanters which have five major components, i.e., ion source, mass analyzer, accelerating power supply, focusing unit, and beam scanner, the PIII system has only a plasma-based ion source and accelerating power supply. PBII has been initially developed for hardening by nitridation of metal parts [137, 138]. Subsequently, most of the work has focused on metallurgical applications [139–141]. Recently published works [142–144], however, confirm a variety of emerging semiconductor applications. To date, the most notable success of the technique has been in the field of large-area doping to meet demands of high throughput. In the last decade PBII has been introduced as a promising and innovative doping technology of silicon ultra-large-scale-integrated circuits (ULSI) due to its characteristics of fast high fluence of $\geq 10^{16}$ cm^{-2} implantation at ultralow ion energies (0.1–10 keV). For shallow junction formation conventional high-current ion implanter has serious shortcomings, due to poor ion beam performance in the ultralow energy range, a low

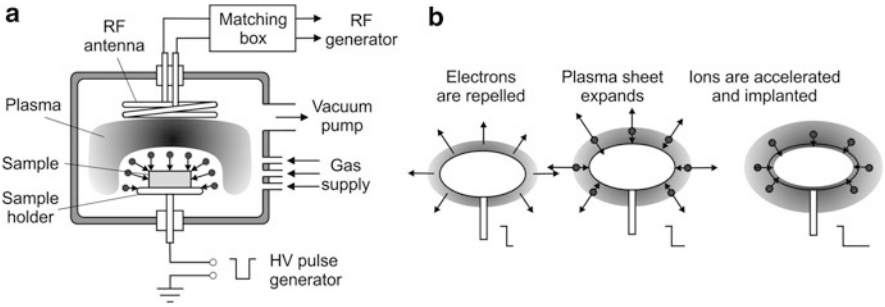

Fig. 3.44 Schematic diagram of a PBII system: (**a**) PBII apparatus and (**b**) development of plasma sheath during PBII treatment

wafer throughput for production, and limitations with doping three-dimensional structures with high-aspect ratios, which are required for advanced CMOS technology.

The principal buildup of plasma-based ion implanters is shown in Fig. 3.44a for the implantation into work pieces with 3D surfaces and into flat samples (wafers). All PBII techniques have in common that the surface of a substrate (or "target") is exposed to, or immersed in, a plasma and that a relatively high negative substrate bias voltage is applied to the sample to accelerate the ions from the plasma to the sample surface. The high ion density plasma (typically 10^{10}–10^{11} cm^{-3}) is generated by means of efficient ionization source, which can be a DC-, RF-, or ECR-power supply. The negative potential applied to the sample creates a plasma sheath around the sample.

Figure 3.44b shows the process in the plasma surrounding the sample in more detail. When the sample is biased to a negative voltage, the electrical field drives electrons which move much faster than ions away from the sample. An ion enriched sheath that is depleted of electrons forms around the sample (and sample holder). Ions are accelerated in the electrical field towards the sample. The plasma sheath expands until the steady-state plasma condition is reached or the high voltage is switched off in the case of pulse biasing. The process chamber is operated at low gas pressure of $\leq$0.5 Pa to avoid ion–neutral collisions in the plasma sheath around the sample. The positively charged ions are accelerated by the electric field in the sheath and implanted into the sample. Depending on the ion–neutral scattering mean free path, the ions are introduced into the substrate with energy and angular distributions determined by the plasma gas pressure, bias voltage, ion charge state, and substrate surface contours. The ion current density depends on the plasma parameters and pulse voltage and is normally in the order of 1–10 mA cm^{-2}. By choosing the pulsed substrate bias charging and arcing on the substrate, sample heating can be well controlled. The positively charged sample surface is neutralized by electrons from the plasma during the bias-off time. Typical pulse duration times between 2 and 100 μs at pulse repetition rates of 100 Hz up to 3 kHz are used in PBII tools.

In comparison to conventional beam-line ion implantation the mean advantages of PBII are:

- PBII equipment is simpler and cheaper than conventional ion implantation equipment
- Treatment of workpieces with complex shape with a certain degree of shape conformity (e.g., trenchwall doping in integrated circuit technology)
- Process time independent of sample size and surface area (large area doping, e.g., large wafers, panels) at high ion fluxes (10^{16} cm^{-2} s^{-1})
- High currents at ultralow energies at $\leq$1 keV, with less radiation damage (for ultra-shallow junctions)
- Minimal charging in pulsed mode operation (insulating materials, e.g., silicon-on-insulators, glass panels with thin film transistors)

whereas the following disadvantageous features are:

- No ion mass separation when polyatomic species or gas mixtures are used in the plasma (impurity contamination), and can therefore not compete with beamline implantation where very high species purity is guaranteed
- Implanted ions energies are not strictly mono-energetic and mainly depend on gas pressure and pulse shape; if the plasma contains only ions of one mass and one charge state, the process can be tuned that one dominant energy exists if the bias pulse shape is essentially rectangular
- In situ dose monitoring is difficult due to sample bias and separate ion fluence calibration will be necessary for each bias voltage

The PBII method is now available for very low energy implantation of various species for ultra-shallow junction dopant profiles and the new higher k gate material modification application. The single wafer chamber design could lead to clustering implantation to other processing steps and this could dramatically change implanter designs in the future [145].

3.6 Electrostatic Ion Accelerator Systems

Ion accelerators are an important and widespread subgroup within the broad spectrum of modern, large particle acceleration devices. They are specifically designed for applications that require high-quality ion beams in terms of energy stability and emittance at ion energies of a few MeV. Their ability to accelerate virtually any kind of ion over a continuously tunable range of energies makes them a highly versatile tool for applications in many fields including nondestructive ion beam analysis, accelerator mass spectroscopy, as well as ion implantation in the manufacture of semiconductor devices. They became powerful tools for new techniques required for analysis and production in many emerging fields, especially analysis of art objects and molecular biology.

The main elements of a high-voltage accelerator are a high-voltage generator, a source of charged particles, and a system for accelerating the particles. The voltage from the high-voltage generator is applied to the electrodes of the accelerating system and generates an electric field inside the system. Charged particles from the

source are accelerated by the field to an energy of $E = e{\cdot}q{\cdot}U$, where e is the elementary electric charge, q is the number of elementary charges on the particle being accelerated, and U is the voltage of the high-voltage generator. The pressure inside the accelerating system must not exceed 10^{-6} mbar, because otherwise the particles being accelerated will undergo considerable scattering by the molecules of the residual gas.

Single- and two-stage electrostatic accelerators can be classified and are mainly named by the working principle and construction of the high-voltage generators which today are usually electrostatic, cascade resonance transformers. An important advantage of high-voltage accelerators over other types of accelerators is the possibility of producing only a small energy spread of the particles, which are accelerated in a uniform electric field that does not vary with time. By using high-voltage accelerators, a relative energy spread of only 10^{-4} can be obtained easily; in some accelerators the spread is as small as 10^{-5}–10^{-6}. For this reason high-voltage accelerators have found extensive application in research in atomic and nuclear physics. Another advantage of high-voltage accelerators is the possibility of building high-power, high-efficiency units. This is of extreme importance for the practical application of the accelerators.

3.6.1 Single-Stage Electrostatic Accelerators

Single-stage electrostatic accelerators using direct voltage technique consist of a high-voltage terminal for generating the high voltage, an ion source of charged particles, and an evacuated acceleration tube through which the particles are accelerated (Fig. 3.45a). The potential drop from the high-voltage terminal to ground potential shown in Fig. 3.45b accelerates the charged particles to an energy equal to the ion charge $e{\cdot}q$ times the terminal voltage U. The accelerator that operates above 10^6 volts (1MV) is usually enclosed in a steel pressure vessel containing electrically insulating, high-pressure gas. The most widely used gas is SF_6 whose dielectric strength is 2.7 times higher than that of air at 1 atm (101 kPa). The dielectric strength rises approximately linearly with pressure to 7 atm, where SF_6 sustains electric fields of ~200 kV cm^{-1}. The electrical breakdown field F can be approximated versus pressure p of SF_6, within a few percent, by the empirical formula $F = 18.6{\cdot}p^{0.6}$ (F in MV m^{-1}, p in MPa), which is independent of the range of peak fields occurring in the different high-voltage terminal designs. For stable operation at high voltages, the insulators of the accelerator support structure and the acceleration tube must be subdivided by metal electrodes that are connected to a resistive voltage divider for voltage grading from the terminal to ground potential.

Single-stage electrostatic accelerators that use an insulating belt to carry a positive charge to the high-voltage terminal are named after Robert Van de Graaff [146]. In this construction, illustrated in Fig. 3.45a, the electric charge is deposited on the insulating belt at the ground end. The motor-driven belt carries the charge to the spherical metal terminal. The belt composed of an insulating material with high dielectric strength is immersed in insulating gas at high pressure.

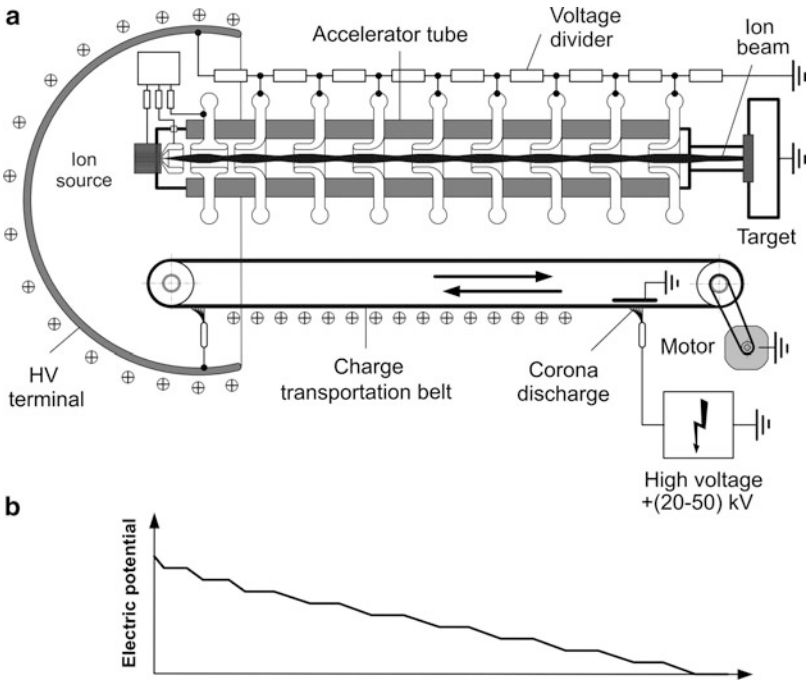

Fig. 3.45 Scheme of the Van de Graaff generator (**a**) and (**b**) the accelerating potential distribution

To charge the belt, a corona discharge is maintained from a brush or comb of metallic wires (sharp needles) held at high voltage to the grounded lower pulley on the opposite side of the belt. The amount of electric charge sprayed onto the belt is controlled by the voltage U_{cor}. If the corona needles are at a positive voltage, the belt surface intercepts positive ions moving from them toward the grounded pulley. The belt carries the positive charge into the spherical terminal, where another corona discharge from another array of needles or a metal brush removes the charge. The charge then passes to the outer surface of the terminal. The positive voltage on the terminal rises until the charging current is matched by current paths to ground which are a combination of current through the resistor chain, the current along the insulating support, and the ion current through the acceleration tube. A negative terminal voltage is produced by operating the charging needles at negative voltage for the acceleration of negative ions (or electrons). The resulting terminal voltage is a function of the diameter of the terminal electrode which behaves like a spherical capacitor with a capacitance $C = 4\pi \cdot \varepsilon \cdot \varepsilon_0 \cdot r_1$, where ε is the relative dielectric constant (e.g., $\varepsilon_{\mathrm{SF6}} = 1.00203$ at 25 °C, 1 bar), ε_0 the absolute dielectric constant, and r_1 the radius of the spherical terminal. If a spherical terminal of radius r_1 is enclosed within a grounded concentric shell of radius r_2, the capacitance C is given by:

$$C = 4\pi \cdot \varepsilon \cdot \varepsilon_0 \cdot \frac{r_1 \cdot r_2}{r_2 - r_1} \tag{3.26}$$

The terminal voltage U_T is proportional to the charge Q transported by the belt to the terminal electrode

$$U_T = \frac{1}{C} \cdot Q \tag{3.27}$$

At constant charging current I_{belt} the equilibrium terminal voltage U_{T0} can be derived from the following equation:

$$\frac{dU}{dt} = \frac{1}{C} \cdot \frac{dQ}{dt} = \frac{1}{C}(I_{belt} - I_{beam} - I_{cor} - I_{res}) \tag{3.28}$$

with I_{beam} the ion beam current through the accelerating tube, I_{cor} the corona current, and I_{res} the electrical current through the resistor chain including the current due to the residual resistance of the insulating column. Typical current–voltage behavior of these current components is shown in Fig. 3.46.

At low terminal voltages where the nonlinear corona current is small and by introducing an effective resistance R of the resistor chain and the insulating column (3.28) can be written as

$$\frac{dU}{dt} = \frac{1}{C}\left(I_{belt} - I_{beam} - \frac{U}{R}\right) \tag{3.29}$$

and analytically solved to

$$U(t) = U_{T0} + (U(0) - U_{T0})e^{-t/\tau} \tag{3.30}$$

where $U_{T0} = R(I_{belt} - I_{beam})$ is the equilibrium terminal voltage and $\tau = RC$ is the time constant.

Equation (3.30) holds as long as the currents I_{belt} and I_{beam} and the effective resistance R are constant and I_{cor} is negligible. The terminal will reach an equilibrium potential U_0 when the charge delivered by the belt is equal to the charge leaving the terminal electrode. The current available to drive an accelerated ion beam is controlled by either the corona discharge current or the belt speed. Typical currents are in the range of 10 μA. Power for ion sources at high voltage can be supplied by a generator attached to the belt pulley inside the high-voltage terminal. Because the horizontal support of long belts and accelerator columns is difficult many high-voltage Van de Graaff accelerators with $U_T = (2...15)$ MV are constructed often vertically. The dimensions of Van de Graaff accelerators with terminal voltages smaller than 2 MV can be significantly reduced and therefore built as horizontal accelerators. Single-stage Van de Graaff accelerators are excellent research tools because they provide a steady-state beam with good energy regulation.

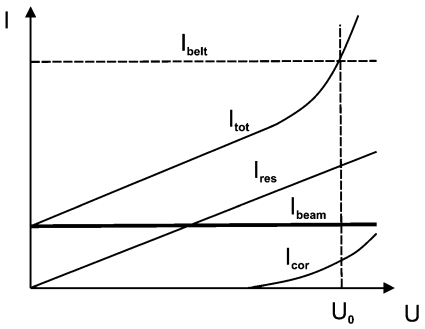

Fig. 3.46 Current–voltage functions for the corona current I_{cor}, ion beam current I_{beam}, resistive current I_{res}, and total current I_{tot} in a Van de Graaff accelerator

Another type of single-stage electrostatic accelerators where the belt-based van de Graaff generator was replaced by the Pelletron generator and known as *Pelletron accelerator* [147] is shown in Fig. 3.47.

In this type of electrostatic accelerators where the belt consists of charging chains which are made of metal pellets (Pelletron, National Electrostatics Corporation, NEC) or metal plates (Laddetron, High Voltage Engineering Company, HVEC) connected by insulating polyamide (nylon) links. The charging chain was developed as an improvement over the older Van de Graaff charging belts. These belts suffered from a number of operational difficulties including terminal voltage instability and susceptibility to spark damage. Also, they generated belt dust which necessitated frequent cleaning inside the accelerator tank. The chain rapidly proved to be more durable than the old belts, while producing a greater terminal stability than had been possible before. It eliminated the belt dust problem as well. As shown in Fig. 3.47, the metal pellets or plates are charged and discharged using the effect of charge influence in an electrostatic field formed by the voltages $\pm U_C$. The electric field between the negatively biased inductor electrode and the pulley rejects electrons from the pellets while they are in contact with the grounded drive pulley. Since the pellets are still inside the electric field as they leave the pulley, they retain a net positive charge which is transported to the high-voltage terminal (up-charging) where the reverse process takes place. Reaching the terminal, the chain passes a negatively biased suppressor electrode which prevents sparking as the pellets make contact with the terminal pulley. The positive charge flows smoothly via the terminal pulley to the terminal. Down-charging works identically to up-charging, except the inductor and suppressor polarities are reversed, and it effectively doubles the charging capacity of the chain. The typical charging currents are in the order of 100–200 μA and high voltages up to 25 MV have been reached. The terminal voltages can be regulated and controlled by varying the charging voltage U_C between inductor and suppressor electrodes and pulleys. Charging voltages up to $U_C = 50$ kV are used. By reversing the polarities of the charging voltages the Pelletron and Laddertron generators can easily be used to accelerate also negative ions.

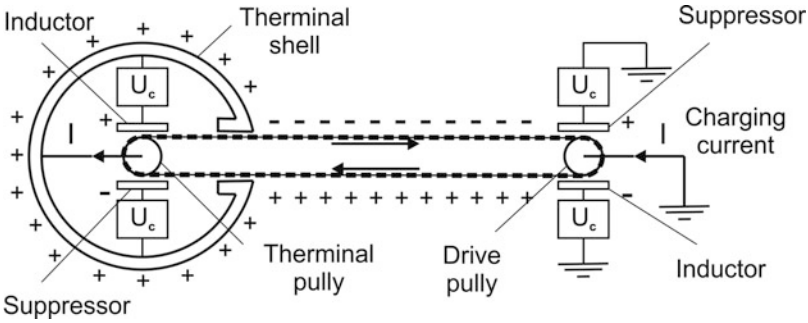

Fig. 3.47 Scheme of the Pelletron and Laddertron HV generator [148, 149]

In a cascade accelerator the voltage source is a cascade generator, which converts a low alternating voltage into a high direct voltage by successively switching of the direct voltages produced in the individual stages of the circuit. Of the several existing schemes for cascade generators, the best known is the *Cockcroft–Walton generator*, whose stages are connected to the power source in series. The advantage of these new cascade generators is uniform distribution of voltage through the stages. A shortcoming of the generators is that the stages must be insulated against the total operating voltage of the apparatus. Voltages of up to 4 MV can be obtained in presently available cascade generators having a power rating of a few tens of kilowatts. The high-voltage transformer has practically no power limitations and is the most promising type of generator for high-power high-voltage accelerators producing an accelerated particle energy of up to ~5 MeV. The linear dimensions of high-voltage accelerators are determined by the voltage of the high-voltage generator and the dielectric strength of its insulation and of the accelerating system. Because of the low dielectric strength of air at atmospheric pressure, it usually is inadvisable to construct an open-type high-voltage accelerator with an energy greater than 1 MeV. Higher energy accelerators are housed in sealed vessels filled with insulating gas at a pressure of 5–15 atmospheres. This approach substantially reduces the size of the accelerators and decreases the construction costs. Particularly effective are electronegative gases, such as Freon and sulfur hexafluoride (SF_6), and mixtures of these gases with nitrogen (N_2) and carbon dioxide (CO_2).

In many existing single-stage electrostatic accelerators as a high-voltage generator a rectifying AC voltage is employed to provide high-current ion beams at energies up to ~5 MeV. The *Cockcroft–Walton accelerator* [150] may be the most convenient one and is shown in Fig. 3.48. The high-voltage (HV) generator of the Cockcroft–Walton accelerator is the cascade generator or voltage multiplier circuit invented by Greinacher [151]. It consists of a HV transformer, HV capacitors, and HV diodes. In Fig. 3.48a cascade generator with four stages is shown.

The capacitors are stacked in two vertical columns capped by a large rounded terminal electrode. The capacitors in the pushing column (P) are charged during the negative half-period of the sinusoidal AC voltage, whereas those of the smoothing

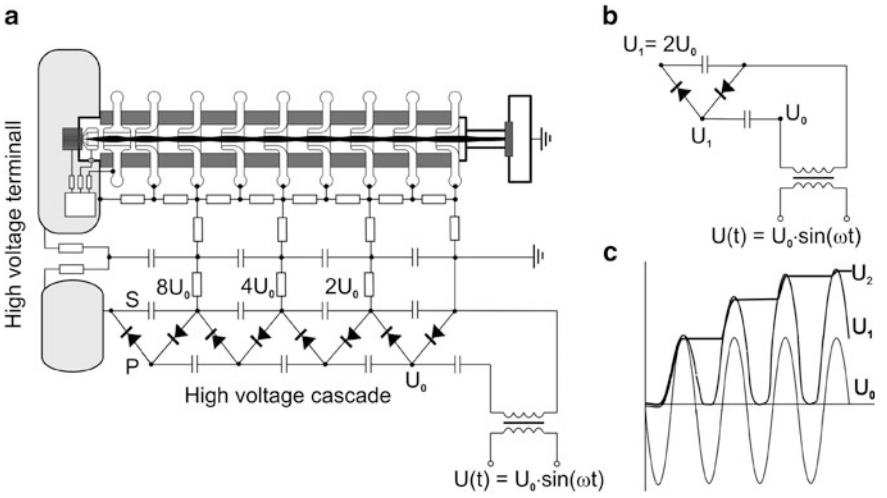

Fig. 3.48 Scheme of a Cockcroft–Walton accelerator (**a**). (**b**) Scheme of one circuit stage and (**c**) voltage oscillograms at different points of the circuit

column (S) during the positive half-period. In steady state the voltages at the break points of the pushing column P amount to $U_0 + U_0 \sin\omega t$, $U_0 + 3{\cdot}U_0 \sin\omega t$, $U_0 + 5{\cdot}U_0 \sin\omega t$, and $U_0 + 7{\cdot}U_0 \sin\omega t$, those of the smoothing column S to $2{\cdot}U_0$, $4{\cdot}U_0$, $6{\cdot}U_0$, and $8{\cdot}U_0$. Here, U_0 is the amplitude of the AC voltage from the transformer. With n stages a high voltage of $2n{\cdot}U_0$ can be achieved. Extracting a DC current causes a mean voltage drop ΔU and a ripple voltage δU which are proportional to the DC current I:

$$\begin{aligned} U &= 2n \cdot U_0 - \Delta U \pm \delta U \\ \Delta U &= \frac{I}{f \cdot C} \cdot \left(\frac{2}{3} n^3 + \frac{3}{4} n^2 + \frac{1}{12} n \right) \\ \delta U &= \frac{I}{f \cdot C} \cdot \frac{n(n+1)}{2} \end{aligned} \tag{3.31}$$

where f is the frequency of the AC voltage and C the capacitance of the capacitors. For small values of ΔU and δU one should choose the frequency f and the capacitance C as large as possible and limit the number n of cascade units. Typical values are $f = 0.5$–10 kHz, $C = 1$–10 nF, and $n = 3$–5. The ripple voltage δU can be reduced by an additional RC filter.

The positively charged ions extracted from the ion source and mass separated by the injector magnet, both at high potential, are accelerated in a tube installed in an evacuated ceramic or glass isolator (see Figs. 3.45 and 3.48). The high voltage is stepwise distributed over several tubes from the terminal to ground. Therefore, the local value of the accelerating electric field E is reduced leading to increased voltage stability. For the same reason the inner electrodes are rounded and polished

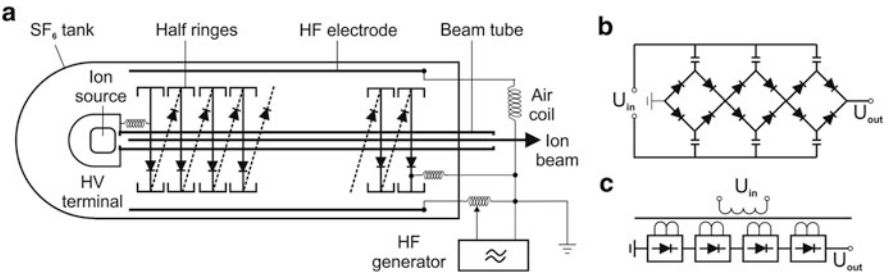

Fig. 3.49 Scheme of the Dynamitron HV generator

with high surface quality allowing electric fields of $\leq$100 kV cm^{-1} in high vacuum. Higher fields cause discharges due to the emission and acceleration of electrons at the electrode surface.

Based on the Cockcroft–Walton type for modern accelerators the *Dynamitron* generator has been developed [152, 153]. The Dynamitron generator (see Fig. 3.49a) is based on an RF oscillator operating at frequencies between 30 and 300 kHz. Driver HF electrodes in the form of half-cylinders (corona half-loops) transmit the RF power via capacitive coupling to coupling half rings (Fig. 3.49b).

Together with an external air coil the two driver electrodes form an oscillator circuit. The high frequency AC field of the LC circuit induces a current in the half-cylinder equipotential rings, which is rectified by the diodes connected in series. The half-cylinder equipotential rings are coupled together by a resistor chain to achieve a homogeneous potential distribution. A Cockcroft–Walton-like cascade generator generates the DC voltage. In modern machines semiconductor diodes are used. RF chokes provide the connection of the rectifier cascade between ground and high-voltage terminal. Like in the classical Cockcroft–Walton generator the achievable high voltage is proportional to the number n of rectifier stages:

$$U = 2 \cdot n \cdot f_c \cdot U_0. \tag{3.32}$$

Here, U_0 is the amplitude of the alternating voltage at the driver electrode D and f_c the coupling factor. A rectifier stage consists of two rectifier diodes. The voltage amplitudes U_0 reach values up to about 100 kV. The advantage of this power supply is a high reliability due to the absence of moving parts inside the pressure vessel. Another advantage compared to the classical Cockcroft–Walton generator is the very low capacitances of the system. Therefore, possible spark-overs are rather harmless. The regulation loop of the Dynamitron generator can be modeled like in a standard electronic power supply. Therefore, the stabilization of the terminal voltage is substantially faster than the classical Van de Graaff belt generator or the Pelletron generator. In another variant of the Dynamitron power supply,

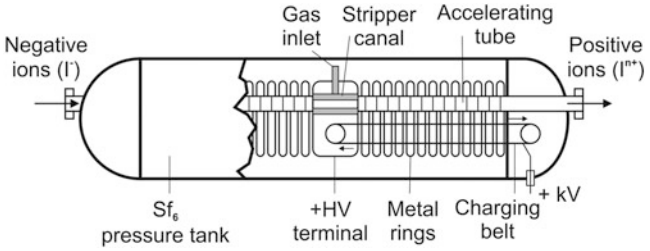

Fig. 3.50 Schematic of a two-stage (tandem) electrostatic accelerator in a pressure tank

the capacitive coupling is replaced by an inductive coupling (Fig.3.49c). Dynamitron generators produce constant high voltages of several MV at ion currents up to some 100 mA.

3.6.2 Two-Stage Electrostatic Accelerators

A decrease in the required voltage of the high-voltage generators and thus a reduction in the dimensions of the high-voltage accelerators can be achieved through charge exchange (changing the sign of the charge) in the process of acceleration. Accelerators of this type are called two-stage *Tandem accelerators*. The two-stage Tandem accelerator concept illustrated in Fig. 3.50 was invented in order to achieve higher ion beam energies than with single-ended Van de Graaff accelerators by accelerating ions twice [17, 154].

In tandem accelerators negative ions injected from the ion source are accelerated in a first tube from ground potential to a positively charged terminal at high-voltage U_T in the middle of the tank. In the terminal, a gas canal (usually nitrogen or argon with gas pressures of ~10^{-2} mbar) or very thin carbon foil (areal density about 2–5 μg cm^{-2} or thickness of ~4–10 μm) strips electrons from the ions. The important drawback of gas stripper is the fact that they must be windowless and this can cause vacuum problems in the accelerating tube resulting in bad ion beam transmission. The solution was to introduce a vacuum pump (turbomolecular or getter pump) in the terminal. About 90 % of the gas is re-injected into the stripper canal. In the case of turbo pumps, the gas is re-injected through a sorption trap to prevent any migration of oil into the accelerator tubes. Higher charge states are obtained with foil strippers except at low energies. Because of energy straggling and angular dispersion, the emittance of the beam is more deteriorated through a foil stripper than through a gas stripper.

An example of the ion charge-state equilibrium after electron stripping in a nitrogen gas canal is shown in Fig. 3.51 for 2.4 MeV negatively charged $^{12}C^-$ ions injected into the gas canal [155].

The resulting positively charged ions are accelerated in a second tube, away from the terminal, back to ground potential. The resulting kinetic ion energy E of an ion depends on the charge q of the positive ions and is given by

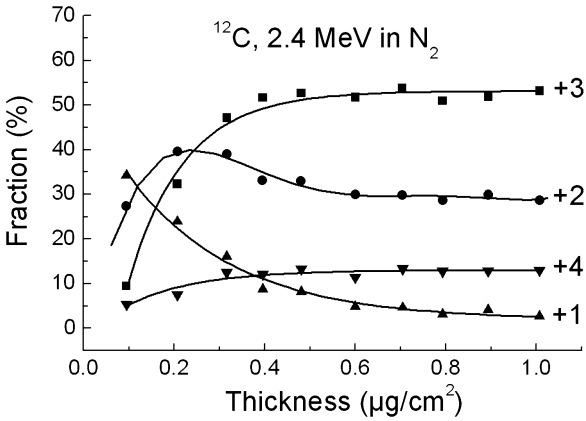

Fig. 3.51 The measured fractions of the charge states $q = 0, +1, \ldots, +4$ for ^{12}C ions leaving a N_2 gas stripper in a tandem accelerator (from [155])

$$E = e \cdot U_T + e \cdot q \cdot U_T = e(1 + q) \cdot U_T, \tag{3.33}$$

where e is the absolute electron charge of the single-charged negative ions and q the positive charge state of ions. For example, mass separated negative ions of H^- or Cl^- are extracted from a duoplasmatron or Cs-sputter ion source, respectively. Subsequently injected into a tandem accelerator operating at a terminal voltage of $U_T = 5$ MV and stripped into positive ions H^+ or Cl^{7+} or Cl^- they are accelerated to final energies of 10 MeV and 40 MeV, respectively. In general, the final ion energy is a little bit higher since negative atomic ions as well as molecular ions are pre-accelerated (ion extraction voltage) to about 50 keV by connecting the negative ion source with a negative potential, the so-called injection voltage U_I. In the case of negative molecular ions with mass M_{neg} (e.g. $(CN)^-$ instead of N^-, see Table 3.1) extracted from the ion source eqn. 3.33 has to be rewritten to

$$E = e\left[(U_I + U_T) \cdot \frac{m_{pos}}{M_{neg}} + q \cdot U_T\right] \tag{3.34}$$

with M_{neg} the mass of the molecular ion (e.g. $(CN)^-$) and m_{pos} the atomic mass of the finally accelerated ion after stripping (e.g. N^+).

With increasing terminal voltage the cascade generators were enclosed in high pressure tanks (Fig. 3.52) and their design continuously improved.

In the Dynamitron [153, 156] (Fig. 3.52a) two RF electrodes are mounted near the inner surface of the tank. This circuit with a resonance frequency around 100 kHz is coupled inductively with an oscillator. Because of high power, the oscillator sits in a separate tank. Parallel coupling of the cascade to the liners is accomplished through the electrode to corona ring capacitance. In Tandetrons manufactured by HVEE [157] with a 30 kHz oscillator the generator is mounted in the pressure vessel perpendicular to the ion beam centerline to protect it against transients associated with vacuum discharges. This setup gives Tandetrons their T-shaped design (Fig. 3.52b).

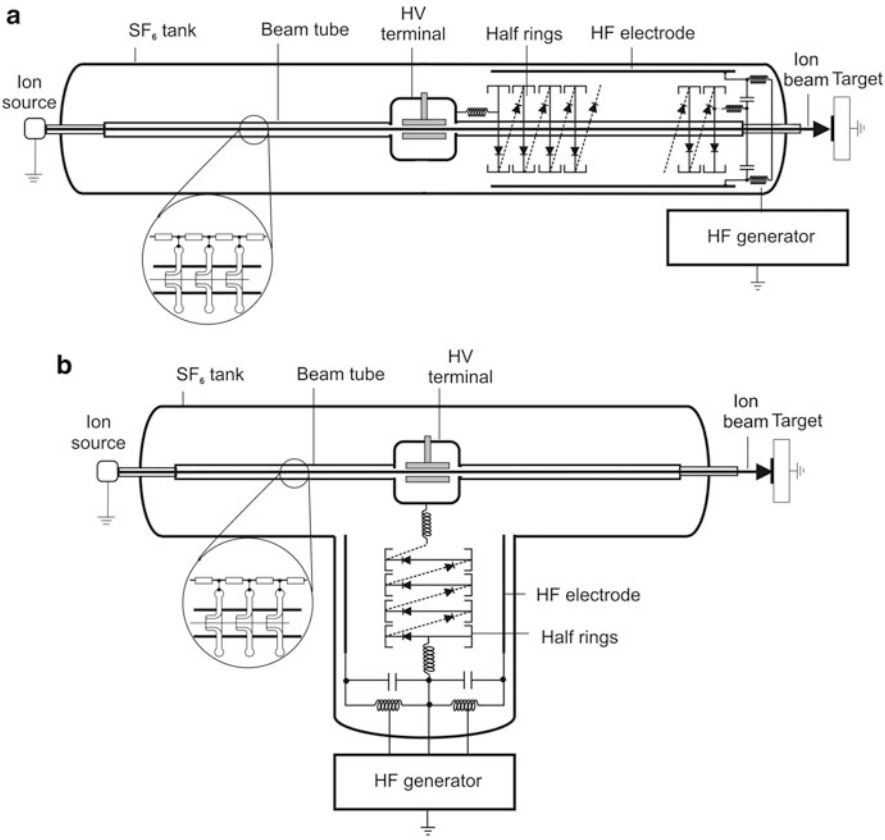

Fig. 3.52 Schematics of (**a**) the Dynamitron, and (**b**) the Tandetron with enclosed cascade generators

Compared to single-stage accelerators Tandem accelerators have the advantage of much higher ion energies for a given terminal voltage. The disadvantage is that the ion charge-exchange process results in a significant reduction of beam intensity. However, for a wide range of applications ion currents of a few μA of accelerated ions are adequate. In contrast to single ended machines, Tandem accelerators have advantageously both ends (ion injection and target chamber) at ground with the high-voltage terminal in the middle of the tank. In modern Tandem accelerators the charging belt has been replaced by high-voltage generators, such as Cockcroft–Walton generator and Dynamitron generator. Nowadays, many tandem accelerators are equipped with two source types for negative ions—Duoplasmatron combined with a charge exchange channel [158] for the supply of He^- and Cs sputter ion source for all other kinds of negative ions (Fig. 3.53). In the charge exchange cell, the electron capture and loss processes, which take place during collisions between energetic ions and atoms in a vapor (mostly alkaline metals of Li and Rb), result in a distribution of charge states of the ion beam as in the stripping process.

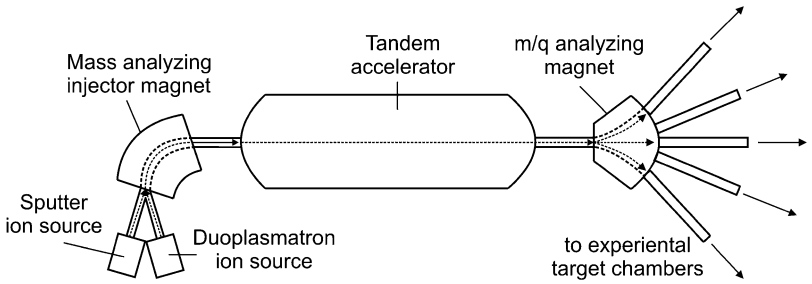

Fig. 3.53 Example of outline of a tandem accelerator for application in research and development

The efficient production of negative ions through charge exchange depends on the ion energy, the electron affinity of the element of interest and of the electron binding energy of the donor. Through charge exchange, some negative ions can be formed in an excited state of the element. That is true for He for instance which is important in ion beam analysis techniques. Different combinations, for example Duoplasmatron ion sources associated with a Li charge exchange channel or RF ion sources equipped with a Rb charge exchange channel can be found in tandem accelerators. As shown in Fig. 3.53 after ion beam formation and before injection of the ion beam into the accelerator, the ions are mass separated by the injector magnet (low energy analyzing magnet) and at the accelerator exit the positive ions with different charge states are energy analyzed by the high energy analyzing magnet. For many research applications, the high energy analyzing magnet can switch the ion beam in different beam lines connected with different chambers of ion beam analysis or ion beam irradiation of different materials (e.g., ion implantation).

For the last 50 years and at present, DC electrostatic accelerators play an essential role in nuclear physics, ion beam analysis like Rutherford backscattering (RBS), particle-induced X-ray emission (PIXE), particle-induced gamma emission (PIGE), nuclear reaction analysis (NRA) and elastic recoil detection (ERD), accelerator mass spectrometry (AMS), and materials modification (e.g., high energy implantation, ion beam mixing). The main properties of these machines are:

- Any charged ion can be accelerated in an energy range ~(0.1–100) MeV
- The energy dispersion is quite low and in the order of $\sim 10^{-4}$
- The terminal voltage and thus the energy of the ions can be varied quite easily
- The maximum terminal voltage is limited to ~25 MV due to voltage breakdowns
- The ion beam currents are continuous and are 10 nA–10 mA (depending on used ion sources and the voltage generators)

Van de Graaff and Tandem Van de Graaff accelerators are still in use for basic research in nuclear physics and in many applications. Cockcroft–Walton and Dynamitron generators are commonly used as high-voltage generators in order to accelerate ions with high beam currents. There was continuously a growing demand for small electrostatic accelerators for applications in industry, medicine, and biology which goes to compact and customized electrostatic accelerators. Modern single-stage Van de Graaff accelerators are equipped with a unique ion source exchange system

that allows for ion source exchange without opening the pressure vessel. Complete single-stage and Tandetron accelerator systems for ion implantation and ion beam analysis and Tandetron systems for accelerator mass spectrometry are available nowadays.

National Electrostatics Corporation (NEC), Middleton, Wisconsin, USA [159] produces three distinct classes of electrostatic accelerators. The U-series are Pelletron accelerators with terminal voltages from about 4 MV up to about 25 MV. They are mainly used for basic nuclear structure research. The S-series are Pelletron accelerators with terminal voltages from <1 MV up to about 5 MV for applications involving MeV ion implantation, surface analysis, micro-beam applications, and advanced research.

High Voltage Engineering Europe (HVEE), Amersfoort, The Netherlands [160] offers air insulated accelerator systems up to 500 kV, single-stage accelerator systems "Singletron" up to 6 MV, and Tandem accelerator systems "Tandetron" up to 6 MV terminal voltage. The high-voltage generator of the Singletron and Tandetron accelerator systems is a SF6 insulated Dynamitron power supply with a very high-voltage stability and a low-voltage ripple resulting in an excellent beam energy resolution.

3.7 Focused Ion Beam Systems

3.7.1 Low Energy Focused Ion Beams

Focused ion beams (FIB) in the ion energy range 1–100 keV are able to modify or to pattern solid state surfaces with sub-µm resolution directly without any lithographic processes. Fundamental processes of ion beam interaction with materials—ion implantation, material removal by sputtering or ion beam assisted gas etching, and ion beam assisted material deposition from the gas phase are used in modern FIB tools having a resolution of ~5 nm at Ga^+ ion beam currents of 0.5 pA [40].

Today, FIB machines are mostly applied as powerful tools in cross-section sample preparation for high resolution transmission electron microscopy (X-TEM) investigations by local ion beam sputtering (or milling) [41]. In contrast to conventional TEM-sample preparation techniques, FIB milling gives the possibility to prepare the TEM specimens locally from large-area samples with high spatial resolution. Furthermore, cross-sectional cuts prepared by FIB milling can be easily investigated by methods of analytical scanning electron microscopy (SEM). For this purpose FIB columns have been combined with SEM columns in one tool to the so-called dual-beam or cross-beam machines [41] which are mainly used for failure analysis in integrated circuits.

The ion sources in FIB systems are always liquid metal (mainly Ga) or metal alloy ion sources (LMIS) providing a point like ion emission (see Sect. 3.2.7). The LMIS has the ability to provide a source of ions of ~5–10 nm in diameter. Gallium (Ga) is mostly used as source material in LMIS for commercial FIB instruments for a number of reasons: (1) its low melting point minimizes any reaction (or interdiffusion)

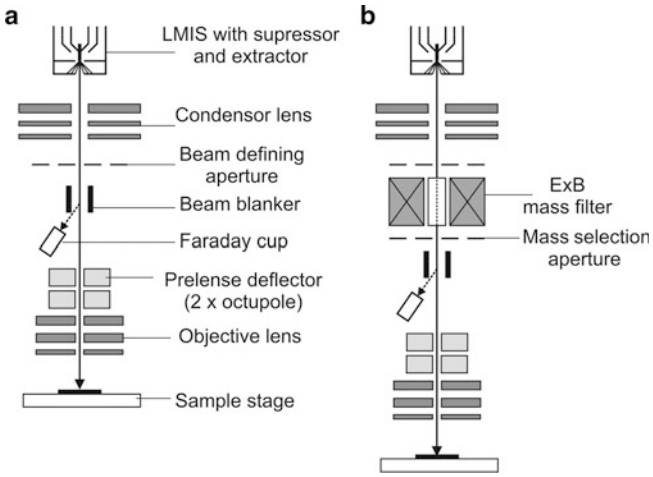

Fig. 3.54 Typical FIB column geometry without (**a**) and with ion mass separator (**b**)

between the liquid and the tungsten needle, (2) the low volatility at the melting point conserves the supply of metal and yields a long source life, (3) its low surface free energy promotes viscous behavior on the tungsten needle, (4) its low vapor pressure allows Ga to be used in its pure form instead of in the form of an alloy source and yields a long lifetime because the liquid will not evaporate, (5) it has excellent mechanical, electrical, and vacuum properties, and (6) its emission characteristics enable high angular intensity with a small energy spread.

The schematic diagram of the FIB column is shown in Fig. 3.54.

The design of the compact ion beam column is similar to that of a scanning electron microscope (SEM). The main difference is the use of an ion beam instead of an electron beam and the forming of the ion beam is carried out by electrostatic instead of magnetic components because the focusing strength of an electromagnetic lens is directly related to the charge/mass ratio q/m of a particle. A vacuum of about 10^{-7} mbar is maintained inside the column. By applying a negative potential of ~−7 kV to the extraction electrode with a small aperture, positively charged ions are emitted from the liquid Ga (or metal alloy) cone by the high electric field (~10^8 V cm^{-1}), which is formed on the tip of a W needle. The beam acceptance aperture of the extraction electrode system with a diameter of ~1 mm selects the central part of the emitted ion beam. For Ga ion sources typical extracted ion currents are in the order of some μA. The ion column itself has two lenses—a condenser lens and an objective lens. Once the ions are extracted from the LMIS, they are accelerated through a potential of typically 5–50 kV applied to the upper condenser lens down the ion column to the grounded sample stage. The condenser lens acts as an ion beam collimating or focusing lens depending on the operating mode: crossover beam path for highest beam current or noncrossover for best imaging performance. The lower objective lens is used to focus the ion beam at the sample surface enabling a best resolution in the sub-10 nm range. Additionally,

a set of beam defining apertures with various diameters (10–400 μm) after the condenser lens help in defining the beam spot size and provides a relatively wide range of ion currents from 1 pA to 100 nA that may be used for different applications. In contrast to conventional broad beam ion implantation, the FIB works at ion current densities which are 4–5 orders of magnitude higher and may be as high as 10 A cm^{-2}.

Optimizing the beam shape is obtained by centering each aperture, tuning the column lenses, and fine tuning the beam with the use of two octopole lenses (double prelens deflector). The cylindrical octupole lenses are used to perform multiple functions such as beam deflection, alignment, and correction of residual spherical aberrations of the beam. In addition, the scan field of the ion beam can be rotated by the octupole lenses. The octupole doublet is used for raster scanning the focused beam over the sample in a user-defined pattern over a maximum area of 400 × 400 μm without scanning field stitching. As a result of the scanning process the deflected beam is guided every time through the central point of the lower electrostatic objective lens. Beam blankers prevent unwanted erosion of the sample by deflecting the beam away from the center of the column. The beam blanker also allows to deflect the beam into the Faraday cup for ion beam current measurement. The relatively large working distance of the FIB with typical values of ~(1–2) cm permits the introduction of samples with varied topography without concern for field variations at the ion beam exit of ion column.

In the case of using liquid metal alloy ion sources, the insert of an ExB mass filter with a mass selection aperture is necessary to select the ion mass and the ion charge state (Fig. 3.54b). The mass resolution of the ExB mass separator is given by the relation [37]:

$$\frac{M}{\Delta M} = \frac{E_x}{2 \cdot U_{\text{acc}}} \cdot \frac{l}{d}\left(\frac{l}{2} + D\right), \tag{3.35}$$

where U_{acc} is the acceleration voltage, E_x the electric field strength in the ExB filter, d the diameter of the mass selecting aperture, l the length of the ExB filter, and D the distance between the mass separator and the aperture. Typical mass resolutions in FIB columns are in the order of $M/\Delta M \sim$ 35–100 depending on the ion energy in the range 30–10 keV, respectively. Such ExB mass separators in FIB columns are able to select single and multiple charged single and cluster ions with mass–charge ratios of $m/q \sim$ (10–1,000) amu/e.

The most important parameter of the ion beam is the beam spot diameter d in the focus (beam diameter at FWHM) on the sample, which is given by [39]. Assuming a Gaussian ion distribution in the beam and consider paraxial particle trajectories (axial ion velocity and energy spread) the spot diameter is expressed by

$$d = \sqrt{\left(M_{\text{c}} \cdot d_{\text{q}}\right)^2 + (d_{\text{s}})^2 + (d_{\text{c}})^2}, \tag{3.36}$$

where $M_c = \alpha_0/\alpha$ is the magnification of the lenses in the ion column determined by the acceptance half angles of the condenser lens α_0 and the convergence half angle of the objective lens α. d_q is the virtual ion source diameter from which the ions are emitted, and d_s and d_c are the spot sizes due to spherical and chromatic aberrations, respectively. d_s and d_c are expressed by the two formulas:

$$d_s = \frac{1}{2} \cdot C_s \cdot \alpha^3, \quad d_c = C_c \cdot \left(\frac{\Delta E}{E}\right) \cdot \alpha, \tag{3.37}$$

where C_s and C_c are spherical and chromatic aberrations coefficients, respectively. In the relation $\Delta E/E$, ΔE denotes the energy spread of the ion beam and E the ion energy. The convergence half angle α is given by

$$\alpha = \sqrt{\frac{I}{\pi \cdot M^2 \cdot \left(\frac{\mathrm{d}I}{\mathrm{d}\Omega}\right)}} \tag{3.38}$$

with I the ion current, M the ion mass, and $\mathrm{d}I/\mathrm{d}\Omega$ the angular ion intensity of the source.

From expressions (3.36) and (3.37) it can be seen that the beam spot diameter in the focal plane on the sample is mainly dominated by spherical and chromatic aberrations due to the ion energy spread ΔE and the ion current I. The ion energy spread ΔE (defined as width at FWHM of the energy distribution) depends on the ion source type, the ion emission current, and on the kinds of emitted ions which is shown in Fig. 3.55 in dependence on the mass–charge ratio m/q for an ion acceleration voltage $U_{acc} = 30$ kV.

From Fig. 3.55 it can be seen that the energy spread for 30 keV Ga^+ ions is ~20 eV, whereas ΔE decreases for lower masses of single charge ions and increases with increasing ratios of m/q and charge state. Low currents minimize ΔE, thereby reducing the spot size d and increasing the ion current density, which is mostly the desired situation.

In the case of low ion currents of a few pA the beam spot size is in the order $d < 10$ nm and smaller than the virtual ion source diameter $d_q \sim 20$–50 nm which depends on the mass of emitted ions and the ion emission current. At often used medium currents of a few hundred pA and medium angular apertures chromatic aberrations dominate the beam spot size, so that $d \propto I^{1/2}$, whereas at high ion currents in the nA range (large angular aperture) the spot size is mainly affected by spherical aberrations and $d \propto I^{3/2}$. For example, the dependence of the FIB spot size from the Ga^+ ion current is shown in Fig. 3.56 for the mostly used commercial FIB columns and for main applications.

Roughly, the applications of FIB can be divided into three classes: (1) the subject of FIB for microsystem technology inspection, metrology, and failure analysis with well-developed procedures for cross-sectioning of TEM- and SEM-specimens; (2) the use of FIB as a tool for maskless micromachining by both subtractive

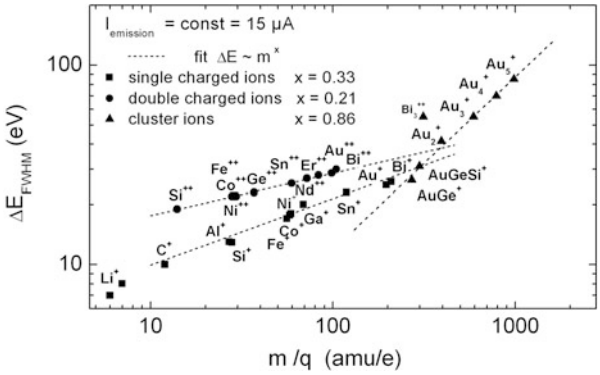

Fig. 3.55 Energy spread as a function of ion mass and charge state obtained at 30 kV acceleration voltage from elemental Ga and Bi LMIS and different liquid metal alloy LMIS ion sources of AuGeSi-, CoNd-, ErFeCrNi-, SnPb-, GaBi-, GaBiLi-, and CCeAl-alloys [161]

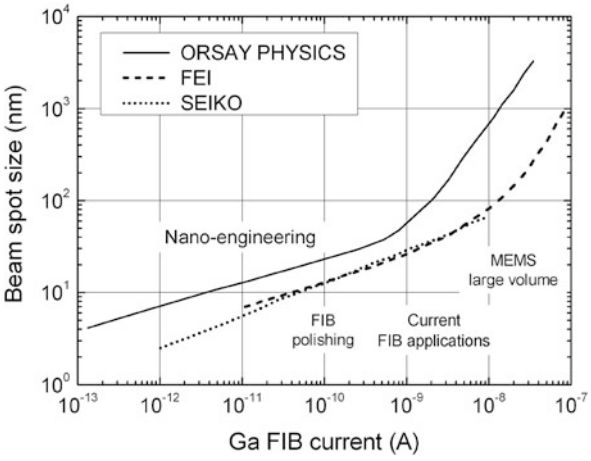

Fig. 3.56 FIB spot size versus ion current for Ga FIB columns from different manufacturers

(layer etching) and additive (layer deposition) techniques, and (3) FIB ion implantation for local doping and ion beam synthesis of new nanoscale phases as well as the combination of FIB implantation into silicon with subsequent selective etching. For all purposes the appropriate processing FIB chambers have been developed which can include a detector for imaging by detection of secondary electrons or ions (only at low FIB currents of <40 pA) using MCPs (or scintillator–photomultiplier combinations) mounted directly above the sample at an angle of 45° to the incident beam, a gas injection system (GIS) for FIB-assisted etching and layer deposition, and an electron gun to prevent surface charging of nonconducting materials, e.g., SiO_2, Si_3N_4, during FIB treatment.

FIB can be used as a deposition tool for fabricating nanostructures. FIB-assisted layer deposition (FIBAD) uses the ion beam to initiate and localize chemical vapor deposition (CVD) in a specific location by a direct-writing technique, also known as FIBCVD. For FIBAD many types of precursor gases have been used for making of

a variety of metallic and insulating structures. For example, the precursor gasses WF_6 [or $W(CO)_6$], $C_7H_7F_6O_2Au$, $(CH_3)_3NAlH_3$, $C_9H_{16}Pt$, $C_{14}H_{10}$ or $C_{16}H_{10}$, and TMOS + O_2 (TMOS—tetra-methyloxysilane) have been used to deposit W, Au, Al, Pt, C, and SiO_2, respectively [162]. The gas nozzle is usually controlled at a height of 0.1–1 mm above the target surface at an angle of 30–60°, with the precursor gas being evaporated from a heated container. In FIB-assisted etching (FIBAE), also known as chemical-assisted or gas-assisted ion etching, an ion beam is used to initiate a chemical reaction between the substrate surface and gas molecules absorbed on the substrate to enhance the material removal rate. By injecting a reactive gas precursor into the milling process, the material removal mechanism can be changed and the associated milled shape can be altered. While ion milling can be used to remove almost all kinds of solid materials, FIBAE can only be applied to certain substrates since a precursor gas must exist to form volatile products with the substrate. Frequently used precursor gases in FIBAE include Cl_2, Br2, I_2, and XeF_2 for etching semiconductors (Si, GaAs, InP), metals (Al, W), and insulators (SiO_2), and H_2O vapor is generally used for the etching of carbon-based materials (PMMA). Also, mixtures have been applied to FIBAE, such as Cl_2/NH_3 for copper [41].

Nowadays, modern dual platform systems (also called dual-beam or cross-beam systems) incorporates a FIB column and a FEB column (focused electron beam, i.e., an SEM) and has advanced capabilities. The electron beam is used for imaging without concern of sputtering the sample surface, which is the case at FIB imaging. As a result, ion beam milling and characterization can be in situ obtained. In addition, electron beam deposition of materials becomes also possible to produce very low energy deposition that will not affect the underlying surface of interest as dramatically as FIBAD. It is possible to integrate the electron and ion beam operation to provide three-dimensional information (FIB tomography) by sputtering the sample in increments of 40–60 nm and obtaining an SEM image of the freshly exposed specimen cross-section after each sputtering cycle. An energy dispersive spectrometry (EDS) detector can be added to provide elemental analysis on the cross-sections.

The geometrical layout and arrangement of the two columns (perpendicular FEB and FIB tilted by ~50°) enables perpendicular tilt of the sample to the ion beam in the coincidence point. To provide full eucentric tilt at all operating conditions a 6-axis eucentric specimen stage (x, y, z, z', tilt and rotate) with a stage position accuracy of ± 1 μm is used in state-of-the-art dual platform systems. The electron and the ion beam coincide at one crossover point some mm below the objective lens of the SEM. The geometrical properties of the two columns allow ion milling on large samples (up to 200 mm wafers) at ion incidence angles up to 90° with respect to the FIB (normal ion incidence). The chamber of dual platform FIB/FEB systems used for TEM specimen preparation is additionally equipped with micromanipulators for lift-out of the FIB milled TEM lamella from the sample and to solder it to the TEM grid [41].

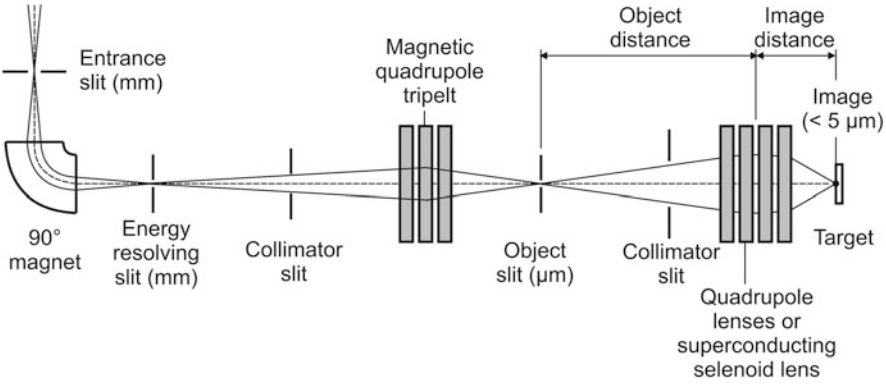

Fig. 3.57 Schematic diagram of a scanning nuclear microprobe

3.7.2 High Energy Focused Ion Beams

Light ion beams, mostly protons, with MeV energies can be focused to beam spot sizes of $\leq$1 µm and scanned in two directions over the sample surface with the availability to image trace element distributions, to measure concentrations of parts per million, and to determine the depth structure of the sample. Such an analytical instrument is called nuclear microprobe or sometimes scanning proton microprobe. Overviews about the nuclear probe formation and operation as well as about applications in materials research and analysis are given in [163–167]. Nuclear microprobes are instruments based around electrostatic accelerators and include a sophisticated high energy focusing system (Fig. 3.57).

The ion beam from the accelerator passes through the object aperture for an imaginary source, the collimator aperture, and the demagnifying lenses, which mostly are combinations of two, three, or four magnetic quadrupole lenses with alternating polarities and different strengths to focus high energy ions [163, 168]. The demagnification is roughly given by the ratio of the object distance and image distance. Demagnifications up to 80 have been achieved, which result in beam spot sizes down to a few 100 nm at focusing the ion beam to an image distance of about 15 cm from the last lens to the image plane (sample surface). The performance of the nuclear microprobes has improved steadily, and as a result spatial resolutions of even 50–100 nm can now be achieved. To obtain large demagnification most nuclear microprobes have lengths of 5–10 m. The ion beam current within the focused beam spot is controlled by the size of the object and collimator apertures whereas the collimator lens defines the beam angular divergence passing into the magnetic quadrupole lenses. By appropriate choosing of the collimator aperture the influence of chromatic and spherical aberrations on the beam spot can be minimized. The beam *xy*-scanning over the sample surface is carried out by two sets of magnetic or electrostatic plates before or after the quadrupole lenses. The arrangement of the scanning system before the lenses leads to a shorter image distance but to limited scanning ranges. In all microprobes the *xy*-coordinates of the

scanning beam are logged by the computer and synchronized with the data acquisition system of the corresponding ion beam analysis method (RBS, ERDA, PIXE, PIGE, etc.), enabling spatially resolved images of element distributions. Problems at fast and effective microanalysis with focused ion beams can arrive due to relatively high ion current densities. For example, the focusing of a proton beam with an ion current of 1 nA into a spot with an area of 1 μm^2 corresponds to an ion flux of 10^{17} cm^{-2} s^{-1} which can cause damage, sputtering, and heating in sensitive materials (e.g., polymers, semiconductors). Therefore, the application of nuclear microprobes with high demagnification optics is concentrated on low-beam current techniques, such as scanning transmission ion microscopy (STIM), transmission channeling, ion beam-induced current (IBIC), ion beam luminescence (IBIL), and single ion event upset imaging where ion beam damage is not a major issue.

On the other hand, higher ion current densities in high-demagnification microprobes can be applied to materials modification in a reasonable short time. A review of nuclear microprobe application to microstructure fabrication in different materials is given in [169]. Examples of these applications are: (1) ion beam writing exposure (lithography) of polymers like PMMA and SU-8 to fabricate micro- and nanostructures with high aspect ratios up to 100, with vertical, smooth sidewalls and low line-edge roughness [170, 171], and (2) local irradiation in semiconductors for damage creation in selected areas, which can be selectively wet etched or electrochemically anodized at different rate, producing patterned micromachined structures in silicon [172].

References

1. Doering H, Nishi J (2008) Handbook of semiconductor manufacturing technology, 2nd edn. CRC Press, Boca Raton, FL
2. Anders A (ed) (2000) Handbook of plasma immersion ion implantation and deposition. Wiley, New York
3. Ziegler JF, Biersack JP, Littmark U (1985) The stopping and range of ions in matter. Pergamon, New York, http://www.srim.org
4. Posselt M (1994) Crystal-TRIM and its application to investigations on channeling effects during Ion implantation. Radiat Eff Defects Solids 130–131:87
5. Möller W, Eckstein W (1984) TRIDYN – a TRIM simulation code including dynamic composition changes. Nucl Instrum Methods Phys Res B 2:814
6. Strobel M, Heinig KH, Möller W (2001) Three-dimensional domain growth on the size scale of the capillary length: effective growth exponent and comparative atomistic and mean field simulations. Phys Rev B 64:245422
7. Posselt M (2001) Atomistic simulation of ion-beam induced defect formation. Mater Res Soc Symp Proc 647:O.2.1.1
8. Lopez GM, Fiorentini V (2004) Structure, energetics, and extrinsic levels of small self-interstitial clusters in silicon. Phys Rev B 69:155206
9. Thomson JJ (1913) Rays of positive electricity. Proc R Soc A 89:1–20
10. Dearnaley G, Freemann JH, Nelson RS, Stephan J (1973) Ion implantation. North Holland, Amsterdam
11. Wilson R, Brewer GR (1973) Ion beams. Wiley, New York

12. Townsend PD, Kelly JC, Hartley NEW (1976) Ion implantation, sputtering and their applications. Academic, London
13. Ryssel H, Ruge I (1978) Ionenimplantation. Akademische Verlagsgesellschaft, Leipzig
14. Helborg R (ed) (2005) Electrostatic accelerators – fundamentals and applications. Springer, Heidelberg
15. Van de Graaff RJ (1931) Electrostatic high voltage generators. Phys Rev 38:1919A
16. Reinhold G, Truempy K (1969) High voltage dc power supplies for beam injectors. IEEE Trans Nucl Sci 16:117
17. Van de Graaff RJ (1960) Tandem electrostatic accelerators. Nucl Instrum Methods 8:195
18. Valyi F (1975) Atoms and ion sources. Wiley, New York
19. Wilson RG, Brewer GR (1973) Ion beams with application in ion implantation. Wiley, New York
20. Alton GD (1993) Ion sources for accelerators in materials research. Nucl Instr Methods B 73:221
21. Brown IG (1989) The physics and technology of ion sources. Wiley, New York
22. Wolf B (1995) Handbook of ion sources. CRC, Boca Raton, FL
23. Chavet I, Bernas R (1967) Experimental study of an ion source for electromagnetic isotope separation with a view to high efficiency operation. Nucl Instrum Methods 51:77
24. Renau A, Smatlak D (1997) A novel ion source for high current ion implantation. In: Ishida E, Banerfee S, Mehta S, Smith TC, Current M, Larson L, Tasch A (eds) Ion implantation technology 96. IEEE, Piscataway, NJ, p 279
25. Freeman JH (1963) A new ion source for electromagnetic isotope separators. Nucl Instrum Methods 22:306
26. Sidenius G (1965) The high temperature hollow cathode ion source. Nucl Instrum Methods 38:19
27. Wolf BH (1972) Characteristics of a cold cathode type Penning source. IEEE Trans Nucl Sci 19:74
28. Penning FM (1937) Ein neues Manometer für niedrige Gasdrucke, insbesondere zwischen $l0^{-3}$ und 10^{-5} mm. Physica 4:71
29. Blanc D, Degeilh A (1961) Les sources d'ions à excitation électrique de haute fréquence. J Phys Radium 22:230
30. von Ardenne M (1956) Tabellen der Elektronenphysik, Ionenphysik und Übermikro-skopie. Deutscher Verlag der Wissenschaften, Berlin
31. Winter H, Wolf BH (1974) Analysis of the duoplasmatron-type discharge as a source of multiply charged heavy ions. Plasma Phys 16:791
32. Lejeune C (1974) Theoretical and experimental study of the duoplasmatron ion source: part I: model of the duoplasmatron discharge. Nucl Instrum Methods 116:417
33. Alton GD, Mills GD (1985) Negative ion sources equipped with continuous annular and spherical geometry surface ionizers. IEEE Trans Nucl Sci NS-32:1822
34. Alton GD, McConnell JW (1988) The emittances and brightnesses of high-intensity negative ion sources. Nucl Instrum Methods A 268:445
35. Friedrich M, Bürger W, Henke D et al (1996) Nucl Instrum Methods Phys Res A 382:357–360
36. Middleton R (1990) A negative-ion cookbook. University of Pennsylvania, Philadelphia, PA, http://www.nd.edu/~nsl/nsl_docs/Making_Beam/SNICS/Negative%20Ion%20Cookbook.pdf
37. Melngailis J (1987) Focused ion beam technology and applications. J Vac Sci Technol B5:469
38. Mackenzie RAD, Smith GDW (1990) Focused ion beam technology: a bibliography. Nanotechnology 1:163
39. Prewett PD, Mair GLR (1991) Focused ion beams from liquid metal ion sources. Wiley, Chichester

40. Orloff J, Utland M, Swanson L (2003) High resolution focused ion beams. Kluwer, New York
41. Giannuzzi LA, Stevie FA (2005) Introduction to focused Ion beams: instrumentation, theory, techniques and practice. Springer, New York
42. Swanson LW (1994) Use of the liquid metal ion source for focused beam applications. Appl Surf Sci 76/77:80
43. Bischoff L (2005) Alloy liquid metal ion sources and their application in mass separated focused ion beams. Ultramicroscopy 103:59
44. Taylor G (1964) Disintegration of water drops in an electric field. Proc R Soc Lond A 280:383
45. Kingham DR, Swanson LW (1984) Shape of a liquid metal ion source. Appl Phys A 34:123
46. Krohn VE, Ringo GR (1975) Ion source of high brightness using liquid metal. Appl Phys Lett 27:479
47. Swanson LW (1983) Liquid metal ion source: mechanism and applications. Nucl Instrum Methods Phys Res 218:347
48. Swanson LW, Schwind GA, Bell AE, Brody JE (1979) Emission characteristics of gallium and bismuth liquid metal field ion sources. J Vac Sci Technol 16:1864
49. Bischoff L, Pilz W, Mazarov P, Wieck AD (2010) Comparison of bismuth emitting liquid metal ion sources. Appl Phys A 99:145
50. Bhaskar ND, Klimcak CM, Fraukolz RP (1990) Liquid metal ion source for cluster ions of metals and alloys. Rev Sci Instrum 61:366
51. Umemura K (1992) Measurement of energy spread and angular intensity of a cesium liquid metal ion source. Appl Phys A 54:115
52. Bischoff L (2008) Application of mass-separated focused ion beams in nano-technology. Nucl Instrum Meth Phys Res B 266:1846
53. Bischoff L, Mair GLR, Akhmadaliev C et al (2005) The post-ionisation of Pb ions from a molten Sn host field-ion emitter. Appl Phys A 80:205
54. Bischoff L, Mair GLR, Mair AWR et al (2004) The mass spectrum of a tin liquid metal ion source. Nucl Instrum Meth Phys Res B 222:622
55. Bischoff L, Akhmadaliev C (2008) An alloy liquid metal ion source for lithium. Phys D Appl Phys 41:052001
56. Bischoff L, Pilz W, Ganetsos T et al (2005) On the temperature dependence of the mass spectra of AuGe and AuGeSi liquid metal alloy ion sources. J Phys Conf Ser 10:214
57. Mair GLR, Bischoff L, Londos CA et al (2005) An in-depth investigation into the temperature dependence of the mass spectra of an $Au_{82}Si_{18}$ liquid metal field emitter. Appl Phys A 81:385
58. Hesse E, Bischoff L, Teichert J (1994) Development of a cobalt liquid alloy ion source. J Phys D Appl Phys 27:427
59. Akhmadaliev C, Pilz W, Bischoff L (2006) European Focused Ion Beam Users Group EFUG, Annual meeting 02.10.2006, Wuppertal, Germany
60. Pilz W, Bischoff L (2011) Emitter for an ion source and method of producing the same, European patent application 04017894.9
61. Bischoff L, Mair GLR, Aidinis CJ, Ganetsos T (2002) Fundamental properties of erbium-ions-producing liquid metal alloy ion sources. Nucl Instrum Meth Phys Res B 197:282
62. Driesel W, Dietzsch C, Hesse E et al (1996) In situ observation of the tip shape of Co-Ge liquid alloy ion sources in a high voltage TEM. J Vac Sci Technol B 14(3):1621
63. Bischoff L, Teichert J (2000) Liquid metal ion source working with an $Er_{70}Fe_{22}Ni_5Cr_3$ alloy. J Phys D Appl Phys 33:L69
64. Mazarov P, Wieck AD, Bischoff L, Pilz W (2009) Alloy liquid metal ion source for carbon focused ion beams. J Vac Sci Technol B 27:L47
65. Reyntjens S, Puers RJ (2001) A review of focused ion beam applications in microsystem technology. Micromech Microeng 11:287
66. Sakudo N, Tokiguchi K, Koike H, Kanomata I (1977) Microwave ion source. Rev Sci Instrum 48:762

67. Hitz D, Girard A, Melin G et al (2002) Results and interpretation of high frequency experiments at 28 GHz in ECR ion sources, future prospects. Rev Sci Instrum 73:509
68. Brainard JP, O'Hagan JB (1983) Single – ring magnetic cusp ion source. Rev Sci Instrum 54:1497
69. Hahto SK, Hahto ST, Ji Q et al (2004) Multicusp ion source with external rf antenna for production of protons. Rev Sci Instrum 75:355
70. Donets ED (1998) Historical review of electron beam ion sources. Rev Sci Instrum 69:614
71. Child CD (1911) Discharge from Hot CaO. Phys Rev 32:492
72. Langmuir I, Compton KT (1931) Electrical discharges in gases. II. Fundamental phenomena in electrical discharges. Rev Mod Phys 3:191
73. Lawson JD (1977) The physics of charged-particle beams. Clarenda Press, Oxford
74. Pierce JR (1940) Rectilinear electron flow in beams. J Appl Phys 11:548
75. Pierce JR (1949) Theory and design of electron beams. Van Nostrand, New York
76. Sloan D, Lawrence E (1931) The production of heavy high speed ions without the use of high voltages. Phys Rev 38:2021
77. Enge HA (1967) Deflecting Magnets. In: Septier A (ed) Focusing of charged particles, vol. 2, New York, Academic, p. 203
78. Seliger RL (1972) E x B mass separator. J Appl Phys 43:2352
79. Cui Z (1996) Investigation of $\mathbf{E} \times \mathbf{B}$ mass filters for focused ion beam systems. Nucl Instrum Methods A 368:288
80. Großer J (1983) Einführung in die Teilchenoptik. B.G. Teubner Verlag, Stuttgart
81. Freeman JH (1976) The boundaries of ion implantation. In: Carter G, Colligon JS, Grant WA (eds) Applications of ion beams to materials 1975, Conference Series no. 28. Institute of Physics, p. 340
82. Ryding G, Wittkover AB (1975) Industrial ion implantation machines. IEEE Trans Manuf Technol 4:21
83. Rose PH, Ryding G (2006) Concepts and designs of ion implantation equipment for semiconductor processing. Rev Sci Instrum 77:111101
84. Leroy C, Rancoity PG (2009) Principles of radiation interaction in matter and detection, 2nd edn. World Scientific, Singapore
85. Lutz G (1999) Semiconductor radiation detectors. Springer, Berlin
86. Laegsgaard E (1979) Position sensitive semiconductor detectors. Nucl Instrum Methods 162:93
87. Wiza JL (1979) Microchannel plate detectors. Nucl Instrum Methods 162:587
88. Adams J, Manly BW (1965) The mechanism of channel electron multiplication. Nucl Sci Electron Eng 37:180
89. Matsuura S, Umebayashi S, Okuyama C, Oba K (1985) Characteristics of the newly developed MCP and its assembly. IEEE Trans Nucl Sci NS-32:350
90. Langstaff DP, Chase T (2007) A multichannel detector array with 768 pixel developed for electron spectroscopy. Nucl Instrum Methods Phys Res A 573:169
91. Mantus DS, Morrison GH (1990) Ion image detection with a microchannel plate evaluated by using a charge coupled device camera. Anal Chem 62:1148
92. Martin C, Jelinsky P, Lampton M et al (1981) Wedge-and-strip anodes for centroid-finding position-sensitive photon and particle detectors. Rev Sci Instrum 52:1067
93. Fulbright HW (1979) III. Ionization detectors, ionization chambers. Nucl Instrum Meth 62:21
94. Döbeli M, Kottler C, Stocker M et al (2004) Gas ionization chambers with silicon nitride windows for the detection and identification of low energy ions. Nucl Instrum Phys Res B 219–220:415
95. Price W (1958) Nuclear radiation detectors. McGraw-Hill, New York
96. Hentschel E, Kotte R, Ortlepp HG et al (1989) Performance of a bragg ionization chamber for depth profiling und surface analyses. Nucl Instrum Methods Phys Res B 43:82
97. Assmann W (1992) Ionization chambers for materials analysis with heavy ion beams. Nucl Instrum Meth Phys Res B 64:267

98. Mayer JW, Eriksson L, Davies JA (1970) Ion implantation in semiconductors: silicon and germanium. Academic, New York
99. Wegman L (1984) The historical development of ion implantation. In: Ziegler J (ed) Ion implantation science and technology. Academic, New York, p 3
100. Rose H (1985) A history of commercial implantation. Nucl Instrum Methods Phys Res B 61:1
101. Rimini E (1995) Ion implantation: basics to device fabrication. Kluwer, Norwell
102. Chason E, Picraux ST et al (1997) Ion beams in silicon processing and characterization. J Appl Phys 81:6513
103. McKenna CM (2000) 12th IEEE international conference ion implantation technology proceedings. IEEE, New York, p 1
104. Horsky T (1998) Indirectly heated cathode arc discharge source for ion implantation of semiconductors. Rev Sci Instrum 69:840
105. Tokiguchi K et al (2002) 14th IEEE international conference on ion implantation technology proceedings. IEEE, New York, p 629
106. Glavish HF (1981) Magnet optics for beam transport. Nucl Instrum Methods Phys Res 189:43
107. Nobes MJ, McLaren MG (1996) Proceedings of the 11th IEEE international conference on ion implantation technology. IEEE, New York, p 379
108. Benveniste V, Kellerman P, Graf MA (1998) Proceedings IEEE international conference on ion implantation technology. IEEE, New York, p 432
109. Howard K (1991) Implant uniformity evaluation using a Varian/Extrion scan compensator module on an electrostatic scanning ion implanter. Nucl Instrum Methods Phys Res B 55:202
110. Campbell OF, Ray AM, Sugitami M, Sato F (1998) Introducing the MC3 medium current 300 mm implanter. Conference on ion implantation technology proceedings. IEEE, New York, p 154
111. Kaim RE, van de Meulin PFHM (1991) The EXTRION 220 parallel scan magnet. Nucl Instrum Methods Phys Res B 55:453
112. Pippins MW (1991) A system and performance overview of the EXTRION 220 medium-kurrent ion-implanter. Nucl Instrum Methods Phys Res B 55:423
113. Harlan JM, Petry K (1998) Proceedings of the IEEE international conference on ion implantation technology. IEEE, New York, p 266
114. Cambell OF, Ray AM (1998) Proceedings of the international conference on ion implantation technology. IEEE, New York, p 154
115. Angel G et al (1998) Proceedings of the IEEE international conference on ion implantation technology. IEEE, New York, p 188
116. Ryding G (1981) Target chambers for ion implantation using mechanical scanning. Nucl Instrum Methods Phys Res 189:239
117. Murrell A et al (2004) Proceedings of the international conference on ion implantation technology. IEEE, New York, p 20
118. Murakami J et al (2008) Proceedings of the international conference on ion implantation technology. IEEE, New York, p 180
119. Sundström H et al (2008) Proceedings of the international conference on ion implantation technology. IEEE, New York, p 184
120. Tokiguchi K et al (2000) Proceedings of the 12th international conference on ion implantation technology. IEEE, Alpbach, Austria, p 372
121. Mera K, Tomita H, Tokiguchi K (2002) High current ion implanter for 300 mm SIMOX wafer production. Hitachi Rev 51:113
122. Blake J et al. (2002) Proceedings 2002 international SOI conference, Williamsburg, p 109
123. Blake J, Richards S (2002) Proceedings of the 14th IEEE international conference on ion implantation technology. IEEE, New York, p 395
124. IBIS Technology Corporation. http://www.ibis.com
125. SOITEC. http://www.soitec.com
126. SHE America. http://www.shin-etsu.com

127. Aspar B, Bruel M, Moriceau H et al (1997) Basic mechanisms involved in the smart-cut® process. Microelectron Eng 36:233
128. SiGen. http://www.sigen.net
129. Sato M et al (2002) Proceedings of the 14th IEEE international conference on ion implantation technology. IEEE, New York, p 383
130. Murata H et al (2006) Uniformity improvement of the Ion implantation system for Low temperature poly-silicon TFTs. J Korean Phys Soc 48:S27
131. Rose PH (1997) Ion implantation, yesterday and today. Solid State Technol 40:129–130
132. Purser KH, Cleland M, Naylor H, Smick T (1985) Concepts and designs of ion implantation equipment. In: Proceedings SPIE advanced applications of ion implantation, vol 0530
133. Turner N, Purser KH, Sieradzki M (1987) Design considerations of VLSI compatible production MeV ion implantation system. Nucl Instrum Methods Phys Res B 21:285
134. Tokoro N, Holbrook N, Hacker D (2000) Proceedings of the 12th international conference on ion implantation technology. IEEE, Alpbach, Austria, p 368
135. Sun HL, Lee W, Xu K et al (2000) Proceedings of the 12th international conference on ion implantation technology. IEEE, Alpbach, Austria, p 385
136. Glavish HF, Bernhardt D, Boisseau P et al (1987) Production high energy ion implanters using radio frequency acceleration. Nucl Instrum Methods Phys Res B 21:264
137. Conrad JR, Radtke J, Dodd RA, Worzala FJ (1987) Plasma source ion-implantation technique for surface modification of materials. J Appl Phys 62:4591
138. Tendys J, Donnelly IJ, Kenny MJ, Pollock JTA (1988) Plasma immersion ion implantation using plasmas generated by radio frequency techniques. Appl Phys Lett 53:2143
139. Anders A (1997) Metal plasma immersion ion implantation and deposition. Surf Coat Technol 93:158
140. Günzel R, Brutscher J, Mändl S, Möller W (1997) The use of plasma source ion implantation for wear protection. In: Pauleau Y, Barna PB (eds) Protective coatings and thin films. Kluwer, Dordrecht, p 635
141. Ensinger W (1998) Modification of mechanical and chemical surface properties of metals by plasma immersion ion implantation. Surf Coat Technol 100–101:341–352
142. Chu PK, Qin S, Chan K (1996) Plasma immersion ion implantation a fledgling technique for semiconductor processing. Mater Sci Eng R17:207
143. Ensinger W (1998) Semiconductor processing by plasma immersion ion implantation. Mater Sci Eng A 253:258
144. Chu PK (2003) Semiconductor applications of plasma immersion ion implantation. Plasma Phys Control Fusion 45:555
145. Liebert C, Walther S, Felch S (2000) Proceedings of the 12th international conference on ion implantation technology. IEEE, Alpbach, Austria
146. Van de Graaff RJ (1931) A 1500000 volt electrostatic generator. Phys Rev 38:1919
147. Herb RG (1974) Pelletron accelerators for very high voltage. Nucl Instrum Methods 122:267
148. Hinterberger F (1997) Physik der Teilchenbeschleuniger und Ionenoptik. Springer, Berlin
149. National Electrostatics Corporation (2002) National Electrostatics Corporation, Middleton, WI. http://www.pelletron.com/charging.htm
150. Cockcroft JD, Walton ET (1932–1934) Experiments with high velocity ions. Proc Roy Soc Lond A136:229 (1932), A137:229 (1932), and A144:704 (1934)
151. Greinacher H (1921) Über eine Methode, Wechselstrom mittels elektrischer Ventile und Kondensatoren in hochgespannten Gleichstrom umzuwandeln. Z Phys 4:195
152. Cleland MR, Morgenstern MR (1960) Low-cost electrons: three manufacturers offer new accelerators. I. Dynamitron. A high-power electron accelerator. Nucleonics 18:52
153. Hanley PR, Cleland CF, Mason P et al (1969) The tandem Dynamitron accelerator. IEEE Trans Nucl Sci 16:90–95
154. Alvarez L (1951) Energy doubling in dc accelerators. Rev Sci Instrum 22:705
155. Kiisk M, Erlandsson B, Faarinen M (2002) The charge state distribution of carbon beam measured at the Pellatron accelerator. Nucl Instrum Methods A 481:1–8

156. Langsdorf A Jr (1983) Reduction of ripple voltage in a dynamitron. IEEE Trans NS-30:1453–1455
157. Mous DJW et al (1992) The HVEE tandetron line; new development and design considerations. Nucl Instum Methods B 62:421–424
158. Philipp G, Scheib U, Hofmann A (1974) He- and Li- ions from a modified charge exchange source. Nucl Instrum Methods 115:507–508
159. National Electrostatics Corporation (NEC). http://www.pelletron.com
160. High Voltage Engineering Europe (HVEE). http://www.highvolteng.com
161. Bischoff L (2008) Application of mass-separated focused ion beams in nanotechnology. Nucl Instrum Methods Phys Res B 266:1846–1851
162. Melngailis J (2001) Applications of ion microbeam lithography and direct processing. In: Helbert JN (ed) Handbook of VLSI lithography. Noyes, Park Ridge, NJ, pp 791–855
163. Breese MBH, Jamison DN, King PJC (1996) Materials analysis with nuclear microprobe. Wiley, New York
164. Breese MBH, Grime GW, Watt F (1992) The nuclear microprobe. Annu Rev Nucl Part Sci 42:1–38
165. Watt F (1997) The nuclear microprobe: a unique instrument. Nucl Instrum Methods Phys Res B 130:1–8
166. Jamison DN (1997) Recent applications of nuclear microprobes analysis to frontier materials. Nucl Instrum Methods Phys Res B 130:706–716
167. Wang Y, Nastasi M (eds) (2010) Handbook of modern ion beam materials analysis, vol 2, 2nd edn. Materials Research Society, Warrendale, PA, pp 285–305
168. Watt F, Grime GW (1987) Priciples and applications of high energy ion microbeams. Adam Hilger, Bristol
169. Watt F, Breese MBH, Bettiol AA, van Kan JA (2007) Proton beam writing. Mater Today 10:20–29
170. Watt F (1999) Focused high energy proton beam micromachining: a perspective view. Nucl Instrum Methods Phys Res B 158:165–172
171. van Kan JA, Sanchez JL, Xu B et al (1999) Resist materials for proton micromachining. Nucl Instrum Methods Phys Res B 158:179–184
172. Teo EJ, Tavernier EP, Breese MBH et al (2004) Three-dimensional micromachining of silicon using a nuclear microprobe. Nucl Instrum Methods Phys Res B 222(513):517

Materials Processing

4

Materials processing by implantation of energetic ions into solid surfaces has been applied in many fields of modern production technologies. For the last 40 years, ion implantation became the key technology especially in semiconductor technology for the production of ultra-large-scale integrated (ULSI) circuits, for example, silicon processors and memory devices. The type and value of semiconductor conductivity can be selected by the type and amount of implanted doping ions, for example, implantation of boron, gallium, or indium ions for p-type doping and of phosphorous, arsenic, or antimony ions for n-type doping of silicon. The necessary dopant concentration to be implanted is below 0.1 at.%. On the other hand by implanting high ion fluences, high impurity concentrations of tens of at.% can be achieved giving the possibility to synthesize buried layers of compound materials, for example SiO_2 layers in Si by high fluence oxygen ion implantation. The well-known relations between ion energy and ion penetration depth for all important dopant–semiconductor combinations meet the demands of microelectronic technology for introducing doping concentrations with an error smaller than ± 1 %. Lateral doping homogeneities over large wafer areas with an error of ~1 %, multiple implantation steps of different ions without significant interaction of the introduced dopants are standard for the ion implantation technique. Ion implantation is the only doping technique for the fabrication of device structures with dimensions in the nanometer range.

The knowledge of fundamentals of ion–solid interactions, mainly the penetration depth or ion depth distribution in the material as described in Chap. 2 is the prerequisite for the application of ion implantation in materials processing.

4.1 Ion Irradiation Effects in Crystalline Materials

At ion irradiation of solids (mostly called ion implantation) energetic ions penetrate into the material to a range R proportional to the ion energy E, whereas the concentration of the introduced impurity atoms N is directly proportional to the ion current density j or the ion fluence Φ. Due to magnetic ion mass separation

B. Schmidt and K. Wetzig, *Ion Beams in Materials Processing and Analysis*,
DOI 10.1007/978-3-211-99356-9_4,

the purity of introduced atoms is extremely high. Furthermore, impurity concentrations above their solubility limit in the solid target can be easily achieved, because ion implantation concerns a thermodynamic nonequilibrium process. The shape and depth position $N(x)$ can be adjusted by variation of the ion energy and the incidence angle of the ion beam relative to the sample surface normal. Usually the low target temperature prevents in-diffusion of disturbing other impurities from the ambient. Doping by ion implantation causes structural changes (radiation damage) which are especially important in crystalline targets (e.g., semiconductors), overlaying the doping process. Therefore, subsequent thermal annealing of ion beam-induced crystal defects by re-crystallization of the crystal lattice and the simultaneous electrical activation of impurity atoms (localization of dopants on crystal lattice sites) is an integral part of ion implantation in many cases.

4.1.1 Depth Profiles and Ion Channeling

The ion distribution $N(x)$ [see (2.26) in Chap. 2] normally distributed around R_p drops by one, two, and five decades at the following depth values x, respectively,

$$\begin{aligned} N(x) &= 10^{-1} \cdot N_{max} \quad \text{at} \quad x = R_p \pm 2 \cdot \Delta R_p, \\ N(x) &= 10^{-2} \cdot N_{max} \quad \text{at} \quad x = R_p \pm 3 \cdot \Delta R_p, \\ N(x) &= 10^{-5} \cdot N_{max} \quad \text{at} \quad x = R_p \pm 4.8 \cdot \Delta R_p. \end{aligned} \tag{4.1}$$

The values x in (4.1) can be used for the estimation of necessary layer thicknesses for implantation masking on patterned substrates.

The three-dimensional $N(x, y, z)$ ion distribution including the transversal ion straggling ΔR_l for example at the edge of an implantation mask in the y-direction can be approximated by simple Gaussian distributions, with two straggling parameters ΔR_p (longitudinal straggling) and ΔR_l (lateral straggling).

The ratio of lateral and longitudinal ion straggling $\Delta R_l/\Delta R_p$ has been determined in [1]. For masks with perpendicular edges one has taken into account that there exists a lateral straggling component underneath the mask but due to masking the opposite component is missing. Therefore, the impurity concentration near to the edge is lower compared to implanted areas which are far from the mask edge at least by the lateral straggling ΔR_l. Directly below the mask edge the concentration amounts $N(y) = N_{max}/2$. For light ions the lateral straggling is slightly higher compared to the longitudinal straggling. For heavy ions the lateral broadening of the profile is nearly constant and the ratio $\Delta R_l/\Delta R_p \approx 0.3$–$0.4$ becomes constant. At implantation in masking windows with small dimensions of <1 μm the lateral ion straggling becomes more important and has to be taken into account. To minimize ΔR_l, the edges of the masking layer are often tapered rather than perfect steep, so that ions are gradually prevented from entering the target.

In practice, R_p, ΔR_p, and ΔR_l are tabulated for most common impurities implanted, for example, into Si, Ge, GaAs, SiO_2, Si_3N_4, Al_2O_3, and photoresists

as a function of ion energy and can be found in [2, 3]. Alternatively, $N(x)$, R_p, and ΔR_p can be easily calculated using the well-known SRIM code (http://www.srim.org) developed by Ziegler et al. [4].

The Gaussian approximation for $N(x)$ represents the most simple approximation for the description of the ion range distribution. This approximation to the profile is good for lower energies, but is less correct of higher energies where the profile becomes asymmetric or "skewed." Nevertheless, the Gaussian profile approximation is very useful as a fit to experimental data for the profile near its peak. For example, the peak value N_{max} is mostly within 1 % of the measured value (except for very shallow profiles).

The ion depth distribution $N(x)$ can be characterized in terms of its moments, where the projected range R_p is the normalized first moment and the standard deviation ΔR_p the second moment. Higher moments are the skewness γ describing the asymmetry of the distribution and the kurtosis β indicating how flat the top of the distribution is. A negative skewness means that the distribution is shifted toward the surface, for example due to back scattering of light ions (e.g., B in Si). This case is common for light ions at high energies. At positive skewness the distribution is shifted away from the surface, for example due to ion channeling [see (2.23) and (2.24) in Chap. 2] and which is common for heavy ions at low ion energies. Several different distributions have been employed to give a more accurate fit to the moments of an ion implant distribution than is possible using one Gaussian. The most popular of these are the semi-Gaussian in the case of small asymmetry of profiles ($\gamma < \Delta R_p$), and the Pearson-IV distribution or dual Pearson-IV distribution for amorphous and crystalline targets, respectively [5–10] in the case of large asymmetries of implanted profiles. These semiempirical models are based on both experimental data and physically based models with verified accuracy.

Another approach which simulates ion implantation depth profiles is based on Monte Carlo simulations using the formalism for the binary collision of primary ion–target atom and secondary target–target atom collisions (see Chap. 2). The Monte Carlo approach is used in the development of the physically based models, and these models help to provide the theoretical foundation required in understanding ion implantation, and in technology development and process control. In the case of amorphous targets with only random ion scattering in the target, the SRIM code (http://www.srim.org) and in the case of crystalline targets with possible ion channeling in the crystal, the Crystal-TRIM code [11] are widely used. These two Monte Carlo simulation codes calculate not only the as-implanted ion depth distribution $N(x)$ but provide also the defect concentration and their distribution over depth. The program Crystal-TRIM simulates ion implantation into single-crystalline targets (e.g., Si, Ge, diamond) with up to ten amorphous overlayers of arbitrary composition (with up to three components). The code can be used to calculate as-implanted range and damage distributions as function of depth. Not only atomic ions but also molecular ions (with up to three components) may be considered. Dynamic simulation of ion-induced damage accumulation in single-crystalline substrates (including the formation of amorphous layers) can be carried out.

The applicability of Monte Carlo computer simulations codes based on the binary collision approximation and mentioned before is limited in that they do not account for the modification of the target composition during ion implantation, target removal by sputtering, and target swelling. Thereby, reliable results can only be expected for relatively low implantation fluences of $\Phi \leq 1 \times 10^{16}$ cm^{-2}. At high fluences, a significant reordering of the lattice atoms due to collision sequences may occur. This leads, for example, to a change of the local concentrations in polyatomic or multilayered substances. Furthermore, the implanted ions may, at sufficiently high concentration, play a significant role in the dissipation of collision cascades. Based on the TRIM code the program TRIDYN developed by Möller and Eckstein [12] simulates the dynamic change of thickness and/or composition of multicomponent targets during high fluence ion implantation in amorphous targets. Up to five different atomic species, including those of the ion beam, may be considered. It is possible to use in the beam up to four different ion species with different energies and angles of incidence. The initial target may consist of up to four different species (up to five if some amount of a beam species is already present in the target). Effects such as ion deposition and reflection, sputtering, and ion mixing at interfaces can be computed. The main fields of application of TRIDYN include high fluence ion implantation, ion beam synthesis, sputtering and ion mixing of polyatomic solids, ion beam- or plasma-assisted deposition of thin film, and ion beam- or plasma-assisted etching. An overview about the development of different models for determining of ion implantation profiles and the conditions under which they can be applied to provide useful predictions can be found in [13].

In crystalline targets, for example semiconductor materials (Si, Ge, GaAs, SiC, etc.), the ion range distribution can be significantly influenced by the ion channeling effect as described in Chap. 2. Selected examples of as-implanted depth distributions in dependence on the tilt angle and the rotation degree are shown in Figs. 4.1 and 4.2. As demonstrated in these figures channeling effects are also successfully simulated in a highly accurate manner by using, for example, the dual Pearson model [14] and the Crystal-TRIM code [17] which are shown in Figs. 4.1 and 4.2, respectively.

Due to beam scan angle α_s and/or the wafer misscut and bow angles α_b, the incidence angle of ions relative to the surface normal can vary across the wafer in the order of $\leq 1°$. The resulting channeling variations cause the depth distribution to vary across the wafer. As the extent of local channeling is difficult to control, channeling must be further reduced by additional methods. Channeling does not occur if there is significant implant damage that turns the implanted layer into an amorphous one. Heavy ions such as P^+ and As^+ at large fluences do not show channeling. Light ions and/or low dose implants are prone to channeling. In such instances, channeling can be prevented by:

- Implanting through a thin amorphous layer (e.g., silicon oxide) to randomize the directions of the ions as they enter the crystal lattice
- Using heavy ions, for example BF_2 or heavier molecules rather than boron

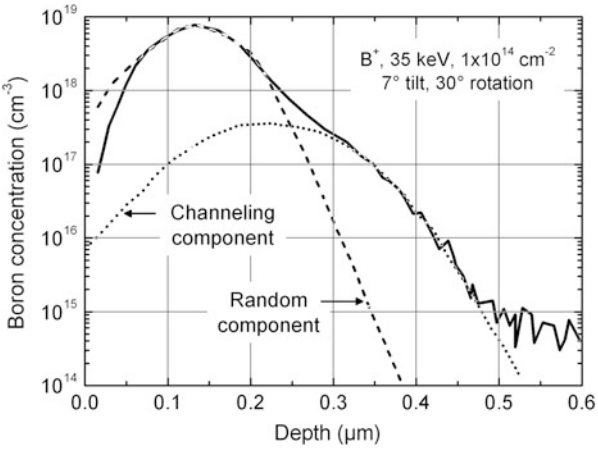

Fig. 4.1 Fit of the one-dimensional dual Pearson distribution (*dotted line*) to the experimental boron profile measured by SIMS (*solid line*) [14]

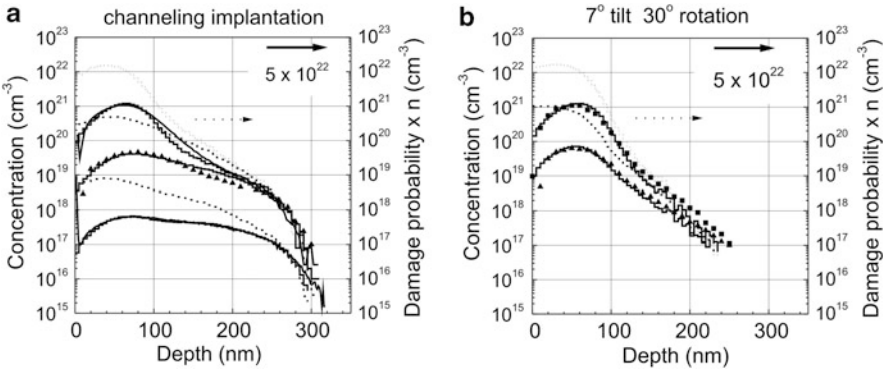

Fig. 4.2 Range and damage distributions for 15 keV B^+ implantations into (100)-Si, in the [15] axial channel direction (**a**), for three different fluences: 1×10^{13} (*bottom curves*), 5×10^{14}, and 8×10^{15} cm^{-2} (*top curves*). The corresponding profiles for tilted implants (**b**) are given for two fluences: 5×10^{14} (*bottom curves*) and 8×10^{15} cm^{-2} (*top curves*). The SIMS data (*continuous lines*, *triangles*, and *squares*) were taken from [16]. The histograms were obtained by Crystal-TRIM simulations [17]. The damage profiles, given by the damage probability multiplied by the atomic density of Si, are shown by *dashed* and *dotted curves*

- Implanting heavy, but electrically inactive species, such as Si or Ge, prior to the actual dopant implantation. The preimplantation turns the wafer surface into an amorphous layer

These and other issues associated with ion channeling are described more in detail in [18].

4.1.2 Implantation-Induced Crystal Damage

Energetic ions traveling through the crystalline target lose their energy in a series of nuclear and electronic collisions and come to rest many atom layers below the surface. Only nuclear collisions with the target atoms result in their displacements referred as damage or disorder. At the collision the ions transfer kinetic energy and momentum to the target atom. The displaced target atom (energetic recoil lattice atom) itself can displace other target atoms resulting in a collision cascade and generation of additional disorder. Along collisional cascades an agglomeration of vacancies and interstitial atoms (Frenkel pairs) and more complex defects (defect clusters) are formed in the crystal lattice. Due to higher nuclear stopping heavy ions transfer more energy to displaced atoms compared to light ions for which electronic stopping dominates. With increasing ion fluence the damaged lattice volumes begin to overlap and finally form a completely amorphous layer without any long-range lattice order. The number of defects and their depth distribution $N_d(x)$ in a target depend on the ion–target mass ratio M_i/M_t, ion energy E, fluence Φ and the fluence rate (or ion flux) J, and the target temperature. As an example the defect evolution in Si at 40 keV P^+ ion irradiation is schematically shown in Fig. 4.3.

Compared to the implanted impurity depth profile the maximum of the damage depth distribution is always shifted to the surface due to the ion energy loss in displacements of lattice atoms $E_d > 0$ [19]. The amorphization fluence Φ_a can be roughly estimated using formula (4.2) if one assumes that all target atoms are displaced:

$$\Phi_a = \frac{2 \cdot E_d \cdot N_t}{(dE/dx)_n}, \tag{4.2}$$

where N_t is the atomic density of the target and $(dE/dx)_n$ the energy loss at nuclear collision per length (depth) unit. In many cases (4.2) underestimate the amorphization fluence because annihilation (annealing) effects during implantation, e.g., outdiffusion of vacancies or collisions with already displaced atoms, are not taken into account. A more correct calculation of the amorphization fluence is given by Morehead and Crowder [20]. Table 4.1 gives calculated and measured amorphization fluences for common ions used for implantation in semiconductors at room temperature.

For some important ions used in silicon technology, the dependence of the amorphization fluence on the silicon target temperature is shown in Fig. 4.4. At the fast rise of the amorphization fluence Φ_a the corresponding temperature T_a means that heating crystalline silicon samples to this temperature amorphization of silicon can be avoided. For example, sample heating to $T_a \approx (400–450)\ ^\circ C$ suppresses amorphization of silicon for all shown ions. Furthermore, Fig. 4.4 demonstrates that for light ions (e.g., boron) amorphization of silicon cannot be achieved at room temperature and at common fluences $<10^{17}\ cm^{-2}$.

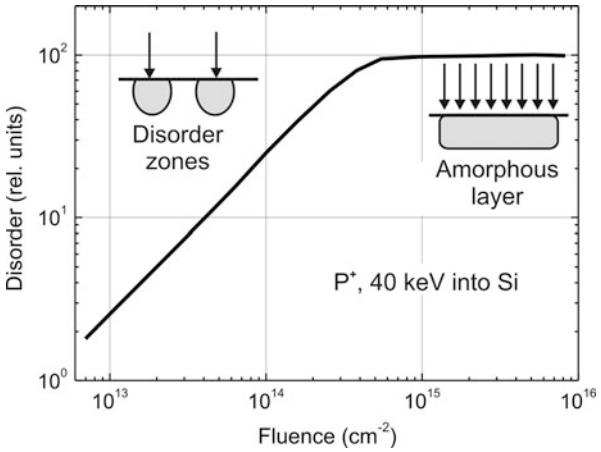

Fig. 4.3 Defect evolution in Si at 40 keV P^+ ion implantation as a function of ion fluence

Table 4.1 Amorphization fluence for common ions in different semiconductors

Semiconductor	Ion	Ion mass of the main isotope	Amorphization fluence Φ_a (cm^{-2})	Reference
Si	B	11	8×10^{16}	[20]
	Al	27	$\geq 5 \times 10^{14}$	[21]
	P	31	6×10^{14}	[20]
	Ga	70	2×10^{14}	[20]
	As	75	2×10^{14}	[20]
	Sb	122	1×10^{14}	[21]
	In	204	1×10^{14}	[21]
	Bi	209	5×10^{13}	[21]
Ge	B	11	2×10^{16}	[20]
	P	31	–	–
	Ga	70	–	–
	As	75	–	–
	In	204	5×10^{13}	[20]
GaAs	C	12	1×10^{15}	[22]
	Si	28	2×10^{14}	[22]
	Zn	64	3×10^{13}	[23]
	Cd	114	3×10^{13}	[23]
GaP	Te	130	1×10^{14}	[24]

For high energy light ions, most of the energy loss is due to electronic collisions which do not produce displacement damage. With increasing penetration depth, light ions lose energy until the cross-over of the electronic and nuclear energy losses $(dE/dx)_e$ and $(dE/dx)_n$, respectively, is reached below which the nuclear stopping becomes dominant (e.g., at $E < 10$ keV for 80 keV B^+). Therefore, most lattice damage occurs in the part of the light ion trajectory beyond this

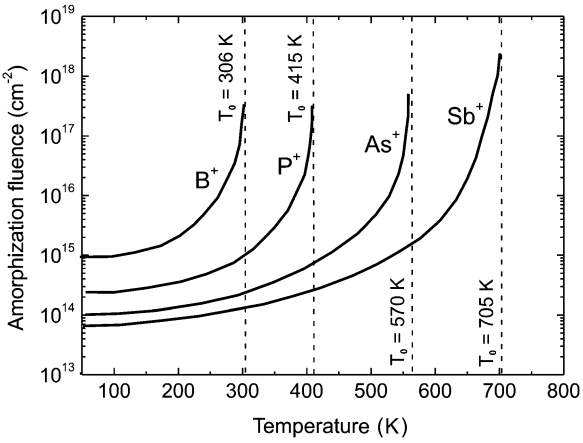

Fig. 4.4 Amorphization fluence as a function of target temperature for common ions used ion implantation into silicon taken from [20]

point. This light ion-induced damage is characterized by a small damage volume density which amounts to ~2 × 10^{20} cm^{-3} and ~0.2 % of Si atoms. Light ions produce only trails of primary Si recoils around the trajectory of the implanted light ion. The low energy recoiled atoms are separated only by small distances from the vacancies they leave. This explains possible dynamic annealing of these defects and therefore no formation of amorphous layers in silicon during room temperature and high fluence B^+ implantation. The light ion-induced damage is thus characterized by primary crystal defects (mostly vacancies and interstitials) which require different annealing procedures compared to crystalline regrowth of implantation-induced amorphous layers. The most important effects of crystal damage and defects induced by ion implantation are summarized in Fig. 4.5.

Comparing experimental data for the amorphization fluence with the number of displaced atoms per ion one can conclude that other effects than only the ion fluence can influence the creation of damage. Besides the target temperature and the ion mass, the defect density around the ion trajectory in the target highly depends on the diffusion of vacancies (V) and interstitial atoms (I). The defect density increases with increasing ion mass because the contribution of the nuclear energy loss to the overall energy loss increases. The mobility of defects becomes higher with increasing target temperature and depends on the remaining crystal order. At low defect density the diffusivity of vacancies and interstitials is higher and thus the probability for their recombination is higher leading to a partial defect annealing during ion implantation. High defect densities prevent the effect of self-annealing and the situation becomes more complicated if interaction between vacancies (formation of di-vacancies, V–V), between vacancies and dopants (e.g., vacancy–boron complex, V–B), and between vacancies and other impurities in silicon (e.g., vacancy–oxygen complex, V–O) with different mobilities takes place.

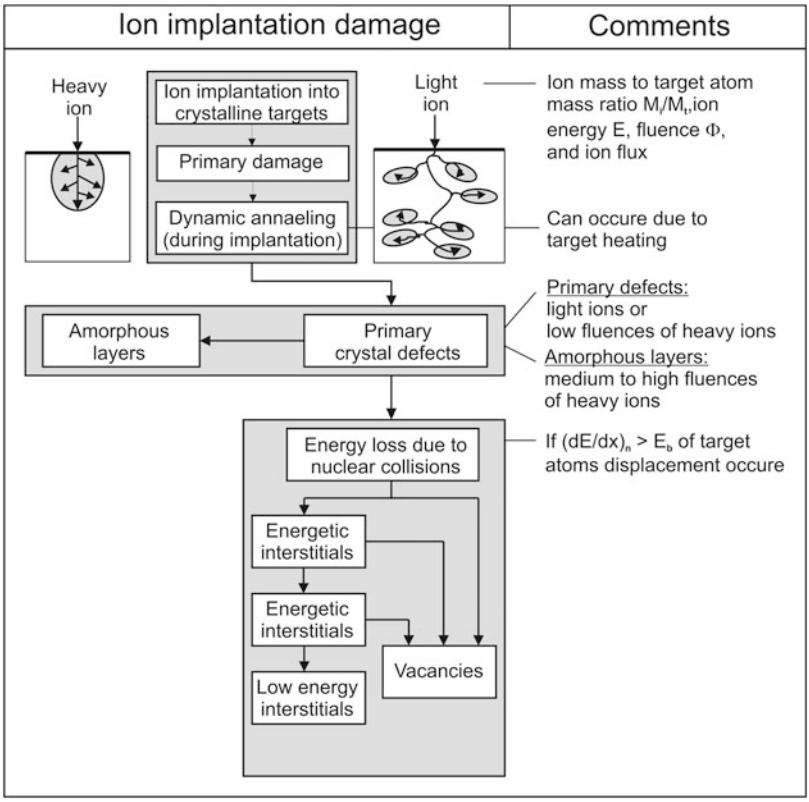

Fig. 4.5 Most important effects of crystal damage and defects induced by ion implantation in crystalline targets

4.1.3 Sputtering Effects and Implanted Profile Change

High fluence ion implantation with $\Phi > 10^{16}$ cm^{-2} leads to effects which usually do not occur in implantations with fluences $<10^{16}$ cm^{-2} performed for conventional implantation doping of semiconductors. The main effects are the dynamical change of the target properties during the implantation process (density, composition, chemical properties, stopping power), diffusion, and surface sputtering. Sputtering (the escape of target atoms, ions, and clusters from the target surface due to physical knock-on process caused by the incident ions) depends on the ion mass and energy as well as the properties of the target material (see Chap. 2). The depth distribution of the implanted atoms for a fluence $\Phi = j{\cdot}t$ (targeted fluence) is then given by Krimmel and Pfleiderer [25]:

$$N(x,\Phi) = \frac{N_t}{2\cdot Y}\cdot\left[\operatorname{erf}\frac{x - R_p + \frac{\Phi\cdot Y}{N_t}}{\sqrt{2}\cdot\Delta R_p} - \operatorname{erf}\frac{x - R_p}{\sqrt{2}\cdot\Delta R_p}\right], \tag{4.3}$$

where Y is the sputtering coefficient and N_t the atomic target density ($N_t = \rho/M_t \cdot m_a$ with ρ the mass density, M_t the target atom mass, and $m_a = 1.66 \times 10^{-24}$ g the atomic mass unit) and with the actual surface being always at $x = 0$. The proportion of re-sputtered implanted ions Φ_s can be approximately calculated by integrating $N(x, \Phi)$ over the range $x \leq 0$ and becomes

$$\Phi_s(\Phi) = \left(\frac{\Phi}{2} - \frac{N_t \cdot R_p}{2 \cdot Y}\right) \cdot \left[\operatorname{erf} \frac{\frac{\Phi \cdot Y}{N_t} - R_p}{\sqrt{2} \cdot \Delta R_p} + 1\right] + \frac{\Delta R_p \cdot N_t}{\sqrt{2\pi}} \cdot \exp \frac{-\left(\frac{\Phi \cdot Y}{N_t} - R_p\right)^2}{2 \cdot \Delta R_p}. \tag{4.4}$$

The difference $\Phi_r = \Phi - \Phi_s$ is that fraction of the implanted ions which is actually deposited in the target (the retained fluence). For high fluence implantation at low ion energies, a saturation of surface concentration is reached which corresponds in the equations above to the case of assuming that Φ is infinite. Then, it follows from (4.4) that the maximum density of implanted atoms at the surface is $\sim N_\infty = N(0, \infty) = N_t'/Y$. For the new target density N_t' it can approximately be assumed that $N_t' = N_t + N_\infty$. Therefore, at the surface the implanted impurity density is $N_\infty = N_t/(Y - 1)$. Furthermore, from (4.4) a saturation fluence of

$$\Phi_\infty = \Phi_r(\infty) = \frac{N_t \cdot R_p}{Y - 1} \tag{4.5}$$

can be found.

As an example, Fig. 4.6 shows Co^+ implantation profiles in silicon calculated from (4.3) for different implantation fluences. For the highest fluence of 1×10^{17} cm^{-2} the distribution corresponds to the saturation case with maximum concentration at the surface. The calculation does not include the effect of cobalt-atom diffusion during implantation.

Calculating retained fluence Φ_r according to (4.4) for 35 keV Co^+ implantation in Si at a sputtering yield of $Y = 3$ and a fluence of 1×10^{17} cm^{-2} we get that the retained to targeted fluence ratio Φ_r/Φ is only in the range of ~50 % if the saturation stage is reached. At saturation the maximum implanted impurity concentration is located always at the target surface and depends on the sputtering coefficient Y which is given at normal incidence by the Sigmund formula [27, 28]. In this formula, target swelling, blistering, and re-deposition of sputtered target material are neglected. With increasing ion mass the sputter yield increases with a maximum of the ion energy dependence usually between 10 and 500 keV depending on the M_t/M_i ratio. Sputter coefficients are extensively investigated for metals irradiated with noble ions (He, Ne, Ar, Kr, Xe) and other ions and can be found for example in [27, 29]. As shown in Fig. 4.7, for Si, sputter coefficients for common ions (B, P, Ga, As, Sb, and Bi) have been measured and calculated by different authors and are published in [27, 30, 31]. Sputtering yields at noble ion

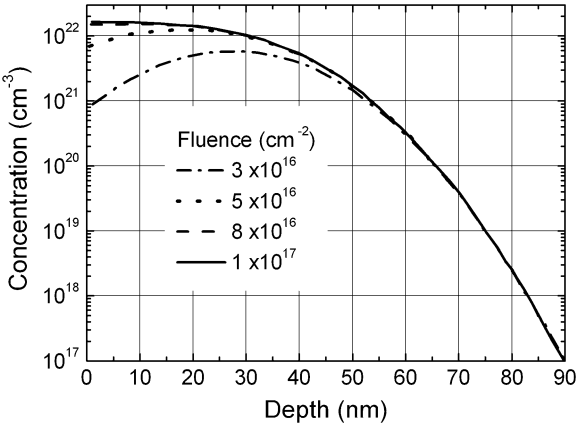

Fig. 4.6 Calculated cobalt concentration profiles for various implantation fluences of 35 keV Co^+ ions in silicon at normal incidence ($R_p = 33$ nm; $\Delta R_p = 12.8$ nm; $Y = 3$) [26]

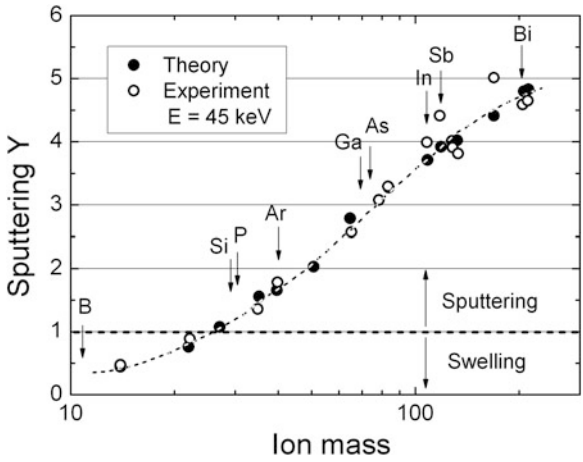

Fig. 4.7 Sputtering yield of 45 keV ions for silicon as a function of ion mass at normal incidence; *open cycles* of experimental data are taken from [30] and *full cycles* of theoretical values are taken from [27]

irradiation of III–V- (GaAs, InP, GaSb, InSb, GaN) and II–VI- (CdS, CdSe, CdTe, HgTe, ZnTe, PbTe) semiconductors also have been intensively investigated and are published in [32, 33].

Applying the TRYDYN simulation code to high fluence ion implantation the change of the profile due to surface layer removal by sputtering can be very well predicted, as shown in Fig. 4.8 for 60 keV Co^+ implantation into silicon at normal incidence. The example in Fig. 4.8 demonstrates that at the surface the maximal atomic fraction of Co in Si introduced by ion implantation is limited to 33 %. The black bars at the beginning of each profile indicate the location of the actual surface for each implanted fluence, or, in other words, the thickness of the sputter-removed

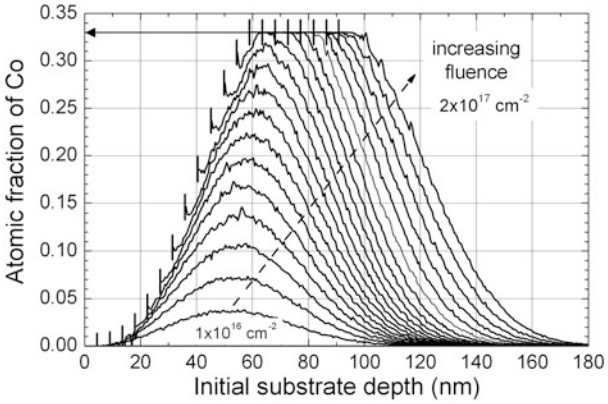

Fig. 4.8 Change and shift of the Co concentration depth profile in dependence on implanted fluence in the range (1–20) $\times$ 10^{16} cm^{-2} for 60 keV Co^+ implantation into silicon. The fluence increment between the profiles is 1 $\times$ 10^{16} cm^{-2} (Röntzsch L private communication)

Si layer which amounts, for example, 90 nm at an implanted Co^+ fluence of 2×10^{17} cm^{-2}.

Because high fluence ion implantation produces drastic changes in the target (target density, target composition, phase changes crystalline to amorphous) at low sputtering yields for light ions (ion mass M_i comparable or smaller than target atom mass M_t), swelling of the target can appear. For sputtering investigations, this effect can be neglected in most cases at very high fluences but at moderately high fluences the swelling effect has to be taken into account. In the case of Si^+ implantation into silicon, the sputter coefficient is around or ≤ 1 depending on ion energy as shown in Fig. 4.9.

The mechanisms and effects of ion implantation-induced damage and ion sputtering in compound semiconductors strongly depend on the semiconductor group. The III–V semiconductors are usually easily amorphized at relatively low fluences (on the order of 10^{14} cm^{-2}), but there is also evidence of some recrystallization taking place at higher fluences. The implantation damage behavior of the II–VI and HgCdTe semiconductors is very similar to that of metals. Several mechanisms can cause bombardment-induced compositional changes in multicomponent materials. For example, in the case of Ar^+ bombardment of InP, the experimental results indicate that the cause of surface compositional changes is mainly preferential sputtering, while for argon bombardment of GaAs, bombardment-induced diffusion and segregation effects are the dominant mechanisms. In general, particular compositional change mechanisms can appear in most mentioned compound semiconductor systems and also in SiC [34, 35]. Especially, for SiC and diamond-like carbon (DLC), for example ta-C layers, in the nonsteady state case, the drastic change of the target density due to amorphization and therefore to swelling must be taken into consideration [36].

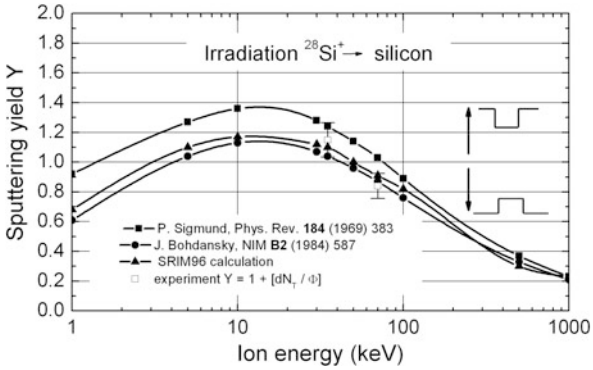

Fig. 4.9 Sputtering yield for Si^{+} ion irradiation of crystalline silicon showing the ion energy dependence of both sputtering and swelling (Bischoff L private communication)

Processes leading to surface sputtering may also inject one species into another through interfaces in a sandwiched target, and therefore lead to transmission sputtering or interface mixing. In general, such processes may give rise to changes in the depth profile of the composition of a multicomponent target.

As described in Chap. 2 one may distinguish between recoil implantation and cascade mixing. The former effect is due to direct ion–target collisions and therefore strongly directional, while the latter process is due to target–target collisions and therefore more or less isotropic. Moreover, recoil implantation involves few atoms with moderate and high energies while cascade mixing strongly peaks toward low recoil energy. Recoil implantation causes a net displacement of the depth profile of the light species relative to that of the heaviest species in the direction of the beam, whereas cascade mixing is roughly equivalent with an interdiffusion, with a diffusion coefficient essentially independent of target temperature [37, 38]. The effect of recoil implantation was intensively investigated for implantation into and through masking layers, for example SiO_2 and Si_3N_4, on silicon, as often used in microelectronic technology [39–42] and applied to direct shallow doping of different substrates using specific surface layers [43, 44].

In general, recoil ion implantation or recoil ion mixing is based on atom relocation by single-collision events. The energy E_R transferred to the recoiled target atom M_2 by the incident ion M_1 with an energy E_0 during single collision at the interface between the substrate S and the layer L is equal to

$$E_R = E_0 \cdot \frac{4 \cdot M_1 \cdot M_2}{(M_1 + M_2)^2} \cdot \cos^2\vartheta, \tag{4.6}$$

where ϑ is the scattering angle. The maximum transferred energy E_{Rmax} is achieved at $M_1 = M_2$ and at $\theta = 0$ (head-on collision) but the most probable collisions are at large angles (soft collisions) with decreasing transferred energy E_R.

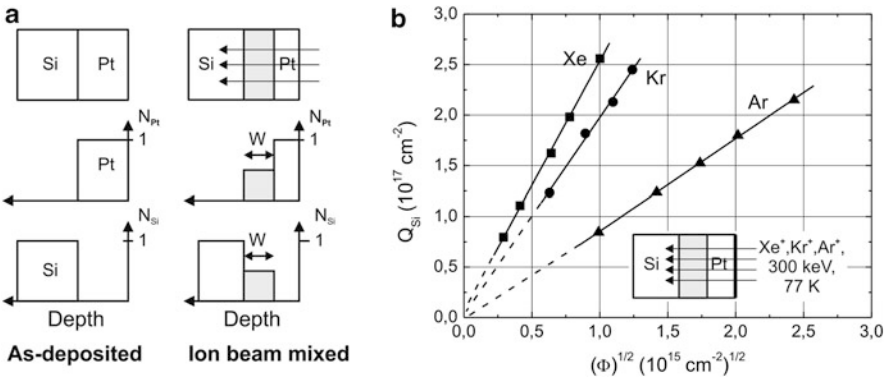

Fig. 4.10 (**a**) Schematic drawing of recoil ion beam interface mixing and (**b**) example of ion mass and fluence effects in an ion mixed Pt/Si layer. The amount Q_{Si} is the amount of silicon in the mixed layer w. The ion mixing rate is proportional to $(\Phi)^{1/2}$ (from [45] and [46])

If w is assumed as the thickness of mixed layer between S and L the amount of mixing Q is equal to the number of S and L atoms in the layer w (Fig. 4.10a). Q increases with ion mass M_1 because $(dE/dx)_n$ scales with ion mass and is proportional to the square root of the fluence Φ or the irradiation time t at constant ion flux (Fig. 4.10b).

Several processes are responsible for the ion mixing effect, all of which are initiated by the interaction of an energetic ion with a solid. Both ballistic and cascade effects depend on the mass of the incident ion. By increasing the mass of the ion the amount of energy deposited in nuclear collisions per unit length traveled by the ion also increases. The influence of mass and fluence effects on ion mixing is clearly evident as shown in Fig. 4.10. The average thickness of reaction at the Pt/Si interface is given in units of Si atoms cm^{-2}, which increases with both increasing mass of the incident ion and the increasing fluence Φ. At the Pt/Si interface the mixing rate for all ion irradiations is proportional to $(\Phi)^{1/2}$. Ion beam mixing gives the ability to produce ion-modified materials with higher solute impurity concentrations at lower irradiation fluences than can be achieved with conventional high fluence ion implantation, for example of an Au/Cu interface [47].

The isotropic broadening observed in thin buried marker layers strongly suggests that a series of single-event, forward-momentum recoils is not the dominant mixing mechanism. Instead, in many cases the symmetric marker broadening appears to be more related to processes dominated by the isotropic displacement mechanism caused by collisional cascades [48].

For the simulation of ion implantation into multilayer systems including recoil implantation and ion mixing at interfaces, the dynamic binary collision code TRIDYN is favored to be used. Because TRIDYN considers both of ballistic interactions of an energetic ion with target atoms (direct ion–target collisions and target–target collisions) as well as dynamic change of depth-dependent composition changes in stacked layers, ion mixing at layer interfaces can be simulated very well. An example of $Si/SiO_2/Si$ stack mixing by Si^+ ion irradiation with the aim of Si nanocrystal formation in thin gate oxides can be found in Sect. 4.3.3.

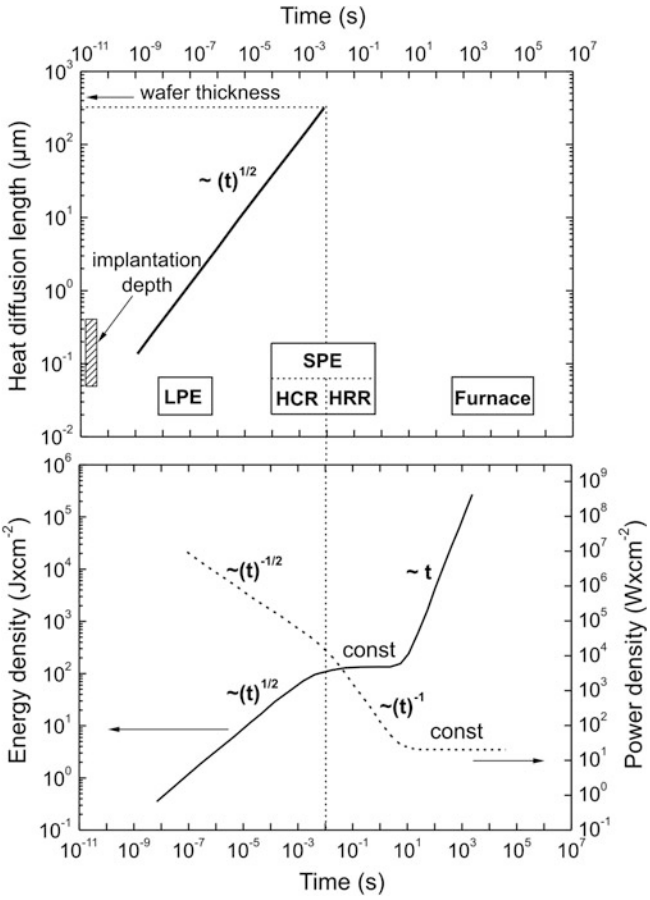

Fig. 4.11 Schematic classification of different regimes for radiation damage annealing in dependence on time of energy transfer to the sample (wafer) during heating [49]. The *upper part* shows the heat diffusion length during energy transfer and the *lower part* the energy density necessary for annealing at different regimes of liquid phase epitaxy (LPE), solid phase epitaxy (SPE), heat conduction regime (HCR), and heat radiation regime (HRR)

4.1.4 Radiation Damage Annealing

The major problem associated with ion implantation in semiconductors (Si, Ge, GaAs, SiC, etc.) is the removal of damage in the substrate lattice which has negative influence on materials and device properties. This is conventionally achieved by furnace annealing at temperatures up to about 1,000 °C. In semiconductors one has to distinguish between defect annealing, re-crystallization of amorphous layers, and electrical activation of implanted dopants by placing them on crystal lattice sites. In Fig. 4.11 characteristic properties of different annealing regimes are summarized as a function of the heating time. In this scheme all methods using heating times less

than 1 s are called nonconventional annealing techniques in which short pulses or writing beams are used to transfer the energy of light into the lattice of the semiconductor.

The two principal annealing regimes are the annealing (recrystallization) in the liquid phase (liquid phase epitaxy) and the annealing in the solid phase (solid phase epitaxy). Extremely short pulses of ≤ 1 μs heat the amorphized layer not long enough to allow a complete recrystallization by solid phase epitaxial regrowth (SPE). Full recrystallization can only be achieved by melting of the damaged layer followed by a liquid-phase epitaxial regrowth process (LPE). In these short pulse times, the diffusion length of the heat is in the same order of magnitude as the implantation depth. That means, only the damaged surface region is thermally affected by the annealing process. At liquid phase epitaxial regrowth the implanted layer melts and recrystallizes with high crystal perfection from the undamaged volume to the surface on a time scale $<10^{-7}$ s and at energy densities of ~1 J cm^{-2}. For this regime, pulsed and scanned lasers are applied. Because impurity diffusion coefficients in liquids are several orders of magnitude higher than in the solid phase, a significant redistribution of the implanted species occurs due to diffusion and segregation [50].

For heating times of 10^{-4} to 1 s the rapid thermal annealing (RTA) process has been shown to take place analogous to the conventional thermal (furnace) annealing by solid phase epitaxial regrowth. As the activation energy for impurity diffusion is higher than that for epitaxial regrowth, the redistribution of the implanted profile is negligible in times required to recrystallize an amorphous layer. During furnace annealing (FA) a noticeable redistribution of impurity atoms can be observed, only due to the fact, that contrary to the nonconventional methods, the necessary annealing time is strongly exceeded. Therefore, the nucleation of small defects (e.g., point defects) to extended defects (e.g., dislocation loops) and their growth observed at thermal furnace annealing can also be altered by nonconventional annealing techniques.

It is appropriate to subdivide the SPE regime into two different time–temperature regimes—the heat conduction regime (HCR) and the heat radiation regime (HRR). At HCR during short pulses (≤ 1 ms, e.g., for silicon wafers with a thickness of >300 μm) there is a strong temperature difference between the illuminated side and the other side of the wafer. This is a consequence of the finite heat diffusion through the wafer during the pulse duration. After the pulse the surface temperature is rapidly lowered due to temperature equalization over the wafer thickness by heat conduction. Before this rapid cooling has taken place the annealing process must be completed. In the HRR during longer pulses (≥ 10 ms), the diffusion length of the heat exceeds the wafer thickness and the heating of the whole sample material is nearly uniform. Provided that the sample is thermally isolated the heat is stored for a long time (typically ~1 s) because the cooling is dominated by heat radiation to the surrounding medium. Because the heating times of both regimes (HCR and HRR) differ by three orders of magnitude, differences in the annealing behavior of the implanted samples can appear.

Within the end of the 1970s years it has been demonstrated that both scanned cw lasers and scanned electron beams [51] offer powerful tools in the solid phase annealing. Nevertheless, only after 20 years especially laser annealing received renewed interest, e.g., for dopant activation, by either melt quenching a surface layer or as a high-temperature submelting pretreatment prior to a standard RTA [52–55].

One of the approaches of rapid thermal processing to the elimination of implantation damage is flash-lamp annealing (FLA) in the time scale of ms [56–58]. It is likely that RTA and FLA steps today play the most important role in Si device fabrication, possibly with more stringent control over time and temperature, as has been the experience with advances in planar CMOS technology [59]. For a number of excellent reviews of RTA methods, the reader is referred to some references [60–63]. Dopant activation by rapid thermal processing requires exquisite control of wafer temperature because diffusion and electrical activation of the dopants are governed by high thermal activation energies, typically in the range 3–5 eV. Controlling diffusion with a tolerance of ± 1 %, as may be required by the silicon IC technology, corresponds to controlling the temperature of 1,000 °C to better than ± 1 K. Thus, temperature control for critical annealing steps would have to be better than ± 1 K across 300 mm wafers. The performance of current advanced RTA equipment is in the range $\pm(2–3)$ K. The RTA techniques can be divided into two categories: (1) rapid wafer transfer between a steady heat source and a heat sink, and (2) a fixed wafer heated by rapid modulation of the heat source. Heat is exchanged for the most part normal to the wafer surface by radiation, gas convection, and gas thermal conduction. The wafer temperature is usually determined by infrared-based optical pyrometers that incorporate systems for measuring wafer radiance and emissivity. Pyrometry is the favored method because it is noncontacting and, owing to Planck's radiation law, the errors in temperature are relatively less than the errors of change of sample radiance and emissivity due to different surface properties (e.g., different patterned of SiO_2, Si_3N_4, poly-Si, thin metal layers, etc.).

In the *LPE annealing regime* energy irradiation sources of high-power pulsed lasers, for example Nd-glass, Nd-YAG, and Yb-YAG lasers, with wavelength in the visible and near-infrared region (1,064–355 nm) as well as XeCl- and KrF-excimer in ultraviolet region (308–248 nm) with energy densities of ≥ 1 J cm^{-2} and pulse duration times of 10^{-7}–10^{-8} s are required. For melting of near-surface layers, there exists a light pulse energy barrier E_L which depends on the light absorption coefficient α, the light wavelength λ, and on the sample temperature. With increasing sample temperature the absorption coefficient increases for most of semiconductor materials. With increasing light pulse length t_p the energy barrier increases with $E_L \sim (t)^{-0.5}$, because the diffusion time of the generated heat from the surface layer into the substrate is also reduced, and at the same time the maximum melting depth d_{max} decreases corresponding to the relation $d_{max} \sim (t)^{0.5}$. For epitaxial regrowth of amorphous layers, the depth of the melted layer must be larger than the thickness of amorphous layer. In this case the formation of defects such as stacking faults, dislocations, and precipitates can be eliminated to high degree

during LPE. The significant redistribution of the implanted dopant profile during LPE is caused by the very high diffusion coefficient in the melt which is orders of magnitude higher compared to that in the solid material. The redistribution of the profile depends on the melt duration t_m, the melt depth d_m, and segregation coefficient k_0, which represents the ratio between the equilibrium dopant solubility in the growing crystalline solid material and that in the liquid near the interface. For silicon the values are <1 [64], which means that during regrowth of the melted layer the dopants are rejected into the melt which becomes progressively enriched with dopants.

In the case of high segregation coefficients (e.g., B, P, As), the redistribution of impurities is mainly driven by their diffusion in the melt, whereas for small coefficients $k_0 < 10^{-2}$ the redistribution is mainly caused by the segregation at the liquid–solid interface. A high amount of impurities is pushed in direction of the surface where eutectic precipitates can be formed. During the high cooling rates during LPE point defects remain in the re-crystallized layer which can be partially removed at subsequent conventional low-temperature annealing, for example in a hydrogen atmosphere. Furthermore, during LPE the thermal solubility limit of dopants in the melt is much higher compared to their solubility in the solid state of silicon which leads to complete electrical activation of introduced high fluence-implanted impurities even above the equilibrium solid state solubility limit [50, 65, 66].

In the *HCR annealing regime with SPE* scanned continuous wave (cw) lasers or pulsed lasers with wavelength in the visible and near-ultraviolet range (~400–800 nm) with irradiation times in the order of 0.5 ms $< t <$ 20 ms are applied to damage annealing [51]. On this time scale of energy supply for damage annealing, higher energy densities up to 100 J cm^{-2} are necessary due to heat loss by heat conduction into the substrate (and the ambient). The laser beam spots have usually diameters of 10–100 µm and must be scanned over the sample surface with appropriate scan velocity or repetition and dwell time. In this regime, no significant redistribution of the implanted profiles and segregation effects at the surface are observed if the concentration of implanted impurities in the substrate is in the order of their solubility at given annealing temperature. For re-crystallization at sufficient energy in the laser beam spot very low concentrations of remaining point defects, especially in <100>-oriented silicon substrates, and a high degree of electrical activation up to 100 % can be achieved.

Among thermal pulsed-laser annealing *flash-lamp annealing (FLA)* [67] can be applied for greater suppression of dopant diffusion effects. FLA uses a high optical flux for faster heating to either melt the surface of the wafer or selectively raise the surface temperature. Upon termination of the light pulse, the surface temperature rapidly cools by thermal diffusion from the near-surface region into the bulk of the sample. The rapid quenching can lead to lattice defects and dopant metastability, and consequently to dopant redistribution during subsequent thermal processing steps. FLA has also been implemented in a lamp-based RTA system as a modification of the chamber shown in Fig. 4.12a, where the upper bank of lamps was replaced by Xe flash-lamps, emitting in the 300–800 nm wavelength range and to produce a 0.5–20 ms pulse at the peak temperature [68].

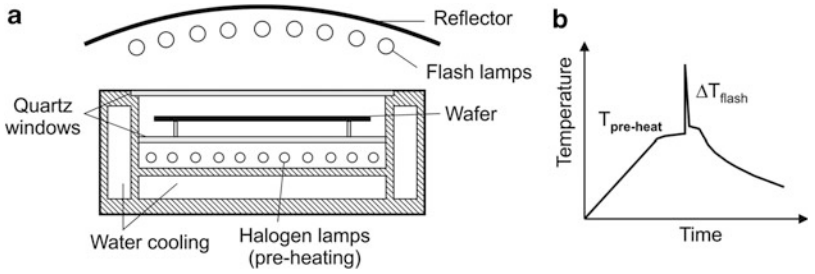

Fig. 4.12 Schematic buildup of a FLA annealing chamber (**a**) and typical $T(t)$ characteristics (**b**)

The heating and cooling rates are very high and in the order of 10^6 K s^{-1}, which can easily lead to sample breakage due to high introduced mechanical stress. The lower bank of incandescent lamps is used to heat the wafer up to about 600 °C. The upper bank of lamps is energized by an electric discharge to produce a short pulse of radiation with an energy density up to 100 J cm^{-2}. Figure 4.12b schematically illustrates the surface temperature versus time profile for FLA. As has been shown, the results indicate a high electrical activation of dopants with negligible diffusion in the region of the junction in the case of BF_2 implantation and several nanometer diffusion in the case of As implantation into silicon [69].

In principle for *SPE in the HRR regime* the same energy sources as in the HCR regime can be applied, but in recent years large area light radiation heaters (mostly arrays of incandescent lamps systems and of high-power arc lamps) became accepted because of higher productivity during annealing of large wafers up to 300 mm diameter. The sample exposure time in this regime is higher than 100 ms. Due to the continuous heating over the sample thickness, the irradiation time can be varied over a broad range without significant change of damage annealing behavior. Shorter times are preferred if diffusion effects (profile broadening) have to be minimized. The annealing conditions do not change if the sample (wafer) is irradiated from the nonimplanted back side. At these conditions possible influence of patterned surface layers on the front side on energy absorption can be excluded. After annealing in the HRR regime residual defects of rod-like dislocation with some tens of nanometer extension, no significant redistribution and phase separated precipitates of impurities have been observed.

Several steady light heat source methods have been developed mainly for purposes of common rapid thermal annealing (RTA) of implantation damage annealing in silicon and other semiconductors. The *cold-wall RTA method* that uses incandescent lamps for heating, wafer rotation for uniformity, and gas levitation for thermal isolation and quench cooling was developed to replace prolonged furnace annealing. Incandescent lamp systems are now most prevalent in IC manufacturing. Figure 4.13a illustrates the process chamber of a modern lamp-based system with wafer heating from the top side and wafer temperature measurement from the bottom side [70]. The heating lamps are arranged in a closed-packed two-dimensional array and are powered in concentric annular zones. The power distribution among the zones is controlled by temperature sensors along the radial direction underneath the wafer.

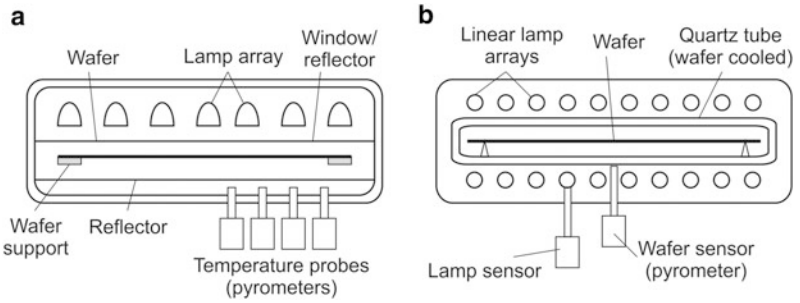

Fig. 4.13 Typical buildups of a cold-wall RTA system: (**a**) asymmetric lamps, single-sided heating, and (**b**) linear lamps, double-sided heated

Another RTA system, illustrated in Fig. 4.13b, has a chamber that efficiently surrounds the wafer with heating lamps [71–73]. The reflective enclosure contains linear lamps arranged in rows with the filaments parallel to the wafer and includes a quartz isolation tube to control the gas ambient. The linear lamps in the upper and lower banks may be mutually parallel or perpendicular. The power distribution among the lamps is adjusted to produce uniform temperature distribution over the wafer. Two radiation probes are used to determine the wafer temperature by a technique denoted as ripple pyrometry [74]. The probe with the view of the wafer collects a mixture of radiation emitted by the wafer and the lamps. The other probe (ripple pyrometer system) samples radiation from the lamps for reference.

High-power arc lamps have been used for RTP, particularly for *spike annealing*. Spike annealing techniques were introduced to control dopant diffusion in shallow junction formation [75]. Current spike annealing methods use infrared heating that is characterized by near thermal equilibrium across the wafer thickness of the wafer, similar to RTA. The variables are heating rates, which depend on the intensity and wavelength of the infrared radiation source, the switching time from heating to cooling, and the cooling rate, which involves radiative, convective, and thermal conductive dissipation of wafer heat. Typical temperature versus time traces for spike anneals with arc and incandescent lamps are shown in Fig. 4.14.

Both curves were produced by abruptly turning off lamp power at or near the peak temperature. Typical heating rates are in the range 100–400 K s^{-1}. The wafers cool by chamber absorption of the emitted radiation at rates up to 150 K/s. Sharper spike peaks are achieved for an arc lamp compared to incandescent lamps, because arc lamp method produces the sharper spike with an inherent response time of ~10 μs. The incandescent lamp method produces a spike with a more rounded peak because of incandescence after-glow in tungsten filaments, which has a time constant of about 0.5 s. In spike annealing wafers are cooled by turning off the heating lamps or by withdrawing the wafer from the heated environment. Initial cooling at high temperature is dominated by radiative heat transfer. Cooling can be augmented by thermal conduction and gas convection at lower temperatures, e.g., by using He gas as the exchange medium.

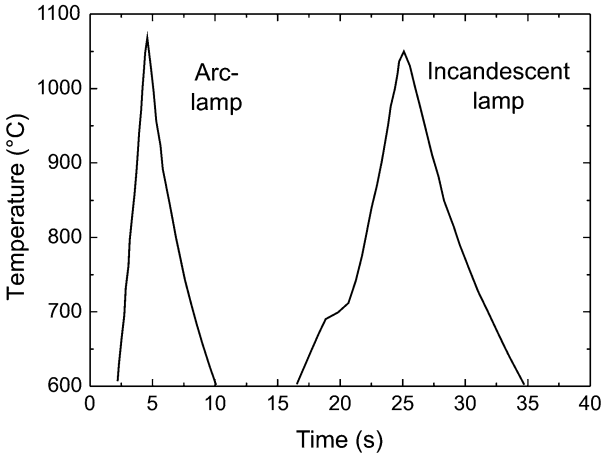

Fig. 4.14 Typical temperature versus time traces for spike anneals with arc and incandescent lamps

In some cases rapid thermal processing is carried out by briefly inserting the sample into a quartz tube furnace. The modern technique is oriented on so-called *hot-wall RTA* in a vertical quartz tube furnace (bell jar furnace) and utilizes the uniformity and reproducibility inherent in a steady furnace-based heat source (Fig. 4.15) [76]. The wafer is transported by fast elevation in a bell jar furnace heated with a vertical temperature gradient. The temperature at the top of the bell jar is several hundreds K higher than the maximum targeted wafer temperature. The desired heating rate and maximum wafer temperature determine the peak furnace temperature. The bottom of the chamber is water cooled and serves as a heat sink for cooling the wafer when it is moved down. The temperature is measured by a pyrometer that detects the wafer radiance and subtracts background interference from the furnace radiation. The pyrometry uses 0.95 μm wavelength, where optical transmission through Si is negligible.

A comprehensive review of the detailed operation of RTA systems with respect to the dynamic response of the sample (wafer) temperature to light irradiation can be found in [77].

During *furnace annealing* on the time scale of >10 min, the implanted and damaged sample is at thermal equilibrium with the surrounding inert gas ambient in a heated high-purity quartz or poly-Si tube. The recrystallization of amorphous Si layers (activation energy 2.3 eV) in most cases takes place in the temperature range of 600–800 °C and the annealing of different kinds of crystal defect as well the electrical activation of dopants in a higher temperature of 800–1,000 °C. If the implantation conditions are not sufficient to create an amorphous layer, lattice repair occurs by the generation and diffusion of point defects in the crystal. This process has an activation energy of about 5 eV and requires therefore higher annealing temperatures to remove all the defects. It is thus easier in many cases

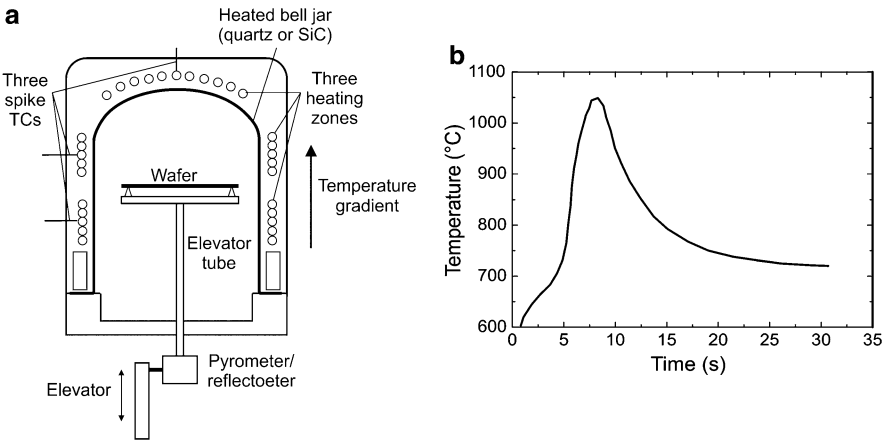

Fig. 4.15 Hot-wall RTA using a vertical quartz (or SiC) tube furnace (bell jar furnace) (**a**) and typical temperature–time trace (**b**)

to repair a fully amorphized layer than a partially damaged one. The result of incomplete annealing is a reduction in the fraction of active dopants which in principle has to be as high as possible. This means that in the furnace regime the recrystallization of amorphous layers in silicon takes place during heating up the furnace to the desired annealing temperature at 800–1,000 °C. The annealing process depends on time–temperature characteristics of heating-up rate, constant temperature annealing time and cooling-down rate because the furnace annealing regime is a thermodynamic equilibrium process. The thickness of the recrystallized layer is given by the expression:

$$d_{\mathrm{R}} = a \cdot v_0 \cdot t \cdot \exp - \frac{E_{\mathrm{a}}}{k \cdot T}, \tag{4.7}$$

where v_0 is the phonon frequency (e.g., in the Si lattice 10^{11}–10^{12} s^{-1}), a is the crystal lattice constant (e.g., for Si 0.543 nm), and E_{a} the activation energy for atom movement (e.g., for Si 2.3 eV).

The phonon frequency v_0 depends on the crystal orientation and the concentration of introduced impurities. The recrystallization velocity of an amorphous Si layer between 1 and 50 nm min^{-1} increases with increasing doping concentrations and in order of B, P, As, Ga, In and of orientations <111>, <110>, <100> as shown in Fig. 4.16. In the nonabrupt transition depth between the amorphous layer and the crystalline substrate, the damage concentration continuously decreases leading to an increased concentration of point defects and dislocations. Therefore, during long-time furnace annealing these defects, depending on annealing conditions, can extend into the crystalline substrate as well into the recrystallized layer.

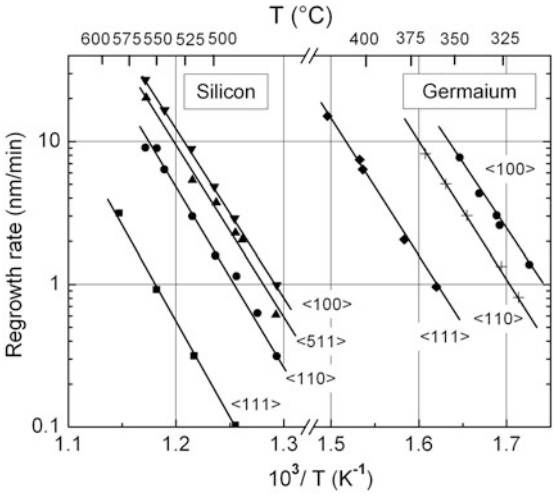

Fig. 4.16 Recrystallization velocity in Si and Ge for different crystal orientations (from [78])

Due to the complexity of processes for defect dissolution, defect generation, recrystallization, electrical dopants activation in crystalline materials, and the placement of annealing processes in the full device fabrication process, many optimized thermal annealing regimes have been developed. Especially multistep annealing at different temperatures and times with different heating and cooling rates are of great importance because low residual defect concentration and high electrical activation can be achieved [79]. The disadvantage of furnace annealing is the redistribution of dopants (lateral and vertical broadening of the as-implanted profile) by defect-enhanced diffusion which is observed already at lower temperatures and thermal diffusion at high temperatures. The emission of vacancies during annealing increases the diffusion coefficient of the implanted atoms. The time constant of vacancy emission is in the order of minutes. In general, implantation induced release of vacancies (V), and, especially, in the case of boron in Si the release of interstitials (I) can increase the diffusion coefficient significantly. The increase of the boron diffusion coefficient denoted as transient enhanced diffusion (TED) is explained by the formation of (I–B) complexes with a high diffusivity in silicon [80–85]. A defect-enhanced diffusion has been also observed for stable dislocation defects often induced by high fluence implantation.

In advanced silicon manufacturing technology, more ion implant annealing is done by RTA in single wafer process tools than in batch furnaces. This is especially true for shallow junction implant annealing, where RTA is believed to be a better method. Depending on the implanted dopants, the ion energy, and fluence, the annealing can require temperatures up to 1,100 °C [86]. The advantage of RTA is to access these high temperatures while minimizing the thermal budget by reducing the annealing time at a given temperature. A very short annealing time at higher temperatures, spike-anneal with a very fast ramp up/down rate has been introduced

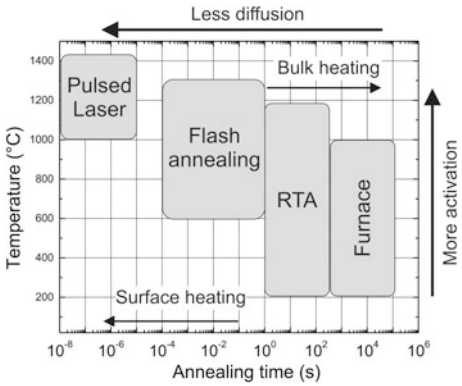

Fig. 4.17 Temperature–time map of various thermal annealing techniques used in the semiconductor industry

as an effective shallow junction implant annealing to electrically activate implant species with no significant diffusion. The annealing time is typically shorter than 1 s. For ultra-shallow junction (USJ) formation with $x_j < 50$ nm, excimer laser-based SLA and nonfilament-based FLA techniques using arc lamps are being actively investigated [68, 87, 88]. For further reduction of the diffusion of implanted species during annealing, SPE of implanted silicon at lower temperatures (600–700 °C) using RTA has been investigated [89].

The temperature–time characteristics of common thermal annealing techniques introduced in silicon processing for VLSI circuits are summarized in Fig. 4.17.

Usually, all the active device regions are located at the near-surface region within a depth of <1 μm on Si substrates (wafers) with a thickness of 400–800 μm. From the viewpoint of minimizing dopant diffusion and defect generation during annealing, selective surface heating without significant heating of the bulk Si wafer is an ideal thermal treatment. The two modes of LPE (surface melting) and SPE (submelt modes) of SLA have been investigated for USJ fabrication [90]. The LPE mode of SLA annealing gives a high electrical activation, but has process integration problems. The SPE mode of SLA annealing reduces the problems of process integration and gives reasonable electrical activation of implanted dopants. For both SLA modes, the annealing area is limited by the size of the laser beam and requires significant pulses repetition, as well as scanning systems for dopant activation over the full wafer surface. In the future, the semiconductor industry will target USJ junction depths below 20 nm. High quality pn-junctions with $x_j < 10$ nm will require annealing techniques without broadening of the implanted profiles or less than <3 nm due to diffusion. There are numerous annealing options which depend on the gate stack structure and on process integration including: (1) high-temperature ms-FLA or SLA, (2) spike-RTA with lower spike annealing temperatures of <900 °C, (3) SPE at higher annealing temperatures of >700 °C, and (4) combinations of spike + ms annealing or ms + spike annealing [91].

4.2 Ion Implantation into Semiconductors

Ion implantation is one of the most important processing steps in semiconductor technology. During the progress of ion implantation technology over the past 30 years, remarkable progress has been made in understanding the particle-solid collision phenomena so that range profiles of implanted dopants in semiconductors can be calculated with considerable accuracy. The annealing conditions to remove the implantation-induced crystal damage in semiconductors and to leave the implanted dopants on lattice sites, and fully electrically active, have also been well explored. The engineering challenges are related to the development of low and high energy implantation processes to accommodate the many implantation steps used in the fabrication of integrated semiconductor circuits. With decreasing dimensions in integrated circuit technology new physical and engineering challenges are focused on the interaction between the defects and dopants introduced during implantation. Now, with device dimensions deep in the submicrometer range, quantitative information about dopant-defect interactions are needed and must be taken into account in modern semiconductor device technology. The flexibility and compatibility of ion implantation with other fabrication processes enables the fast implementation of changes in new and advancing technology.

4.2.1 Ion Implantation into Silicon

Silicon is the most important semiconductor in the microelectronics industry and the basic material in VLSI and ULSI technology. Compared, for example, to germanium silicon has a larger bandgap ($E_g = 1.1$ eV) resulting in lower leakage currents allowing the device operation at higher temperatures up to ~150 °C. With the widespread and intensive silicon processing developments in integrated circuit technology based on MOS (or CMOS) device structures, ion implantation replaced the conventional diffusion doping for almost all planar silicon device structures. Ion implantation has become an essential doping process for manufacturing of MOS, CMOS, BiCMOS, and bipolar solid state silicon devices [92]. Therefore, the developments in ion beam processing of silicon mainly for CMOS technology stimulated the development of appropriate ion implantation tools and the application of ion implantation for other kinds of silicon devices, for example silicon detectors and sensors.

In *advanced CMOS technology* much more than 100 process steps are required to fabricate silicon integrated circuits (memory and processor devices). The wafers have to be lithographically patterned, doped, etched, and coated with various thin films. The advances in device design and shrinking of transistor dimensions require well-controlled fabrication processes, such as ion implantation, capable of uniform, controlled, and reproducible introduction of dopants into silicon. Ion implantation has become quite complex to meet the demands of small device structures such as the typical gate lengths of $<$100 nm in a complementary MOS (CMOS) device

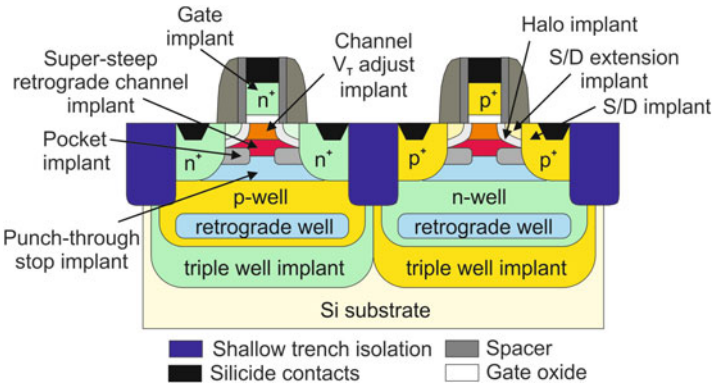

Fig. 4.18 Ion-implanted regions in a common CMOS transistor

shown in Fig. 4.18. The basic parts of the CMOS device are two MOS field-effect transistors (MOSFETs) consisting of one p-channel FET and one n-channel FET. To form both types of transistors in the same substrate, regions of opposite doping types are required separated by a shallow trench isolation (STI).

Figure 4.18 illustrates the sophistication of current implantation technology. More than 20 different implantations covering a wide range of energies (0.1 keV–1 MeV), fluences of 10^{11}–10^{16} cm^{-2}, and dopant species (mainly B, P, As, In) are typically used to tailor dopant profiles during device fabrication. The lowest energies are for junction formation and the highest for substrate or well doping. As shown in Fig. 4.18 ion implantation plays an important role in the fabrication of various integral parts of a CMOS transistor, where the most important ones are the formation of the transistor channel and the contact areas of source and drain as well as the doping of the wells. Scaling down the transistors in size, many implantation processes must meet the requirements for lower energies and higher doses to improve advanced transistor performance. Therefore, implantations such as source-drain extension implants, halo formation, and gate-electrode doping in the low energy regime have attracted widespread attention. All implantation processes in the fabrication of advanced silicon CMOS devices are summarized in the ion fluence-energy map of Fig. 4.19.

For all implantation processes shown in Fig. 4.19 the typical implantation parameters are summarized in Table 4.2.

Most of efforts in shallow pn-junction fabrication are focused on the formation of shallow source/drain junctions. Since boron has much higher diffusivity than phosphorous and arsenic, shallow p^+n-junctions have proven to be more difficult to form in CMOS devices compared to P- or As-doped shallow n^+p-junctions. The formation of shallow boron p^+n-junctions is limited by three effects: (1) small ion mass of boron and therefore relatively large projected range (penetration depth) requires ultra-low energy implantation with $E \leq 1$ keV, (2) increasing channeling of boron with decreasing ion energy, and (3) anomalous diffusion in the tail region

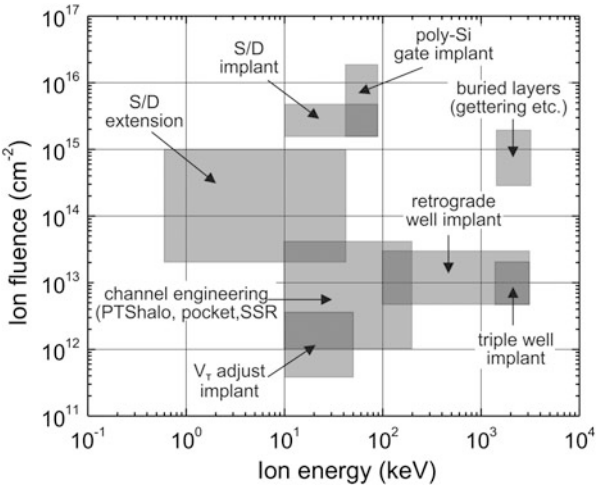

Fig. 4.19 Ion fluence–energy map of different ion implantations for silicon MOS-device and process technology (adapted after [93])

Table 4.2 Implantation processes and parameters for advanced CMOS transistor technology

Transistor region	Ions	Energy (keV)	Fluence (cm^{-2})	Remarks
Channel formation	P, B	10–80	1×10^{12}–5×10^{13}	Halo, PTS, LATIPS, Pocket, SSR
	As, In, Sb	80–200		High tilt angles and wafer re-depositioning
Transistor threshold voltage adjust	B, BF_2, As	10–50	4×10^{11}–4×10^{12} ($\rightarrow 1 \times 10^{11}$)	Transistor threshold voltage
Source/drain deep contacts	As, BF_2, B	10–80 ($\rightarrow$1–30)	2×10^{15}–8×10^{15} ($\rightarrow 1 \times 10^{15}$–$4 \times 10^{15}$)	Conducting source/drain areas
Source/drain extension	As, BF_2, B	0.5–30	3×10^{13}–1×10^{15}	Electric field reduction near S/D
poly-Si gate doping	B, BF_2, P	30–80 ($\rightarrow$2–30)	3×10^{15}–2×10^{16} ($\rightarrow 1 \times 10^{15}$–$8 \times 10^{15}$)	Conducting gate material
Preamorphization	Ge, Si	5–50	5×10^{13}–2×10^{15}	Channeling suppression
Retrograde wells	B, P	1,500–3,000	5×10^{12}–3×10^{13}	Off-state leakage current reduction
Triple wells	P, B	1,200–3,000 ($\rightarrow$5,000)	5×10^{12}–3×10^{13}	p- and n-well separation
Buried layers	B, P	1,500–3,000	2×10^{13}–5×10^{13}, 3×10^{14}–2×10^{15}	Subcollector in bipolar transistors
Proximity gettering	C, N, O, F, Si	1,500–3,000	5×10^{14}–5×10^{15}	Carrier lifetime improvement
SOI wafer fabrication	O	30–100	3×10^{16}–1×10^{17}	SIMOX
	H, He			Smart-Cut

of the implanted profile during high-temperature annealing due to transient-enhanced diffusion (TED).

Furthermore, scaling of supply voltage does not happen as fast as geometrical device scaling, such as gate length and gate oxide thickness. Because of this, the electric field in the device increases with scaling, resulting in aggravation of short-channel effect (SCE). Short channel effects impact MOSFET device characteristics such as threshold voltage V_{th}, subthreshold currents, and I–V behavior beyond threshold. In addition, it has been recognized that also increased reliability concerns such as hot carrier effect (HCE) and gate oxide reliability. Various transistor design techniques have been proposed and investigated to deal with SCE and HCE. One of the most important developments in transistor design to deal with SCE and HCE is the use of lightly doped drain (LDD) in conjunction with polysilicon gate sidewall spacer (see Fig. 4.18). Various other ion beam processing steps have been adopted in transistor fabrication. These include retrograde channel implantation, super-steep retrograde channel (SSR) implantation, halo or pocket implant with a large tilt angle, preamorphization implant (PAI), punch-through stopper (PTS), and large tilt-angle punch-through stopper implantation (LATIPS). Because silicon CMOS technology is one of the most developed semiconductor technologies, the used ion beam processing steps will be described in the principal sequence of their application to the CMOS transistor fabrication (see Fig. 4.18):

- Twin-well processing (or triple-well process)
- n-well and p-well processing
- Transistor channel processing
- n- and p-type source and drain processing
- Poly-Si gate processing

The principal ion implantation sequence in the advanced CMOS device manufacturing process starts with high energy implantation to form the retrograde wells, after that the medium energy implantation for punch-through stop (PSS) and low energy implantation for threshold voltage (V_{th}) adjustment. After gate patterning low energy source/drain extension (SDE) implantation, and halo implantation under high tilt angles are carried out. The final implantation steps are the doping of deep S/D areas by medium energy implantation.

Step 1: Retrograde n- and p-wells implants

The areas where the transistors will be fabricated—the n-channel MOSFET in the p-well and the p-channel MOSFET in the n-well—are achieved by high energy implantation of B^+ and P^+ (or As^+) ions, respectively, at energies ranging from a few 100 keV to several MeV with a peak concentration at a depth of about 1–2 μm below the surface. The ion energy depends on the device type and its application for high speed logic (processor) and DRAM memory devices with relatively shallow wells and for SRAM and flash memories with deeper wells. In former fabrication processes, the p- and n-wells were formed by medium energy implantation followed by a deep thermal in-diffusion which is eliminated in modern technology, allowing the use of RTA with a small thermal budget. This eliminates lateral dopant diffusion and permits better device scaling (higher transistor packing density). Retrograde well implantation is normally self-aligned to the already performed

oxide-filled shallow trench isolation (STI). Profiled well implantation can be performed with an arbitrary impurity distribution to optimize many device characteristics almost independently. Buried layers with n-profiled and p-profiled wells are fabricated alternatively using multiple high energy ion implantations (B^+ for a p-well and P^+ for an n-well) by controlling ion energy and fluence independently. The resulting multiple depth profile is usually called triple well structure. The application of triple well structures provides important advantages to several different CMOS devices. They include memory devices (DRAM, flash, and SRAM) and embedded CMOS technologies with memory and logic devices on the same chip [94]. In triple well technology, the addition of moderate fluence high energy P^+ and B^+ ion implants allows the creation of separate p-wells and n-wells which are isolated from p- and n-substrates, respectively. To take full advantage of triple well structures, high energy (2–3 MeV) ion implantation is preferred over other approaches, like deep diffusion with long thermal treatment at high temperatures (~1,150 °C). In typical triple well processes, the deep n-well that forms the added isolation of the third well requires P^+ implantation with an ion energy up to 3 MeV at a fluence of 1×10^{13}–1×10^{14} cm^{-2} Additionally, the boron p-well, which is implanted into the deep n-well, will require up to 1 MeV at a fluence of 1×10^{13}–1×10^{14} cm^{-2}. Typically, these processes form 2.5–3.5 μm deep buried n- and p-wells with a retrograde dopant profile (low subsurface dopant concentration). In order to pattern and mask the very deep implants, thick photoresist masks are required with thicknesses of 3.5–5.5 μm. Thermal diffusion treatment is not required, and dopant activation and implantation damage recovery can be achieved by the subsequent thermal processes, for example during the gate oxidation step. Retrograde triple well processing allows the formation of a buried n-well beneath selected n- and p-wells without surface compensation of dopants, which can lead to improved device performance. The impurity concentration at each depth determines the respective CMOS-FET device characteristics, such as threshold voltage, hot carrier generation, punch-through voltage, junction breakdown voltage, junction capacitance, latch-up susceptibility, soft-error immunity, etc. Isolation characteristics, inter-well or intra-well, are also determined by impurity concentrations at certain well depths. Since a high energy implanted well can usually be made shallower than a conventional diffused well, the trenches for isolating wells also become shallower and easier to fabricate.

Step 2: Anti-punch-through and threshold shift implants

The anti-punch-through implant following the well implantations is applied to create a higher doped region between the transistor channels and the maximum of the well-implanted profiles to prevent punch-through from the drain depletion regions extending to source depletion regions. The anti-punch-through implantation is usually carried out at medium ion energies of 50–200 keV and low fluences of 10^{12}–10^{13} cm^{-2}. The natural threshold of the NMOS transistor is about 0 V and that of the PMOS transistor is about –1.2 V. An implantation for p-type doping is used to make the NMOS transistor harder to invert and the PMOS transistor easier resulting in both threshold voltages balanced around $V_{th} \approx 0$. The threshold voltage can be adjusted to the desired level by increasing the doping level through a low energy

and low fluence ion implantation into the channel region. The threshold adjust implantation is very sensitive to doping variations and requires very reproducible ion beam energies and fluences. The energy depends on the thickness of the gate oxide present during implantation. The threshold voltages of both n-type (V_{thn}) and p-type (V_{thp}) transistors are adjusted to typically equal values of +0.6 V and −0.6 V, respectively.

In modern CMOS technology for V_{th} adjustment implantation, light ions B^+ and P^+ are often substituted by heavy ions (e.g., In^+ for B^+ in n-channel MOSFETs and Sb^+ for P^+ in p-channel MOSFETs) to reduce its diffusivity and dopant redistribution during subsequent thermal processes [95]. These so-called super-steep retrograde (SSR) channel profiles allow the fabrication of deep-submicron MOSFETs with suppressed punch-through effect, improved electron mobility, and lowered interface dopant concentration level [96]. The need for nonuniform channel doping is described more in detail by Taur and Ning [97].

Step 3: Implantation of lightly doped source/drain regions

After patterning of the gate insulator and gate electrode, shallow doped ($\sim 10^{20}$ cm^{-3}) source and drain regions next to the more lightly doped ($\sim 10^{18}$ cm^{-3}) active channels of the MOSFETs are fabricated in a self-aligned manner by low energy and low fluence implantation. These shallow S/D profiles are called S/D extensions and are commonly found in modern MOS device designs. The doping profiles in the S/D regions have a profound impact on the channel performance (e.g., short channel effects). As a result, considerable effort has been also put into the optimization of the S/D. The shallow S/D extension was originally motivated by a desire to relieve high electric fields and the resulting breakdown of the device due to hot electron effects [15]. For modern high performance devices however, the S/D extension is stronger motivated by the trade-offs between short channel effects and the S/D resistance. The S/D extensions represent a shallow effective S/D junction to the channel regions, while at the same time, minimize the contribution of the S/D regions to extrinsic resistance through the presence of the deep S/D regions. The S/D extensions are formed by using of low dose and low energy dopant implantations.

Step 4: Source/drain halo implantation

Lateral channel engineering is used extensively to improve device performance. Typically, lateral engineering is accomplished by angled implants into the channel region following gate patterning. The halo implant is normally performed under high angles of 30–60° to counterdope the source/drain extension regions, which is done after poly-silicon gate patterning but before nitride spacer formation. Halo implants need to be performed with four 90° rotations of the wafers to dope both sides of the differently orientated transistors. The lateral implants cause an increase in doping concentrations near the edges of the SDE regions. The use of halo implants can improve short channel effects [98] and thereby control the so-called threshold voltage roll-off [99]. For devices with long channel lengths, the impact of the halo implant is minimal. As the channel length is decreased, the portion of the channel with an increased dopant level becomes more and more significant, leading to an increase in the effective channel doping level with decreasing channel length.

Step 5: Implantation of the heavily doped sources/drain regions

Only after the formation of the spacers, the higher fluence and higher energy dopant implantations are then followed to form the source/drain region by using the spacers as masks. Additionally to the completed sources and drain doping, this step provides the implantation of ohmic contact areas into the p- and n-wells and into the substrate. For S/D- (and well) contact areas it is important that they have a lowest possible resistance which requires medium energy (10–80 keV) and high fluence implantation with fluences in the order of ~(1–5) $\times$ 10^{15} cm^{-2} for As^+ in the case of n-channel MOSFETs and for B^+ (or BF_2^+) in the case of p-channel MOSFETs. At these implantation conditions highly doped ($>10^{20}$ cm^{-3}) S/D contact areas adjacent to the more slightly doped (~10^{18} cm^{-3}) S/D-extensions are formed. As^+ ions are preferred due to their low diffusivity and higher solubility in Si compared to P^+ ions. Because boron has a higher diffusivity it is more difficult to fabricate shallow S/D-junctions in p-channel MOSFETs. S/D areas have an opposite conductivity to create a pn-junction and a good isolation to the surrounding wells. Junction depths of $\leq$100 nm are typical for scaled MOSFETS with channel length below 0.25 μm [100].

Step 6: Poly-Si gate implantation

As a gate contact material polycrystalline silicon (poly-Si) with a thickness of ~300 nm is deposited by LPCVD on top of the gate insulator and subsequently highly doped by high fluence implantation. This step is carried out simultaneously with the S/D implantation because ion energies and fluences in both cases are comparable. n^+-type poly-Si doping for n-channel MOSFETs and p^+-type poly-Si doping for p-channel MOSFETs are usually achieved by P^+ or As^+ and B^+ (BF_2^+) implantation, respectively. The dopant activation in poly-Si during subsequent annealing must be done carefully to avoid their diffusion through the gate insulator (SiO_2, HfO_2, etc.) into the transistor channel, which can lead to undesired V_{th} variation [101]. For p^+-type doping of poly-Si low energy B^+ is preferred because of fluorine enhanced diffusion of boron through ultrathin gate oxides that occurs at annealing of BF_2-implanted poly-Si [102]. This effect can be reduced by forming a gate oxinitride, either during oxidation or by N^+ co-implantation.

In order to fabricate more and more shallow pn-junctions, recent efforts are done with respect to the following ion implantations: (1) lowering the ion energy to around 100 eV, (2) use of heavier ion species and in some cases of molecular and gas cluster ions (e.g., decaborane $B_{10}H_{14}$, octadecaborane $B_{18}H_{22}$), and (3) preamorphization by Si^+, Ge^+, or Xe^+ ion implantation to avoid channeling effects.

Co-implantation of N^+, F^+, and C^+ ions together with boron implantation for shallow source/drain doping is often used in deep submicron MOSFET fabrication to suppress transient-enhanced diffusion (TED) of boron [103] and boron deactivation (so-called reverse annealing) [104] during subsequent thermal annealing. Furthermore, applying N^+ co-implantation to the gate doping, the gate silicon oxide can be nitrided, thus suppressing the boron penetration through the SiO_2 and improving the reliability and hot carrier resistance of the gate oxide.

The different ion implantation processes described earlier are included in advanced CMOS technology to fabricate MOSFETs with 28 nm gate length and

with metal/high-K gate structures. As dopant ions B^+, BF_2^+, P^+, As^+, Sb^+, and In^+ as well as heavy boron molecule and cluster ions are implanted to form several types of MOS transistors. Implantation steps with Ge^+ or Xe^+ ions for silicon preamorphization, the stress memorization by As^+ implantation into the poly-Si gate electrode to increase the charge carrier mobility in the transistor channel [105], and co-implantation of C^+, F^+, N^+ are employed. Thus, the application of all these implantation steps results nowadays in a total number of 40–50 ion implantations.

Discrete high-power devices with current handling capability ranging from 100 A to several 1,000 A at high voltages can be divided into majority carrier devices (Schottky diodes, power MOSFETs, junction field-effect transistors—JFETs) and minority carrier devices (thyristors, bipolar transistors, isolated gate bipolar transistors—IGBT and pin-diodes).

The charge carrier lifetime significantly influences the operation parameter of bipolar power devices such as diodes, thyristors, and IGBTs. High charge carrier lifetime (~0.1–1 ms) is required, in order to keep on-state charge carrier losses low. On the other hand, power devices required to operate at high frequencies need a short carrier lifetime in certain device regions, in order to achieve a fast turn-off state and a minimization of the reverse recovery charge. The reduction of the carrier lifetime can be achieved by introducing recombination centers either by in-diffusion of metallic impurities (e.g., Au, Pt) before final device contact metallization or by irradiation with high energy light ions (H^+, He^+) from the device back side, which is usually the last step in power device processing sequence. Compared to diffusion of metal impurities the advantages of high energy ion irradiation with H^+ and He^+ ions are the local decrease of carrier lifetime by ion-induced defects with precise spatial damage location and defect density in the device depletion zone, no metal contamination, and low device leakage current [106–108]. H^+ and He^+ (or He^{++}) irradiation are carried out at typically 1–10 MeV ion energy with fluences of about 10^{10}–10^{12} cm^{-2}. At these irradiation conditions the mostly damaged regions (depth of the Bragg peak) are located in a depth of 10–500 μm and of 3–70 μm for 1–10 MeV H^+ and 1–10 MeV He^+ irradiations, respectively. Among other created defects (single vacancies, interstitials, vacancy-impurity complexes, etc.) the most useful ion induced defects in these regions are silicon singly negative-charged divacancies ($V_2{}^{-1}$) with a deep level in the band gap ($E = E_C$−0.41 eV, [109]) and a concentration of about ~10^{14}–10^{16} cm^{-3} at typical irradiation with 5 MeV H^+ and He^+ ions and a fluence of 1×10^{12} cm^{-2}, respectively. The silicon divacancy is of special interest because it is temperature stable until 300 °C which is important for reliable device operation. At this deep level an enhanced charge carrier recombination can be achieved due to a low recombination lifetime τ_R preserving at the same time a high generation lifetime τ_G time for low reverse currents. Consequently, the aim of lifetime engineering in power devices by high energy ion irradiation is a maximization of the lifetime ratio τ_G/τ_R and therefore to ensure increased switching speed (higher frequencies) and decrease of power losses (heat reduction).

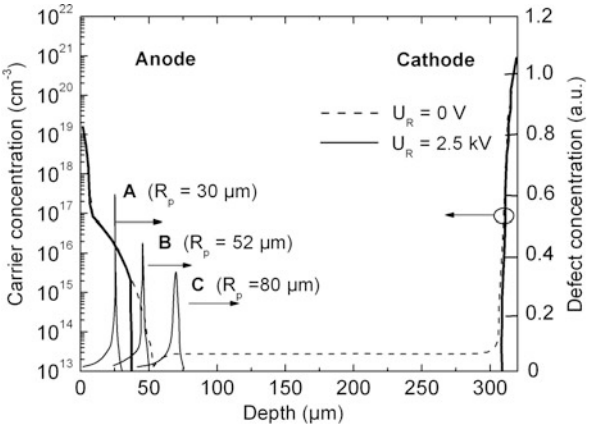

Fig. 4.20 Charge carrier profiles in a P^+PNN^+ diode at reverse voltages of $U_r = 0$ V (*dashed*) and $U_r = 2.5$ kV (*solid*) with simulated profiles of the damage resulting from ion irradiation into regions A, B, C

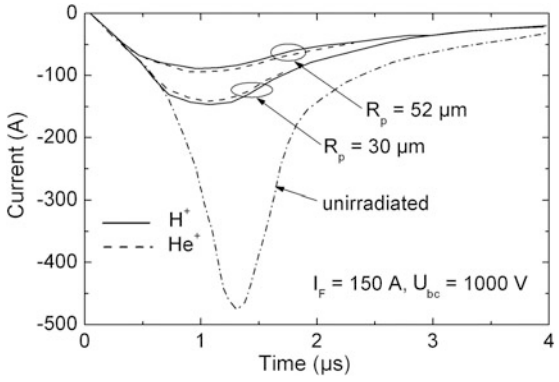

Fig. 4.21 Reverse recovery waveforms of an unirradiated diode and diodes irradiated by H^+/He^{2+} ions (fluence $5 \times 10^{12}/5 \times 10^{11}$ cm^{-2}, *solid/dashed*)

As an example of local lifetime engineering in power diodes, the implantation conditions and the resulting reverse current recovery behavior are shown in Figs. 4.20 and 4.21, respectively [108, 110].

In this case, ion energies of 1.8, 2.4, and 3.0 MeV for H^+ and 7.1, 9.6, and 12.1 MeV for He^{2+} were chosen in that way to place the damage peak into three qualitatively different regions of the diode [anode side of the junction outside (A) and inside (B) of the space charge region, and the N-base side of the junction (C)]—see Fig. 4.20. The chosen ion energies guarantee identical projected ranges in silicon R_p (30, 52, and 80 µm) for both projectiles. The fluences were set differently for H^+ and He^{2+} ions (2×10^{11}–5×10^{12} and 2×10^{10}–5×10^{11} cm^{-2},

respectively) to provide equivalent carrier recombination rates. After irradiation, all diodes were annealed at 200 °C for 60 min to stabilize the radiation defects.

The effect of H^+ and He^{2+} irradiation on the turn-off characteristics (Fig. 4.21) is identical, if the H^+/He^{2+} fluence ratio is set to 10. As can be seen, local lifetime control by ion irradiation can speed-up the diode switching and soften the current recovery by leaving enough charge on the cathode side. Moving of the projected ion range R_p close to the anode (from region C to A) reduces the storage time and fastens the space charge region development. Nevertheless, the effect of local lifetime control on reverse current I_r and break-down voltage U_{br} is more complex and varies according to the location of the damage maximum [110, 111].

It is shown that optimal lifetime structuring over device depth giving superior recovery characteristics is achieved by a well-balanced combination of two or more consecutive local lifetime treatments. Beside the ion irradiation fluence, the irradiation procedure involves a proper choice of irradiation energy [112]. Since any radiation defect profile can be created by superposition of several irradiation steps, the combination of ion and electron irradiation provided further device improvement.

Another example for improvement of power device performance by back-side high energy ion irradiation of metal oxide semiconductor gate turn-off thyristors (MOS-GTOs) is given in [113]. This type of power device seems to be very promising especially in high voltage applications, thanks to a very low voltage drop and good switching performances. He^+ ion irradiation was executed at ultra-high ion energy of 40 MeV in the fluence range of (0.25–1.0) $\times$ 10^{10} cm^{-2} using a cyclotron in order to obtain a local damage peak at a depth of ~700 μm for charge carrier lifetime lowering at the transition between N^- drift and N^+ buffer layers of the MOS-GTOs. The irradiation in this case was performed with He irradiation from the back side of the wafer thus avoiding any damages at the gate oxide of MOSFET placed on the device front side. Experimental results show that He^+ irradiation can significantly improve the turn-off switching performances of the MOS-GTO without affecting its on-state and turn-on switching characteristics. A proper localization of defect peak concentration, obtained by changing the parameters of the irradiation (energy and fluence), has been used to optimize the device characteristics and to improve significantly its switching performances. A reduction by more than 30 % of the turn-off energy losses compared to nonirradiated MOS-GTO devices was demonstrated using ultrahigh He^+ ion irradiation.

Among ion irradiation based local defect engineering, ultrahigh energy boron implantation for doping of deep pillar-like p-type regions into depths up to 40 μm is of great interest for high-voltage super-junction devices (SJDs) and was firstly introduced by Infineon's CoolMOS technology between 1998 and 2000 [114–116]. The CoolMOS™ high voltage MOSFET devices do not show bipolar current contribution like the well known tail current observed during the turn-off phase of IGBTs. Advantageously, the CoolMOS™ device virtually combines the low switching losses of a MOSFET with the on-state losses of an IGBT.

For the vertical p-type pillars devices, the state of the art successive epitaxial growth of n^--type layers (overall thickness ~35 μm) combined with local p-type

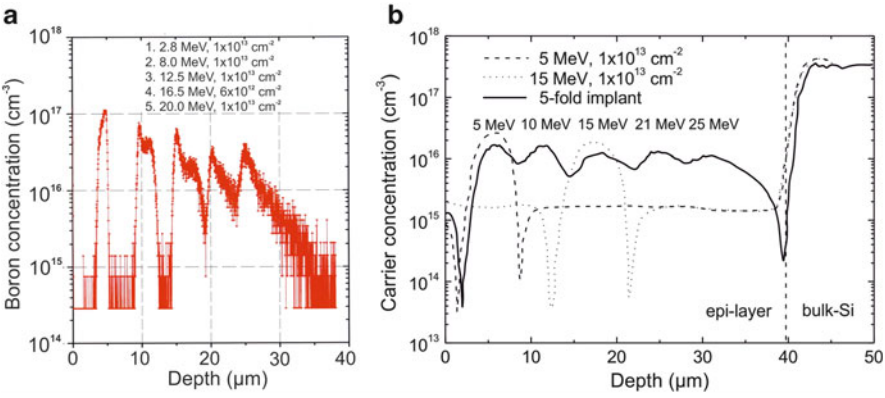

Fig. 4.22 (**a**) Boron depth profile measured by SIMS of a fivefold B^+ implantation using ion energies between 2.8, 8.0, 12.5, 16.5, and 20 MeV, and (**b**) corresponding charge carrier depth profile obtained by spreading resistance measurement. The n-type epi-layer has a thickness of 40 μm and a carrier concentration of 2×10^{15} cm^{-3}. The high charge carrier concentration of the n^+-substrate is ~4×10^{17} cm^{-3} [118]

diffusion and/or low energy ion implantation is time consuming and cost intensive. As an alternative low cost vertically structured doping process, recently ultra-high energy boron implantation was proposed to form the vertical p-type pillars [117, 118]. This concept represents a major simplification of SJDs fabrication since the overall number of process steps is drastically reduced.

For the patterned implantation of high-energetic boron ions, silicon stencil masks are placed in proximity to the wafer. In order to ensure safe masking even for 25 MeV, B^+ ions with a projected range of $R_p = 34$ μm the thickness of the silicon mask had to be 45 μm [118]. The ultra-high energy boron implantation consists of a fivefold implantation sequence with B^+ ion energies between 2.5 and 25 MeV and fluences from 5×10^{12} to 1×10^{13} cm^{-2} per implantation step. Due to the high aspect ratio (7:1) of the Si stencil mask the implantation was carried out perpendicular to the wafer surface. The as-implanted boron profile measured by SIMS in Fig. 4.22a clearly shows the well-separated boron doped regions of the fivefold implantation sequence. Each peak shows a characteristic distribution with contributions from channeled and dechanneled ions.

The strong influence of axial channeling is evident as the implantations were performed under normal incidence conditions. Whereas for the lowest energy the peak distribution is mainly determined by channeled ions the influence of the channeling decreases with increasing energy. To obtain a continuously p-type doped pillars the wafers were subsequently annealed at 1,150 °C for 6 h enabling p-type regions with charge carrier concentrations of $n_A \sim 10^{16}$ cm^{-3} in a depth between 2 and 40 μm and a sufficient homogeneity in the spatial carrier concentration which was confirmed by spreading resistance depth profiling shown in Fig. 4.22b [118]. It was demonstrated that the developed high energy implantation process yields fully functional high-voltage MOS transistors with high blocking voltages and low reverse leakage currents. A more detailed description of the device properties is given in [119].

Today, silicon planar technology including ion implantation is being utilized extensively to advanced *silicon sensor and detector technologies* [120–125]. In these areas, attention was first focused on microsensor (i.e., microfabricated sensor) development.

Today, common ion implantation is implemented in sensor and detector technology to fabricate doped regions in different device structures (diodes transistors, resistors, etc.). In some sensor applications, ion implantation is often followed by a diffusion step to get wanted impurity profiles going deeper than a few parts of a micrometer normally achieved by implantation. In this way, ion implantation is used as a predeposition technique, using its high ion fluence accuracy to improve the accuracy of the doping concentration. So, boron-implanted resistors for piezoresistive micromachined sensors have a resistance value accuracy down to 1 %, which is much better than that achievable with the thermal diffusion technique. Therefore, ion implantation is the dominating way of making advanced piezoresistive sensors.

In the field of radiation detectors (photodetectors, charged particle, and X-ray detectors), high responsivity and collection efficiency of charge carriers generated by radiation are required. This can be only reached using low damage shallow pn-junctions in the radiation entrance window of the radiation sensing device. Although radiation sensors are relatively simple in design with relatively large structure sizes in comparison with integrated microelectronic circuits the requirement of maintaining the high-quality silicon properties (e.g., extreme low impurity concentration, high minority charge carrier lifetime of $\geq$1 ms) during processing did not allow a straightforward application of the microelectronic planar technology. The requirements on ion beam processing in some aspects are more stringent due to the processing of commonly used high purity Float-Zone silicon (FZ-Si) without degradation of its properties, for example, by the introduction of impurities or the creation of defects, the processing of both wafer sides without damaging the opposite surface, and the production of even wafer-sized defect-free radiation detectors.

Using the flexibility of ion implantation, for example, tailoring of doping profiles with exact location of its maximum at the SiO_2/Si interface implanting through thin SiO_2 layers or producing of buried doping profiles is easily possible. In the following selected examples for the application of high energy ion implantation to the fabrication of advanced radiation sensing devices will be described. The aim of high energy ion implantation for the fabrication of buried doping layers is the optimization of the electric field distribution $E(x)$ and the increase of the high electric field strength in the device depletion region without breakdown. This approach has been introduced to replace high-temperature deep diffusion processes and epitaxial growth of doped silicon layers in the fabrication process of radiation sensing devices.

In *Avalanche Photodiodes* (APD) a high electric field is necessary to reach the regime of photon generated charge carrier multiplication up to a level of $M \sim 10^2$–10^3 at low dark currents. Figure 4.23 shows typical doping profiles and electric field distribution for a conventional silicon $N^+P\pi P^+$ APD with a deep diffused P-layer (Fig. 4.23a) and an $N^+\pi P\pi P^+$ APD with a buried MeV-implanted P-profile [126] (Fig. 4.23b), respectively.

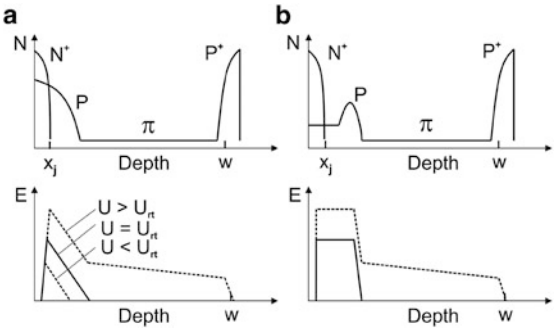

Fig. 4.23 Principal doping profiles and typical electric field distributions of a conventional silicon $N^+P\pi P^+$ APD with a deep diffused P-layer (**a**) and an $N^+\pi P\pi P^+$ APD with a buried MeV-implanted P-profile (**b**). U_{rt} is the so-called reach-through voltage

As can be seen in Fig. 4.23a the highest electric field in the $N^+P\pi P^+$ structure is restricted to a very small depth region at the N^+P-junction whereas for the $N^+\pi P\pi P^+$ structure in Fig. 4.23b with a buried MeV-implanted P-profile the electric field has a constant high value of (1–3) $\times$ 10^5 V cm^{-1} over a certain depth region. As an advantage of high energy boron implantation, the width of the constant high electric field region and the electric field strength can be precisely tuned by changing the ion energy and the ion fluence, respectively. For the deep B^+ ion implantation, the maximum of the buried P-layer is located at a distance of 2.75 and 3.1 μm from the surface for ion energies of 1.5 and 1.8 MeV, respectively. The ion fluence is low—in the range of (1–2) $\times$ 10^{12} cm^{-2}—and has to be carried out with high demands to homogeneity and fluence accuracy with errors <1 % [126]. Precise control of the conditions for the two implantation steps ensures good process reproducibility, which is particularly easy to do for epitaxial π/P^+ wafers, and also a good fabrication yield. APDs obtained in this way offer excellent photoelectric performance, e.g., low dark current ($I_0 < 1$ nA) close to the breakdown, high gain of $M > 150$, resulting in a sensitivity greater than 75 A/W, as well as excellent uniformity in the avalanche set point (ASP) of $\leq \pm 5$ % and improved correction of ASP temperature dependence.

The sensitive area of APDs could be also increased thanks to the excellent spatial homogeneity offered by the implantation technique compared to APDs fabricated only by diffusion processes. Figure 4.24 shows, for example, typical dependence of the multiplication factor M on the bias voltage U of an APD with $x_j = 400$ nm of the N^+p-junction for different B^+ ion fluences implanted at 1 MeV. As can be seen the $M(U)$ characteristics of the APD depend very sensitive on the B^+ ion fluence.

Silicon PIN diodes are also widely used for the detection and spectrometry of ionizing radiation, in particular of charged particles, e.g., electrons (e), protons (H^+), α-particles (He^+), and heavier ions (see also Sect. 3.4.5). Today ion implantation is the standard doping process for the fabrication of shallow p^+n-junction regions and n^+-contacts in n-type high resistivity silicon using low energy

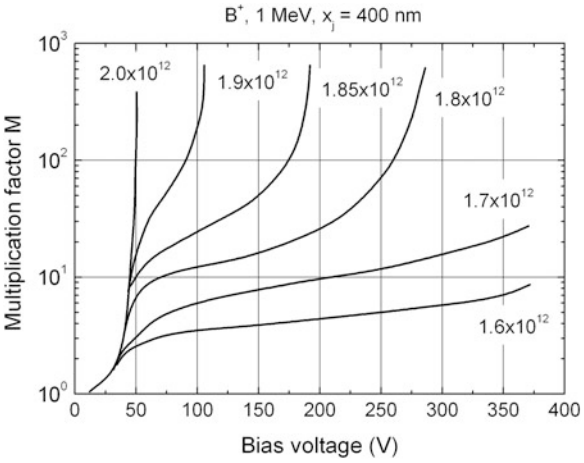

Fig. 4.24 Typical dependence of the multiplication factor M on APD bias voltage *U* for different B^+ ion fluences (in cm^{-2}) implanted at an ion energy of 1 MeV [127]

implantation of boron and arsenic/phosphorous (10–30 keV, 10^{14}–10^{15} cm^{-2}), respectively, which was introduced by the pioneer works of Kemmer [128, 129]. This detector technology and a variety of advanced structures such as strip or pixel detectors, the silicon drift chamber detectors (SDCDs), or fully depleted junction charge-coupled devices (CCD's) have been further developed during the last decade [123–125, 130]. Besides, relatively high energy ion implantation (300–600 keV) has been used to implant deep $n^{(+)}$ or $p^{(+)}$ layers into high resistivity silicon for fully depleted CCDs, SDCDs, or for junction field-effect transistors (JFETs) monolithically integrated on these detectors [131, 132].

In the following some examples for applications of the MeV ion implantation technique in the detector fabrication technology will be discussed. The motivation, as also in the case of APDs, arises from the fact that local changes of the substrate doping can be used to modify the vertical electric field distribution of silicon pn-junction detectors. Low dose MeV implantation of phosphorous in n-type silicon has been applied to realize pn-junction detectors with high field regions (HFR) extending from the surface to a depth of several micrometer ($p^+nn^{(-)}n^+$ structure). Using silicon pn-junction detectors with classical $p^+n^{(-)}n^+$ structure for heavy ion spectroscopy two particular problems arise, namely the plasma delay and the pulse height defect (PHD). This PHD is usually defined as the energy difference obtained in the spectrum between the peak position of heavy ions and protons (or α-particles) of the same incidence energy. The PHD is caused by three effects: the nonnegligible energy loss of heavy ions in the detector entrance window (front contact and p^+-layer), the increasing contribution of the nonelectronic nuclear stopping with increasing ion mass, and the deficit due to the plasma recombination of charge carriers along the ionization track of the incident particle. It is well known that the effective silicon dead layer and the plasma recombination at ionization densities

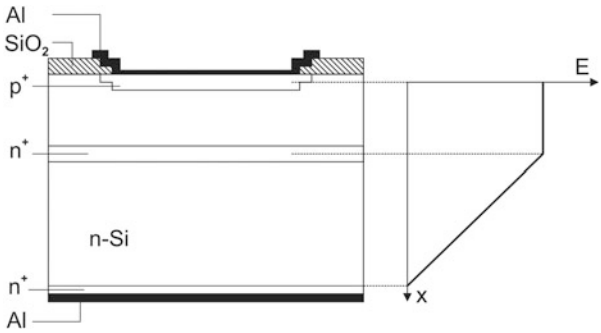

Fig. 4.25 Schematic view of the modified detector structure with a buried n^+ doping profile and the electric field distribution of the reverse bias detector

$\geq 10^{19}$ e/h-pairs per cubic centimeter depends on the electric field strength [133, 134]. Therefore, detectors with enhanced internal electric fields of $E > 10\,\text{kV cm}^{-1}$ are preferred for the spectroscopy of heavy ions owing large electronic stopping power. Silicon detectors with such high internal electric field have been fabricated applying MeV ion implantation of P^+ ions into high resistivity n-type detector-grade silicon [135, 136]. The novel silicon detector structure proposed in [135] with a high internal field strength up to $E = 200\ \text{kV cm}^{-1}$ is shown schematically in Fig. 4.25.

The conventionally employed p^+n-junction structure based on high resistivity n-type material ($\rho \geq 2{,}000\ \Omega$ cm) is modified by a 10 MeV P^+ high energy ion implantation at low fluences in the range of 1×10^{11}–$1 \times 10^{12}\ \text{cm}^{-2}$ leading to a buried region of enhanced n-type bulk doping with the maximum of the profile at a depth of 4.75 μm. The depth of the HFR and the maximum electric field strength can be established separately by the energy and the fluence of the MeV implantation, respectively, as shown Fig. 4.26.

Figure 4.26 shows the calculated electric field distribution for a detector modified by a P^+-implantation at 10 MeV with different fluences. The local enhancement of the bulk doping due to the MeV implantation results in an increased and nearly constant electric field up to the depth of the buried layer at ~4 μm. Behind the $n^{(+)}$ layer the electric field linearly decreases analogous to the conventional detector configuration. This field distribution is similar to diodes, which are produced using epitaxial $n^{(+)}$ layers on high resistivity material. Implantation fluences above $\Phi > 2.5 \times 10^{11}\ \text{cm}^{-2}$ result in high field regions with $F > 50\ \text{kV cm}^{-1}$, which exceed those of conventional heavy ion detectors. For an implantation fluence of $1 \times 10^{12}\ \text{cm}^{-2}$ even an electric field strength above $100\ \text{kV cm}^{-1}$ can be easily realized, which is more than a factor of ten higher compared to conventional $p^+n^{(-)}n^+$-diodes. The performance of detectors with different high field regions has been tested using oxygen ions with energies between 0.9 and 8.5 MeV [135]. Figure 4.27 shows the measured ion energies as a function of the electric field strength. The bias voltage for all detectors was changed from 5 up to 200 V to obtain an electric field overlap between detectors with different HFRs.

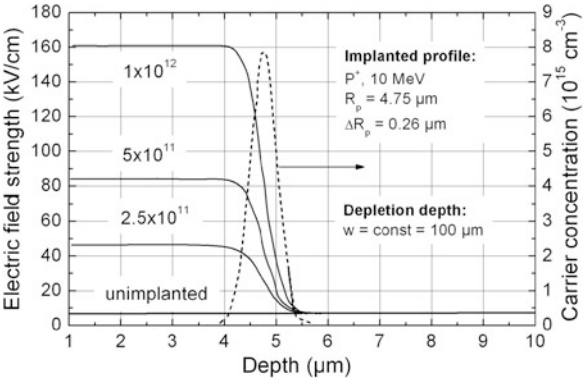

Fig. 4.26 Electric field strength versus depth of a HFR silicon detector (P^+, 10 MeV) as a function of ion fluence for a fixed depletion depth of 100 μm

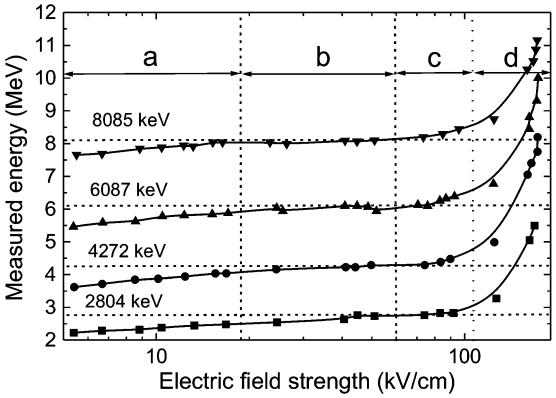

Fig. 4.27 Measured signal amplitudes of different HFR detectors in dependence on the electric field strength for various ion energies of oxygen (2.80, 4.27, 6.09, and 8.09 MeV); parameter: P^+, 10 MeV: (a) unimplanted, (b) 2.5×10^{11} cm^{-2}, (c) 5.0×10^{11} cm^{-2}, (d) 1.0×10^{12} cm^{-2}

Three regions can be clearly distinguished. The measured energy continuously increases with the electric field up to a constant value, which is obtained at around $F = 35$ kV cm^{-1}. The following nearly constant part of the curves can be interpreted as the region of maximum carrier collection from the window and the ionized track in the depletion zone. At electric fields above 100 kV cm^{-1} a significant enhancement of the pulse height was measured caused by charge carrier multiplication (avalanche effect). The beginning avalanche multiplication at moderate field strength of about 80 kV cm^{-1} is surprising and gives rise to the conclusion that the electric field is strongly enhanced near to the end of the "conducting needle" of the plasma track.

Recently, silicon detectors with HFR have been also developed for the detection of electrons in modern electron lithography tools [136]. In principle the electron detector consists of a conventional p^+n-junction diode where the pn-junction area is covered with an additional electron beam patterned heavy metal layer (2.5 μm thick Cr/W layer), which possesses well-defined windows of various dimensions in the micrometer and nanometer range. This heavy metal layer acts as an absorber allowing the electrons to penetrate the sensitive junction area only through these windows. From the evaluation of the detector signal arising from a scanned beam across windows of different size one can derive information about the properties of the incoming beam such as spot size, homogeneity, current density, skewness, etc. [137]. The requirements for electron beam lithography tools are closely related to the use of higher electron energies (30–50 keV to maintain better pattern fidelity) and higher electron current densities (to increase the throughput). Even more critical, tighter beam specifications have become more and more important. Consequently, the diagnostics and control of the e-beam parameters in the e-beam writer are of fundamental relevance. One main problem of conventional Si pn-junction detectors applied for the diagnostics of intense electron beams is the nonlinearity between the incoming electron current and the detector response measured as an output voltage after external signal processing. For typical electron beam current densities of several ampere per square centimeter, ionization leads to the formation of a nearly spherical volume with a high electron/hole (eh) concentration of 10^{17}–10^{18} eh-pairs/cm^3 (often called plasma cloud). During the characteristic plasma time (some ns), this cloud screens the external field and eh-recombination is favored. Standard Si detectors made from high resistivity Si (resistivity ~ kΩ cm) which are characterized by a triangular field distribution with a maximum field strength of only 2–3 kV cm^{-1} do not enable complete eh-separation without any charge loss for the diagnostics of intense electron beams (the same problem as for heavy ion detection). Because the plasma time is roughly inverse proportional to the electric field strength an increase of the electric field is necessary to lower plasma-based charge losses in such electron detectors. For this purpose, detectors with an enhanced electric field strength of about 10–20 kV cm^{-1} have been fabricated in a standard planar process including a high energy (MeV) ion implantation step with nearly the same implantation parameters as used for heavy ion detectors. Considerations concerning the ion energy are derived from the electron ionization depth distribution shown in Fig. 4.28a.

The stopping power peak shifts from 1 μm to about 5.5 μm by increasing the electron beam energy from 20 to 50 keV. Furthermore, for higher energies the distribution is characterized by a larger width and a lower value of the stopping power. As shown in Fig. 4.28b over the interesting depth the electric field strength between 20 and 30 kV cm^{-1} can be easily varied by choosing an appropriate implantation fluence in the range (1.0–2.5) × 10^{11} cm^{-2}. As the HFR is formed only at a small part (~3.5 %) of the larger p^+n-junction area (52 mm^2) implantation masks suitable for MeV ion implantation are required. Low implantation fluences allow to use thick film photoresist masks of 20–25 μm thickness. The fabrication of the p^+- and n^+-layers (see Fig. 4.25) was carried out in a conventional procedure

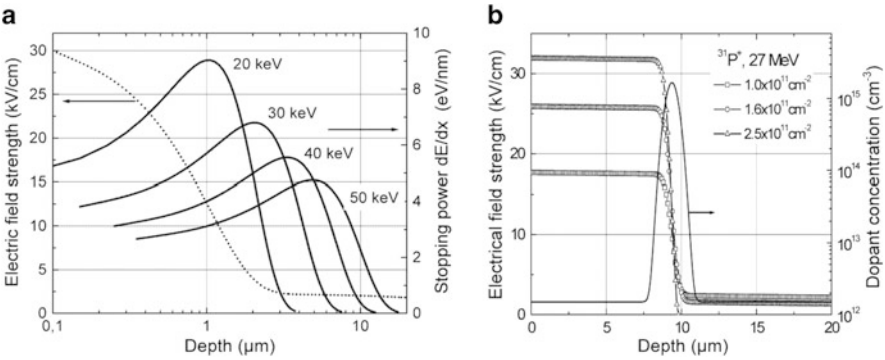

Fig. 4.28 (**a**) Stopping power due to ionization for electrons ($E = 20$–50 keV) in Si and electric field distribution for conventional deep diffused n^+-region limited to about 2 μm. (**b**) Electric field distribution of the HFR pn-junction detector with a buried implanted $n^{(+)}$ layer ($^{31}P^+$, 27 MeV) determined for a reverse bias detector voltage of 30 V which represents different values of the depletion layer width w (115, 80, 9.8 μm) for implantation fluences of 1.0, 1.6, and 2.5×10^{11} cm^{-2}, respectively

using ion implantation of B^+ and P^+ ions at 50 keV with fluences of 5×10^{14} cm^{-2}, respectively. Measurements of the linearity behavior of the electron detectors were performed with electrons of 50 keV energy using different incident electron currents (beam spot area $A < 2$ μm^2). It was demonstrated that the linearity range extends with increasing implantation fluence and increasing detector bias. For the highest P^+ ion fluence of 3.7×10^{11} cm^{-2}, high e-beam currents up to 200 nA corresponding to a very high current density of 20 A cm^{-2} have been detected without significant charge carrier loss. If the linearity range is plotted versus the electric field strength, a linear correlation was obtained (Fig. 4.29).

This behavior agrees with the assumption that deviations from the linearity are caused by charge loss due to plasma related recombination, which is in first order inversely proportional to the electric field strength [138, 139].

4.2.2 Ion Implantation into Germanium

Although the first transistor was made of germanium (Ge), today most integrated circuits are fabricated using silicon substrates. The main reasons for the change from Ge to Si are the excellent physical properties of the SiO_2/Si interface which are crucial in CMOS technology. Today SiO_2 is increasingly replaced by high-k dielectrics. This fact and the advantage that the carrier mobility in Ge is higher than in Si (3,900 cm^2 V^{-1} s^{-1} compared to 1,450 cm^2 V^{-1} s^{-1} of Si) have led to a renewed interest in germanium as a candidate for future integrated devices, such as high mobility transistors [140] and high quality photodetectors [141]. For successful device applications of Ge, however, low resistivity, shallow, and low leakage germanium pn-junctions are required.

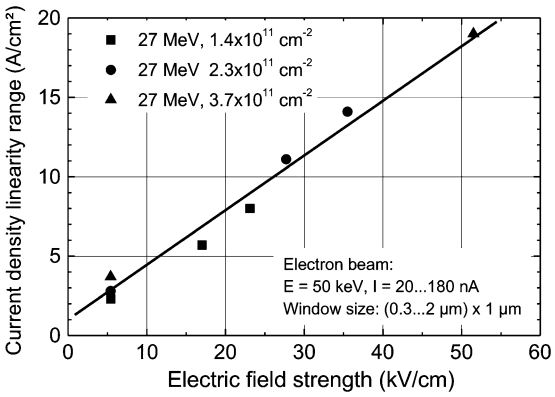

Fig. 4.29 Dependence of the linearity range of the electron detectors on the electric field strength in the HFR. *Different symbols* for the same implantation fluence represent different detector bias values

Recent investigations on the formation of ultra-shallow junctions by ion beam processing have shown that p^+-doping using B^+ ion implantation yields junctions that meet the requirements for the 22 nm technology node, whereas the formation of n^+p-junctions by P^+ or As^+ ion implantation is complicated by the high diffusivity, the low solubility of these dopants in germanium, and by low activation of these dopants and the difficulty in defect annihilation during subsequent annealing [142]. Ga^+-implanted ions as p-type dopants in Ge are another interesting alternative for shallow junctions because their higher atomic mass reduces both the ion straggling and the channeling of the as-implanted profile, as demonstrated for P^+ and As^+ ion implantation in Ge-MOSFET device fabrication [143]. Additionally, compared to boron Ga has a very high solubility in Ge of ~5×10^{20} cm^{-3}. However, Ga that seemed to be very attractive for p-type doping suffers from an important dose loss due to evaporation during annealing [142].

Because boron has a very low diffusivity in Ge the as-implanted profile defines the pn-junction depth. For example, as shown in Fig. 4.30 for 6 keV B^+ implantation into Ge at a fluence of 3×10^{15} cm^{-2} followed by RTA annealing up to a temperature of 400 and 600 °C for 60 s no movement of B takes place and the as-implanted and annealed profiles overlap [144].

Sheet resistance measurements showed that a higher activation level of 1×10^{19} cm^{-3} (dashed line in Fig. 4.30a) compared to the solid solubility of B into Ge of 6×10^{18} cm^{-3} (full line in Fig. 4.30a, b) was reached. Therefore, results for B^+ ion implantation for p-type junctions in Ge are promising. To reduce boron channeling (deeply extended tail of the boron profile into the bulk in Fig. 4.30a) an amorphization of Ge over a depth of ~100 nm can be performed by self-implantation of Ge^+ ions at 100 keV and a fluence of 1×10^{15} cm^{-2}. During annealing the amorphous layer re-crystallizes by solid phase epitaxial Ge regrowth with activation of B atoms onto substitutional sites. As shown in Fig. 4.30b, the

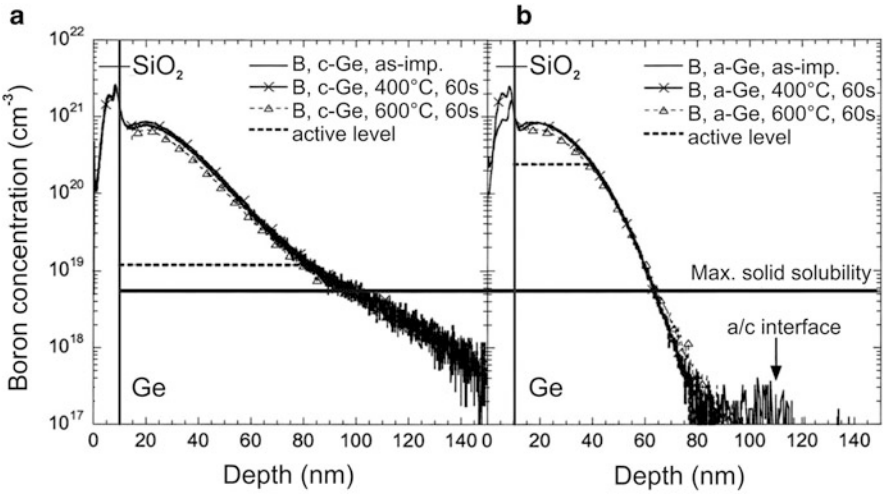

Fig. 4.30 6 keV B^+, 3×10^{15} cm^{-2} as-implanted, and annealed at 400 and 600 °C for 60 s, boron depth profiles in Ge measured by SIMS without (**a**) and with (**b**) preamorphization by a Ge implant of 100 keV Ge + ions to a fluence of 1×10^{15} cm^{-2} [144]

activation level reaches 2×10^{20} cm^{-3} (dashed line), which is two orders of magnitude above the equilibrium solid solubility (full line in Fig. 4.30a, b). However, at the maximum of the implanted profile the boron concentration reaches 1×10^{21} cm^{-3}. Evidently, an important part of the B atoms is not activated.

The application of Ga^+ ion implantation to the fabrication of p^+n-junctions in Ge was recently investigated to study the diffusion behavior of the implanted Ga at RTA annealing for 60 s in the temperature range of 300–700 °C with SiO_2 capping layers to prevent Ga outdiffusion during heat treatment [145]. The results suggest that Ga has nearly the same diffusion behavior as B in Ge. Implanting Ga^+ ions (40 and 80 keV, 3×10^{15} cm^{-2}) into crystalline Ge, no diffusion was observed after the RTA annealing at 300–700 °C. For annealing 60 s at 550 °C, an electrical activation level of 4.4×10^{20} cm^{-3} was achieved which is close to the Ga solubility in Ge. Ge preamorphization followed by SPER did not yield a higher activation level, although ion channeling was suppressed. Additionally, an increased Ga diffusivity in the amorphous phase was observed at temperatures >400 °C. The high activation level and the absence of diffusion make Ga^+ ion implantation in c-Ge to form p^+n-junctions very promising for implementation in a Ge technology.

The formation of n^+-doped junctions by P^+ ion implanation is more critical as phosphorous and does not show a high level of active concentration. Maximum concentrations of $(5–6) \times 10^{19}$ cm^{-3} have been reached, which are below its equilibrium solid solubility of 2×10^{20} cm^{-3} [146]. It has been assumed that most of the P atoms are not in an electrically active configuration and are possibly paired with point defects such as vacancies. At phosphorous concentrations above $(2 - 3) \times 10^{19}$ cm^{-3}, the diffusion coefficient in Ge is dopant concentration dependent leading to a box-like profile during annealing (Fig. 4.31) [147].

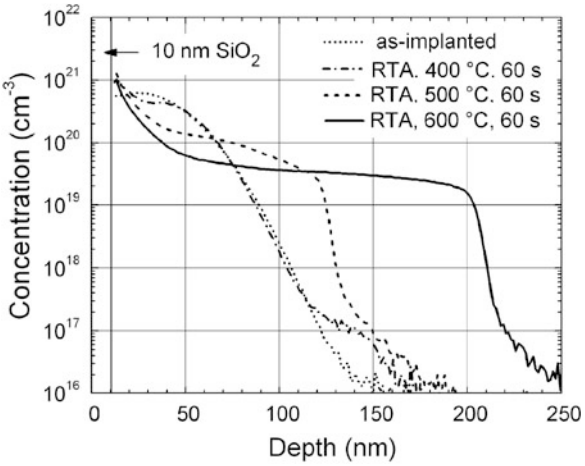

Fig. 4.31 Phosphorous profiles after 60 s RTA at 400 °C (*dashed/dotted line*), 500 °C (*dashed line*), and 600 °C (*thick line*). The as-implanted profiles are shown for comparison (*dotted line*). Before annealing the thickness of the amorphous layer was 150 nm. The P profiles were measured by SIMS

Prior to ion implantation of the profiles in Fig. 4.31, the samples were capped with 10 nm SiO_2 by sputter deposition. Preamorphization implantation (PAI) was performed by Ge^+ ions at energies of 150 keV and at a fluence of 1×10^{15} cm^{-2}. Phosphorous was implanted at 30 keV and 3×10^{15} cm^{-2} and rapid thermal annealing (RTA) of the samples was performed at 400, 500, and 600 °C for 60 s. Recently, for suppression of phosphorous diffusion and achievement of a high activation degree at the same time, FLA in the ms range instead of RTA has been applied [148]. Shallow n^+ layers in Ge were formed by P^+ ion implantation (30 keV, 3×10^{15} cm^{-2}) and subsequent millisecond (3 and 20 ms) flash-lamp annealing. In contrast to conventional RTA annealing, a high activation up to 6.5×10^{19} cm^{-3} is achieved without any dopant redistribution and noticeable phosphorous diffusion. Furthermore it was shown that the optimum of FLA treatment should not strongly depend on the pretreatment by preamorphization implantation (PAI), preannealing by RTA, and the solid phase epitaxial recrystallization (SPER) of amorphous layers. The results suggest that independently of pretreatment the maximum activation should be obtained at a flash energy that corresponds to the onset of P diffusion. To obtain a high electrical activation, the thermal annealing needs to be carefully designed so that phosphorous can be effectively activated before diffusion. Optimized RTA or FLA annealing process can yield a maximum active P concentration of $\sim 1 \times 10^{20}$ cm^{-3}, which is its solid solubility limit. Usual RTA temperatures for Ge, about 400–600 °C, are used for less than 60 s.

In general annealing behavior for high fluence-implanted phosphorous, doping levels can be quite complicated due to outdiffusion of phosphorous (losses to gas phase or capping SiO_2 layer), indiffusion deeper into the sample, and precipitation

of P-containing clusters at locations of peak concentration [149]. These undesirable effects can be avoided if P^+ ions are implanted to concentrations at the peak activation level of $\leq 5 \times 10^{19}$ cm^{-3} [143].

Compared to other n-type dopants phosphorous is preferred for the implantation of highly doped n^+p-junctions. This is related to the fact that high fluence implantation above 5×10^{14} cm^{-2} of the heavier dopant ions (As, Sb, Bi) and also Ge for preamorphization creates serious roughening of the surface, near-surface void formation, or even porous surface layers [150]. The formation of voids and clusters of voids has been observed in Ge during ion implantation of heavy ions such as Ga, Ge, As, In, and Sb into Ge at ion energies $\geq$30 keV and fluences above ~1×10^{15} cm^{-2}. A complete surface coverage with cluster voids and pronounced porous layers often appears at higher fluences of $\geq 1.0 \times 10^{16}$ cm^{-2} [150, 151]. The morphology of the near-surface damage strongly depends on ion mass. For example, in the case of Ga^+ and As^+ ion implantation the induced surface roughness is purely a surface related effect which can be prevented by adding a 10–30 nm SiO_2 capping layer prior implantation. In the case of In^+, Sb^+, and heavier ion (e.g., Bi^+), implantation subsurface void formation by the clustering of vacancies takes places. This subsurface void formation appears abruptly at fluences between 5×10^{14} and 10^{15} cm^{-2} and cannot be removed during subsequent thermal treatment. The initial void and porous structure formation is discussed in the literature in terms of very effective vacancy clustering [152–156] and "microexplosion" theories [157–159]. Nevertheless, results of extended investigations indicate that neither the vacancy clustering nor microexplosion theory can solely explain void formation [151]. In summary, surface roughening, near-surface void, and porous layers formation in germanium suggest that ion implantation conditions must be chosen carefully in Ge-based device processing with common p- and n-type dopants (Ga^+, In and As^+, Sb^+, respectively) and with Ge^+ ions for preamorphization. Ion fluences above 5×10^{14} cm^{-2} could result in void and porous layer formation which cannot be removed via annealing.

Among the increasing use in microelectronic technology, Ge with high doping by ion implantation recently becomes interesting in research and development of new Ge-based superconducting and spintronic devices [160, 161].

4.2.3 Ion Implantation into Compound Semiconductors

In comparison with group IV semiconductors (Si, Ge) ion implantation into *III–V semiconductors* exhibits some peculiarities which are connected with the physical properties of these compound materials. Nevertheless, ion implantation is extensively used to fabricate n-, p-doped layers in III–V compounds because no reliable diffusion technology exists due to the low evaporation temperature (already above 500 °C) of the group V species (As, P). Furthermore, the annealing for damage removal and dopant activation is more complicated compared to Si and Ge (different temperature regions for recrystallization, annealing of defects, and electrical activation of implanted dopants [162–164]). It has been shown that it is much more

difficult to obtain high degree of dopant activation in GaAs compared with Si, that the achieved activation levels and mobility values of the carriers in some cases are lower than the theoretically expected ones. Usually, the highest activation is obtained if amorphization of the crystalline material is prevented and the best electrical device performances are obtained using rapid thermal annealing (RTA) in combination with suitable capping layers. RTA is chosen in the temperature range 500–900 °C for some seconds. As mentioned, the surface of III–V wafers has to be protected from thermal decomposition during annealing which is achieved by dielectric layer deposition (e.g., of SiO_2, S_3N_4, or Al_2O_3, etc.) and/or by same wafer material proximity or the maintenance of group V over pressure in the annealing ambient [165–167].

Ion implantation processes in III–V compound semiconductor technology were developed for shallow n-type, shallow p-type doping, and for material compensation by deep level impurities in most commonly used GaAs, $Al_xGa_{1-x}As$, InP, $In_{0.53}Ga_{0.47}As$, $In_{0.48}Al_{0.52}As$, and InSb [168]. The most preferred implanted ion is Si^+ to obtain n-type doping because of its easy activation at relatively low temperatures and its low diffusivity (e.g., $D_{Si} \approx 10^{-14}$ cm^2 s^{-1} in GaAs). Other possible ions for n-type doping are S^+, Se^+, Te^+, Sn^+, and Ge^+, but they do not meet demands on low diffusivity and thermal stability (S), low crystal damage (Se, Te, and Sn), and high activation (Ge) [169]. For Si^+ ion implantation, for example, into the source and drain regions of GaAS-MOSFETS fluences of ~(1–5) $\times$ 10^{14} cm^{-2} at ion energies $\leq$200 keV are used. Implanted silicon is usually activated by rapid thermal annealing at 850–1,000 °C (800–875 °C) and l–10 s for GaAs (InP, InGaAs), respectively. At relatively poor activation of Si the maximum electron concentration one can achieve in GaAs is limited to (2–3) $\times$ 10^{18} cm^{-3}, whereas in the case of InP an activation of 80–100 % has been obtained and the electron peak concentration reaches ~10^{19} cm^{-3} [170]. At increased high Si^+ fluences, to avoid amorphization and to obtain higher Si activation, the implantation can be performed at elevated target temperatures of ~200 °C. But also in this case the maximum electron concentration is limited to $\approx 10^{19}$ cm^{-3}. Another attempt to obtain high electron concentrations is the co-implantation of Si^+ and S^+ ions. Both Si and S are donor impurities in III–V compounds occupying group III and V lattice positions, respectively. Using Si^+ and S^+ co-implantation, a maximum electron concentration of 3 $\times$ 10^{18} cm^{-3} in GaAs and 2 $\times$ 10^{19} cm^{-3} in InP have been obtained. A high Si activation giving an electron concentration of $\approx$ 10^{19} cm^{-3} was observed in $In_{0.43}Ga_{0.57}As$ too [166].

For p-type doping of III–V semiconductors, the most preferred implanted ion is Be^+ with low ion mass (low crystal damage), but also other ions, such as Zn^+, Mg^+, and Cd^+, are often used. The p-doping by these ions is more problematic compared to n-doping due to their relatively high diffusivity during annealing [165, 167, 171].

In contrast to n-dopants (Si^+, S^+, Se^+, Te^+, Sn^+ ions), for p-type dopants (Be^+, Mg^+, Cd^+, Zn^+ ions) implanted into GaAs, an activation close to 100 % can be obtained for peak concentrations up to $\approx$2 $\times$ 10^{19} cm^{-3} [172]. It is interesting to note that, in Ga-based III–V compounds the maximum achievable electron concentration by donor implantation doping is limited to values of $<$4 $\times$ 10^{18} cm^{-3},

whereas hole concentrations $>10^{19}$ cm^{-3} can be easily achieved by acceptor doping. In indium-based III–V compounds there is the opposite situation. Implantation of nearly all ion species of group II, IV, VI, and inert gases into GaAs and other III–V compound semiconductors have been reported in the literature.

High energy (MeV) ion implantation is extensively used in III–V compound semiconductor technology (GaAs, InP) to obtain buried doped layers (Si^+ implantation), deep material compensation (high resistivity layers), and selective area device isolation implants (O^+ implantation) [170, 173, 174]. MeV O^+ ion implantation is used in order to isolate thick multilayer device structures, for example in heterojunction bipolar transistors and a variety of semiconductor lasers. As reported in [173] the formation of high resistivity layers in highly doped n- and p-type epitaxial GaAs (and InP) layers has been achieved in the fluence range of 5×10^{13}–5×10^{15} cm^{-2} by 25–50 MeV O^+ ion implantation with projected ranges of these ions of 14.0 and 28.8 μm in GaAs, respectively. The sheet resistance of thin (0.5 μm) epitaxial surface device layers exposed to such ions increases roughly by two orders of magnitude with fluence in the range 10^{13}–10^{15} cm^{-2} but, depending on the initial doping concentration, may decrease slightly again at higher O^+ fluences. For the fabrication of buried, highly doped, layers in GaAs, an InP high energy (30–70 MeV) Si^+ ion implantation at ion fluences of 5×10^{14} cm^{-2} has been also investigated [173]. From sheet resistance measurements it was concluded that the electrical activation of implanted Si in GaAs and InP slightly increases by ~50 % with increasing ion energy from $\leq$200 keV to high energies of 10–100 MeV for conventional Si^+ implantation and high energy implantation, respectively. Possible applications for high energy ion implantation are the fabrication of thick (>4 μm) multilayer photonic devices such as quantum infrared detectors and III–V semiconductor lasers which contain several different III–V materials and in which low energy ions are insufficient to penetrate the active layer structure.

Among oxygen ion implantation, the compensation of III–V compound semiconductors (radiation damage, local introduction of compensating deep or mid-gap levels) has been achieved also by implantation of other chemically inactive ion species such as H^+, He^+, Ne^+, N^+, etc. [168] or by implanting chemically active substitutional impurities like transition metal ions (Fe^+, Co^+, Ti^+, etc.). To create deep compensation levels, implanted transition metal ions have to be driven into the substitutional sites by annealing the material at (750–900) °C, whereas at light gas ion bombardment the implantation damage itself provides these levels. Compensation by light ion bombardment has a poor thermal stability at temperatures above 500 °C, whereas substitutional compensation by transition metal ion implantation is thermally stable enabling further processing of the material at high temperatures.

With improving crystal quality of the *group III-nitride materials (GaN, AlN, InN)* ion implantation becomes an emerging doping technique in exploring new dopant species and device structures. The reasons for recent intense research are possibilities in fabrication of high brightness light emitting diodes as well as in fabrication of electronic devices that operate at high power or high temperature [175]. Already heterostructure field effect transistors, junction field effect transistors, and heterojunction bipolar transistors have been demonstrated. For

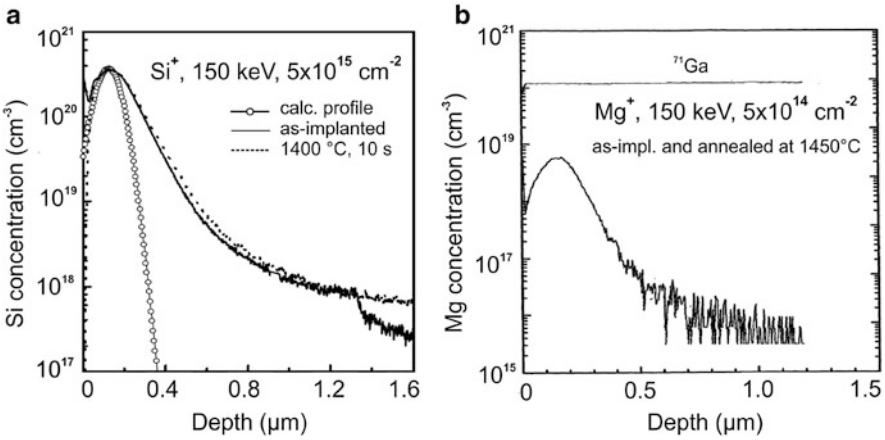

Fig. 4.32 Depth profiles of Si^+- (**a**) and Mg^+-(**b**) implanted GaN before and after annealing at 1,400 and 1450 °C, respectively (the profiles practically coincide) [177, 178]

III-nitride ion implantation is used for improvement of device luminescence, material doping, and local compensation in these materials [176]. Common dopant ions for S/D formation in III-nitride FETs are Si^+, S^+, Te^+, Be^+, Mg^+, C^+, Ca^+, and Zn^+, where for n-type doping mostly Si^+ but also S^+, Te^+ ions (energy 100–600 keV, fluence 5×10^{14}–5×10^{14} cm^{-2}) and for p-type doping Be^+, Mg^+, C^+, and Ca^+ ions (50–150 keV, (3–5) $\times 10^{14}$ cm^{-2}) often with co-implantation of P^+ ions have been used. Channel implantation in III-nitride FETs is carried out at lower fluences in the range of 10^{13}–10^{14} cm^{-2}. For the annealing of crystal damage in GaN and activation of implanted impurities usually higher temperatures of $\geq$1,000 °C are necessary. Both conventional furnace annealing and rapid thermal annealing (RTA) have been tried, using annealing temperatures up to 1,200–1,500 °C. At such high temperatures, annealing of GaN is complicated due to material decomposition (loss of nitrogen from the GaN surface), which becomes pronounced for prolonged annealing times already at temperatures of above 800 °C. Therefore, GaN surfaces have to be protected during annealing by appropriate capping layers (e.g., AlN) or the annealing must be carried out under high pressure N_2 ambient. For example, it was shown that for Si^+-implanted and AlN-capped GaN a high activation with almost 100 % of Si on Ga sites can be achieved at 1,100 °C, 15 s RTA annealing.

Most of the common acceptor and donor ions implanted into GaN show a very low diffusivity at high temperatures [177], as shown, for example, for Si as a n-type dopant in Fig. 4.32a and for Mg as a p-type dopant in Fig. 4.32b.

This behavior is important for the fabrication of GaN-based power devices such as thyristors and insulated gate bipolar transistors that will require creation of doped well or source/drain regions by implantation. The low diffusivities of implanted dopants in GaN allow a quite precise control of the junction and there will be fewer problems with lateral diffusion of the source/drain regions towards the gate. A comprehensive overview of ion implantation into GaN and related phenomena is given in [179].

O^+ ion implantation into GaN has been investigated with respect to selective area isolation between device structures. For this purpose multienergy O^+ ion implantation with different fluences has been applied, e.g., 50 keV, 1×10^{14} cm^{-2}; 100 keV, 2×10^{14} cm^{-2}; 200 keV, 3×10^{14} cm^{-2}, resulting in a total fluence of 6×10^{14} cm^{-2}. At these implantation conditions the sheet resistance of the as-grown GaN was increased approximately by six orders of magnitude up to 10^9–10^{10} Ω sq^{-1} [180]. Selective area isolation in GaN can be achieved also by implantation of n- and p-type GaN with Ti^+, Fe^+, or Cr^+ ions forming deep defect levels and insulating layers with maximum sheet resistances of ~10^{12} Ω sq^{-1} in n-type and ~10^{10} Ω sq^{-1} in p-type GaN.

The *wide bandgap compound semiconductor SiC* is the favored material for high-temperature, high-power, and high-frequency device applications [181]. In the last years, intensive research has been performed on n-type doping of SiC by N^+, P^+, S^+, and Sb^+ and on p-type doping of SiC by Al^+, B^+, and Ga^+ ion implantation which is reviewed, for example, in [182]. Whereas N^+ implantation has been mostly applied in order to produce low resistivity, n-type SiC regions, the development of efficient processes for p-type doping is still a challenging task. High fluence Al^+ implantation seems to be the most promising procedure to fabricate low resistivity, p-type regions in SiC and, therefore, many studies have been performed in this field in order to find out the optimum conditions for the implantation and the subsequent damage annealing. Compared to silicon processes, ion implantation into SiC requires much higher temperatures at subsequent annealing (~1,200–1,800 °C) to achieve acceptable electrical activation of donor or acceptor ions. Annealing of implanted SiC needs to be performed in high-purity inert gas ambient such as argon. High-temperature annealing in nitrogen ambient produces thin nitride layers on the surface of SiC. One of the issues related to ion implantation is to achieve doping levels of ~10^{19} cm^{-3} in order to get ohmic contacts with specific contact resistance below 10^{-5} Ω cm [183]. Another issue is the need of high energy (MeV) ion implantation to form deep p^+n-junctions. Since introduction of dopants by thermal diffusion is not possible in SiC, MeV ion implantation of acceptor ions (Al^+, B^+, Ga^+) is necessary to create p-wells for CMOS field-effect transistors and other devices that require deep p-type regions [184]. Most of these ion beam processes are based on carrying out implantation at elevated temperatures (~500–800 °C) using patterned high-temperature masking materials (e.g., SiO_2, Si_3N_4). The target temperature during implantation promotes some self-annealing during the implantation, so that damage and segregation of displaced Si and C atoms do not become excessive, especially at high fluence implantation employed for ohmic contact formation. Protecting the SiC wafer surface during implantation annealing is very important. Annealing performed without SiC surface protection results in surface roughening due to the sublimation and re-deposition of Si species such as Si, Si_2C, SiC_2, etc. on the crystal surfaces. The Si sublimation results in SiC surface material and implanted impurity loss during annealing [185]. For high-temperature annealing above 1,400 °C, capping layers of SiO_2 and Si_3N_4 are not applicable due to their volatility at these high temperatures required for annealing implanted SiC. AlN encapsulation has proved useful in protecting the SiC sample surface

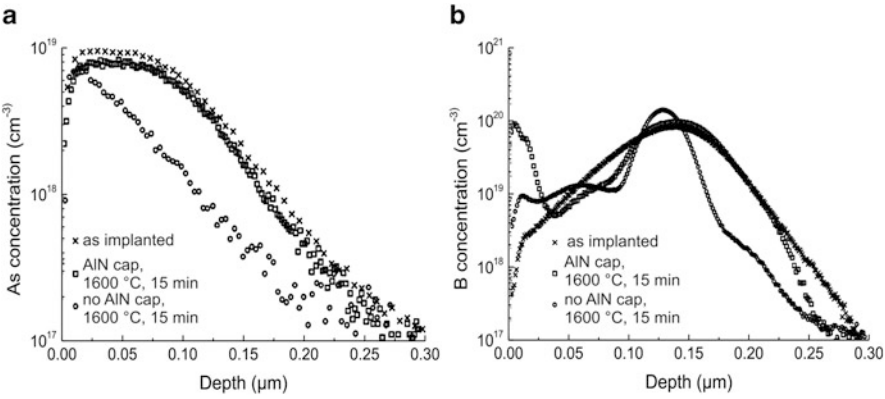

Fig. 4.33 SIMS depth profiles for (**a**) As^+-, and (**b**) B^+-implanted SiC before and after annealing with and without AlN encapsulant [186]

during postimplantation annealing up to 1,650 °C for 10 min [186]. The importance of this capping layer at high-temperature annealing of SiC is demonstrated in Fig. 4.33 where, for example, the depth profiles of As^+- and B^+-implanted SiC after annealing with and without an AlN capping layer are shown.

The As profiles in Fig. 4.33a were achieved after a multiple As^+ implantation (20, 40, 80, 140, and 220 keV) with a total ion fluence of 1.2×10^{14} cm^{-2} at 800 °C target temperature. For the B-profiles in Fig. 4.33b, the implantation conditions were 50 keV, 8.8×10^{14} cm^{-2} at an implantation temperature of 700 °C.

It was demonstrated that N, P, and Al dopants are thermally stable in SiC during postimplant annealing, with or without encapsulation. In the case of shallow As^+ and Sb^+ implantations, when the annealing was performed at 1,600–1,650 °C without capping layer, more than 50 % of the implanted ions are lost due to sublimation related surface damage, but these implantation profiles remained thermally stable when annealed with an AlN capping layer. The AlN capping layer could not prevent the out-diffusion of B near the SiC surface over a depth of ~(50–100) nm (see Fig. 4.33b) and the redistribution of the B profile. It is assumed that the redistribution is associated with the implantation-induced defects and not with the defects created at the surface during annealing. Nevertheless, in the case of a multiple energy B^+ implantation over a depth of 0.7 μm the uniform B concentration profile remained stable everywhere except at the surface [184].

Among conventional furnace and RTA annealing, FLA was used for crystal recovery and activation of high fluence Al-implanted SiC wafers [187]. In comparison with furnace and RTA, the free hole concentration can be remarkably increased to higher acceptor atom concentrations ($N_A \geq 10^{20}$ cm^{-3}). Aluminum was implanted into n-type SiC epitaxial layers at 400 °C with four different energies and fluences in order to obtain a box-shaped (500 nm thick) profile with plateau concentrations of Al up to 1.5×10^{21} cm^{-3}. The samples were annealed in Ar

ambient by FLA at maximum sample temperatures during the flash (duration 20 ms) of about 2,000 °C. As demonstrated, FLA is a promising annealing technique for the formation of very high doped p^+(Al)-layers in SiC-based electronic devices because of the higher hole concentrations and lower resistivity as well as the weak temperature dependence of the electrical material parameters for Al concentrations $\geq 5 \times 10^{20}$ cm^{-3}.

4.3 Ion Beam Synthesis of New Phases in Solids

Except the application of ion implantation in microelectronic device and integrated circuit technologies ion beams became a valuable and innovative tool for processing, for example, of advanced materials with novel electrical, optical, and magnetic properties. At conventional low and medium fluence ($<10^{16}$ ions/cm^2) ion implantation in microelectronics, the concentration of introduced dopants is usually below their solubility limit in semiconductor materials. At certain annealing temperatures the impurity atoms are solved in Si and located on crystal lattice sites or, as a small part, remain as soluted interstitial atoms. If the concentration of impurity atoms introduced by high fluence implantation ($\geq 10^{16}$ cm^{-2}) exceeds the solubility limit, ion implantation leads to a far-from-equilibrium state (supersaturated solid) which relaxes towards thermodynamic equilibrium during subsequent annealing by phase separation through precipitation and ripening (Ostwald ripening) of nanoclusters (NC) [188].

Phenomenologically, ion beam synthesis (IBS) can be divided into several stages, schematically shown in Fig. 4.34:

Accumulation and supersaturation. After ions have been slowed down by electronic and nuclear stopping, they are incorporated into the target material. Thermal activation at common implantation temperatures is usually too low to allow impurity diffusion over larger length. The impurity distribution remains frozen in, especially at low impurity concentrations.

Nucleation or early phase separation. Upon annealing, thermal fluctuations could initiate phase separation through the (homogeneous) nucleation of precipitates. The necessary energy barrier can either be reduced by heterogeneities (defects) in the substrate giving rise to inhomogeneous nucleation or by considerably higher supersaturations.

Growth. Second phase precipitates formed by nucleation grow as long as the local monomer concentration is above the equilibrium concentration of these precipitates. All precipitates grow on the expense of the reservoir of dissolved impurity atoms.

Coarsening and Ostwald ripening. The monomer concentration decreases during further annealing and a competitive coarsening process called Ostwald ripening takes place. Large NCs grow on the expense of smaller one, which finally dissolve.

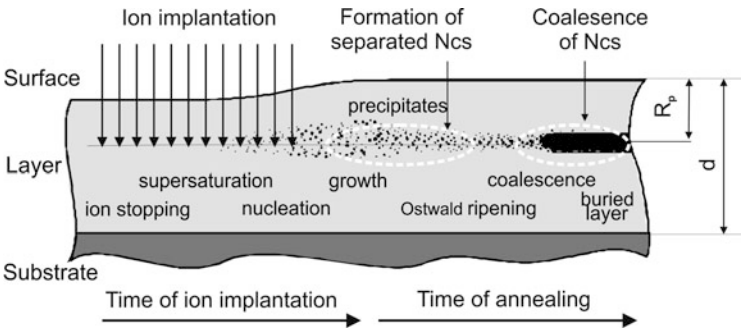

Fig. 4.34 Scheme of major stages at ion beam synthesis (IBS) of new phases. NCs nucleate and grow during ion implantation or, for impurity atoms immobile during implantation, during subsequent thermal treatment. The mean NC size as well as their spatial and size distribution changes during Ostwald ripening. At very high fluences, buried compound layers can form by coalescence of NCs

Coalescence and percolation. During NC growth, neighboring NCs might touch each other and coalesce to a larger one. This process is more likely for very high ion-fluence implantations aimed at the formation of buried continuous layers.

According to the classical nucleation theory (CNT) the initial supersaturation of impurity atoms dispensed in a matrix is metastable and thermal fluctuations may lead to the precipitation of second-phase nanocrystals. In general, the nucleation rate I can be written as $I = A{\cdot}\exp(-W/kT)$, where W is the thermodynamic nucleation barrier and A a dynamical factor increasing with impurity concentration. This case is referred to as homogeneous nucleation. In contrast, the so-called inhomogeneous nucleation is triggered by system inhomogeneities, such as defects, grain boundaries, interfaces, or impurities. The inhomogeneous reaction rate $I_i = A_i{\cdot}\exp(-W_i/kT)$ can be much higher than the homogeneous one, since mostly, due to an effectively lower interface energy contribution to the nucleation barrier, $W > W_i$. According to classical nucleation theory, the energy barrier for homogeneous nucleation decreases with increasing supersaturation and the nucleation rate increases with the concentration of dissolved impurity atoms and (exponentially) with temperature. The single second-phase precipitates nucleated from an initial supersaturation interact with the initial phase by monomer exchange. Thereby, the equilibrium concentration of monomers near the phase boundaries is reached if the attachment and detachment rates are equal, which is also a function of the local curvature of the phase boundary. For spherical precipitates, this relation is given for the diffusion controlled case by the Gibbs–Thomson (GT) relation formula [189]:

$$c^{\mathrm{GT}}(R) = c_\infty \cdot e^{\left(\frac{R_c}{R}\right)}, \quad R_c = \frac{2 \cdot \sigma \cdot V_a}{k \cdot T}, \tag{4.8}$$

where c_∞ denotes the impurity equilibrium concentration at a flat phase boundary (i.e., the solidus concentration), and R_c the capillary length given by the material

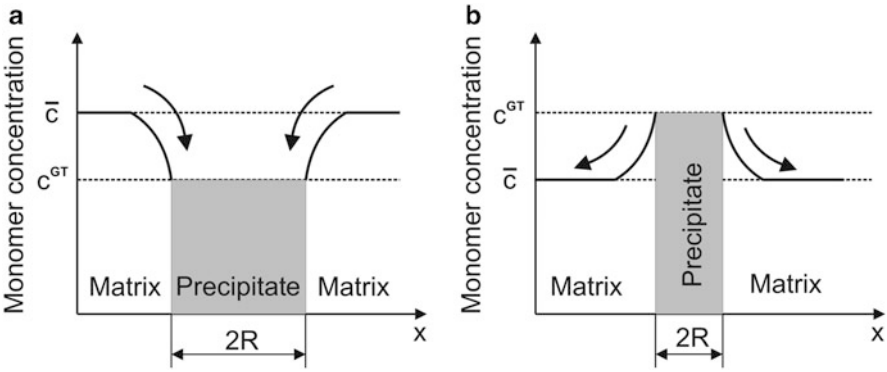

Fig. 4.35 Concentration profile of dissolved monomers near a precipitate. Depending on the average monomer concentration the cluster grows at $\bar{c}>c^{GT}$ (**a**) or shrinks at $\bar{c}<c^{GT}$ (**b**)

parameters surface tension σ and atomic volume V_a. The precipitate will grow if the average surrounding concentration $\bar{c}$ is higher than c^{GT}, the cluster acts as a sink for the diffusing monomers leading to cluster growth. On the opposite, for a lower average concentration $\bar{c}$ of surrounding monomers compared to c^{GT} the cluster emits monomers and therefore acts as a source and will shrink, as shown in Fig. 4.35.

In an early growth stage after nucleation all clusters will feeded from the reservoir of dissolved monomers. At that stage the average monomer concentration is still large compared to the equilibrium concentration c^{GT} of the individual clusters. The clusters do not interact directly with each other and the total volume of the precipitated second phase increases in time at a constant rate. However, when supersaturation becomes insufficient to dominate the system evolution, the system tends to diminish its free energy via a decrease of the total interfacial area. This minimization occurs by diffusional mass transfer from smaller (dissolving) to larger (growing) precipitates, which results in an increasing average precipitate size but decreasing total surface area. This stage of phase transition is also known as Ostwald ripening [190] or coarsening. If the density of NC is high, it is possible that NC touch, and then rapidly minimize their energy by surface diffusion of adatoms, such that a larger spherical cluster emerges (coalescence). The theory of Ostwald ripening, developed by Lifshitz and Slyozov [191] and by Wagner [192], is known as LSW theory. A more recent theory including the case of ripening during ion-implantation can be found in [193–195]. The LSW theory predicts the time evolution of the particle size distribution $f(R, t)$ and yields in the asymptotic limit $t \to \infty$ the following temporal power laws:

$$\overline{R}(t) = k_R^D \cdot t^{1/3} \quad N(t) = k_R^D \cdot t^{-1} \quad \text{(coarsening regime)} \tag{4.9}$$

for the time evolution of the average particle radius $\overline{R}(t)$ and the particle density $N(t)$. If the evolution is instead interface controlled, the growth law reads as

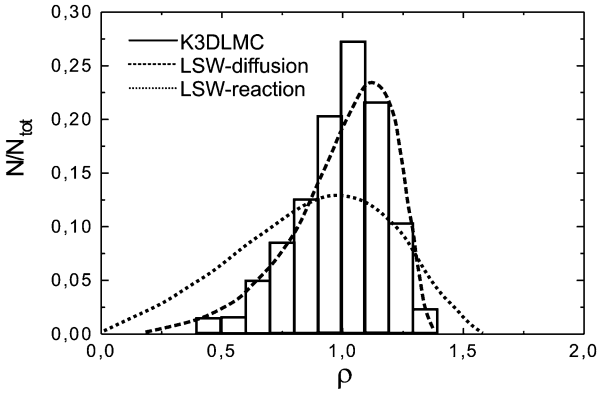

Fig. 4.36 Histogram of the nanoparticle radius distribution with $\rho = R/\overline{R}$ obtained by kinetic Monte Carlo simulation of second-phase precipitation. Both stationary distributions of the LSW theory are included [195]

$$\overline{R}(t) = k_{\mathrm{R}}^{\mathrm{D}} \cdot t^{1/2} \quad N(t) = k_{\mathrm{R}}^{\mathrm{D}} \cdot t^{-3/2} \quad \text{(diffusion limited growth regime)}. \quad (4.10)$$

The corresponding rate constants $k_{\mathrm{R}}^{\mathrm{D}}$ can be found in [191, 192] and have been reexamined for the more realistic case of nonzero solubilities and nonideal solution [196, 197]. The LSW theory further predicts that the particle size distribution $f(R, t)$ is time invariant (for $t \to \infty$) under the scaling of the average particle size $\overline{R}$.

For the modeling of ion beam synthesis, atomistic approaches such as the kinetic 3D lattice Monte Carlo (K3DMC) method were developed by Heinig et al. (see [195] and references therein) which allow to study the evolution of a given distribution of impurity atoms in a neutral matrix also for a time-dependent concentration of impurity atoms. An example of Monte Carlo simulations for studying the NC formation and determining the nanoparticle size distribution is shown in Fig. 4.36.

As can be seen in Fig. 4.36 the nanoparticle size distribution is in reasonable accordance with the stationary form (LSW) of the particle radius distribution of diffusion-limited Ostwald ripening (OR), but it is on the average somewhat smaller and seems to be more symmetric.

In the above description effects of interfaces, surfaces, spacial gradients of supersaturation, and the finite size of the supersaturation region were neglected although they have a significant influence on the evolution of spatial and size distribution of nanoparticles. So, the effect of sharp gradients in the initial concentration of impurity atoms has been discussed by Reiss et al. [193] for ion beam synthesis of buried SiO_2 structures (see Sect. 4.3.1).

The division of IBS in all these stages is to some degree artificial. The borders between the individual steps are rather ill-defined and depend on the specific implantation and annealing parameters. Tailoring of the size and size distribution of NCs could be achieved by a control of implantation parameters (ion energy, flux

and fluence, sample temperature) and annealing parameters (temperature, time, ambient conditions, etc.). Phase separation of ion-implanted, immiscible impurity atoms from the surrounding matrix, i.e., the formation of NCs, can also occur during the implantation process if the impurity atoms are sufficiently mobile due to collisional ion mixing; otherwise a subsequent annealing is always necessary.

Phase separated precipitates or NCs can lead to significant modification of the electrical, mechanical, magnetic, and optical properties of the host material. Formation of nanoclusters by ion beam synthesis (IBS) has been documented for a large variety of ion species and host materials. The examples include metal NPs [198] and semiconductor NCs in inert hosts [199], compound NCs formed as a result of chemical reaction between the implanted and substrate atoms, e.g., silicide formation for metal implantation into Si [200], metal alloys [201], and compound semiconductors formed by co-implantation or sequential implantation of various atom types, e.g., II–VI, III–V, or IV–IV semiconductor NCs in SiO_2 [202], Al_2O_3 [203], or Si [204]. In the following chapters, selected examples of ion beam synthesis with technological relevance, namely IBS of insulating and silicide layers buried in silicon as well as ion beam synthesis of semiconducting nanocrystals in insulators will be described.

4.3.1 Buried Insulating Layers in Silicon

An example for high fluence ion implantation into silicon where the concentration of implanted ions exceed the solid solubility limit is the O^+ ion implantation leading to highly oxygen supersaturated silicon. During subsequent high-temperature annealing, this state relaxes to thermodynamic equilibrium through phase separation into SiO_2 and Si, SiO_2 precipitation, Ostwald ripening of SiO_2 precipitates, and their coalescence to a continuous buried SiO_2 layer. This technique of ion beam synthesis was called *S*eparation by *IM*planted *OX*ygen (SIMOX) [205, 206] and is today well established in microelectronic device fabrication to produce thin silicon layers of high crystalline quality with an abrupt interface to a stoichiometric buried SiO_2 layer [207]. Similar IBS techniques were developed with high fluence nitrogen implantation (*S*eparation by *IM*planted *NI*trogen—SIMNI) [208, 209] and separation by high fluence implantation of both oxygen and nitrogen (SIMON) [210].

In the frame of the SIMOX technology, the buried oxide (BOX) is synthesized by internal oxidation following the deep implantation of O^+ ions at high fluences of 1.8×10^{18} cm^{-2} into the crystalline Si substrate at elevated temperatures (~500 °C) (Fig. 4.37). Annealing at high temperature (~1,300 °C, for some hours) is necessary to recover a suitable crystalline quality of the top Si film. High current implanters (100 mA, 180–200 keV) have been developed to produce 200 mm wafers with good thickness uniformity, low defect density (except threading dislocations with an areal density of 10^4–10^6 cm^{-2}), sharp Si–SiO_2 interfaces, and high charge carrier mobility in the top Si device layer.

As shown in Fig. 4.37, during high fluence O^+ implantation a Gaussian-like distribution in the depth of the substrate is created which in the annealing stage

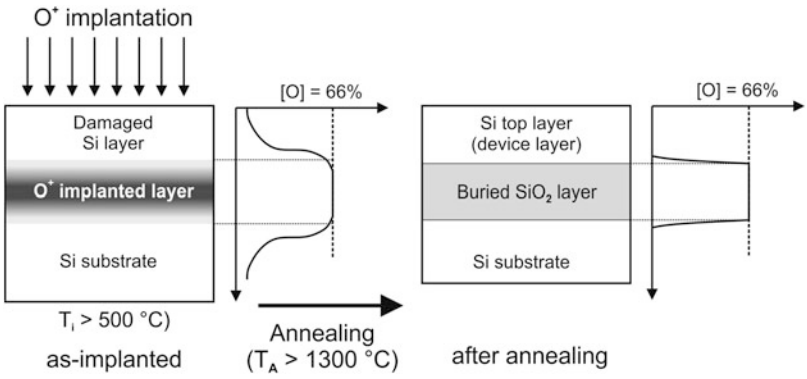

Fig. 4.37 SIMOX process for BOX formation at 0.4–1.8 × 10^{18} cm^{-2}, 100–200 keV, 1,320–1,350 °C, 6 h in Ar/O_2

redistributes into a rectangular shape and forms the desired buried layer. During ion implantation and the subsequent annealing, different steps of evolution merging into one another are run through. At the beginning an oxygen supersaturation in the Si substrate is created, followed by the nucleation of SiO_2 compound precipitates. Immediately after nucleation, the SiO_2 precipitates grow at the expense of the oxygen supersaturation. Later on, while annealing is in progress, the mean radius of SiO_2 precipitates increases due to Ostwald ripening which diminishes the interface energy. Finally, the SiO_2 precipitates become so large that they may overlap and coalesce towards a closed buried SiO_2 layer, thereby further diminishing the interface energy. Especially, the Ostwald ripening is recognized as the principal mechanism for the redistribution of the implanted profile [193]. The modeling approach for Ostwald ripening [188] for BOX layers gives consistent results using the experimentally confirmed initial condition of a band of homogeneously distributed precipitates.

The evolution of the oxygen depth profiles during high fluence oxygen implantation into silicon has been modeled by Maydell-Ondrusz and Wilson [211] and by Jäger [212–214]. The model takes into account the change of the ion range profile with changing target composition, the swelling of the target by the collected oxygen, and the surface sputtering. If the implanted oxygen exceeds the SiO_2 stoichiometry, initially at the profile maximum, the excess oxygen is assumed to diffuse readily to substoichiometric regions, i.e., towards surface and bulk, thereby oxidizing silicon in the interface region to SiO_2. In this way, the shape of the oxygen depth profile changes with the increasing fluence from Gaussian-like to flat topped profile as shown in Fig. 4.38.

The model describes the modification of the profiles by in situ "internal oxidation" during the implantation process. The microstructure of the top Si and buried SiO_2 layers as well as the redistribution of oxygen affected by postimplantation or in situ annealings are not taken into account. Nevertheless, the calculations reproduce fairly well the thickness and the depth position of the buried oxide layer, but

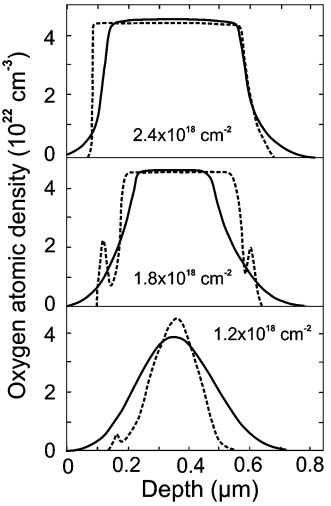

Fig. 4.38 Depth profiles of the oxygen concentration in samples implanted with 150 keV O^+ ions to various fluences. The theoretical results (*solid lines*) are given together with AES depth profiles (*dashed lines*). The experimental profiles have been measured in annealed samples and these data have been normalized by assuming a stoichiometric oxygen concentration for the plateaus [213]

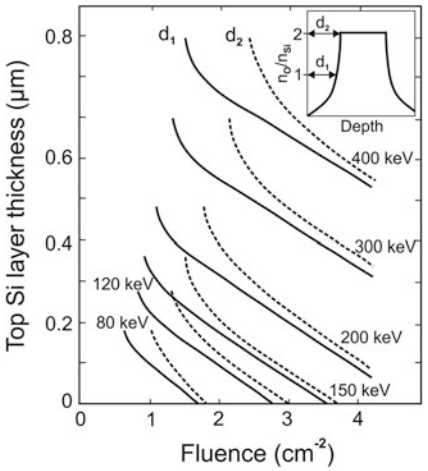

Fig. 4.39 Surface silicon device layer thicknesses versus implanted oxygen fluence for various implant energies [213]

allow only rough estimates of the width of the interphase region between the SiO_2 layer and the single-crystal surface layer in the SOI substrates. The results shown in Fig. 4.39 are considered to be of practical relevance. The thickness of the top silicon device layer is shown in dependence on the implanted O^+ fluence and for various ion energies, and is in good agreement with available experimental data. The two

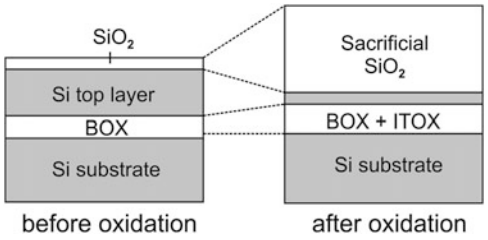

Fig. 4.40 Schematic representation of the ITOX process (low fluence SIMOX)

distances d_1 and d_2 given there indicate the width of the transition region to the BOX layer. If with increasing implanted fluence the oxygen depth profile becomes more and more rectangular, the two curves in Fig. 4.39 approach each other and have the same slope. The thickness of the BOX layer is not shown since it depends essentially only on fluence, but not on ion energy.

For considering the O^+ ion fluence required to reach an oxygen-to-silicon ratio of 2.0 in the sample (so-called the stoichiometric fluence) it was concluded that the stoichiometric fluence increases with increasing ion energy. At IBS of BOX layers as substrates for SOI wafers, the material should receive fluences which exceed the theoretical value given in [213]. Otherwise, no homogeneous SiO_2 layer (usually 200–400 nm thick) but a mixture of amorphous SiO_2 precipitates and Si nanocrystals may be obtained. For ion energies $E \geq 150$ keV the formation of the oxide layer starts at a depth coinciding with the projected range R_p of the O^+ ions in silicon. At these ion energies the effects of sputtering and changing ion range compensate that of target widening (swelling).

To improve the quality of the BOX layers in SIMOX wafers, high-temperature annealing in oxygen containing atmosphere for internal thermal oxidation (ITOX) has been applied. At these annealing conditions the ion fluence can be significantly reduced from 1.8×10^{18} cm^{-2} (for Si^+, 200 keV) to 4×10^{17} cm^{-2} (low fluence SIMOX) [215–217]. The ITOX process improves the stoichiometry of the BOX and slightly increases the overall thickness of the buried oxide, which is shown in Fig. 4.40.

The lower oxygen fluences are needed for large SIMOX wafers with ultrathin silicon device layers and BOX layers for ultra-large-scale integrated (ULSI) CMOS circuits and implies a considerable gain in IBS processing time and wafer cost. The material properties for standard SIMOX and low fluence SIMOX wafers together with the corresponding process parameters of ion beam synthesis are summarized in Table 4.3.

The flexibility of ion beam processing allows also the fabrication of double SIMOX structures with a Si device top layer and a Si layer sandwiched between the two buried oxides which, for example, can serve for interconnects, wave guiding, additional gates, or electric shielding. Furthermore, if the O^+ ion implantation is carried out through a patterned masking layer (e.g., patterned SiO_2), laterally isolated single-transistor islands and interrupted BOX layers as SOI regions

Table 4.3 SIMOX wafer material properties and process parameters

Wafer parameter	Standard SIMOX	LF-SIMOX (ITOX)
Wafer diameter	≤200 mm	≤300 mm
Si device layer thickness	210 nm	20–145 nm
Si device layer thickness uniformity	±0 nm	±2 nm
BOX layer thickness	375 nm	135, 145 nm
BOX layer thickness uniformity	±10 nm	±5 nm
Surface roughness	0.7 nm	<0.15 nm
Dislocation density	$<10^3$ cm^{-2}	$<10^3$ cm^{-2}
BOX pipe (pinhole) areal density	<0.1 cm^{-2}	<0.1 cm^{-2}
BOX dielectric electric field breakdown	$>5 \times 10^6$ V cm^{-2}	$>7 \times 10^6$ V cm^{-2}
IBS process parameters	Standard SIMOX	LF-SIMOX (ITOX)
O^+ ion energy	150–200 keV	≤100 keV
O^+ ion fluence	1.8×10^{18} cm^{-2}	4×10^{17} cm^{-2}
Implantation temperature	~500 °C	~500 °C
Annealing process	1,320–1,350 °C (Ar)	1,320–1,350 °C (Ar/O_2)

integrated into a bulk Si wafer can be fabricated [218]. The advantages of ion beam synthesis of buried SiO_2 layers compared to other SIO techniques are that SIMOX is compatible with silicon device processes (ion implantation and thermal annealing). On the other hand, as a disadvantage high fluence implantation up to ~2×10^{18} cm^{-2} and high-temperature annealing up to ~1,350 °C require special implantation and annealing equipment demanding attention to impurity contamination during both processes. Compared to crystalline Si bulk material remaining crystal defects (e.g., threading dislocations) and SiO_2 precipitates in the top Si layer as well as pin holes, trapped charges, and Si precipitates in the BOX layer can influence the electrical properties of devices fabricated in SIMOX wafers.

4.3.2 Ion Beam-Synthesized Silicide Layers

Using high fluence ion implantation, this problem can be solved and buried crystalline silicide layers can be fabricated in both (111)- and (100)-oriented substrates with satisfying electrical characteristics. The internal silicide growth process during annealing after high fluence ion implantation is often called "mesotaxy" by analogy with epitaxy which refers to single-crystal growth on surfaces [219, 220].

The formation of metal-silicide layers in silicon by ion beam synthesis is a two-step process, in which a sufficient amount of metal ions such as Co^+, Ni^+, Fe^+, or Cr^+ with high fluence is first implanted into heated Si substrates (300–500 °C) to retain crystallinity during implantation. During the second step, the Si substrates are subsequently annealed at elevated temperatures (600–1,000 °C) until a monocrystalline planar silicide layer epitaxially embedded in monocrystalline silicon is formed. A detailed description of these processes can be found, for example, in [200].

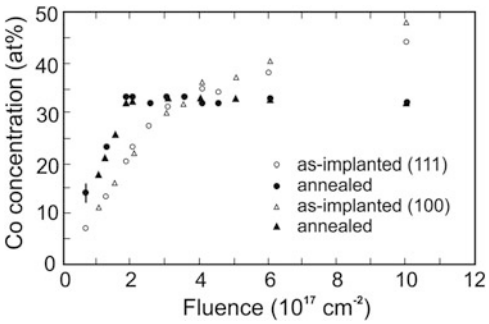

Fig. 4.41 Co peak concentration in as-implanted and annealed (100)- and (111)-oriented Si samples as a function of ion fluence for a Co^+ ion energy of 200 keV [200, 222]

The most thoroughly investigated silicides with metallic behavior formed by ion beam synthesis are $CoSi_2$ and $NiSi_2$ because of their superior material properties and therefore of their possible applications as contacts and electrical interconnects in silicon technology. $CoSi_2$ and $NiSi_2$ with a cubic CaF_2 lattice structure have a lattice constant which is close to that of Si and the lattice mismatches relative to Si amounts to only -1.2 % for $CoSi_2$ and -0.4 % for $NiSi_2$ leading to well-controlled epitaxial growth of crystalline layers in silicon. For ion beam synthesis of $CoSi_2$, Co^+ ions in the energy range of ~(100–250) keV high fluences of (1–5) $\times$ 10^{17} cm^{-2} are implanted into silicon at a substrate temperature of 350 °C. The annealing is carried out in two steps: at 600 °C for 1 h in vacuum (or inert gas atmosphere) to initiate the silicide precipitation and regrowth of the silicon followed by a 1,000 °C, 30 min, annealing step for the coalescence of the cobalt silicide precipitates to a well-defined 110 nm thick $CoSi_2$ layer buried under a crystalline silicon overlayer with a thickness of ~60 nm in the case of a 200 keV Co^+ implantation [221]. Experimentally it was found that for ion beam synthesis of buried $CoSi_2$ layers a Co peak concentration $c_{peak} \sim 18$ at.% is required. Therefore, at an ion energy of 200 keV ion fluences exceeding 10^{17} cm^{-2} are necessary. For the 200 keV Co^+ implantation carried out at 350 °C, Fig. 4.41 shows the dependence of the Co peak concentration on ion fluence in Si for as-implanted and annealed samples [222].

As can be seen, in the as-implanted state the Co peak concentration depends linearly on the ion fluence up to $\Phi \approx 3 \times 10^{17}$ cm^{-2} beyond which the dependence becomes nonlinear. This value nearly coincides with the calculated value of ~2.7×10^{17} cm^{-2} at which the peak concentration achieves the composition of $CoSi_2$ [200]. In the region of linear fluence dependence, the synthesized layers after implantation are Si-rich and consist of isolated $CoSi_2$ precipitates. At a fluence above 3×10^{17} cm^{-2}, where the slope changes, the peak concentration reaches the stoichiometric value for $CoSi_2$ and epitaxial aligned $CoSi_2$ layers are already formed during ion implantation.

For samples annealed at $T \geq 1{,}000$ °C, the dependence of the Co peak concentration on ion fluence in the region of $\Phi < 1.8 \times 10^{17}$ cm^{-2} increases compared to

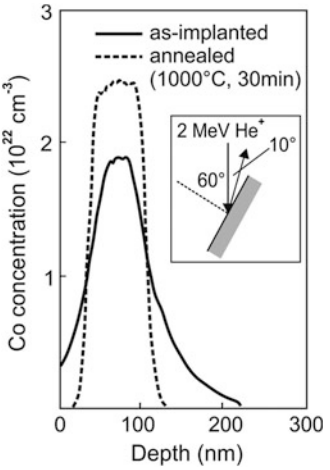

Fig. 4.42 Co concentration profiles obtained from RBS measurements after 170 keV Co^+ implantation of 2×10^{17} cm^{-2} and subsequent annealing at 1,000 °C for 30 min [223]

the as-implanted state. At fluences above 1.8×10^{17} cm^{-2} a distinct discontinuity appears in the slope and the Co concentration becomes constant where $CoSi_2$ layers of stoichiometric composition are formed. As can be concluded from Fig. 4.41 for a critical Co^+ ion fluence of $\Phi_{crit} = 1.8 \times 10^{17}$ cm^{-2}, the Co concentration in the maximum of the implanted profile amounts to $c_{crit} = 19$ at %. The criterion for the peak concentration $c_{peak} > c_{crit}$ where continuous $CoSi_2$ layers can be formed by IBS is only a necessary, but not a sufficient condition for the formation of a uniform planar buried layer, because IBS depends on implantation and annealing conditions. The epitaxial growth of $CoSi_2$ during annealing is shown in Fig. 4.42 where Co depth profiles obtained by RBS measurements for the as-implanted (170 keV, 2×10^{17} cm^{-2}) and the annealed (1,000 °C, 30 min) are compared [223].

The steep increase and decrease of the Co concentration at the boundaries of the buried silicide layer shows that this layer is very uniform and has sharp interfaces to the silicon substrate. During growth of the silicide layer from the initial Gauss-like depth profile, a depletion of Co occurs in the tails of the initial profile due to the dissolution of Co from smaller silicide precipitates, followed by diffusion of Co towards larger $CoSi_2$ precipitates in the region of increasing Co concentration (Ostwald ripening). The ripening leads to a contraction of the initial depth distribution towards the maximum concentration of the profile. With increasing annealing time precipitates grow and finally coalesce to a continuous buried layer. For Co and other silicides, the reaction is nucleation controlled and the moving species are the metal atoms.

As confirmed by structural investigations (TEM) the single-crystalline $CoSi_2$ layers have atomically abrupt interfaces in both (100)- and (111)-oriented Si. The observation of misfit dislocations at the $Si/CoSi_2$ interfaces indicates that the silicide is not pseudomorphic with the Si crystal. The achieved resistivities of

the ion beam-synthesized $CoSi_2$ layers in (100)-Si are about ~1 μΩ cm and lower by a factor of two than those of the best UHV-deposited $CoSi_2$ layers [224]. Because the structural quality of the silicide layers is not as high as for MBE grown layers this unexpected result may be due to the inherent cleanliness of the IBS process. Since the silicide layers form beneath the surface of the silicon substrate prior cleaning procedures of the Si surface are not critical. Moreover, the Co^+ ions are mass selected and do not contain common contaminants (e.g., oxygen, nitrogen, carbon) present in typical evaporation sources.

For the other cubic disilicide $NiSi_2$ similar results have been achieved [225, 226]. In general, ion beam-synthesized films of nickel disilicide have a much higher residual resistivity than those of $CoSi_2$, perhaps because of residual crystal defects, but comparable to or better than MBE grown films. Since $NiSi_2$ melts at 980 °C, the annealing is limited to lower temperatures than for the $CoSi_2$, which may be the reason for some of the structural and electrical differences. The structural and electrical characteristics of ion beam-synthesized $NiSi_2$ films strongly depend on the postannealing temperature and time. The poly-crystalline nickel disilicide already forms during ion implantation with a fluence of 1×10^{17} cm^{-2} at a sample temperature of ~100 °C. A good sheet resistance of $NiSi_2$ film correlated with the Si/Ni ratio has been achieved at ion fluences of ~1×10^{17} cm^{-2} and subsequent annealing at 550 °C for 30 min. The achieved minimum sheet resistance of $NiSi_2$ layers is in the order of 50 μΩ cm and somewhat larger compared to $CoSi_2$. The thickness of a buried silicide layer can be tailored by the choice of the ion energy and the ion fluence. If the implanted ion fluence exceeds the threshold value Φ_{crit} nearly all the implanted atoms will be located in the synthesized layer after high-temperature annealing. The thickness d of the buried layer depends linearly on the ion fluence Φ and is given by $d = \Phi/n$ for $\Phi > \Phi_{crit}$ where n is the atomic density of the metal atoms in the silicide. Layers in the thickness range between 15 and 400 nm have been prepared, using ion energies between 20 keV and 6 MeV.

Ion beam synthesis of other metallic silicides has been also investigated, for example, WSi_2 with regard to the possibility of using them as a gate and interconnect metallization material in semiconductor devices [227]. It was shown that good sheet resistance of tungsten silicide films is achieved and continuous epitaxial layers of WSi_2 with smooth surface morphology can be effectively produced with 40 keV W^+ ions at an ion fluence of 1×10^{17} cm^{-2} with a one-step annealing at 800 °C for 30 min. The ion beam synthesis of semiconducting transition metal silicides ($CrSi_2$ [228], β-$FeSi_2$ [229]) and Ru_2Si_3 [230] has been studied extensively because of their direct or indirect band gap in the order of ~(0.3–0.8) eV and of promising applications in silicon heterostructures (e.g., narrow base hetero-bipolar transistors) and optoelectronic devices in silicon (e.g., efficient light sources in silicon). Ion beam-synthesized rare earth silicides ($ErSi_2$ [231], and $ErSi_{1.7}$, $YSi_{1.7}$, and $Er_{0.5}Y_{0.5}Si_{1.7}$ [232]) are of technical interest with regard to application in infrared light detection and in ohmic contacts.

As minimum feature sizes decrease in integrated circuit technology, ion beam synthesis of silicides without the requirement for a defining mask to delineate the implanted area can be carried out with a focused ion beam (FIB) [233–235].

The FIB implantation of Co^+ ions is an alternative to the critical and costly process of transferring submicrometer patterns where the masking layer must withstand high-fluence implantation. As has been demonstrated the ion beam synthesis of $CoSi_2$ structures by FIB with deep submicron feature sizes can be achieved either by conventional two-step furnace annealing or by short-time flash-lamp annealing (FLA) in the melting regime. At FLA the common physical process of $CoSi_2$ precipitation and coalescence is replaced by the physical process of local melting and recrystallization [236]. During FLA (3 ms pulse, energy density $J = 120$ J cm^{-2}, 700 °C preheating) regions of transiently molten silicon are selectively formed at locations where the implanted patterns provide efficient nucleation centers. The implanted Co dissolves in the molten region immediately. During rapid cooling of the wafer surface, the recrystallization of molten regions lasts only a fraction of a second. During resolidification, the strong segregation of Co at the moving solid–liquid interface results in an increase of the Co concentration in the melt. This process stops when the eutectic concentration is reached which is close to the concentration of Co in the stoichiometric $CoSi_2$. The final width of the $CoSi_2$ NWs is proportional to the amount of implanted cobalt within the transiently molten region, assuming the formation of a stoichiometric silicide in the stripe.

With the FIB a small beam spot (typically <200 nm in diameter) is rastered across the sample to form the implanted silicide. Compared to conventional broad-beam ion implantation with ion current densities of ~10 μA cm^{-2} the current densities of FIB systems are typically ~1 A cm^{-2}. At such high current densities ion fluence rate (ion flux) effects at implantation into Si for ion beam synthesis must be taken into account [234]. It was found that the damage of the Si lattice has a strong influence on the $CoSi_2$ layer formation and that the increased damage accumulation at long dwell times of the FIB prevents the formation of continuous $CoSi_2$ layer. Cobalt disilicide layers have been produced by 70 keV Co^{++} implantation with a spot size of 200–300 nm into silicon heated to a temperature of 400 °C. The beam was scanned meander-like on an area of 40 × 40 μm^2 using subsequent pixels with a distance of 80 nm. The total fluence was about 1×10^{17} cm^{-2}, corresponding to 3×10^1 and 3×10^3 frames at dwell times of 100 and 1 μs, respectively. The samples were furnace annealed by the usual two-step procedure for 60 min at 600 °C and 30 min at 1,000 °C in a nitrogen atmosphere. The annealed samples show that continuous $CoSi_2$ layers can only be formed using sufficiently short pixel dwell times of the FIB spot (see Fig. 4.43).

When the dwell time is increased, the layers exhibit holes and are completely disintegrated at a dwell time exceeding 100 μs. The use of short dwell times results in a lower damage of the target. For example, for the implantation using 1 μs dwell time the silicon surface layer remains crystalline, whereas for a dwell time of 250 μs the surface layer becomes amorphous. Thus, it was concluded that different dwell times (ion fluxes) result in a different degree of damage due to dynamic defect annealing.

Co^+ ion implantation with a FIB was applied in [235] to study ion beam synthesis of $CoSi_2$ nanowires (NW) in silicon (see Figs. 4.44 and 4.45). Two

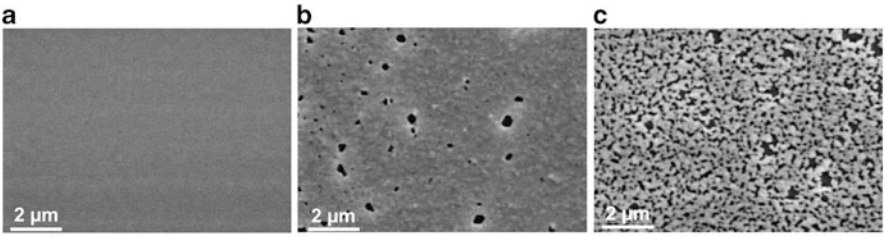

Fig. 4.43 Plane view SEM images of the influence of different FIB dwell times on $CoSi_2$ layer formation. (**a**) $CoSi_2$ layer fabricated with a short pixel dwell time of 1 µs. The layer is continuous and smooth. (**b**) The dwell time is increased to 50 µs and the layer shows some holes and an enhanced roughness. (**c**) Increase of dwell time to 100 µs leads to totally disintegrated layer. Experimental parameters are: (111) Si substrate, fluence of 1×10^{17} cm^{-2}, ion beam spot size of 300 nm, ion current density of 1 A cm^{-2} [234]

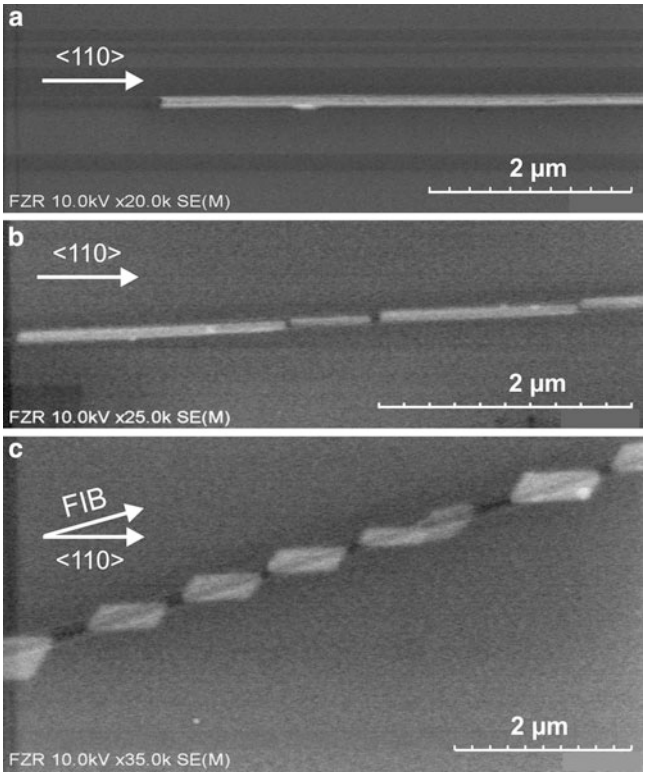

Fig. 4.44 $CoSi_2$ nanowires in (100)-Si (**a**), in (111)-Si with a small misalignment (**b**), and with a misalignment angle of about 15° (**c**). The Co^{++} FIB implantation fluence was 1×10^{17} cm^{-2} [235]

mechanisms of $CoSi_2$ nanowire formation were investigated: first, conventional synthesis by Co^{++} FIB implantation at elevated temperatures into silicon along in-

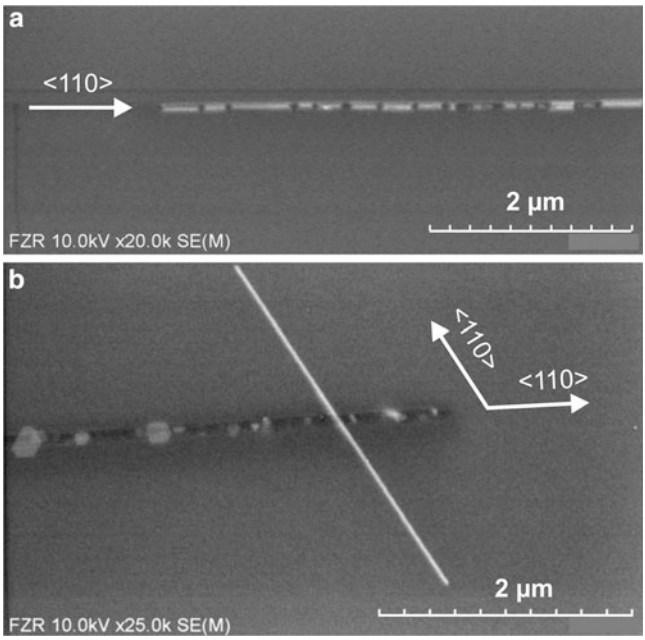

Fig. 4.45 $CoSi_2$ NW in (100)-Si implanted with a fluence of 7×10^{16} cm^{-2} (**a**) and in (111)-Si, implanted with a fluence of 3×10^{16} cm^{-2} (**b**) [235]

plane ⟨110⟩ Si crystal direction and subsequent conventional two-step annealing, and second, self-aligned $CoSi_2$ nanowire growth in cobalt supersaturated silicon on defects induced by FIB at room temperature during subsequent annealing.

Conventionally synthesized NWs (Co^{++}, 60 keV, 1×10^{17} cm^{-2}) showed lengths of 10–20 µm and diameters of 100–150 nm in the case of FIB implantation along the chosen ⟨110⟩ direction. A small deviation of the FIB trace from this direction leads to a decay of the NW into shorter fragments and larger angles of FIB trace misalignment cause the formation of chains of more or less prolonged $CoSi_2$ nanoparticles. Further reduction of the NW diameter was expected by decreasing the concentration of Co atoms implanted in silicon at the same FIB spot. NWs synthesized at lower fluences of 1×10^{16}–7×10^{16} cm^{-2} are not stable and decay into shorter NW fragments with a diameter of about 50 nm. Moreover, because of the existence of the other ⟨110⟩ crystalline directions crossing the FIB trace, there is a certain probability of spontaneous and self-aligned NW growth in these two directions. This effect has been explained by the existence of the well-known {311} defects in silicon induced during FIB implantation [237]. These defects are closed between two {311} planes and are elongated in the ⟨110⟩ direction. During annealing the implanted and solved Co atoms diffuse and can be gettered in the {311} defects. They react with silicon and form silicide precipitates along these defects, i.e., along the ⟨110⟩ direction which is the most preferable direction for the one-dimensional $CoSi_2$ crystalline structure growth. This process stabilizes the

defect structure and hinders dissolution of the rod-like defects. Subsequent Oswald ripening of the silicide precipitates along this ⟨110⟩ direction leads to the formation and alignment of initial oblong $CoSi_2$ nanoparticles at the defect position. During further heating the solved cobalt atoms are still available around the nanoparticles and diffuse to them promoting the growth of crystalline $CoSi_2$ NWs. This finally results in the formation of some micrometer long NWs. In contrast to conventional ion beam synthesis of $CoSi_2$ NWs by high-fluence FIB implantation along a narrow trace, the defect induced and self-aligned NWs seem to be more stable.

4.3.3 Ion Beam Synthesis of Nanocrystals in Insulators

With the combined utilization of ion–solid interactions that lead to far-from-equilibrium states and thermodynamic processes resulting in relaxation toward equilibrium, tiny nanostructures [often called nanoparticles (NP), nanoclusters or nanocrystals (NC)] of controlled composition can be formed in virtually any matrix. Still, the size of the nanostructures obtained in this self-organization approach is much below the capabilities of present days direct structuring techniques, as, e.g., extreme ultraviolet optical lithography or direct writing electron beam lithography. By now literature contains a wealth of publications on different ion–matrix combinations that potentially might trigger applications of these novel nanoscale materials [238–242]. The properties of nanoparticles are dominated mainly by two effects:

1. Increasing surface energy associated with increasing surface-to-volume ratio for small NPs which determine their physical and thermodynamic properties (e.g., melting point, solid phase transition, and bulk modulus)
2. With decreasing NP size change of the band structure (e.g., transition from indirect to direct semiconductors, widening of band gap) and electron confinement in NPs

Both effects lead to novel electronic properties showing a wide range of effects, for example, large nonlinear optical susceptibility of metal nanoparticles, effective photoluminescence, and charge storage properties of semiconducting NPs.

Ion beam synthesis of metal NPs (e.g., Au, Ag, Cu) in an inert dielectric medium (e.g., SiO_2, Al_2O_3) concerns to change or improve the properties of optical materials such as reflectivity, absorption, refractive index, and luminescence. This application of IBS is driven by the demands on optical materials with higher data transfer velocity and the fabrication of purely optical devices and integrated circuits. For example, metallic NPs in a dielectric matrix enhance the third-order susceptibility near the surface plasmon resonance frequency (see, for example [243]). Due to the nonlinearity in the refractive index caused by this effect, these systems have attracted much interest for use in all-optical switching devices. Additionally, the frequency of light absorbed by these metallic NPs shifts to shorter wavelengths as a function of decreasing NP size. Thus, measuring the absorption spectra of an ensemble of embedded NPs is an indirect method of determining their size. Typical process parameters in fabrication of metallic NPs for changing of

Table 4.4 Implantation and annealing conditions at IBS of Cu, Ag, and Au NPs

Process parameter	Cu	Ag	Au
Energy E (keV)	30–160; 3,500	50–300; 3,500	1,500–4,400
Fluence Φ (cm^{-2})	(1–10) × 10^{16}	(0.1–60) × 10^{16}	(0.1–15) × 10^{16}
Current density j (μA cm^{-2})	0.7–10	0.2–14	0.5–2.0
Target temperature T_i (°C)	RT–1,100	RT–600	LN_2, RT-600
Annealing temperature T_A(°C)	–	400–700	700–1,200
Annealing time t_A (h)	1 (at implantation)	12 ns–1 h	0.5–36
Annealing atmosphere	Vacuum (implant. chamber)	Vacuum (implant. chamber)	Air, O_2, Ar + 4% H_2 (furnace)

linear absorbance, luminescence, and producing of nonlinear optical effects are summarized in Table 4.4.

At ion beam synthesis of metal NPs in optical materials the ion energy is chosen in a broad range from some tens of keV up to some MeV with corresponding high fluences in the range of ~1 × 10^{15}–1 × 10^{17} cm^{-2} to achieve impurity concentration in the order of (1–10) at % in the maximum of the implanted profile. The annealing conditions are selected specifically for the kind of implanted metal ions. The NP growth kinetics and the NP size distribution are significantly influenced by the implantation as well as annealing parameters. In contrast to Au, the NP formation during ion irradiation without subsequent annealing is more pronounced for Cu (and sometimes for Ag) ions implanted into silica. Annealing for the formation of certain Ag and Au NP cluster sizes is usually carried out at (400–700) °C and (600–1,200) °C, respectively. The influence of the target temperature during implantation into quartz glass and the ion current density on the NP size distribution has been investigated in [244, 245]. At room temperature implantation and at relatively low ion current densities a more sharp NP size distribution with a mean NP diameter of (5–10) nm is formed. With increasing both the target temperature T_i and ion current density j, the NP size rises up to (25–30) nm with a broader distribution.

For Cu the distribution of NP size in dependence on the impurity concentration in the maximum of the Cu depth profile shows a linear behavior with $d_{NP}(nm) = 0.15\ N_{Cu}(cm^{-3})$ [246]. For example, such correlations are helpful in tuning the metal NP sizes during IBS.

The formation of Ag NPs has been observed already at 150 keV Ag^+ ion implantation into different types of glasses without annealing where the mean cluster diameter is in the range of 6–40 nm for ion fluences of 2 × 10^{16} cm^{-2} and 7.6 × 10^{17} cm^{-2}, respectively [247, 248]. For Ag NPs it was found that the chemical composition of the glass can influence the NP growth and the final size distribution. Subsequent annealing of Ag^+-implanted glasses leads to dissolution of large NPs into smaller ones and at higher annealing temperatures (or heated samples during implantation) and to an increased Ag solution in the glass matrix [249].

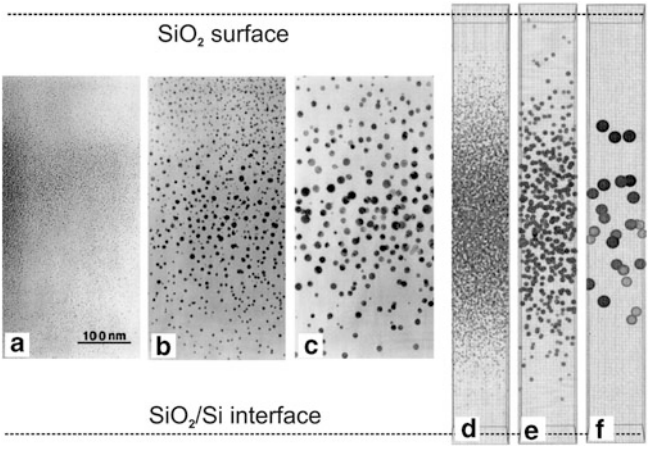

Fig. 4.46 *Left*: Cross-section TEM images of 2.75 MeV Au^+-implanted fused silica for a fluence of 1.5×10^{17} cm^{-2} and implantation temperatures at (**a**) room temperature, (**b**) 400 °C, and (**c**) 600 °C (TEM images were taken from the central region of the implanted profile). *Right*: KLMC simulation results of Au NP formation during ion implantation. (**d**)–(**f**) show the NC distributions immediately at the end of implantation for the investigated parameter T_i and a constant j (taken from [252])

The IBS of Au NPs is usually carried out using MeV Au^+ ion implantation with fluences 3×10^{16}–1.5×10^{17} cm^{-2} where the nucleation and NP growth depend on implantation temperature T_i and ion current density j [250, 251] and can be additionally changed at subsequent annealing. In the as-implanted state, Au NPs with a mean size of <5 nm have been observed. During subsequent annealing at (900–1,100) °C, the mean Au NP size increases up to ~30 nm. Investigations of the NPs growth kinetics showed a time dependence of the NP growth with $\overline{R} \sim (t)^{1/3}$, which is typical for Ostwald ripening. Kinetic 3D lattice Monte Carlo (KLMC) method has been applied to describe nucleation and growth of Au NPs in SiO_2 [252]. This system is well suited for fundamental studies of the mechanisms of NP formation, because (1) Au does not tend to form an oxide or silicide since Au atoms are chemically inert with respect to the constituents of the host material and (2) Au is observed to precipitate during the implantation stage. The basic dependences of the depth-dependent NC size distribution on the main implantation parameters, i.e., the implantation temperature T_i and the ion current j (ion flux) have been modeled. Using the KLMC model, the principal dependences of the observed particle size distributions can be understood and are qualitatively in good agreement with corresponding experiments.

In Fig. 4.46 fused silica or thermally oxidized silicon wafers with an oxide thickness of 1.7 μm were implanted with Au^+ ions at an energy of 2.75 MeV to fluences in the range of 3×10^{16}–1×10^{17} cm^{-2}. At this energy the projected range of the Au^+ ions is about 0.9 μm. The current density j was approximately 1 μA cm^{-2} and the substrate temperatures during implantation T_i have been varied

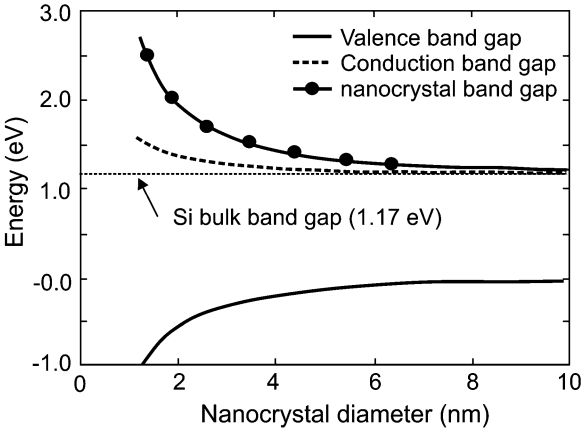

Fig. 4.47 The band gap energy as function of the NP radius shown for spherical Si quantum dots [254]

from room temperature to 600 °C. As shown in Fig. 4.46 a qualitatively good agreement between simulated and experimentally observed NC size distributions has been observed with respect to the different implantation temperatures.

In many publications among the structural (NP size and distribution) and chemical properties (compound formation, embedding into the host matrix), the optical properties have been investigated intensively, for example in [238, 245, 251, 253]. It must be mentioned that for ion beam-synthesized metallic NPs a volume fraction of NPs in the range of (1–10) % can be achieved. This value is by a factor of 10^3–10^4 higher compared to incorporation of colloidal NPs during glass melting at thermodynamic equilibrium. Consequently, one can expect approximately the same absorbance of a 0.2 µm thick ion beam modified layer compared to ~1 mm thick conventional optical glasses.

In contrast to metallic NPs, semiconducting NPs (Si, Ge) show for sizes of a few nanometers pronounced luminescence, due to the fact that with decreasing NP size the electronic band structure changes and direct electron transition into the conduction band becomes possible. As an example, the size-dependent energy gap for Si NPs is shown in Fig. 4.47, which inherently affects the electronic and optical behavior of ion beam-synthesized NPs.

The recombination of electrons into the valence band is accompanied by photoemission (photo- or electroluminescence). Due to the tininess, the NP can be considered as a "quantum dot," i.e., its electronic states are quantized and the density of states is singular, i.e., an electron can occupy the quantized energy level. The energetic spacing between neighboring energy levels increases with decreasing cluster size. For an insulating matrix surrounding the NP, the NP can be regarded as a potential well of finite depth. In this context, the NP acts as a trap for electrons or holes, since it confines them. This effect of quantum (or rather electron/hole) confinement is a principal aspect of semiconducting NPs for

electronic and opto-electronic applications in charge carrier storage and electroluminescent devices, respectively. So, band-to-band recombination of confined excitons in the NCs yields a near-infrared luminescence which is much more efficient than that of bulk silicon (photoluminescence quantum efficiency of about 59 % [255]). Moreover, the surface-to-volume ratio of NPs is significantly larger in comparison with bulk materials which implies that the electrical and optical properties of the NPs are remarkably determined by NP surface or rather NP-insulator interface contributions. Si (and also Ge) nanocrystals (NCs) are a very promising material in silicon-based memory and optoelectronic technologies (e.g., Si NC-based laser devices [256] and photovoltaic solar cells [257]) fully compatible to modern complementary metal oxide semiconductor (CMOS) processing.

The development of luminescing device structures based on ion beam-synthesized Si and Ge nanocrystals in a well-controlled fabrication process requires information about the depth distribution of the nanoclusters embedded usually in the SiO_2 layer thermally grown on silicon. Implanted metals (e.g., Au, Ag, Cu) in a glassy or SiO_2 matrix often show a significant redistribution after thermal treatment with preferred accumulation of metal NPs at the surface or internal interfaces (e.g., [258]). On the contrary, the low diffusion coefficient of Si and Ge in SiO_2 suggests a depth distribution of semiconductor nanoclusters, which corresponds to the as-implanted profile [259, 260].

The implantation (ion energy and fluence) and annealing (temperature and time) conditions at ion beam synthesis of Ge and Si NPs depend on the provided application and on the substrate material. As substrates often fused silica, sapphire and SiO_2 layers thermally grown on silicon are used. For optical and electronic device applications, thermally grown SiO_2 is the common insulator material, allowing the device and circuit fabrication in a CMOS compatible process. Depending on the SiO_2 layer thickness, the Si^+ and Ge^+ ion energies are used in a wide range from low to high ion energies (1 keV–1 MeV) at relatively high ion fluences in the order of $\sim(1–10) \times 10^{16}$ cm^{-2}. The phase separation through precipitation and Ostwald ripening is achieved usually at annealing temperatures of $T_A \approx$ (600–1,200) °C in inert gas atmosphere using RTA or furnace annealing for $t_A \approx$ (30–300) s and $\approx$ (0.5–4) h, respectively. In contrast to the formation of metallic NPs in a glassy matrix, the ion current density during ion implantation does not have an observable influence on NP size and size distribution. However, the impurity redistribution and NP evolution can be strongly influenced by the annealing ambient as has been reported in [261] for Ge-implanted SiO_2 layers. The origin of this behavior is the in-diffusion of an oxidant from the annealing atmosphere, which changes substantially the Ge depth profile and NP distribution. It should be emphasized that even for atmospheres having oxidant (moisture) concentrations as low as a few ppm, such unusual Ge redistributions have been found [262]. These effects of influence of the annealing ambient, for example, on the microstructure of Ge-implanted SiO_2, have been studied by annealing in N_2, Ar, or dry O_2 atmospheres with different concentrations of chemical reactive components (H_2O, O_2). 500 nm thick SiO_2 layers thermally grown on (100)-oriented Si wafers were implanted with 350 keV Ge^+ ions and fluences between

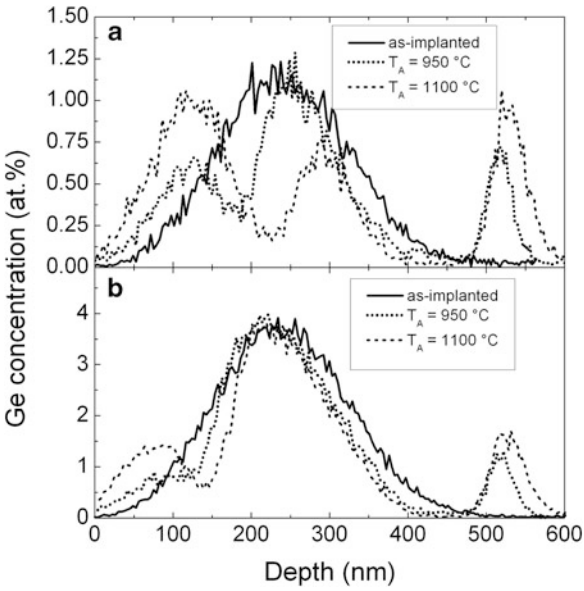

Fig. 4.48 Ge concentration profiles obtained from RBS spectra of 500 nm thick SiO_2 layers on Si which were implanted with 350 keV Ge^+ and subsequently annealed in N_2 for 1 h. (**a**) $\Phi = 1.5 \times 10^{16}\ cm^{-2}$, (**b**) $\Phi = 5.0 \times 10^{16}\ cm^{-2}$ [262]

5×10^{15} and $5 \times 10^{16}\ cm^{-2}$, which results in peak concentrations of implanted Ge of (0.4–4.0) at.%, respectively. The annealing was performed at 950, 1,000, and 1,100 °C in a standard furnace for 15–180 min using the "inert" gases of N_2, Ar, or the "reactive" gas of dry O_2 (all of 5.0 purity). In Fig. 4.48 the Ge depth distributions measured by RBS are shown. The as-implanted Ge profiles are located inside the SiO_2 layer, i.e., the Ge concentrations at the surface and the Si/SiO_2 interface are below 1 % of the peak concentration.

For both fluences the RBS spectra show unusual changes in the Ge depth distributions after annealing at 950 °C in N_2. Three well-separated peaks are found, whose separation from each other increases with increasing annealing temperature. The width and height of the central Ge peak decrease and the two satellite peaks grow. As it has been shown by STEM-EDX analysis [263], the Ge at the Si/SiO_2 interface is located within a thin Si layer at the Si/SiO_2 interface where it forms a few monolayers of a Si–Ge alloy. At the higher annealing temperature of 1,100 °C, Ge diffuses partly into the Si substrate as it can be expected from the complete miscibility of Ge and Si. After annealing (see Fig. 4.49b, c), in the center of the SiO_2 layer Ge NPs appear which are related to the central peak in the RBS spectrum (see Fig. 4.48b).

For the Ge nanocluster distribution of Fig. 4.49c, a mean cluster size of 6 nm was observed, which is in good agreement with the mean cluster size of (6.4 ± 0.7) nm measured by XRD. Towards the SiO_2 surface, the Ge cluster band is terminated by a very narrow (11.1 nm) edge region, which is in contrast to the smooth tail of nanoclusters facing the Si substrate. No Ge clusters were found between the sharp edge of the cluster band and the SiO_2 surface, where a pronounced subsurface peak

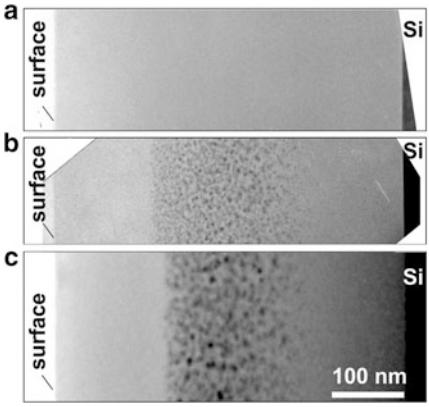

Fig. 4.49 Cross-sectional TEM micrographs of 500 nm thick SiO_2 on Si implanted with 5×10^{16} cm^{-2} at 350 keV prior to annealing (**a**) as well as after annealing at 950 °C for 1 h (**b**) and 1,100 °C for 1 h (**c**) [262]

of Ge was observed by RBS (Figs. 4.48 and 4.49). XPS measurements reveal that Ge 2p3/2 photoelectrons coming from the central, cluster-related peak and from the interface peak can be attributed to elemental Ge, whereas the energy of photoelectrons from the subsurface peak is shifted indicating Ge–O bonds [264]. The Ge redistribution and nanocluster evolution of identically implanted but Ar annealed SiO_2 layers are quite similar to the samples annealed in N_2. However, the Ge redistribution can be largely suppressed by the deposition of a 20 nm thick capping layer of LPCVD-Si_3N_4 on top of the SiO_2 layer before ion implantation. The disappearance of the drastic Ge redistribution during annealing in samples protected by a diffusion barrier underlines the strong influence of the annealing ambient on Ge and Si NP formation in SiO_2. After annealing in dry O_2 for 15 min (Fig. 4.50a) the general features of the NP depth and size distribution appear to be similar to samples annealed in N_2 (Figs. 4.48 and 4.49) or in Ar. However, the evolution of NPs is faster and/or occurs at lower temperatures. At longer annealing times (30 and 45 min) the sharp edge of the NP band of elemental Ge shifts progressively into the depth of the layer. In contrast to annealing in N_2 (or Ar), on the rear side of the moving sharp edge of the Ge NP band a layer of diffuse precipitates was observed (Fig. 4.50b, c).

In comparison to annealing in N_2 (or Ar), annealing in dry O_2 increases the surface concentration of the oxidant by orders of magnitudes which overcompensates the smaller diffusivity of O_2 compared to H_2O. Thus, the zone of GeO_2 formation shifts towards the edge of the nanoparticle band. Finally, the arriving oxidant cannot be consumed completely by dissolving Ge which results in direct oxidation of Ge nanocrystals. These GeO_2 nanoclusters can be seen in the TEM images of Fig. 4.50d. Due to their lower specific Ge density and amorphous structure, they can be distinguished from Ge NPs by a lower Z-contrast, diffuse boundaries, and the absence of lattice plane imaging by HRTEM. For the explanation of Ge redistribution due to chemical effects, the following model was proposed [262]: Ge^+ ion implantation forms a highly supersaturated solution of Ge in SiO_2.

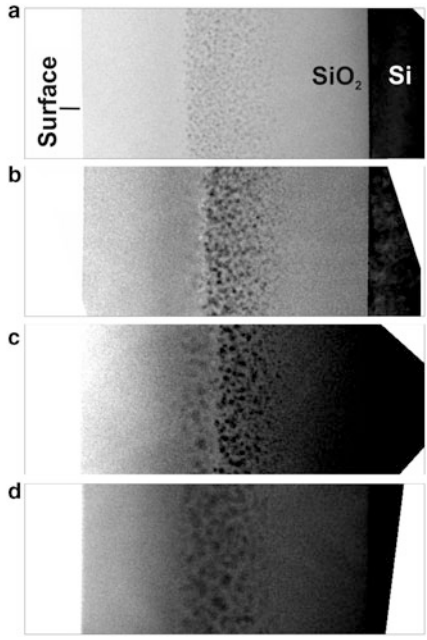

Fig. 4.50 Cross-sectional TEM images of 500 nm SiO_2 layers on Si implanted with 5.0×10^{16} cm^{-2} at 350 keV after annealing at 950 °C in pure O_2 for 15 min (**a**), 30 min (**b**), 45 min (**c**), and 90 min (**d**). Amorphous diffuse GeO_2 nanoclusters can be seen in (**c**) and (**d**) [262]

At the initial stage of annealing most of Ge (Si) precipitates to tiny Ge NPs, whereas a small fraction of Ge (Si) remains dissolved in SiO_2. The concentration c of dissolved Ge (Si) around a nanoparticle is given by the Gibbs–Thomson relation (4.26). In an ensemble of nanoparticles, the average supersaturation $\langle c - c_{sol} \rangle_{av}$ is proportional to $1/R_{av}$, where R_{av} is the mean NP radius. During annealing an oxidant (e.g., moisture) can diffuse into SiO_2 where it oxidizes dissolved Ge (Si). Assuming for both species comparable diffusion coefficients, the zone of GeO_2 formation should be between the surface and the cluster band. This explains two features of the experimental data: (1) As the oxidant reacts with Ge dissolved in SiO_2, the resulting GeO_2 does not form NPs within the SiO_2 matrix. Thus, the Ge accumulated there as GeO_2 can be seen as a peak in the RBS spectra, however NPs were not observed in cross-sectional TEM images. (2) The small distance between the sink (the zone of GeO_2 formation) and the source (the layer of Ge NPs) of Ge monomers leads to a steep gradient of dissolved Ge. Therefore, an effective dissolution of nanoparticles occurs only within a narrow layer of the nanoparticle band whose width is in the order of the diffusional screening length $\lambda = (4\pi R_{av} n_{NP})^{-1/2}$, where n_{NP} is the NP density. Estimating R_{av} from Fig. 4.49 and calculating n_{NP} with the aid of the implanted fluence, the diffusional screening length can be calculated to be $\lambda = 10$ nm. This value is in excellent agreement with the width of the edge of the nanoparticle band. At the Si/SiO_2 interface (see Fig. 4.48) the concentration c of Ge dissolved in SiO_2 is lower than c_{sol} because the Ge–Si bond strength is more than 10 % larger than the Ge–Ge bond strength. In

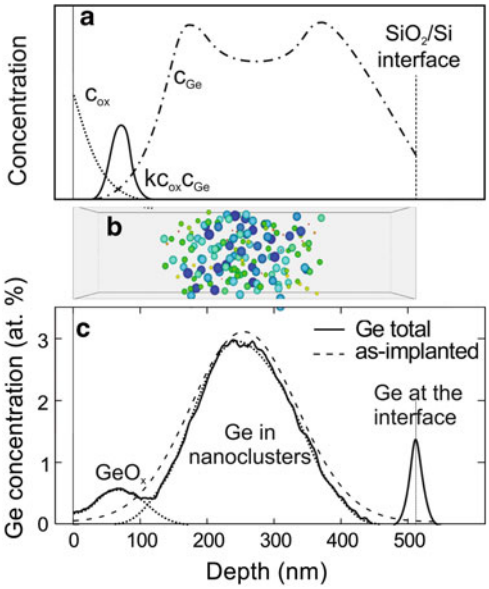

Fig. 4.51 KLMC simulation of the Ge redistribution and cluster formation in a 500 nm Ge^+ ion-implanted SiO_2 layer on Si during annealing. (**a**) Scheme of the oxidant (H_2O) concentration c_{ox}, the Ge monomer concentration c_{Ge}, and the Ge oxidation rate $k \cdot c_{ox} \cdot c_{Ge}$ in SiO_2. (**b**) The spatial and size distribution of Ge NPs. (**c**) The calculated total Ge depth profile (*full curve*), which evolved from the as-implanted profile (*dashed curve*) during annealing, consists of the three Ge components: (1) GeO_x (subsurface peak), (2) Ge in nanocrystals (*central peak*), and (3) Ge accumulated at the interface [265]

the nanocluster region c is higher than c_{sol}, therefore, the resulting concentration gradient leads to a diffusion flux and to an accumulation of Ge at the interface. There, Ge can either grow epitaxially on top of the Si substrate, or, for sufficiently high annealing temperatures, it can diffuse into the Si substrate.

Kinetic 3D lattice Monte Carlo (KLMC) computer simulations of Ge precipitation, diffusion, and oxidation as well as of cluster coarsening were performed supporting the proposed model [265]. In the simulation code, two kinds of impurities (Ge, oxidant) have been considered. Figure 4.51b, c show the results of a KLMC simulation. The Ge atoms have been deposited into the SiO_2 layer according to a Gaussian depth profile (dashed line in Fig. 4.51c).

Using appropriate diffusion coefficients for H_2O and Ge in SiO_2 as well as the Ge–Ge and Ge–Si bond strength, the total Ge profile (full line in Fig. 4.51c) is in excellent qualitative agreement with the RBS spectrum shown in Fig. 4.48b. The KLMC simulations facilitate the understanding of the driving forces for Ge redistribution, nucleation, and Ostwald ripening of NPs in SiO_2. The results of Ge redistribution were additionally supported by XPS depth profiling measuring the depth-dependent chemical bond states of Ge in the SiO_2 layer [264].

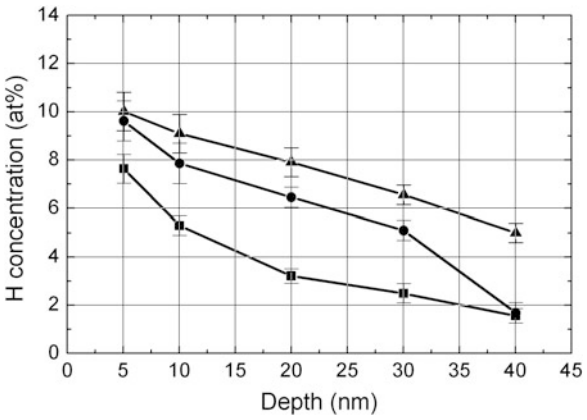

Fig. 4.52 Hydrogen depth profiles of Si^+-, Ge^+-, and Sn^+-implanted SiO_2 after storage. The ion fluence was 5×10^{15} cm^{-2} for all ions [(*filled square*) Si^+, $E = 13$ keV; (*filled circle*) Ge^+, $E = 22$ keV; (*filled triangle*) Sn^+, $E = 26$ keV] [268]

Redistribution of Ge- and Si-implanted SiO_2 by partial oxidation, possible out-diffusion, and diffusion to underlying interfaces becomes more and more critical with decreasing oxide layer thickness. For example, one of specific applications is the IBS of Si nanocrystals in thin gate oxides (SiO_2) for nonvolatile memories with a very promising performance as proposed by Tiwari et al. [266]. Because for this application the SiO_2 layer thickness of the gate oxide in the MOS-FET has been reduced below 20 nm, an increased impact of ambient on the ion beam damaged thin oxide not only during subsequent annealing but also during sample storage has to be expected.

High-fluence ion implantation (1×10^{15}–1×10^{17} cm^{-2}) for IBS of NPs in SiO_2 layers leads to a high degree of destruction of the amorphous network. In the case of low energy ion implantation ($E < 30$ keV) into SiO_2, the damaged layer will be located very near to the SiO_2 surface. The large number of broken bonds in the SiO_4-tetrahedra due to displaced Si and O atoms results in rearrangements of the fundamental ring structure within the glassy network [267] in which moisture from the ambient can be absorbed. Water molecules adsorb at the surface, and damage-enhanced inward diffusion can take place. Therefore, chemical reactions of the implanted impurities with hydrogen and oxygen must be expected during subsequent annealing which can interfere with precipitation and Ostwald ripening of nanocrystals. The incorporation of water from the ambient in stored, as-implanted SiO_2 layers and during different preparation steps in the IBS of NPs has been studied by hydrogen depth profiling using NRA [268]. The results of H depth profiling after storage (at 40 % rel. humidity in clean room) are shown in Fig. 4.52 for ions of different ion masses, implanted into SiO_2.

Concentrations of hydrogen up to 10–12 at.% due to water absorption from the ambient at a depth of 5 nm and 6–8 at.% at the projected range R_p (20 nm of different implanted ions) were measured. Moreover, this penetration of hydrogen atoms was found to increase with the energy losses provided by the implantations, i.e., increased with the fluence and the atomic mass of the implanted ions. The high amounts of incorporated hydrogen and oxygen are sufficient to interfere significantly with the precipitation and Ostwald ripening of NPs during IBS, namely to

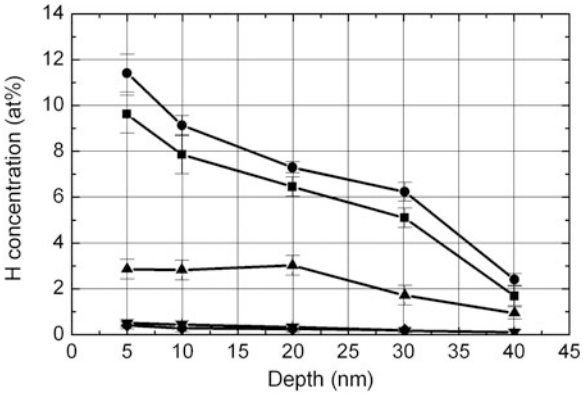

Fig. 4.53 Hydrogen depth profiles in Ge^+-implanted SiO_2 after different preparation steps [(*filled square*) storage after implantation, (*filled circle*) wet chemical cleaning (SPM), and (*filled triangle*) 600 °C annealing for 10 min in dry N_2]. For comparison, the H concentration profiles in the unimplanted, as-grown, oxide (*filled inverted triangle*) and in oxide, which was only wet-chemically treated (Piranha clean, H_2O_2/H_2SO_4) (*filled diamond*), are included [268]

enhance the precipitation and ripening process by the presence of hydrogen on one hand and to oxidize the implanted impurities partially or fully by incorporated oxygen on the other hand.

Figure 4.53 shows the results of H depth profiling after different preparation steps (storage, wet chemical cleaning, and 600 °C annealing for 10 min in dry N_2). For comparison, the H concentration in the unimplanted as-grown SiO_2 and in SiO_2 that was only wet-chemically treated (Piranha clean, H_2O_2/H_2SO_4) is included. The measured H concentration in these samples was smaller than 0.5 at.%, which is near the NRA sensitivity limit of 0.05 at.%. Wet chemical cleaning of the as-implanted samples slightly increases the H content in SiO_2 by nearly 2 at.%. Therefore, it was concluded that the H concentration up to a SiO_2 depth of (40–50) nm is caused by water absorption from the air humidity and defect-enhanced inward diffusion at room temperature. The annealing reduces the H concentration approximately by a factor of two in the depth of R_p. The reduction of the H content near the SiO_2 surface is more pronounced due to possible outward diffusion of H and OH^- and/or H_2O molecules during thermal treatment. From the measured H depth profiles, one can conclude that half of the H concentration is equal to an oxygen concentration of 3–4 at.% (most probably OH groups are present) at R_p, which is of the same order of impurity concentration in the maximum of the implanted profile. Therefore, one can expect in the initial state of postimplantation annealing (sample heating up) a very fast redistribution of the implanted profile occurs, due to the rapid formation, for example, of SiH_x and GeH_x compounds, leading to fast precipitation and even H-stimulated outward diffusion of the implanted atoms. With increasing temperature and time, oxidation (like wet oxidation of Si) of the implanted atoms Si, Ge, and Sn or of precipitates and nanocrystals takes place. The penetration and final concentration of H_2O molecules do not depend on the relative humidity in the

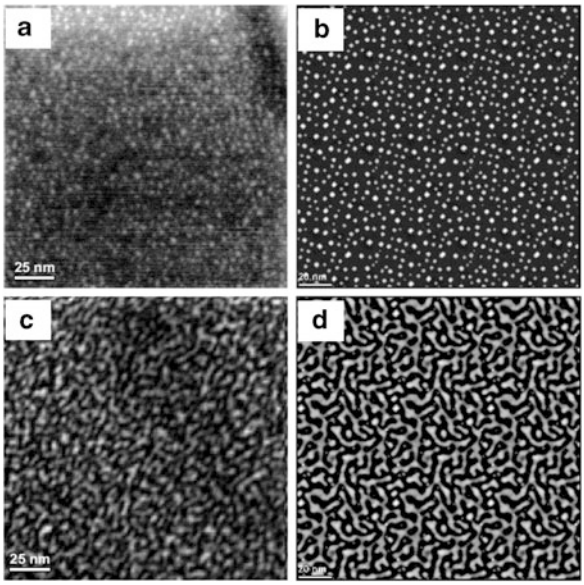

Fig. 4.54 Comparison between the morphologies of phase separated Si NPs in SiO_2 obtained by XTEM (PEELS-STEM) imaging [*left*, (**a**, **c**)] and KMC simulations [*right*, (**b**, **d**)]. Nucleation of Si NCs is observed (**a**) for a Si fluence of 1×10^{16} cm^{-2} and predicted with the same morphology for (**b**) 3×10^{15} cm^{-2}. Spinodal patterns are imaged (**c**) for 2×10^{16} cm^{-2} and simulated (**d**) for 8×10^{15} cm^{-2}. *Bright* and *dark regions* correspond to Si and SiO_2 phases, respectively (from [271])

atmosphere but are mainly limited by the degree of damage, i.e., the concentration of defects, in the SiO_2 matrix.

Unexpected nanocrystal distributions, especially in very shallow implanted SiO_2 layers, can be explained by these chemical effects during IBS. The observed water incorporation is very important in IBS for the case of Si, Ge, and Sn NPs in ultrathin gate oxides (10–30 nm thick) that were intensively investigated because of their potential application in nanocrystal-based nonvolatile memory devices [269]. For example, studies on low energy 1 keV Si^+ ion beam synthesis of Si NP embedded in 10 nm thick SiO_2 layers have been done [270, 271]. The morphology of Si NPS thin gate oxide layers has been investigated by TEM imaging (PEELS-STEM) and compared with kinetic three-dimensional lattice Monte Carlo (KLMC) simulation. Remarkable agreement between the atomistic simulations and the PEELS-STEM images was found. However, the predicted Si^+ ion fluences are significantly lower than the experimental ones. A substantial fraction of the implanted Si is lost by parasitic oxidation with atmospheric humidity as shown in Fig. 4.54.

The quantitative analysis of the characteristics of Si NPs populations shows that only a fraction of the implanted fluence (up to 40 %) has precipitated into NPs. Furthermore, the KMC simulation well predicts the transition from isolated NCs, obtained through the nucleation and growth, towards a network of connected particles, obtained through the spinodal decomposition of a highly supersaturated matrix.

Besides extensive fundamental research, e.g., on quantum confinement of charge carriers or on effects in structural phase transitions, semiconducting NPs exhibit promising applications as well as large technological potential: (1) for opto- and

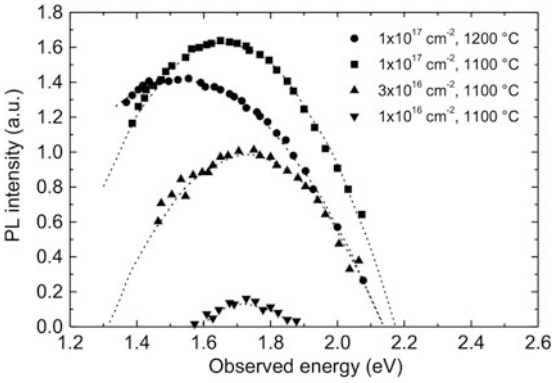

Fig. 4.55 PL spectra from Si NPs in a 100 nm SiO_2 layer implanted with 40 keV Si^+ ions at given fluences and annealed at indicated temperatures (1 h, for 3×10^{16} cm^{-2} 5 h). The PL was excited by irradiation of the samples at a wavelength of $\lambda = 355$ nm [280]

electro-luminescence from Si and Ge NCs in SiO_2 the understanding and controlling of their microstructure seems to be vital for a tailoring of efficient devices [272, 273], and (2) within the challenges of miniaturization in microelectronics the promising use of Si (and Ge) NPs in nonvolatile memories [274] and even as single-electron transistors [275].

Typically, for Si-NPs, the photoluminescence (PL) and electroluminescence (EL) spectra extend from 600 to 1,000 nm. The effects on the luminescence spectrum of the NP density, size and distribution, annealing temperature and time, ion fluence, and the sample temperature during implantation have been extensively studied. Most investigations on IBS of Si NPs report a PL peak at around 1.7 eV (728 nm). The often reported blue–violet PL in the region of (2.7–3.2) eV in Si^+-, Ge^+-, and Sn^+-implanted SiO_2 appears to come from oxygen deficiency centers in the implanted SiO_2 matrix or at the interface between NPs and SiO_2 rather than the NPs themselves [273]. The position of the luminescence peak at around 1.7 eV appears to be dependent on the implanted fluence of silicon [272, 276–278], with a red shift in PL peak position generally with an increasing fluence and depends on the experimental conditions. The highest PL peak intensity has been reported for implanted SiO_2 with an excess Si content of ~10 at.% Si [276, 277]. For SiO_2 containing 10 at.% Si, the PL intensity initially increases with annealing time, after which it saturates. During the initial stages of annealing, among Si NP growth some kind of NP surface passivation takes place [279]. Reaching a critical radius during annealing the Si NP size stabilizes, as does the number of dangling bonds at the Si/SiO_2 interface. Furthermore, it was found that a second annealing step at 500 °C in forming gas (95 % N_2, 5 % H_2) results in an increase in PL intensity and a red shift in the emission peak. This increase in PL intensity may be a result of the passivation of nonradiative defects by hydrogen (e.g., Si dangling bonds) [278]. For example, a typical PL spectrum from Si NPs in thermally grown SiO_2 on silicon is shown in Fig. 4.55 [280].

The PL spectrum in Fig. 4.55 was obtained from 100 nm thick SiO_2 layers implanted with fluences from 1×0^{16} cm^{-2} to 1×10^{17} cm^{-2} of Si^+ ions at 40 keV corresponding to a silicon excess between 2 and 25 at.% at a depth $R_p \approx 60$ nm in

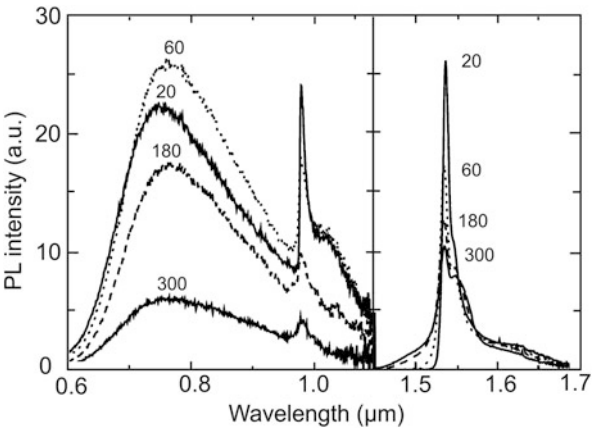

Fig. 4.56 PL spectra at different temperatures (in K) showing a broad Si NP spectrum in the wavelength region of 600–1,100 nm, and two sharp Er luminescence lines at 982 and 1,536 nm. The Er concentration was 1.8 at.%. The PL was excited at $\lambda = 458$ nm with a pump power of 1 mW [283]

the SiO_2 layer. The annealing was carried out at 1,000, 1,100, and 1,200 °C for 0.5–5 h in dry N_2.

Recently, it was shown that if additionally Er^+ ions are implanted into silicon dioxide containing Si NPs fabricated by IBS room temperature, photoluminescence (and electroluminescence) at near-infrared wavelength of $\lambda = 1.54$ μm is observed [281–283]. The PL (EL) shown in Fig. 4.56 is of interest because Erbium-doped optical amplifiers are important components in optical telecommunication because the optical transition of Er^{3+} at 1.54 μm is in the region of optimum transmission of silica-based glass fibers.

The Er and Si NP doped SiO_2 was fabricated by Si^+ ion implantation at 35 keV with a fluence of 6×10^{16} cm^{-2} into a 100-nm-thick thermally grown SiO_2 layer and by subsequent annealing at 1,100 °C for 10 min in vacuum resulting in Si NPs with sizes in the range 2–5 nm and a concentration of ~10^{19} cm^{-3}. The Si NP doped SiO_2 was then implanted with 125 keV Er^+ ions and a fluence of 5.1×10^{15} cm^{-2}. The peak of the implanted Er profile with a peak concentration of 1.8 at.% is located at a depth of ≈ 50 nm which coincide with the maximum of the Si NP depth distribution. Vacuum annealing at 1,000 °C was carried out to remove Er^+ implantation-induced damage. At least the samples were annealed at 800 °C for 30 min in forming gas (N_2 + H_2) to reduce defect-related luminescence. It was shown that at 1.8 at.% Er concentration the Er/Si NP ratio ≈100:1. Nevertheless, the observed maximum excitable Er concentration was only ≈(1–2) $\times$ 10^{19} cm^{-3} and therefore in the order of the Si NP volume concentration, which means that a single Si NP can effectively excite only ~1–2 Er ions. The model proposed by Polman [284] suggests that strong coupling between the Si NPs and the implanted Er atoms (existing as ionized Er^{3+} in SiO_2) effectively enables the Si NPs to pump the Er. The excitation cross section of the Er increases in the presence of Si NPs compared to Er excitation in the pure SiO_2. In the presence of a Si NP, the

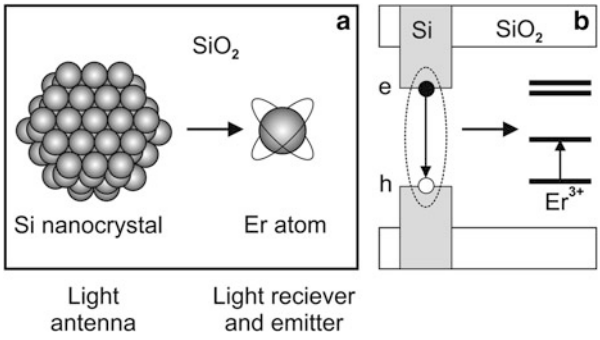

Fig. 4.57 Schematic Er excitation model, showing (**a**) a Si NP and an Er^{3+} ion embedded in SiO_2, and (**b**) the electronic band structure of Si NP doped SiO_2 and the Er energy levels (adapted from [284])

wavefunction of an electron–hole pair ("exciton") in a Si NP can couple to a nearby Er^{3+} at a distance of ~1 nm in SiO_2, as shown schematically in Fig. 4.57a.

An optically generated exciton (dotted line) confined in the Si NP will recombine nonradiatively and excite Er^{3+} from the ground state to the first excited state (Fig. 4.57b). The excited Er ions radiatively decay emitting photons at a wavelength of $\lambda = 1.536$ μm as shown in Fig. 4.56. Silica-based materials containing Si NPs and Er synthesized by ion beams enable the fabrication of a new class of miniature waveguide amplifiers as proposed by Polman [284].

More information about device applications of Si NPs and toward their microelectronic chip-based uses, the reader can find in the two books of Koshida [285] and Pavesi and Turan [286]. In these books alternative fabrication techniques for Si NPs are also described, namely plasma-enhanced chemical vapor deposition (PECVD) and physical vapor deposition (PVD) by sputtering or evaporation producing substoichiometric (or Si-rich) SiO_x (with $x < 2$) layers.

In microelectronics memory architectures charge storage devices for high-density, low-voltage, low-power, and fast write/erase data storage are needed to meet the International Technology Roadmap for Semiconductors (ITRS) requirements in the future. At present, two types of charge trapping memories are used: the polysilicon-blocking oxide–nitride-tunneling oxide-silicon (SONOS) memory, including the nitride read-only memory (NROM), and the nanocrystal floating-gate memory as proposed by Tiwari et al. [274]. A nanocrystal floating-gate memory consists of single-transistor memory-cell structures in which the conventional poly-Si floating-gate (FG) is replaced by Si NPs as isolated charge trapping centers as shown in Fig. 4.58.

The main advantage of the Si nanocrystal-based multidot floating gate memory is, however, the isolation of the Si NPs from each other that allows to reduce reliability constraints arising from charge leakage and hence improving reliability. As shown in Fig. 4.58a,b possible conduction paths originating from oxide defects, either process or operation related, have only a very local effect and cannot lead to a complete discharging of the distributed NC floating gate layer. As a result, the injection oxide thickness between the NPs and the transistor channel can be reduced to <5 nm. At these distances, electrons can tunnel by direct electron tunneling at

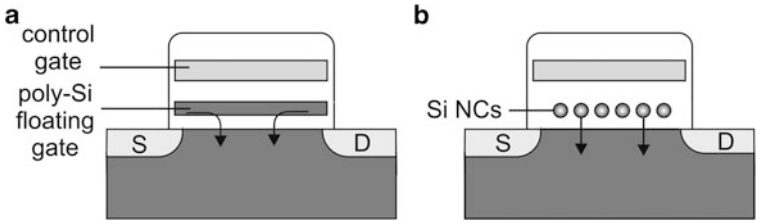

Fig. 4.58 Schematic buildup of (**a**) a poly-Si floating-gate memory cell, and (**b**) a nanocrystal floating-gate memory cell

Table 4.5 Implantation and annealing conditions at Si NP synthesis in thin gate oxides for memory applications

IBS process parameters	Values
SiO_2 thickness (nm)	5–30
Si^+ ion energy (keV)	1–15
Si^+ ion fluence (cm^{-2})	5×10^{15}–5×10^{16}
Si excess at implanted profile peak (at.%)	10–50
Annealing temperature (°C)	950–1,150
Annealing time (min)	0.5–30
Annealing ambient	N_2, $N_2 + O_2$, Ar, vacuum

low gate voltages into the Si NPs. Thicker injection oxides would require charging by defect generating Fowler–Nordheim tunneling (hot electron injection) at higher gate voltages. The last processes are known to limit the memory endurance upon repeated write and erase cycles which is not the case for direct tunneling.

IBS by low energy ion implantation into thin gate oxides allows the formation of a multidot floating gate layer made of Si NCs at a location from the SiO_2/Si interface (transistor channel) that can be tailored for DRAM-like (volatile) or EEPROM-like (nonvolatile) memory applications. Typical implantation and annealing conditions for the formation of Si NP containing gate oxides are summarized in Table 4.5.

Using very low ion energies of $E < 5$ keV (typically 1 keV) promises several advantages for the fabrication of Si NP memories: (1) Shallow and narrow depth profiles of Si excess are achieved. Phase separation is expected to result in a thin layer of Si NCs embedded in the SiO_2. (2) The depth position of the NC layer should be easily controllable by the ion energy and the total amount of Si contained in the NPs by the ion fluence, while the annealing temperature determines the mean NC size. (3) Little ion damage at the SiO_2/Si interface is expected due to the low ion energy; irradiation damage created within the SiO_2 is largely recovered during annealing. The ion energy at Si NP synthesis is one of the critical parameters in relation with the thickness of the gate oxide because after full processing the injection distance between the Si NC layer and the transistor channel can be too small preventing true nonvolatile memory operation. In this case only a DRAM-like

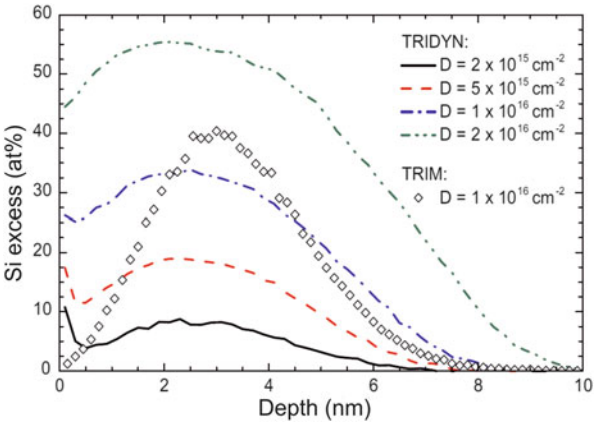

Fig. 4.59 Depth profiles of Si excess for 1 keV Si^+ implantation into SiO_2 calculated by TRIDYN in comparison with TRIM [270]

volatile memory transistor operation with fast programming and erasing at low electric fields (write/erase voltage $<+10$ V/-10 V), which ensures a high endurance, will be possible. The formation of well depth-localized layers of Si (and Ge) NPs for different implantation and annealing conditions given in Table 4.5 and their applications in nonvolatile (EEPROM-like) memory devices has been successfully achieved [287–291].

For a typical example of Si NP synthesis by ion implantation into thin (<10 nm) gate oxide, Fig. 4.59 shows the Si excess depth profiles for 1 keV Si^+ implantation. The ion fluence increases from 1×10^{15} cm^{-2} up to 2×10^{16} cm^{-2}.

As can be seen the Si excess increases for higher Si^+ ion fluences, while the profile broadens considerably due to ion beam mixing, sputtering, and swelling. The slight Si enrichment at the target surface is observed as the result of preferential O sputtering. For comparison, a Si implantation profile calculated by TRIM has been added to Fig. 4.59, which is much sharper than the corresponding TRIDYN profile. Accordingly, the Si peak concentration is significantly overestimated by TRIM and the profile broadening observed by TRIDYN calculations cannot be described by TRIM. Therefore, TRIDYN simulations are required to predict a correct profile for high-fluence implantation. With the given initial Si excess distribution phase separation can be modeled by KMC simulations the result of which is shown in Fig. 4.60.

The Si atoms in Fig. 4.60 are colored according their coordination to other Si atoms. The red color corresponds to atoms with no bonds to neighboring Si excess atoms, while blue indicates fully coordinated atoms. The first chart on the left-hand side depicts the as-implanted SiO_2. The Si excess atoms are dispersed in the oxide with a distribution tail reaching almost up to the SiO_2/Si interface. Bonds between neighboring Si atoms have not yet formed (indicated by the red color). In the first stage of annealing, small Si NCs form rapidly and are visible as tiny (green) dots. With increasing annealing time the NC density visibly decreases and the average

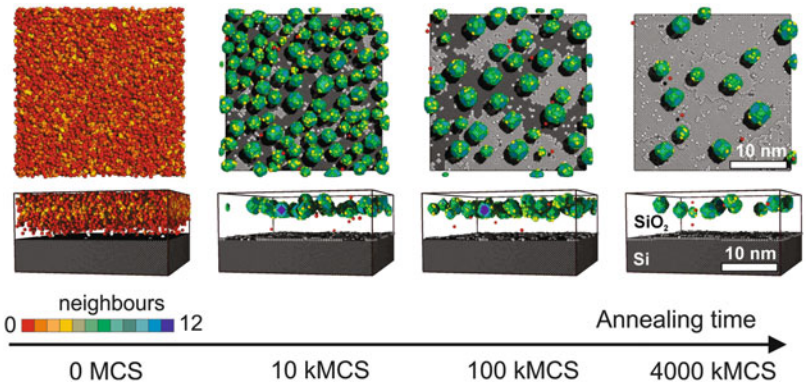

Fig. 4.60 Results of a KMC simulation (*top view* and *cross sections*) for 1 keV Si^+ implantation into 8 nm thick SiO_2 on silicon. At a fluence of 2×10^{15} cm^{-2}, Si NCs form during annealing and dissolve with increasing annealing time due to Si loss to the absorbing SiO_2/Si interface [270]

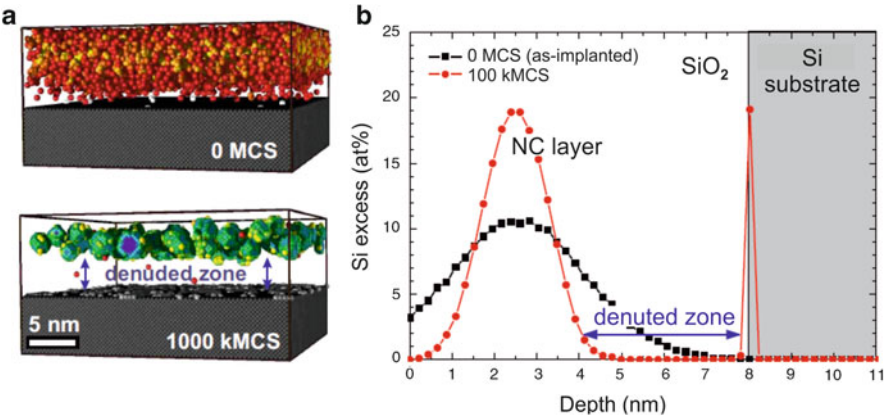

Fig. 4.61 Formation of a denuded zone free of NC at the SiO_2/Si interface during phase separation as predicted by KMC simulations. (**a**) Two KMC simulation snapshots (*cross section view*) are shown for 1 keV Si^+ implantation into 8 nm thick SiO_2 to a fluence of 2×10^{15} cm^{-2}. The first one refers to the as-implanted case while the second was taken after 100 kMCS. (**b**) Corresponding Si excess depth profiles

size of the NCs increases. This behavior of phase separation is important for NC size and density control in fabrication of nonvolatile NC memories. Finally, long-lasting annealing (right chart) leads to a considerable amount of Si loss to the absorbing SiO_2/Si interface. Si atoms attached there are colored in light gray, and it is apparent that a complete Si monolayer has grown epitaxially onto the silicon substrate. The SiO_2/Si interface acts as a strong sink for diffusing Si atoms, and therefore leads to a NC-depleted zone parallel to the interface as shown in Fig. 4.61. This denuded zone will serve as tunneling oxide in the NC memory and isolates the NC from the transistor channel.

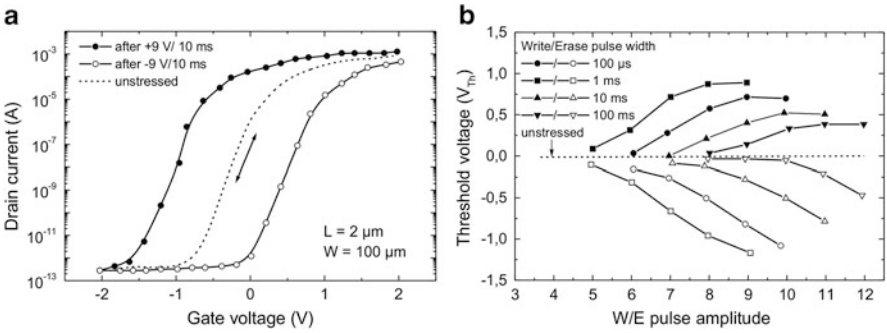

Fig. 4.62 (**a**) Transfer characteristic for Si NP floating-gate nMOS transistor. (**b**) Threshold voltage shift versus write/erase voltages for different pulse durations [289, 290]

At charge injection during the write pulse, electrons have to overcome the barrier by Fowler–Nordheim tunneling or by quantum mechanical direct electron tunneling. In both cases, the width of the injection oxide critically determines the memory properties as writing speed required for charging of the NCs and charge retention. The ion energy and oxide thickness can directly be used to control the distance between Si NCs and the Si/SiO_2 interface. Furthermore, the width of the denuded zone is influenced by the annealing time. For the nonvolatility Si NC memory under normal read and retention conditions, the thickness of the injection oxide has to remain larger than 4 nm [292, 293]. In order to accomplish this target, Si NC n-channel MOSFETs have been fabricated using 1 keV Si^+ implantation to a fluence of 2×10^{16} cm^{-2} into 7 nm thick SiO_2. Subsequent annealing has been done in diluted O_2 atmosphere (N_2/O_2) at 950 °C for 30 min. Swelling due to oxidation has lead to a total oxide thickness of 14 nm. A typical transfer characteristic (drain current I_D versus gate voltage V_G) of such a transistor is shown in Fig. 4.62a.

The threshold voltage shift V_{th} resulting from applied write/erase pulses is plotted in Fig. 4.62b as a function of the pulse amplitude. At 100 ms pulse duration, write/erase pulse amplitudes of ±6 V are high enough to achieve a threshold voltage shift of +0.5 and −0.25 V, respectively. However, shorter pulses require progressively higher write and erase voltages. At 100 µs more than 10 V must be applied to get comparable threshold voltage shifts. Endurance measurements plotted in Fig. 4.63a do not indicate a degradation of the tunneling oxide at this voltage after 10^6 write and erase cycles, and the threshold voltage window does not close after more than 10^4 s waiting time (see Fig. 4.63b), i.e., negligible charge is lost during this period.

However, temperature activated retention measurements reveal a much faster charge loss at elevated temperatures (150 °C), which is not observed in competing memory technologies, e.g., in SONOS type memories using either Si_3N_4 or oxynitrides as a charge trapping layer.

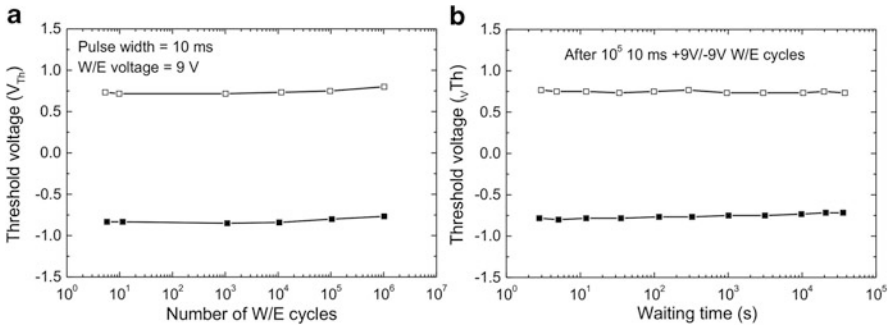

Fig. 4.63 (**a**) Endurance and (**b**) data retention characteristics of a Si NP floating-gate nMOS transistor. The endurance was measured using +9/−9 V write/erase pulses of 10 μs duration. The charge retention has been measured at room temperature after 10^5 write/erase cycles [289, 290]

Low energy IBS of Si NCs in thin gate oxides seems to be a simple technique being advantageous over more complex SiO_x deposition approaches (e.g., CVD). In principle the NC synthesis can be tuned with four process parameters only: the ion fluence Φ and ion energy E controlling the buildup of a supersaturated solid solution of excess Si in the SiO_2 and the annealing time t_A and annealing temperature T_A affecting the NC phase separation. Unfortunately, the situation is much more complex and additional process parameters influence the Si NC formation at low energy IBS. Some of these factors are:

- *Charge neutralization*, which is necessary to prevent a charge buildup at the isolating SiO_2 surface and charge breakdowns through the thin oxide (oxide damage) during implantation [294]
- *Contamination of the SiO_2 by impurities* (e.g., carbon or boron) during ion implantation, sputtered from the mechanical implanter parts or coming from the residual gas atmosphere [290]
- *Absorption of humidity* in the ion-damaged SiO_2 after the sample has been exposed to air [268]
- *Wafer cleaning* (standard RCA and Piranha wet cleaning) affecting the topmost SiO_2 [290]
- *Partial oxidation of implanted Si* during annealing either by residual humidity from the annealing ambient or by humidity that has penetrated before into the damaged oxide [268, 290]
- *Oxide swelling*, which appears after low energy IBS. It could result from various effects such as ion sputtering (negative swelling), incorporation of implanted material, Si oxidation, changed SiO_2 density, or defect creation [290, 295]
- *Reactive annealing ambient* (e.g., N_2/O_2 mixture), which reduces the amount of implanted Si by oxidation but on the other hand improves electrical properties due to the better curing of oxide defects [288]

Irradiation-based concepts for synthesis of Si NCs based on ion beam mixing of interfaces [296] could deliver in particular an alternative to low energy IBS that eliminates external influences on the NC formation at phase separation. For that

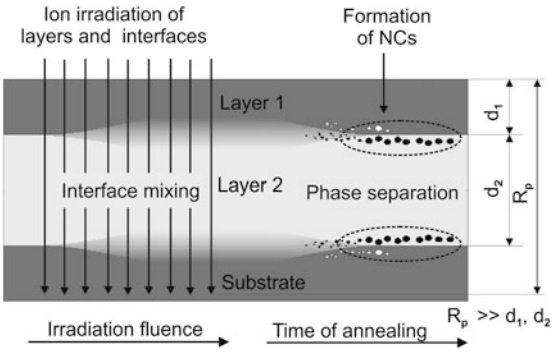

Fig. 4.64 Scheme of ion beam-induced self-alignment of a NC δ-layer near a layer/substrate interface by ion irradiation through the interface and subsequent thermal treatment leading to the phase separation in the ion mixed nonstoichiometric near-interface layer through precipitation and Ostwald ripening of NCs

purpose, the complete transistor gate stack (gate oxide and poly-Si gate electrode) is irradiated by Si ions and will be described in the following chapter.

4.4 Ion Beam Mixing of Interfaces

Although there are possibilities to tailor the mean NC size (mainly by variation of ion fluence, annealing temperature, and time) at conventional IBS, the possibilities for tailoring the NC size distribution by the variation of ion implantation parameters are rather limited. Ion irradiation not only causes supersaturation and damage to the substrate but also affects the interface between a thin layer and the substrate or interfaces between thin stacked layers. As schematically shown in Fig. 4.64 primary energetic ions produce collisional cascades which cause substantial interface mixing leading to nonstoichiometric and nonstable phases near the interface.

Subsequent annealing restores the interface region rapidly via spinodal decomposition. However, the tails of the mixing profiles do not reach the recovered interfaces by diffusion, thus, phase separation proceeds via nucleation and growth of NCs near the interface. The competition between interface restoration and nucleation self-aligns nearly monodispersive δ-layers of NCs in proximity to the interface. Self-organization of a δ-layer of Ge NCs in SiO_2 has been found [262, 297] close to the Si/SiO_2 interface after appropriate Ge^+ implantation into a SiO_2 layer on a Si substrate. The NC δ-layers were found when the following conditions were fulfilled: (1) a negligibly small amount of ions is implanted in the Si/SiO_2 interface region, and (2) the cascade of energetic O and Si recoils produced by primary collisions initiate a few displacements per atom (dpa) in the Si/SiO_2 region. Different contributions to the self-organization of NC δ-layers have been described and investigated by kinetic MC simulations and reaction–diffusion equations [298]. As an example, the positioning of a Ge-NC δ-layer near the SiO_2/Si interface without Ge^+ implantation into this region is shown in Fig. 4.65. The Ge^+ implantation ($E = 350$ keV, $D = 5 \times 10^{16}$ cm^{-2}) into a 500 nm thick SiO_2 layer was carried out in such a way that the maximum of the implanted profile ($R_p = 211$ nm)

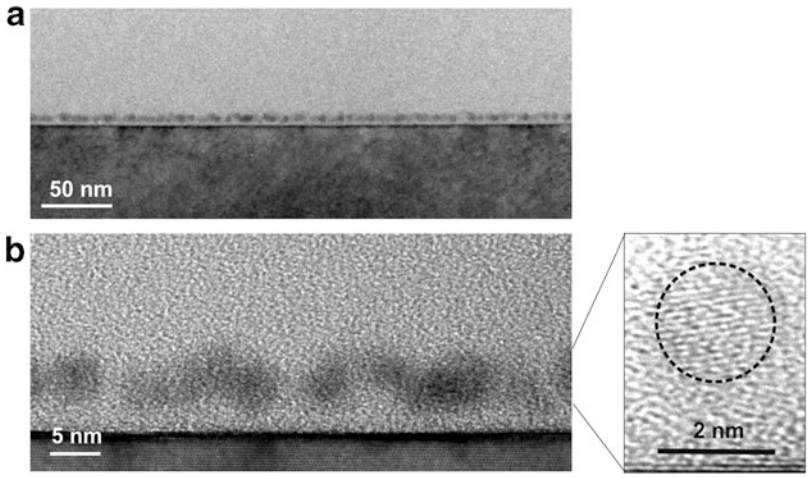

Fig. 4.65 Formation of NCs at flat interfaces under ion irradiation: (**a**) XTEM image overview of a Ge NC δ-layer next to the SiO_2/Si interface; (**b**) HRTEM cross-sectional image of an individual Ge NC with resolved <111> crystal lattice planes of the nanocrystal

is located far away from the SiO_2/Si interface. The Ge concentration in the tail of the implanted profile reaching the interface is below 0.5 at.% and can be neglected.

After annealing of this sample no Ge NCs have been observed near the interface. Ion irradiation (Si^+, $E = 450$ keV, $D = 5 \times 10^{15}$ cm^{-2}, $R_p \approx 720$ nm) through the SiO_2/Si interface before or after Ge^+ implantation in SiO_2 induces a self-aligned δ-layer of Ge NCs as shown in Fig. 4.65. In the ion mixed nonstoichiometric SiO_x ($x < 2$) layer during annealing (1,000 °C, 1 h), tiny Si precipitates form to which Ge atoms attach during diffusion towards the Si substrate. The miscible Ge/Si precipitates grow with increasing annealing time forming nearly pure Ge NCs with a denuded zone of ~3 nm in between the NC layer and the substrate.

Ion irradiation not only affects flat interfaces but also curved interfaces of embedded NCs [298–300]. Thus, NC atoms can be mixed out by recoils of collisional cascades into the surrounding matrix. If these atoms are mobile in the host matrix, their steady state concentration is given by the detailed balance of detachment and attachment processes at the NC interface. The attachment of impurity atoms at the NC interface is mainly a thermally activated process whereas detachment of atoms from NCs can be thermally activated or caused by displacements of the collisional cascade. At higher irradiation temperature, the thermally activated detachment dominates and at low-temperature detachment of NC atoms becomes temperature independent, i.e., detachments are governed by ion beam mixing. An analytical model of the steady state of a NC under ion irradiation, which includes ion beam mixing at interfaces of NCs and impurity diffusion in the host matrix was developed and checked using kinetic lattice Monte Carlo simulations by Heinig et al. [298]. Based on this model a new method of re-assembling of a given NC size distribution using ion-induced "inverse Ostwald

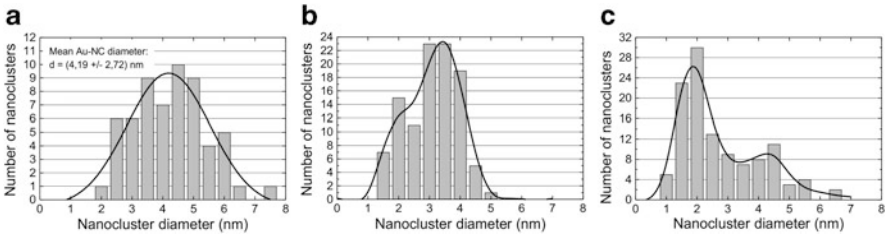

Fig. 4.66 Evolution of the size distribution of Au NCs formed by 330 keV Au^+ implantation with a fluence of 2×10^{16} cm^{-2} and annealing at 1,000 °C for 1 h in dry O_2 (**a**), under subsequent 4.5 MeV Au^+ irradiation of 5×10^{15} cm^{-2} at 190 °C target temperature (**b**), and 1×10^{16} cm^{-2} at 200 °C target temperature (**c**)

ripening" (IOR) was predicted, which should allow even the formation of monodispersive NC distributions. An experiment has been performed [300] in order to prove the predictions for IOR. In a 480 nm thick SiO_2 layer, Au NCs were synthesized by Au^+ implantation ($E = 330$ keV, $\Phi = 2 \times 10^{16}$ cm^{-2}, $R_p = 102$ nm) and subsequent annealing at 1,000 °C for 1 h in dry oxygen. The evaluation of high resolution XTEM images showed that the mean NC diameter d_{NC} in the depth region ($R_p \pm 15$ nm) was 4.2 nm with a FWHM of 2.7 nm (Fig. 4.66a).

The same sample was after it irradiated with 4.5 MeV Au^+ ions at 200 °C with a flux density of 3.9×10^{11} $cm^{-2}s^{-1}$ to study the evolution of the initial NC size distribution under ion irradiation. 4.5 MeV Au^+ ions had a projected range of $R_p = 1.06$ μm and they came to rest deep in the Si substrate, i.e., no Au^+ ions were deposited in the region of the initial Au NC depth distribution. The mean size of Au NCs decreases with increasing fluence of 5×10^{15} cm^{-2} and 10×10^{15} cm^{-2} (see Fig. 4.66b, c, respectively). Furthermore, an increase of the NC density and a decrease of the width of the size distribution with increasing ion fluence were found. This experimental result is in good agreement with theoretical predictions. A quantitative comparison fails due to the lack of reliable values of diffusivity and solubility of Au in SiO_2.

The approach for ion irradiation induced self-alignment of Si NCs near SiO_2/Si interfaces also has been applied to the fabrication of nonvolatile multidot floating gate memory devices [296]. For this application a MOS-like Si/SiO_2/Si structure was selected and submitted to Si^+ ion irradiation to mix the interfaces of this layer stack. Thus, sandwiched between the stable phases of SiO_2 and Si, unstable nonstoichiometric SiO_x ($x < 2$) phases are formed. Annealing restores the upper and lower SiO_2/Si interfaces by spinodal decomposition. However, the tails of the Si atom mixing profiles do not reach the recovered interfaces by diffusion, thus, phase separation proceeds via nucleation and growth of Si NCs in SiO_2. The competition between interface restoration and nucleation self-aligns δ-layers of Si NCs in SiO_2 along the two interfaces. This self-alignment of δ-layers of Si NCs with the SiO_2/Si interfaces has been predicted by atomistic computer simulations [301] and is shown in Fig. 4.67.

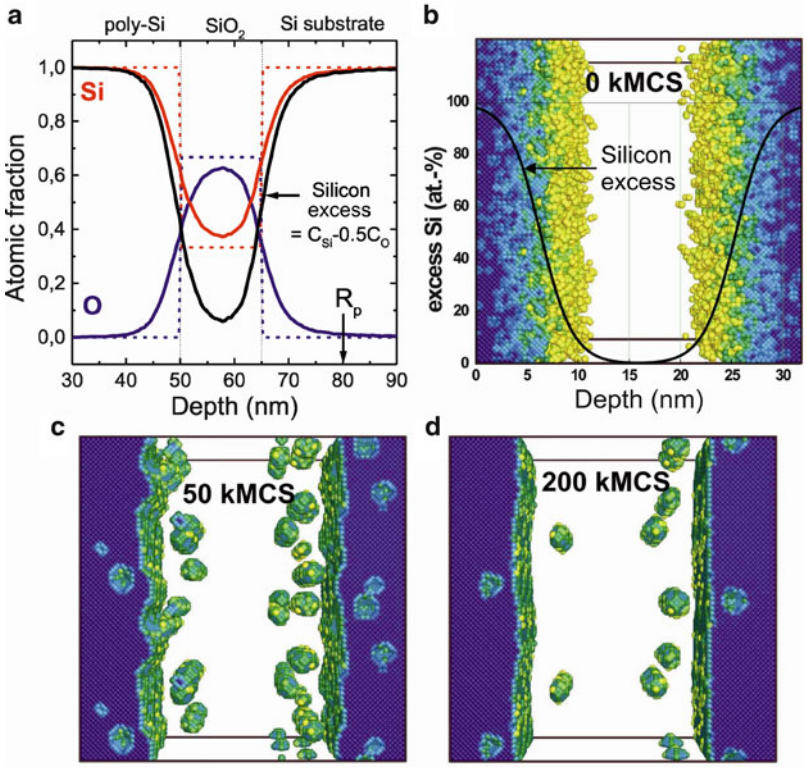

Fig. 4.67 Self-aligned Si NC formation by ion irradiation of SiO_2/Si interfaces: (**a**) TRIDYN results of Si ion irradiation ($E = 50$ keV, $\Phi = 1 \times 10^{16}$ cm^{-2}) through a layer stack of 50 nm poly-Si, 15 nm SiO_2, into the Si substrate. KLMC simulation snapshots referring (**b**) to the as-irradiated state, (**c**) to the early state of phase separation, and (**d**) to a later stage

As shown in Fig. 4.67 the Si precipitates in SiO_2 have developed to Si NC δ-layers which are aligned with the SiO_2/Si interfaces. The mean Si NC diameter is 2 nm and the mean distance from the interfaces is 2 nm, too. In each δ-layers, the Si NC areal density is in the order of 10^{12} cm^{-2}. This prediction has been verified experimentally by energy filtered transmission electron microscopy (EFTEM) [302]. As can be seen in Fig. 4.68, bright and dark areas are visible in dark and white regions of the SiO_2 layer, respectively.

These spherical regions refer to Si NCs in the oxide. Accordingly, the Si NCs are separated from the SiO_2/Si interfaces by a mean distance of 3 nm, i.e., they are aligned in a δ-layer at each interface. The mean diameter of the NCs was estimated to be 3 nm. These morphological features are in accordance with the KLMC simulation predictions from [301].

For memory device fabrication, the ion irradiation-based concept for synthesis of Si NCs experiments was carried out on 150 mm (100)Si wafers covered with a 15 nm thermally grown SiO_2 layer and a 50 nm poly-Si layer deposited by LPCVD

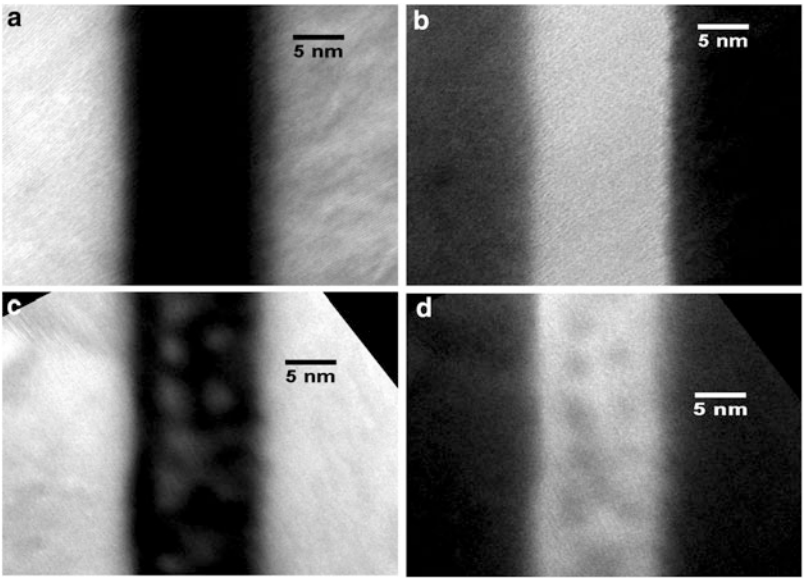

Fig. 4.68 Energy-filtered (X)TEM images of the poly-Si/SiO_2/Si structure: (**a**, **b**) referring to the as-deposited state and (**c**, **d**) after Si^+ ion irradiation ($E = 50$ keV, $\Phi = 7 \times 10^{15}$ cm^{-2}) and postirradiation annealing ($T = 1{,}050$ °C, $t = 120$ s) [302]. In EFTEM images (a,c) recorded with electrons of an energy loss between 14 and 18 eV the Si substrate and the poly-Si layer appear bright – in contrast to dark SiO_2 regions. For an energy loss window between 20 and 36 eV, the Si substrate and the poly-Si layer appear dark, the SiO_2 regions however bright (b,d).

on top of the SiO_2 layer. The upper poly-Si layer was used as a capping layer to prevent any influence of contaminants from ambient and annealing atmosphere (mainly humidity) on the NC formation process in the thin gate oxide [268]. The poly-Si/SiO_2/Si stack was irradiated with 50 keV Si^+ ions at fluences in the range of 3×10^{15}–1×10^{16} cm^{-2}. After ion irradiation a highly n^+-doped and 250 nm thick poly-Si gate was deposited onto the irradiated stack. Subsequently, the samples were annealed (RTA) at different temperatures (950–1,100 °C) and times (5–180 s) and further processed for the fabrication of n-channel MOSFETs in a standard 0.6 µm CMOS process line. Electrical measurements of memory properties show that devices exhibit significant memory windows at low gate voltages. Devices with a memory window of about 0.5 V for write/erase voltages of –7 V/+7 V and a programming time of $t_{pp} = 10$ ms have been achieved. In terms of memory window and transistor characteristics, an ion irradiation fluence of (5–7) $\times 10^{15}$ Si^+ cm^{-2} and annealing at $T_A = 1{,}050$ °C for $t_A = 30$ s appear as promising conditions for devices fabrication (see Fig. 4.69a). The memory window can be increased by annealing at higher temperatures ($T = 1{,}100$ °C) and/or for longer times (>120 s) proceeding to further phase separation Si NC formation. As shown in Fig. 4.69b, in this case a large stable memory window of $\Delta V_{th} \sim 3$ V can be achieved.

No degradation in memory windows was observed for NC memory devices after 10^7 write/erase cycles with $V_{pp} = +7$ V/−7 V, $t_{pp} = 1$ ms programming conditions

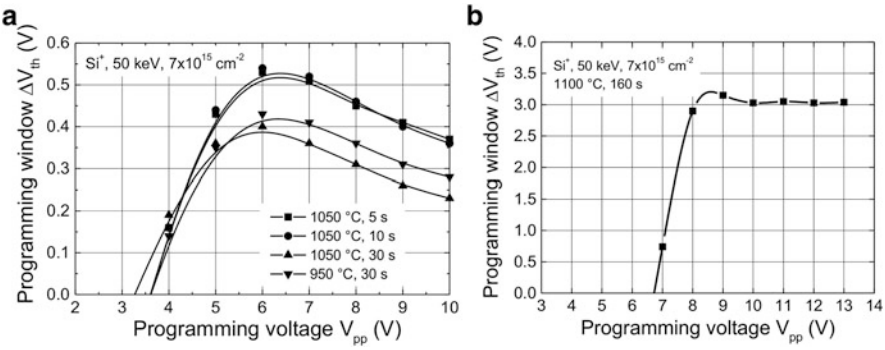

Fig. 4.69 Memory window ΔV_{th} versus programming voltage V_{pp} (pulse length $t_{pp} = 10$ ms) of n-channel MOSFETs with self-aligned Si NCs in the gate oxide. Si^+ irradiation was performed at an ion energy of 50 keV and a fluence of 7×10^{15} cm^{-2}: (**a**) for low thermal budget at different RTA annealing parameters; (**b**) for high thermal budget and annealing at $T = 1{,}100$ °C for 160 s

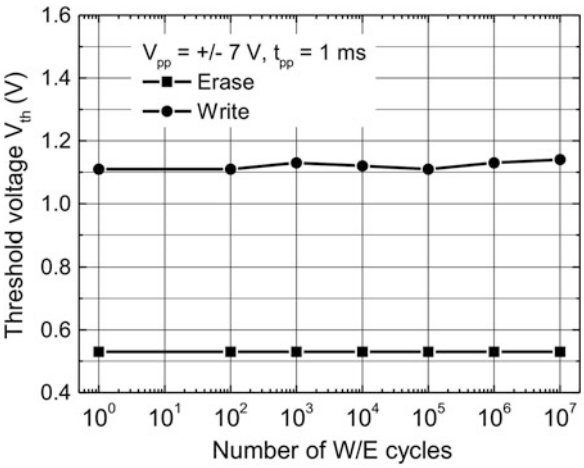

Fig. 4.70 Endurance characteristics of nMOSFETs obtained with write/erase voltages of $V_{pp} = \pm 7$ V and pulses of $t_{pp} = 1$ ms. The sample was irradiated with 50 keV Si^+ ions at a fluence of 7×10^{15} cm^{-2} and annealed at 1,050 °C for 30 s

(Fig. 4.70), which means that the fabricated memory devices exhibit a superior endurance. It was found that data retention time tested at 85 °C is too low for EEPROM application (100 days at room temperature and 8 h at 85 °C). The fabricated nMOS devices exhibit maximum memory windows at low gate voltages indicating that the charge storage nodes are located near to the Si/SiO_2 interface. This implies the possibility of direct charge carrier tunneling into Si NCs during low programming voltages. The lowering of the programming window at programming voltages $V_{pp} > 6$ V (Fig. 4.69a) can be explained by trap-assisted tunneling

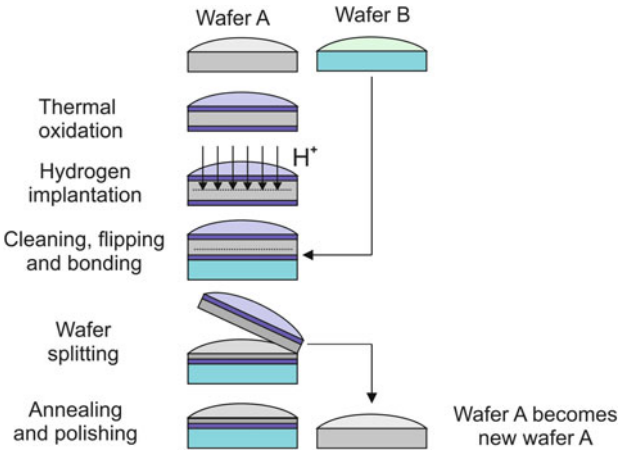

Fig. 4.71 Schematic process flow of SOI wafer fabrication by Smart Cut based on hydrogen implantation, wafer bonding, layer splitting, and final wafer polishing. Wafer A can be reused as substrate for SOI processing

through the gate insulator. Besides retention, all electric parameters of the devices fulfill current requirements to nonvolatile memory devices. The low data retention might be explained by direct re-tunneling of charge carriers to the channel which could be a common problem of multidot floating-gate memories.

4.5 Ion Beam Slicing of Thin Layers (Smart-Cut for SOI and Solar Cells)

High fluence of inert gases or hydrogen can be used for exfoliation of thin layers of crystalline materials to be placed on any kind of substrates (dielectric, glass, plastic, quartz, amorphous silicon, crystalline semiconductor, etc.). This technology, called "Smart Cut" (or Ion Cut), was developed at LETI Laboratories, Grenoble, France, in 1991 and involves the implantation of H^+ ions into silicon. Among the SIMOX process (see Sect. 4.3.1) the Smart Cut process is mostly used for SOI wafers production. SOI wafers made by Smart Cut technology possess less defects in the top Si device layer compared to SOI wafers made by SIMOX. As shown in Fig. 4.71 the Smart Cut process is based on the principles of ion implantation and wafer bonding [303–305].

This process requires two starting silicon wafers (A—seed wafer and B—handle wafer) to produce the SOI wafer. The first step is the thermal oxidation of wafer A. The oxide layer with a thickness in the range of some tens of nanometer until some micrometer will become the buried oxide (BOX) in the final SOI wafer. High-fluence ion implantation of light ions (H^+, He^+) through the SiO_2 into the underlying silicon substrate forms a damaged layer at and around the projected ion range

R_p. After that wafer A is bonded to wafer B, forming the substrate of the final SOI wafer. The bonded wafer pair is subsequently heated so that the wafers split along the gas-implanted plane. The removed portion of the wafer A will now become substrate for another smart cut wafer. The Smart Cut SOI wafer is now annealed at high temperature, after that polished and ready for device processing. The main process parameters are the following:

- High-fluence ion implantation (H^+) through the SiO_2 layer forms the layer for later cutting. The ion fluence is in the range of 3.5×10^{16}–1×10^{17} cm^{-2}. At this stage microcavities or micro bubbles are formed at R_p, the size and density of which depend on the implanted fluence, implantation energy, fluence rate, and implantation temperature. The thickness of the Si layer to be splitted later can be tailored in the range from 0.1 μm up to 13.5 μm by selecting corresponding ion energies between 10 keV and 1 MeV, respectively.
- Hydrophilic bonding of the implanted wafer to a handle wafer (either bare or SiO_2 capped) at room temperature [306]. The handle wafer plays a key role as a stiffener and provides the bulk silicon under the BOX layer in the SOI structure. Before bonding the two wafers are cleaned by a modified RCA cleaning procedure to remove particles, contaminants, and to form hydrophilic surfaces on both wafers. The bonded wafer pair undergoes a heat treatment at ~200 °C to form a strong chemical bond at the bond interface between the wafers.
- Two-step thermal treatment of the joined wafer pair leads to splitting. The first annealing is carried out typically at 400–600 °C during which the implanted hydrogen ions diffuse within the implanted layer (defect-enhanced diffusion) forming H_2 gas bubbles of high internal pressure. The evolution of these bubbles proceeds via Ostwald ripening. Finally, with increasing annealing time the bubbles coalesce leading to crack propagation along the plane of the bubble network leaving a thin monocrystalline Si layer on the surface of the carrier wafer on top of the thermal grown SiO_2 layer. The subsequent high-temperature annealing step is typically performed at 1,100 °C for 2 h to remove any silanol groups from the bonding interface and to achieve a high quality SiO_2/Si interface.
- Final chemical mechanical polishing (CMP) of the Si top layer (about 50–100 nm) of the SOI structure is carried out to remove micro-roughness and surface defects. Standard parameters of the micro-roughness and the Si layer thickness uniformity are 0.15 nm (RMS) and ±10 nm, respectively [307]. For modern integrated circuit applications (e.g., processors), the thickness of the top Si device layer can be further reduced up to some tens of nanometer.

The defect formation during H^+ implantation and the coarsening (Ostwald ripening) of H_2 microcavities has been intensively investigated and is schematically illustrated in Fig. 4.72. It was shown by TEM investigations that the defective region of the implanted profile (mostly around R_p) contains small platelet-like microcavities with dimensions of about 10 nm long and about 1 nm thick. They appear mostly aligned parallel to the surface, i.e., in a (100)-oriented Si crystal lattice plane. After implantation, the nucleation stage of the cavities is not completed and, for example, at 500 °C an annealing time of ~5 min is required

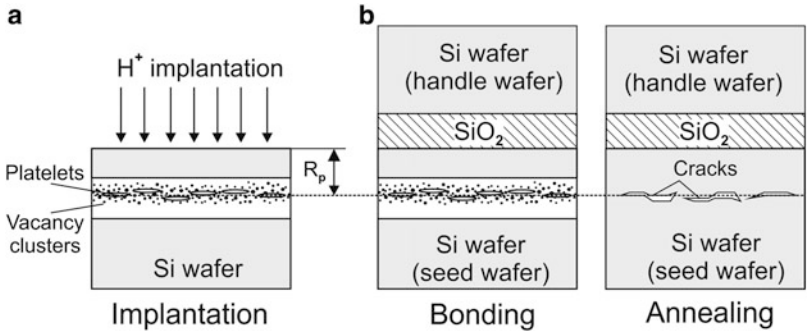

Fig. 4.72 (**a**) Formation of defects (vacancies, vacancy clusters) and H_2 filled microcavities/bubbles during H^+ implantation around R_p in the seed wafer. (**b**) Formation of crack network in the seed wafer during annealing of the bonded wafer pair

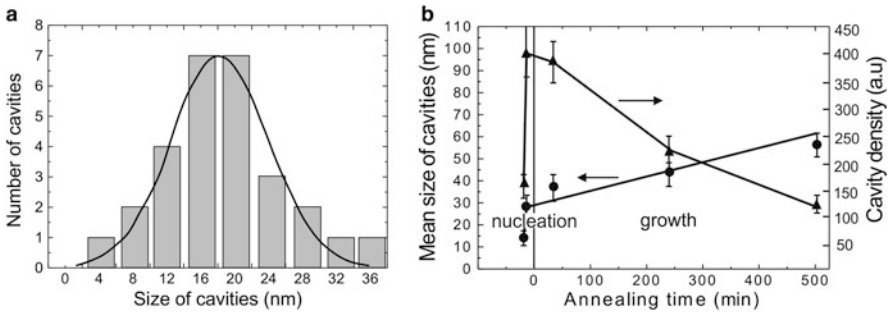

Fig. 4.73 Typical initial distribution of the cavity size (**a**) and (**b**) their evolution in size and density as a function of annealing time at $T_A = 500\ ^\circ C$ (taken from [304])

for coarsening of the cavities [304]. As usually observed in the Ostwald ripening stage, the microcavities grow in size and reduce in density, as shown in Fig. 4.73.

The splitting time has been experimentally measured and varies from a few seconds to some hours sensitively depending on the annealing temperature but also on implantation conditions (ion fluence and energy), Si material properties (doping concentration), and bonding parameters. Remarkably, two temperature ranges with different activation energies for splitting have been identified. In the high-temperature range ($T_A > 530\ ^\circ C$), an activation energy of $E_a \approx 0.5$ eV is obtained which is comparable with the activation energy of 0.48 eV for atomic hydrogen diffusion in silicon. Therefore, it is assumed that in the high-temperature range splitting is controlled by H diffusion. In the low-temperature range ($T_A < 500\ ^\circ C$), the activation energy is higher [$E_a = (2.2–2.5)$ eV] and assumed as the sum of two activation energies involving hydrogen diffusion (0.48 eV) and dissociation of Si–H bonds. The dissociation of Si–H bonds greatly depends on experimental conditions. The transition temperature between low- and high-temperature regimes was observed at $\approx 550\ ^\circ C$ [308].

Table 4.6 Smart Cut wafer material properties and process parameters

Wafer parameter	Values
Wafer diameter	$\leq$300 mm
Si device layer thickness	50–100 nm
Si device layer thickness uniformity	$\pm$0.5 nm
BOX layer thickness	100 nm–3 μm
BOX layer thickness uniformity	$\pm$0.1 nm
Surface roughness	0.15 nm
Dislocation density	~100 cm^{-2}
BOX pipe (pinhole) areal density	Non
BOX dielectric electric field breakdown	$>5 \times 10^6$ V cm^{-1}
Implantation parameters	Standard Smart Cut
H^+ ion energy	20–200 keV
H^+ ion fluence	~5×10^{16} cm^{-2}
Implantation temperature	RT–350 °C
Annealing process	500 + 1,100 °C (N_2, Ar)

The thickness of the cleaved Si layer measured by cross-section SEM and TEM imaging is somewhat smaller than the depth R_p of the implanted H profile [309, 310]. As can be obtained from SRIM calculations, the maximum of the H concentration peak is somewhat deeper than the maximum of the damage profile which supports this observation. The results are consistent with the proposed mechanism of preferential H microcavity and bubble formation in the depth region where the highest concentration of defects (damage) is induced by the implantation process.

The Smart Cut process used for mass production significantly lowers the production costs of SOI wafer fabrication, since the H^+ (or He^+) ion fluence is one order of magnitude lower compared to oxygen fluence for SIMOX. The gas implantation can be carried out at room temperature using standard high current ion implantation tools. Compared to the SIMOX process, where high temperatures of $T_A > 1{,}200$ °C and special annealing tools are necessary, at Smart Cut the heat treatment for wafer splitting proceeds in standard furnaces. The material properties for standard Smart Cut SOI wafers together with the corresponding process parameters of H^+ ion implantation for ULSI CMOS circuits are summarized in Table 4.6.

Due to the flexibility of the Smart Cut process it has been used, for example, in crystalline SiC structures which have enabled it to be bonded onto silicon substrate [311]. For other semiconductor materials, the process has been used successfully, for example in Ge [312], GaAs [313], GaN [314], InP [315], and in other materials, e.g., in ferroelectric $BaTiO_3$ (BTO) crystals [316].

The cutting process based on H^+ implantation exhibits an effective and economical method of transferring thin materials layers from bulk substrates onto another substrate material to achieve hetero-material integration. This advantage of the Smart Cut process recently became an interesting technology in the fabrication of thin film solar cells, where thin layers of high quality crystalline semiconductor

materials are transferred and bonded to glass and/or other photovoltaic materials (http://www.sigen.com). Nevertheless, the Smart Cut process has not yet been applied to solar cell mass production. The thickness of the transferred layer is defined by the penetration depth of the H^+ ions which for conventional microelectronic applications is typically <1 μm. Applying high-fluence, high energy implantation of H^+ ions in the energy range of (1–4) MeV, the exfoliation of silicon layers with thicknesses of (15–150) μm, respectively, will be possible. This thickness range represents the thickness gap between thin film solar cells (a-Si, a-Si/μc-Si, CIGS, typically <15 μm thick) and conventional single- or polycrystalline Si solar cells (typically >150 μm thick). The introduction of the Smart Cut process into solar cell fabrication requires electrostatic accelerators supplying H + ions in the MeV ion energy range, which are still too expensive for cost-effective production.

4.6 Ion Beam Erosion, Sputtering, and Surface Patterning (Ripples and Dots)

Surface patterning by ion beam erosion represents nanoscale surface morphologies spontaneously developing from uniform ion bombardment of an initially flat surface in a nonequilibrium self-organization process. Ion beam erosion is routinely used in surface analysis, depth profiling, surface cleaning, and micromachining [317]. Depending on the chemical–physical properties of the eroded substrates and the erosion conditions, it is possible to create ordered submicron, nanoscale surface features like dots and ripples. Highly ordered ripple and dot patterns are observed at erosion with different ions on the surfaces of various substrates, for example of crystalline semiconductors (e.g., Si, Ge, GaSb, and InP), amorphous glasses and thermally grown SiO_2, single-crystalline (e.g., Cu, Ag) and polycrystalline metals (e.g., Ag, Au, Pt). Some elected examples of patterned semiconductor and SiO_2 surfaces are shown in Fig. 4.74.

In Fig. 4.74a–c the direction of the incident ion beam is marked by the arrow. The ion irradiation conditions at off-normal beam direction in Fig. 4.74a–c were the following: (a) Kr^+ ions, $E = 1.2$ keV, $\Phi = 2.2 \times 10^{18}$ cm^{-2}, angle of incidence 15° with respect to the surface normal; (b) Xe^+ ions, $E = 2$ keV, $\Phi = 6.7 \times 10^{18}$ cm^{-2}, angle of incidence 5°; (c) Ar^+ ions, $E = 1$ keV, $\Phi = 1 \times 10^{18}$ cm^{-2}, angle of incidence 45°. In Fig. 4.74d the ion irradiation was carried out at normal incidence with Ar^+ ions at low energy of $E = 0.42$ keV and a fluence of $\Phi = 4 \times 10^{18}$ cm^{-2}.

Ion erosion-induced nanodots, in general, are observed on some materials only during normal incidence of the ion beam onto the substrate surface. In the case of surface ripples, depending upon the off-normal ion beam angle of incidence, ripples with wave vectors either parallel or perpendicular to the beam direction are observed in semiconductors, metals and dielectric materials, and for different and mostly used ion species including Ar^+, Kr^+, and Xe^+. Most results indicate that ripple patterns appear only within a limited range of angles of incidence, which vary between 30° and 70°. However, in contrast to usual observations, Ziberi et al.

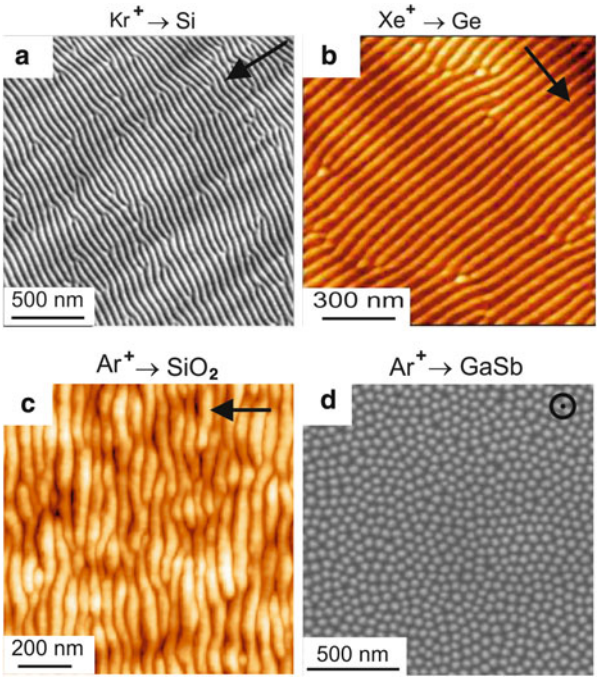

Fig. 4.74 AFM imaged surface pattern induced by ion beam erosion on various substrates. (**a**) ion-eroded (111)Si surface [318]. (**b**) ion-eroded (001) Ge surface from [319]. (**c**) Ion-eroded SiO_2 surface from [320]. (**d**) Hexagonal ordered nanodots with dot size ≈50 nm on GaSb fabricated by normal-incidence ion beam erosion [321]

[319] found that highly ordered ripples occur on 2 keV Xe^+ ion-eroded Si and Ge surfaces at smaller angles of incidence from 5° to 30° (see Fig. 4.74b). They report, that ripple patterns disappear and the surface gets smoothed between 30° and 60°, and evolve again on the surface at incidence angles above 60°. In most cases at incidence angles below a critical angle, which is ~(70–75)°, ripples perpendicular to the ion beam projection on the surface are formed. This critical angle depends mainly on the substrate material, ion species, and ion energy. At incidence angles larger than this critical angle, ripples parallel to the ion beam projection on the surface are formed (see, for example, [322]). Besides the ion beam direction the main process parameters affecting the features of surface pattern are the ion mass, the ion energy, the ion flux and fluence, and the substrate temperature during irradiation. A comprehensive overview about ripple formation under various ion irradiation conditions was published by Chan and Chason [323].

Most experimental studies show that the amplitude of perpendicular-mode ripples and dots increases exponentially with the time up to saturation with increasing fluence. The amplitude saturation may be related to nonlinear effects that become effective after a certain erosion time. At room temperature the ripple wavelength is, in general, not affected by the ion fluence, whereas for samples heated to $T \geq 400$ °C an increase of the wavelength with increasing ion fluence and ion flux was found [324]. At low temperatures, the ripple wavelength is

independent of sample temperature and increases with the ion energy. At higher temperatures, the ripple wavelength λ scales with the following Arrhenius law

$$\lambda \propto (1/T^{1/2}) \exp(-E_\lambda/2kT) \tag{4.11}$$

with T the sample temperature and E_λ an activation energy with values in the range of 0–1.7 eV depending on experimental conditions (e.g., ion mass, ion flux, ion energy) [323].

Furthermore, the wavelength λ is inversely proportional to the square root of ion energy $(E)^{1/2}$. The ripple evolution on heated surfaces and metallic substrates where the crystallinity remains under ion irradiation is more sensitive to the ion flux and ion fluence than on ion beam-amorphized surfaces. Additionally, the ripple and nanodot formation can be significantly influenced by other conditions at high-fluence ion irradiation, for example, by possible deposition of metal contaminants co-sputtered by the incident ion beam from the sample surrounding. As reported in [325, 326] under ion bombardment with Ar^+ ions at normal incidence, the co-deposition of metals can trigger the formation of dot arrays on Si surfaces, which cannot be observed under clean conditions. For example, ion beam erosion experiments performed in ultrahigh vacuum and taking care that the ion beam hits the Si(001) surface only, no ion beam-induced pattern forms on Si for incident angles $\leq 45^\circ$ with respect to the surface normal using 2 keV Kr^+ and fluences of $\approx 2 \times 10^{18}\,\mathrm{cm}^{-2}$ [327]. Therefore, pattern formation at normal or small off-axis ion beam incidence may be substantially influenced by metal impurities coming from broad beam ion sources or which are deposited by sputtering from the target holder surrounding the sample. Ion beam properties, like angle divergence and energy distribution of the ions also significantly influence the evolution and features of surface pattern, which was investigated, for example by Ziberi et al. [328].

Summarizing published studies, focused and unfocused ion beams with varying diameters from tens of nm (FIB) up to ~(1–20) cm (broad beam ion sources) have been used. Though mostly low energies (up to 2 keV) are used, higher ion energies of (4–50) keV for self-organization of surface pattern have also been applied. The wavelength of the ripples λ ranges over two orders of magnitude from several micrometers to several decades nanometers, depending on ion beam parameters and intrinsic materials properties. For example, on semiconductor surfaces (Si and Ge), these surface patterns are nanometer-scale structures, typically with a peak-to-valley amplitude between 0 and 10 nm and a periodicity between 30 and 300 nm. Recently, very regular surface pattern of dots and ripples with an unusual high aspect ratio (amplitude-to-wavelength ratio) of about one were observed at ion irradiation of Ge surfaces with heavy Bi cluster ions [329, 330].

There exist some theoretical models that try to explain the resulting surface topography during ion irradiation. Nevertheless, a complete understanding of the physical processes has not been achieved yet. At present it is widely accepted that the reason for the spontaneous buildup of a self-organized regular pattern is the competition between surface roughening induced by sputter removal of atoms and

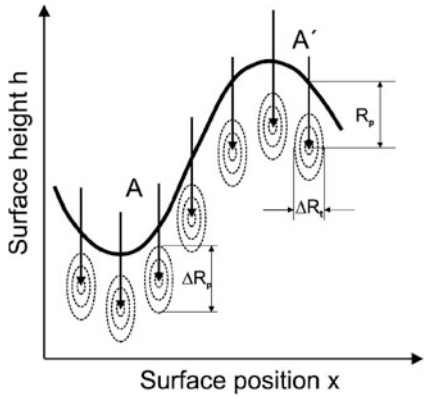

Fig. 4.75 Scheme of the ion erosion-driven Sigmund-instability of planar surfaces. The ellipses contours represent the iso-energy contours of energy deposition. R_p, ΔR_p, and ΔR_t are the projected ion range, the longitudinal and transversal ion straggling, respectively

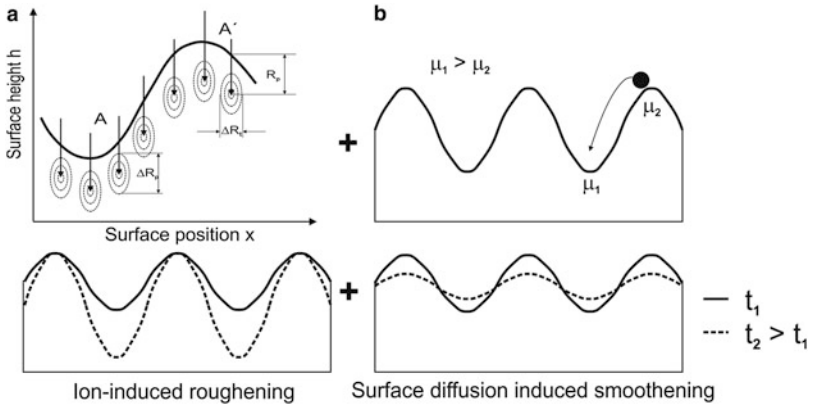

Fig. 4.76 Formation of periodically modulated ripple structures. (**a**) Ion induced roughening due to higher sputter yield at regions of positive surface curvature. (**b**) Surface smoothing by surface migration (diffusion) of atoms transporting material from negative curvature to positive curvature regions

diffusive surface smoothing mechanisms. Most theoretical explanations are based on the Bradley and Harper (BH) erosion-smoothing mechanism [331]. In this continuum model a linear continuum equation is used, which describes the surface topography as a continuous function, and the atomic near-surface structure is not considered to provide a physical understanding of associated atomistic mechanisms.

The BH model describing the sputter morphology evolution and the main features of ripple formation is based on the sputter theory developed by Sigmund [27, 332], which relates the erosion rate to the energy deposition onto the surface by sputtering. As shown in Fig. 4.75 the energy deposition with ellipsoidal shape differently depends on the local surface curvature—it takes place closer to the

surface at convex areas than of concave areas. Thus, the average energy and also the erosion rate are larger in points with positive curvature (A) than in those with negative curvature (A'). Obviously, the surface becomes unstable and the initial surface roughness gets amplified. According to the BH model the curvature dependent erosion rate induced surface roughening competes with opposite processes of smoothing the surface, which leads to the formation of periodically modulated ripple structures, as schematically shown in Fig. 4.76.

In general, the BH model successfully predicts some experimental observations such as ripples orientation, and the exponential growth of the amplitude at short ion irradiation times. However, at long erosion times, the ripples amplitude saturates and this fact cannot be explained by this model. Another implication of BH model is that the wavelength of the ripples should decrease for increasing ion energy, but at room temperature the opposite effect has been experimentally observed. Furthermore, the BH model implies that flat surfaces would remain flat due to the absence of valleys and hills. However, experimental observations show that under ion bombardment, in many cases, different types of structures evolve on initially flat surfaces. To overcome these problems more generalized continuum theories (higher order extensions of the BH equation) have been developed taking into account, for example:

- Nonlinear effects related to the incidence angle dependent sputtering yield which are responsible for the surface roughness saturation with time [333]
- Ion-induced effective surface diffusion (ESD) as a relaxation mechanism [334]
- Stabilizing effect of ion impact induced lateral mass redistribution to offset the BH destabilizing erosive mechanism at low angles [335]
- Other nonlinearities and higher order terms into a most general nonlinear equation [336]
- Re-deposition of eroded material during sputtering onto the surface [337]

However, to explain the self-organization of nanostructures due to ion erosion, more complex mechanisms responsible for the morphological evolution on different material surfaces must be taken into account. Moreover, during the ion bombardment the surface of the substrate is far from equilibrium and many atomistic surface processes become effective. Therefore, atomistic models, based on kinetic Monte Carlo (KMC) and Molecular Dynamic (MD) simulations can give additional useful information about the physical mechanisms behind the macroscopic surface pattern formation (see, for example, [338] and [339], respectively). It has been shown by KMC simulations that the combination of curvature-dependent sputtering based on the Sigmund model with thermally activated surface defect diffusion can produce surface patterns similar to those predicted by the BH theory. The results of MD simulations which take into account the surface mass re-arrangement caused by finite atomistic crater rims can explain, for example, the experimental observation of ripple amplitude saturation, which cannot be accurately predicted by the BH model or any other known numerical or analytical model for the sputter erosion surface instability.

Nowadays, ion-induced nanopatterns become interesting for various technological applications. By controlling the surface pattern down to the nanoscale, the

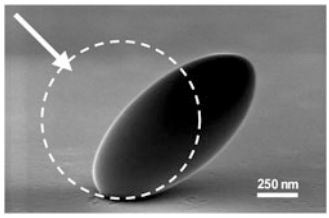

Fig. 4.77 Silica particle on silicon after irradiation with 4 MeV Xe^+ ions to a fluence of 4×10^{14} cm^{-2} at 90 K. The ion beam direction indicated by the *arrow* was tilted 45° from the surface normal. The initially spherical silica particle is indicated by the *dashed circle* [344]

structure and properties of thin films deposited on these surfaces can be tuned. For example, nanostructured ripple surfaces can be used as templates for the growth of thin metal films with predefined magnetic anisotropy [340]. In addition, the self-organized alignment of physical-vapor deposited metal nanoparticle chains or arrays of metallic nanowires with anisotropic optical properties, e.g., dichroitic plasmonic properties, have been recently demonstrated [341].

4.7 Ion Beam Shaping of Nanomaterials

The controlled anisotropic deformation of nanomaterials (e.g., NPs) by their irradiation with high energy ion beams is usually called "ion beam shaping." The energy loss of heavy high energy ions (>2 MeV) in the target is dominated by electronic stopping S_e. Due to the large mass difference between the ion and the electrons, the ion track remains roughly straight and the target atoms around the ion track are electronically excited. The energy in the electronic subsystem is subsequently transferred to the atomic subsystem by means of electron–phonon coupling, resulting in a local lattice temperature which can exceed several thousands of Kelvin [342, 343]. This can lead to the formation of a cylindrically shaped molten ion track with a typical diameter of several nanometers. These processes, called thermal spike model, can therefore induce structural changes in the target material such as amorphization, defect generation, and structural transformations, and finally macroscopic, anisotropic deformation of micro- and nanoscale objects as a result of microscopic processes occurring in the ion track (thermal spike) of individual ion impacts.

Anisotropic deformation of colloidal particles and nanoparticles assembled on a surface or embedded in insulating materials by MeV heavy ion irradiation has been intensively studied in recent years. As shown in Fig. 4.77 the deformation of micrometer-sized colloidal silica ensembles on Si surfaces by irradiation with 0.3–4 MeV Xe^+ ions was employed to change their spherical shape into oblate spheroids [345–347].

Under MeV ion irradiation amorphous silica NPs change their shaping rate into oblate ellipsoids depending on the ion energy and irradiation temperature. The final shaping anisotropy is determined by the ion fluence and the deformation increases with ion fluence and is independent of the ion flux. Size aspect ratios as large as ten

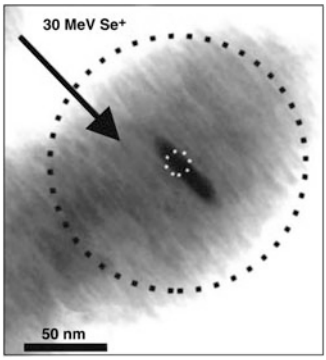

Fig. 4.78 Core–shell particle with a 14 nm-diameter Au core and a 72 nm-thick silica shell after 30 MeV Se^+ ion irradiation at an incidence angle of 45° (*indicated by the arrow*) at a fluence of 2×10^{14} cm^{-2}. The original *spherical shape* of the Au core and the silica shell are indicated by *white* and *black dashed circles*, respectively [351]

have been achieved. It was also found that small silica NPs (~40 nm) show less deformation than large particles (~1,000 nm). The deformation characteristics, expansion in the direction perpendicular to the ion beam and the shrinkage in the direction parallel to the ion beam with remaining constant particle volume, are explained by the viscoelastic thermal spike model of Trinkaus and Klaumünzer [348, 349]. Ion beam modified colloidal ensembles as photonic crystals and colloidal masks are of great interest due to their unique nano- or microstructures with distinct optical properties [350].

Many investigations show that the deformation characteristics for metallic NPs are quite different compared to amorphous silica particles. In [351, 352], for example, core/shell particles with a Au core of 14 nm diameter surrounded by a 72 nm thick silica shell were irradiated with 30 MeV Si^+ ions at a fluence of 2×10^{14} cm^{-2} (see Fig. 4.78).

The observed deformation of the silica shell was consistent with the anisotropic deformation described earlier. However, the Au core has deformed into rods with dimensions of 6 by 38 nm with the major axis along the direction of the ion beam and the minor axis perpendicular to it. Size aspect ratios up to nine were observed for the Au nanorods. Experiments with Au core/silica glass shell NPs have shown that the Au core particle only deforms when the silica shell surrounding the particle is thicker than a critical thickness of ~30 nm. This different deformation behavior of the metallic NP is attributed by the authors to the in-plane mechanical stress in the silica shell acting on the radiation-softened Au core.

Similar ion beam shaping of crystalline metallic NPs was observed, for example, for Co [353], Pt [354], Ag [355], and extensively investigated for Au NPs embedded in silica glass or in thermally grown SiO_2 [352, 356, 357]. As an example, Fig. 4.79 shows a typical shape transformation from spherical NPs with an original diameter of ≈20 nm and embedded in SiO_2 (Fig. 4.79a) into Au nanorods (or nanowires) aligned parallel to the direction of the ion beam.

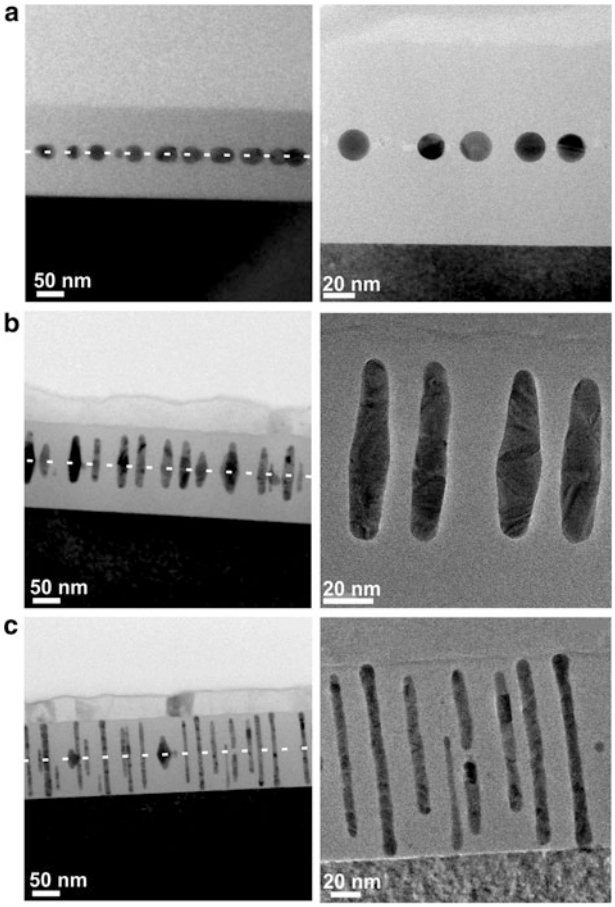

Fig. 4.79 Ion beam shaping of nearly monodispersive spherical Au NPs with a mean diameter of ≈20 nm using 38 MeV I^{7+} ions: (**a**) Au NPs embedded nearly in the middle of a 130 nm thick SiO_2 layer, (**b**) Au particle elongation after irradiation with a fluence of 1×10^{14} cm^{-2}, and (**c**) Au nanorod formation after irradiation with an ion fluence of 2.5×10^{14} cm^{-2}. The *dashed line* indicates the depth plane in which the initial NPs were located

The elongation progressively increases with increasing ion fluence as shown in Fig. 4.79b, c. The Au NPs have been irradiated with 38 MeV I^{7+} ions with a fluence of 1×10^{14} cm^{-2} (Fig. 4.79b) and 2.5×10^{14} cm^{-2} (Fig. 4.79c) leading first to prolate-like nanorods with a length of ≈72 nm, a width of ≈15 nm, and an aspect ratio of about 5 and to pronounced nanowires with a length of ≈140 nm, a width of ≈8 nm, and an aspect ratio of about 17, respectively.

The deformation of spherical Au NPs into nanorods does not follow the visco-elastic thermal spike model and other mechanisms must be the reason. Compared to amorphous insulators it is noteworthy that crystalline metals or freestanding metallic NPs do not deform under high energy ion irradiation, which is ascribed to the

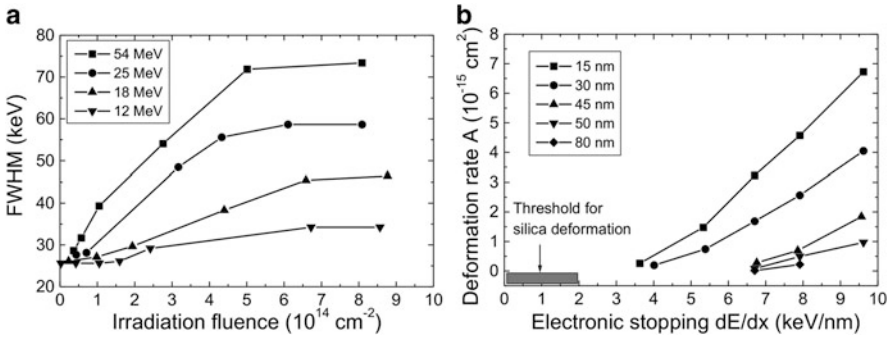

Fig. 4.80 (**a**) Au peak width (FWHM) measured by RBS, representing the Au nanorod size versus fluence for 15 nm Au NPs embedded in SiO_2 under Ag^+ ion irradiation at different ion energies. (**b**) Deformation rate A as a function of electronic stopping S_e in SiO_2 for Au NPs with different diameter of (15–80) nm irradiated with Ag^+ ions [358]

absence of ion track formation due to the large electron mobility of metals, and to fast recrystallization that restores the original state of the material. Thus, the formation of nanorods must be a result of processes that affect both the metal and the surrounding silica matrix and cannot be attributed only to the in-plane mechanical stress in the surrounding silica matrix acting on the radiation-softened Au NP. The shaping behavior of crystalline metallic NPs (e.g., Au) in dependence on ion fluence Φ and deposited energy by electronic energy loss $S_e(x)$ has been investigated in detail by Dawi et al. [358].

The results show the existence of two thresholds, an energy loss threshold (Fig. 4.80a) and a fluence threshold (Fig. 4.80b) for metallic NP elongation, which depend on both NP size and electronic stopping power S_e (ion mass and energy) of the incoming ions. As can be concluded from Fig. 4.80a the energy loss thresholds for elongation of Au NPs with (15–30), (40–50), and 80 nm diameter are around 3.5, 5.5, and (7–8) keV nm^{-1}, respectively. In general, the data from irradiations with different kinds of ions and at different ion energies indicate that a mean threshold of (4–8) keV nm^{-1} in the electronic energy loss can be expected above which deformation of the metallic NPs occurs. In comparison, the electronic energy loss threshold for amorphous NPs (e.g., silica) is much lower and in the range of $S_e \approx$ (0.1–1.8) keV nm^{-1}. The deformation rate A(cm^2) of the NPs in Fig. 4.80a is defined as the relative differential RBS Au peak width change dE per unit fluence dΦ, $A = (1/E)(dE/d\Phi)$. Taking into account the first data points (above the threshold) of the relative change of the Au RBS peak FWHM versus fluence, and defining $dE/d\Phi$ as the slope of the linear width increase, A can be plotted versus the electronic energy loss S_e in the SiO_2 matrix. In general, the ion fluence threshold depends on the ion mass and energy and decreases with increasing ion energy and ion mass. With increasing NP size the fluence threshold for NP deformation increases. Typical values of the fluence threshold for metallic NP deformation can be expected in the range between 5×10^{13} and 5×10^{14} cm^{-2}.

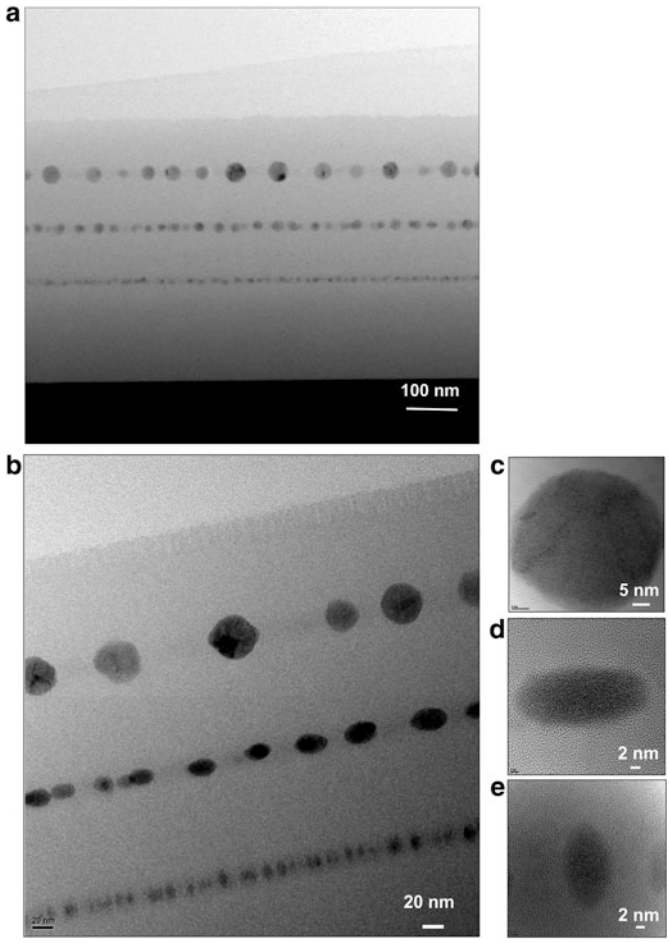

Fig. 4.81 Cross-section (X)TEM image of the as prepared sample with Ge NPs with different sizes of 8, 18, and 37 nm from top to down (**a**). Overview image (**b**) and high-resolution images (**c**–**e**) of the sample after irradiation with 38 MeV I^{7+} ions at a fluence 1×10^{14} cm^{-2}. The largest Ge nanoparticles remain spherically and consist of a mixture of polycrystalline and amorphous regions (**c**). The oblate (**d**) and rod-like (**e**) Ge particles are completely amorphous

Thermal spike calculations of the temperature elevation around the NP are in correlation with the increase of the deformation rate with increasing ion track radius, i.e., with increasing electronic stopping power of the incoming ions. For the deformation of metallic NPs embedded in a silica matrix, two possible mechanisms for deformation can be considered: (1) The nanoparticle responds to the stress field generated in silica by ion tracks squeezing the NP by the surrounding matrix (indirect mechanism). (2) The ion track overlaps with both the NP and the silica matrix, giving rise to transient gradients (chemically, thermally, mechanically) acting on the involved metal atoms of the NP (direct mechanism). In experiments for metallic NP deformation (elongation) in SiO_2, the energy loss

by electronic stopping is higher than the threshold for silica deformation and in-plane stress fields in the silica matrix are always present.

Contrarily to ion beam shaping of metallic NPs embedded in silica, the deformation of crystalline semiconducting Ge NPs evolves with shrinking of the NP in the ion beam direction and expanding perpendicular to the direction of the ion beam which was experimentally observed by Schmidt et al. [359, 360]. As shown in Fig. 4.81 at given irradiation conditions (38 MeV I^{7+} ions at a fluence 1×10^{14} cm^{-2}) the deformation and the shape depend on the size of the spherical Ge NPs.

The largest Ge nanospheres in the top layer kept spherical (cf. Fig. 4.81c), whereas medium-size Ge spheres in the middle layer became oblates (cf. Fig. 4.81d), and smaller ones, in the bottom layer, shaped rod-like (cf. Fig. 4.81e). The high-resolution cross-section (X)TEM image in Fig. 4.81c shows that the large unshaped spherical Ge nanoparticles are in a mixed polycrystalline and amorphous state. The oblate and rod-like Ge particles in Fig. 4.81d, e, respectively, reveal a completely amorphous structure. At a higher fluence of $\approx 5 \times 10^{14}$ cm^{-2} the larger Ge NPs of Fig. 4.81c become smaller, obviously due to partial ion-induced Ge dissolution into SiO_2. These Ge NPs reduced in size start to deform too. This effect was also observed during irradiation of metallic NPs embedded in silica, for example in [357].

At present, the different shape evolution of metal (Au, Ag, Pt, etc.) and semiconductor (Ge) NPs is not yet fully understood. One possible approach for the physical description accounts for the well-known in-plane stress generated by ion tracks in the surrounding silica matrix and for ion tracks overlapping with the NPs the electronic energy relaxation in the whole nanoparticle.

Molten SiO_2 tracks are expected if the energy of electronic stopping in SiO_2 per length unit exceeds the threshold of $dE_{el}/dx > 2$ keV nm^{-1}. In most cases the molten track diameter is small compared to the nanoparticle diameter. The interaction of the molten tracks with the nanoparticles seems to dissolve some material from the NPs in the SiO_2 matrix [357, 359], which has been not yet considered by the model. Whereas in SiO_2 the deposited electronic stopping energy relaxes within a rather confined volume into the phonon system leading to narrow molten tracks, in metals and in Ge the electronic energy relaxes in larger volumes, here we assume in the melts if the following relation is fulfilled:

$$\frac{dE_{NP}^{el}}{dx} \cdot L_{NP} \geq \frac{4\pi}{3} \cdot R_{NP}^3 \cdot H_{NP}^{melting} \cdot \rho_{NP}, \tag{4.12}$$

where L_{NP} is the length of the ion track in the nanoparticle, R_{NP} is the radius of the nanoparticle, $H_{NP}^{melting}$ is the heat of melting, and ρ_{NP} is the density of the NP. Thus, for a given electronic stopping power a spherical nanoparticle melts under the condition that

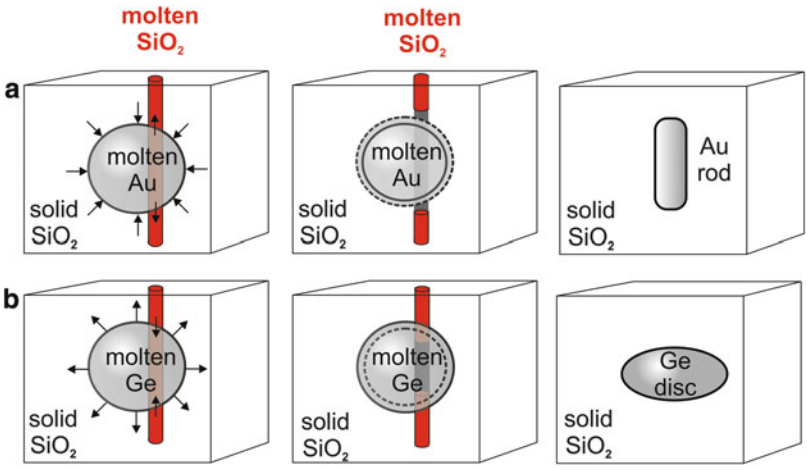

Fig. 4.82 Scheme of different deformation for metal (Au) and semiconducting (Ge) NPs proposed by Heinig (private communication). (**a**) NP elongation in direction of the ion beam direction due to the expansion of the molten metal into the molten SiO_2 track. (**b**) NP shrinking in direction of the ion beam due to the contraction of the molten semiconductor material

$$R_{\mathrm{NP}}^{\max} \leq \sqrt{\frac{3 \cdot \mathrm{d}E_{\mathrm{NP}}^{\mathrm{el}}/\mathrm{d}x}{2\pi \cdot H_{\mathrm{NP}}^{\mathrm{melting}} \cdot \rho_{\mathrm{NP}}}}. \tag{4.13}$$

where melting of NPs is restricted to $L_{NP} \leq 2{\cdot}R_{NP}$. If we set both sides of (4.13) equal we find the largest spherical NP with radius $R_{\mathrm{NP}}^{\max}$ which can be molten by electronic stopping. For example, in the case of 38 MeV I^{7+} ion irradiation the electronic stopping power in Ge is $\mathrm{d}E_{\mathrm{el}}/\mathrm{d}x = 7.7\ \mathrm{keV\ nm^{-1}}$ and we get a maximum particle radius of $R_{\mathrm{NP}}^{\max} \approx 16\,\mathrm{nm}$, which means that Ge particles with smaller sizes will be molten. This estimated size threshold for melting is in agreement with the experimentally found shaping of the three different nanosphere sizes (Ge NPs of 9 nm radius are shaped, whereas NPs of 18.5 nm radius remain spherically, see Fig. 4.81c). The particle radius of 18.5 nm for the largest Ge nanoparticles is above the threshold of $R_{\mathrm{NP}}^{\max} \approx 16\,\mathrm{nm}$. It should be noted that below the shaping threshold, which can be assumed to be $R_{\mathrm{NP}}^{\max}$, two shaping modes have been identified (Fig. 4.81d, e): NPs with radii being much larger than the molten track diameter shape into disks, whereas rod-like shaping is found for NPs with radii comparable with the molten ion track radius. It appears that both are necessary for Ge NP shaping with swift heavy ions, molten tracks in SiO_2, and molten Ge NPs.

The following driving forces for tailoring of NP size distributions, shapes, and anisotropies of nanoparticles by high energy heavy ions can be assumed: (1) the materials dependent electronic stopping power, (2) the volume change of the silica matrix and the NPs upon melting, (3) the asymmetric hydrodynamic flow due to stress field hysteresis, (4) the far-from-equilibrium steady-state solubilities, and (5) the strongly anisotropic diffusion coefficients. One of the most striking effects upon melting of the NPs as schematically shown Fig. 4.82 is its volume change $\pm\Delta V/V_{\mathrm{s}}$

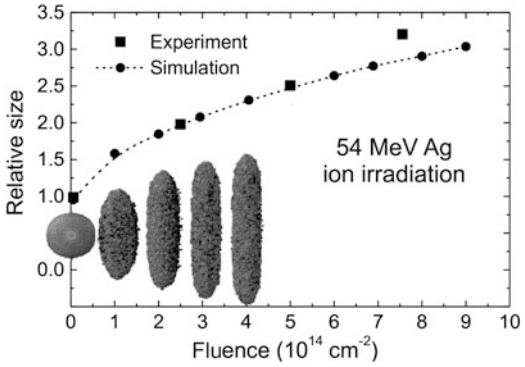

Fig. 4.83 KLMC simulation of the Au nanoparticle deformation. The relative particle size $l/2R_0$ is shown as function of the fluence for 54 MeV Ag^+ ion irradiation. l is the length of the Au rod and R_0 is the radius of the initially spherical Au NP. The insets show the simulated Au NP shapes after irradiation with 1×10^{14}, 2×10^{14}, 3×10^{14}, and 4×10^{14} cm^{-2} (Heinig KH, private communication)

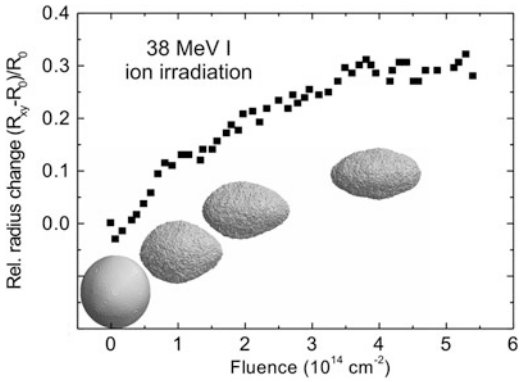

Fig. 4.84 KLMC simulation of the Ge nanoparticle deformation. Shown is the relative particle radius change $(R_{xy}–R_0)/R_0$ as a function of the fluence for 38 MeV I^{7+} ion irradiation. Here, R_{xy} is the larger radius of the oblate spheroid and R_0 is the radius of the initially spherical Ge NP. The insets show the simulated Ge nanoparticle shapes after irradiation with fluences of 1×10^{14}, 2×10^{14}, and 4×10^{14} cm^{-2} [360]

with V_s the solid state volume, for example, contraction by ≈ -5 % for Ge or expansion by about $\approx +5$ % for Au.

When the NP melts it is forced to expand (Au) or to reduce (Ge) its volume. Because it is embedded in SiO_2 a high tensile stress is built up. During the extremely short melt periods of 10...100 ps, this stress can relax only partly via the molten SiO_2 track, not via the solid SiO_2 matrix. Thus, the intersection interfaces between molten SiO_2 and molten Au moves outward and the molten Ge moves into the NP to allow for the molten Au expansion and for the molten Ge contraction, thereby reducing the tensile stress. Within a few tens of picoseconds the molten NPs cool down, reaching due to the extreme cooling rate a strongly

under-cooled liquid state. From that state it re-solidifies suddenly without a chance of re-contraction (Au) or re-expansion (Ge) in the track, which is now solid. Thus, after melting and re-solidification of NPs in SiO_2 a hysteresis of the volume change appears. In the proposed model, this hysteresis is assumed to be the driving force for NP shaping into rods or disks. Based on this model kinetic Monte Carlo simulations described in [195] have been carried out taking into account spatio-temporal temperature profiles of the molten tracks, the volume change of the silica matrix and the NPs upon melting, and the temperature-dependent solubility and diffusivity of the NP material in molten silica surrounding the NP. Two examples of KLMC simulation results for the deformation behavior during high energy ion irradiation of Au and Ge nanoparticles are shown in Figs. 4.83 and 4.84, respectively.

KLMC simulation results in Fig. 4.83 are compared with experimental results taken from [358] for the irradiation of Au NPs with 54 MeV Ag ions for different fluences. The simulation was performed for an Au NP size of 15 nm, a track radius of 4.5 nm, and a minimum track length L_{NP} inside the NP of $R_0/2$. The insets in Fig. 4.83 show the side views of the NPs at the positions of corresponding fluences. The transformation of the spherical Au NPs into elongated nanorods agrees very good with the relative size change experimentally observed by Davi et al. [358] (see experimental data in upper curve in Fig. 4.80b). Assuming that ~1 % of the Au NP volume change upon melting and subsequent shrinking during resolidification is pressed into each ion track the simulation results nicely fit the experimental data.

The simulation in Fig. 4.84 was performed for a Ge NP size of 16 nm, a track radius of 3.8 nm, and a minimum track length L_{NP} of $R_0/2$. The insets of Fig. 4.84 show the side views of NPs at the positions of the fluence which they experienced. The shaping agrees nicely with the experimentally found shapes (see Fig. 4.81b, d), even the required fluences agree. The saturation of shaping at high fluences seen in Fig. 4.84 results from the minimum track length L_{NP}, because too flat Ge NPs will be no longer molten. The model works only for NPs being larger than the track radius, and therefore small Ge NPs becoming elongated (Fig. 4.81e) cannot be modeled. Additionally, a fluence-dependent dissolution of Ge NPs has been observed experimentally which decreases the size of initially not deforming NPs until they shrink below the critical size of (4.12). Afterwards they get a prolate shape too.

The striking agreement between the experiments and the KLMC simulations suggests that the driving force for ion beam shaping is inherently included in the model for atomistic simulations. Finally, the task to identify the microscopic physical origin of driving forces of ion beam shaping remains difficult. Nevertheless, the main behavior of ion beam shaping not only for metal but also for Ge nanoparticles can be satisfyingly described. The experimentally observed growth of very long (~200 nm) Au nanowires at the expense of shorter ones [357] requires an Au transport through the silica matrix which has been also considered in KLMC simulation of ion beam shaping, and a preferred growth of longer nanowires has been observed too (Heinig KH, private communication). Subsequent ion tracks which overlap with the volume of former tracks enable the dissolved Au to diffuse away from the NP, and gold can diffuse track by track from one nanoparticle to another. As the driving force for the preferred Au diffusion from shorter Au

nanorods to longer ones some kind of Ostwald ripening has been identified and KLMC simulations reproduce nicely that experimental finding. The driving force identified so far is related to a strong anisotropy of the mean Au diffusion along the ion track and perpendicular to the track into the surrounding silica matrix.

From application point of view, especially metal nanoparticles (Au, Ag, Cu) are studied extensively, because their near-field and far-field optical response promise, for example, nanophotonic applications for subwavelength light guiding in nanoparticle chains, plasmonic light sources, plasmon lasers, enhanced LEDs, and enhanced solar cells. For these purposes nanorods and nanowires are of special interest since their plasmon resonance frequencies can be tuned over a wide range by varying the aspect ratio and length of the nanoparticles.

4.8 Ion Beam Processing of Other Materials

Ion implantation is a unique technique to modify the near-surface region of a wide range of solid materials independently of many of the constraints associated with conventional processing methods. In most cases materials, such as metals and most semiconductors, are rather insensitive to the electronic part of the energy deposition. Other materials, for example insulating and dielectric materials such as ionic solids, alkali and silver halides, dielectric glasses, and amorphous materials, are quite sensitive to the energy deposited in their electronic systems. The high sensitivity of these materials to ion irradiation makes them particularly attractive for ion beam modification.

Besides the wide application of ion implantation and ion beam synthesis in the semiconductor industry, ion beam methods found application, for example, to the synthesis and modification of metal-nitride layers in metal alloys, and the modification of polymers, insulating optical materials and ceramics. Two general ion beam processing methods are widely used for surface modification of nonsemiconductor materials: scanned or broad beam ion implantation, in which the ion beam is directed toward mostly planar substrate surfaces, and plasma immersion implantation, where the ions hit the surface of nonplanar, three-dimensional, workpieces from all directions. The ion beam treatment is designed to modify only the surface properties of materials without changing their bulk properties. Some of the surface properties that can be modified by ion beam processing are hardness, fatigue, toughness, adhesion, wear, friction, corrosion oxidation, dielectric properties, magnetic properties, superconductivity, resistivity, and catalysis.

4.8.1 Ion Implantation into Metals

The first application of ion implantation into metals was reported in 1969 by Dearnaley [361], who addressed the possibility of improving mechanical and corrosion behavior of steels that are of relevance to the metal processing industry. Ion implantation into metals has shown remarkable improvement in properties, for example, of nitrogen-implanted alloy steels and of nitrogen-implanted aluminum tools for machining high-temperature alloys. An extended overview of ion implantation into metals the reader can find in [362]. Plasma immersion ion implantation (PIII) has introduced another set of opportunities for metal surface treatment by ions and a rapid increase of PIII facilities which are now commercially available. The PIII treatment of metals introduced by Conrad et al. [363] in 1986 can achieve advantages over directed beam implantation. The effects of implanting nitrogen into metal surfaces previously or simultaneously enriched, for instance with carbon and/or boron by vapor deposition which is known as ion beam-assisted deposition (IBAD), also have been found application to metals.

As demonstrated in many studies (see, for example, [364–368]) ion implantation can modify the surface-sensitive mechanical (wear, friction, hardness, adhesion, fatigue) and chemical (corrosion, oxidation, electrochemistry, catalysis) properties of steels. For example, fatigue life has been extended by as much as a factor of two, the coefficient of sliding resistance can be reduced by as much as a factor of 100, the surface hardness can be increased by 2–3 times, and the wear resistance increased by a significant amount. Studies have concentrated on the use of nitrogen ions, but the use of C^+, B^+, Ti^+, and Mo^+ ions has also shown promising results. Today the PSII processing is already used in large-scale manufacturing, such as of automotive parts. A very useful application of this process is in the ion implantation of medical prostheses based on Ti alloys (e.g., Ti6Al4V). For instance, artificial hip joints with complicated shapes have been implanted with nitrogen ions for wear and hardness improvement to increase the lifetime of such devices [369].

N^+ is the most common ion used for metallurgical applications and causes pegging of microcracks, filling of lattice spaces in crystalline structures of the polycrystalline material, and chemical reactions to form nitride compounds, giving new lattice properties. One example is N^+ ion implantation of different austenitic stainless steels (e.g., DIN 1.4301 or AISI 304) with high chromium content where a substantial increase in hardness by converting Cr in the near-surface layers to chromium nitride and a wear improvement (reduction factor) up to a factor of 30 have been achieved. Improvements by B^+ and C^+ implantation into steels have been also reported. These improvements are explained in analog to metallurgical boridizing and carburizing of metal surfaces to form metal-boride and -carbide phases. N^+ ion implantation alone or combined N^+/C^+ implantations are also applied to mold steels which are usually made from FeCr ferritic stainless steels with higher carbon content (e.g., Cr12MoV, X36CrMo17, or X155CrVMo12.1) [370, 371]. These materials do not withstand high-temperature thermal processing, often suffering significant distortions or significant decrease of hardness at temperatures

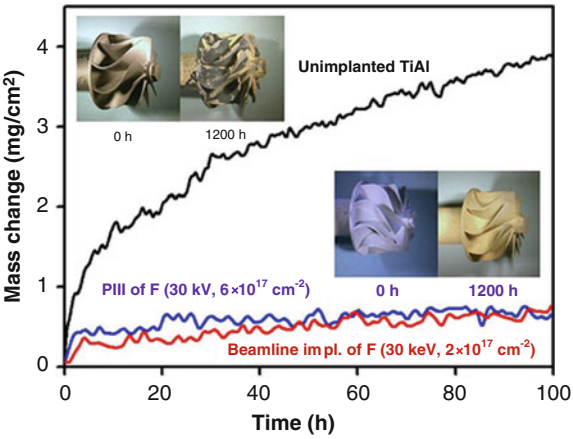

Fig. 4.85 Comparison of the oxidation behavior of γ-TiAl before and after processing by BLII and PIII with F^+ ions. Insets: As-received (untreated) turbo-charger rotor (*top left*). Exposure in air at 1,050 °C for 100, 600, and 1,200 h. The same rotor after fluorine treatment (*bottom right*). Exposure in air at 1,050 °C for 100, 600, and 1,200 h

above (200–300) °C. Ion implantation can substantially improve the surface properties with negligible distortion or oxidation effects, and induce high surface hardnesses (~1,100–2,000 Vickers hardness) resulting in substantial increases in tool lifetimes [372]. For injection and extrusion screws used, for example, in molten plastic pumps ion implantation produces a low friction, wear-resistant surface on the screw and allied components. Interesting industrial applications of N^+ ion beam processing of metals are, for example, in manufacturing of steel knives for cutting meat, plastic, paper, or rubber for which a life improvement by a factor of four to seven could be reached. Compared to other ion applications, for example, to tooling the field of medical implants, such as steel knives was advancing more quickly. This is because ion implantation appears to be the only surface modification technique that can successfully harden titanium alloy's surface (e.g., Ti/6AI/4V) without compromising surface finish, dimensionality, or cosmetic appearance.

Other examples are titanium alloys (titanium aluminides) which are used as light weight materials where ion implantation (PIII) can help to improve substantially materials properties under harsh environmental conditions. Despite of their good mechanical properties they cannot be applied yet, for example, in aero engines due to their insufficient oxidation resistance at temperatures above roughly 800 °C. Using implantation of halogens, especially F^+ ions, into the subsurface zone of the TiAl components the oxidation behavior of TiAl alloys can be improved significantly [373–376]. For turbine blades, as examples for real TiAl components, PIII implantation of F^+ ions extracted from a Ar/CH_2F_2-RF-plasma (400 W, 500–750 Hz) by negative pulses of −30 kV, 10 ms using a total number of 1×10^6 pulses was carried out leading to a retained fluorine dose of $\approx 6 \times 10^{17}$ cm^{-2}. The investigations showed an increased high-temperature oxidation resistance after PIII treatment due to the formation of thin protective alumina layer on the surface in contrast to a fast growing, nonprotective thick mixed oxide layer (TiO_2/Al_2O_3) on untreated samples during high-temperature

oxidation in air. The formation of a growing Al_2O_3 layer is promoted by the fluorine. This so-called fluorine effect leads to the preferential intermediate formation of gaseous aluminum fluorides at elevated temperatures if the fluorine content at the surface is being kept within a certain concentration range. These fluorides are then converted into solid Al_2O_3 due to the high oxygen partial pressure of the high-temperature environment forming protective pure Al_2O_3. The thin Al_2O_3 surface layer is not be damaged by high-temperature corrosion and is stable even under thermocyclic conditions and in wet and aggressive environments which are typical for technical high-temperature applications [377, 378].

Fig. 4.85 shows an example for improvement of high-temperature oxidation resistance of TiAl alloys by plasma-immersion ion implantation (PIII) and beamline ion implantation (BLII) of fluorine ions. The curves for mass change versus time representing the oxidation behavior were measured by thermogravimetric analysis (TGA) and studied during thermocyclic exposure. The ion beam treated samples (red and blue curve) show a significant lower mass gain (higher oxidation resistance) than the untreated sample (black curve). After optimization of implantation parameters for the F^+ ion PIII the same good TGA results compared to optimum beamline implantation of fluorine (25 keV, 2×10^{17} cm^{-2}) were found. In this case, the PIII parameters were the following: pulse length 10 ms, bias voltage 30 kV, RF power 400 W, frequency 750 Hz, 1×10^6 pulses, gas flow CH_2F_2/Ar = 15/5 sccm. The retained fluorine fluence was 6×10^{17} cm^{-2}. For comparison, the upper left and bottom right insets in Fig. 4.85 show the change of turbine rotor tools during high-temperature exposure before and after ion treatment, respectively.

For other Al alloys and Al, the improvement of tribological properties by the formation of an aluminum nitride surface layer has been also demonstrated using low energy (1–10 keV) N^+ ion implantation into heated samples. AlN exhibits high hardness and wear resistance as well as significantly enhanced corrosion resistance. The kinetics of aluminum ion beam nitriding has been intensively investigated by Telbizova et al. [379–381]. It was shown that a thin stoichiometric nitride layer is formed at the aluminum surface by diffusion of aluminum atoms from the bulk underlying the AlN layer. An inhomogeneous AlN layer may form if the process of ion beam nitriding is limited by Al diffusion rather than by N^+ ion supply. At otherwise identical conditions, an increased sample temperature will result in a more homogeneous nitride layer.

The ion implantation into metals and metal alloys is continuing to develop in different metallurgical areas. Ions other than nitrogen are increasingly used, for example, rare earth elements such as yttrium to produce high lubricity and corrosion-resistant surfaces. These developments of ion implantation will continue to extend the options to use moderate temperature processing methods while still achieving improved surface properties for increasing tool life. Ion implantation in metals becomes an important and promising technique for surface nanomodification, especially in case of ultra precision tools where the depth of modification

should be in range of 30–100 nm. Important advantage of this technique is the fact that surface dimensions are not changed after implantation. This is especially important for ultra precision tools where the subsequent dimension correction would be extremely difficult.

4.8.2 Ion Implantation into Polymers

Conventional ion beam implantation has been introduced to modify the surface properties of polymers, giving an improvement in such qualities as hardness, conductivity, and biocompatibility. Plasma immersion ion implantation (PIII) as an alternative method has the advantages of high implantation rates and conformal treatment of three-dimensional polymer or plastic surfaces. Ion beam treatments modify the outermost surfaces of polymers without affecting their bulk properties. The ion beam processing of polymers has led to dramatic improvements in their hardness. For example, after implantation, the surfaces of some polymers may become harder than stainless steel, although the process may actually be a result of carbonization of the polymer rather than by the synthesis of new compounds by implantation itself. Physical and chemical effects appearing during ion implantation into polymers are described more in detail in [382].

The effects of ion implantation in the energy range from several keV to MeV on polymers have been widely reported. The energy release of fast ions in polymers produces pronounced changes in their chemical and physical properties associated with the breaking and rearrangement of the original chemical bonds. Changing the ion fluence three main modifications in polymers can be distinguished: (1) at low ion fluences (~10^{14} cm^{-2}) cross-linking between chains and chain scissions is observed; (2) with increasing ion fluence ($\geq 10^{15}$ cm^{-2}) the original polymer structure is heavily damaged and exhibit properties close to those of hydrogenated amorphous carbon; (3) at very high fluences (~10^{16} cm^{-2}) graphitization of the material occurs [383].

In contrast to ion irradiation of semiconductors and metals in polymers, the electronic stopping (S_e) and nuclear stopping (S_n) act simultaneously and both are responsible for the change of their properties. It has been assumed that a complete modification of irradiated polymer already occurs in the single-ion track, forming a graphitized ion track due to the so-called linear energy transfer [LET—energy deposited per unit ion path length (eV nm^{-1})]. The successive overlap of many ion tracks with increasing ion fluence induces a complete change of chemical bonds of the material. Thus, characteristic saturation fluences for each combination of ion mass and energy are observed. The results of differently generated chemical effects, such as modification of functional groups, destruction of the aromaticity, formation of a three-dimensional compacted network, depend not only on the implantation parameters (total deposited energy, electronic stopping S_e, nuclear stopping S_n, and ion fluence) but also upon the chemical composition and structure of polymers [384, 385].

A particularity during ion irradiation of polymers is that various gaseous molecular species are released, for example hydrogen and less abundant heavier molecules which are scission fragments. Cross-linking occurs when free dangling ion or radical pairs on neighboring molecular chains join. Mechanical, physical, and chemical property changes in polymers are determined by the magnitude of cross-linking and scission. Cross-linking enhances the mechanical stability (increase of hardness, improvement of wear, and starch resistance) and decreases the in-diffusion and solubility of chemical solvents while scission degrades mechanical strength and increases dissolution of polymers in solvents. The electrical conductivity and optical density increase by ion irradiation due to the formation of cross-links and conjugated double and triple bonds in the polymer. Furthermore, the charge carrier mobility can be increased by cross-linking which facilitate the transport of charge carriers across molecular chains of the polymer. Additionally, ion irradiation induces changes in the electronic structure and induces defects such as anions and radicals (donors) and cations (acceptors). Thus, electrons can be excited by visible light, and colour changes occur because of increased light absorbance. With increasing ion fluence more energetic blue light is absorbed first and the color changes from pale yellow to reddish brown and eventually to a dark color. At very high ion fluences, a metallic luster appears because light is scattered by electrons similar to the effect of free electrons in metals. Industrial application examples are:

- The fabrication of conductive integrated circuit trays using N^+ or Ar^+ ion implantation into modified poly-phenylene oxides to prevent IC failure caused by static electricity
- The fabrication of scratch, UV absorbent and oxygen penetration protected transparent polymers by N^+, C^+, or He^+ ion implantation for sun caps, goggles, cosmetic bottles, touch screens, etc.

The application of ion beams to polymer modification can be roughly classified into three main fields: (1) surface modification of mechanical, chemical, and electrical properties mostly by noble gas and metal ion implantation, (2) modification of optical properties by nitrogen and noble gas ion implantation, and finally, (3) synthesis of polymer composite materials containing metal NPs by implanting metal ions, which is motivated by potential optical applications, such as magnetooptic data storages and nonlinear optical devices [386]. The nonlinear optical properties of polymer composites containing metal NPs, for example Ag NPs in PMMA, are based on the dependence of their refractive index on incident light intensity. The metallic NPs embedded in a polymer which exhibit an enhancement of local electromagnetic field enhancement stimulates the linear optical absorption of metal NPs (surface plasmon resonance, SPR). Between suitable dielectric materials (e.g., SiO_2, Al_2O_3, MgO) for embedding metallic NPs, polymers will be of increasing interest.

Mainly noble gas and nitrogen ion, but also metal ion (Ag, Cu, Fe, Cr, Pt, Pd, W, Ti, etc.), halogen ion (F, Cl), and silicon ion implantations have been investigated. For polymer modification the selected ion energies are in the medium energy range (30–500 keV) and relatively high fluences in the range from 10^{14} to 10^{17} cm^{-2} are

implanted. The large number of different polymers and the change of their properties by ion implantation/irradiation cannot be described considerably in the frame of this chapter.

4.8.3 Ion Implantation into Insulating Optical Materials

Ion implantation is one of the most effective techniques for alteration of optical properties including reflectivity, absorption, luminescence, and refractive index in a large number of insulating optical materials [238, 387]. The ion beam-induced optical properties are closely dependent on ion species, ion energy, and ion fluence. Mostly investigated insulating optical materials are noncrystalline glasses, nonlinear optical crystals, photorefractive crystals, and laser crystals. The ion implantation in optical crystals is mainly focused on the investigation and optimization of ion-implanted planar and channel waveguides because optical waveguide structures are the most fundamental parts of integrated optical circuits in the field of modern optical communication. Recent activities in this field of research and development have been reviewed by Chen et al. [388, 389]. It is evident that until now, ion implantation has been used to produce waveguide structures in more than 100 optical materials, including glasses, inorganic crystals, semiconductors, and organic materials (e.g., PMMA).

Ion irradiation (H^+, He^+, Ar^+, etc.) induced defects and compaction of the glass network in different *glasses* lead to an increase of the refractive index (RI) by a few percent [390]. Implanting chemically active ions (e.g., N^+, Li^+) into fused silica (SiO_2) the RI can be increased significantly, for example from 1.46 to 1.96 with increasing Li^+ ion fluence [391]. *Fused silica* is widely used in the manufacture of optoelectronic devices because the coupling between fused silica and optical fibers is much easier resulting from the small difference between their RIs. Different planar waveguides have been produced in fused silica by high energy ion implantation of light (e.g., H^+, 0.5–1.0 MeV, ~10^{16}–10^{17} cm^{-2}) and heavy (C^+, 2–3 MeV, ~1×10^{15} cm^{-2}) ions. *Amorphous silicate and phosphate glasses* are important optical materials due to their good mechanical performance, high chemical stability, and very high transparency in the infrared wavelength region. Rear earth doped (e.g., Nd^{3+} and Er^{3+}) glasses have been extensively used as hosts of waveguide amplifiers and waveguide lasers with RIs tailored by high energy ion irradiation (e.g., O^+, ~5 MeV, ~1×10^{15} cm^{-2}).

For optical waveguide applications, the change of the refractive index n by ion implantation/irradiation has been intensively investigated in *crystalline optical materials*. In these insulating covalent crystals (e.g., niobates), the value of n is linked with the bond polarizability α of the lattice ions and the material density (volume) via the Lorentz–Lorenz expression:

$$\left(\frac{\Delta n}{n}\right) = \left(\frac{(n^2-1)\cdot(n^2+2)}{6n^2}\right)\cdot\left(\frac{\Delta V}{V}+\frac{\Delta\alpha}{\alpha}+F\right), \tag{4.14}$$

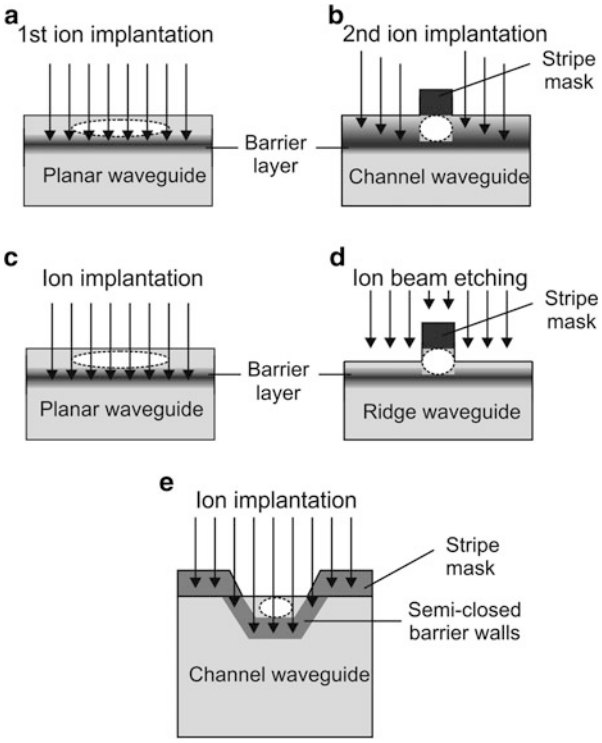

Fig. 4.86 Ion beam processing for barrier-confined waveguides. (**a**) Planar waveguide on the sample surface formed by single implantation step to create a buried vertical barrier wall; (**b**) channel waveguides produced by multiple ion energy implantations to build the side barrier walls with a stripe mask; (**c**) vertical barrier-confined planar waveguide; (**d**) selective etching of the planar waveguide surface regions by patterned etching; (**e**) ion implantation with stripe masks of wedged cross sections, constructing trapezoid cross-section channel waveguides confined by closed barrier walls inside the substrate

where the value of F accounts for the ion beam-induced structural changes of composition, lattice structure, density, and stress of the insulator material. Materials crystallinity implies an efficient packing density of lattice ions and therefore radiation damage, and finally amorphization, reduces the density and then the RI is reduced, for example in $LiNbO_3$, the RI can be lowered up to 10 % by ion irradiation [392].

In the development of integrated optics for communications and signal processing, the control of the RI in a lithographically patterned and well-defined region of the surface or in a buried region is essential. The prerequisite for optical devices is the definition of optical waveguiding paths which result from the trapping of light in a region of high refractive index. Ion implantation in insulating materials always changes the refractive index and, depending on the target material and the ion processing, can either increase or reduce the value of RI. Therefore, if the RI is raised the ion implantation is made into the guiding region. Alternatively, if the RI is decreased, ion irradiation is used to implant the regions adjacent to the guide. Hence, for optically active devices it may be preferable to reduce the index of the regions which act as waveguide boundaries, and so to preserve the optimum crystal quality within the guide. Different waveguide structures have been proposed and realized combining photolithographic patterning, etching, and ion implantation/

irradiation. The ion beam processing for the fabrication of planar, channel, and ridge waveguides is schematically shown in Fig. 4.86.

By optimization of ion implantation and, if necessary, annealing parameters most of these implanted materials show good light guiding properties with acceptably low loss and only minor degradation of bulk crystal properties.

In the majority of cases, the ion implantation in waveguide technology is carried out by high energy (0.5–5 MeV), light ion implantation (H, He), and sometimes by heavy ion implantation (C, O, P, Si, etc.). The light ion implantation requires higher fluences of 10^{15}–10^{16} cm^{-2} than the heavy ion implantation to form the waveguide structure. In some materials, fluences of only ~10^{13} cm^{-2} are sufficient for the heavy ion-implanted waveguide formation. Usually, when high energy H^+ and He^+ ions are implanted into optical crystal substrates, an optical barrier with a lower RI compared to the substrate will be formed, leaving a nearly undisturbed region between the optical barrier and the substrate surface. In the case of heavy ions implanted into the optical crystal, the electronic energy loss S_e is strong enough to change the optical properties in the near-surface region. This change surely weaks the birefringence of the implanted region, resulting in the increase of the RI. The confinement of light in this type of waveguides relies on the enhanced RI layer so that they are sensitive to light polarization direction.

References

1. Furukawa S, Matsumura H, Ishiwara H (1972) Theoretical considerations on lateral spread of implanted ions. Jpn J Appl Phys 11:134
2. Ryssel H, Ruge I (1978) Ion implantation. Akademische Verlagsgesellschaft Geest & Portig K.-G, Leipzig
3. Gibbons JF (1968) Ion implantation in semiconductors – part I: range distribution theory and experiments. Proc IEEE 56:295
4. Ziegler JF, Biersack JP, Littmark U (1985) The stopping and range of ions in matter. Pergamon, New York
5. Maes H, Vandervorst W, van Overstraten R (1981) Impurity profiles of implanted ions in silicon. In: Wang FY (ed) Impurity doping processes in silicon. North-Holland, Amsterdam, p 443, Ch. 7
6. Gibbons JF, Mylroie S (1973) Estimation of impurity profiles in ion implanted amorphous targets using joined half-Gaussian distributions. Appl Phys Lett 22:568
7. Hofker WK (1975) Implantation of boron in silicon. Philips Res Rep Suppl no. 8, pp 1–126
8. Tasch AF, Shin H, Park C et al (1989) An improved approach to accurately model shallow B and BF_2 implants in silicon. J Electrochem Soc 136:810
9. Tasch AF, Yang SH, Morris SJ (1995) Modeling of ion implantation in single-crystal silicon. Nucl Instrum Methods Phys Res B 102:173
10. Zhang H, Gao M, Xu L et al (2008) United Gauss-Pearson-IV distribution model of ions implanted into silicon. Solid State Ionics 179:832
11. Posselt M (1994) Crystal-Trim and its application to investigations on channeling effects during ion implantation. Radiat Eff Def Solids 130–131:87
12. Möller W, Eckstein W (1984) TRIDYN – a TRIM simulation code including dynamic composition changes. Nucl Instrum Methods Phys Res B 2:814
13. Wolf S, Taylor RN (2000) Silicon processing for the VLSI Era, vol. 1: process technology, 2nd edn. Lattice Press, Sunset Beach, CA, p 375

14. Klein K, Park C, Tasch AF et al (1991) Analysis of the tilt and rotation angle dependence of boron distributions implanted into <100> silicon. J Electrochem Soc 138:2102
15. Roy K, Mukhopadhyay S, Mahmoodi-Meimand HS (2003) Leakage current mechanisms and leakage reduction techniques in deep-sub micrometer CMOS circuits. Proc IEEE 91:305
16. Klein KM, Park C, Tasch AF (1991) Modeling of cumulative damage effects on ion-implantation profiles. Nucl Instrum Methods 59–60:60
17. Posselt M, Schmidt B, Murthy CS et al (1997) Modeling of damage accumulation during ion implantation into single-crystalline silicon. J Electrochem Soc 144:1495
18. Simonton R Tash AL (1996) Channeling effects in ion implantation into silicon. In: Ziegler J (ed) Ion implantation science and technology. Ion Implantation Technology Co., pp 293–390
19. Gibbons JF (1972) Ion implantation in semiconductors – part II: damage production and annealing. Proc IEEE 60:1062
20. Morehead FF, Crowder BL, Title RS (1972) Formation of amorphous silicon by ion bombardment as a function of ion, temperature, and dose. J Appl Phys 43:1112
21. Meyer JW, Erikson L, Davies JA (1970) Ion implantation in semiconductors. Academic, New York
22. Harris JS (1971) The effects of dose rate and implantation temperature on lattice damage and electrical activity in ion- implanted GaAs. In: Ruge I, Graul J (eds) Ion implantation in semiconductors. Springer, Berlin, pp 157–167
23. Westmoreland JE, Marsh OJ, Hunsperger RG (1970) Lattice disorder produced in GaAs by 60-keV Cd ions and 70-keV Zn ions. Radiat Eff 5:245
24. Haskell JD, Grant WA, Stephens GA, Whitton LJ (1971) The influence of various parameters on radiation damage in GaP. In: Ruge I, Graul J (eds) Ion implantation in semiconductors. Springer, Berlin, pp 193–198
25. Krimmel EF, Pfleiderer H (1973) Implantation profiles modified by sputtering. Rad Eff 19:83
26. Teichert J, Bischoff L, Hessey E et al (1996) Cobalt disilicide interconnects for micromechanical devices. J Micromech Microeng 6:272
27. Sigmund P (1969) Theory of sputtering. I. Sputtering yield of amorphous and polycrystalline targets. Phys Rev 184:383
28. Winterbon KB, Sigmund P, Sanders JB (1970) Spatial distribution of energy deposited by atomic particles in elastic collisions. Mat Fys Medd Dan Vid Selsk 37(14):1–73
29. Colligon JS (1961) Ion bombardment of metal surfaces. Vacuum 11:272
30. Anderson HH, Bay HL (1975) Heavy-ion sputtering yield of silicon. J Appl Phys 46:1919
31. Behrisch R (ed) (1981) Sputtering by ion bombardment. Springer, Berlin
32. Malherbe JB (1994) Sputtering of compound semiconductor surfaces. I. Ion-solid interactions and sputtering yields. Crit Rev Solid State Mater Sci 19:55
33. Malherbe JB (1994) Sputtering of compound semiconductor surfaces. II. Compositional changes, radiation-induced topography and damage. Crit Rev Solid State Mater Sci 19:128
34. Heera V, Prokert F, Schell L et al (1997) Density and structural changes in SiC after amorphization and annealing. Appl Phys Lett 70:3531
35. Bischoff L, Teichert J (1998) Focused ion beam sputtering of silicon and related materials. Research report, FZR-217, Research Center Rossendorf, pp 25–32
36. Philipp P, Bischoff L (2011) Investigations of conducting nano-structures on ta-C films made by FIB lithography. Nucl Instrum Methods Phys Res B. doi:10.1016/j.nimb.2011.08.057
37. Andersen HH (1979) The depth resolution of sputter profiling. Appl Phys 18:131
38. Schwarz SA, Helms CR (1979) An ion knock-on mixing model with application to Si-SiO_2 interface studies. J Vac Sci Technol 16:781
39. Chu WK, Müller H, Mayer JW, Sigmon TW (1974) Residual disorder in Si from oxygen recoils in annealed "through-oxide" arsenic implants. Appl Phys Lett 25:297
40. Sigmon TW, Chu WK, Müller H, Mayer JW (1975) Enhanced residual disorder in silicon from recoil implantation of oxygen and nitrogen by arsenic implants through dielectric layers. In: Namba S (ed) Ion implantation in semiconductors. Plenum Press, New York, pp 633–639
41. Muline RA, Cullis AG (1975) Residual defects in Si produced by recoil implantation. Appl Phys Lett 26:551

42. Petkov MP, Chen CM, Atwater HA et al (2000) A relation between surface oxide and oxygen-defect complexes in solid-phase epitaxial Si regrown from ion-beam-amorphized Si layers. Appl Phys Lett 76:1410
43. Liu HL, Gearhart SS, Booske JH, Cooper RF (2000) Recoil implantation method for ultrashallow $p(^+)$/n junction formation. J Appl Phys 87:1957
44. Shao L, Lu X, Jin J et al (2000) Depth profiles of high-energy recoil implantation of boron into silicon. Mater Res Soc Symp 610:B6.8.1
45. Nastasi M, Mayer JW (1994) Ion beam mixing in metallic and semiconductor materials. Mater Sci Eng R Rep 12:1
46. Tsaur BY, Lau SS, Liau ZL, Mayer JW (1979) Ion-beam-induced intermixing of surface layers. Thin Solid Films 63:31
47. Mayer JW, Lau SS (1983) Ion beam mixing. In: Poate JM, Foti G, Jacobson DC (eds) Surface modification and alloying by laser, ion, and electron beams. Plenum, New York, p 241
48. Matteson S, Paine BM, Grimaldi MG et al (1981) Ion beam mixing in amorphous silicon I. Experimental investigation. Nucl Instrum Methods 182–183:43
49. Heinig KH, Hohmuth K, Klabes R et al (1982) Flash lamp annealing of ion implanted silicon. Radiat Eff Def Solids 63:115
50. Heinig KH, Klabes R, Woittennek H (1980) A description of the laser-induced annealing and diffusion behaviour of implanted silicon crystals. Radiat Eff 47:157
51. Appleton BR, Celler GK (eds) (1982) Laser and electron beam interactions with solids. Elsevier North Holland, New York
52. Shima A (2006) Laser annealing technology and device integration challenges. In: 14th IEEE international conference on advanced thermal processing of semiconductors – RTP 2006, pp 11–14
53. Friedrich D, Bernt H, Hanssen H et al (2007) Laser annealing of power devices. In: 15th IEEE international conference on advanced thermal processing of semiconductors – RTP 2007, pp 263–269
54. Paetzel R, Brune J, Simon F et al (2010) Activation of silicon wafer by excimer laser. In: 18th IEEE international conference on advanced thermal processing of semiconductors – RTP 2010, pp 98–102
55. Chen S, Wang X, Thompson M (2010) Characterization of dopant activation, mobility and diffusion in advanced millisecond laser spike annealing. In: 18th IEEE international conference on advanced thermal processing of semiconductors – RTP 2010, pp 66–70
56. Cohen RL, Williams JS, Feldman LC, West KW (1978) Thermally assisted flash annealing of silicon and germanium. Appl Phys Lett 33:751
57. Bomke HA, Berkowitz HL, Harmatz M et al (1978) Annealing of ion-implanted silicon by an incoherent light pulse. Appl Phys Lett 33:955
58. Lue JT (1980) Arc annealing of BF_2^+ implanted silicon by a short pulse flash lamp. Appl Phys Lett 36:73
59. Fiory AT (2001) Rapid thermal annealing. In: Buschow KHJ et al (eds) Encyclopedia of materials: science and technology. Permagon, Elsevier Science, Amsterdam, pp 8009–8017
60. Kamgar A (1989) Rapid thermal processing of silicon. In: Watts RK (ed) Submicron integrated circuits. Wiley Interscience, New York
61. Roozeboom F, Parekh N (1990) Rapid thermal processing systems: a review with emphasis on temperature control. J Vac Sci Technol B 8:1249
62. Fair RB (ed) (1993) Rapid thermal processing: science and technology. Academic, New York
63. Roozeboom F (ed) (1996) Advances in rapid thermal and integrated processing. Klewer, Dordrecht
64. Sze SM (2002) Semiconductor-device-physics-technology, 2nd edn. Wiley, New York
65. Krynitzky J, Suski J, Ugniewski S (1977) Laser annealing of arsenic implanted silicon. Phys Lett A 61:181
66. Celler GK, Poate JM, Kimerling LC (1978) Spatially controlled crystal regrowth of ion implanted silicon by laser irradiation. Appl Phys Lett 32:464

67. Skorupa W, Gebel T, Yankov RA, Paul S et al (2005) Advanced thermal processing of ultra-shallow implanted junctions using flash lamp annealing. J Electrochem Soc 152:G436–G440
68. Gebel T, Voelskow M, Skorupa W et al (2002) Flash lamp annealing with millisecond pulses for ultra-shallow boron profiles in silicon. Nucl Instrum Methods Phys Res B 186:287
69. Gelpey J, Elliott K, Camm D (2002) Advanced annealing for sub-130 nm junction formation. In: 201st electrochemical society meeting, symposium Q1, rapid thermal and other short-time processing technologies III, May 12–17, 2002, p 735
70. Peuse B, Miner G, Yam M, Elia C (1998) Advances in RTP temperature measurement and control. Mater Res Soc Symp Proc 525:71
71. Singh R (1988) Rapid isothermal processing. J Appl Phys 63:R59–R114
72. Nguyenphu B, Fiory AT (1999) Wafer temperature measurement in a rapid thermal processor with modulated lamp power. J Electron Mater 28:1376
73. Hauf M, Balthasar H, Merkl C, Müller S, Streibel C (1999) Emissivity compensated wafer temperature measurement using intensity-modulated lamp light. In: Roozeboom F et al (eds) Advances in rapid thermal processing. Electrochemical Society, Pennington, NJ, pp 383–390
74. Schietinger C, Adams B, Yarling C (1991) Ripple technique: a novel non-contact wafer emissivity and temperature method for RTP. Mater Res Soc Symp Proc 224:23
75. Saito S, Shishiguchi S, Mineji A, Matsuda T (1998) Ultra shallow junction formation by RTA at high temperature for short heating cycle time. Mater Res Soc Symp Proc 532:3
76. Hebb J, Shajii A (1999) Temperature measurement, uniformity, and control in a furnace-based rapid thermal processing system. In: Roozeboom F et al (eds) Advances in rapid thermal processing. Electrochemical Society, Pennington, NJ, pp 375–382
77. Timans P, Sharangpani R, Thakhur RPS (2000) Rapid thermal processing. In: Nishi Y (ed) Handbook of semiconductor manufacturing technology. Decker, New York
78. Lau SS, Mayer JW, Tseng W (1980) Handbook of semiconductors. North-Holland, Amsterdam
79. Kannan VC, Casey D (1977) Two-step annealing of arsenic-implanted <111> silicon. Appl Phys Lett 31:721
80. Michel AE, Rausch W, Ronsheim PA (1987) Implantation damage and the anomalous transient diffusion of ion-implanted boron. Appl Phys Lett 51:4487
81. Sedwick TO, Michel AE, Deline VR, Cohen SA (1988) Transient boron diffusion in ion-implanted crystalline and amorphous silicon. J Appl Phys 63:1452
82. Fair RB (1990) Point defect charge-state effects on transient diffusion of dopants in Si. J Electrochem Soc 137:667
83. Cowern NEB, Jansen KTF, Jos HFF (1990) Transient diffusion of Ion-implanted B in Si: dose, time, and matrix dependence of atomic and electrical profiles. J Appl Phys 68:6191
84. Jaraiz M, Gilmer GH, Poate JM, de la Rubia TD (1996) Atomistic calculations of ion implantation in Si: point defect and transient enhanced diffusion phenomena. Appl Phys Lett 68:409
85. Suzuki K (2003) Model for transient enhanced diffusion of ion-implanted boron, arsenic, and phosphorous over wide range of process conditions. Fujitsi Sci Technol J 39:138
86. Jones KS, Rozgonyi GA (1993) Extended defects from ion implantation and annealing. In: Fair RB (ed) Rapid thermal processing science and technology. Academic, Boston
87. Talwar S, Wang Y, Gelatos C (2000) Laser thermal processing (LTP) for fabrication of ultra-shallow, hyper-abrupt, highly activated junctions for deca-nanameter MOS transistors. Electrochemical Society Symposium Proceedings PV 2000-9 95
88. Tichy RS, Elliott K, McCoy S, Sing D (2001) Annealing of ultra-shallow implanted junctions using arc-lamp technology: achieving the 90 nm node. In: Proceedings of 9th international conference on advanced thermal processing of semiconductors – RTP 2001, pp 87–93
89. Talwar S, Markle D, Thompson M (2003) Junction scaling using lasers for thermal annealing. Solid State Technol 46:83
90. Borland JO, Matsuda T, Sakamoto K (2002) Shallow and abrupt junction formation: paradigm shift at 65-70 nm. Solid State Technol 45:79
91. Borland JO (2007) 32 nm node USJ implant and annealing options. 15th IEEE international conference on advanced thermal processing of semiconductors – RTP 2007, p 181

92. Mayer JW, Lau SS (1990) Electronic materials science. Integrated circuits in Si and GaAs. Macmillan, New York, pp 183–222
93. Simonton RS, Class W, Erokhin Y et al (2000) In: Nishi Y, Doehring R (eds) Handbook of semiconductor manufacturing technology. New York, Decker
94. Borland JO, Kawski J (1998) Triple well applications profit from MeV implant technology. Semicond Int 21:67
95. Venkatesan S, Lutze JW, Laga C, Taylor WJ (1995) Device drive current degradation observed with retrograde channel profiles. Tech Dig IEDM-95:419–422
96. Parrill TM, Namaroff MJ (1999) Ion implantation productivity for advanced applications. Eur Semicond 1999:44
97. Taur Y, Ning TH (1998) Fundamentals of modern VLSI devices. Cambridge University Press, New York, NY
98. Hori A, Mizuno B (1999) CMOS device technology toward 50 nm region-performance and drain architecture. IEDM Technical Digest International, Washington, DC, pp 641–644
99. Rodder M, Amerasekera A, Aur S, Chen IC (1994) A study of design/process dependence of 0.25 μm gate length CMOS. International electron devices meeting. Technical Digest International, San Francisco, CA, pp 71–74
100. Osborn CM (1990) Formation of silicided, ultra-shallow junctions using low thermal budget processing. J Electron Mater 19:67
101. Schaber H, Criegern RV, Weitzel I (1985) Analysis of polycrystalline silicon diffusion sources by secondary ion mass spectrometry. J Appl Phys 58:4036
102. Aoyame T, Suzuki K, Tashiro H et al (1995) Effect of fluorine on boron diffusion in thin silicon dioxides and oxynitride. J Appl Phys 77:417
103. Murakami T, Kuroi T, Kawasaki Y et al (1997) Application of nitrogen implantation to ULSI. Nucl Instrum Methods Phys Res B 121:257
104. Colombeau B, Smith AJ, Cowern N et al (2004) Electrical deactivation and diffusion of boron in preamorphized ultrashallow junctions: interstitial transport and F co-implant control. Technical Digest IEEE IEDM (2004) p. 971
105. Ota K, Shugihara K, Sayama H et al (2002) Novel locally strained channel technique for high performance 55 nm CMOS. Technical Digest IEEE IEDM (2002) p. 27
106. Hazdra P, Vobecky J, Galster N (2000) A new degree of freedom in diode optimization: arbitrary axial lifetime profiles by means of ion irradiation. ISPSD 2000, May 22–25, Toulouse, France
107. Hazdra P, Brand K, Rubes J, Vobecky J (2001) Local lifetime control by light ion irradiation: impact on blocking capability of power P-i-N diode. Microelectron J 32:449
108. Hazdra P, Vobecky J, Brand K (2002) Optimum lifetime structuring in silicon power diodes by means of various irradiation techniques. Nucl Instrum Methods Phys Res B 186:414
109. Nakano Y, Ishiko M, Tadano H (2002) Deep level centers in silicon introduced by high-energy He irradiation and subsequent annealing. J Vac Sci Technol B 20:379
110. Hazdra P, Brand K, Vobecky J (2001) Effect of defects produced by MeV H and He ion implantation on characteristics of power silicon P-i-N diodes. In: Proceedings of 11th international conference on ion implantation technology 2000, IEEE Press, p 135
111. Hazdra P, Komarnitskyy V (2007) Local lifetime control in silicon power diode by ion irradiation: introduction and stability of shallow donors. IET Circuits Devices Syst 1:321–326
112. Vobecky J, Hazdra P, Homola J (1996) Optimization of power diode characteristics by means of ion irradiation. IEEE Trans Electron Devices 43:2283
113. Ronsisvalle C, Enea V, Abbate C (2011) Effects of back-side He irradiation on MOS-GTO performances. In: Proceedings of 23rd international symposium on power semiconductor devices and ICs (ISPSD) 2011, May 23–26, IEEE Press, San Diego, CA, pp 144–147
114. Deboy G, Marz M, Stengl JP et al (1998) A new generation of high voltage MOSFETs breaks the limit of silicon. Technical Digest IEDM 98, San Francisco, CA, p 683

115. Lorenz L, Deboy G, Knapp A, März M (1999) COOLMOS – a new milestone in high voltage power MOS. Proceedings of ISPSD 1999, Toronto, pp 3–10
116. Saggio M, Fagone D, Musumeci S (2000) MDmesh™: innovative technology for high voltage power MOSFETs. Proceedings of ISPSD 2000, Toulouse, p 65
117. Meijer J, Burchard B, Ivanova K et al (2004) High-energy ion projection for deep ion implantation as a low cost high throughput alternative for subsequent epitaxy processes. J Vac Sci Technol B 22:152
118. von Borany J, Friedrich M, Rüb M et al (2005) Application of ultra-high energy boron implantation for superjunction power (CoolMOS) devices. Nucl Instrum Methods Phys Res B 237:62
119. Rüb M, Bär M, Deboy G et al (2004) 550V superjunction 3.9 Ohmmm^2 transistor formed by 25 MeV masked boron implantation. Proceedings of ISPSD 2004, Kitakyushu, Japan, p 455
120. Schmidt B, Schubert D (1986) Siliciumsensoren. Akademie-Verlag, Berlin
121. Reichel H et al (1989) Halbleitersensoren: Prinzipien, Entwicklungsstand, Technologien, Anwendungsmöglichkeiten. Expert Verlag, Ehningen bei Böblingen
122. Sze SM (1994) Semiconductor sensors. Wiley, New York
123. Lutz G (1999) Semiconductor radiation detectors: device physics. Springer, Berlin
124. Hartmann F (2009) Evolution of silicon sensor technology in particle physics. STMP 231. Springer, Berlin
125. Spieler H (2005) Semiconductor detector systems. Oxford University Press, Oxford
126. Lecrosnier D, Pelous G, Amouroux C et al (1975) Optimization of avalanche silicon photodiodes. Technical digest – international electron devices meeting, Washington, DC, p 595
127. Ripoche G, Harari J (2009) Avalanche photodiodes. In: Decoster D, Harari J (eds) Optoelectronic sensors. ISTE Ltd., London, pp 80–87
128. Kemmer J (1980) Fabrication of low noise silicon radiation detectors by the planar process. Nucl Instrum Methods 169:499
129. Kemmer J, Burger P, Henck R, Heijne E (1982) Performance and applications of passivated ion-implanted silicon detector. IEEE Trans Nucl Sci NS-29:733
130. Kemmer J (1990) Advanced concepts for semiconductor nuclear radiation detectors. Nucl Instrum Methods B 45:247
131. Radeka V, Rahek V, Rescia P et al (1989) Implanted silicon JFET on completely depleted. IEEE Trans Electron Devices Lett ED-10:91
132. Strüder L (1989) Recent developments in semiconductor detectors and on-chip electronics. Nucl Instrum Methods A 283:387
133. Caywood JM, Mead CA, Mayer JW (1970) Influence of carrier diffusion effects on window thickness of semiconductor detectors. Nucl Instrum Methods 79:329
134. Kanno I (1987) Models of formation and erosion of a plasma column in a silicon surface-barrier. Rev Sci Instrum 58:1926
135. von Borany J, Schmidt B, Grötzschel R (1996) The application of high energy ion implantation for silicon radiation detectors. Nucl Instrum Methods Phys Res A 377:514
136. von Borany J, Beyer V, Schmidt B, Schnabel B (2003) A novel silicon detector for energetic electrons with improved linearity characteristics. Microelectron Eng 67–68:140
137. Deutscher M (1989) Ein Justierdetektor für Elektronenformstrahlen. Habilitations-schrift, Teil D, AdW der DDR
138. Seibt W, Sundström KE, Tove PA (1973) Charge collection in silicon detectors for strongly ionizing particles. Nucl Instrum Methods 113:317
139. Finch EC, Asghar M, Forte M (1979) Plasma and recombination effects in the fission fragment pulse height defect in a surface barrier detector. Nucl Instrum Methods 163:467
140. Hellings G, Mitard J, Eneman G et al (2009) High performance 70-nm germanium pMOSFETs with boron LDD implants. IEEE Electron Device Lett 30:88
141. Jones R, Thomas S, Bharatan S et al (2002) Fabrication and modeling of gigahertz photodetectors in heteroepitaxial Ge-on-Si using a graded buffer layer deposition by low

energy plasma enhanced CVD. Proceedings of international electron devices meeting (IEDM), 2002, p 793
142. Simoen E, Satta A, D'Amore A et al (2006) Ion-implantation issues in the formation of shallow junctions in germanium. Mater Sci Semicond Process 9:634
143. Brunco DP, De Jaeger B, Eneman G et al (2008) Germanium MOSFET devices: advances in materials understanding, process development, and electrical performance. J Electrochem Soc 155:H552
144. Satta A, Simoen E, Clarysse T et al (2005) Diffusion, activation, and recrystallization of boron implanted in preamorphized and crystalline germanium. Appl Phys Lett 87:172109
145. Hellings G, Wuendisch C, Eneman G et al (2009) Implantation, diffusion, activation, and recrystallization of gallium implanted in preamorphized and crystalline germanium. Electrochem Solid State Lett 12:H417
146. Chui CO, Kulig L, Moran J, Tsai W, Saraswat KC (2005) Germanium n-type shallow junction activation dependences. Appl Phys Lett 87:091909
147. Posselt M, Schmidt B, Anwand W et al (2008) Implantation into preamorphized germanium and subsequent annealing: Solid phase epitaxial regrowth, P diffusion, and activation. J Vac Sci Technol B 26:430
148. Wündisch C, Posselt M, Schmidt B et al (2009) Millisecond flash lamp annealing of shallow implanted layers in Ge. Appl Phys Lett 95:252107
149. Satta A, Simoen E, Duffy R et al (2006) Diffusion, activation, and regrowth behavior of high dose P implants in Ge. Appl Phys Lett 88:162118
150. Janssens T, Huyghebaert C, Vanhaeren D et al (2006) Heavy ion implantation in Ge: dramatic radiation induced morphology in Ge. J Vac Sci Technol B 24:510
151. Darby BL, Yates BR, Rudawski NG et al (2011) Insights for void formation in ion-implanted Ge. Thin Solid Films 519:5962
152. Kögler R, Mücklich A, Skorupa W et al (2007) Vacancies in high energy ion implanted SiGe. J Appl Phys 101:033508
153. Holland OW, Appleton BR, Narayan J (1983) Ion implantation damage and annealing in germanium. J Appl Phys 54:2295
154. Huber H, Assmann W, Karamian SA et al (1997) Void formation in Ge induced by high energy heavy ion irradiation. Nucl Instrum Methods Phys Res B 122:542
155. Nitta W, Taniwaki M, Hayashi Y, Yoshiie T (2002) Formation of cellular defect structure on GaSb ion-implanted at low temperature. J Appl Phys 92:1799
156. Romano L, Impellizzeri G, Tomasello MV et al (2010) Nanostructuring in Ge by self-ion implantation. J Appl Phys 107:084314
157. Wilson IH (1982) The effects of self-ion bombardment (30–500 keV) on the surface topography of single-crystal germanium. J Appl Phys 53:1698
158. Ghaly M, Nordlund K, Averback RS (1999) Molecular dynamics investigations of surface damage produced by kiloelectronvolt self-bombardment of solids. Philos Mag A 79:795
159. Kim JC, Cahill DG, Averback RS (2005) Surface defects created by 20 keV Xe ion irradiation of Ge(111). Surf Sci 574:175
160. Herrmannsdoerfer T, Heera V, Ignatchik O et al (2009) Superconducting state in a gallium-doped germanium layer at Low temperatures. Phys Rev Lett 102:217003
161. Zhou S, Bürger D, Mücklich A et al (2010) Hysteresis in the magnetotransport of manganese-doped germanium: evidence for carrier-mediated ferromagnetism. Phys Rev B 81:165204
162. Sealy BJ (1988) Ion implantation doping of semiconductors. Int Mater Rev 33:38
163. Wesch W, Götz G (1986) Rapid annealing of ion-implanted GaAs. Physica Status Solidi A 94:745
164. Pearton SJ, Poate JM, Sette F et al (1987) Ion implantation in GaAs. Nucl Instrum Methods Phys Res B 19/20:369
165. Dodadalapur A, Streetman BG (1990) Implantation in InP-the role of stoichiometric imbalances. Electrochem Soc Symp Proc 90–13:66

166. Rao MV (1992) Rapid thermal annealing of ion-implanted InP, InGaAs, and InSb. Proc SPIE 1595:108
167. Pearton SJ, Chakrabarti UK (1992) Novel dry etch chemistries for InP and related compounds. In: Katz A (ed) Indium phosphide and related materials: processing, technology and devices. Artech House, Norwood, MA, pp 420–426
168. Rao MV (1993) Ion implantation in III–V compound semiconductors. Nucl Instrum Methods Phys Res B 79:645
169. de Souza JP, Sadana DK (1992) Ion implantation in gallium arsenide MESFET technology. IEEE Trans Electron Devices ED-39:166
170. Rao MV, Nadella RK, Holland OW (1992) Elevated temperature 3 MeV Si and 150 keV Ge implants in InP:Fe. J Appl Phys 71:126
171. Rao MV, Nadella RK (1990) Be^+/P^+, Be^+/Ar^+, and Be^+/N^+ coimplantations into InP:Fe. J Appl Phys 67:1761
172. Gill SS, Sealy BJ (1986) Review of rapid thermal annealing of ion implanted GaAs. J Electrochem Soc 133:2590
173. Pearton SJ, Jalali B, Abernathy CR et al (1992) Isolation properties and experimental ranges of high energy ions in GaAs and InP. J Appl Phys 71:2663
174. Vellanki J, Nadella RK, Rao MV (1993) Highly conductive buried n^+ layers in lnP:Fe created by MeV energy Si, S, and Si/S implantation for application to microwave devices. J Electron Mater 22:73
175. Pearton SJ, Zolper JC, Shul RJ, Ren F (1999) GaN: processing, defects, and devices. J Appl Phys 86:1
176. Zolper JC (1997) Ion implantation in group III-nitride semiconductors: a tool for doping and defect studies. J Cryst Growth 178:157
177. Wilson RG, Zavada JM, Cao XA et al (1999) Redistribution and activation of implanted S, Se, Te, Be, Mg, and C in GaN. J Vac Sci Technol A 17:1226
178. Cao XA, Abernathy CR, Singh RK et al (1998) Ultrahigh Si^+ implant activation efficiency in GaN using a high-temperature rapid thermal process system. Appl Phys Lett 73:229
179. Kucheyev SO, Williams JS, Pearton SJ (2001) Ion implantation into GaN. Mater Sci Eng R Rep 33:51–107
180. Cao XA, Pearton SJ, Dang GT (2000) Creation of high resistivity GaN by implantation of Ti, O, Fe, or Cr. J Appl Phys 87:1091
181. Neudeck PG (1994) Progress towards high temperature, high power SiC devices. Institute of Physics Conference Series 141: Compound Semiconductors, pp 1–6
182. Rao MV (2003) Maturing ion-implantation technology and its device applications in SiC. Solid State Electron 47:213
183. Choyke WJ, Matsunami H, Pensl G (2004) Silicon carbide recent major advances. Springer, Berlin
184. Handy EM, Rao MV, Holland OW et al (2000) Al, B, and Ga ion-implantation doping of SiC. J Electron Mater 29:1340
185. Capano MA, Ryu S, Melloch MR et al (1998) Dopant activation and surface morphology of ion implanted 4H- and 6H-silicon carbide. J Electron Mater 27:370
186. Handy EM, Rao MV, Jones KA (1999) Effectiveness of AlN encapsulant in annealing ion-implanted SiC. J Appl Phys 86:746
187. Wirth H, Panknin D, Skorupa W, Niemann E (1999) Efficient p-type doping of 6H-SiC: Flash-lamp annealing after aluminum implantation. Appl Phys Lett 74:979
188. Reiss S, Heinig KH (1994) Ostwald ripening during ion beam synthesis – a computer simulation for inhomogeneous systems. Nucl Instrum Methods Phys Res B 84:229
189. Goodrich FC, Rusanov AI (eds) (1981) The modern theory of capillarity. Akademie Verlag, Berlin
190. Ostwald W (1897) Studien über die Bildung fester Körper. 1. Abhandlung: "Übersättigung und Überkaltung". Z Phys Chem 22:289
191. Lifshitz LM, Slyozov VV (1961) The kinetics of precipitation from supersaturated solid solutions. J Phys Chem Solids 19:35

192. Wagner C (1961) Theorie der Alterung von Niederschlägen durch Umlösen (Ostwald-Reifung). Z Electrochem 65:581
193. Reiss S, Weber R, Heinig KH, Skorupa W (1994) Experimental study and modeling of structure formation in buried layers at ion beam synthesis. Nucl Instrum Methods Phys Res B 89:337
194. Strobel M (1999) Modeling and computer simulations of ion beam synthesis of nanostructures. Ph.D. dissertation, University of Technology, Dresden, Germany
195. Strobel M, Heinig KH, Möller W (2001) Three-dimensional domain growth on the size scale of the capillary length: effective growth exponent and comparative atomistic and mean-field simulations. Phys Rev B 64:245422
196. Schmitz G, Haasen P (1992) Decomposition of an AlLi alloy – the early stages observed by HREM. Acta Metallurgica et Materialia 40:2209
197. Calderon HA, Voorhees PW, Murray JL, Kostorz G (1994) Ostwald ripening in concentrated alloys. Acta Metallurgica et Materialia 42:991
198. Mazzoldi P, Arnold GW, Battaglin G et al (1994) Peculiarities and application perspectives of metal-ion implants in glasses. Nucl Instrum Methods B 91:478
199. Atwater HA, Shcheglov KV, Wong SS et al (1994) Ion beam synthesis of luminescent SI and GE nanocrystals in a silicon dioxide matrix. Mater Res Soc Symp Proc 316:409
200. Mantl S (1992) Ion beam synthesis of epitaxial silicides: fabrication, characterization and applications. Mater Sci Rep 8:1
201. Zuhr RA, Magruder RH, Anderson TA, Wittig JE (1994) Nanosize metal alloy particle formation in AG and CU sequentially implanted silica. Mater Res Soc Symp Proc 316:457
202. Zhu JG, White CW, Budai JD et al (1995) Growth of Ge, Si, and SiGe nanocrystals in SiO_2 matrices. J Appl Phys 78:4386
203. White CW, Budai JD, Zhu JG et al (1995) Compound semiconductor nanocrystals formed by sequential ion implantation. Mater Res Soc Symp Proc 358:169
204. White CW, Budai JD, Zhu JG et al (1996) Ion beam synthesis and stability of GaAs nanocrystals in silicon. Appl Phys Lett 68:2389
205. Christoloveanu S (1989) Advanced silicon on insulator materials: processing, characterization and devices. In: Harbeke G, Schulz MJ (eds) Semiconductor silicon. Springer, Berlin, pp 223–249
206. Colinge JP (1997) Silicon-on-insulator technology: materials to VLSI, 2nd edn. Kluwer, Boston, pp 32–44, Chapter 2
207. Celler GK, Cristoloveanu S (2003) Frontiers of silicon-on-insulator. J Appl Phys 93:4955
208. Reeson KJ (1987) Fabrication of buried layers of SiO_2 and Si_3N_4 a using ion beam synthesis. Nucl Instrum Methods Phys Res B 19–20:269
209. Hatzopoulos N, Bussmann U, Robinson AK, Hemment PLF (1991) Buried insulator formation by nitrogen implantation at elevated temperatures. Nucl Instrum Methods Phys Res B 55:734
210. Zhang E, Yi W, Chen J et al (2005) Research on the effect of nitrogen implantation doses on the structure of separation by implantation of oxygen and nitrogen. Smart Mater Struct 14: N42
211. Maydell-Ondrusz EA, Wilson IH (1984) A model for the evolution of implanted oxygen profiles in silicon. Thin Solid Films 114:357
212. Jäger HU, Hensel E, Kreissig U et al (1985) A model for the oxidation of silicon by high dose oxygen implantation. Thin Solid Films 123:159
213. Jäger HU (1986) Model investigations of the oxidation of silicon by high dose implantation. Nucl Instrum Methods Phys Res B 15:748
214. Jäger HU (1987) Improved modeling of oxygen depth profiles in high dose oxygen-implanted silicon. Phys Stat Sol (a) 103:K75
215. Nakashima S, Katayama T, Miyamura Y et al (1994) Thickness increment of buried oxide in a SIMOX wafer by high-temperature oxidation. In: Proceedings of IEEE International SOI Conference (1994), pp 71–72

216. Kawamura K, Deai H, Morikawa Y et al (1996) Gate oxide integrity on ITOX-SIMOX wafers. In: Proceedings of IEEE International SOI Conference (1996), pp 162–163
217. Maszara WP, Bennett J, Boden T et al (1997) Low dose SIMOX and impact of ITOX process on quality of SOI film. In: Proceedings of IEEE International SOI Conference (1997) pp 18–19
218. Dong Y, Chen M, Chen J et al (2004) Patterned buried oxide layers under a single MOSFET to improve the device performance. Semicond Sci Technol 19:L25
219. White AE, Short KT, Dynes RC et al (1987) Mesotaxy: single-crystal growth of buried $CoSi_2$ layers. Appl Phys Lett 50:95
220. White AE, Short KT (1988) Synthesis of buried oxide and silicide layers with ion beams. Science 241:930
221. White AE, Short KT, Dynes RC et al (1989) Mesotaxy: synthesis of buried single-crystal silicide layers by implantation. Nucl Instrum Methods Phys Res B 39:253
222. Mantl S, Jebasinski R, Hartmann D (1991) The effect of dose on the growth of buried $CoSi_2$ layers in (111) and (100) Si produced by ion implantation. Nucl Instrum Methods Phys Res B 59–60:666
223. Van Ommen A, Bulle-Lieuwma CWT, Ottenheim JJM, Theunissen AML (1990) Ion beam synthesis of heteroepitaxial Si/$CoSi_2$/Si structures. J Appl Phys 67:1767
224. Hensel JC, Tung RT, Poate JM, Unterwald FC (1984) Electrical transport properties of $CoSi_2$ and $NiSi_2$ thin films. Appl Phys Lett 44:913
225. Vanheilemont J, Bender H, Wu MF et al (1993) Implantation temperature dependent distribution of $NiSi_2$ formed by ion beam synthesis in silicon. Appl Phys Lett 62:2795
226. Hsu JY, Liang JH (2005) An investigation of annealing effect on forming nickel disilicide by ion beam synthesis. Nucl Instrum Methods Phys Res B 241:543
227. Liang JH, Chao DS (2001) Formation of tungsten silicide films by ion beam synthesis. Surf CoatTechnol 140:116
228. White AE, Short KT, Maex K et al (1991) Exploiting Si/$CoSi_2$/Si heterostructures grown by mesotaxy. Nucl Instrum Methods Phys Res B 59–60:693
229. Radermacher K, Mantl S, Dieker C, Lüth H (1991) Ion beam synthesis of buried α-$FeSi_2$ and β-$FeSi_2$ layers. Appl Phys Lett 59:2145
230. Homewood KP, Reeson KJ, Gwilliam RM et al (2001) Ion beam synthesized silicides: growth, characterization and devices. Thin Solid Films 381:188
231. Golanski A, Christie WH, Galloway MD et al (1991) Ion beam induced diffusion and crystallization in high-dose Er implanted Si. Nucl Instrum Methods Phys Res B 59–60:444
232. Hogg SM, Vantomme A, Wu MF, Langouche G (2000) Electrical properties of rare earth silicides produced by channeled ion beam synthesis. Microelectron Eng 50:211
233. Bischoff L, Heinig KH, Teichert J, Skorupa W (1996) Submicron $CoSi_2$ structures fabricated by focused ion beam implantation and local flash lamp melting. Nucl Instrum Methods Phys Res B 112:201
234. Hausmann S, Bischoff L, Teichert J (1998) Dose rate effects in focused ion beam synthesis of cobalt disilicide. Appl Phys Lett 72:2719
235. Akhmadaliev C, Schmidt B, Bischoff L (2006) Defect induced formation of $CoSi_2$ nanowires by focused ion beam synthesis. Appl Phys Lett 89:223129
236. Heinig KH (1984) Effects of transient local melting on semiconductor surfaces. In: Proceedings of international conference on energy pulse modification of semiconductors and related materials, EPM '84. Dresden, p 265
237. Calvo P, Claverie A, Cherkashin N et al (2004) Thermal evolution of 113 defects in silicon: transformation against dissolution. Nucl Instrum Methods Phys Res B 216:173
238. Buchal C, Withrow SP, White CW, Poker DB (1994) Ion implantation of optical materials. Annu Rev Mater Sci 24:125
239. Meldrum A, Haglund RF, Boatner LA, White CW (2001) Nanocomposite materials formed by ion implantation. Adv Mater 13:1431

240. Heinig K, Müller T, Schmidt B et al (2003) Interfaces under ion irradiation: growth and taming of nanostructures. Appl Phys A Mater Sci Process 77:17
241. Skorupa W, Rebohle L, Gebel T (2003) Group-IV nanocluster formation by ion-beam synthesis. Appl Phys A Mater Sci Process 76:1049
242. Mazzoldi P, Mattei G (2007) Some aspects of ion implantation technique in nanostructured materials. Phys Stat Sol (a) 204:621
243. Flytzanis C, Hache F, Klein MC et al (1991) Nonlinear optics in composite materials. In: Wolf E (ed) Progress in optics, vol 29. North-Holland, Amsterdam, pp 321–411
244. Magruder RH, Kinser DL, Wittig JE, Zuhr RA (1992) Structure property relationships of nanometer-size metal clusters in glasses. Proc SPIE 1761:180
245. Magruder RH, Haglund RF, Yang L et al (1994) Physical and optical properties of Cu nanoclusters fabricated by ion implantation in fused silica. J Appl Phys 76:708
246. Hosono H, Fukushima H, Abe Y et al (1992) Cross-sectional TEM observation of copper-implanted SiO_2 glass. J Non Cryst Sol 143:157
247. Matsunami N, Hosono H (1993) Colloid formation effects on depth profile of implanted Ag in SiO_2 glass. Appl Phys Lett 63:2050
248. Matsumi N, Hosono H (1993) Anomalous fringe pattern of Ag colloid in phosphate glasses by implantation. Nucl Instrum Methods Phys Res B 80/81:1233
249. Mazzoldi P, Tramontin L, Boscolo-Boscoletto A et al (1993) Substrate effects in silver-implanted glasses. Nucl Instrum Methods Phys Res B 80/81:1192
250. Magruder RH, Yang L, Huglund RF et al (1993) Optical properties of gold nanocluster composites formed by deep ion implantation in silica. Appl Phys Lett 62:1730
251. White CW, Zhou DS, Budai JD, Zuhr RA (1994) Colloidal Au nanoclusters formed in fused silica by MeV ion implantation and annealing. Mater Res Soc Symp Proc 316:499
252. Strobel M, Heinig K, Möller W (1999) Ion beam synthesis of gold nanoclusters in SiO_2: computer simulations versus experiments. Nucl Instrum Methods Phys Res B 147:343
253. Fukumi K, Chayahara A, Kadono K et al (1994) Gold nanoparticles ion implanted in glass with enhanced nonlinear optical properties. J Appl Phys 75:3075
254. KimerIing LC, Kolenbrander KD, Michel J, Palm J (1996) Light emission from silicon. Solid State Phys 50:333
255. Walters RJ, Kalkman J, Polman A et al (2006) Photoluminescence quantum efficiency of dense silicon nanocrystal ensembles in SiO_2. Phys Rev B 73:132302
256. Pavesi L, Dal Negro L, Mazzoleni C et al (2000) Optical gain in silicon nanocrystals. Nature 408:440
257. Conibeer G, Green M, Corkish R et al (2006) Silicon nanostructures for third generation photovoltaic solar cells. Thin Solid Films 511–512:654
258. Alfond TL, Theodore ND (1994) Backscattering and electron microscopy study of mega-electron volt gold implantation into silicon. J Appl Phys 76:7265
259. Wendler E, Herrmann U, Wesch W, Dunken HH (1996) Structural changes and Si redistribution in Si^+ implanted silica glass. Nucl Instrum Methods Phys Res B 116:332
260. Zhu JG, White CW, Budai JD, Withrow SP, Chenb Y (1995) Growth of Ge, Si, and SiGe nanocrystals in SiO_2 matrices. J Appl Phys 78:4386
261. von Borany J, Grötzschel R, Heinig KH et al (1997) Multimodal impurity redistribution and nanocluster formation in Ge implanted silicon dioxide films. Appl Phys Lett 71:3215
262. Heinig KH, Schmidt B, Markwitz A et al (1999) Precipitation, ripening and chemical effects during annealing of Ge^+ implanted SiO_2 layers. Nucl Instrum Methods Phys Res B 148:969
263. Markwitz A, Schmidt B, Matz W et al (1998) Microstructural investigation of ion beam synthesised germanium nanoclusters embedded in SiO_2 layers. Nucl Instrum Methods Phys Res B 142:338
264. Oswald S, Schmidt B, Heinig KH (2000) XPS investigation with factor analysis for the study of Ge clustering in SiO_2. Surf Interface Anal 29:249
265. Borodin VA, Heinig KH, Schmidt B (1998) Modeling of Ge nanocluster evolution in ion-implanted SiO_2 layer. Nucl Instrum Methods Phys Res B 147:286

266. Tiwari S, Rana F, Chan K et al (1995) Volatile and non-volatile memories in silicon with nano-crystal storage. IEEE International Electron Devices Meeting Technical Digest, p 521
267. Devine RAB (1994) Macroscopic and microscopic effects of radiation in amorphous SiO_2. Nucl Instrum Methods Phys Res B 91:378
268. Schmidt B, Grambole D, Herrmann F (2002) Impact of ambient atmosphere on as-implanted amorphous insulating layers. Nucl Instrum Methods Phys Res B 191:482
269. Claverie A, Bonafos C, Ben Assayag G et al (2006) Materials science issues for the fabrication of nanocrystal memory devices by ultra low energy ion implantation. Defect Diffus Forum 258–260:531
270. Müller T, Heinig KH, Möller W (2002) Materials science issues for the fabrication of nanocrystal memory devices by ultra low energy ion implantation. Appl Phys Lett 81:3049
271. Müller T, Heinig KH, Möller W et al (2004) Multi-dot floating-gates for nonvolatile semiconductor memories: their ion beam synthesis and morphology. Appl Phys Lett 85:2373
272. Brongersma ML, Polman A, Min MS et al (1998) Tuning the emission wavelength of Si nanocrystals in SiO_2 by oxidation. Appl Phys Lett 72:2577
273. Skorupa W, Rebohle L, Gebel T (2003) Group-IV nanocluster formation by ion-beam synthesis. Appl Phys A 76:1049
274. Tiwari S, Rana F, Hanafi H et al (1996) A silicon nanocrystals based memory. Appl Phys Lett 68:1377
275. Fu Y, Dutta A, Willander M, Oda S (2000) Carrier conduction in a Si-nanocrystal-based single-electron transistor – I. Effect of gate bias. Superlattices Microstruct 28:177
276. Lopez M, Garrido B, Bonafos C (2001) Model for efficient visible emission from Si nanocrystals ion beam synthesized in SiO_2. Nucl Instrum Methods Phys Res B 178:89
277. Iwayama TS, Hama T, Hole DE, Boyd IW (2002) Optical and structural properties of encapsulated Si nanocrystals formed in SiO_2 by ion implantation. Surf Coat Technol 158–159:712
278. Cheylan S, Elliman RG (1999) The effect of ion dose and annealing ambient on room temperature photoluminescence from Si nanocrystals in SiO_2. Nucl Instrum Methods Phys Res B 148:986
279. Bonafos C, Columbeau B, Altibelli A et al (2001) Kinetic study of group IV nanoparticles ion beam synthesized in SiO_2. Nucl Instrum Methods Phys Res B 178:17
280. Linnros J, Lalic N, Galeckas A, Grivickas V (1999) Analysis of the stretched exponential photoluminescence decay from nanometer-sized silicon crystals in SiO_2. J Appl Phys 86:6128
281. Kik PG, Brongersma ML, Polman A (2000) Strong exciton-erbium coupling in Si nanocrystal-doped SiO_2. Appl Phys Lett 76:2325
282. Kik PG, Polman A (2000) Exciton–erbium interactions in Si nanocrystal-doped SiO_2. J Appl Phys 88:1992
283. Kik PG, Polman A (2001) Exciton–erbium energy transfer in Si nanocrystal-doped SiO_2. Mater Sci Eng B 81:3
284. Polman A (2002) Photonic materials: teaching silicon new tricks. Nat Mater 1:10
285. Koshida N (ed) (2006) Device applications of silicon nanocrystals and nanostructures. Springer, Berlin
286. Pavesi L, Turan R (2010) Silicon nanocrystals: fundamentals, sythesis and applications. Wiley-VCH, Weinheim
287. von Borany J, Gebel T, Stegemann KH (2002) Memory properties of Si^+ implanted gate oxides: from MOS capacitors to nvSRAM. Solid State Electron 46:1729
288. Normand P, Kapetanakis E, Dimitrakis P et al (2003) Effect of annealing environment on the memory properties of thin oxides with embedded Si nanocrystals obtained by low-energy ion-beam synthesis. Appl Phys Lett 83:168
289. Dimitrakis P, Kapetanakis E, Tsoukalas D et al (2004) Silicon nanocrystal memory devices obtained by ultra-low-energy ion-beam synthesis. Solid State Electron 48:1511

290. Normand P, Kapetanakis E, Dimitrakis P et al (2004) Nanocrystals manufacturing by ultra-low-energy ion-beam-synthesis for non-volatile memory applications. Nucl Instrum Methods Phys Res B 216:228
291. Beyer V, von Borany J, Klimenkov M, Müller T (2009) Current-voltage characteristics of metal-oxide-semiconductor devices containing Ge or Si nanocrystals in thin gate oxides. J Appl Phys 106:064505
292. Compagnoni CM, Ielmini D, Spinelli AS (2003) Study of data retention for nanocrystal Flash memories. In: Proceedings of the 41st annual international reliability physics symposium, pp 506–512
293. Tiwari S, Wahl JA, Silva H et al (2000) Small silicon memories: confinement, single-electron, and interface state considerations. Appl Phys A 71:403
294. Normand P, Dimitrakis P, Kapetanakis E et al (2004) Processing issues in silicon nanocrystal manufacturing by ultra-low-energy ion-beam-synthesis for non-volatile memory applications. Microelectron Eng 73–74:730
295. Carrada M, Cherkashin N, Bonafos C et al (2003) Effect of ion energy and dose on the positioning of 2D-arrays of Si nanocrystals ion beam synthesised in thin SiO_2 layers. Mater Sci Eng B 101:204
296. Schmidt B, Heinig KH, Röntzsch L et al (2006) Ion irradiation through SiO_2/Si interfaces: non-conventional fabrication of Si nanocrystals for memory applications. Nucl Instrum Methods Phys Res B 242:146
297. von Borany J, Grötzschel R, Heinig KH et al (1999) The formation of narrow nanocluster bands in Ge-implanted SiO_2-layers. Solid State Electron 43:1159
298. Heinig KH, Müller T, Schmidt B, Strobel M, Möller W (2003) Interfaces under ion irradiation: growth and taming of nanostructures. Appl Phys A 77:17
299. Heinig KH, Schmidt B, Strobel M, Bernas H (2001) inverse ostwald ripening and self-organization of nanoclusters due to ion irradiation. Mater Res Soc Symp Proc 650:R9.6/O14.6
300. Schmidt B, Heinig KH, Mücklich A (2001) Evolution of ion beam synthesized Au nanoclusters in SiO_2 under ion irradiation. Mater Soc Symp Proc 647:O11.20
301. Röntzsch L, Heinig KH, Schmidt B (2004) Experimental evidence of Si nanocluster δ-layer formation in buried and thin SiO_2 films induced by ion irradiation. Mater Sci Semicond Process 7:357
302. Röntzsch L, Heinig KH, Schmidt B et al (2005) Direct evidence of self-aligned Si nanocrystals formed by ion irradiation of Si/SiO_2 interfaces. Phys Stat Sol (a) 202:R170
303. Bruel M (1995) Silicon on insulator material technology. Electron Lett 31:1201
304. Aspar B, Bruel M, Moriceau H (1997) Basic mechanisms involved in the Smart-Cut® process. Microelectron Eng 36:233
305. Bruel M (1996) Application of hydrogen ion beams to Silicon on Insulator material technology. Nucl Instrum Methods Phys Res B 108:313
306. Tong QY, Gösele U (1999) Semiconductor wafer bonding: science and technology. Wiley, New York
307. Bruel M, Aspar B, Auberton-Herve AJ (1997) Smart-Cut: a new silicon on insulator material technology based on hydrogen implantation and wafer bonding. Jpn J Appl Phys 36:1636
308. Aspar B, Lagahe C, Moriceau H et al (1998) Kinetics of splitting in the Smart-Cut^R process. Proc IEEE Int SOI Conf 1998:137–138
309. Nastasi M, Mayer JW (2006) Ion implantation and synthesis of materials. Springer, Berlin, p 152
310. Tesmer JR, Nastasi M (eds) (1995) Handbook of modern ion beam analysis. Materials Research Society, Pittsburgh, PA
311. Di Cioccio L, Leitec Y, Letertre F et al (1996) Silicon carbide on insulator formation using the Smart Cut process. Electron Lett 32:1144

312. Akatsu T, Deguet C, Sanchez L et al (2006) Germanium-on-insulator (GeOI) substrates – a novel engineered substrate for future high performance devices. Mater Sci Semicond Process 9:444
313. Jalaguier E, Aspar B, Pocas S et al (1998) Transfer of 3 in GaAs film on silicon substrate by proton implantation process. Electron Lett 34:408
314. Tauzin A, Akatsu T, Rabarot M et al (2005) Transfers of 2-inch GaN films onto sapphire substrates using Smart Cut^{TM} technology. Electron Lett 41:668
315. Moriceau H, Fournel F, Aspar B et al (2003) New layer transfers obtained by the Smart Cut process. J Electron Mater 32:829
316. Izuhara T, Gheorma IL, Osgood RM et al (2003) Single-crystal barium titanate thin films by ion slicing. Appl Phys Lett 82:616
317. Carter G (2001) The physics and applications of ion beam erosion. J Phys D Appl Phys 34:R1
318. Ziberi B, Frost F, Höche T, Rauschenbach B (2005) Ripple pattern formation on silicon surfaces by low-energy ion-beam erosion: experiment and theory. Phys Rev B 72:235310
319. Ziberi B, Frost F, Rauschenbach B (2006) Formation of large-area nanostructures on Si and Ge surfaces during low energy ion beam erosion. J Vac Sci Technol A 24:1344
320. Keller A, Facsko S, Möller W (2009) The morphology of amorphous SiO_2 surfaces during low energy ion sputtering. J Phys Condens Matter 21:495305
321. Facsko S, Dekorsy T, Koerdt C et al (1999) Formation of ordered nanoscale semiconductor dots by ion sputtering. Science 285:1551
322. Carter G, Nobes MJ, Paton F et al (1977) Ion bombardment induced ripple topography on amorphous solids. Radiat Eff Defects Solids 33:65
323. Chan WL, Chason E (2007) Making waves: kinetic processes controlling surface evolution during low energy ion sputtering. J Appl Phys 101:121301
324. Brown AD, Erlebacher J (2005) Temperature and fluence effects on the evolution of regular surface morphologies on ion-sputtered Si(111). Phys Rev B 72:075350
325. Ozaydin G, Ozcan AS, Wang YY (2005) Real-time X-ray studies of Mo-seeded Si nanodot formation during ion bombardment. Appl Phys Lett 87:163104
326. Zhou J, Facsko S, Lu M, Möller W (2011) Nanopatterning of Si surfaces by normal incident ion erosion: influence of iron incorporation on surface morphology evolution. J Appl Phys 109:104315
327. Macko S, Frost F, Ziberi B et al (2010) Is keV ion-induced pattern formation on Si(001) caused by metal impurities? Nanotechnology 21:085301
328. Ziberi B, Frost F, Tartz M (2008) Ripple rotation, pattern transitions, and long range ordered dots on silicon by ion beam erosion. Appl Phys Lett 92:063102
329. Bischoff L, Pilz W, Schmidt B (2011) Amorphous solid foam structures on germanium by heavy ion irradiation. Appl Phys A 104:1153
330. Bischoff L, Heinig KH, Schmidt B et al (2012) Self-organization of Ge nanopattern under erosion with heavy Bi monomer and cluster ions. Nucl Instrum Methods Phys Res B 272:198–201
331. Bradley RM, Harper JME (1988) Theory of ripple topography induced by ion bombardment. J Vac Sci Technol A 6:2390
332. Sigmund P (1973) A mechanism of surface micro-roughening by ion bombardment. J Mater Sci 8:1545
333. Cuerno R, Barabasi AL (1995) Dynamic scaling of ion-sputtered surfaces. Phys Rev Lett 74:4746
334. Makeev MA, Barabasi AL (1997) Ion-induced effective surface diffusion in ion sputtering. Appl Phys Lett 71:2800
335. Carter G, Vishnyakov V (1996) Roughening and ripple instabilities on ion-bombarded Si. Phys Rev B 54:17647
336. Makeev MA, Cuerno R, Barabasi AL (2002) Morphology of ion-sputtered surfaces. Nucl Instrum Methods Phys Res B 197:185

337. Munoz-Garcia J, Castro M, Cuerno R (2006) Nonlinear ripple dynamics on amorphous surfaces patterned by ion beam sputtering. Phys Rev Lett 96:086101
338. Chason E, Chan WL (2009) Kinetic Monte Carlo simulations compared with continuum models and experimental properties of pattern formation during ion beam sputtering. J Phys Condens Matter 21:224016
339. Kalyanasundaram N, Freund JB, Johnson HB (2009) A multiscale crater function model for ion-induced pattern formation in silicon. J Phys Condens Matter 21:224018
340. Liedke MO, Liedke B, Keller A (2007) Induced anisotropies in exchange-coupled systems on rippled substrates. Phys Rev B 75:220407(R)
341. Oates TWH, Keller A, Noda S, Facsko S (2008) Self-organized metallic nanoparticle and nanowire arrays from ion-sputtered silicon templates. Appl Phys Lett 93:063106
342. Toulemonde M, Dufour C, Wang Z, Paumier E (1996) Atomic and cluster ion bombardment in the electronic stopping power regime: a thermal spike description. Nucl Instrum Methods Phys Res B 112:26
343. Toulemonde M, Costantini JM, Dufour C (1996) Track creation in SiO_2 and $BaFe_{12}O_{19}$ by swift heavy ions: a thermal spike description. Nucl Instrum Methods Phys Res B 116:37
344. Snoeks E, van Blaaderen A, van Dillen T et al (2000) Colloidal ellipsoids with continuously variable shape. Adv Mater 12:1511
345. Vossen DLJ, de Dood MJA, van Dillen T et al (2000) Novel method for solution growth of thin silica films from tetraethoxysilane. Adv Mater 12:1434
346. Snoeks E, van Blaaderen A, van Dillen T et al (2001) Colloidal assemblies modified by ion irradiation. Nucl Instrum Methods Phys Res B 178:62
347. van Dillen T, Polman A, van Kats CM, van Blaaderen A (2003) Ion beam-induced anisotropic plastic deformation at 300 keV. Appl Phys Lett 83:4315
348. Trinkaus H, Ryazanov AI (1995) Viscoelastic model for the plastic flow of amorphous solids under energetic ion bombardment. Phys Rev Lett 74:5072
349. Klaumünzer S (2004) Ion hammering of silica colloids. Nucl Instrum Methods Phys Res B 215:345
350. van Dillen T, van Blaaderen A, Polman A (2004) Shaping colloidal assemblies. Mater Today 7:40
351. Roorda S, van Dillen T, Polman A et al (2004) Aligned gold nanorods in silica made by ion irradiation of core–shell colloidal particles. Adv Mater 16:235
352. Penninkhof JJ, van Dillen T, Roorda S et al (2006) Anisotropic deformation of metallo-dielectric core–shell colloids under MeV ion irradiation. Nucl Instrum Methods Phys Res B 242:523
353. D'Orleans C, Stoquert JP, Cerruti C et al (2003) Anisotropy of Co nanoparticles induced by swift heavy ions. Phys Rev B 67:220101(R)
354. Giulian R, Kluth P, Araujo LL et al (2008) Shape transformation of Pt nanoparticles induced by swift heavy-ion irradiation. Phys Rev B 78:125413
355. Penninkhof JJ, Polman A, Sweatlock LA et al (2003) Mega-electron-volt ion beam induced anisotropic plasmon resonance of silver nanocrystals in glass. Appl Phys Lett 83:4137
356. Mishra YK, Singh F, Avasthi DK et al (2007) Synthesis of elongated Au nanoparticles in silica matrix by ion irradiation. Appl Phys Lett 91:063103
357. Dawi EA, Rizza G, Mink MP et al (2009) Ion beam shaping of Au nanoparticles in silica: particle size and concentration dependence. J Appl Phys 105:074305
358. Dawi EA, Vredenberg AM, Rizza G, Toulemonde M (2011) Ion-induced elongation of gold nanoparticles in silica by irradiation with Ag and Cu swift heavy ions: track radius and energy loss threshold. Nanotechnology 22:215607
359. Schmidt B, Mücklich A, Röntzsch L, Heinig KH (2007) How do high energy heavy ions shape Ge nanoparticles embedded in SiO_2? Nucl Instrum Methods Phys Res B 257:30
360. Schmidt B, Heinig KH, Mücklich A, Akhmadaliev C (2009) Swift-heavy-ion-induced shaping of spherical Ge nanoparticles into disks and rods. Nucl Instrum Methods Phys Res B 267:1345

361. Dearnaley G (1969) Ion bombardment and implantation. Rep Prog Phys 32:405
362. Ashworth V, Grant WA, Procter RPM (1982) Ion implantation into metals. Franklin Book Co., Elkins Park, PA
363. Conrad JR, Radtke JL, Dodd RA et al (1987) Ion bombardment and implantation. J Appl Phys 62:4591
364. Dearnaley G (1983) Applications of ion implantation in metals. Thin Solid Films 107:315
365. Picraux ST (1984) Ion implantation in metals. Annu Rev Mater Sci 14:335
366. Dimigen H, Kobs K, Leutenecker R et al (1985) Wear resistance of nitrogen-implanted steels. Mater Sci Eng 69:181
367. Dearnaley G (1994) Historical perspective of metal implantation. Surf CoatTechnol 65:1
368. Dearnaley G (1990) Ion beam modification of metals. Nucl Instrum Methods Phys Res B 50:358
369. Hirvonen JK (1989) Ion beam processing for surface modification. Annu Rev Mater Sci 19:401
370. Kliauga AM, Pohl M, Klaffke D (1998) A comparison of the friction and reciprocating wear behaviour between an austenitic (X 2 CrNiMo 17 13 2) and a ferritic (X 1 CrNiMoNb 28 4 2) stainless steel after nitrogen ion implantation. Surf CoatTechnol 102:237
371. Thorwarth G, Mändl S, Rauschenbach B (2000) Plasma immersion ion implantation of cold-work steel. Surf CoatTechnol 125:94
372. Woolley E (1997) Surface hardening by ion implantation. Materials World 5:515
373. Schumacher G, Dettenwanger F, Schütze M et al (1999) Microalloying effects in the oxidation of TiAl materials. Intermetallics 7:1113
374. Donchev A, Gleeson B, Schütze B (2003) Thermodynamic considerations of the beneficial effect of halogens on the oxidation resistance of TiAl-based alloys. Intermetallics 11:387
375. Donchev A, Kolitsch A, Schütze M, Yankov R (2009) Plasma-immersion-ion-implantation of fluorine to protect TiAl-components against high-temperature oxidation. Plasma Process Polym 6:434
376. Neve S, Masset PJ, Yankov RA (2010) High temperature oxidation resistance of fluorine-treated TiAl alloys: chemical vs. ion beam fluorination techniques. Nucl Instrum Methods Phys Res B 268:3381
377. Masset PJ, Yankov R, Kolitsch A, Schütze M (2010) Comparison of fluorination treatments to improve the high temperature oxidation resistance of TiAl alloys in SO_2 containing environments. Mater Sci Forum 638–642:1374
378. Donchev A, Kolitsch A, Schütze M, Yankov R (2011) Combined Al- plus F-treatment of Ti-alloys for improved behaviour at elevated temperatures. Mater Corros 62:695
379. Telbizova T, Parascandola S, Prokert F (2001) Ion nitriding of Al: growth kinetics and characterisation of the nitride layer. Surf CoatTechnol 142–144:1028
380. Telbizova T, Chevolleau T, Möller W et al (2001) Nitrogen incorporation and loss during ion nitriding of Al. Nucl Instrum Methods Phys Res B 184:347
381. Möller W, Parascandola S, Telbizova T et al (2001) Surface processes and diffusion mechanisms of ion nitriding of stainless steel and aluminium. Surf CoatTechnol 136:73
382. Fink D (2004) Fundamentals of ion-irradiated polymers. Springer, Berlin
383. Calcagno L, Foti G (1991) Ion irradiation of polymers. Nucl Instrum Methods B 59–60:1153
384. Marletta G (1990) Chemical reactions and physical property modifications induced by keV ion beams in polymers. Nucl Instrum Methods Phys Res B 46:295
385. Lee EH (1999) Ion-beam modification of polymeric materials – fundamental principles and applications. Nucl Instrum Methods Phys Res B 151:29
386. Stepanov AL (2010) Synthesis of silver nanoparticles in dielectric matrix by ion implantation: a review. Rev Adv Mater Sci 26:1
387. Townsend PD (1987) Optical effects of ion implantation. Rep Prog Phys 50:501
388. Chen F, Wang XL, Wang KM (2007) Development of ion-implanted optical waveguides in optical materials: a review. Opt Mater 29:1523

389. Chen F (2008) Construction of two-dimensional waveguides in insulating optical materials by means of ion beam implantation for photonic applications: fabrication methods and research progress. Crit Rev Solid State Mater Sci 33:165
390. Bayly AR (1973) Optical properties of ion bombarded silica glass. Radiat Eff 18:111
391. Standley RD, Gibson WM, Rodgers JW (1972) Properties of ion-bombarded fused quartz for integrated optics. Appl Optics 11:1313
392. Wie DTY, Lee WW, Blom LR (1975) Large refractive index change induced by ion implantation in lithium niobate. Appl Phys Lett 25:329

Ion Beam Preparation of Materials

5

5.1 Removal of Target Atoms by Sputtering

Ions impinging onto a solid can cause different ion–solid interaction effects because of nuclear and electronic energy losses of the striking ions. Typical secondary effects of these interactions are illustrated in Fig. 5.1.

To these belong

- The generation of secondary electrons, ions, photons, and phonons
- The implantation of impinging ions
- The removal of target atoms by sputtering

Typical interaction parameters for the bombardment of a Si surface by Ga^+ ions with 30 keV are shown in Table 5.1 [1].

Ion bombardment-induced sputtering is a very sensitive tool for removing atoms from solid surfaces, combined with a modification of surface topography. The displacement of target atoms by ion sputtering allows controlled ion beam preparation of materials. It can be used for surface cleaning, surface etching, target thinning, and cutting for layer's cross sections. For high primary ion fluences ($>10^{13}$ cm^{-2}), the sputter equilibrium is reached at depths greater than the primary ion implantation depth R_p.

A permanent ion bombardment causes different processes influencing the sputter effects, as

- Preferential and selective sputtering for compound targets
- Atomic mixing for layered targets
- Influence of channeling for crystalline targets
- Crater bottom roughening
- Charging effects (for insulators)

These effects are well understood from the literature (e.g., [1–5]).

Ion sputtering can be defined as the target erosion by ion bombardment. In this process surface atoms are removed by physical knock-on processes caused by collisions between incident primary ions and secondary recoiled target atoms with near-surface atoms of a target. The basic quantity is the sputtering yield Y:

B. Schmidt and K. Wetzig, *Ion Beams in Materials Processing and Analysis*,
DOI 10.1007/978-3-211-99356-9_5,

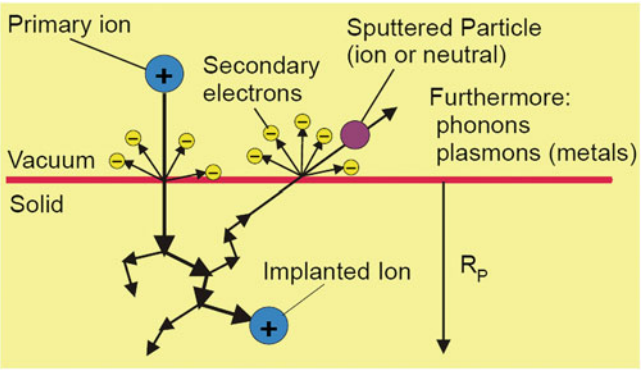

Fig. 5.1 Possible ion–solid interactions of an ion impinging onto a solid

Table 5.1 Typical interaction parameters for a Ga^+ 30 keV ion bombardment of a Si target [1]

Parameter	Typical value
Secondary electron yield	1–5
Secondary ion yield	10^{-1}–10^{-5}
Photon yield	~10^{-2}
Sputtering yield Y	2.4
Implantation depth R_p	~10 nm

Table 5.2 Measured sputtering yields Y and sputter rates S (in μm^3/nC) for different targets and ion sources (ion energy 30 keV) [5]

Ion source	Ga^+		Al^+		In^+	
Target	Y	S	Y	S	Y	S
Si	2.1	0.26	0.9	0.11	2.9	0.36
Cu	1.8	0.13	0.9	0.07	5.2	0.39
Zr	2.5	0.36	1.2	0.18	1.9	0.28
Mo	1.1	0.10	0.8	0.07	2.0	0.19
Ta	3.5	0.40	1.3	0.15	2.0	0.22
W	1.1	0.11	0.8	0.08	2.1	0.21

$$Y = \frac{\text{mean number of sputtered atoms}}{\text{bombarding ion}}.$$

The sputtering yield typically lies in the range 0.5–20 (see Table 5.2).
It depends upon

- Ion species
- Ion energy
- Ion beam direction
- Target material composition

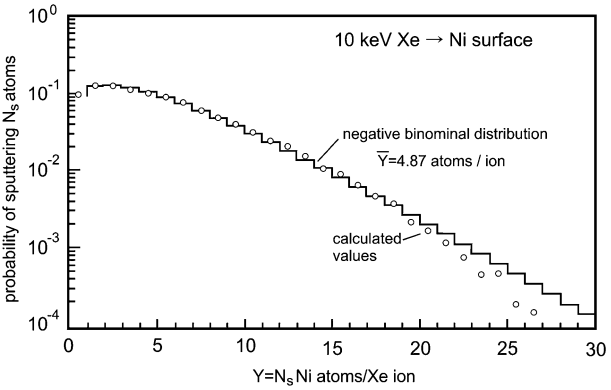

Fig. 5.2 Probability distribution for sputtering N_S atoms per incident ion. Normal 10 keV Xe^+ bombardment of amorphous Ni [6]

It is inversely proportional to the concentration of implanted species quantity, and it can be modified by the chemical reactivity of the ions. The bombarding ion transfers energy to target atoms, which are recoiled with sufficient energy to generate other (near-surface) recoils (typically 1–2 for 20 keV Ar^+ ion bombardment on Si) that can escape from the solid. They mainly account for the sputtering yield.

The particles that are emitted from the ion bombarded target predominantly consist of neutral atoms in the ground state with broad energy and angular distributions. The mean energy of the emitted particles is in the order of ~10 eV.

They are sputtered products in a narrower sense with a mean energy in the order of ~10 eV that can be transferred to the emitted material. Only a very small fraction of the emitted particles are excited atoms or secondary ions (compare the low secondary ion yield in Table 5.1).

The sputtering yield for individual ions may show large deviations from the mean value of Y. These fluctuations can be studied by computer simulations. Figure 5.2 shows the probability distribution for sputter ejection of N_S atoms for 10 keV Xe^+ bombardment of amorphous Ni at normal incidence, as calculated by Eckstein with TRIM [6]. The probability can be well approximated by a negative binominal distribution. From Fig. 5.2, it is evident that about 10 % of the bombardment impacts do not cause any sputtering ($N_S \rightarrow 0$). The most probable event is the emission of 2–3 Ni atoms, whereas the probability for 27 sputtered Ni atoms is still 10^{-4}. These values correspond to a mean sputtering yield $Y = 4.87$.

5.2 Effects on Sputtering Yield

The ion sputtering yield depends on different parameters. Besides the ion beam characteristics as its mass, its energy and incident direction, it also depends on the target material composition [7, 8]. For multicomponent targets, there exists the so-called preferential sputtering; for polycrystalline and/or heterogeneous targets,

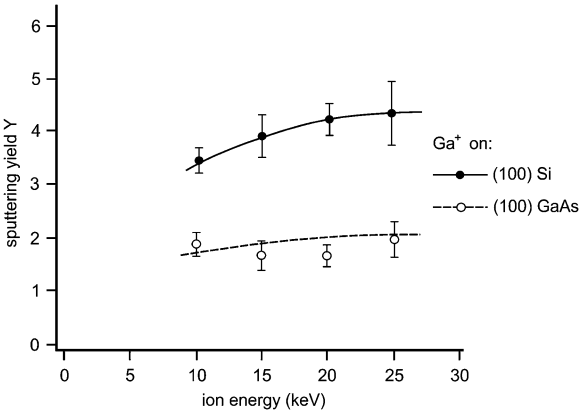

Fig. 5.3 Sputtering yield Y as a function of the ion energy for Ga^+ ions impinging on (100)Si or on (100)GaAs respectively [5]

selective sputtering takes place. Furthermore, the sputtering yield of crystalline solids is influenced by the channeling effect.

5.2.1 Ion Energy and Ion Atomic Number

The sputtering yield Y should be proportional to the number of displaced or recoil atoms per impinging ion. As already mentioned in the general Chap. 2, for medium mass ions as Ga with an energy E_0 the number of recoils is proportional to the energy deposited at the surface [8]:

$$Y = \Lambda \cdot F_D(E_0) \tag{5.1}$$

with Λ the materials factor, and $F_D(E_0)$ the deposited energy at the surface.

The nuclear energy deposited on the surface can be expressed as

$$F_D(E_0) = \alpha \cdot N \cdot S_n(E_0) \tag{5.2}$$

with α the correction factor, N the atomic density of target atoms, and $S_n(E_0)$ the nuclear stopping cross section at energy E_0.

The product $N{\cdot}S_n(E) = dE/dx$ is the nuclear energy loss rate. In the low keV energy sputtering regime the nuclear stopping cross section $S_n(E)$ is proportional to E, and therefore $S_n \sim F_D \sim Y \sim E$.

This dependence $Y(E)$ is experimentally confirmed for the low energy range (e.g., [9]), and also shown in Fig. 5.3 [5, 10]. The important observation is that the sputtering yield saturates at around 30 keV.

For higher ion energies, the sputtering yield decreases again. This is evident from Fig. 5.4, showing the sputtering yield of a Ni target in dependence on the

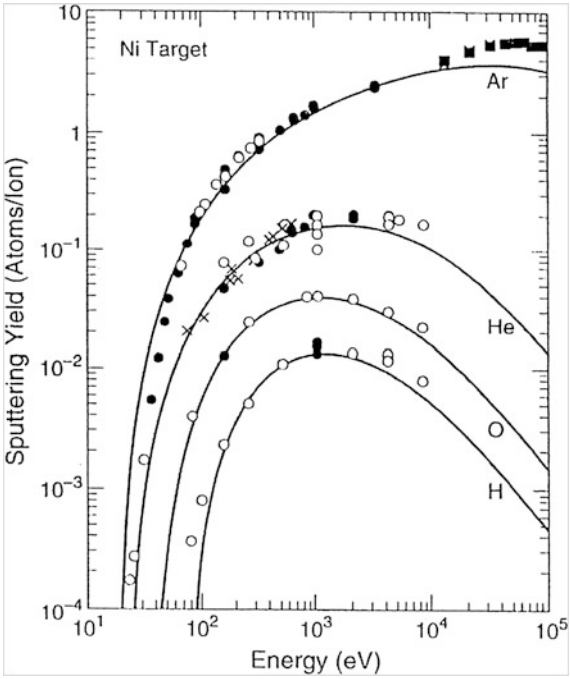

Fig. 5.4 Sputtering yield of a Ni target in dependence on the bombarding energy and the mass of different impinging ions [11]

bombarding energy and the mass of different impinging ions. The experimental data were measured by Yamamura and Muraoka [11], whereas the continuous graphs follow an empirical formula by Matsunami et al. [12].

From Fig. 5.4, it follows that the curve progression is the more flat the higher the corresponding ion mass is. Explicitly, the sputtering yield curve for Ar does not decrease in the given energy range. Even for the mass number of Ga which is higher than that of Ar, the $Y(E)$ dependence of Fig. 5.3 fits in very well.

With increasing atomic number Z_1 of the impinging ions, the deposited energy and with it the sputtering yield also grow [13]. This is illustrated in Fig. 5.5 for bombardment of Si with 45 keV ions of different atomic numbers Z_1. The continuous curve is the result of Sigmund's calculations [13], and the data are taken from Andersen and Bay [14]. For very heavy ions, the interaction energy and with it the sputtering yield Y saturate to a constant value.

A survey of measured sputtering yields Y and sputter rates S (in $\mu m^3\ nC^{-1}$) is given in Table 5.2 for different targets and 30 keV primary ions Ga^+, Al^+ and In^+ [5]. In some cases of ion beam-assisted target preparation Ga^+ ions must be replaced by other ions as Al^+ or In^+ to avoid deleterious effects and to maximize the sputter rate, respectively. Here, In^+ has shown promise as a useable alternative to Ga^+ [5]. The results of Fig. 5.5 are in very good agreement with those of Table 5.2.

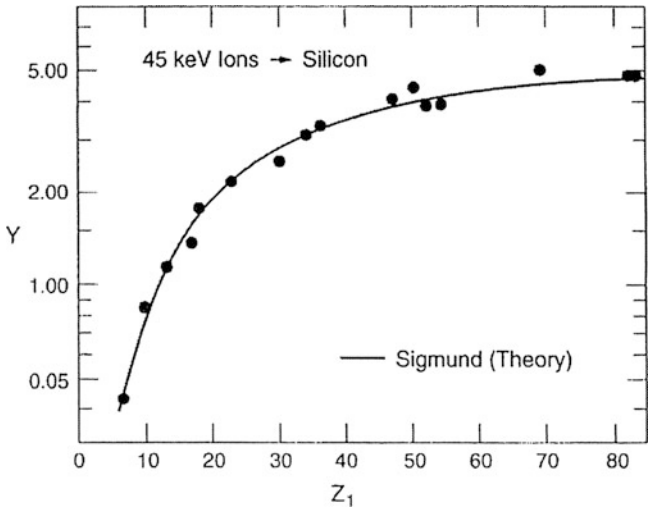

Fig. 5.5 Sputtering yield Y for bombardment of Si with 45 keV ions of different atomic numbers Z_1 [13, 14]

5.2.2 Ion Incident Direction

For the dependence of sputtering yield on ion incident angle Θ, different theories exist. For isotropic, homogeneous and polycrystalline targets, the Sigmund model gives an angular dependence of the sputtering yield Y as

$$Y(\Theta) = Y(0) \cdot \cos^{-f}(\Theta) \tag{5.3}$$

where f is a constant depending mainly on the target atom/primary ion mass ratio [8, 13].

Yamamura proposed another theoretical expression that analytically describes the angle dependence of the sputtering yield over a wide range of incident angles:

$$Y(\Theta) = Y(0) \cdot t^f \cdot e^{-S\cdot(t-1)}, \tag{5.4}$$

where $t = 1/\cos\,\Theta$ and S and f are adjustable parameters [15]. Measurements of Kaito (1999, Personal communication, referred by Vasile et al. in J Vac Sci Technol B 17: 3090) for 30 keV Ga^+ ion irradiation of Si, extending the incident angle Θ to near perpendicular incidence, are shown in Fig. 5.6.

Experimental data show good agreement with both the Sigmund and Yamamura theories at low angles of incidence. At higher angles however, the Yamamura theory gives better agreement with the experimental data. The sputtering yield reaches a maximum near 80°, and then falls rapidly as the incident angle approaches 90°, where surface ion channeling begins to dominate the interaction.

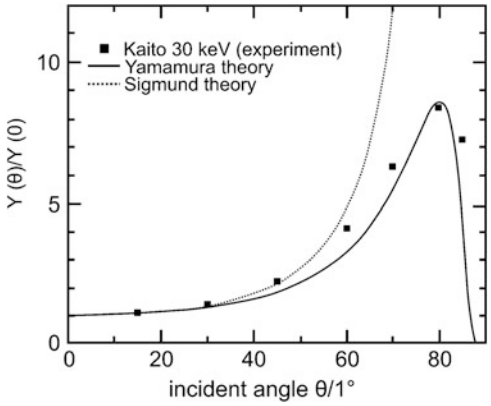

Fig. 5.6 Comparison of sputtering yields (30 keV Ga^+ on Si) calculated by Sigmund and Yamamura with experimental data of Kaito [5]

Channeling occurs in crystalline target materials. When ions enter a low-index axial crystal direction or planar channel in a crystal, electronic and nuclear stopping will be reduced considerably. The mean maximum penetration depth R_P of ions incident along main crystallographic directions in the crystal can exceed their range in an amorphous target by factors of more than one order of magnitude [16, 17]. This is caused by moving the collision cascade further away from the surface.

As an example, Fig. 5.7 shows the sputtering yield Y of a (100)Cu single crystal bombarded with 27 keV Ar^+ ions under different incident angles Θ [18]. Due to the channeling effect the sputtering yield Y shows pronounced minima in "open," i.e., low index <111>, <211> and <411> lattice directions. Generally, the sputtering yield values for single crystalline materials are higher compared to amorphous or polycrystalline targets. Ion channeling is one of the reasons for selective sputtering effects.

5.2.3 Selective Sputtering Due to Ion Channeling

If a parallel ion beam bombards a polycrystalline and/or heterogeneous target surface, so-called selective sputtering will take place. This effect results from ion channeling (see Sect. 2.4) and it was extensively investigated by Hauffe (e.g., [2, 19, 20]). Figure 5.8 shows the ion beam-induced shaping of grain microstructures at the target surface. In case (a) the different ion incident directions with respect to the crystal orientations of the individual grains cause different displacement rates, that means different sputter rates/yields. In case (b) additionally the different materials composition of the heterogeneous target may have different sputter rates, and therefore selective sputtering takes place.

In contrast to chemical etching, selective ion sputtering forms pronounced steps at the grain boundaries [21, 22]. Thus, the internal grain structure can be revealed, if

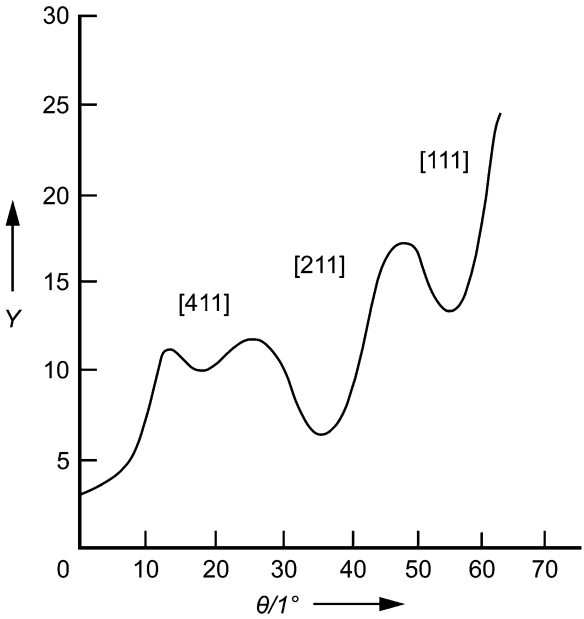

Fig. 5.7 Sputtering yield Y of a copper (100) single crystal with 27 keV Ar^+ ion bombardment, demonstrating the channeling effect [17, 18]

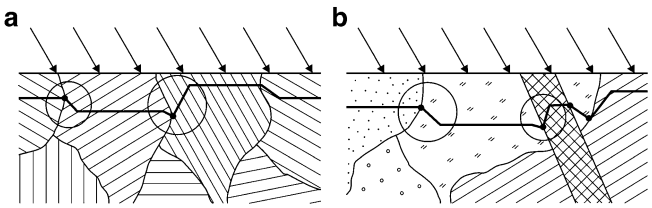

Fig. 5.8 Selective sputtering of polycrystalline (**a**) and heterogeneous (**b**) target surface, bombarded with a parallel ion beam (after Hauffe [19])

the initial target surface is chemically very clean and very smooth. As an example, the SEM image of Fig. 5.9 shows a distinct surface pattern after selective sputtering on an electrolytically polished polycrystalline Cu surface after bombardment with 10 keV Ar^+ ions at 40° ion incidence with respect to the surface normal [23].

Systematic investigations of selective sputtering effects and their comparison with chemical etching done by Hauffe resulted in the development of a model for grain boundary attack. This model explains the surface relief formation in detail, e.g., groove generation at normal incidence and special sputtering effects at grazing incidence [2, 19, 23]. Further results are discussed in Sect. 5.3.1

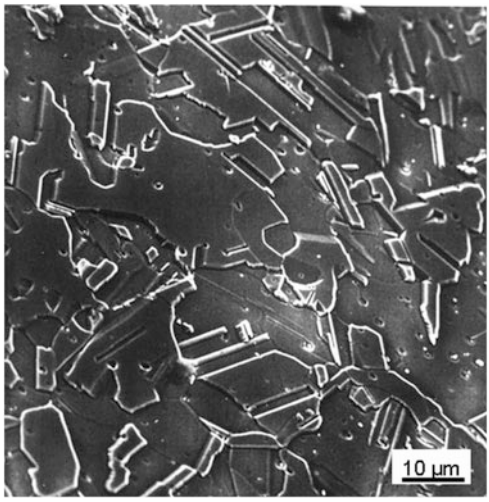

Fig. 5.9 SEM image of a clean polycrystalline Cu surface after bombardment with 10 keV Ar^+ ions at 40° ion incidence with respect to the surface normal [23]

5.2.4 Target Material

The dependence of the sputtering yield Y on the atomic number Z_{target} of bombarded target atoms can be understood by the linear collision cascade model of Sigmund [13]. After this theory both energy and momentum are transferred from the bombarding primary ions to target atoms, which recoil with sufficient energy to generate other recoils (cascades of binary collisions). Some of these backward recoils will approach the surface with enough energy to escape from the solid. Sputtering of target atoms occurs if the transferred energy is high enough to overcome the binding energy of surface target atoms. That means the sputtering yield will strongly depend on this binding energy and therefore on the target atomic number Z_{target}.

For ion energies E_0, the sputtering yield according to Sigmund's theory is given by

$$Y(E_0) = \frac{4.2 \times 10^{14} \cdot \alpha \cdot S_{\text{n}}}{U_{\text{s}}} \tag{5.5}$$

with

$$\alpha = 0.15 + 0.13 \cdot \left(M_{\text{target}}/M_{\text{PI}}\right), \tag{5.6}$$

$$S_{\text{n}} = \frac{8.462 \cdot s_{\text{n}}(\varepsilon) \cdot M_{\text{PI}}}{M_{\text{PI}} + M_{\text{target}}} \cdot \frac{Z_{\text{PI}} \cdot Z_{\text{target}}}{\left(Z_{\text{PI}}^{2/3} + Z_{\text{target}}^{2/3}\right)^{1/2}}, \tag{5.7}$$

and U_{s} the surface potential.

Table 5.3 Sputtering yields Y for different ion–target combinations, calculated with Sigmund's model (ion energy 30 keV) [5]

	Bombarding ion	Bombarding ion	Bombarding ion
Target	Ar^+	Ga^+	In^+
Al	3.2	5.2	6.6
Si	2.5	4.0	5.1
Ti	3.4	5.4	6.9
Cu	5.8	9.1	11.7
Zr	4.0	6.2	8.1
Mo	3.8	5.9	7.6
Ta	4.3	6.7	8.7
W	4.0	6.1	8.0

$S_n(\varepsilon)$ is defined as

$$S_{\mathrm{n}}(\varepsilon) = \frac{0.5 \cdot \ln(1+\varepsilon)}{\varepsilon + 0.14 \cdot \varepsilon^{0.42}} \tag{5.8}$$

with

$$\varepsilon = \frac{a \cdot M_{\mathrm{target}} \cdot E}{Z_{\mathrm{PI}} \cdot Z_{\mathrm{target}} \cdot e^2 \cdot (M_{\mathrm{target}} + M_{\mathrm{PI}})} \tag{5.9}$$

and a the Thomas–Fermi screening radius.

Furthermore, theoretical models are given by Matsunami [24] and Yamamura [15].

Sputtering yield values for selected ion–target combinations, calculated with Sigmund's model, are summarized in Table 5.3 [5]. The calculated values of sputter yield are generally higher than those which were found experimentally (compare Table 5.2), because redeposition and other artifacts diminish the experimental sputtering yield results [5]. A graphic demonstration of sputtering yields for 30 keV Ar^+ bombardment of different targets with atomic numbers from $Z_{\mathrm{target}} = 4$ (Be) up to $Z_{\mathrm{target}} = 52$ (Te) is given in Fig. 5.10. An interesting result of Fig. 5.10 is the strong variation of the sputter yields for one order of magnitude. This can be used to optimize specific ion–target combinations. The periodic fluctuations of sputtering yields as demonstrated in Fig. 5.10 are effected by the interatomic potentials, which are responsible for the physical properties of the individual targets.

If the periodic behavior $Y = f(Z)$ is correlated with other periodic fluctuating target parameters, very interesting results can be found. Figure 5.11 shows the correlation between sputtering yield Y and melting temperature T_{m} for targets with atomic numbers $Z = 13$–30 under 25 keV Ga^+ ion beam bombardment at an incidence angle $\Theta = 80°$ [1]. The sputtering yield shows an inverse correlation with T_{m}. This relationship is evident because the melting temperature is a measure

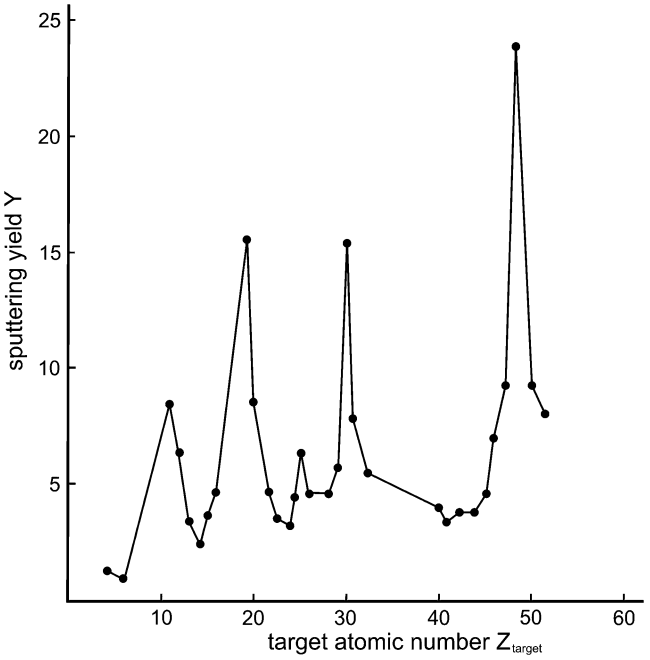

Fig. 5.10 Experimental data for the sputtering yield of 30 keV Ar^+ ion bombardment on different target materials (after [5])

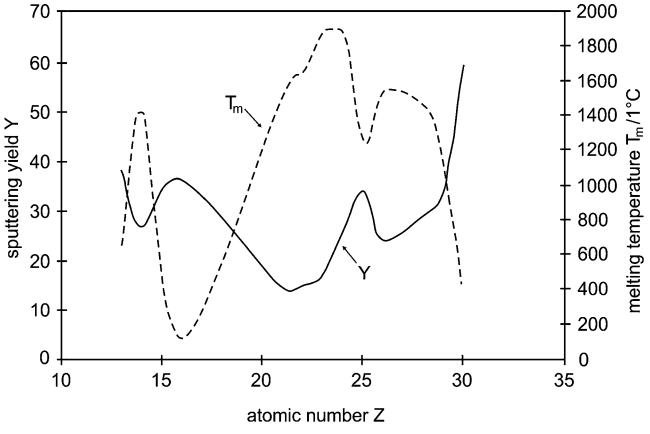

Fig. 5.11 Correlation between sputtering yield Y and melting temperature T_m of different targets ($Z = 13$–30) at 25 keV Ga^+ ion bombardment

of the atomic binding strength. Atoms with a very strong bond have a low probability to be sputtered from the target.

5.2.5 Preferential Sputtering

According to (5.5), the sputtering yield is inversely proportional to the surface potential U_s. The surface potential can be inserted as the surface binding energy E_{Bi}; so from (5.5) it follows that $Y \sim 1/E_{Bi}$. A second dependence of Y exists on the energy transfer: Y increases with increasing energy transfer from the bombarding ion to the target atoms. Both binding energy and energy transfer may be different for the different atomic species in a multicomponent target material. As an example, we look at a system consisting of two atomic components A and B with atomic concentrations N_A and N_B respectively.

The partial sputtering yields are defined by $Y_{A,B}$ = number of ejected atoms/incident ion. They are proportional to the corresponding atomic concentrations:

$$\frac{Y_A}{Y_B} = r \cdot \frac{N_A}{N_B} \neq \frac{N_A}{N_B}. \tag{5.10}$$

For low fluences, the total sputtering yield Y_{total} can be superposed from the partial sputtering yields:

$$Y_{total} = Y_A + Y_B. \tag{5.11}$$

In (5.10) r is the so-called sputtering factor, which takes into account differences in surface binding energies $E_{Bi;A,B}$, in sputter escape depths and energy transfers within the collision cascades. Typical values of r are 0.5–2. For $r \neq 1$ one of the two components A, B is sputtered preferentially. The complicated concentration depth profiles that may result have been discussed, e.g., by Andersen [25] and by Betz [26]. During sputtering, the surface concentrations and yields will change from their initial values toward a stationary state in the bulk:

$$\frac{Y_A(\infty)}{Y_B(\infty)} = \frac{{N_A}^{bulk}}{{N_B}^{bulk}}, \tag{5.12}$$

where $Y_{A,B}(\infty)$ mean the stationary partial sputtering yields and ${N_{A,B}}^{bulk}$ the bulk atomic fractions.

For $r > 1$, the sputtering yield of component A is greater than that of B, and therefore the near-surface region will be enriched with component B. This produces an increase in the sputtering yield of B—because of more B atoms—and a decrease in the sputtering yield of A. Thus the increased concentration of B just balances out the preferential sputtering of A, and at steady state the real bulk concentrations will be measured, according to (5.12).

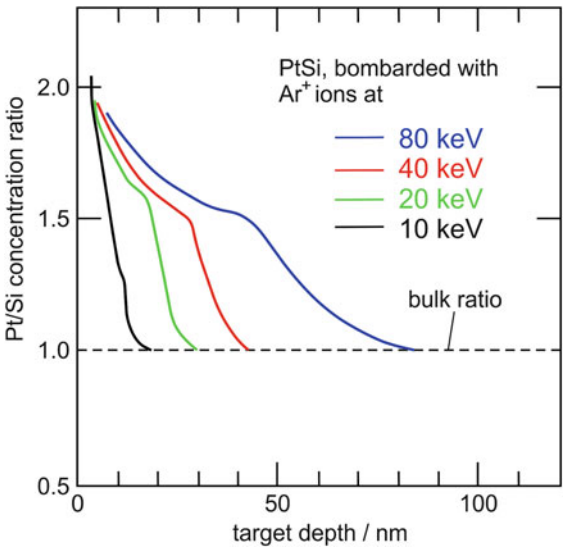

Fig. 5.12 Preferential sputtering of a PtSi target by Ar^+ ion bombardment at different energies and fluences [27]

As an example preferential sputtering of a PtSi target with a bulk concentration ratio of $Pt^{bulk}/Si^{bulk} = 1$ shall be discussed [27, 28]. The diagram in Fig. 5.12 shows concentration depth profiles of the target after bombardment with Ar^+ ions of different energies between 10 and 80 keV, and with ion beam fluences of some 10^{17} cm^{-2}. The bulk concentration ratio of 1 is reached after different ion bombardment depths of some 10 nm, proportional to the ion energies. In the near-surface region, the bulk concentration ratio Pt/Si = 1 is falsified because of preferential sputtering.

This change in the composition of a near-surface layer of PtSi can also be demonstrated by Rutherford Backscattering (RBS, see Chap. 6). The RBS spectrum of Fig. 5.13 was received with 2 MeV $^4He^+$ ions after sputtering by 20 keV Ar^+ ions. It shows an enrichment of the Pt concentration in the near-surface region (shaded area) as a result of the enhanced Si sputtering.

The measured curves in Fig. 5.14 show partial sputtering yields of Si and Pt as a function of the Ar^+ ion dose or Ar^+ fluency respectively. At low bombardment fluencies, the sputtering yield of Si is significantly higher than that of Pt. At the onset of preferential sputtering, the ratio $Y_{Si}(0)/Y_{Pt}(0)$ is about 3. The equality of the Si and Pt yields reflects the fact that the stationary state, that means the bulk state, has been reached. The total stationary sputtering yield $Y_A(\infty) + Y_B(\infty)$ of a two-component target material is a function of the bombarding ion energy.

This is demonstrated in Fig. 5.15 for a TaC target during $^4He^+$ bombardment, by both the experiment and TRIDYN computer simulation [27]. Initially, carbon is sputtered preferentially, denuding at the surface. Therefore its partial sputtering yield decreases, whereas the Ta partial yield increases. Both values converge to a ratio $Y_{Ta}(\infty)/Y_C(\infty) = 1$, and its sum increases with increasing $^4He^+$ ion energy.

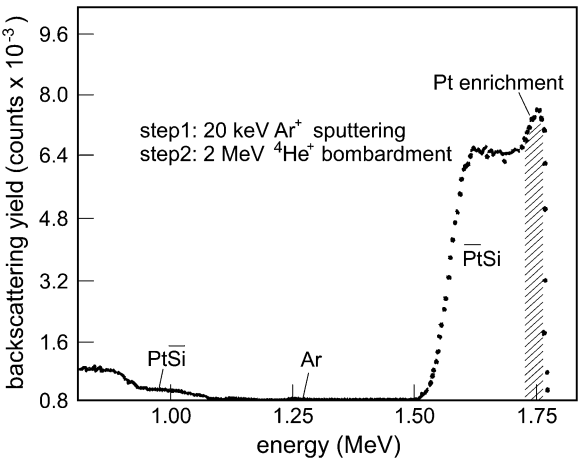

Fig. 5.13 RBS spectrum of PtSi with 2 MeV $^4He^+$ ions after sputtering by 20 keV Ar^+ ions [27]

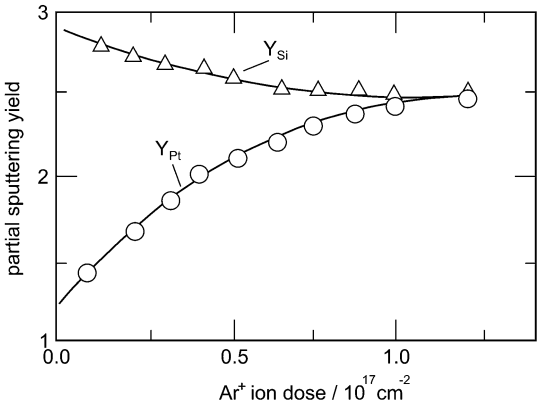

Fig. 5.14 Partial sputtering yields of Si and Pt as a function of fluence for 40 keV Ar^+ bombardment of a PtSi layer [27]

5.3 Preparation Steps by Ion Beam Irradiation

By ion bombardment of a target, different ion beam-induced modifications of this target will take place as part of the materials preparation process. In detail, a bombarding ion beam will be useful for the following target treatments:

- Ion beam-induced cleaning and etching
- Ion beam-induced material deposition
- Ion beam depth profiling
- Ion beam cutting
- Ion beam thinning

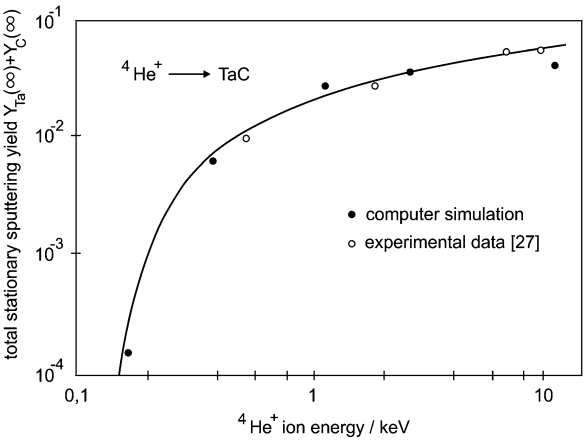

Fig. 5.15 Total stationary sputtering yield $Y_{Ta}(\infty) + Y_C(\infty)$ of TaC during $^4He^+$ bombardment as a function of the ion energy [27]

5.3.1 Ion Beam-Induced Cleaning and Etching

As discussed in Sect. 5.2.3, ion beam sputtering, or often called etching, of a crystalline surface has various reasons (see also Fig. 5.8). The different ion incident directions with respect to crystals orientation give rise to different atomic sputter rates $Y = f(\Theta_i)$, causing an ion beam etched surface. Furthermore, a heterogeneous target commonly has different etching rates for different material components: $Y = f(Z_{mat})$, effecting an additional contribution to the ion beam etching (sputter-eroded) process.

A precondition for pure microtopography development by ion beam etching and its visualization is the existence of a very clean surface. This is especially induced by electrolytical or chemical polishing but can be also reached by ion bombardment with very smooth ion beam parameters [3].

In that case, the ion beam only removes the physically and chemically adsorbed atoms and molecules from the target surface. As an example, Fig. 5.16 shows the FIB micrograph of a Cu interconnect line, bombarded by Ga^+ ions with $I = 2 \times 10^{-10}$ A and $U_B = 30$ kV [29]. The cleanliness of the surface is demonstrated by the orientation contrast of Ga^+ ion-induced emitted electrons.

The characteristics of ion beam etching in comparison with chemical etching have been studied systematically by Hauffe [2, 19]. For polycrystalline targets, he developed a model for grain boundary attack by ion etching. The visible steep slopes depend on the angle of ion incidence, and their number can be enhanced by consecutive etching under different angles. In Fig. 5.17a, an etched structure of polycrystalline Cu after 10 keV Ar^+ bombardment at different angles (in a final step at 35°) is visible. In spite of it, ion etching of single crystalline or of amorphous surfaces causes microrelief structures consisting of facets, as demonstrated in Fig. 5.17b for a Cu single crystal surface, also bombarded by 10 keV Ar^+ ions. A faceting model also developed by Hauffe [22, 23] describes the nucleation and growth mechanism of these faceting structures.

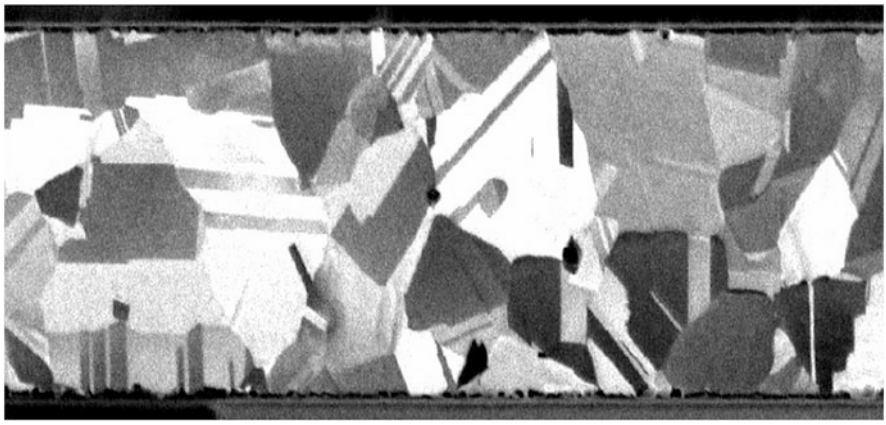

Fig. 5.16 FIB micrograph of a clean Cu interconnect line (line width 8 μm, Ga^+ bombardment with $I = 2 \times 10^{-10}$ A, $U_B = 30$ kV) [29]

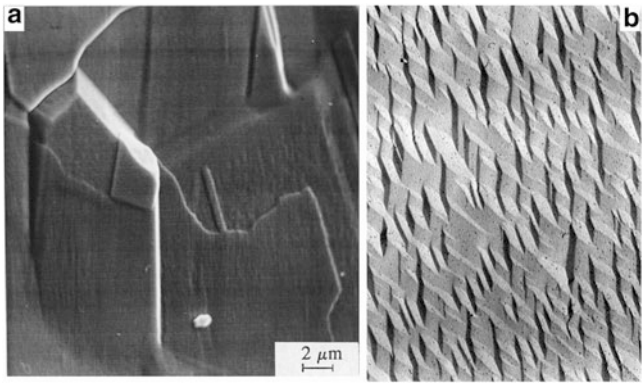

Fig. 5.17 Ion beam etched Cu surfaces, after 10 keV Ar^+ bombardment [19]: (**a**) polycrystalline Cu, and (**b**) mono-crystalline Cu

The topography of ion beam etched surfaces is decisively influenced by the initial surface state, as by the existence of a contamination layer. As an example, Fig. 5.18a reproduces the SEM micrograph of a (852)-oriented Ag surface with such a protecting contamination layer [2, 22]. The visible cones developed under oblique 10 keV Ar^+ bombardment, with $\Theta_0 = 51°$. They may be caused by screening particles protecting the underlying material. Their growing and removal conditions are discussed by Hauffe (e.g., [22]), and they are drawn schematically in Fig. 5.18b, with $I =$ ion beam current and v_p, v_w, $v_s =$ cutting velocities of the cone peak, the cone wall and the (852) Ag surface, respectively. Both, the growth and the removal of such cones can be influenced not only by impinging and reflected ions but also by the redeposition of sputtered atoms.

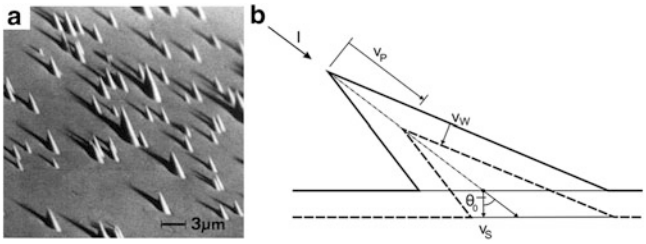

Fig. 5.18 Cone formation on a coated, (852)-oriented Ag surface during 10 keV Ar^+ ion bombardment under $\Theta_0 = 51°$ [2, 22]: (**a**) SEM image, and (**b**) growth and removal of cones (schematically)

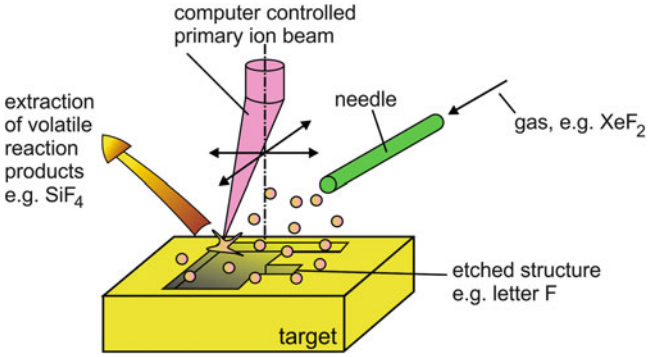

Fig. 5.19 Enhancement of the ion beam etching rate by gas assistance (schematically)

The ion beam etching rate can be enhanced by gas assistance [3]. The reaction mechanism is an interaction of the gas with the target surface to produce a volatile chemical compound that will be removed by the vacuum system. The enhanced ion beam etching mechanism is schematically demonstrated in Fig. 5.19.

A reactive gas, e.g., XeF_2 or an other halide, is introduced into the reaction chamber by a fine needle gas valve. The gas is physically or chemically adsorbed on the target surface. It reacts with the surface either spontaneously—as XeF_2 on Si—or under the influence of the primary ion beam. The developing volatile reaction products are desorbed from the surface and then extracted. The spontaneous reaction of XeF_2 (gaseous: g) with Si (solid: s) proceeds as follows [30]:

$$XeF_2(g) + Si(s) \rightarrow SiF_2(s) + Xe(g) \tag{5.13}$$

and after it

$$SiF_2(s) + XeF_2(g) \rightarrow SiF_4(g) + Xe(g). \tag{5.14}$$

The extracted gaseous reaction product is then SiF_4. By computer controlling of the primary ion beam, patterns can be written on the surface because of the

Table 5.4 Etching rate enhancement versus milling by gas assistance (30 keV Ga^+) [3]

Gas	Target Si	Target SiO_2	Target Al	Target W	Target PMMA
I_2	5–10	1	5–15	–	2
XeF_2	7–12	7–10	1	7–10	4
Cl_2	11	1	5–10	1	1
Br_2	6–10	1	10–20	1	1

enhanced etching rate at spots where ions impinge. As a schematic example in Fig. 5.19, the letter "F" is formed as a result of the etched microstructure by the writing focused ion beam (FIB).

The etching rate enhancement by gas assistance versus milling is summarized in Table 5.4 for different gas–target combinations in the presence of Ga^+ ion beam.

The interaction of chlorine and bromine with silicon is similar to that of XeF_2 [3]. However, both chlorine and bromine need the presence of the ion beam for a gas-enhanced etching rate, because no spontaneous reaction between these gases and the target surface takes place. On the other hand, the necessity of a present ion beam is preferable, because this allows a better control of the ion beam etching process [3]. The etching rate enhancement is evident not only for semiconducting targets, but also for metals, insulators and organic materials, as the acrylic glass (PMMA).

5.3.2 Ion Beam-Induced Material Deposition

The ion beam bombardment of a specimen surface for preparation can be applied for material deposition on the sample surface using the following deposition techniques:

- By direct current (DC) plasma sputtering of a target
- By direct ion beam sputtering of a target
- By deposition of metal atoms from a metallo-organic compound under ion beam bombardment

Ion beam-induced material deposition by means of target sputtering nowadays is the most common coating technique because of particular advantages compared with other techniques, as, e.g., material evaporation. Decisive advantages of target sputtering with ions are low sputtering times of only few minutes and the formation of homogeneous thin coating layers.

In Fig. 5.20, the principles of the two different types of sputter coating are schematically demonstrated. The direct current (DC) plasma sputter coater is equipped with two electrodes (Fig. 5.20a). The positively charged electrode is the specimen holder with some specimen, and the negatively charged is the target, typically gold. A glow discharge is formed, and the sputtered Au particles move from the target to the specimen surface, where they are deposited. The sputter yield may be enhanced by use of a magnetron head. Usually Ar is used, and a suitable low pressure is achieved by the vacuum system. The grain size of the deposited gold layer is then (2–5) nm, and to achieve a continuous conductive surface layer its thickness has to be typically (10–20) nm.

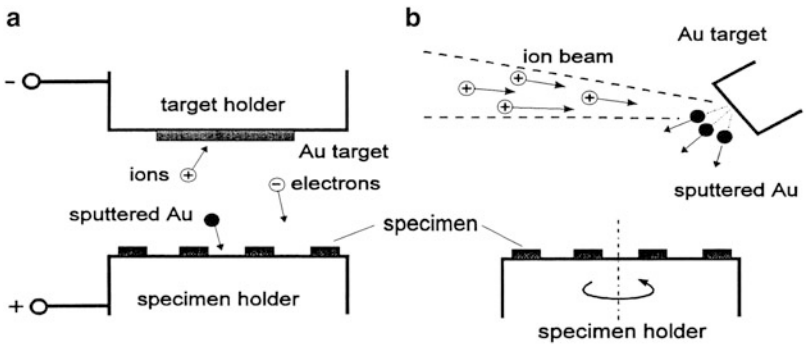

Fig. 5.20 Ion sputter coating by (**a**) direct current (DC) plasma sputtering, (**b**) ion beam sputtering (schematically)

Thinner deposition layers can be attained with direct ion beam sputtering, though this process needs longer deposition times (Fig. 5.20b). An inert gas ion beam—e.g., of Ar ions—is used for bombardment of the target, which preferably consists of gold. The sputtered Au particles cover the specimen placed on a rotating specimen holder, to avoid directional sputter deposition.

The rate of ion beam-induced material deposition can be enhanced by gas assistance, in a similar way as ion beam etching [3].

The gas-assisted ion beam-induced deposition is a direct material deposition by using a focused ion beam together with a gaseous compound precursor. Because of the narrow localized ion beam spot, the deposition process also takes place in a very local area where the controlled ion beam is scanning the specimen surface.

The gas-assisted deposition process is schematically reproduced in Fig. 5.21, and it can be described by the following steps:

- A gaseous metallo-organic compound, acting as precursor, is introduced into the reaction chamber through a fine needle in vicinity to the ion beam spot on the sample surface
- The gas molecules adsorb at the target surface. By the bombarding ion beam, these molecules are decomposed into volatile and nonvolatile fractions
- The volatile fractions as oxygen, gaseous carbon compounds and hydrogen are desorbed from the surface and then extracted by the vacuum system. The nonvolatile reaction products, mostly metals, are deposited on the surface

By computer controlling of the primary ion beam patterns can be written on the surface because of metal deposition under ion bombardment. As an example in Fig. 5.21, the letter "F" is written as a deposited metallic pattern.

The first ion beam-induced metal deposition (Al) under gas assistance with a trimethyl aluminum precursor was described by Gamo et al. [31]. Actually, a lot of different precursors are well-known for successful ion beam-induced deposition not only of metals (Ta, Pt, Au, Cu, Fe) but also of insulators (SiO_2) and carbon. A summary of precursor gases and deposited materials at ion beam-induced deposition processes is given in Table 5.5.

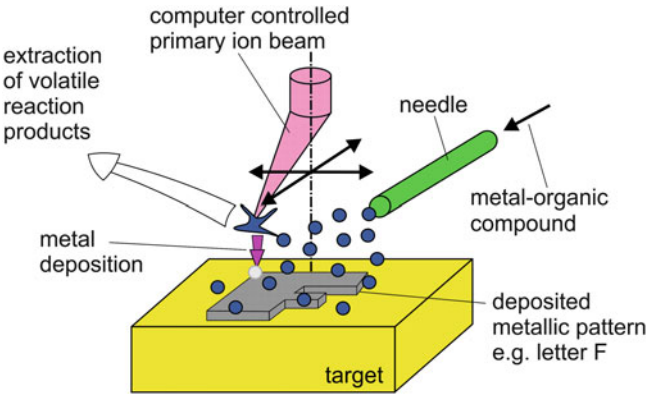

Fig. 5.21 Ion beam-induced material deposition under gas assistance (schematically)

Table 5.5 Precursor gases and deposits for ion beam-induced material deposition

Precursor gas		Deposited material	References
Trimethyl aluminum	$Al_2(CH_3)_3$	Al	[31]
Tungsten hexacarbonyl	$W(CO)_6$	W	[32]
Dimethyl gold hexafluoro acetylacetonate	$C_7H_7O_2F_6Au$	Au	[33]
Trimethyl platinum	$C_9H_{16}Pt$	Pt	[34]
Pentaetoxy tantalum	$Ta(OC_2H_5)_5$	Ta	[35]
Palladium acetate	$[Pd(O_2CCH_3)_2]_3$	Pd	[36]
Mixture siloxane/oxygen	$Si(OCH_3)_4$	SiO_2	[37]
Naphthalene	$C_{10}H_8$	C	[38]

An important precondition for successful material deposition is the right flow rate of the gas precursor. In the case the gas fluence is too high the deposition rate will be very small, but if the fluence is too low the sputtering process of the specimen surface by the incident ion beam will take place. Therefore, the gas flow must be carefully adjusted by a nozzle which is placed inside the needle shown in Fig. 5.21.

The deposition rate also depends on the primary ion current density, the scanned area, and the pixel dwell time [3]. Therefore, also the ion flux will be a decisive parameter for optimization of the material deposition process. The most efficient deposition rate will be reached with intermediate beam current densities of some 10^{-12} A μm^{-2} for $C_9H_{16}Pt$, that is for Pt deposition and of some 10^{-10} A μm^{-2} for $W(CO)_6$ in the case of W deposition [39].

5.3.3 Ion Beam-Induced Depth Profiling

Most of materials characterization techniques are limited to two-dimensional representations of materials, usually of their surfaces. This applies to the microstructure, but also to the phase and element analysis of specimen surfaces.

For example, X-ray diffraction, spectroscopic and imaging techniques allow two-dimensional mappings or near-surface measurement modes. However, during the last decade both structural and chemical depth profile characterization of bulk materials, thin layers and multilayer systems have become more and more important [40]. Also the understanding of interface structures is of growing interest [41]. These arrangements are determined by the depth profile of microstructure, but also of element concentrations, chemical states and phase concentrations, as evaluated by principal component analysis [42].

Because thin films down to monolayers are of growing interest, problems of layer modification during ion sputtering, ion mixing, implantation and similar processes become more and more awkward. From these problems follows the demand for a low information depth (few nanometers) and for a good depth profile resolution down to the nm range.

Ion beam depth profiling in combination with surface-sensitive analytical techniques is mainly used to investigate such depth concentration profiles. As discussed also in Sect. 6.7.1, the concentration depth profile $c = f(z)$ must be evaluated from the measured intensity–time profile $I = f(t)$. This will be done by two calibrations:

- Depth calibration $z = f(t)$
- Element or phase calibration $c = f(I)$

To reveal the true depth concentration profile $c = f(z)$ one must consider that by ion beam sputtering both the composition and the morphology of an uncovered target surface will be changed [43].

Generally, c is the element concentration, but in some cases it can also be interpreted as a phase concentration because of different bonding states, resulting in different peak shapes. Figure 5.22 illustrates schematically this fact for a TiC–C multilayer system. Because C exists in both phases—C and TiC—its element concentration $c_{\mathrm{elem}}(z)$ is always different from zero. An interesting fact is the nonlinear transformation from the sputter time axis t_{Sp} to the sputter depth axis z because of different sputtering rates of the individual layers. The phase depth profile interprets the real carbon concentrations in the alternating TiC and graphitic C layers.

To achieve the depth calibration $z = f(t)$, the sputtering rate $\dot{z}$ must be given:

$$z(t) = \int_0^t \dot{z} \cdot \mathrm{d}t. \tag{5.15}$$

Under the assumption of a constant sputtering rate $\dot{z}$ (5.15) can be simplified:

$$\dot{z} = \frac{z_0}{t_0} = \text{const.} \tag{5.16}$$

with $t_0 =$ erosion time and $z_0 =$ erosion depth. The depth calibration is then carried out by an erosion crater depth measurement.

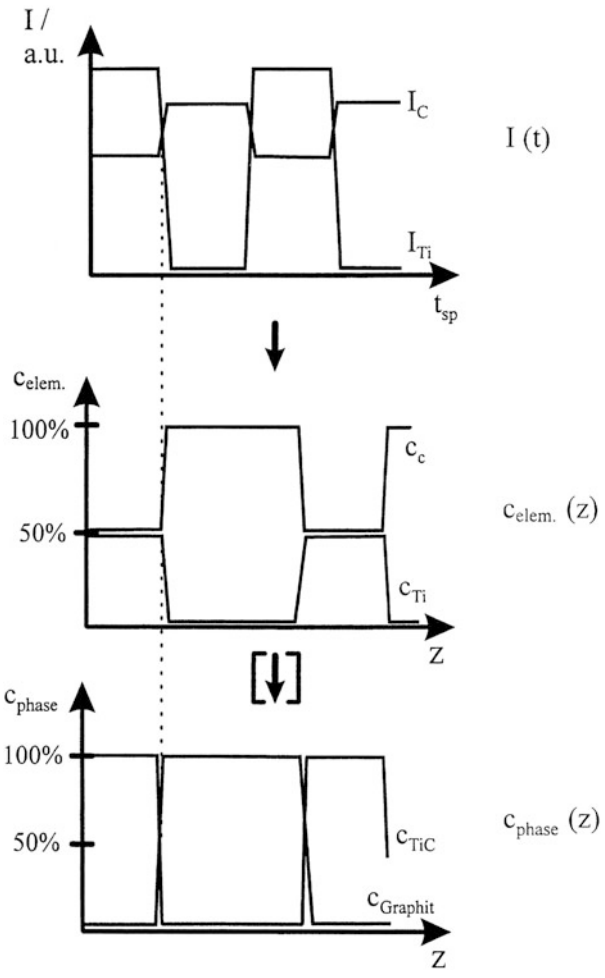

Fig. 5.22 Determination of concentration depth profiles for a TiC/C multilayer system (schematically) [40]

Considering the means of obtaining the concentration depth profile $c(z)$ from the measured intensity–time profile $I(t)$, modern methods for ion beam depth profiling can be divided into two groups:

1. The surface layer is alternately removed by ion sputtering and analyzed by means of Auger or photoelectron spectrometry (AES, XPS).
2. The sputtered part of the surface is immediately used for depth profile analysis. This is the case for secondary ion and sputter neutral mass spectrometry (SIMS, SNMS) and for glow discharge optical emission spectrometry (GDOES).

Furthermore, nondestructive depth profiling methods exist such as total reflection X-ray fluorescence (TXRF), Rutherford Backscattering (RBS) or angle resolved photoelectron spectrometry (ARXPS). Some of these techniques (SIMS, SNMS, RBS) will be discussed in Chap. 6.

Each of the ion beam depth profiling methods in group (1) and group (2) has special advantages. AES combines a depth resolution of only few nm with best lateral resolution values of about 20 nm [44]. The main advantage of XPS is the possibility of obtaining chemical bonding information. Trace analyses down to hydrogen ($Z = 1$) with detection limits below the ppm range can be obtained with SIMS and SNMS. GDOES is a fast method with sputtering rates up to 100 nm s^{-1} [45], without the requirement of high vacuum. On the other hand, one must renounce microscopic lateral resolution.

An important parameter for the accuracy of the depth profile obtained by successive sputter removal of the sample material is the depth resolution Δz, which is limited by ion-induced surface roughening and atomic mixing. Therefore, ion sputtering parameters [40] must be carefully selected to minimize these disturbing effects. The depth resolution Δz has been further improved by the development of special deconvolution techniques. Präßler improved the quantitative depth determination for GDOES depth profiles by the addition of information on the crater formation process into the time-to-depth transformation [46]. For that he demonstrated the mathematical handling of deconvolution for GDOES analysis of multilayer systems. Because of a non-Gaussian relation for the signal response, the quantitative evaluation of GDOES depth resolution Δz can be carried out using

$$\Delta z = \frac{\Delta c}{(\mathrm{d}c/\mathrm{d}z)_{\max}} \tag{5.17}$$

Without deconvolution, the depth resolution in Fig. 5.23 degrades proportional to the depth of the ion beam sputtered crater. This is in accordance with the crater profiles of Fig. 5.24, which show an increasing roughening of the crater bottom [47]. In contrast, the roughness remains constant at $\Delta z = 20$ nm using the deconvolution technique. That means, the depth resolution and thereby also the quantification become then almost independent of the sputtering depth.

The principle and the schematic function of GDOES are shown in Fig. 5.25. The glow discharge source after Grimm [48] consists of a ring-shaped anode and opposite to it the sample, which serves as the cathode. During the discharge, the cathode is bombarded by positive ions of a noble gas. This bombardment induces a surface erosion of the sample causing a typical sputtering crater. By ion collision processes and further interactions in the plasma the sputtered material, both atoms and ions, is excited for optical transitions in the visible and ultraviolet ranges. The generated photons correspond to characteristic spectral lines of the elements in the plasma, giving information on the element depth profiles of the sample which is removed layer-by-layer by the ion sputtering process.

Sputtering rates up to 100 nm s^{-1} are possible. The emitted light is analyzed in an optical spectrometer which consists of a concave grating in a Rowland circle and calibrated photomultiplier tubes. The measured intensity –time profiles have to be converted for quantitative analysis into concentration depth profiles. For that purpose, the quantification algorithm by Bengtson [49] is commonly used very successfully.

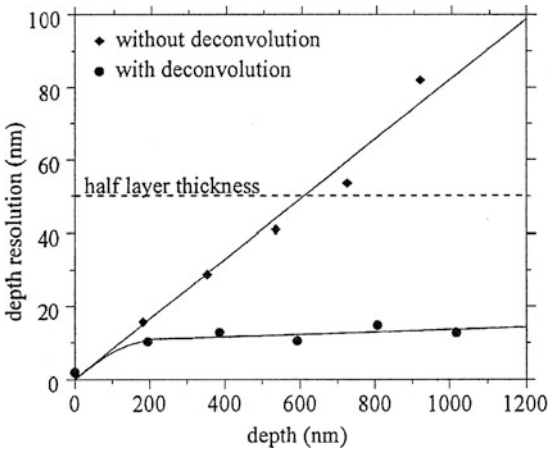

Fig. 5.23 Comparison of the depth resolution of a Cu/CrNi multilayer system with and without deconvolution technique (Ar at 770 Pa) [40]

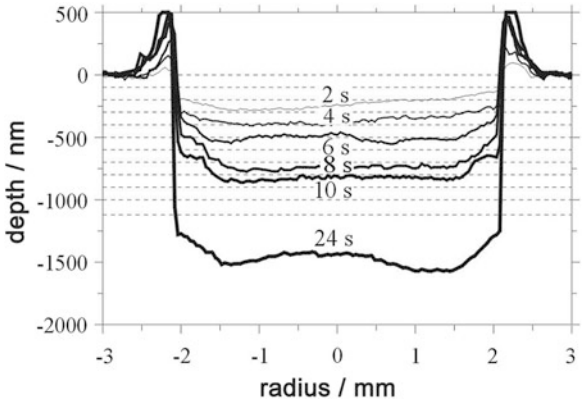

Fig. 5.24 Crater depth profiles of a Cu/CrNi multilayer system after different sputter times (rf-sputtering, $p_{Ar} = 770$ Pa, $U = 1{,}350$ V, depth in nm) [47]

Similar or better values of depth resolution could be reached for other ion beam-based depth profiling methods such as AES, XPS, dynamic SIMS and SNMS [40, 50]. They are usually in the (1–10) nm range. Because the total depth is often greater than the analytical depth resolution, a combination of alternating surface spectroscopy and progressive removal of the surface by ion sputtering is used.

As an example, Fig. 5.26 shows the AES concentration depth profile of an as-deposited spin-valve sample using 800 eV Ar^+ ions for sputtering [51]. At the interface FeMn/CoFe, an excess of Fe is calculated as expected for a CoFe alloy layer. This is represented by the bold line in Fig. 5.26. In the other "CoFe" layers, a much lower Fe signal was found. Annealing at 350 °C leads mainly to oxidation of the Ta capping layer, but no evidence for a demixing of the Cu and Co layers was found [52]. The depth resolution of this concentration depth profile is $\Delta z < 5$ nm.

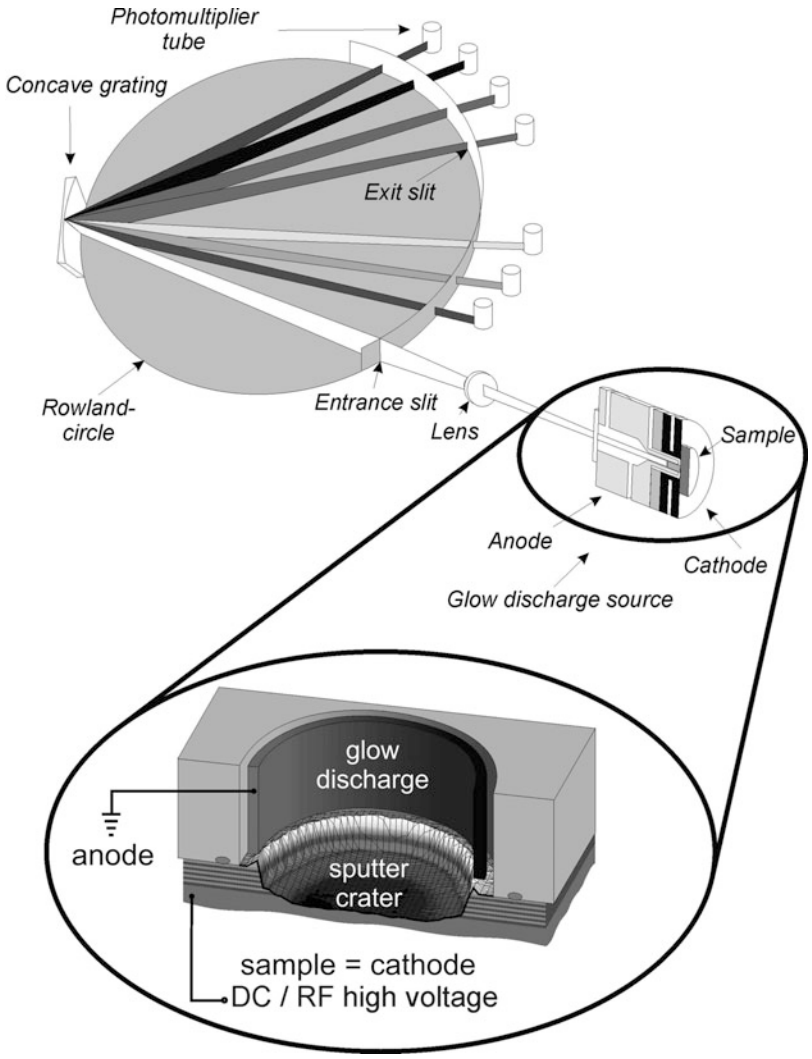

Fig. 5.25 Principle of glow discharge optical emission spectroscopy (GDOES)

Chemical states of elements can be determined from both AES and XPS spectra by the so-called chemical shift. This is the observed peak shift of a particular element when the chemical state of this element changes. The chemical shift is particularly distinct in XPS spectra. It is caused by the alteration in the valence electron density when an atom combines with another atom or atom group. The binding energy (BE) of the core electrons therefore changes, giving rise to shifts in the corresponding photoelectron peaks. For the identification of unknown chemical states, tabulations of chemical shifts have been made by many authors (e.g., [53]).

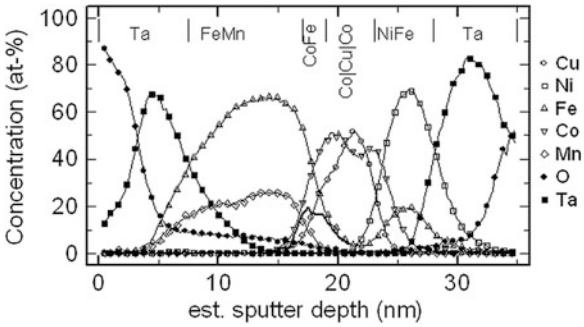

Fig. 5.26 AES concentration depth profile of an as-deposited spin valve sample [50]

During analysis of thin films and layer systems by ion beam depth profiling, the chemical states of their elements often change in dependence on the layer depth. This can be shown graphically by the binding energy shift of photoelectron peaks in depth profiles. As an example, Fig. 5.27 demonstrates the binding energy shift of the XPS peaks of Ta 4f and Si 2p for increasing thickness of a Ta layer sputtered on Si [54]. Tantalum was deposited by magnetron sputtering up to a thickness of 10 nm. At the interface, the Ta 4f photoelectron peak shows a significant shift of 0.6 eV to higher binding energy compared to metallic Ta, which is observed at a layer thickness of 10 nm (left image). The shifted peak at the interface agrees very well with the $TaSi_2$ reference spectrum. A shift in the binding energy of the Si 2p peak was also observed (right image), which is an additional hint for silicide formation at the Ta/Si interface.

5.3.4 Ion Beam Cutting

Cross-sectional cutting of samples is another example of ion beam applications in microanalytics. Ion beam cutting generates representative cross sections through heterogeneous materials [19, 22]. This method can be used to most targets, especially to materials with very different components as metal-matrix composites, brittle insulators, porous materials and organic samples. Ion beam cutting can be carried out, for example, in situ under electron microscopic control in an SEM. This has two advantages. The cutting process can be immediately studied and the virgin cross section can be investigated without any air exposure or transport problems. Furthermore, ion beam cutting is an advantageous preparation method to get cross sections for microanalytical methods as AES, XPS, SIMS, and also analytical TEM.

The ion beam cutting technique is possible as an ion beam slope cutting, using a broad ion beam (BIB), or a focused ion beam (FIB) in the scanning mode. Ion beam cutting is mainly used

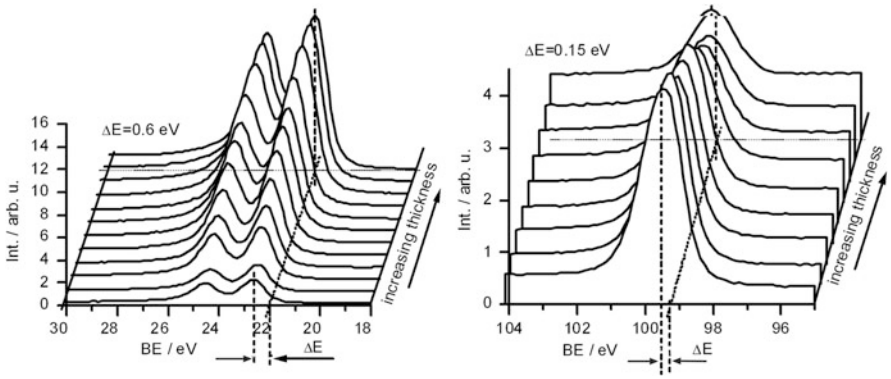

Fig. 5.27 Binding energy (BE) shift of XPS peaks for increasing Ta layer thickness (up to 10 nm) on Si (*left*: Ta 4f peaks, *right*: Si 2p peaks) [54]

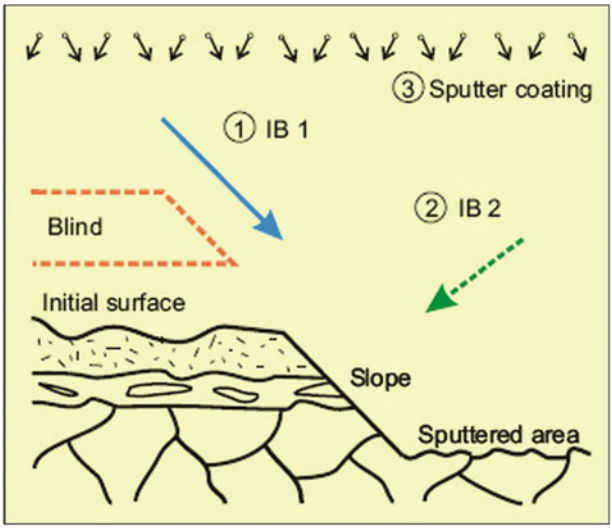

Fig. 5.28 Principle of the ion beam slope cutting technique (after Hauffe [55, 56])

- For element and phase distribution investigations on cutted surfaces
- For analysis of the microstructure along different cross sections
- For three-dimensional failure analysis
- For fabrication of specialized micro- and nano-tools

In this section the ion beam slope cutting technique with BIB will be discussed in more detail, whereas sample preparation and applications of the FIB method will be the subject of the special Sect. 5.4.

Figure 5.28 shows the principle of ion beam slope cutting [2, 55, 56]. A parallel broad ion beam (not focused) strikes the initial surface up to a sharp borderline,

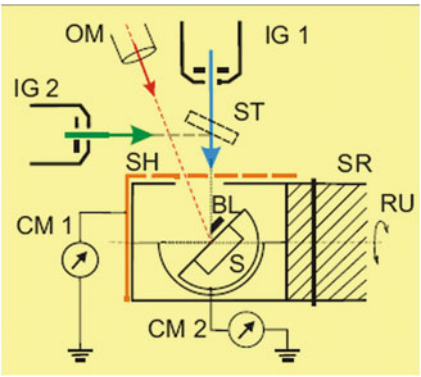

Fig. 5.29 Arrangement of ion guns, sample stage, manipulation and control attachments in the modified Gatan PECS [55]; *IG 1* ion gun for cutting and etching, *IG 2* ion gun for coating, S sample, *BL* blind mounting, *SR* sample rod, *RU* rocking/rotation unit, *SH* shutter, *OM* optical microscope, *CM* 1 absorbed shutter ion beam current, *CM* 2 absorbed sample ion beam current, *ST* sputter target

which is given by the shadow projection of a protective shield usually from Ta or other materials with a low sputtering yield. The bombarding ions produce a virgin slope between the protected and the sputtered area, which is free of impurities. For its three-dimensional investigation, three processing steps are necessary:

- Ion beam slope cutting ①
- Ion beam selective etching ②
- Sputter coating ③

Whereas the direction of the cutting ion beam is given by the blue arrow, both the selective etching and a possible SEM observation of the initial surface, the slope area and the sputtered area take place in the direction of the dashed green arrow.

In practice, a single ion beam apparatus should allow multitasking and combining several functions as well as multistep processing. The Gatan Precision Etching and Coating System (PECS) fulfills these requirements [55]. Figure 5.29 shows schematically the arrangement of ion guns (IG1, IG2) for ion cutting, etching, cleaning, polishing and coating as well as the control, observation (OM) and measurement (CM1, CM2) capabilities. The stage allows samples positioning, tilting and rotation (RU), blind mounting (BL) and adjustment with precise sample transfer into the SEM for testing the results after the different ion bombardment steps. Reproducible positioning in SEM and PECS is important for multistep preparation with processing parameters specified for the selected task and modified depending on the observation results. The inert or reactive ions in the ion guns have typically energies up to 10 keV and current densities up to 40 μA mm^{-2}. The multistep ion beam preparation technique is suitable for ion beam slope cutting as well as for selective ion etching and for sputter coating. Ion beam slope cutting is carried out with parallel impinging Ar^+ or Kr^+ ions and the cutting depth is measured by calibration of the bombardment time.

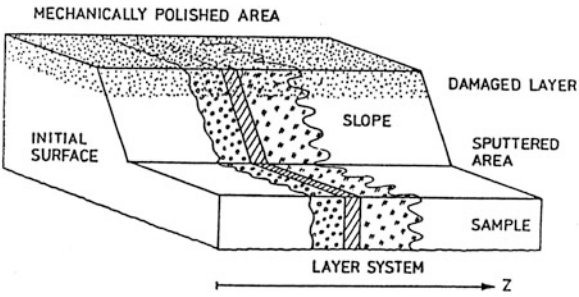

Fig. 5.30 Ion beam slope cutting of a sample with damaged surface layer (after Hauffe [2])

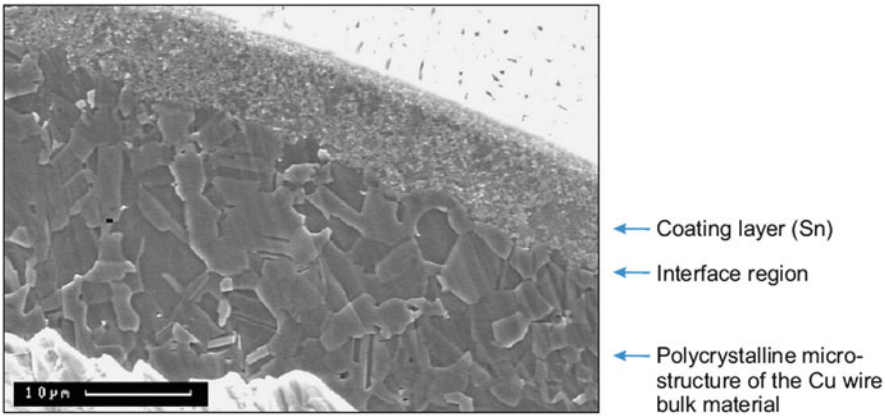

Fig. 5.31 SEM image of ion beam slope cut through a Sn-coated polycrystalline Cu wire after selective ion etching [55]

A modification of ion beam slope cutting for analyzing samples with a damaged surface layer is demonstrated in Fig. 5.30. The damaged layer is caused by mechanical polishing, and the ion beam slope cutting starts from the polished area through the damaged layer into the undisturbed region. In this way, the sample can be investigated in the direction z to each arbitrary depth. This method can be successfully used for rough surfaces and for heterogeneous samples (e.g., [2]).

Figure 5.31 shows the SEM image of ion beam slope cut through a Sn-coated polycrystalline Cu wire [55]. The sample was cut under 45° for 1 h and etched with 7 keV Ar^+ ions for 150 s. In Fig. 5.31 both the microstructure of the polycrystalline Cu wire bulk and the coating layer system are clearly visible after the selective Ar^+ ion etching. Especially the interface region between Cu bulk and Sn coating is shown to be deformation-free without mechanical treatment. By multiple ion cutting also the 3D microstructure of the Cu wire can be observed [55].

Preferentially, ion beam slope cutting is applied in all cases where classical cutting techniques are not effective or even impossible. Thus, favored application fields are:

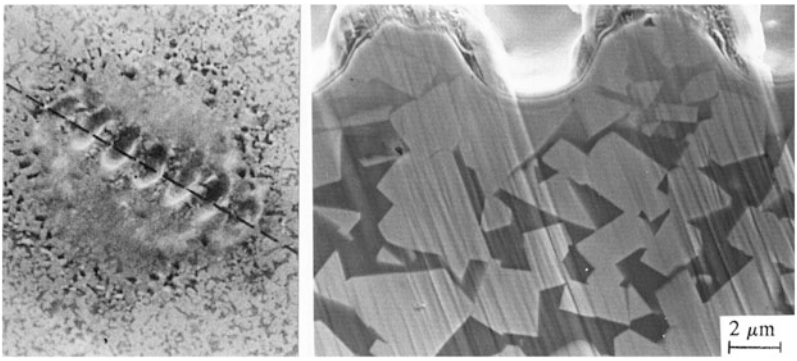

Fig. 5.32 SEM image of ion beam slope cutting of a laser-modified WC-Co hard metal: *left*—periodic surface structure; *right*—ion cut cross section

- The uncovering of interfaces between materials with very different properties, such as of brittle and ductile components
- The use of ion beam slope cutting as an in situ method, in combination with other analyzing techniques or analytical tools in a multicomponent apparatus

As an application example, Fig. 5.32 shows SEM images of ion beam slope cutting of a laser-modified WC-Co hard metal. Both laser bombardment and ion beam-induced cutting were carried out in situ in an SEM [19, 57]. Cemented carbides with higher binder contents were irradiated with a CO_2-pulse laser inside the SEM to investigate the structural development in more detail. The decisive medium is the melting Co binder which dissolves the refractory tungsten carbide phase. In this way, a superficial layer of a supersaturated solid solution with highly dispersed secondary carbides is produced [57]. At higher laser pulse numbers, a periodic structure is engraved in the surface by local evaporation as a result of a self-amplifying phenomenon. This is evident in the left field of Fig. 5.32. This periodic structure is strictly correlated with polarization direction and wavelength of the CO_2-pulse laser [58]. Now an ion beam slope cut was implemented in situ into the hard metal sample along the dashed line. The resulting cross section is given in the right field of Fig. 5.32, and it shows

- A changed phase concentration in the near-surface region
- A redeposition of Co in the evaporated laser spots

These results prove the potential of ion beam cutting in combination with further analyzing techniques.

5.3.5 Ion Beam Thinning

The aim of ion beam sample thinning is the production of thin material lamellas which can be penetrated by a fast electron beam, e.g., in a transmission electron microscope (TEM). For typical electron acceleration voltages of about (100–400) kV, the required lamella thickness must be in the order of some

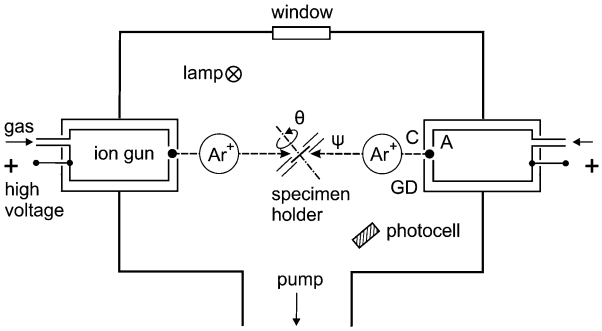

Fig. 5.33 Principle of sample thinning by ion beam milling (after Murr [57])

10 nm. The ion beam sample thinning can be realized with two different bombardment techniques:

- Conventional oblique ion bombardment in the keV range, so-called ion beam milling
- Focused ion beam (FIB) technique

  Sample thinning by focused ion beams will be discussed in Sect. 5.4.

The principle of ion beam milling, firstly described by Murr [59], is demonstrated in Fig. 5.33. In an evacuated preparation chamber, a sputter process with inert gas ions (commonly Ar^+) will take place on the sample surface. For uniform thinning, the sample rotates in a specimen holder up to its perforation around the oblique axis (angle ψ). The evenness of the sputter process is enhanced by the simultaneous operation of two opposite located ion guns with glow discharge (GD). The glow discharge works at high voltage between a grounded tube C and a positively charged tube A. Typical bombardment conditions are:

- Ion energy (1–10) keV
- Ion current density (1–200) μA mm^{-2}

The ion gun bombardment stops after sample perforation, which is detected by a lamp and a photocell at opposite site. In the surrounding of the perforation, the sample thickness grows wedge-shaped from only few nm. So the near-perforation sample region can be transmitted by electrons for TEM imaging.

The ion beam milling technique is successfully used for the preparation of heterogeneous and/or isolating materials. As a drawback of ion beam milling, several hours bombardment are necessary to obtain sample perforation. This will be overcome by the FIB thinning technique (see Sect. 5.4).

A special ion beam thinning task is the preparation of cross sections for TEM investigation with conventional ion beam milling. It is also named “face-to-face” technique because of the face-to-face sticking together of sample stripes in one preparation step. The different preparation activities to produce TEM lamellas are illustrated in Fig. 5.34. The following intermediary steps are necessary:

- Breaking or sawing of sample stripes
- Sticking together of two stripes

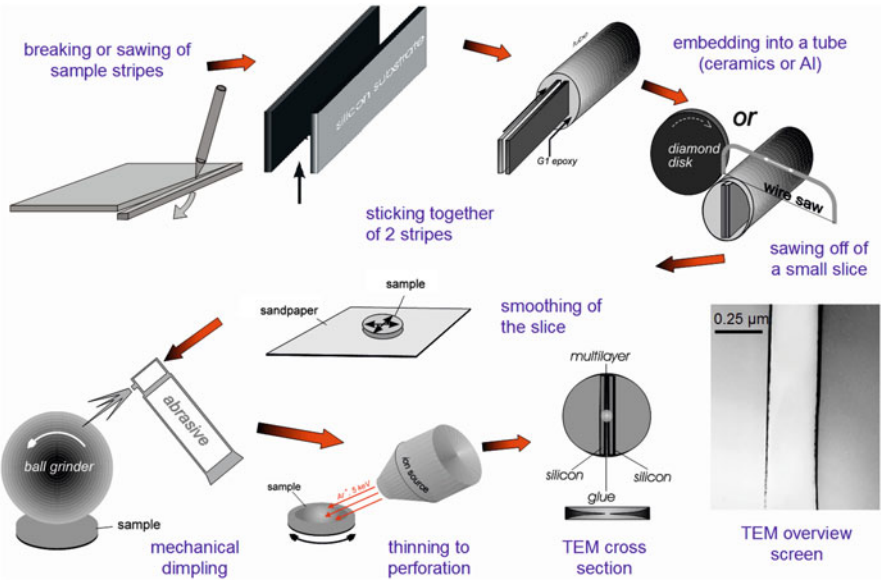

Fig. 5.34 Preparation of TEM lamellas by conventional ion beam milling (so called face-to-face technique)

- Embedding of this double-stripe into a ceramic tube
- Sawing off of a small slice with a diamond saw
- Smoothing of the slice on sandpaper
- Mechanical dimpling by a ball grinder
- Thinning to perforation by ion beam milling
- Putting of this cross section into the TEM sample holder

The image contrast of such a TEM cross section is a function of local sample thickness. Because of the wedge-shaped increase in thickness with growing distance from the specimen edge atomic resolution is only possible in the very thin wedge of the close-by region. This is evident in the left upper part of Fig. 5.35, near the perforation edge of a $Cs(Nb, W)_5O_{14}$ compound. Here, individual atomic stacks are visible as bright spots.

A modified ion beam thinning technique for TEM enlarging the observation area can be realized by combination of ion milling with preformed sample bars (e.g., [2]). The preparation principle is shown in Fig. 5.36. It is a two-step ion milling technique with a Mo grid of some 100 µm wide mesh placed above the sample. At normally incident ion beam, the masking grid is projected onto the sample surface (Fig. 5.36a). After removal of the grid conventional ion milling takes place on the rotating sample (Fig. 5.36b). The developing crossbar structure stabilizes the sample, and the thin regions are suitable for TEM observation (Fig. 5.36c).

As an example, Fig. 5.37 shows a glass sample after thinning for TEM observation by the two-step ion milling process. The Mo grid is still in place, and the crossbar structure with thin electron transmissive regions is visible.

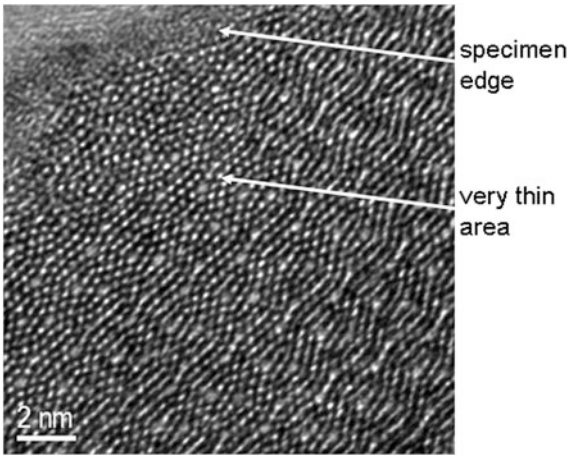

Fig. 5.35 Atomic stacks in the surrounding of perforation edge of a $Cs(Nb, W)_5O_{14}$ sample (HRTEM image)

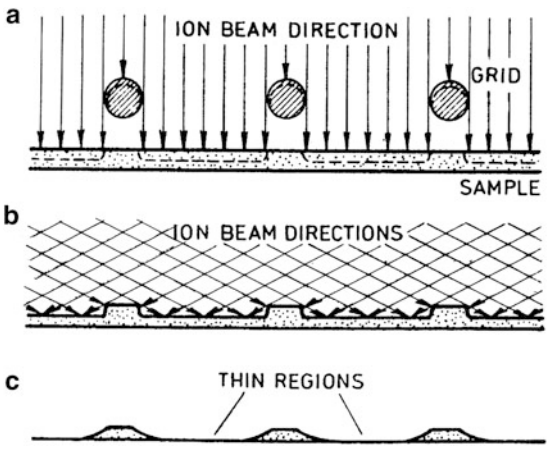

Fig. 5.36 Two-step ion milling with integrated grid for TEM (**a**) grid projection onto the sample by the ion beam; (**b**) ion milling under oblique ion incidence and sample rotation; (**c**) final TEM object (after Hauffe [2])

A further thin film specimen preparation method was developed by Yasuhara [60]. This technique is based on broad ion beam milling, but because of almost grazing incidence of the ion beam sample damaging is strongly reduced. The thinning principle of this so called ion slicer is demonstrated in Fig. 5.38. As shown in Fig. 5.38a, a thin shield plate is mounted on the top of the specimen, which is pre-prepared mechanically. An Ar^+ ion beam sputters the specimen from both sides, while it is tilted up to $\pm 6°$. As the side view of Fig. 5.38b shows, the shield plate causes a smooth ion beam incidence on both sides of the specimen.

The ion beam thinning process is finished when perforation occurs in the specimen. The surrounding thin-film area with a thickness <100 nm can then be transmitted by electrons in a TEM. To avoid nonuniformity of the ion beam milling

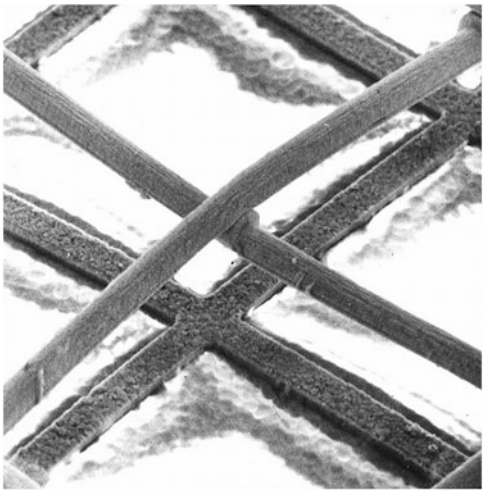

Fig. 5.37 SEM micrograph of a glass sample thinned for TEM by the two-step ion milling process of Fig. 5.36 [2]

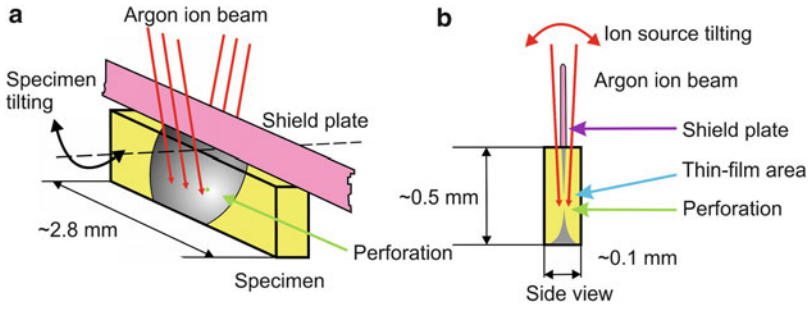

Fig. 5.38 Principle of thin film preparation with Ar^+ ions and a shield plate (**a**) top view; (**b**) side view (after Yasuhara [60])

procedure, the specimen together with the fixed shield plate is tilted up to $\pm 30°$ with respect to the ion source tilting plane. After ion beam thinning, the specimen is adhered to a reinforced ring and can be inserted into the TEM.

5.4 Focused Ion Beam Preparation

Over the past few years, the focused ion beam technique (usually abbreviated with FIB technique) has become an important tool for solid state microanalysis [1, 5]. It is widely accepted in materials research for microelectronics, especially for SEM imaging, cross-section preparation failure analysis, and device modification in the semiconductor industry.

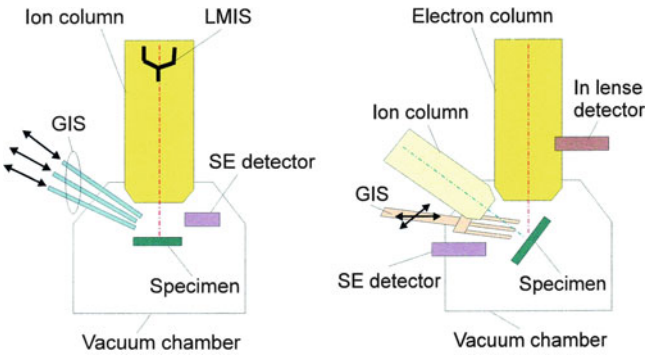

Fig. 5.39 Principle of focused ion beam preparation in a single beam (*left*) and dual beam (*right*) scanning ion microscope

FIB sample preparation possesses two decisive advantages: it combines a fast material removal with low damage generation in the near-surface region. Modern FIB instruments can prepare TEM specimen in less than 1 h in an almost nondestructive state. Both FIB technical configuration and its operating parameters are described in Chap. 3. Therefore, here the features of FIB will be given only in a highly condensed manner.

The basic instrumental concept is a scanning ion microscope using a liquid metal ion source (LMIS), in the same way as an electron beam is used in scanning electron microscopy (SEM). The operating mode is shown in Fig. 5.39. In the so-called single beam mode (left), a strong electric field extracts positively charged Ga^+ ions from the LMIS. The Ga^+ ion beam is focused by electrostatic lenses in an ion column and scanned over the specimen surface. There it can produce a secondary electron (SE) image with the aid of an SE detector, but primarily the ion sputtering effect removes material from the specimen-producing FIB-induced cross sections or thin film lamellas. The top surface of such thin film lamellas is usually protected against ion sputtering by the deposition of chemical reaction products, which are set off from metallo-organic compounds. These compounds come from gas incidence sources (GIS) and are introduced by needles into the vacuum chamber. A so-called dual beam system represents the combination of a FIB apparatus with an SEM, the electron column of which is visible in the right image of Fig. 5.39.

FIB columns can be also incorporated into other analytical instruments such as transmission electron microscopes (TEM), AUGER electron spectrometers (AES) or secondary ion mass spectrometers (SIMS).

Typical FIB applications in materials science are:

- High channeling contrasted imaging for 3D microstructure analysis
- 3D failure analysis of devices structures
- Device edits and their modifications
- Probe preparation for scanning force microscopy
- TEM specimen preparation
- In-situ imaging of FIB milling processes

Some of them will be described in the following sections.

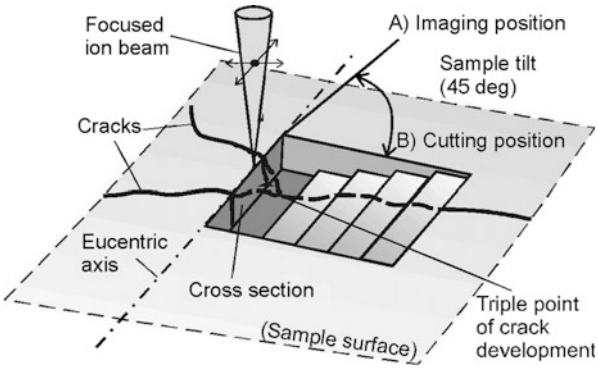

Fig. 5.40 Operating mode of in situ cross-section preparation ("cut and view") by FIB technique [61]

5.4.1 FIB-Induced Cross-Section Preparation

The most frequent application of FIB technique is the in situ cross-section preparation, allowing localized depth analysis, especially in thin layers or bulk near-surface regions. Its operating mode is evident from Fig. 5.40. It is also named "cut and view technique" because of the alternating sample cutting and imaging position, generating a growing patterning of the sample surface [61].

In the cutting position B of the sample surface the focused ion beam removes material, the quantity of which depends on the local position, forming a step pattern. After cutting, the sample can be tilted 45° around the eucentric axis to reach its imaging position A. The cut-step pattern allows to produce channeling contrasted SEM images from the cross section.

Typical parameters of the FIB cross-section stage are compiled in Table 5.6.

As an example for 3D failure analysis, Fig. 5.40 shows schematically crack propagations from the surface into the cross section. The SEM image of Fig. 5.41 demonstrates the depth propagation of microcracks in a 5 µm thick TiAlN hard coating on a WC-6%Co substrate. From such investigations, the thermo-mechanical damage mechanism based on relaxation processes can be understood [62]. Generally, failure investigations using FIB cross-sectional cutting are preferred because samples are damaged only locally in the µm-range and have not been destroyed completely by conventional metallographic preparation procedures. Therefore, using this FIB technique a thermo-mechanical loading by laser shocks and sequential investigation of cutting tools was possible for damage analysis.

FIB cuts with exposing and imaging of cross sections can help to understand the mechanical behavior of Cu-Ag metallization layers produced by electrochemical deposition (ECD) under cyclic thermo-mechanical loading. Cu alloy layers with up to 2 at.% Ag are shown to be promising for better performance of metal interconnects in terms of metal layer damage, induced by alternating current loading, that means by alternating temperature loading. After stabilization of microstructure during the first heat cycle, in further cycles an enhanced elastic region up to a temperature of 220 °C could be observed which is better than in pure Cu films [63].

Table 5.6 Operation parameters of a FIB cross-section stage

Parameter	Typical value
Bombarding ions	Ga^+
Ion beam current	$(1–10^4)$ pA
Spot size	8 nm–1 µm
Stage and apertures	Motorized
Switch possibility	Microscope → milling
GIS sources	Pt, W, H_2O, J, F, …

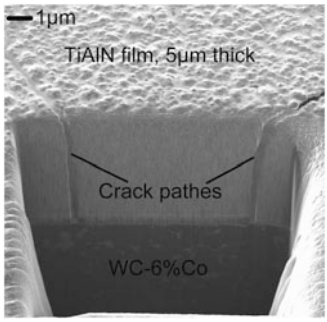

Fig. 5.41 Crack paths in a FIB cross-section preparation of a 5 µm TiAlN hard coating on WC-6 % Co substrate (SEM image)

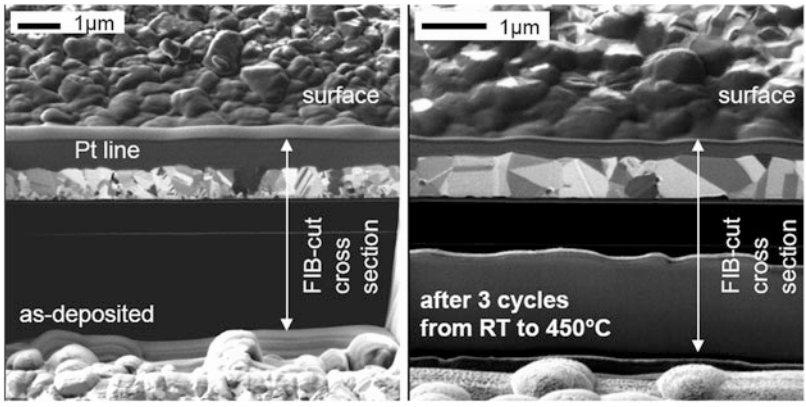

Fig. 5.42 FIB microscopic analysis of microstructure of electroplated Cu (0.5 at.% Ag) metal layers under temperature cycling [63] *left*: as-deposited state; *right*: after three temperature cycles

The changes in microstructure of Cu (0.5 at.% Ag) metallizations during the first heat treatment are demonstrated in Fig. 5.42 by FIB cuts before and after heating. Shown are the FIB-cut cross sections of the metallization layers below a Pt protection line in the as-deposited state (left-hand) and after three temperature cycles between room temperature (RT) and 450 °C (right-hand). The grain size increases distinctly, and the Cu seed is recrystallized together with the Cu-Ag film. The texture before and after heating does not differ remarkably, and it is

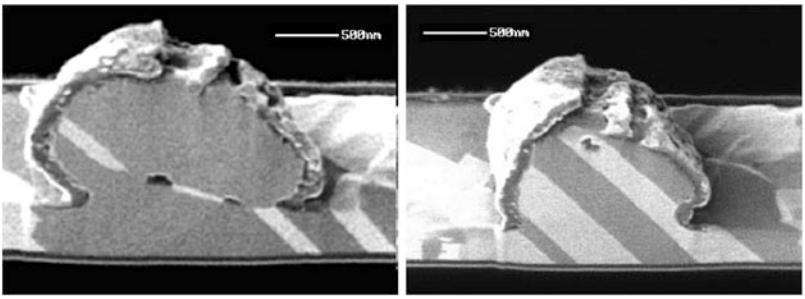

Fig. 5.43 FIB cuts through two hillocks after electro-migration test ($j = 3 \times 10^6$ A cm^{-2}, $T = 260$ °C) of an electroplated Cu interconnect line [64]

comparable to that of pure ECD-Cu films. The results of investigation of the Cu-Ag metallization are essential for processes optimization and improvement of device interconnect performance.

Because of continuing downscaling of device dimensions in microelectronics, the current densities in metallization layers have become extremely high, up to some 10^6 A cm^{-2}. Together with increasing operation temperatures caused by high clock frequencies of integrated circuits (today in the GHz range), the impulse forces of conduction electrons may become so high that their momentum transfer to atoms of the interconnect line can generate a net material transport. This effect is known as electro-migration and can cause circuit failures in the form of voids and short circuits through so-called hillocks [64]. To avoid this dangerous phenomenon, the conditions for void and hillock formation including their intergrowth with interconnects have been studied in detail also by FIB-induced cross sectioning.

As an example, Fig. 5.43 shows FIB cuts through two hillocks after an electro-migration test on an electroplated Cu interconnect line. The interconnect line was loaded with a current density of $j = 3 \times 10^6$ A cm^{-2} at $T = 260$ °C. The images were taken with Ga^+ ion-induced secondary electrons and show a distinct orientation contrast. Furthermore, the hillock of the right image has grown epitaxially through the interconnect line. The hillock cap layers have probably been formed by oxidation processes and also by carbon contamination produced in the SEM under particle irradiation.

Another example of FIB-produced cross sections is their application as probes in magnetic force microscopy (MFM) (Menzel S (2005) private communication, unpublished). This probe fabrication allows the realization of Fe containing MFM cantilevers and well-defined tip length and diameter. For this purpose, a hole is drilled by FIB from the backside in the tip of a Si_3N_4 cantilever and afterwards a Fe-filled multiwall carbon nanotube (MWCNT) is thread through the hole with a typical diameter in the 100 nm range. Prior to that, a suitable MWCNT is selected from a nanotube bundle after its FIB-cutting (Fig. 5.44). The chosen Fe-filled MWCNT is transferred from the bundle into the hole of the cantilever under observation inside an SEM, and finally its length is corrected by FIB with respect to Fe-filling and MWCNT stiffness (Fig. 5.44).

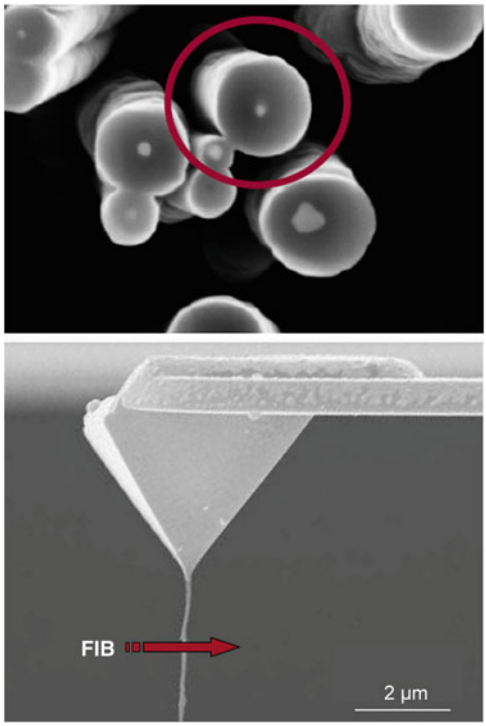

Fig. 5.44 SEM images of probe production for magnetic force microscopes (MFM) *above*: selection of one CNT from Fe-filled CNT bundle (FIB cross section); *down*: MFM cantilever with CNT probe, cut by FIB

5.4.2 FIB-Based Thin Film Preparation

Besides FIB cross section preparation (see Sect. 5.4.1), the most frequent application of FIB is thin film specimen preparation, e.g., for the fabrication of TEM lamellas. The physical principle of FIB-based thin film specimen preparation in comparison with conventional ion beam thinning is illustrated in Fig. 5.45. In the conventional thinning mode, a broad ion beam (typical diameter 10 µm) with oblique incidence (typically about 7°) and medium energy (typically 5 keV) strikes the sample surface (left). It produces a wedge-shaped thin film, which is transmissive for electrons in the region near the perforation. FIB thinning is realized by a focused ion beam (typical diameter 10 nm) with parallel incidence at higher energy (typically 30 keV, right). It produces a coplanar, very thin film of the specimen which is transmissive for electrons all over the film surface.

Special advantages of the FIB technique in comparison with conventional ion beam induced thinning are

- Uniform and lower film thickness
- Reduced concentration of implanted ions because of nearly parallel ion incidence with respect to the thin film surface

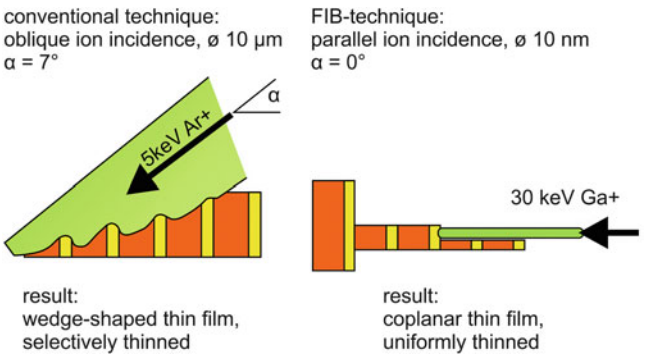

Fig. 5.45 Thin film preparation with ion beams: *left*: conventional technique; *right*: FIB technique

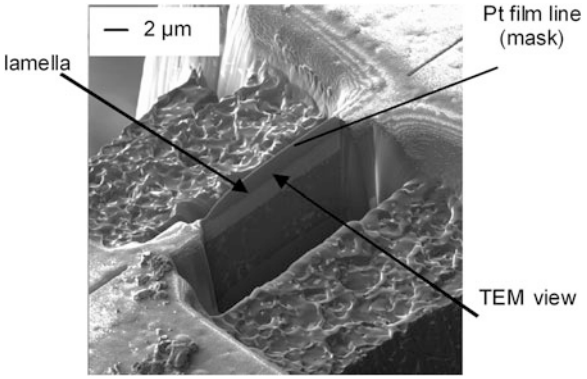

Fig. 5.46 SEM image of a FIB prepared TEM lamella in a TiN/Al_2O_3 multilayer system [64]

In practice, FIB-based sample thinning can be achieved by material removal according to Fig. 5.40, but from both sides. Using a metallo-organic vapor injection system, some different FIB-assisted CVD processes can be performed to deposit a heavy metal film as a mask on top of the lamella. As an example, Fig. 5.46 shows the lamella prepared from a TiN/Al_2O_3 multilayer system on a hard metal substrate.

The transport of the thinned lamellas and their investigation inside a TEM can be realized in two different ways. Quite simple is to tilt the whole sample of Fig. 5.46 by 90° for direct TEM investigation of the lamella. A second way is to quarry out the lamella from the bulk system, to pick it up with a tungsten tip, to transport it by a manipulator into the TEM and to site it onto a Cu grid inside the sample holder. This procedure is named "lift-out" technique and is demonstrated in Fig. 5.47.

The whole FIB-assisted lamella preparation process can be divided into the following four steps:

- Cutting out of the sample volume of interest (e.g., on a wafer)
- Polishing or cutting from both sides to a thickness of (10–50) µm

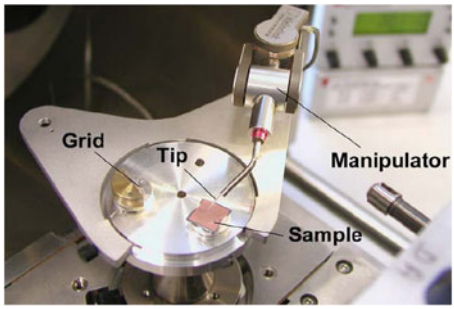

Fig. 5.47 "Lift-out" lamella transport and positioning from the FIB preparation unit into the TEM

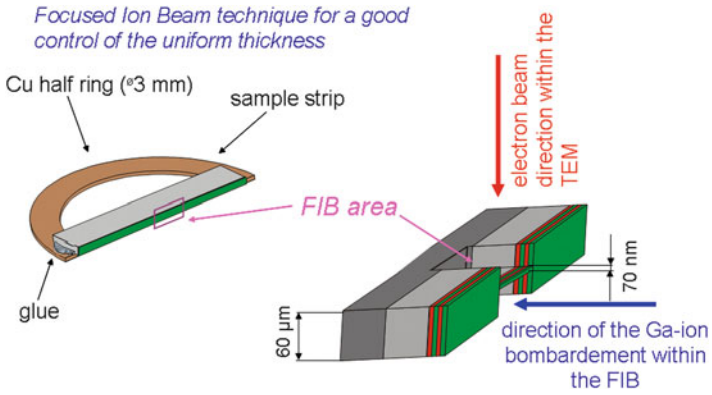

Fig. 5.48 Sample preparation by FIB technique for elemental depth profiling (schematically)

- Materials removal by FIB bombardment down to some 10 nm
- Reaction with injected gas components for deposition or etching

The FIB-assisted thin film preparation process can be performed in a modified way allowing elemental depth profiling perpendicular to the sample surface by using analytical capabilities of TEM. This is demonstrated in Fig. 5.48. A sample with a multilayer system on top is bombarded with a Ga^+ FIB normally to the surface. The ion bombardment occurs above and beneath a thin residual bar of some 10 nm (in Fig. 70 nm). Afterward the sample strip is glued on a Cu half ring sample holder and transmitted by electrons within the TEM. The FIB processed area of the specimen can be immediately imaged and analyzed in the TEM and represents the two-dimensional element distribution (mostly the depth profile) of the multilayer system. It has to be mentioned that the focused ion beam technique allows a good control of the sample thickness uniformity which is necessary for subsequent TEM investigations.

As an example, Fig. 5.49 shows the image of the elemental depth distribution in a Co/Cu multilayer stack obtained by analytical (energy-filtered) TEM investigations [64, 65]. Images of Co (red) and Cu (green) are overlaid.

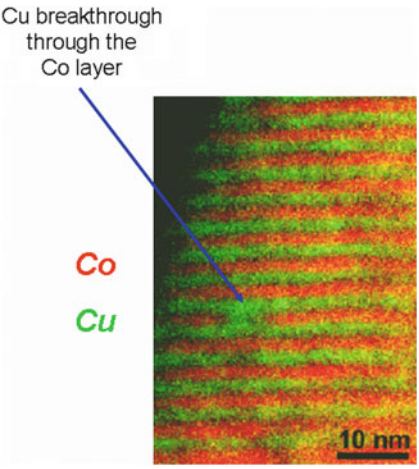

Fig. 5.49 Energy filtered TEM image of a Co/Cu multilayer with 2 nm single layer thickness after annealing at 400 °C [64, 65]

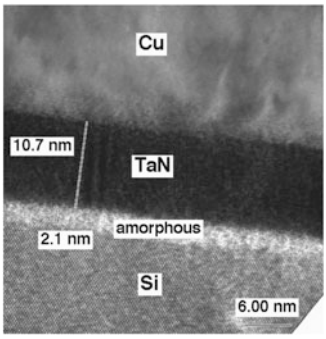

Fig. 5.50 Highly resolved TEM cross-section image of a Cu interconnect sample prepared by FIB

The thickness of each single layer is about 2 nm. Such multilayer Co/Cu systems are of interest because they show a distinct giant magnetoresistance [66].

An interconnect between two Cu layers through a Co layer was found after annealing at 400 °C and is marked by the arrow. The driving force for pinhole formation in individual thin layers may be caused by different free surface energies of Co and Cu layers, respectively [65].

The energy-filtered TEM technique can be used to aid element-selective chemical analysis of the sample. Improved elemental maps can be obtained by taking a series of images, allowing quantitative analysis and improved accuracy of mapping where more than one element is involved. Artifacts introduced in the sample during FIB preparation are not essential in this kind of analysis.

Figure 5.50 shows a highly resolved cross-section TEM image of a FIB-prepared sample with a Cu interconnect layer and a TaN diffusion barrier on Si. The micrograph displays an intact TaN barrier layer after annealing at 600 °C. An amorphous Si layer (thickness 2.1 nm) appears beneath the TaN barrier layer. This

Table 5.7 Limiting effects at FIB-assisted preparation

Parameter	Limiting effect	Reason
Quality of spot size	Noncircular spots	High ion current
Material removal	V-shaped cross-section profile	Material redeposition
Sample microstructure	Amorphization	Ion implantation
Sputter angle distribution	Backscattering	Ion scattering
Thinning of multilayers	Thin layer deformation	Intrinsic stresses

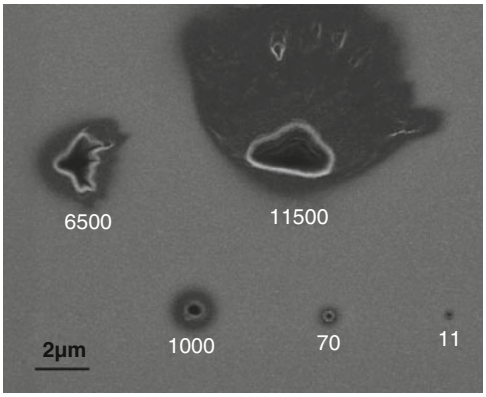

Fig. 5.51 SEM image of FIB spot sizes in a Ga^+ ion beam-perforated Al film (ion energy: 30 keV; ion current: numerical values in pA)

layer has also been observed in the as-deposited state and is caused by the TaN physical vapor deposition process [64, 67].

5.4.3 Limiting Effects at FIB Preparation

As described in Sect. 5.4.2, a special advantage of FIB-assisted sample preparation in comparison with conventional ion beam preparation technique is its low ion implantation and therefore its low damage generation in the near-surface region. This is essentially the result of nearly parallel FIB incidence (see also Fig. 5.45).

Nevertheless, the amount of implanted Ga^+ ions depends on the ion energy and the current density of impinging ions, on their angle of incidence, and the target material. Because ion implantation into the specimen becomes noticeable with growing ion fluence, it can cause limiting effects for FIB preparation at unsuitably high FIB ion currents and/or irradiation times. Most important limiting effects are summarized in Table 5.7.

Figure 5.51 shows spot sizes in a polycrystalline Al film after 30 keV ion bombardment with different Ga^+ ion currents (numerical values in 10^{-12} A) (Menzel S (2005) private communication, unpublished). For higher FIB currents the beam spot size increases and the shape of the beam profile becomes broader and noncircular because adjustment errors of the beam relative to the ion-optical axis of

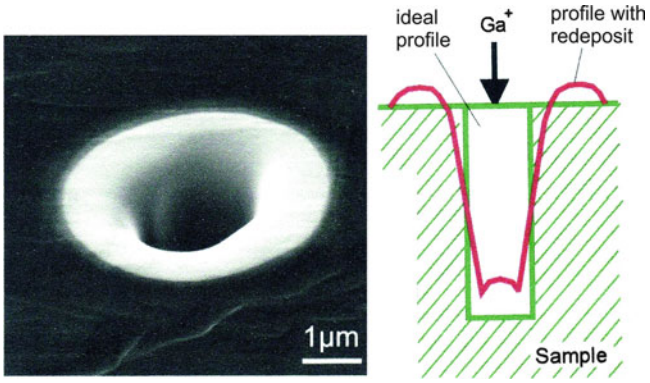

Fig. 5.52 Material redeposition after removal by Ga^+ FIB bombardment (Menzel S (2005) private communication, unpublished); *left*: SEM image of crater profile; *right*: V-shaped profile with redeposit

the FIB column become more critical. Accordingly, the asymmetry of spot sizes limits the application of thin film preparation at high FIB currents.

Redeposition of FIB-induced sputtered material is an artifact changing the cross-section crater profile to a profile with an additional ring-shaped bulge (see Fig. 5.52) [68]. The ideal box-like crater profile in Fig. 5.52 is only hypothetic, because in reality it must be a copy of the Gaussian-like FIB profile. Redeposition must be taken into account for successful and rapid specimen preparation, especially of TEM lamellas.

The redeposition depends on:

- Kinetic energy of leaving (sputtered) atoms
- Sticking coefficient of the target material
- Geometry of the feature being milled
- Sputtering yield of the target material
- Conductivity of the target material

The effect of redeposition can be suppressed by reactive gas addition (as Cl_2, I_2, XeF_2, etc.). The gas reacts with the redeposited material, and as a result this material can become volatile and then removed by the vacuum system [69]. A further possibility to prevent a V-shaped cross-section profile is the alteration of the ion beam incidence angle. The required alteration is material-dependent, ranging from (1–2)° to more than 10° [1].

The geometry of a deep sputter crater restricts the escape of the sputtered material. This causes an enhanced localized partial pressure p of sputtered atoms in the gas phase, and as a result the mean free path λ between particle collisions in the confined hole is reduced:

$$\lambda = \frac{k \cdot T}{\sqrt{2} \cdot d^2 \cdot p} \tag{5.18}$$

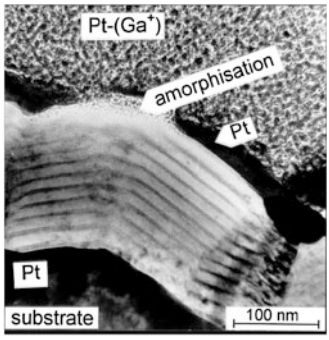

Fig. 5.53 SEM image of an amorphous zone up to 50 nm in depth induced during Pt–line deposition

with λ the mean free path, p the localized partial pressure, d the collision parameter, T the absolute temperature, and k the Boltzmann's constant.

The collisional mean free path λ very strongly depends on the localized pressure p. So λ decreases down to 10 orders of magnitude when the local pressure p increases by 2 orders of magnitude [68]. Thus, the probability of sample/sputtered atom collisions increases, resulting in redeposition, and must be taken into consideration for an estimation of the redeposition effect.

Sample preparation by FIB uses the process relies on ion bombardment to remove sample material locally and selectively. Atoms that are displaced from their equilibrium positions by impacts of energetic ions generate a collision cascade within the target material. Sputtering occurs if sufficient momentum is transferred to a surface atom. Simultaneously, ion implantation induces the development of a near-surface amorphous phase. The amorphous phase induced in crystalline materials by ion bombardment is typically metastable, and its formation depends on crystal properties, complexity of chemical ordering and the width of an intermetallic phase field (Nastasi [27]).

As an example, Fig. 5.53 shows an amorphous zone up to 50 nm in depth induced during FIB-assisted Pt–line deposition. The multilayer cross section consists of 8 nm Pt/175 nm $BaTiO_3/SrTiO_3$—multilayer/Pt on $Ti/SiO_x/Si$.

A pronounced backscattering effect under FIB bombardment is observed when an incident Ga^+ ion is scattered directly or after multiple collisions out of the target. Generally, sample materials with high sputtering yield have a high backscattering yield of incident Ga^+ ions, too.

A further artifact which limits FIB preparation is the deformation of thinned foils by high internal compressive stresses. This is the case especially for multilayer thin films. As an example, Fig. 5.54 shows the top view on a Cu-coated Si substrate with a thin Pt protection layer on its surface (Menzel S (2005) private communication, unpublished). The lamella is thinned from above and below (see arrows) with a

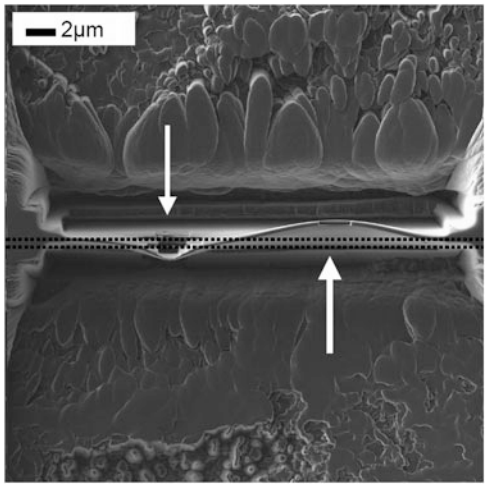

Fig. 5.54 Top view of a FIB thinned and deformed lamella of Cu layered Si substrate (SEM image)

decreasing ion current down to 50 pA. Redeposited crystals are clearly visible in the upper image part. The former initial thickness is indicated by the dotted lines, but because of the bended foil the thinned areas of interest are removed at both sides during FIB polishing. This artifact can be overcome by ion etching of support bars into the FIB windows (Thomas J (2004) private communication, unpublished).

References

1. Giannuzzi LA, Stevie FA (2005) Introduction to focused ion beams. Springer, New York
2. Hauffe W (1991) Production of microstructures by ion beam sputtering. Top Appl Phys 64:305–338
3. Yao N (2007) Focused ion beam systems. Cambridge University Press, Cambridge
4. Hellborg R, Whitlow HJ, Zhang Y (2009) Ion beams in nanoscience and technology. Springer, Heidelberg
5. Orloff J, Utlaut M, Swanson L (2003) High resolution focused ion beams: FIB and its applications. Kluwer, New York
6. Eckstein W (1988) Statistics of sputtering. Nucl Instrum Methods Phys Res B 33:489–492
7. Behrisch R (2007) Sputtering by ion bombardment. Springer, Berlin
8. Sigmund P (2006) Ion beam science – solved and unsolved problems. Mat Fys Medd Dan Vid Selsk 52:1–755
9. Zhou XW, Wadley HNG, Sainethan S (2005) Low energy sputtering of Ni by normally incident Xe ions. Nucl Instrum Methods Phys Res B 234:441–457
10. Crow GA (1990) Focused ion beam micromachining of Si and GaAs using Ga and Au liquid metal ion sources. PhD thesis, Beverton, OR
11. Yamamura Y, Muraoka K (1989) Over-cosine angular distributions of sputtered atoms. Nucl Instrum Methods Phys Res B 42:175–181
12. Yamamura Y, Matsunami N, Iton N (1983) A universal relation for the sputtering yield of monatomic solids. Radiat Eff 71:65f
13. Sigmund P (1977) Sputtering processes: collision cascades and spikes. In: Tolk NH (ed) Inelastic ion-surface collisions. Academic, New York

14. Andersen HH, Bay HL (1981) Sputtering yield measurements. In: Behrisch R (ed) Sputtering by particle bombardment. Berlin, Springer
15. Yamamura Y (1996) Energy dependence of the yields on ion- induced sputtering of monatomic solids. At Data Nucl Data Tables 62:149f
16. Hosler W, Palmer W (1993) Effects of crystallinity on depth resolution in sputter depth profiles. Surf Interface Anal 20:609–620
17. Kempshall BW, Schwarz SM, Prenitzer BI et al (2001) Ion channelling effects on the FIB milling of Cu. J Vac Sci Technol B 19:749–754
18. Molchanov VA, Telkovski VG, Chicherov VM (1961) Anisotropy of cathodic sputtering of single crystals. Sov Phys Doklady 6:222–229
19. Hauffe W (1995) Ion bombardment experiments. In: Wetzig K, Schulze D (eds) In situ scanning electron microscopy in materials research. Akademie Verlag, Berlin, pp 195–218
20. Hauffe W (1978) Proceedings of National Conference on the Physics of Semiconductor Surfaces, AdW GDR, Binz, p 1
21. Wetzig K, Wittig H (1970) Emissionselektronenmikroskopische Untersuchungen zur selektiven Materialabtragung durch Ionenätzen an intermetallischen Verbindungen. Krist Tech 5:561–576
22. Hauffe W (1978) Untersuchung der Richtungsverteilung emittierter Atome und der Oberflächenveränderungen bei der Ionenstrahlzerstäubung von Festkörpern. Habilitationsschrift, TU Dresden
23. Hauffe W (1971) Development of the surface topography on polycrystalline metals by ion bombardment. Phys Stat Sol (a) 4:111
24. Matsunami N (1984) Energy dependence on the yields of ion- induced sputtering of monatomic solids. At Data Nucl Data Tables 31:1f
25. Andersen HH (1984) Ion bombardment induced composition changes in alloys and compounds. In: Williams JS, Poate JM (eds) Ion implantation and beam processing. Academic, Sydney
26. Betz G, Wehner GK (1981) Sputtering in multicomponent materials. In: Behrisch R (ed) Sputtering by ion bombardment II. Springer, Berlin
27. Nastasi MA, Mayer JW, Hirvonen JK (1996) Ion-solid interactions, Cambridge solid state science series. University Press, Cambridge
28. Holloway PH, Bhattacharya RS (1982) Preferential sputtering of PtSi, $NiSi_2$, and AgAu. J Vac Sci Technol 20:444–448
29. Wetzig K (2008) Ion beam research in materials science, Lecture course book. TU, Dresden
30. Winters HF, Coburn JW (1992) Surface science aspects of etching reactions. Surf Sci Rep 14:161–270
31. Gamo K, Takaruka N, Samoto N et al (1984) Ion beam assisted deposition of metal organic films. Jpn J Appl Phys 23:293–295
32. Stewart DK, Stern LA, Morgan JC (1989) Electron beam, X-ray and ion beam technologies. Proc SPIE 1089:18–25
33. Shedd GM, Dubner AD, Thompson CV et al (1986) Tunable UV laser photolysis of organometallics. Appl Phys Lett 49:1584–1586
34. Puretz J, Swanson LW (1992) Focused ion beam deposition of Pt containing films. J Vac Sci Technol B 10:2695–2698
35. Gamo K, Takakura N, Hamamura Y et al (1986) Maskless ion beam assisted deposition of W and Ta. Microelectron Eng 5:163–170
36. Harriott LR, Cummings KD, Gross ME et al (1986) Decomposition of palladium acetate films with a microfocused ion beam. Appl Phys Lett 49:1661–1662
37. Komano H, Ogawa Y, Takigawa T (1989) Study of precursor gases for focused ion beam insulator deposition. Jpn J Appl Phys 28:2372–2375
38. Hillsboro OR (2003) Carbon deposition, Technical note, FEI Company, PN 4035 272 27241-A
39. Hillsboro OR (2003) Platinum deposition, Technical note, FEI Company, PN 4035 272 21851-B

40. Wetzig K, Baunack S, Hoffmann V et al (1997) Quantitative depth profiling of thin layers. Fresenius J Anal Chem 358:25–31
41. Lorenz WJ, Plieth W (1998) Electrochemical nanotechnology. Wiley, Weinheim
42. Oswald S, Baunack S (1997) Application of XPS and factor analysis for non-conducting materials. Surf Interface Anal 25:942–947
43. Hofmann S (2005) Characterisation of nanolayers by sputter depth profiling. Appl Surf Sci 241:113–121
44. Linsmeier C (1994) Auger-electron spectroscopy. Vacuum 45:673–690
45. Hoffmann V, Dorka R, Wilken L et al (2003) Present possibilities of thin layer analysis by GDOES. Surf Interface Anal 35:575–582
46. Präßler F, Hoffmann V, Schumann J et al (1996) Quantitative depth profiling in glow discharge spectroscopies. Fresenius J Anal Chem 355:840–846
47. Präßler F, Hoffmann V, Schumann J et al (1995) Comparison of depth resolution for direct current and radiofrequency modes in GDOES. J Anal At Spectrom 10:677–680
48. Grimm W (1968) Eine neue Glimmentladungslampe für die optische Emissionsspektralanalyse. Spectrochim Acta B 23:443–454
49. Bengtson A (1985) A contribution to the solution of the problem of quantification in surface analysis. Spectrochim Acta B 40:631–639
50. Magee CW, Honig RE (1982) Depth profiling by SIMS. Surf Interface Anal 4:35–41
51. Baunack S, Menzel S, Brückner W et al (2001) AES depth profiling multilayers of 3d transition metals. Appl Surf Sci 179:25–29
52. Menyhard M, Sulyok A, Pentek K et al (2000) Demixing in spin valve structures: an AUGER depth profiling study. Thin Solid Films 366:129–134
53. Seah MP, Briggs D (1990) Practical surface analysis, part 1. Wiley, Chichester
54. Zier M, Oswald S, Reiche R et al (2003) XPS investigations of thin Ta films on a Si surface. Anal Bioanal Chem 375:902–905
55. Hauffe W (2007) Broad ion beam slope cutting through Sn coated copper wires. Microsc Microanal 13(Suppl 2):584
56. Hauffe W (1977) Patent DD 139670: Vorrichtung zur Vorbereitung der Stoffprobe für die Untersuchung
57. Müller H, Wetzig K, Schultrich B et al (1990) In situ laser irradiation of WC-Co hard metals inside a SEM. J Mater Sci 25:4440–4448
58. Birnbaum MJ (1965) Semiconductor surface damage produced by ruby lasers. J Appl Phys 36:3688–3689
59. Murr LE (1970) Electron optical applications in materials science. Mc Graw-Hill, New York
60. Yasuhara A (2005) Development of ion slicer. JEOL News 40:46–48
61. Menzel S, Wendrock H, Wetzig K (2004) The focused ion beam (FIB) technique in materials research. Acta Metallurgica Slovaka 10:692–694
62. Klotz K, Bahr HA, Balke H et al (2002) Creep analysis and laser induced cracking of (Ti, Al) N coatings. Thin Solid Films 413:131–138
63. Wetzig K (2004) Migration processes in thin metallic structures. Acta Metallurgica Slovakia 10:40–47
64. Wetzig K, Schneider CM (2006) Metal based thin films for electronics. Wiley, Weinheim
65. Bobeth M, Hecker M, Pompe W et al (2001) Thermal stability of nanoscale Co/Cu multilayers. Z Metallk 92:810–819
66. Parkin SSP, Li ZG, Smith DJ (1991) Giant magnetotesistance in antiferromagnetic Co/Cu multilayers. Appl Phys Lett 58:2710–2712
67. Hecker M, Fischer D, Hoffmann V et al (2002) Influence of N content on microstructure and thermal stability of TaN. Thin Solid Films 414:184–191
68. Ishitani T, Tsuboi H, Yaguchi T et al (1994) TEM sample preparation using a focused ion beam. J Electron Microsc 43:322–326
69. Thayer ML (1993) Enhanced focused ion beam milling applications. In: Proceedings of the 19th International Symposium for Texting and Failure Analysis, pp 425–429

Materials Analysis by Ion Beams

6

6.1 Introduction

The emphasis of materials analysis using ion beams is directed towards the composition and structure of surfaces and near-surface layers on the depth scale from nm up to μm. Ion beam-based analytical techniques concern with ion sources, ion beams, the kind and cross section of ion interaction with matter, the emerging radiation (e.g., sputtered secondary ions, scattered ions, ion-induced photon, and electron emission), and appropriate radiation detection systems.

For materials analysis with ion beams there exist a variety of experimental techniques, which are summarized in Fig. 6.1 as an ion mass–ion energy map. As shown in Fig. 6.1, one can divide all methods into three ion energy ranges (1) low-energy range of some keV, (2) medium-energy range of 30–300 keV, and (3) high-energy range of ~0.5–100 MeV. In relation to the primary ion mass, light ions ($M < 10$, mostly H^+, He^+) in a wide energy range are used for scattering techniques (LEIS, MEIS, RBS) and particle-induced photon emission techniques (PIXE, PIGE). Heavier ions (e.g., N, O, Cl, etc.) are necessary mainly for the techniques of NRA and ERDA. Low-energy (some keV) heavy ions ($M_i \geq M_{\text{Oxygen}}$) with a certain sputter yield of target atoms are necessary in the widely used analytical technique of secondary ion mass spectrometry (SIMS).

Characteristic differences between photon, electron, and ion interactions with matter are illustrated in Fig. 6.2, which compares the radiation range or penetration depth as well as the electron and ion trajectories in silicon obtained by Monte Carlo calculations. Typical X-rays of some 10 keV photon energy exhibit a very deep penetration depth in the mm range with exponential intensity decay by photon absorption. Typical electron energies are some 10 keV, and the interaction range is restricted to some 10 μm. The electron penetration into the solid is characterized by a large longitudinal and transversal straggling (pear-shape profile) and a low-beam damage because of small electron mass. In contrast, medium- and low-energy heavy ion irradiation, for example with 60 keV Ga^+ ions, interacts with the solid only in a very shallow depth region of <100 nm with high-target damage and target

B. Schmidt and K. Wetzig, *Ion Beams in Materials Processing and Analysis*,
DOI 10.1007/978-3-211-99356-9_6,

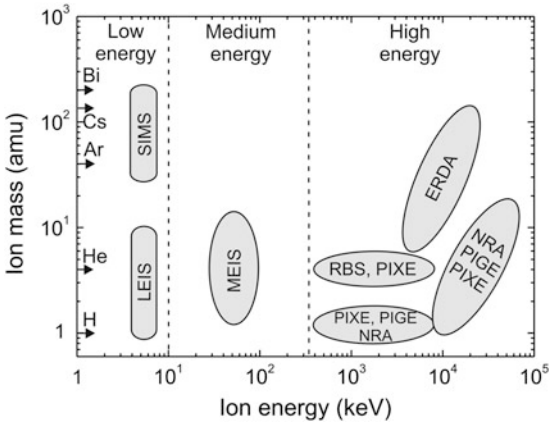

Fig. 6.1 Ion beam-based analytical techniques in relation to primary ion mass and ion energy: *SIMS* secondary ion mass spectrometry, *LEIS* low energy ion scattering, *MEIS* medium-energy ion scattering, *RBS* Rutherford backscattering, *ERDA* elastic recoil detection analysis, *PIXE* particle-induced X-ray emission, *PIGE* particle-induced gamma-ray emission, and *NRA* nuclear reaction analysis

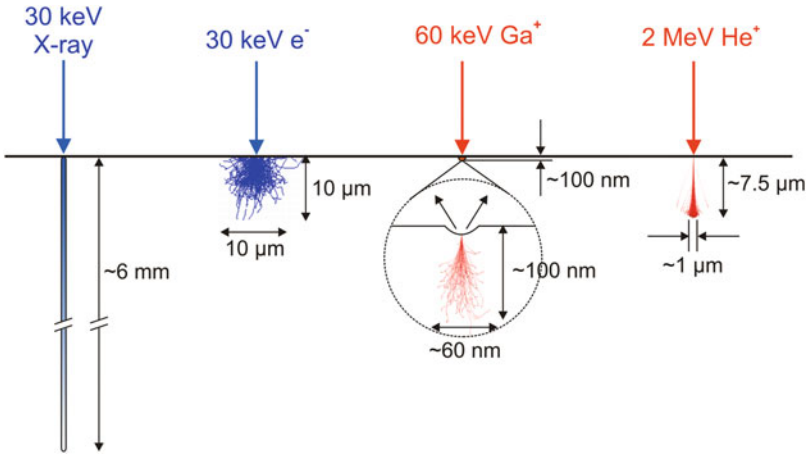

Fig. 6.2 Comparison of penetration depth and particle trajectories of radiation in silicon

material removal by sputtering. These interaction processes are of special importance for SIMS. On the other hand, high-energy light ions, for example, 2 MeV He^+ used for RBS, cause a deep probe beam of some µm with well-defined depth and collimation (small lateral ion straggling due to weak interactions) and with a small low-damage region of about ~0.5–1.0 µm size located in the Bragg-peak at end of ion range.

Compared to many other analytical techniques, including SIMS, ion beam analytical methods with high-energy ions (usually in the literature called IBA)

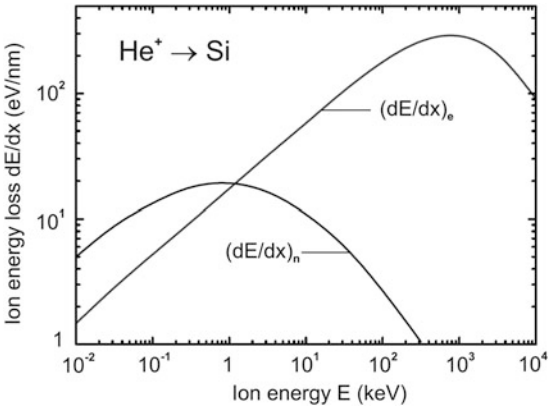

Fig. 6.3 Nuclear stopping and electronic stopping as a function of ion energy for He^+ ion irradiation of silicon

have the advantage that they are nondestructive, easy to use, and provide quantitative interpretation of measurements. The high accuracy of these ion beam techniques is mainly due to the precise knowledge of cross sections of the involved atomic and nuclear processes.

As described in Chap. 2 and schematically shown in Fig. 6.2, ions impinging the target undergo a series of elastic [with nuclear energy loss $S_n = (dE/dx)_{nuclear}$] and inelastic [with electronic energy loss $S_e = (dE/dx)_{electronic}$] collisions with the host atoms until they stop at some depth.

Depending on ion mass M and ion energy E, both ion-stopping processes S_n and S_e can appear together or one of them dominates [1, 2]. For example, in the low-energy range of 10–200 keV, typical for ion implantation of heavy ions, usually S_n is the dominating stopping process. High-energy light ions in the MeV region loss their energy predominantly by electronic stopping S_e [3]. As an example, Fig. 6.3 shows the distributions of the nuclear and the electronic stopping over a wide energy range for He^+ ions in silicon.

At ion beam analysis (IBA) using light ions (H, He) in the 1–3 MeV range, the dominating energy loss is given by the electronic stopping $S_e = (dE/dx)_e$ as can be seen in Fig. 6.3. Therefore, in the near-surface layer, which is analyzed, no defects are created. From the figure it can be also concluded that only at the end of the ion trajectories in the solid, where the ion energy is slowed down below some keV, nuclear stopping becomes comparable or higher compared to electronic energy loss. Thus, only in these depth regions ion-induced damage occurs, and therefore, RBS is assumed as a nondestructive analysis technique.

Ions accelerated to different energies and entering the target cause different interaction phenomena at both the atomic and the nuclear level leading to the emission of particles or photons with energies characteristic for elements in the target (see Fig. 6.4) [4]. In some analytical techniques, the same incident and emerging ions are employed, as in ion-scattering techniques (e.g., RBS, but also

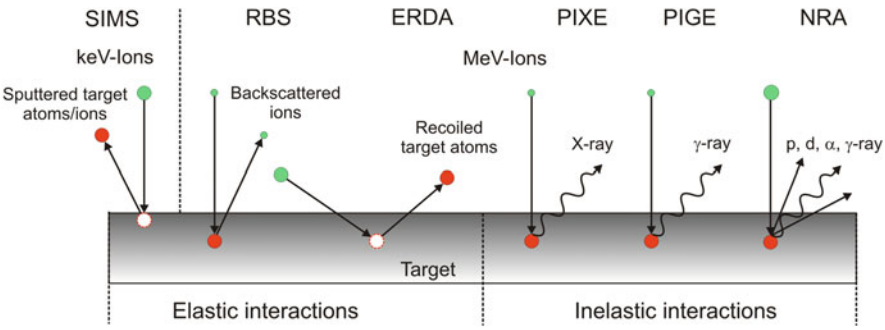

Fig. 6.4 Schematic representation of ion–target interaction. MeV ion induced elastic and inelastic interaction processes are related to common ion beam analysis (IBA), whereas primary heavy ions of some keV are used to sputter secondary target ions or atoms which are mass analyzed by SIMS [4]

MEIS, LEIS). In other cases, the primary incident ion, the emerging ion, and photon radiation from the target differ, which is indicated as:

- Primary ion in, target ion/atom out: ERDA (and also SIMS)
- Primary ion in, X-ray or γ-ray out: PIXE or PIGE, respectively
- Primary ion in, nuclear reaction products out (e.g., protons, deuterons, α-particles, γ-rays, etc.): NRA

Except SIMS, LEIS and MEIS common ion beam analysis of materials requires high-energy ions in some 100 keV and MeV range which are produced by accelerators as described in Sect. 3.6. Accelerator-based high-energy ion beams are in many cases more sensitive compared to other photon and electron-based probe techniques. The reason is that ions carry high momentum and interact more strongly with target electrons and nuclei through Coulomb forces between them. The basics of these ion–solid interactions have been described in Chap. 2.

Elastically backscattered light ions are detected in RBS and elastically recoiled (secondary) target atoms are detected in ERDA. X-rays and γ-radiation emitted from the target give element-specific information due to characteristic photon emission at relaxation of excited electron clouds (X-rays) or of excited atomic nuclei. This information is detected in the analytical methods of particle-induced X-ray emission (PIXE) or particle-induced gamma emission (PIGE), respectively. Nuclear reaction analysis (NRA) is a pure nuclear technique as it is governed by nuclear reactions and kinematics. If the primary ion energy exceeds the Coulomb barrier and the ion penetrates into the nucleus, it performs a nuclear reaction. In NRA, the primary ion is absorbed by the nucleus of target atoms at some resonance energies, and subsequently different secondary particles (proton, deuteron, neutron, or α-particle) or γ-rays are promptly emitted which can be detected. It must be mentioned that, in principle, PIGE is also an IBA technique, which is based on nuclear reactions. The proton (particle)-induced γ-ray emission (PIGE) is restricted to the detection of γ-rays emitted in (p,γ), (p,pγ), and (p,αγ) reactions.

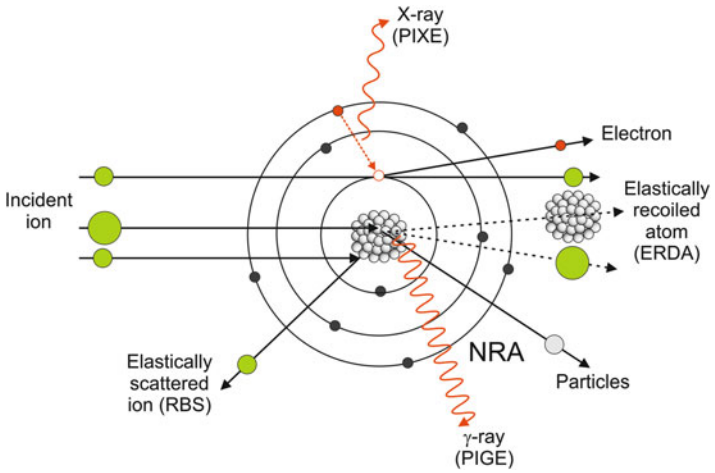

Fig. 6.5 Ion–target atom interaction at relevant IBA techniques

The incident ions interact either with atomic electrons or atomic nuclei of target atoms, as schematically shown in Fig. 6.5. The interaction with an atomic electron is purely Coulomb, and therefore it is governed by Coulomb's law. The Coulomb interaction of the ion with electrons can eject an electron from an inner orbital (as shown in Fig. 6.5) or excite electrons into higher orbitals. The ejected secondary electrons can ionize or excite further target atoms. In both cases, ionized or excited target atoms decay via emission of characteristic X-rays into their ground state which can be analyzed by PIXE. At high energies sufficient to overcome the Coulomb barrier, the incident ion enters the target atomic nucleus and induces a short living ($\sim 10^{-14}$–10^{-18} s) compound nucleus or an excited nucleus. There exist different decay channels through which the compound or excited nucleus returns to its ground state, accompanied by the emission of γ rays (mainly used for PIGE) or secondary reaction particles of ^{1}H (proton), ^{2}H (deuteron), ^{3}He(triton), ^{4}He (α-particle), or neutrons which can be detected in NRA. Additionally, Fig. 6.5 shows schematically a light ion elastically scattered at the target atomic nucleus and a target atom elastically recoiled by the incident ion, which are detected in RBS and ERDA, respectively.

The effects of ion–target atom interactions are summarized in Table 6.1. Nuclei are unaffected in the case of elastic ion scattering and inelastic collision. The interaction force is Coulomb, and the ion only changes its direction (elastic scattering) or is decelerated and causes bremsstrahlung (inelastic collision). If the bombarding ion energy is high enough to negotiate the Coulomb barrier, nuclei of target atoms will be excited. This can be caused by Coulomb excitation and also by inelastic scattering. In the latter process, the interaction force is nuclear. Nuclear interaction forces can also affect nuclear reactions with nucleus transformation.

A special case is the interaction of highly charged ions with solid state surfaces, as schematically demonstrated in Fig. 6.6 [5]. Important results were published by

Table 6.1 Effects of ion–target atom interactions

Interaction type	Interaction force	Ion impact	Nucleus impact
Elastic scattering	Coulomb	Direction changed	No effect
Inelastic collision	Coulomb	Energy loss, ionization, excitation, bremsstrahlung	No effect
Coulomb excitation	Coulomb	Direction changed, energy reduced	Excitation
Inelastic scattering	Nuclear	Direction changed, energy reduced	Excitation

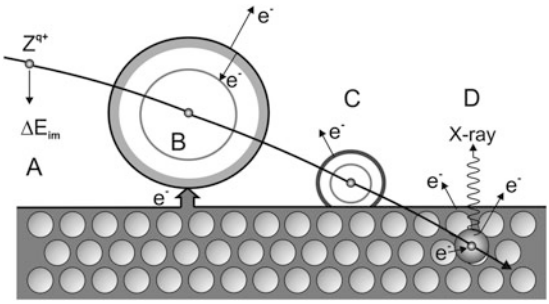

Fig. 6.6 Interaction of highly charged ion with a solid state surface (schematically) [5]

Burgdörfel et al. (e.g., [5–7]). Highly charged ions have a large amount of potential energy, which for slow ions may exceed their kinetic energy. Because of the small surface interaction area of some nm^2 and the very short interaction time of some 10^{-15} s a very high-power flux of 10^{13} W cm^{-2} is realized. The ions are accelerated towards the surface (A) and a "hollow atom" will form up (B). At impact with the surface electron emission takes place (C). The relaxation below the surface (D) is accompanied by target modifications and by radiation emission of X-rays and AUGER electrons, which can be used for analytical investigations. However, the use of highly charged primary ions is of minor importance for their application in materials analysis. Nevertheless, they have attracted interest for basic investigations of ion–surface interaction phenomena.

Besides all ion-induced particle and wave radiations mentioned above, secondary ions are also emitted from an ion-bombarded target surface and can be used for analytical aims. For this purpose, the emitted ions are analyzed in a mass spectrometer, and consequently this method is named secondary ion mass spectrometry (SIMS). It is described in more detail in Sect. 6.7. Furthermore, a direct visualization of target surfaces is possible by different ion beam-imaging techniques as field ion microscopy and ion microscopy with stationary or scanning ion beam, respectively. These imaging techniques are the subject of Sect. 6.8.

As described before common IBA techniques (RBS, ERDA, PIXE, PIGE, NRA) concern with ion energies in the usual range of several MeV. Compared to RBS, the two other scattering techniques MEIS and LEIS use ions with energies of

30–300 keV or only of some keV, respectively. For these techniques high-voltage accelerators are not necessary and common ion sources together with appropriate ion extraction or acceleration stages are applied providing the desired ion beams.

Differently, in the other kinds of ion analytical techniques, such as SIMS, only secondary ions emitted from the solid surface are analyzed by their mass. In order to use these methods to determine concentration depth profiles, it is necessary to remove layers with controlled thickness of the sample. This surface layer removal is carried out by surface bombardment with low energy (0.5–20) keV heavy ions with masses $M_i \geq M_O$ (O^+, Ar^+, Cs^+, Bi^+), which sputter target atoms from the surface. The analysis of secondary ions then can be carried out after each layer is removed to determine the composition of the new surface. The fundamentals and processes of sputtering have been described in Chap. 2. In contrast to IBA methods SIMS and related techniques (e.g., SNMS) exhibit destructive analytical methods.

Consequently, the content of this chapter is divided into two main parts:

1. The description of common IBA methods, namely, ion-scattering techniques in Sect. 6.3, particle-induced photon emission in Sect. 6.4, and nuclear-based IBA methods in Sect. 6.5
2. Low-energy ion beam techniques analyzing secondary light and electron emission in Sect. 6.6, methods based on sputter depth profiling with analysis of secondary ions in Sect. 6.7, and finally ion beam imaging techniques (Sect. 6.8).

6.2 Ion Beam Analytical Techniques: A Survey

Common ion beam analytical (IBA) techniques allow the detection of specific elements in near-surface layers of solids and the determination of their concentration. Furthermore IBA techniques permit the determination of thickness, position, and concentration of individual layers in a multilayer target. Special characteristics of IBA techniques are:

- Generally nondestructive (except for SIMS)
- Typically a multielement method
- Simple and quick sample preparation
- Microtechnique with small sample quantities (mg) and detection ranges (μm)

Primary ions interact with the surfaces, and subsequently different particle and wave radiations will be emitted from the surface. These beams give characteristic knowledge on the solid state surface, and therefore they are mediator for analytical information.

The different kinds of radiations emitted from a target surface after bombardment with high-energetic primary ions are illustrated in Fig. 6.7. As shown in Fig. 6.7a, the primary ions were mass selected, accelerated up to some MeV, then energy analyzed (charge state) by a second magnet, and focused on the sample surface by a focusing ion lens. Different particle and photon radiations are emitted from the target. Emitted particles are elastically backscattered incidence ions [Rutherford backscattering (RBS) and medium-energy ion scattering (MEIS)], particles from nuclear reactions [nuclear reaction analysis (NRA)] and recoil

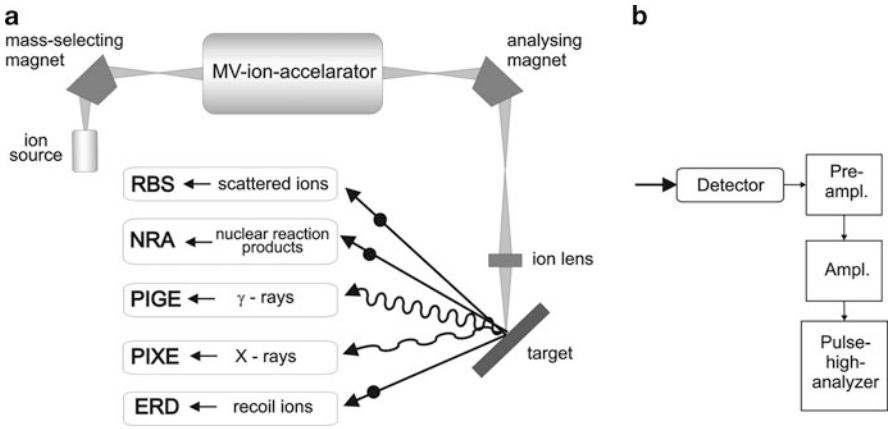

Fig. 6.7 Schematic overview of accelerator-based IBA techniques (**a**) and radiation detection system arrangement (**b**) for particle and photon radiations emitted from a target surface during ion–solid interaction

atoms as forward scattered ions [elastic recoil detection analysis (ERDA)]. Emitted photon radiations are γ-rays [particle induced gamma emission (PIGE)] and X-rays [particle induced X-ray emission (PIXE)]. As shown in Fig. 6.7b, each kind of secondary radiation from the target is detected by radiation specific detection systems using semiconductor detectors (semiconductor Si-, Si(Li)-, Ge(Li)-, HP-Ge detectors), scintillator-PM combinations, Bragg-ionization chambers, MCPs, etc. (see Sect. 3.4.5). Usually the signals from the detectors are electronically amplified and shaped and analyzed in pulse high-multichannel analyzer.

The different emitted radiations and the resulting IBA techniques are summarized in Table 6.2. Often two or more of these techniques are used simultaneously in one experimental setup to obtain additional, complementary information.

Very important preconditions for high-efficient IBA techniques are appropriate ion mass and energy of bombarding ions. These parameters are compiled in Table 6.3. As obvious from this table H^+ and He^+ are the most frequently used ion beams for hydrogen depth profiling. This so-called light ion ERD analysis (LI-ERDA) is a special case because in a straight forward manner the conventional ion energy detection setup (like in RBS with a simple silicon particle detector, only in forward direction) can be used. However, because the H and He projectile masses are low, other heavier elements cannot be examined simultaneously with hydrogen, since the projectile mass needs to be higher than the mass of recoils. For this purpose, heavy ions are used and the ERDA technique is known as heavy ion ERDA (HI-ERDA), where ^{16}O, ^{20}Ne, $^{28}Si^+$, $^{35}Cl^+$,^{127}I, etc. as primary ions with higher energies are used. For RBS with light ions (H^+, He^+) the incident ion energy must be lower than 2 MeV, because for higher energies non-Rutherford scattering becomes significant. If the projectile is lighter than the scattering target atoms, it can be scattered at all angles between 0 and 180°. However, for the ERDA

Table 6.2 Emitted particles/photon radiations and corresponding ion beam analysis techniques

Emitted radiation	IBA technique	Abbreviations
Elastically backscattered ions	Rutherford backscattering	RBS
Elastically backscattered ions	Medium-energy ion scattering	MEIS
Elastically backscattered ions	Low-energy ion scattering	LEIS
Recoiled target nuclei	Elastic recoil detection	ERDA
Characteristic X-rays	Particle-induced X-ray emission	PIXE
Emitted γ-rays	Particle-induced γ-ray emission	PIGE
Particles from nuclear reactions	Nuclear reaction analysis	NRA

Table 6.3 Typical ion beams and incident energies used in various IBA techniques

IBA technique	Ion beam	Incident energy (MeV)	Remarks
RBS	$^{4}He^{+}$, H^{+}	<2	>2 MeV → non-Rutherford scattering
MEIS	$^{4}He^{+}$, H^{+}	0.1–0.3	Medium-energy case of RBS
LEIS	$^{3}He^{+}$, $^{4}He^{+}$, Ne^{+}, Ar^{+}	0.003–0.010	Low-energy elastic scattering, but non-Rutherford
PIXE	H^{+}	1–4	Maximum sensitivity for $13 < Z < 35$ and $75 < Z < 85$
PIGE	He^{+}, H^{+}	0.5–2.5	Maximum sensitivity for $3 < Z < 20$
ERDA	$^{3}He^{+}$, $^{4}He^{+}$	1–3 (LI-ERDA)	Mass of incident ion larger than target nucleus
	^{16}O, ^{20}Ne, $^{28}Si^{+}$, $^{35}Cl^{+}$, ^{127}I, ...	~20–200 (HI-ERDA)	
NRA	$^{1}H^{+}$, $^{2}H^{+}$, $^{3}He^{+}$	0.4–5	Reactions used include (p,γ), (p,αγ), (d,p), (d,pγ) for hydrogen detection
	^{15}N, ^{19}F	6–20	

technique, where the projectile is heavier (M_1) than the target nuclei (M_2), there exists a maximum scattering angle of $\theta_{max} = \arcsin^{-1}(M_2/M_1)$. If the particle detector is placed at an angle of $\varphi > \theta_{max}$, no scattered projectiles (unwanted) but only recoiled ions/atoms are detected [2].

The capabilities of different ion beam analytical techniques are determined by various technical parameters, such as the number of detectable elements, sensitivity, detection limit, depth localization, and depth resolution. The most important techniques are summarized in Table 6.4.

PIXE and PIGE are IBA techniques typically applied for the investigation of trace elements and composition of bulk materials. They have only poor depth resolution in the range from some μm to some 10 μm, but very high-element sensitivity in the ppm range. Typical problems for RBS, MEIS, LEIS, and ERDA are the determination of thickness and composition of near-surface regions. The detectable elements nearly cover the whole periodic system up to U, and these IBA techniques are characterized by very high-depth resolution between monolayer

Table 6.4 Capabilities of ion beam analytical (IBA) techniques

IBA technique	Typical problems	Elements detected	Sensitivity	Depth resolution
RBS	Composition and thickness of near-surface regions	Li–U	Best for heavy elements on light substrates (≈10 ppm)	1–10 nm
MEIS	Composition and thickness of near-surface regions	C (Li)–U	See RBS	Few monolayers
LEIS	Surface-sensitive and monolayer detection	Li–U	Composition of outermost atomic layer	≤1 monolayers
PIXE	Trace element composition of bulk materials	Al–U	Element sensitivity from 1 ppm (Fe) to 100 ppm	2–30 μm
PIGE	Trace element composition of bulk materials	Li–P	Element dependent, from 1 ppm (F) to 50 ppm (Al)	2–50 μm
ERDA	Composition and structure of near-surface regions	H–U	>0.1 %	10–20 nm
NRA	Isotopic tracing and profiling in surfaces and bulks	H–Si	Element dependent, from 1 to 100 ppm	2–10 nm

depth and 10 nm. The detection sensitivity is element dependent and differs considerably. For RBS and MEIS sensitivity is best for heavy elements in light element substrates; it reaches from 10 ppm for U up to 1 % for Li [3, 8]. In contrast, the detection sensitivity of ERDA is limited to about 0.1 %, but all elements from H to U in principle can be detected.

Nuclear reaction analysis (NRA) not only allows the investigation of trace elements (1–100 ppm) with a depth resolution in the nm range, but also isotopic tracing and profiling in near-surface regions, interfaces and bulks are possible.

An example of a schematic setup for combined IBA experiments is illustrated in Fig. 6.8. The target is installed usually on a goniometer (sample tilting and rotation) in the center of an evacuated chamber and bombarded by an incident ion beam, which is focused and collimated to beam spot size of ≤1 mm, or for ion beam microprobes of ≤1 μm. Different particle and photon radiations are emitted by the target and collected by diverse detector systems.

In the present example, silicon particle detectors (SPD) are installed behind and in front of the target. The former one is a SPD for LI-ERDA, whereas the SPD in front of the target is installed for collecting of scattered RBS, MEIS and NRA light particles. The nuclear reaction process also generates γ-radiation (PIGE) which is detected by specially designed γ-ray detectors (large volume HP-Ge detectors or scintillator-PM combination). High-detection efficiency is advantageous for the balance between ion beam-induced target damage and the detectable concentration of the elements of interest. Therefore, a special high-efficient γ-ray detector consisting of a large volume NaI (Tl) or BGO scintillator is applied [11]. PIXE is usually detected by conventional Si(Li)- and Ge(Li)-X-ray detectors or modern silicon drift detectors (SDD), which are also installed in front of the target.

As schematically shown in Fig. 6.8, in the case of combined LI- and HI-ERDA, the full analyzing system for simultaneous detection of light and heavy ions is more

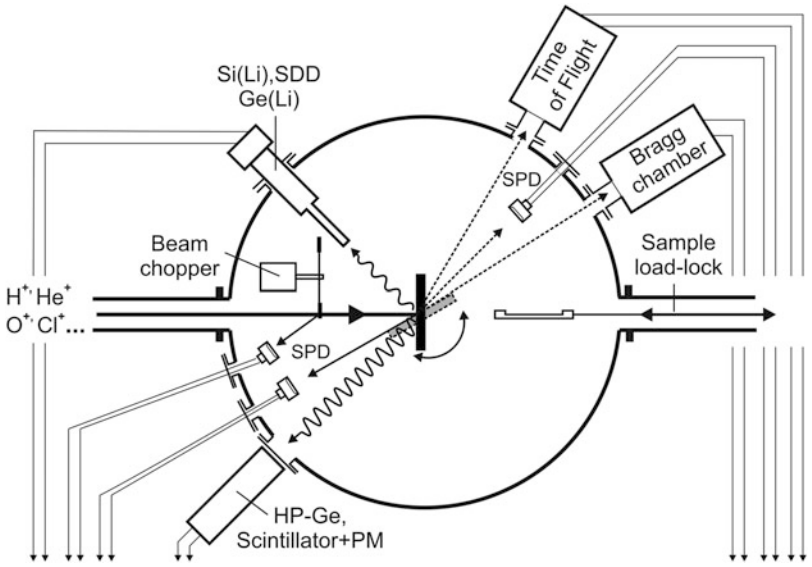

Fig. 6.8 Experimental setup for combined IBA techniques (schematically, after [9, 10])

complicated. Modern ERD systems consist of a SPD (for light recoils of H and He), a Bragg ionization chamber (BIC) (see Sect. 3.4.5), and/or a time-of-flight-energy (ToF–*E*) detector for the detection of heavy recoiled ions/atoms [12]. The use of BIC and ToF–*E* detection techniques was introduced in ERDA for both of recoil mass identification and depth information (depth resolution). The ion beam chopper together with one SPD is installed in the vacuum chamber to monitor and to measure the number of incident ions over the measuring time of IBA. For this purpose the ions of the beam are backscattered periodically from gold-covered-winged wheel rotating through the beam.

All detectors are connected with their specific preamplifiers, amplifiers, and high-voltage supplies. The amplified detector signals are usually converted by analog–digital converters (ADC), and processed with respect to their pulse-heights in multi-channel analyzers (MCA). For the combination of all IBA methods in one vacuum chamber, the samples must be mounted onto the sample holder connected with a goniometer to tilt the sample into position for analysis, that is in backward direction or, alternatively, into position for ERDA analysis in forward direction. The goniometer is also necessary if RBS channeling measurements are performed, which need precise alignment of the sample crystal orientation relative to the direction of the incident ion beam. Most IBA chambers are equipped with a load lock for fast sample transfer.

6.3 Ion Beam-Scattering Techniques

Ion-scattering techniques operate across a large ion energy range, from 1 keV to some tens of MeV, each with different benefits and different aspects that can be investigated with each technique. Compared to other surface analytical techniques, the physics-governing ion scattering is relatively simple. Some of the most common ion beam analysis techniques, as Rutherford backscattering, medium- and low-energy ion spectroscopy as well as elastic recoil detection analysis are based upon the physical principle of binary elastic scattering of energetic ions at sample atomic nuclei (see Chap. 2).

To obtain quantitative information about different elements present at the surface or in the near-surface region of a sample, it is necessary to understand the interaction potentials due to the effects of ion neutralization and scattering cross section. Ion scattering is described by a Coulomb type interaction of the two particles, but only at high energies in the MeV range it can be considered to be purely Coulomb. At low energies, because of the longer interaction times, electron screening must be taken into account. The interaction potential falls off faster than $1/r$, with the Coulomb interaction being multiplied by a so-called screening function [(2.22) in Chap. 2].

Because the scattering cross sections can be calculated with good accuracy, the scattering techniques RBS, MEIS, LEIS, and ERDA are standard-free quantitative analytical methods. The measurement of the energy loss of incident ions by energy measurement of outcoming, scattered ions allows information about the depth of scattering events in the sample. The obtainable depth resolution is determined mainly by the energy resolution of the detection system. For example in "standard" RBS, conventional Si particle detectors (SPD) restrict the depth resolution to about 10 nm.

6.3.1 Rutherford Backscattering

Rutherford backscattering is the most frequently used ion beam analysis method [2, 3, 13–16]. The principle of the RBS method is demonstrated in Fig. 6.9.

RBS bases upon the elastic collision between a high-energetic beam (MeV range) of light ions (E_0, M_1, Z_1, typically $^4He^+$) and near-surface atoms of the investigated sample (M_2, Z_2). The energy of the elastically backscattered ions is measured under different backscattering angles Θ with respect to the direction of the incident ion beam by a detector. The measured energy E_1 depends on the mass M_2 of sample atoms and on the depth t where the scattering process takes place. The depth can be determined by the ion energy loss on the way to and from the point of scattering interaction with the target atom. This allows to profile the element concentration and composition of the sample close to the surface.

The *element identification* of a target atom requires the knowledge of the so-called kinematic factor K. This factor is defined by the ratio between the energies of the primary ion after the collision E_1 and before the collision E_0:

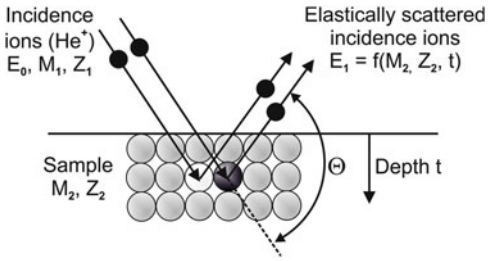

Fig. 6.9 Physical principle of Rutherford backscattering (schematically)

$$K \equiv \frac{E_1}{E_0}. \tag{6.1}$$

The formula for the kinematic factor K at ion scattering can be derived assuming binary elastic collision of the projectile with the target atom (see Fig. 6.9). Taking into account, conservation of energy and momentum the factor K for an ion (M_1) scattered at an angle θ by a target atom (M_2) can be expressed by the following equation [see also (2.8) in Sect. 2.2):

$$K(\theta, M_1, M_2) = \left(\frac{M_1}{M_2 + M_1}\right)^2 \cdot \left(\cos\theta + \sqrt{\left(\frac{M_2}{M_1}\right)^2 - \sin^2\theta}\right)^2. \tag{6.2}$$

As can be seen from (6.2), for elastic scattering the kinematic factor K is independent of the incident ion energy E_0 and depends only on the mass ratio M_1/M_2 and the scattering angle θ. Furthermore, K is more sensitive to M_2 at high values of M_2 for larger scattering angles θ and consequently, RBS measurements are often carried out at angles around 170° (maximum of K at $\theta = 180°$). Since the target element identification is made on the basis of the kinematic factor K the backscattered energy E_1 consequently is equivalent to the mass scale (see Fig. 6.10).

The *mass resolution* δM at RBS analysis can be derived from (6.1) and (6.2). Two target atoms can be distinguished if their mass difference ΔM_2 causes an energy difference ΔE_1 which corresponds approximately to double energy resolution (FWHM) of the overall detection system:

$$\Delta E_1 = E_0 \cdot \frac{dK}{dM_2} \cdot \Delta M_2 \Rightarrow \delta M_2 = \frac{\delta E_1}{E_0} \cdot \left(\frac{dK}{dM_2}\right)^{-1}, \tag{6.3}$$

where $\delta E_1 = (\delta E_d{}^2 + \delta E_s{}^2)^{1/2}$ is the total energy resolution including energy resolution of the detection system δE_d and energy straggling δE_s. Equation (6.3) indicates that the mass resolution δM_2 decreases with increasing projectile energy

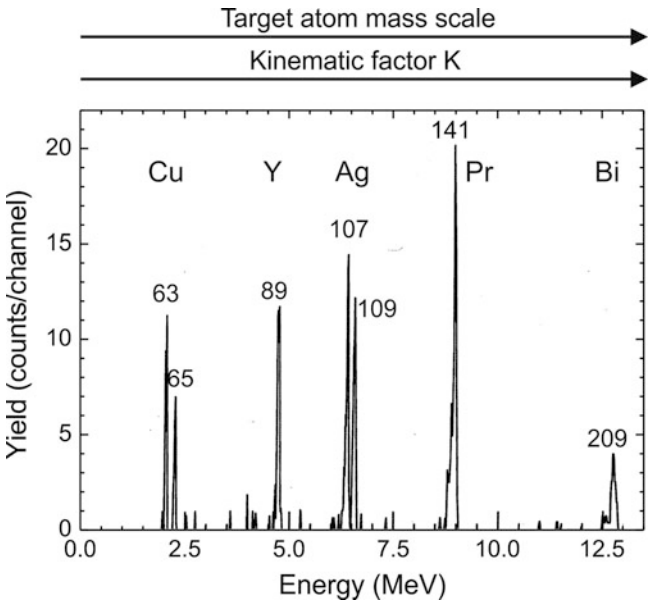

Fig. 6.10 Example of RBS spectrum demonstrating high-mass discrimination. Incident ions: 25 MeV ^{35}Cl; target composition: thin layer target of 0.23 nm Bi, 0.33 nm Pr, 0.33 nm Ag, 0.46 nm Y, 0.72 nm Cu, and 1.4 nm Mn on a high-purity Al substrate (taken from [17])

E_0 and also for heavier target atoms M_2. For the back scattering geometry with $\theta \approx 180°$, we get from (6.3)

$$\delta M_2 \approx \frac{\delta E_1}{E_0} \cdot \frac{(M_2 + M_1)^3}{4M_1(M_2 - M_1)}. \tag{6.4}$$

From (6.4) it follows that for a fixed ratio $\delta E_1/E_0$(~0.01) projectile ions heavier than $^4He^+$ will result in a better mass resolution, but δE_1 increases leading to a reduced energy resolution. If the incident ions are heavier than $^4He^+$, the RBS technique is known as heavy ion Rutherford backscattering spectrometry (HI-RBS). HI-RBS differs from conventional RBS by the use of time-of-flight detectors (ToF detectors) with large scattering solid angles instead of common silicon particle detectors. The advantages of using heavier ions (e.g., ^{12}C, ^{16}O, ^{28}Si, ^{35}Cl) are a better mass resolution for heavy target elements and improved mass sensitivity, for example of metal surface contaminants on silicon wafers.

As an example for improved mass sensitivity, Fig. 6.10 shows the high-mass resolution in RBS analysis of a thin layer (overall thickness 3.57 nm) with six different heavy atom masses deposited on a light mass Al substrate [17].

The sample was bombarded with 25 MeV ^{35}Cl ions under a scattering angle of 175°, and backscattered Cl ions were detected by a ToF detector with micro-channel plates. HI-RBS is suited for the analysis of thin surface layers. Compared

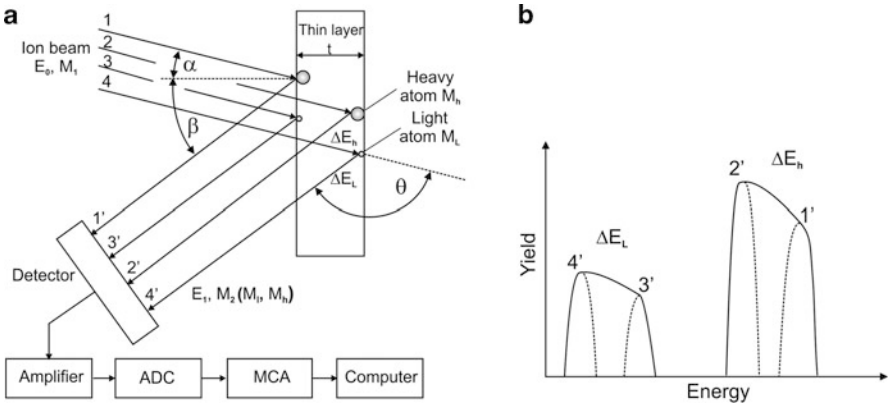

Fig. 6.11 Principal setup of a Rutherford backscattering spectroscopy (**a**) with θ the scattering angle, α the ion incidence angle, and β the ion emergent angle with respect to the surface normal. Schematic RBS spectrum of light and heavy target ions at different depths (**b**)

to conventional ^{4}He-RBS mass and depth resolution at the very surface of the sample can be significantly increased. As demonstrated in Fig. 6.10 even isotopes of Cu and Ag can be resolved.

The common schematic Rutherford backscattering setup is schematically shown in Fig.6.11. An incident ion beam (E_0, M_1) bombards a chemically inhomogeneous thin sample of heavy atoms (atomic mass M_h) and light atoms (atomic mass $M_l < M_h$). The backscattered energy depends on both the atomic mass of the bombarded sample atoms and the depth of the scattering event (here at the front side and at the backside of the thin layer target). The energy differences between the ions backscattered from the front and the backside are ΔE_h or ΔE_l, respectively, as shown schematically in the spectrum in Fig. 6.11b.

Depth scale: The signal from an atom at the sample surface will appear in the energy spectrum at a position $E_1 = K{\cdot}E_0$ (edges $1'$ and $3'$ for heavy and light atoms, respectively). The signal from atoms of the same mass in a depth t below the sample surface will be shifted by the amount of energy loss (edges $2'$ and $4'$ for heavy and light atoms, respectively), while the incident ions pass through the sample, both before [$\Delta E_{in}(x_1)$] and after a collision [$\Delta E_{out}(x_2)$]. Formulas usable in RBS analysis are the following:

$$\text{Energy loss inward}: \quad \Delta E_{in}(x_1) = \frac{t}{\cos\alpha}\int_0^t \left(\frac{dE}{dx}\right)_{in} dt' \cong \frac{1}{\cos\alpha}\left.\frac{dE}{dx}\right|_{in} \cdot t$$

$$\text{Energy at depth } t: \quad E_t = E_0 - \Delta E_{in}(x_1) \tag{6.5}$$

$$\text{Energy loss at scattering}: \quad \Delta E_S = (1-K)\cdot E_t$$

$$\text{Energy loss outward}: \quad \Delta E_{out}(x_2) = \frac{t}{\cos\beta}\int_t^0 \left(\frac{dE}{dx}\right)_{out} dt' \cong \frac{1}{\cos\beta}\left.\frac{dE}{dx}\right|_{out} \cdot t$$

The energy of the scattered ions $E_1(t)$ as a function of scattering depth t at the detector entrance is equal to

$$\begin{aligned} E_1(t) &= K(E_0 - \Delta E_{\text{in}}(x_1)) - \Delta E_{\text{out}}(x_2) \\ &= K\left(E_0 - \frac{t}{\cos\alpha}\cdot\left.\frac{\mathrm{d}E}{\mathrm{d}x}\right|_{\text{in}}\right) - \frac{t}{\cos\beta}\cdot\left.\frac{\mathrm{d}E}{\mathrm{d}x}\right|_{\text{out}} \\ &= K\cdot E_0 - \left(\frac{K}{\cos\alpha}\cdot\left.\frac{\mathrm{d}E}{\mathrm{d}x}\right|_{\text{in}} + \frac{1}{\cos\beta}\cdot\left.\frac{\mathrm{d}E}{\mathrm{d}x}\right|_{\text{out}}\right)\cdot t \\ &= K\cdot E_0 - S\cdot t, \end{aligned} \tag{6.6}$$

where x_1 is the path length from the sample surface to the scattering point, x_2 the path length from the scattering point back to the surface, and $\mathrm{d}E/\mathrm{d}x$ is the specific energy loss (also called stopping power) of the ions over the path lengths. The energy losses are caused by inelastic collisions of the light MeV ions with the electrons of the target atoms (electronic energy loss). The factor S is often called the energy loss factor. In (6.6) $K{\cdot}E_0$ corresponds to the edges $1'$ and $3'$ and $K{\cdot}E_0 - S{\cdot}t$ to the edges $2'$ and $4'$ in the RBS spectrum of Fig. 6.11 for heavy and light atoms in the layer, respectively. At normal incidence of the primary ion beam onto the sample surface, (6.6) simplifies to:

$$E_1(t) = K\cdot E_0 - \left(K\cdot\left.\frac{\mathrm{d}E}{\mathrm{d}x}\right|_{\text{in}} + \frac{1}{\cos\theta}\cdot\left.\frac{\mathrm{d}E}{\mathrm{d}x}\right|_{\text{out}}\right)\cdot t \tag{6.7}$$

with θ the scattering angle.

For every target atom mass M_i (here light M_l and heavy M_h) with the kinematic factor K there exist separate energy-depth scales in the RBS spectrum (as shown in Fig. 6.12), which can be calculated from (6.6) and (6.7).

The mostly used detector in Fig. 6.11 is a Si particle detector with a reverse-biased p-n-junction. Each scattered ion creates electron–hole pairs, the number of which is proportional to the energy of the scattered ion. The induced charge pulses are transformed into voltage pulses and amplified by the detection electronics. A computer switches a multichannel analyzer MCA. Each channel possesses an energy width much smaller than the energy differences ΔE_l and ΔE_h. So a yield spectrum of backscattered ions in dependence of the ion energy appears (Fig. 6.11b), which is a superposition of scatter events at different atoms in different depth. Both axes in Fig. 6.11b can be calibrated in order to get mass concentrations in relation to scattering elements and scattering depth.

The specific energy loss or stopping power $\mathrm{d}E/\mathrm{d}x$ represents a mean energy loss $<\delta E>$ of a large number of ions travelling through the infinitesimal thickness $\mathrm{d}x$. Due to the atomic character of energy loss, an indication of thickness in length units without consideration of the atomic density N_i (cm^{-3}) in the analyzed layer is not reasonable. Therefore, in ion beam analysis, the stopping cross-section $\varepsilon(x)$ is used, which is given in units of eV cm^2. Thus,

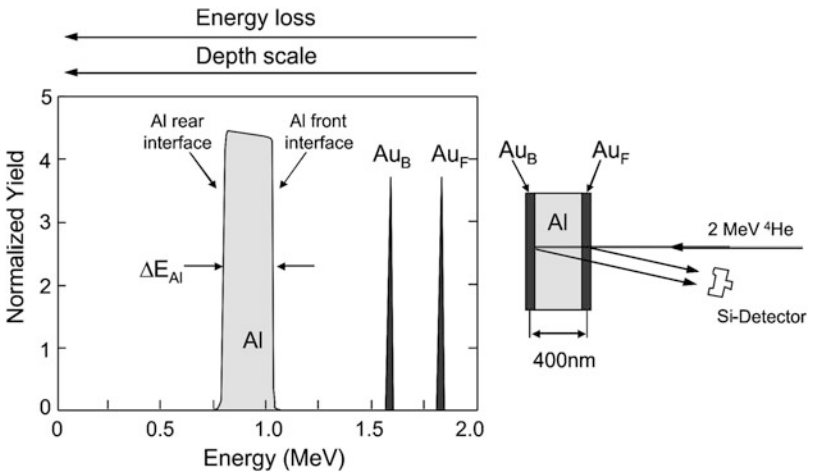

Fig. 6.12 Interpretation of the energy loss and depth scale in RBS spectra of a Au–Al–Au thin film multilayer [3]. The RBS spectrum was recorded using 2 MeV He^+ ions at normal incidence and a scattering angle of $\theta = 170°$

$$\varepsilon(x) = -\frac{1}{N_i} \cdot \frac{\mathrm{d}E}{\mathrm{d}x} \tag{6.8}$$

which represents the mean energy loss $<\delta E>$ per crossed atomic areal density $N_i \cdot \Delta t$.

The interpretation of the energy loss and depth scale is demonstrated in Fig. 6.12, where a 400-nm thick Al layer with ~1 nm Au (≈3 monolayers) deposited on its front and rear side is investigated by RBS [3]. The backscattering spectrum was taken at $\theta = 170°$ with 2 MeV $^4He^+$ ions. One can clearly discriminate between the two gold thin layers Au_F, Au_B and the Al layer. Thus, the RBS spectrum is an overlay of the two depth profiles of gold and aluminum, present in the target material.

The *depth resolution* δt of RBS is equal to

$$\delta t = \frac{\delta(E)}{N_i \cdot \left(\frac{K \cdot \varepsilon_{\mathrm{in}}}{\cos\alpha} + \frac{\varepsilon_{\mathrm{out}}}{\cos\beta}\right)} \quad \text{or} \quad \delta t = \frac{\delta(E)}{N_i \cdot \left(k \cdot \varepsilon_{\mathrm{in}} + \frac{\varepsilon_{\mathrm{out}}}{\cos\theta}\right)} \quad \text{for} \quad \alpha = 0, \tag{6.9}$$

where $\delta E = (\delta E_d^{\,2} + \delta E_s^{\,2})^{1/2}$ is the total energy resolution including energy resolution of the detection system δE_d and energy straggling δE_s.

The yield Y of ions back scattered from a thin layer Δt containing atoms N_i and measured by the detector (see Fig. 6.13) is given by

$$Y_i(t) = N \cdot \Omega \cdot N_i \cdot \Delta t \cdot \sigma \tag{6.10}$$

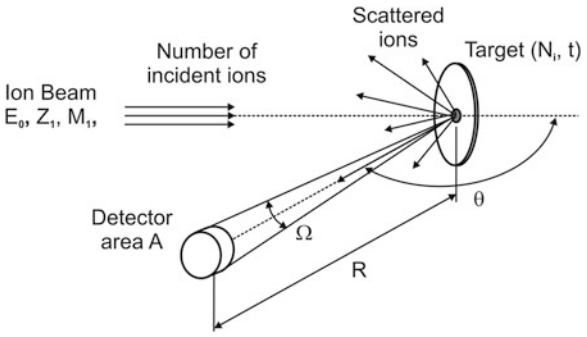

Fig. 6.13 Schematic RBS geometry with normal ion beam incidence showing the scattering angle θ and the solid angle $\Omega = A/R^2$ with R the distance of the detector from the sample for the calculation of the differential cross-section

and depends on the number of incident particles N, the size of the silicon particle detector (solid angle Ω), the number of scattering atoms (atomic areal density $N_i \cdot \Delta t$), and the probability of scattering (backscatter cross-section σ).

The cross-section σ transforms the coordinate space before scattering into the angle space after scattering. The quotient $d\sigma/d\Omega$ denotes the differential backscatter cross section and is expressed by the well-known Rutherford formula (see also Chap. 2) in the center of mass system,

$$\left.\frac{d\sigma}{d\Omega}\right|_{CM} = \left(\frac{Z_1 \cdot Z_2 \cdot e^2}{16\pi \cdot \varepsilon_0 \cdot E_{CM}}\right)^2 \cdot \left(\frac{1}{\sin^4\left(\frac{\theta_{CM}}{2}\right)}\right), \tag{6.11}$$

and in the laboratory system for $M_2 >> M_1$,

$$\left.\frac{d\sigma}{d\Omega}\right|_{Lab} = \left(\frac{Z_1 \cdot Z_2 \cdot e^2}{16\pi \cdot \varepsilon_0 \cdot E_0}\right)^2 \cdot \left(\frac{1}{\sin^4\left(\frac{\theta}{2}\right)}\right). \tag{6.12}$$

The knowledge of the differential backscatter cross section allows the standardless quantification of elements M_i in a thin layer Δt with an areal density of $N_i \cdot \Delta t$ from the measured yield $Y_i(t)$ in (6.10). The observed energy spectra are line spectra, where the energy values of the lines are identified by the kinematic factors of the atom masses M_i and their intensity (yield) ΔY_i by the differential cross section and the number N of incidence primary ions. The corresponding areal densities of target atoms N_i

$$N_i \cdot \Delta t = \frac{\Delta Y_i}{N \cdot \Omega \cdot \left(\frac{d\sigma}{d\Omega}\right)_i} \tag{6.13}$$

can be measured by RBS with a high-accuracy because N and Ω are known within ≤ 1 %. The accuracy for the determination of element composition using RBS is in the range of a few percent, typically ≤ 5 %.

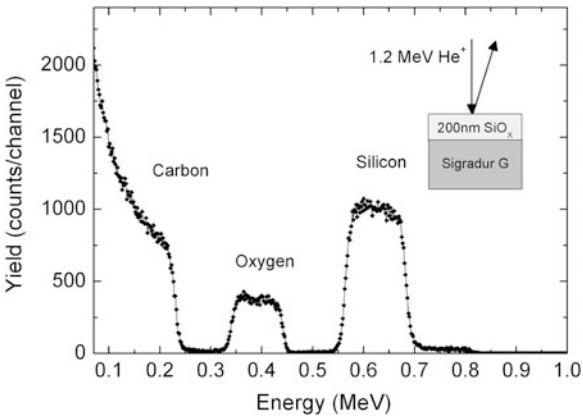

Fig. 6.14 RBS spectrum of a 200 nm thick SiO_x sputter layer deposited on a carbon substrate

Taking into account the solid angle $\Omega = A/R^2$, one can derive from (6.12) and (6.13) the following expression for the yield (detected back scattered ions):

$$\Delta Y_i = \left(\frac{Z_1 \cdot Z_2 \cdot e^2}{16\pi \cdot \varepsilon_0 \cdot E_0}\right)^2 \cdot \frac{N \cdot N_i \cdot \Delta t}{\sin^4(\theta/2)} \cdot \frac{A}{R^2}. \tag{6.14}$$

From (6.14) follows that the Rutherford scatter yield is very forward directed, going as $1/\sin^4(\theta/2)$, which is advantageously used in HR-RBS detecting forward scattered ions by a magnet spectrometer (see Fig. 6.17). The scatter yield increases with decreasing incident ion energy E_0 proportional to $1/{E_0}^2$. Furthermore, (6.14) shows that since $d\sigma/d\Omega$ and therefore Y are proportional to ${Z_1}^2 \cdot {Z_2}^2/{E_0}^2$, the sensitivity increases with increasing Z_1 and Z_2 and decreases with E_0. The increased sensitivity for high-Z_1 incident ions and high-Z_2 target atoms has been demonstrated already in Fig. 6.11.

In the case of compound layers containing more than one element, for example, elements A and B with the chemical formula A_xB_y, the stopping cross-section ε is determined on a molecular basis ε_{AxBy} assuming Bragg's rule of linear additivity of elemental ε, namely $\varepsilon_{AxBy} = x \cdot \varepsilon_A + y \cdot \varepsilon_B$. To take a specific example of Co_2Si, the stopping cross section is written as $\varepsilon_{Co2Si} = 2 \cdot \varepsilon_{Co} + 1 \cdot \varepsilon_{Si}$. If we are interested in the stoichiometry of compound layers A_xB_y with thickness t, we have to determine from the RBS spectrum the ratio of the A and B areal densities $(N \cdot t)_A/(N \cdot t)_B$. From (6.13) and (6.14), it follows that

$$\frac{N_A \cdot t}{N_B \cdot t} = \frac{N_A}{N_B} = \frac{Y_A \cdot \sigma_B}{Y_B \cdot \sigma_A} = \frac{Y_A}{Y_B} \cdot \left(\frac{Z_B}{Z_A}\right)^2 \tag{6.15}$$

because Z_1, E_0, and the scattering angle θ are the same for the elements A and B. Because RBS is a standard-free analytical method composite surface layers (e.g.,

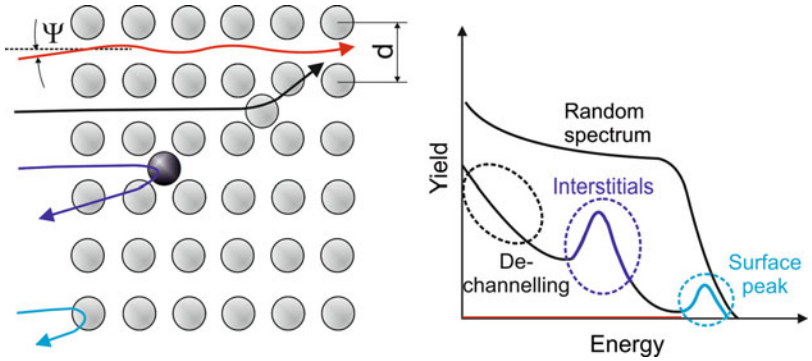

Fig. 6.15 Schematic illustration of channeling RBS: (*left*) ion channeling and scattering on top-surface target atoms and interstitially located impurity and/or target atoms, and (*right*) corresponding C-RBS spectrum in comparison with a random spectrum. Ψ and d denote the critical angle for channeling and d the crystal lattice spacing, respectively (see Chap. 2)

silicides, oxides, nitrides, ceramic glasses) and multicomponent metal alloys are investigated by this method to determine their stoichiometry and composition with sufficient accuracy. For example, Fig. 6.14 shows a typical RBS spectrum of a sub-stoichiometric SiO_x ($x \approx 1$, thickness 200 nm) layer deposited by magnetron sputtering on a glassy carbon substrate (SIGRADUR G®). The sample was analyzed using 1.2 MeV He^+ ions at a scattering angle of 160°. As can be seen, the RBS peaks for oxygen and silicon are clearly separated from the light mass carbon substrate. The ratio of the integrated areas of the O and Si peaks directly gives the areal densities, respectively, and the excess Si content or the stoichiometry x can be determined. In the present case, the Si excess was equal to (22.3 ± 0.1) at.% corresponding to a stoichiometry of $x = 1.07 \pm 0.05$.

In many analytical cases, the samples are crystalline and *ion channeling phenomena* can occur (see Chap. 2). In the case of normal scattering, the incident ions are scattered randomly because target atoms are also distributed randomly in the target matrix (e.g., amorphous materials). If a crystalline sample is properly oriented with respect to the direction of the ion beam, target atom rows or planes can steer incident ions by means of correlated series of small angle collisions. Chains of atoms in the bulk are then shadowed, and, as a result, the probability of scattering from these atoms is reduced, which leads to reduced and totally different scattering yields Y_i from the near-surface in the RBS spectrum. The probability of scattering from sub-surface atoms of crystalline target is reduced by at least one order of magnitude for ions incident along channeling direction. At exact channeling conditions (axial and planar channeling), the scatter yield Y_i consists predominantly scattering events from top-surface atoms (only "surface peak" in the RBS spectrum) of a perfect crystal. Channeling-RBS (C-RBS) is well suited for investigations of interstitial impurity atoms and crystal defects introduced by ion implantation into semiconductors as shown schematically in Fig. 6.15.

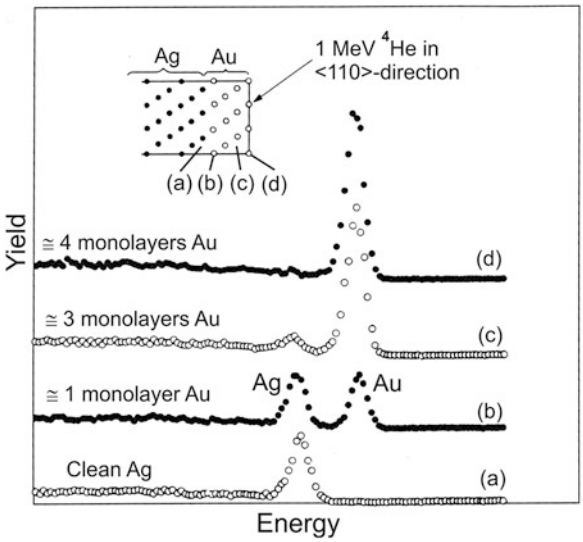

Fig. 6.16 RBS spectra of a Ag surface covered with Au monolayers [18]

C-RBS allows the determination of the degree of impurity activation (atoms on substitutional lattice sites) and defect removal after subsequent damage annealing.

Furthermore, C-RBS is very useful and sensitive for the investigation of ultrathin surface layers (monolayer deposition or surface contaminants). As an example, Fig. 6.16 shows C-RBS of an Ag surface which is covered with adsorbed Au monolayers [18]. In the aligned crystal with the <110> axis parallel to the incident ion beam 1.0 MeV He ions penetrate along the <110> axis of (a) a clean Ag (111) surface and (b), (c), and (d) for Au-covered surfaces. Because the gold atoms shadow the underlying Ag atom rows the He ion scattering at inner Ag atoms diminishes. Therefore the Ag surface peak decreases with increasing Au coverage. Besides the Ag peak the Au peak appears, which grows with increasing Au layer thickness, from one (b) to four (d) monolayers.

In channeling experiments, the orientation of crystals is precisely carried out by a goniometer such that primary ions incident in alignment with the atomic crystal structure. C-RBS measurements are ideal for providing depth distribution of crystal lattice disorder, thickness of amorphous/amorphized surface layers, location of impurity atoms, as well as strain in heterocrystal and superlattice structures. A survey can be found, for example, in Tesmer and Nastasi [8].

Because modern functional layers and layer systems demand nanometer or even sub-nanometer depth resolution instead of SPDs special magnetic spectrometers are applied [19] to perform high-resolution RBS (HR-RBS).

The principal function of such a spectrometer is illustrated in Fig. 6.17. Charged particles which were scattered from the sample with different momenta pass the field of a dipole magnet and are focused to different positions in the focal plane where a position-sensitive detector is located. As detectors, position-sensitive

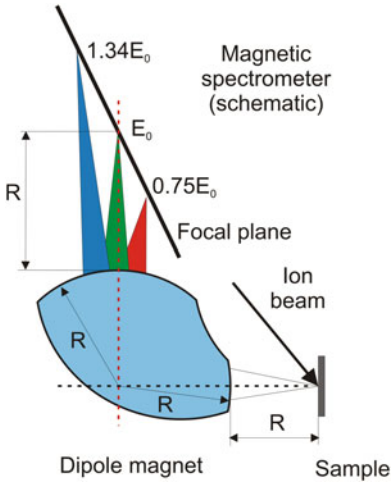

Fig. 6.17 High-resolution ion beam analysis

silicon detectors (Si-PSD) or position-sensitive multichannel plates (MCP-PSD) are used. By this way the problem of energy resolution is converted into a problem of position resolution. At HR-RBS the energy of scattered particles can be measured with an increased accuracy of $\Delta E/E < 10^{-3}$, and the depth resolution reaches values smaller than 1 nm, which is more than one order of magnitude better compared to conventional RBS. However, this value is related only to near-surface regions. Due to energy straggling, the depth resolution rapidly degrades with increasing depth.

As an example for high-depth resolution ion-scattering analysis, Fig. 6.18 shows a HR-RBS spectrum of a multilayer consisting 5 (0.57 nm $Ta_{0.1}Si_{0.9}$/5.2 nm Si) on Si. The HR-RBS spectrum was measured in forward direction with 2 MeV C^{2+} ions at a scattering angle of 35.5° using a magnetic spectrometer of the type as shown in Fig. 6.17. The individual layers are clearly resolved, also because the forward scattering angle increases the path length of both incoming and outcoming ions in the sample [20]. Due to the arrangement of the magnet spectrometer in direction of forward scattering, this technique can be easily applied also to LI-ERDA of hydrogen [14].

Finally, RBS measurements can be accomplished using solid alpha particle radiation sources usually made from radioactive actinide isotopes (e.g., ^{241}Am, ^{239}Pu, ^{252}Cf, and others) instead of a ^{4}He ion beam provided by an accelerator. As an example, the concept of Rutherford backscattering was applied as part of the scientific mission of Surveyor VI at its moon landing in 1967 [21]. An alpha particle-scattering detector head was employed on the moon surface for first analysis of lunar soil by bombardment with primary alpha particles emitted from a ^{242}Cm source with an energy of $E_\alpha = 5.353$ MeV. Lunar surface atoms were identified by two particle detectors, measuring the energy of scattered alpha

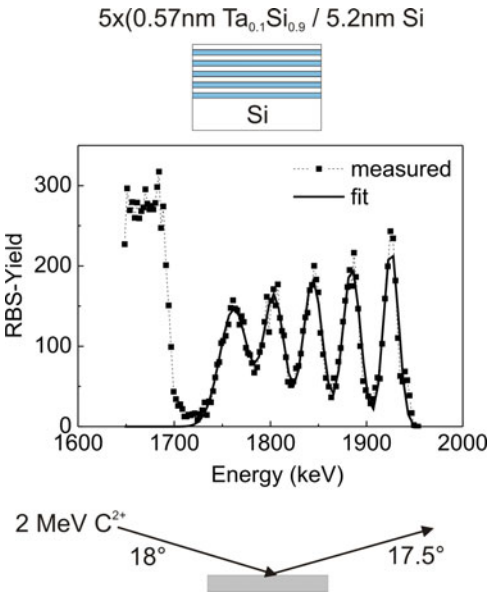

Fig. 6.18 High-resolution RBS spectrum of a multilayer 5 (0.57 nm $Ta_{0.1}Si_{0.9}$/5.2 nm Si) on Si [19]

particles and by a proton detector, measuring the energy of protons emitted by alpha particle-induced nuclear reactions. The findings suggested that large portions of the lunar soil resemble basalt in composition [21]. Nowadays, in an improved specification this prototype is still used in space research. One of the main drawbacks of RBS is its relative poor sensitivity for light elements present in a matrix of heavier elements, which is in the range of 1–10 at.% for $Z < 20$, 0.01–1 at.% for $20 < Z < 70$, and 0.01–0.001 at.% for $Z > 70$. The reasons are (1) the low value of backscattering cross-section σ_{RBS} for light elements which is proportional to Z^2 and (2) the low energy E_2 of ions backscattered from light target atoms. In principle, the sensitivity in Rutherford backscattering analysis can be increased by

- Increasing the number of probing particles N
- Increasing the detector solid angle Ω
- Increasing the detector efficiency
- Increasing the scattering cross-section σ by using heavier probing ions M_1 and decreasing ion energy E_0 and scattering angle θ, respectively

Rutherford backscattering is a very flexible ion beam analysis method. It allows the successful study of the following problems:

- Absolute thickness of thin films and surface layers (areal density in atoms cm^{-2})
- Element concentration profiles as a function of depth
- Interdiffusion kinetics of thin films (silicides, metals, oxides, etc.)
- Analysis of elemental composition in complex materials (phase identification, alloy films, oxides, ceramics, etc.)
- Highly sensitive detection of surface contaminants (surface and interface contaminants, adsorbates, etc.)

Table 6.5 Main features of RBS

Elements	Be–U
Standard conditions	2 MeV ^{4}He beam, silicon detector, 10 min per sample
Precision	Stoichiometry: <1 % relative, thickness: <5 %
Sensitivity	Bulk: some % to 10^{-4}, depending on Z surface: 1–10^{-4} monolayers
Depth resolution	1–10 nm
Remarks	Accessible depth range ~1 μm; no light elements detectable on heavy substrates

- Defect analysis in crystalline materials (as after ion implantation and annealing)
- Quantitative implantation dopant profiles in crystalline semiconductors
- Quantitative control of total amount of impurities implanted into the materials [measured areal impurity density $N{\cdot}t$ (cm^{-2}) is directly equal to the implanted ion fluence Φ (cm^{-2})]
- Quantification of implantation standards necessary for other analytical methods such as SIMS (see Sect. 6.7)
- Quantitative process control, e.g., composition and contaminants
- HR-RBS and element mapping with focused incident ion beam

In summary, the mean features of Rutherford backscattering are given in Table 6.5.

6.3.2 Medium-Energy Ion Scattering

Compared to conventional RBS medium-energy ion scattering (MEIS) is performed at lower incident H^+ and He^+ ion energies in the range of (20–200) keV and with higher resolving detectors (e.g., electrostatic analyzers, magnet spectrometers, and ToF detectors). It is a fairly new technique firstly described by van der Veen [22]. MEIS technique allows quantitative information about sample composition, sample surface, and element concentration depth profiles. The following quantities can be measured by MEIS:

- Angular distribution of ions backscattered from near-surface regions, giving information about atomic locations with ~10^{-2}–10^{-3} nm accuracy in the best case
- Energy distribution of backscattered ions, giving information about atomic composition and about atomic depth distribution with best resolution of ~10^{-1} nm

Therefore, two types of MEIS spectra are gathered from the experimental data: energy spectra and angular spectra. MEIS offers a superior depth resolution while maintaining the same spectra interpretation as RBS. It is also a quantitative technique because the scattering yields Y_i can be measured in absolute units.

Modern research topics which were handled by medium-energy ion scattering are mainly related to depth profiling of ultrathin films, as for application in

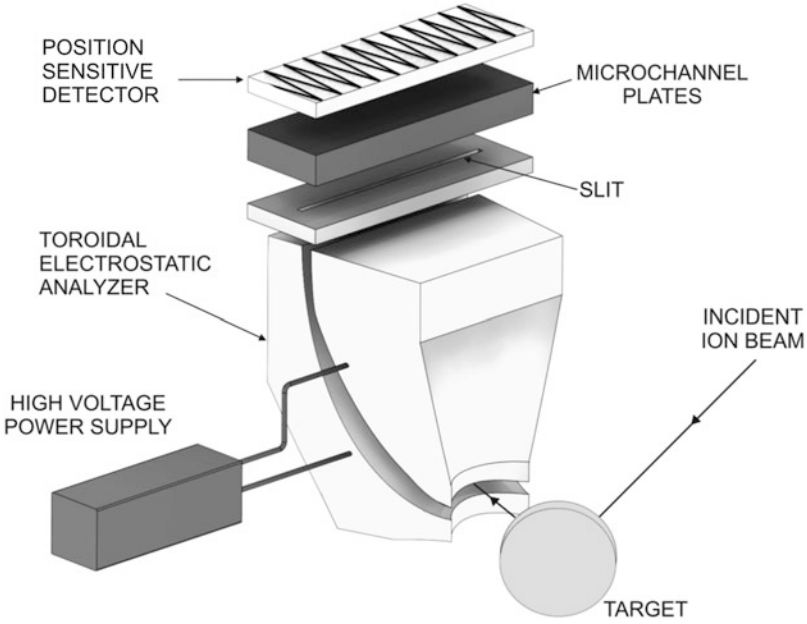

Fig. 6.19 Schematic setup of a medium-energy ion scattering (MEIS) spectrometer

microelectronics. A special advantage of MEIS is here the information about not deeply buried interfaces with a depth resolution in the monolayer range.

Because of the low energy of scattered ions and demands for very high-depth resolution of the MEIS technique, conventional Si particle detectors as for Rutherford backscattering cannot be applied because of their limited energy resolution. As usual detectors for MEIS special toroidal electrostatic analyzers together with position sensitive detectors were developed [23] which achieve an energy resolution $\Delta E/E \approx 10^{-3}$. It is schematically sketched in Fig. 6.19.

A collimated incident beam of H^+ or He^+ ions bombards a target mounted on a goniometer and aligned along specific crystallographic directions. A 6-axis goniometer is used to perform, for example, channeling-in and blocking-out MEIS measurements, which means that the crystal must be aligned along a major crystallographic direction, for both incident beam, and outgoing backscattered ions (so-called double alignment geometry). The principle of these measurements allows, for example, to determine the position of surface atoms with an accuracy of ~0.01 nm. This is due to the restriction of scattering only from top-surface atoms without scattering from underlying substrate atoms. Both the energy and the angle of scattered ions are analyzed simultaneously in a toroidal electrostatic analyzer. The position sensitive detector is an array anode combined with multichannel plates, which convert the ion energy into a proportional amount of electrons. The electrostatic analyzer allows an energy resolution of about 150 eV at a primary ion energy of $E_0 = 100$ keV and an angular resolution of ~0.3°. The position sensitive

detector yields a one- or two-dimensional image, where both the energy and the angle are registered for a certain analyzer voltage, which is stepwise changed to analyze all target masses. The simultaneous analysis of energy and angle of scattered ions allow MEIS to measure atomic mass, depth, and atomic surface structure.

The main application fields of MEIS analysis are:

- Structure of reconstructed single crystal surfaces
- Study of surface melting
- Investigation of composite and alloy surfaces
- Initial stages of oxide growth (e.g., SiO_2 on Si, ZrO_2, HfO_2 on SiO_2)
- Structure of buried layer interfaces (e.g., strain in epitaxial grown layers with certain lattice mismatch, growth of Ni-, Co-, and rare-earth silicides and germanides)
- Analysis of the layer-by-layer composition of bimetallic surfaces (e.g., PbSe (111)-, PtNi(111)-, and CuPd(110)-surfaces)
- Characterization of ultra-shallow pn-junctions in silicon (fluence control, dopant depth distribution, extent and depth of the implant damage in (100)Si)

Furthermore, a rather new research field for MEIS became the study of composition and size of semiconducting and metal nanocrystals [24–26]. As an example for the investigations of surface nanoparticles, Fig. 6.20 demonstrates a typical MEIS spectrum and its interpretation [27]. ZnS and CdSe were deposited on a SiO_2 surface layer on a Si substrate forming nanoparticles with different shape and composition. The surface was analyzed with 130 keV H^+ ions, and the normalized backscattering yield from surface nanoparticles was measured at a scattering angle $\Theta = 135°$. The open circles depict the measuring points, whereas the colored curves represent results of two different model simulations. For both models, the following assumptions for element areal densities of Cd = 0.10 and Se = 0.12 ($\times 10^{15}$ atoms cm^{-2}), and concentration ratio of ZnS:CdSe = 20:1 were made. Furthermore, a $C_xH_yO_z$-capping layer was introduced in the simulations. As Fig. 6.20 demonstrates the best accordance can be achieved by model II, assuming a mixture of ZnS (or of CdSe in ZnS shells) and CdSe nanoparticles.

In summary, the mean features of medium-energy ion scattering are given in Table 6.6.

6.3.3 Low-Energy Ion Scattering

The energy distribution of low-energy ions (1–8 keV) scattered at some specific angles from a solid surface provides information on the mass and the number of surface atoms from the energy position and magnitude of corresponding peaks in the LEIS spectrum [28]. The scattering technique in this ion energy range has been called low-energy ion scattering (LEIS), ion-scattering spectroscopy (ISS), or noble gas ion reflection mass spectroscopy (NIRMS). The acronym LEIS is preferred since the emphasis is on the low ion energies. In LEIS the analyzed depth is restricted only to a few atom layers as schematically shown in Fig. 6.21.

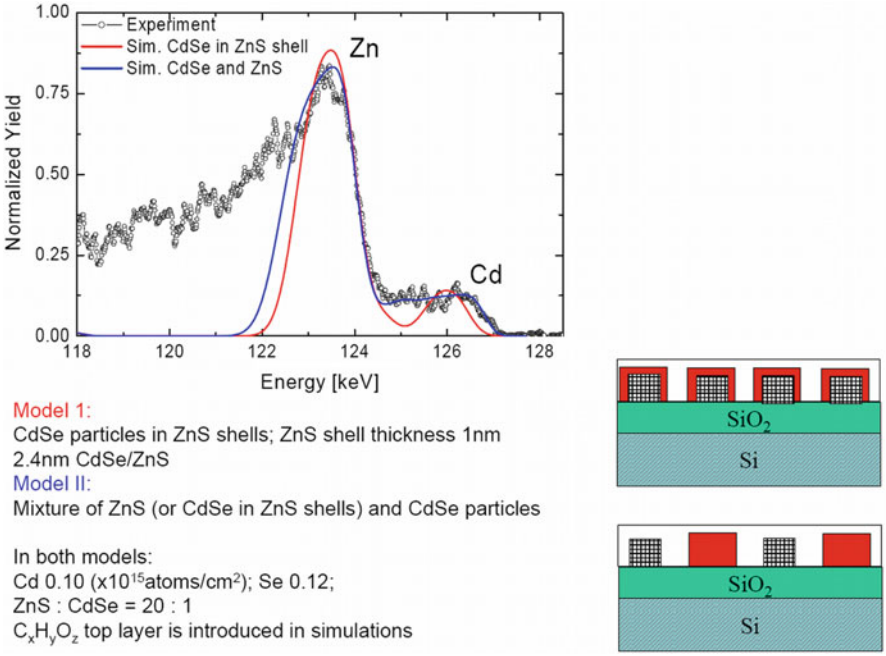

Fig. 6.20 Formation of CdSe and ZnS core–shell nanoparticles on a SiO_2 surface: MEIS experiment and model simulations (after [27])

Table 6.6 Main features of MEIS

Elements	C–U
Standard conditions	10–100 keV $^4He^+$ or H^+ beam; position sensitive ion detector, 30 min per sample
Precision	Atomic location: down to 0.001 nm accuracy
Sensitivity	Bulk: relatively poor
	Surface: 10^{-2} monolayers
Depth resolution	0.1–1 nm right at the surface
Remarks	Composition and structure of buried interfaces with monolayer-level resolution

In the case of single crystal, surface structure or atom location information can be derived from scatter shadowing and multiple scattering effects. In the case of scattering low-energy ions, the scattering cross section is different from the Rutherford cross section, as the distance of closest approach of the impinging ion to the target atom R_{min} is rather large. Thus, electronic screening of the interaction between the nuclei is important. The screened scattering potential $\varphi(r)$ (see also Chap. 2) is expressed as

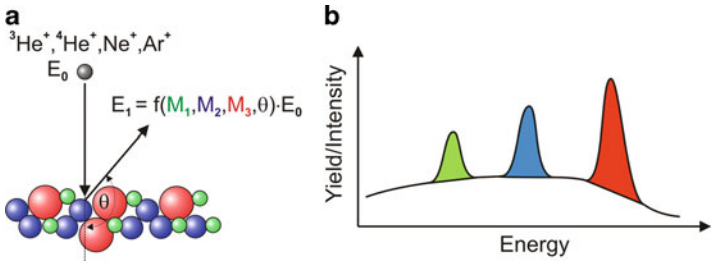

Fig. 6.21 Schematics of LEIS analysis (**a**) and of corresponding LEIS spectrum (**b**) of outermost atomic layer composition

$$\varphi(r) = \varphi_C(r) + \varphi_e(r) = \varphi_C(r) \cdot \Phi\left(\frac{r}{a}\right), \tag{6.16}$$

where $\varphi_C(r)$ and $\varphi_e(r)$ are the potential of target nucleus (Coulomb repulsion) and target electrons, respectively. $\Phi(r/a)$ is the screening function, which describes how the Coulomb potential is weakened by the electronic screening. Φ is a function of the reduced distance r/a with a, the screening length, which is characteristic of the ion–target combination. At low ion energies <10 keV, scattering cross sections are of the same order of magnitude as atomic dimensions and increase with decreasing energy. Thus, the ions have a relatively low probability of penetrating beyond the surface, and those which do have even less chance of scattering back. Moreover, the ions which penetrate and undergo multiple scattering at near-surface atoms, have a longer interaction time with the target atoms and can be neutralized [29].

The atomic surface concentration N_i can be calculated (in a similar manner as in RBS and MEIS) from the yield of backscattered ions Y_i according to

$$Y_i = \frac{I_p}{e} \cdot t \cdot f \cdot R \cdot \eta_i \cdot N \tag{6.17}$$

with I_p—the primary ion current and e the elementary charge, t—the measuring time, f—an instrumental factor (including detector solid angle, detector efficiency, and analyzer transmission), R—a factor, which includes surface roughness and shielding by neighboring atoms, and η_i—the elemental sensitivity factor.

The sensitivity factor includes the differential cross-section $d\sigma_i/d\Omega$ (calculated for given scattering potentials) and the fraction of charged backscattered ions Pi^+ and is given by

$$\eta_i = P_i^+ \cdot \frac{d\sigma_i}{d\Omega}. \tag{6.18}$$

Quantitative surface composition analysis is based on (6.17). However, the elemental sensitivity factor is only known for a few combinations of elements, incident ions, ion energies, and scattering angles [30]. Therefore, quantitative

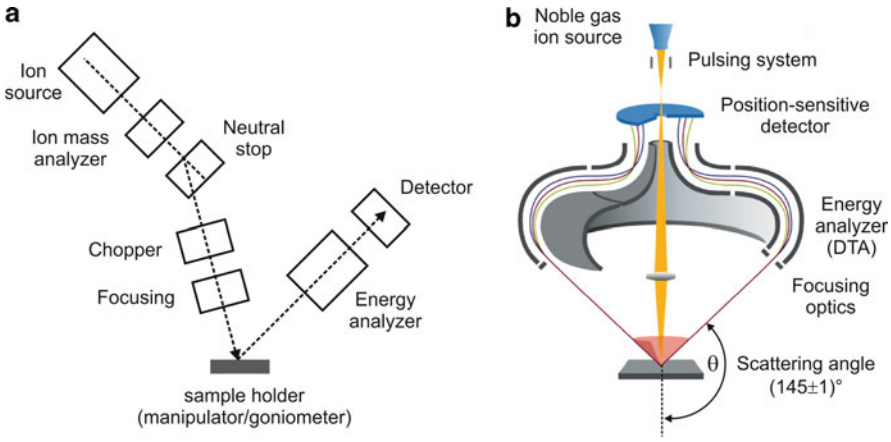

Fig. 6.22 (**a**) Schematic of the different components of a standard LEIS setup. The chopper in the primary ion beam is used in ToF measurements. (**b**) Modern LEIS setup with a double toroidal energy analyzer with parallel energy detection and ToF filtering (from [29, 32])

analysis often requires calibration against reference samples with known surface concentrations. The surface sensitivity of LEIS is largely due to the fact that only scattered ions are analyzed. In general, most of the incoming ions are neutralized upon impact. Therefore, knowledge about neutralization is a necessary requirement for the understanding of the sensitivity factor [29].

Different kinds of LEIS instruments have been developed. For a detailed review of experimental setups the reader is referred to [31]. Nevertheless, each setup has the same basic components. A schematic of a LEIS with its basic components is shown in Fig. 6.22a.

In contrast to RBS and MEIS which need high- and low-energy ion accelerators, in LEIS relatively small ion sources are required, resulting in compact analysis tools. The ion source provides ions of noble gases (He, Ne, Ar) in the energy range from 0.5 to 10 keV with a low energy spread of <0.5 % of primary energy. An isotopic clean ion beam can be selected by the ion mass filter (e.g., ExB Wien filter) with a mass resolution of $\Delta M/M \leq 0.1$. Possible neutrals will contribute to the LEIS signal but not to the current measurement, and therefore it must be filtered out by use of a neutral stop. The neutral stop deflects ions by a small angle onto an aperture located before lenses and collimators, which limit the divergence of the ion beam. The spot size of usually ≈1 mm at the target should be smaller than the acceptance area of the analyzer on the sample. The requirements for the sample manipulator used in composition analysis are less strict than in structure analysis, where at least the angle of incidence and the azimuthal angle must be selected with an accuracy of typically $\leq 1^\circ$ for angular orientation. Cylindrical mirror analyzers (CMAs) with external coaxial ion source or with a built-in ion source often used for LEIS are characterized both by a well-defined scattering angle ($\theta > 90^\circ$, $\Delta\theta \approx 1^\circ$–$2^\circ$) and a large azimuthal acceptance angle (ideally 360°). Large $\Delta\theta$

yields a high sensitivity, but at the expense of the energy (mass) resolution. This is different for the double toroidal analyzer (DTA) in Fig.6.22b, where a large energy window is imaged onto a position sensitive detector. Using energy imaging of the DTA parallel ion detection and, therefore, an increased sensitivity by a factor of ~10^3 have been achieved in comparison to CMA. The acceptance angle of the DTAs, which amounts 1°–4°, gives a high-mass resolution.

For the detection of backscattered ions most LEIS setups use electron multipliers, like channeltrons or a microchannelplate.

For the evaluation of data information recorded by the DTA, quantitative element identification and depth distribution of thin layers can be obtained, with a very high-atomic depth resolution of $\leq$1 nm. LEIS is able to detect all elements heavier than He. The detection limits obtained so far are in the range $\geq$1 % of one monolayer for the elements Li–O, 1–0.05 % of one monolayer for the elements F–Cl, and 500–10 ppm of one monolayer for all element heavier than K. Using sputter depth profiling in dual beam mode (Ar, Kr, Cs,. . . as sputter beam and He, Ne, . . . as MEIS analyzing beam), for example, ultra-shallow As-doping profiles in silicon can be measured. However, compared to SIMS the detection limit is significant higher.

Finally, two examples will be given showing the high-surface sensitivity and depth resolution of LEIS. Figure 6.23 shows LEIS energy spectra taken with a 3 keV He^+ primary ion beam from $ZnAl_2O_4$ samples as a characteristic example of mixed oxides (spinel type crystal). As can be seen in $ZnAl_2O_4$ (solid line) there is no Zn surface peak since Zn atoms are below the outer surface. The tail from the energy of Zn to lower energies agrees with the ZnO spectrum (dashed line), indicating that Zn atoms are present in the second or deeper layers [33].

The example in Fig. 6.24 is related to metal–polymer interfaces which play an important role in the development of organic light-emitting diodes (OLEDs). As shown in this figure, most of Ba diffuses into the polymer already during evaporation of Ba on PPV. From the comparison of the measured peak shape (red line) with the signal from a sub-monolayer of Ba (blue line), a depth of the diffused Ba layer of 7 nm was determined. One of the important problems in development of OLEDs is the minimization of metal diffusion (narrow depth distribution) into the polymer to achieve higher light emission efficiency.

6.3.4 Elastic Recoil Detection Analysis

Elastic recoil detection analysis (ERDA) is governed by simple binary elastic collisions between the projectiles and the target atoms like for the other ion scattering techniques (RBS, MEIS, LEIS) described before [3]. The schematic physical principle of ERDA is demonstrated in Fig. 6.25.

ERDA bases on the elastic collision between heavy ions (e.g., O, Cl, I, Ag, Au) with energies in the MeV range and target atoms of the investigated sample (M_i, Z_i). Contrary to Rutherford backscattering in ERDA knocked-on or recoiled

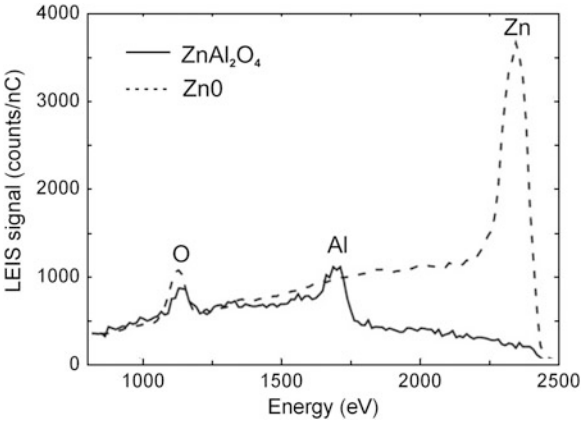

Fig. 6.23 LEIS spectra of 3 keV He^+ backscattered from $ZnAl_2O_4$ (*solid line*) and ZnO (*dashed line*) [33]

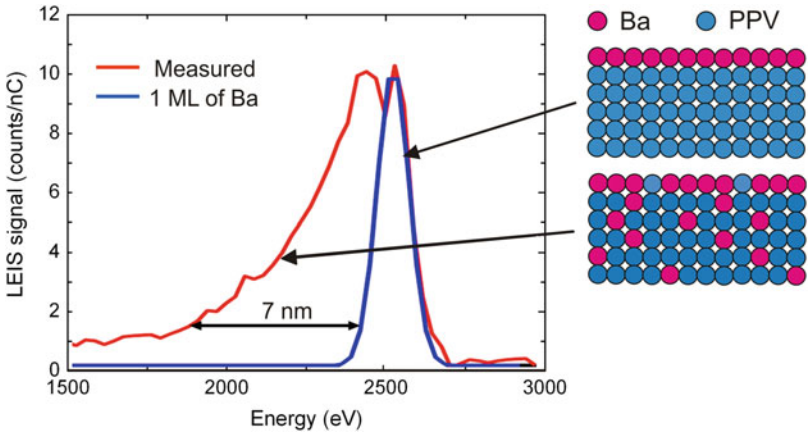

Fig. 6.24 Ba signal in the LEIS spectra of two different poly(phenylenevinylene) (PPV) samples showing Ba present in the outermost layer only (*blue line*) and Ba additionally present in the bulk (*red line*) (taken from [34])

target atoms are detected in the forward direction, as firstly reported by L'Ecuyer et al. [35].

As incident projectiles usually heavy ions are applied, because in accordance with (6.10)–(6.14) the cross-section σ_I and therefore the yield Y_i of the recoiled target atoms increase with increasing atomic number Z_1 of primary ions. The energy of target atoms recoiled under the angle ϕ can be calculated from

$$E_i = K_r \cdot E_0 = \frac{4 \cdot M_1 \cdot M_i}{(M_1 + M_i)^2} \cdot \cos^2\phi \cdot E_0 \tag{6.19}$$

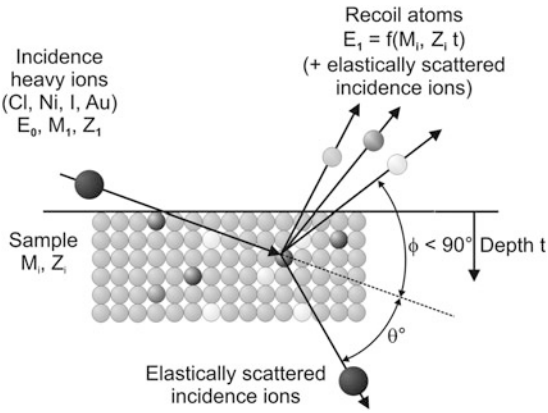

Fig. 6.25 Physical principle of elastic recoil detection analysis (ERDA) with θ the scattering angle and ϕ the recoil angle which is actually the detector angle

with K_r the kinematic factor (here energy fraction transferred from primary to recoiled particles). The kinematic factor for the simultaneously scattered primary ions K_s is given by (6.2). If the projectile mass, its energy, and the recoil angle remain fixed under a given experimental condition, atoms of different masses M_i in the sample come out with different recoil energies E_i as governed by (6.19). The kinematic factor K_r for ERDA is a function of the mass ratios M_i/M_1 and the recoil angle ϕ. According to (6.19) one can conclude that for ERDA the mass resolution is high at small recoil angles ϕ (maximum of dK_i/dM_i at $\phi = 0$). At small angles, also the values K_r are large because the energy transfer from the projectile to target atoms is high and the energy spread will be low. This allows to use relatively large detector solid angles Ω compensating at the same time the fact that the differential scattering cross-section $d\sigma/d\Omega$ has its maximum at $\phi = 90°$. In ERDA $d\sigma/d\Omega$ is given by

$$\left(\frac{d\sigma_i}{d\Omega}\right)_{\text{recoil}} = \left(\frac{Z_1 \cdot Z_i \cdot e^2}{2E_0}\right)^2 \cdot \left(1 + \frac{M_1}{M_i}\right) \cdot \frac{1}{\cos^3\phi}. \tag{6.20}$$

In contrast to RBS, (6.20) shows that for $M_1 >> M_i$ the term Z_i^2 is compensated by the $1/M_i^2$ dependence and the sensitivity is roughly constant for most element present in the sample. From the dependence $1/\cos^3\phi$ it follows that the recoil cross-section is high for angles close to $\phi = 90°$.

Generally, for ERDA the mass of an incident particle is greater than that of the target atoms. Therefore ERDA is a very convenient analyzing method for hydrogen detection using light ^{3}He or ^{4}He incident ions and, more general, for simultaneous element detection using heavy incident ions $M_1 >> M_i$. Usually, ERDA is carried out at very small incidence and recoil leaving angles α and β with respect to the sample surface (glancing geometry). The conversion of measured recoil energies into the depth scale t is given by the energy losses of the incoming projectile and the outcoming recoil or the corresponding energy loss factor S [see (6.5)]. The energy

difference ΔE between a recoil from the surface and a recoil from the depth t is given by

$$\Delta E = E_2 - E_3 = \left(\frac{K_2}{\sin \alpha} \cdot \left. \frac{\mathrm{d}E}{\mathrm{d}x} \right|_{\text{in}} + \frac{1}{\sin \beta} \cdot \left. \frac{\mathrm{d}E}{\mathrm{d}x} \right|_{\text{out}} \right) \cdot t = S \cdot t, \tag{6.21}$$

where $E_2 = K_2 \cdot E_0$ is the energy of the recoil originating from the surface. The energy loss factor S also relates the energy resolution δE to depth resolution $\delta t = \delta E/S$.

As in RBS, the simplest way to use ERDA is the measurement of the recoil yield as an energy spectrum $Y(E_i)$ which contains information about the concentration depth profiles $N_i(x)$ within the analyzed layer. However, ERDA is connected with two difficulties (1) The recoil mass M_i and the depth t of scattering event cannot unambiguously determined, which is referred as "mass-depth ambiguity" (different masses emerging from different depth can reach the detector with equal E_i). (2) A recoiled target atom M_i and a scattered projectile M_1 from different events cannot be unmistakably distinguished, which is referred as "recoil-projectile ambiguity" [36]. Therefore, different elastic recoil detection setups have been developed to solve these problems:

1. Use of absorber foils in front of a common silicon particle detector (SPD) to discriminate heavy-scattered projectiles (resolving recoil-projectile ambiguity) in conventional ERDA for depth profiling of light elements, e.g., hydrogen isotopes [37].
2. Use of time-of-flight (ToF) arrangement to identify recoil masses and scattered projectiles (resolving mass-depth ambiguity) in heavy ion ERDA (HI-ERDA) [38].
   According to $E_i = (1/2) \cdot M_i \cdot v_i^2$ with $v_i = L/t_i$, where L is the flight path and t_i is the flight time, the measurement of the flight time t_i allows not only the identification of recoil masses M_i but also an improvement of the depth resolution. The relative accuracy of the time measurement $\delta t_i/t_i$ can be made much better than the relative accuracy of an energy measurement $\delta E_i/E_i$ just by elongation of the flight path L [8].
3. Use of ΔE–E telescope configurations (combinations of a thin, transmissive ΔE–SPD and a thick stop SPD [39] or combination of a transmissive gas ionization chamber (GIC) with a stop SPD [40]).
4. Use of Bragg ionization chamber (BIC, see Chap. 3) as ion mass and energy dispersive detector to resolve both ion masses M_1, M_i (from the Bragg peak) and energies of scattered incidence E_1 and recoil ions E_i (from the total energy) [41].

At present, in most cases of heavy ion ERDA ToF–E, ΔE–E telescope configurations and BIC detectors are applied. The BIC detector is in principle also a (ΔE–E) ionization chamber which separates recoils only at sufficient high energies (10–100 MeV). In contrast to BIC, in ToF–ERDA works also at lower ion energies of $<$10 MeV [42, 43].

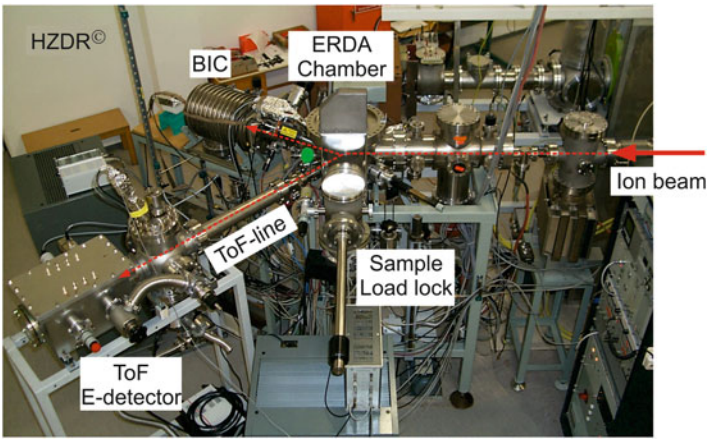

Fig. 6.26 ERDA setup at Helmholtz-Zentrum Dresden-Rossendorf (HZDR), installed at the 6 MV tandem accelerator (6 MV Tandetron from High Voltage)

Using ToF measurements it is possible to identify and separate different masses M_i from a two dimensional scatter plot of flight time t_i versus energy E_i. In the case of recoil measurements by ΔE_i–E_i telescopes and BIC detectors the masses are identified from a scatter plot of ΔE_i versus E_i. The advantage of all ERDA detection methods is the simultaneous recording of depth profile for all target elements lighter than the projectile. Therefore a special application field of ERDA is the characterization of elemental composition and depth profile investigation of light elements in heavy element substrates which cannot be detected by RBS [3]. During ERDA in some cases sample damaging by heavy incident ions with high energies can be a problem. Therefore, much lower ion energies are of growing interest because they are much less damaging. The prospects of low energy ERDA are reviewed by Döbeli et al. [43].

As a typical example, Fig. 6.26 shows the ERDA setup at the Helmholtz-Zentrum Dresden-Rossendorf (HZDR), which is installed at the 6 MV-tandem accelerator (6 MV-Tandetron from High Voltage). The ERDA setup combines a ToF–E detector and a BIC detector-analyzing channel for different analytical purposes.

As characteristic examples, Figs. 6.27 and 6.28 show two-dimensional scatter plots from ToF measurement using a ΔE_i–E_i telescope with a GIC detector and from recoil analysis using a BIC detector, respectively. Figure 6.27 demonstrates the high-mass resolution (~35) which can be seen from the isotope resolution for B, Si and K obtained from a quartz glass substrate. The measurements were performed using 12 MeV ^{127}I ions under an angle of ~35° of the ToF spectrometer relative to the direction of the incident ion beam.

The film areal density and composition were obtained from measurements with 35 MeV $^{35}Cl^{7+}$ ions impinging at an angle of 15° relative to the film surface. The backscattered ions and the recoils were detected with a BIC detector placed at a

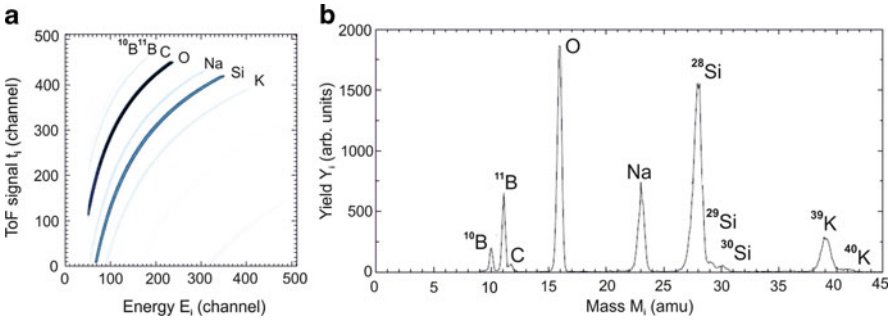

Fig. 6.27 (**a**) Two-dimensional scatter plot (ToF–*E* histogram) from a quartz glass surface obtained with 12 MeV ^{127}I ions using a ToF setup combined with a high-resolution gas ionization chamber (GIC) for energy measurement. (**b**) Corresponding recoil mass spectrum obtained from the ToF–*E* histogram (taken from [44])

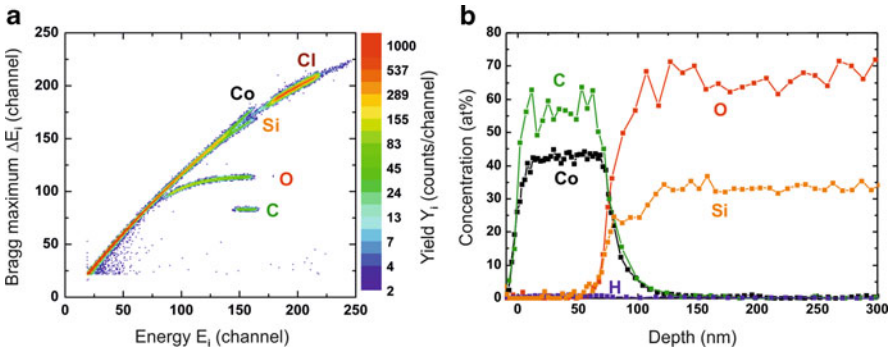

Fig. 6.28 (**a**) Two-dimensional scatter plot (Δ*E*–*E* histogram) from C–Co composite layer co-sputter deposited at room temperature on SiO_2 and subsequently annealed at 300 °C. The spectra were obtained with 35 MeV $^{35}Cl^{7+}$ ions using a Bragg ionization chamber (BIC) for Δ*E* and *E* energy measurements. (**b**) Corresponding depth profiles of all elements present in the sample obtained from the Δ*E*–*E* histogram [45] [Munnik F (2011) Private communication, unpublished]

scattering angle of 30°. Additionally, a standard Si detector was located at a scattering angle of 38° for hydrogen detection. In this case, an aluminum foil was employed in front of the detector to stop heavier recoils and backscattered $^{35}Cl^{7+}$ ions.

Figure 6.28 demonstrates that the ERDA data evaluation of the two-dimensional ΔE_i–E_i histogram results in depth profiles with sufficient high-depth resolution (~5 nm at the surface and ~10 nm at a depth of 75 nm) for all elements present in an C–Co composite layer deposited on SiO_2 [45] (Munnik F (2011) Private communication, unpublished).

For obtaining elemental depth profiles from measured ERDA spectra there exist suitable analysis procedures for which the reader is referred to [46, 47] and available analysis software, e.g., SIMNRA or NDF, referred to [48–50].

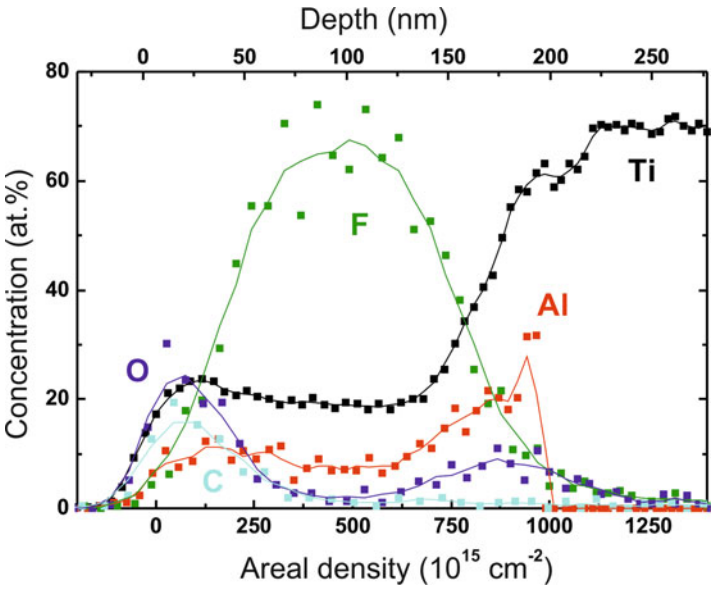

Fig. 6.29 ERDA depth profiles in a TiAl alloy after fluorine plasma immersion ion implantation

A typical example for ERDA application is the measurement of depth profiles in TiAl alloys after ion implantation [51, 52]. Gamma-phase TiAl is an attractive light weight material for advanced applications in aerospace and in power generation plants, e.g., as a material for turbocharger rotors. To overcome its poor oxidation resistance at temperatures above 700 °C, plasma immersion ion implantation of halogens (notably chlorine and fluorine) has been applied. As a result the modified TiAl alloys were protected against environmental oxidation and showed an improved structural and mechanical integrity (see also Sect. 4.8.1) [51].

In Fig. 6.29, the depth profiles of element concentrations in a TiAl alloy are shown, which were measured by ERDA after plasma immersion ion implantation (PIII) of fluorine. As a result it was concluded from the obtained Al and O profiles that fluorine ion implantation initiate TiAl surface passivation at higher temperatures by forming a surface Al_2O_3 layer. The concentrations of both O and C are minimized in a wide depth region around 100 nm, where the F concentration has its maximum concentration of more than 60 at.%. In Fig. 6.29, the depth resolution of ERDA measuring points is about 10 nm (compare Table 6.7).

Special advantages of ERDA compared to Rutherford backscattering are:

- Depth-dependent chemical composition of samples can be determined which is not possible with RBS
- In contrast to RBS, where $\sigma \sim Z_i^2$, in ERDA the cross section depends only slightly on the atomic number and therefore light elements in the target become detectable
- The scattering probabilities are larger with heavier incidence ions

Table 6.7 Main features of ERDA

Elements	H–U (mainly applied for hydrogen)
Standard conditions	~100 MeV heavy ion beam; (2 MeV ^{4}He beam for H detection); gas ionisation detector
Precision	Stoichiometry : 1 % relative
	Thickness: <5 %
Sensitivity	Bulk : % to 10^{-5}, depending on Z
Depth resolution	1–10 nm
Remarks	Simultaneous profiles of all Z; depth range ~1 μm; light elements detectable on heavy substrates

Deciding disadvantages of ERDA are:

- The signal of recoiled particles is covered by interfering effects of backscattered incidence and recoiled particles (recoil-projectile ambiguity) and by a background of forward scattered projectiles
- For the detection of recoiled heavy ions with smaller energies compared to backscattered ones more challenging on the base of time-of-flight arrangements with SPDs or GICs as well as BICs are required

In summary, the mean features of ERDA are compiled in Table 6.7.

For ion beam-assisted nanoscale depth profiling of ultrathin layers with thicknesses of only a few nm, e.g., films deposited by atomic layer deposition (ALD) on semiconductors, high-resolution RBS and ERDA in combination with magnet spectrometers are used [19, 53–55]. From the application point of view in many cases medium- and low-energy ion-scattering techniques (MEIS and LEIS) are increasingly preferred because no accelerators are necessary and these tools can be built in a much more compact manner.

6.4 Ion Beam-Induced Photon Emission

As a result of high-energy ion–solid state interactions, photons are emitted from the target surface which can be analyzed with respect to their energy. The physical principle is schematically demonstrated in Fig. 6.30.

The photon emission results from the interaction between high-energetic (1–3 MeV) light incident ions (usually protons) with the sample atoms. The incident ion can excite electrons of the target atoms or eject them from inner shells of the atoms. During the de-excitation process of the excited target atoms they emit photons with energies of ~(1–30) keV (X-rays). If the energy of the incident light ion is sufficiently high to overcome the Coulomb barrier it enters the target atomic nucleus and induces a short living compound nucleus or an excited nucleus. There exist decay channels through which the compound or excited nucleus returns to its ground state, accompanied by the emission of photons with energies of ~(0.5–10) MeV (γ rays).

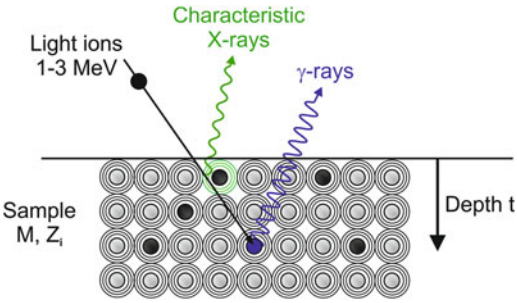

Fig. 6.30 Physical scheme of ion induced photon emission from atomic electron shells (X-ray) or atomic nuclei (γ-ray)

The energies of X- and γ-ray photons are characteristic for the target atoms emitting them. The composition of ion-bombarded target samples thus can be determined by measuring the yield and the energy of the emitted photons with a detector. Usually semiconductor Si(Li) or Ge semiconductor detectors are used, and the spectrum is viewed on a multichannel analyzer [3, 56]. In the case of emitted X-rays, the measuring technique is called particle-induced X-ray emission (PIXE), for emitted γ-rays it is called particle-induced gamma emission (PIGE). Since the heavier elements with $Z > 11$ cannot be detected by PIGE, this method is frequently combined with the PIXE technique.

The ion beam-induced photon emission has some typical advantageous parameters. It allows trace element analysis in bulk materials with sensitivity down to some ppm, a simultaneous multielement analysis of the whole element spectrum (Li–U) and a nondestructive analysis at air with short measuring times. The analysis depth is typically 1 μm. Limitations are the poor depth resolution and missing information about chemical bonding states. Typical investigated materials are metals, glass, ceramics, and biomedical objects.

Recently, some interesting developments were done concerning PIXE and PIGE element mapping with focused MeV ion beams [57, 58]. This was done with the aim of high-resolution biomedical imaging. With conventional PIXE and PIGE element mapping, a lateral resolution comparable with optical microscopy (200–500 nm) could be attained, whereas the best resolution with a direct scanning transmission ion microscopy was ~50 nm [58].

6.4.1 Particle-Induced X-Ray Emission

Particle-induced X-ray emission is an ion beam analysis method which utilizes characteristic X-rays induced via ion beam interactions with the electron cloud of target atoms. The energy of the emitted X-rays is determined by the spacing of the energy levels of the electrons in the atom. This gives rise to a number of characteristic line series (K, L, M, etc.) depending on the final shell. The energy of X-emitted characteristic X-rays depends on the atomic number Z of the target atom. Useful element ranges are for K-series F–Ag, for L-series Cu–U, and for M-series Pt–U.

Tables of X-ray energies can be found in reference books or for example on the NIST Web site [59].

Most of PIXE experiments are made with high-energetic protons producing high-energy X-rays with only small absorption along the path from their origin to the sample surface. As a result detections from deep inside of the target—typically in the mm range—are possible [60]. A typical experimental setup for PIXE analysis is shown Fig. 6.8 for samples mounted in a vacuum chamber and in Figs. 7.13 and 7.14 (see Sect. 7.2) for investigations under air using an external ion beam.

The principle of PIXE is comparable with that of energy dispersive X-ray analysis (EDX), where instead of light ions electrons are used as primary particles. However, due to the complete absence of electron induced bremsstrahlung the sensitivity of PIXE is enhanced by a factor of about 100 compared to EDX and is in the order of ppm for most elements [4].

As an example, Fig. 6.31 shows energy spectra of a bronze sample taken by PIXE with 3 MeV protons and by EDX with 20 keV electrons (after [4]). It is evident that by PIXE also minor elements can be identified because of its enhanced sensitivity, which cannot be seen at all in the EDX spectrum.

For PIXE analysis four main physical processes are of importance:

1. The incident charged particle encounters numerous inelastic collisions with the sample atoms
2. The energy of the ion along its trajectory decreases according to the specific energy loss $(\mathrm{d}E/\mathrm{d}x)_{\mathrm{el}}$ (electronic stopping power)
3. Some of the many atoms ionized along the particle path may emit characteristic X-rays with a probability given by the X-ray production cross-section σ
4. X-rays emerging from the point of emission are attenuated by the factor μ in the material

The target composition influences the particle energy loss $(\mathrm{d}E/\mathrm{d}x)_{\mathrm{el}}$, the X-rays attenuation μ, and the X-ray production probability σ. Generally, the X-ray yield Y_i for characteristic X-rays of the ith element in a sample with the thickness t toward the direction of the detector is

$$Y_i = N \cdot \beta_i \cdot \int_0^t N_i(x) \cdot \sigma_i(E(x)) \cdot \mathrm{e}^{-\frac{\mu x}{\cos\theta}} \mathrm{d}x, \tag{6.22}$$

where N is the total number of incident ions, $N_i(x)$ is the concentration depth profile, σ_i is the X-ray production cross section, μ is the X-ray attenuation factor, θ is the X-ray emission angle with respect to the sample surface normal, and β_i characterizing the energy loss by the X-rays from the incidence to the detector [9]. In the case that $N_i(x)$ is constant (homogeneous bulk samples) and that the X-ray detector has an efficiency ε, the relationship between the observed X-ray line intensity and the element concentration is given by

$$I_i = N \cdot N_i \cdot K_i \quad \text{with} \quad K_i = \varepsilon \cdot \int_0^t \sigma_i(E(x)) \cdot \mathrm{e}^{-\frac{\mu x}{\cos\theta}} \mathrm{d}x. \tag{6.23}$$

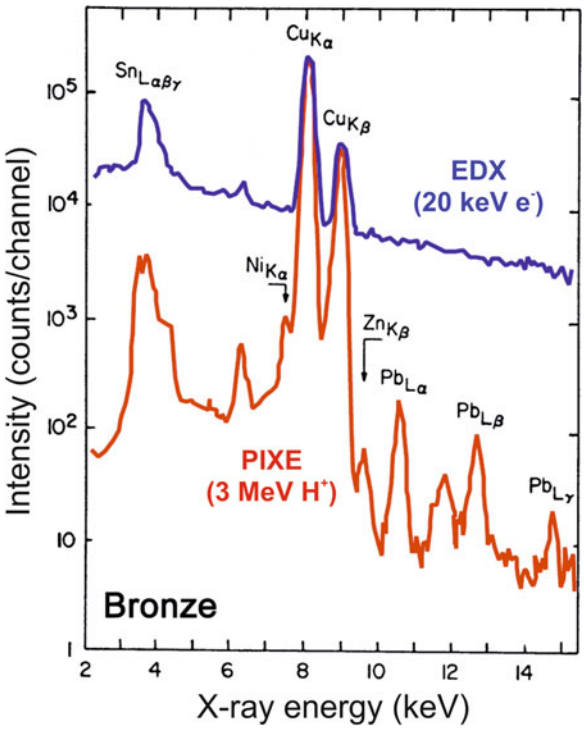

Fig. 6.31 Comparison of PIXE (*red line*) and EDX (*blue line*) spectra taken from a bronze sample. PIXE is generally about 100 times more element sensitive [4]

If both the experiment geometry and the sample matrix composition do not change, K_i is independent of the sample. For quantitative PIXE analysis one can either use the approach by calculating K_i from X-rays production cross-section σ_i, incident ion stopping power $S(E)$, and X-ray attenuation μ, or compare the unknown sample with standards by measuring K_i experimentally, which is most often the case. The determination of target element concentrations from the measured yield Y_i can be realized with especially developed software packages (see for example [61]).

A typical PIXE spectrum obtained with 2.5 MeV protons is shown in Fig. 6.32 [62]. PIXE measurements were done on a thin Mylar foil which is often used as backing foil for the MicroMatter thin standards (http://www.micromatter.com) for calibration purposes in XRF and PIXE. The Mylar foil contains lots of elements that can affect the correctness of the concentration determination and the system calibration for particular energies. The continuous background with a bump present in the low energy part of the PIXE spectrum is mainly caused by secondary electron bremsstrahlung (SEB). The SEB is caused by electrons ejected from the target atoms by the ionizing proton beam and decelerating in the Coulomb field of other atoms.

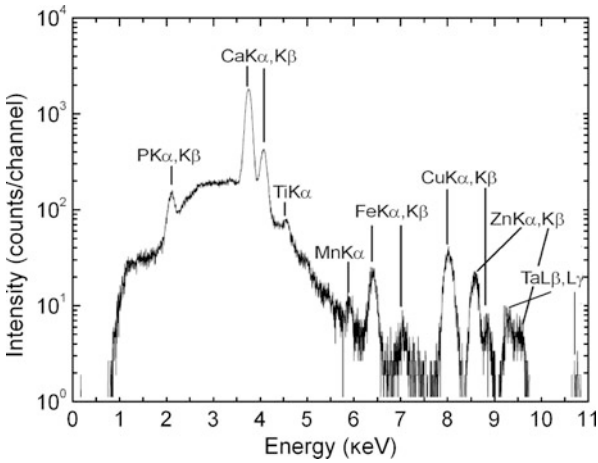

Fig. 6.32 PIXE spectrum of a 6.3 μm thick Mylar foil irradiated with 2.5 MeV protons. The spectrum was recorded with a high-resolution silicon drift detector (SDD) [62]

Though most of ions used for PIXE are 2–3 MeV protons, the use of heavy ions (e.g., $^{3}He^{+}$, $^{12}C^{+}$, $^{14}N^{+}$, $^{16}O^{+}$) has several particularities. A decisive fact is the higher cross-section σ_{ion} for an incident heavy ion of atomic number Z_{ion}, mass number M_{ion} and energy E_{ion}, compared with that for a proton σ_{proton}:

$$\sigma_{ion}(E_{ion}) \approx Z_{ion}^{2} \cdot \sigma_{proton}\left(\frac{E_{ion}}{M_{ion}}\right) \tag{6.24}$$

The cross-section σ_{ion} depends on the velocity ($E_{ion} \propto v_{ion}^{2}$) and on the square of the ion atomic number ($\sigma_{ion} \propto Z_{ion}^{2}$). For example, incident $^{16}O^{+}$ ions with an energy of 50 MeV have about the same velocity as 3 MeV protons, but its cross section is larger by nearly two orders of magnitude as compared to the protons. That means that PIXE measurement with $^{16}O^{+}$ at 50 MeV requires less data acquisition time by a factor 64 compared to analysis with protons of 3 MeV. Another advantage of high-energy heavy ions as compared to protons is their lower background (bremsstrahlung) in the spectra, especially in the case of light target atoms. This circumstance is particularly advantageous for biological and biomedical samples, which are an object of increasing interest [3].

As an example for such a biomedical application, Fig. 6.33 shows a PIXE spectrum of tumor tissue section of a hamster [63]. PIXE analysis of this tissue section was carried out with a Tandem accelerator based microbeam of heavy ^{16}O ions at an energy of 50 MeV. This kind of PIXE technique has revealed itself as a powerful multielement analytical tool. The ion beam was focused to an area of some μm^{2}, and this so-called Micro-PIXE was successfully utilized for the study of multielement distribution on μm-scale in the tissue section (multielement 2D mapping). As a result of such investigations, for example, the drug copper tetra-phenyl-carboranyl porphyrin (CuTCPH), which was given in discrete doses to a test animal, was found to be inhomogeneously distributed within the tumor.

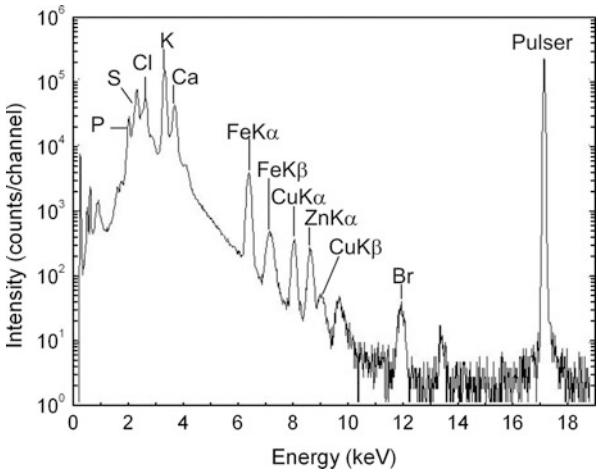

Fig. 6.33 PIXE spectrum of tumor tissue section of a hamster [63]

In general, heavy ion PIXE leads to more complex element spectra because the electron excitation is more complex and multiple ionization can take place (e.g., X-ray lines are broadened and shifted to higher energies). Moreover, heavy ion PIXE is not yet well established because only a few investigations of cross sections for the K- and L-X-ray production of selected target element-projectile combinations are available. Damaging of the sample by heavy ions can also become a problem.

A wide field for PIXE applications is the study of art objects (see also Chap. 7). As an example, Fig. 6.34 shows the so-called Sky disc of Nebra (left) and the corresponding PIXE spectrum (right) (Neelmeijer C (2008) Sky Disc of Nebra. Private communication, unpublished). The sky disc was found in Nebra (Saxony-Anhalt, Germany) in 1997 and is dated to the bronze age. For each detail on the disc the gold composition was measured in order to clarify whether it belongs to the original design or possibly to a later additive. Furthermore, the Ag/Au and Cu/Au concentration ratios have been used for characterization of the particular gold applications. As a result, the genuineness of the "Sky disc of Nebra" could be definitely confirmed.

Particle-induced X-ray emission (PIXE) is particularly appropriate for analysis of metallurgical (alloys), ceramic, geological (minerals), environmental (pollution analysis) and many other materials, being existent as solids, powders, particularly collected in filter substrates or liquids. PIXE has been increasingly used in biology, medicine, and archeology.

In summary the mean features of PIXE are given in Table 6.8.

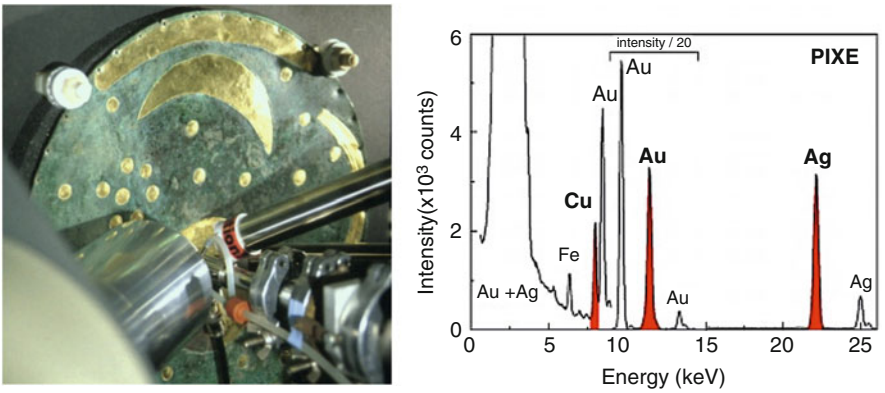

Fig. 6.34 "Sky disc of Nebra". Position for Au analysis with an external proton beam (*left*) and the corresponding PIXE spectrum (*right*) [Neelmeijer C (2008) Sky Disc of Nebra. Private communication, unpublished]

Table 6.8 Main features of PIXE

Elements	Al - U
Standard conditions	3 MeV proton beam; Si(Li) or Ge detector 10 min per sample
Precision	Stoichiometry: 5 % relative; trace element analysis; quantification by standards
Sensitivity	1–100 ppm, depending on Z and matrix
Depth resolution	Poor depth information
Remarks	Probed depth from some 10 μm to some 10 mm; often used with raster imaging (p microprobe)

6.4.2 Particle-Induced γ-Ray Emission

As has been shown in Sect. 6.4.1, light elements from hydrogen to fluorine cannot be analyzed by PIXE. Depth profiling of light elements in samples consisting heavy elements with RBS is limited because RBS is dominated by the Z-dependence of the heavy element scattering cross-section σ. However, low-Z elements can be detected using nuclear reactions with high-energy ions (under resonance conditions) emitting γ-rays or secondary particles.

The particle-induced γ-ray emission (PIGE) bases on a nuclear reaction between high-energetic (typically some MeV), light incident ions ($^1H^+$, $^2H^+$, $^3He^+$, $^4He^+$) and the sample atoms. During the de-excitation process of the excited target nuclei, they emit high-energetic photons (γ-rays), schematically illustrated in Fig. 6.30.

The principal analytical possibilities of PIGE are illustrated in Fig. 6.35. High-energetic incident light ions excite the atoms nuclei of the bombarded sample with an element concentration depth profile $N(x)$. The energies E_γ of the γ-rays which are emitted during the de-excitation process are characteristic for the emitting atoms (Z_i, M_i). Thus, the element composition of the sample and their depth profiles can be

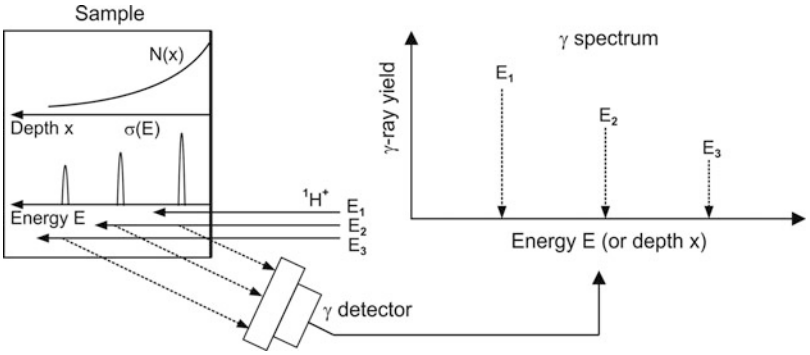

Fig. 6.35 Scheme of PIGE analysis

determined by measuring the yield of γ-photons with conventional Ge detectors or scintillators (NaI(Tl), BGO) combined with photomultipliers (see Fig. 6.8). Contrary to PIXE, PIGE does not show continuous sensitivity. Both the energy of the incident ion and the probability of a nuclear reaction are functions of depth determining the γ-reaction cross-section $\sigma_\gamma(E)$.

PIGE is often used in conjunction with PIXE for analyzing light elements such as B, Na, Mg, Al, and Si in aerosols and geological samples [64]. PIGE is also used for the light element investigation of art objects as paintings or historical glasses [65].

As an example in Fig. 6.36, the PIGE identification of lapis lazuli pigments in a medieval painting is illustrated. This picture, a Madonna painted by Leonardo da Vinci in 1501, was investigated both with PIXE (heavy elements) and additionally with PIGE (light elements) in order to control its genuineness [66]. The upper PIGE spectrum is taken from original lapis lazuli mineral. It shows a clear Na peak at 441 keV. The spectrum below shows part of virgin's gown. Here the Na peak has disappeared. The PIXE spectrum of heavy elements of the gown was also modified. These results identify this investigated painting detail to be a restored part.

Another common application of PIGE is the determination of F in biomedical samples through the reaction ^{19}F (p,p′γ) ^{19}F. The emitted γ-rays have then an energy $E_\gamma = 110$ keV with a detection limit of 3×10^{-9} g/cm^2 [3].

6.5 Nuclear Reaction Analysis

As the previous IBA techniques, nuclear reaction analysis (NRA) is a nondestructive, isotopically sensitive method with high-mass resolution. NRA is mostly used for light elements analysis (concentration and depth distribution of H, D, Li, B, C, N, O, F, Na, and P). Ions with energies of a few MeV excite the target nuclei and form compound nuclei. At subsequent nuclei decays from the detection of the decay products (usually γ-rays but also particles) absolute impurity concentrations can be determined. Moreover, if crystalline samples are irradiated in channeling direction

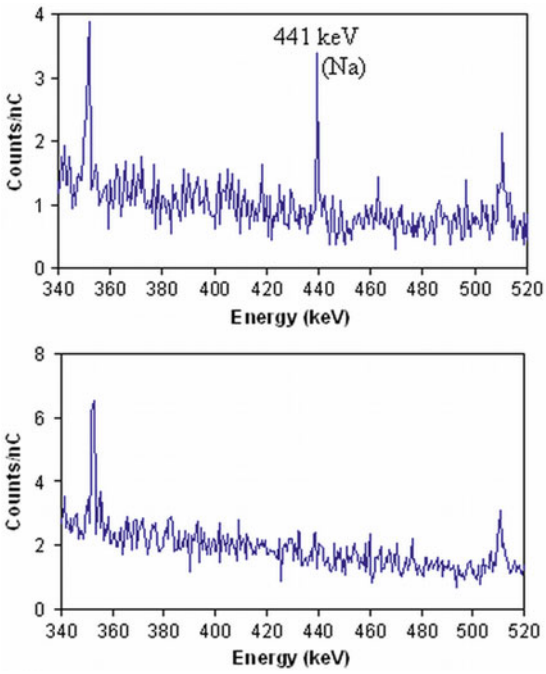

Fig. 6.36 PIGE identification of lapis lazuli pigments in a Madonna painting of Leonardo da Vinci [66]. *Top*: original lapis lazuli mineral; *below*: part of virgin's gown

NRA can be used to determine the lattice location of impurities and the defect distribution depth profile in single crystals. The physical principle of NRA is illustrated in Fig. 6.37 which shows two typical nuclear reactions. Nuclear reaction frequently occurs with light (Fig. 6.37a) and heavier (Fig. 6.37b) incident ions at energies of some MeV, impinging on a sample with light to medium heavy atoms (M_i, Z_i) [67]. As depicted in Fig. 6.37 two groups of experimental requirements for NRA exist—first, the detection of emitted light particles (protons and α-particles) by conventional SPDs to measure their number and energy and, second, the detection of emitted γ-rays by Ge-detectors or scintillator/photomultiplier detectors to measure the intensity of photons (see Sect. 6.4.2: PIGE). In the case of particle detection, the depth profiles are obtained from the energy spectra because particles emitted from deeper layers have a lower energy than reaction products emitted from the surface. The concentration is determined from the number (intensity) of reaction particles with a certain energy. At γ-detection only the intensity of photons is measured by detectors arranged usually outside the ion-scattering chamber, which relatively easily allows to enhance the detector efficiency by increasing the solid up to almost 4π [10]. From the counted number of photons, only the concentration of the specific isotope can be deduced. For depth profiling the γ-yield must be measured as a function of the ion energy E_0 for an equal number of incident projectiles (determination of the excitation curve $N_\gamma(E_0)$).

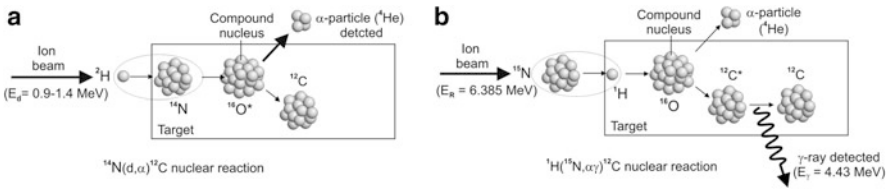

Fig. 6.37 Physical principle of nuclear reaction analysis (NRA) for two typical reactions: (**a**) ^{14}N(d,α)^{12}C nuclear reaction with detection of the emitted α-particle for depth profiling of nitrogen, and (**b**) ^{1}H(^{15}N,αγ)^{12}C nuclear reaction with the detection of the emitted γ-ray for depth profiling of hydrogen

The measured energy spectra $E_p(x)$ of emitted particles and the excitation curve $N_\gamma(E_0)$ depend on the concentration depth profile $N(x)$ of the analyzed element and on the nuclear cross-section $\sigma(E(x))$ where $E(x)$ is the energy of the projectile at the depth x. The evaluation of the concentration profiles $N(x)$ from $E_p(x)$ and $N_\gamma(E_0)$ is simplified for two special behavior types of $\sigma(E(x))$:

1. Nonresonant nuclear reaction: $\sigma(E)$ is constant in an energy interval ΔE and, therefore, the recorded energy spectrum of the reaction particles directly reflects the concentration depth profile in a depth interval Δt corresponding to ΔE (e.g., in the case of the reaction ^{14}N(^{2}H,α)^{12}C in Fig. 6.37a)
2. Resonant nuclear reaction: $\sigma(E)$ has a strong resonance at in a small energy interval of ~(0.1–1.0) keV around the resonance energy E_R and is small for all other energies $E < E_R < E$, which allows to determine the concentration depth profile by measuring the excitation curve $N_\gamma(E)$ (e.g., in the case of the reaction ^{1}H(^{15}N,αγ)^{12}C in Fig. 6.37b).

At nonresonant NRA the depth resolution depends on the stopping powers of incident $(d\sigma/dx)_{in}$ and emerging ions $(d\sigma/dx)_{out}$ and the energy resolution of the detector. The depth scale can be obtained from the energy measurement of the emitted particle. The relationship between energy differences $\Delta E(x) = E(x = 0) - E(x)$ and depth x can be found, similarly to RBS and ERDA.

In the case of resonant NRA incident ions initially having an energy E_0 are slowed down until the resonance energy E_R is reached at depth x, where the nuclear reaction will occur at a rate proportional to the impurity concentration. The depth x and the incident beam energy E_0 are then related by the equation

$$x = (E_0 - E_R) \cdot \frac{\cos\theta}{\left(\frac{dE}{dx}\right)_{in}}, \tag{6.25}$$

where θ is the angle between the incident beam and the surface normal, and $(dE/dx)_{in}$ the stopping power for the incident projectile. The yield curve $Y_\gamma(x)$ can be converted into the concentration depth profile by simply changing scales of yield and energy to corresponding scales of concentration $N(x)$ and depth x. The depth resolution δx for resonant NRA is determined by the energy width of the resonance

reaction $\Gamma/2$, the fluctuation of the projectile energy δE and other statistical fluctuations (Doppler broadening, straggling) and is given by

$$\delta x = \frac{\delta E + \Gamma/2}{\left(\mathrm{d}E/\mathrm{d}x\right)_{\mathrm{in}}}. \tag{6.26}$$

Typical achievable depth resolutions are ~(1–10) nm in the depth region of (10–2,000) nm, respectively. Therefore, NRA can be used as a high-sensitive depth profiling ion beam analysis technique to measure the concentration and the depth profile of a certain element in a sample with known qualitative composition down to some ppm [68]. Because nuclear reactions are element (isotope) specific for specific incident ions NRA is not able to probe the sample composition of an unknown sample, like in PIXE or RBS.

The nuclear reaction can be represented by the following equation:

$$A(M_0) + X(M_i) \rightarrow (A + X)^* \rightarrow C(M_{\mathrm{rec}}) + B(M_{\mathrm{emit}}) + n \cdot \gamma \tag{6.27}$$

with A the incident particle nucleus of mass M_0, X the target nucleus of mass M_i, $(A + X)$ the transient compound nucleus, dissociating into C the residual (recoil) nucleus of mass M_{rec} and B the emitted particle with mass M_{emit}, and $n{\cdot}\gamma$ the cascade in which $n{\cdot}\gamma$-photons are emitted during the decay process of the excited compound nucleus. Nuclear reactions described by (6.27) are usually expressed in an abbreviated form by $X(A, B\gamma)C$. For different NRA techniques the reader is referred to [8, 69, 70] and for nuclear cross sections to [71]. A summary of common and important ^{1}H, ^{2}H, ^{3}He, and ^{4}He ion induced nuclear reactions used in NRA can be found in [3].

Ion-induced nuclear reactions are suitable for analysis of target elements up to atomic mass 30 (phosphorus). For heavier target nuclei the nuclear reactions diminish due to largely decreased reaction cross sections. The calculation of absolute concentration values is possible with the help of standards and of specific software packages, for example, SIMNRA [72] or SENRAS [73].

As a typical example, Fig. 6.38 shows the NRA setup at the Helmholtz-Zentrum Dresden-Rossendorf (HZDR), which is installed at the 6-MV tandem accelerator (6-MV Tandetron from High Voltage).

For NRA with the setup shown in Fig. 6.38, $^1H^+$, $^2H^+$, $^4He^+$, and $^{15}N^+$ ion beams with energies in the range of 0.8–10 MeV are mostly used. Usual ion beam currents are in the order of some tens of nA. The γ-rays emitted from the sample are detected with a large area, high-efficiency scintillator ($4'' \times 4''$ BGO) and a photomultiplier.

Some examples for typical NRA investigations with nonresonant and resonant reactions will be shortly described in the following. Figure 6.39 shows measuring results of the deuteron induced nonresonant nuclear reaction $^{14}N(d,\alpha)^{12}C$ which is often applied to the determination of nitrogen concentration depth profiles of nitride layers (e.g., CVD $Si_3N_4/Si_xN_yO_z$ layers, or steel surface layers nitrided by ion implantation).

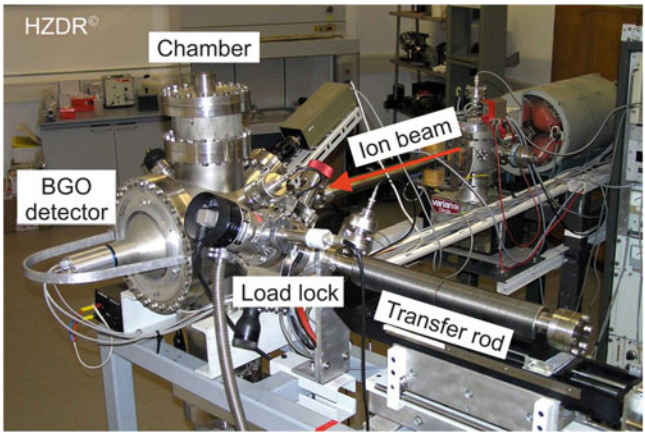

Fig. 6.38 NRA setup at Helmholtz-Zentrum Dresden-Rossendorf (HZDR), installed at the 6-MV tandem accelerator (6-MV Tandetron from High Voltage)

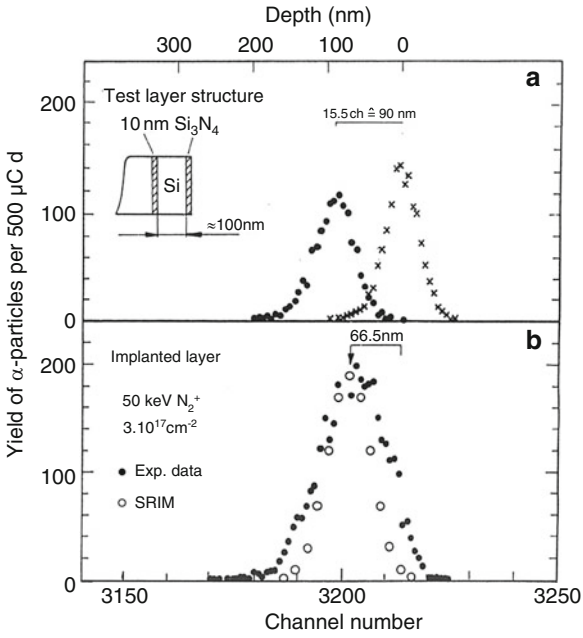

Fig. 6.39 ^{14}N depth profiles of a $Si_3N_4/Si/Si_3N_4$ layer stack on silicon (**a**) and ion implantation profiles in 210Cr46 tool steel (**b**) examined by the $^{14}N(d,\alpha)^{12}C$ nuclear reaction at a deuteron energy of $E_d = 1.4$ MeV [74]

The measured implanted nitrogen profiles were found to agree well with N profiles simulated by SRIM (see Fig. 6.39b). For the $^{14}N(d,\alpha)^{12}C$ reaction the cross-section $\sigma(E)$ is constant in an energy interval $E_0 = (1.0–1.4)$ MeV and, therefore, the recorded α-particle energy spectrum directly reflects the N concentration depth profile in a depth interval (0–400) nm. For NRA with particle

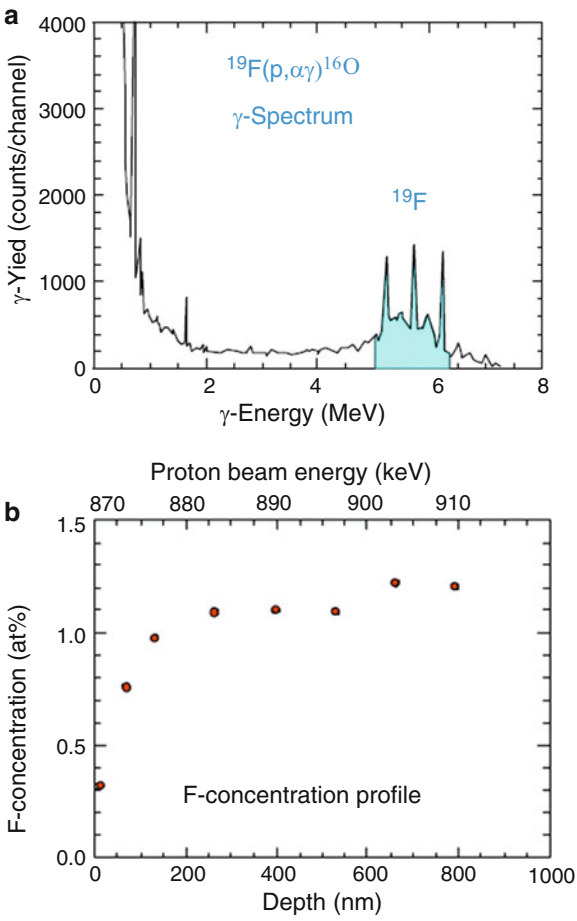

Fig. 6.40 NRA analysis of a plastic foil using the ^{19}F (p,α γ)^{16}O reaction [4]. (**a**) γ energy spectrum; (**b**) F concentration depth profile

detection deuteron projectiles are more commonly used than proton projectiles [75] if thin surface layers (contamination layers) must be investigated. For example, other useful nonresonant reactions for the determination of C and N are the ^{12}C (d,p)^{13}C and ^{14}N (d,p)^{15}N reactions.

As an example of a proton-induced resonant nuclear reaction, in Fig. 6.40 the results of NRA investigations of a plastic foil are shown [4]. The upper Fig. 6.40a shows the γ energy spectrum of the ^{19}F(p,αγ)^{16}O reaction with a resonance at a proton energy of $E_0 = 872$ keV. By step-wise increasing of the incident proton energy the depth location of the reaction resonance was successively shifted into the depth of the sample and a depth profile of the fluorine concentration was obtained with a depth resolution in the 10 nm range (Fig. 6.40b).

Desired or undesired, hydrogen exists in many materials and has a decisive effect on the materials properties. For example, the penetration and inclusion of

hydrogen in metals leads to material embrittlement and stability reduction. In a-C:H or a-Si:H, the change of the hydrogen fraction results in altering of electrical, optical, thermal, and tribological properties which at present is an active field of research—with NRA as a powerful tool for such studies.

Besides elastic recoil detection analysis (ERDA), resonant reactions are used for hydrogen depth profiling. The most often used standard resonant reaction for this purpose is the reaction $^{1}H(^{15}N,\alpha\gamma)^{12}C$ with a large cross section (see Fig. 6.37b), allowing nondestructive quantitative hydrogen analysis in a solid sample with high sensitivity and depth resolution [76] :

$$^{15}N + {}^{1}H \rightarrow {}^{12}C + {}^{4}He + \gamma(4.43\,\mathrm{MeV}). \tag{6.28}$$

Because of the narrow resonance width $\Gamma/2$ of only about 5 keV at a ^{15}N ion energy of 6.385 MeV the depth where the reaction takes place can be varied by changing the incidence energy. Thus, hydrogen concentration depth profiles can be precisely obtained. For incident ^{15}N ion energies of (6.3–12) MeV the analysis depth reaches from the near-surface region up to some μm, with a detection limit in the 10 ppm range and a depth resolution of about 10 nm (for Si in the near-surface region the depth resolution is ~8 nm).

For grazing incidence of the ^{15}N ion beam a hydrogen depth resolution of about 1 nm can be obtained, as demonstrated in Fig. 6.41. Here the hydrogen depth profiles of H_2 and N_2 annealed thin layers of Al_2O_3 and of ZrO_2 with thicknesses of ~10 nm are shown (Grambole D (2010) Private communication, unpublished). The layers were deposited by Atomic Layer Deposition (ALD) on Si, and as can be seen from Fig. 6.41, hydrogen is mostly accumulated in the region of the interface between the layer and the substrate. After an additional N_2 annealing (open measuring points), the hydrogen depth profile in ZrO_2 layers remains unchanged, whereas the hydrogen distribution in the Al_2O_3 layer shifts slightly by ~1 nm to larger depths. At these measuring conditions resonant NRA for hydrogen depth profiling proves to be a very sensitive and accurate method of ion beam analysis.

In summary, the mean features of nuclear reaction analysis are given in Table 6.9.

6.6 Ion Beam-Induced Electron and Light Emission

As shown schematically in Fig. 6.5 particle and photon radiations with energies in the keV and MeV region are emitted from a target surface during high-energy ion–solid interactions. To the particle emission also belong electrons, both free and AUGER electrons, which are illustrated in Fig. 6.42.

Because of the band structure of a bombarded target atom a variety of interactions will take place. The impinging ion may ionize the inner electron shells, if its energy is high enough. The following emission processes are possible:

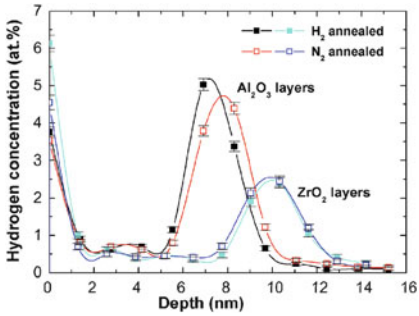

Fig. 6.41 H depth profiling of Al_2O_3 and ZrO_2 layer by NRA using the resonant reaction ^1H (^{15}N,αγ)^{12}C [Grambole D (2010) Private communication, unpublished)

Table 6.9 Main features of NRA

Elements	H–P
Standard conditions	~1 MeV proton beam (^{15}N, ^{19}F for H detection) Ge detector; ~5 h per profile
Precision	Composition: 5 % relative absolute concentrations only by standards
Sensitivity	10 ppm to some %, depending on element
Depth resolution	1–20 nm probed depth: ~μm

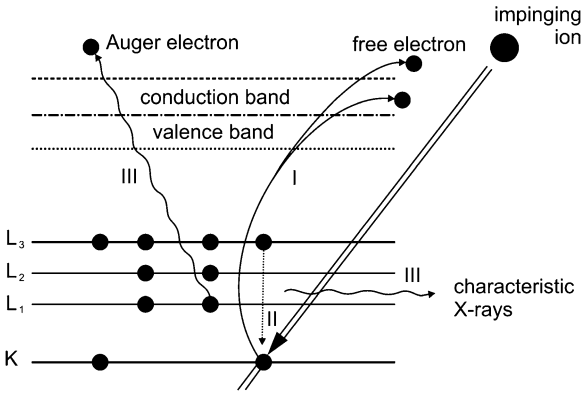

Fig. 6.42 Emission of electrons and photons by ion radiation of a target atom

1. Electron emission: As visible in Fig. 6.42, an ion-bombarded target atom also emits electrons, immediately as free electrons and also in a twice ionized state as AUGER electrons. A further electron emission mechanism for low energy impinging ions of some tens or hundreds of eV energy is caused by their neutralization when approaching the target surface [77]. Yet, because of their low yield and their poor quantification these emitted electrons do not present a competition to analytical techniques with keV electron or X-ray induced electron emission, as for AES or XPS, respectively. Low-energy electrons can be

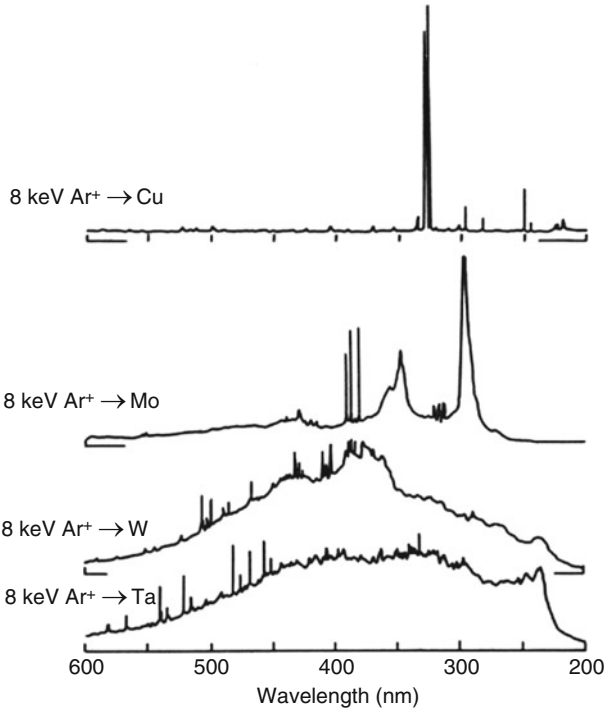

Fig. 6.43 Optical spectra induced by irradiation of Cu, Mo, W, and Ta surfaces with 8-keV Ar^+ ions

only used for imaging in ion induced Scanning Electron Microscopy (see Sect. 6.8).

2. Photon emission: The wavelength depends on the energy of the impinging ion. For H^+ or He^+ ions with energies in the MEV range the inner electron shells are excited, whereby characteristic X-rays from the near-surface region are emitted. This X-ray emission is used in PIXE analysis as described in Sect. 6.4.1. For ion bombardment in the keV range, the emitted photons have energies only of a few eV, or with other words, wavelengths from infrared to UV region of the optical light spectrum. One reason for this light emission is a broad band excitation of higher electron levels, but also a recombination of electron–hole pairs exists [78]. As an example Fig. 6.43 shows optical spectra that were induced by the impact of 8 keV Ar^+ ions on Cu, Mo, W and Ta surfaces, respectively.

6.7 Secondary Ion Emission

Besides all ion-induced particle and photon radiations described in Sects. 6.1–6.6, secondary ions are also emitted from an ion-bombarded target surface. These secondary ions can be also used for analytical aims. For this purpose, the emitted

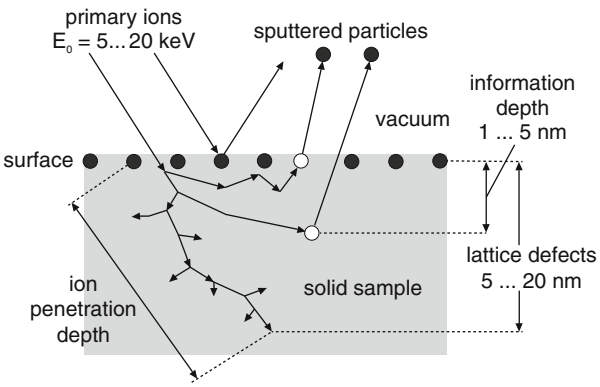

Fig. 6.44 SIMS: interactions of primary ions with atoms of the bombarded surface

ions are analyzed in a mass-selective spectrometer and consequently this method is named secondary ion mass spectrometry (SIMS) [79–81]. One may distinguish between static SIMS and dynamic SIMS. The former one is a nondestructive surface analysis technique with low incident ion current densities, whereas dynamic SIMS is a sputter technique where the sputtered part of the target is immediately used for depth profile analysis of impurities. A similar analytic technique is the Sputtered Neutral particle Mass Spectrometry (SNMS), which analyzes post-ionized neutral particles emitted from the ion-bombarded surface.

Figure 6.44 shows schematically the interaction of relatively low energy primary ions (E_0 = 5–20 keV) with atoms of the bombarded sample surface. Secondary ions (SI) are ejected from the surface by primary collisions of incident ions with target atoms, and also by secondary collision processes of recoiled atoms with target atoms. The primary ion beam produces lattice defects over a depth up to some 10 nm. The SIMS information depth is lower compared to most of IBA techniques and amounts to only few nm. The sputtered material consists not only of SI but also of further neutral and charged particles of the sample material and self-sputtered primary ions. The emitted secondary ions are extracted via an electrical potential and analyzed using a mass spectrometer. Though a semi-quantitative SIMS analysis is possible only by standardization, the detection limit of SIMS is much better than that of comparable depth profile methods. It lies in the ppm range depending on element and materials composition, whereas typical detection limits for AES and XPS are about 10^{-1} at.%.

Basic mechanisms of secondary ion emission are:

- The sputtering process, which theoretically is well understood
- The ionization process, which is described by different models, valid only under limited conditions

There exist different possibilities for ionization:

- Splitting of a surface composition by collision ionization
- Ionization of neutral emission products just in front (<5 nm) of the surface, as by
- Electron emission/electron catching

- Charge exchange
- Auto-ionization from an excited state

The secondary ion (SI) current can be expressed by the following equation:

$$I_{SI} = I_P \cdot S \cdot \beta^{+/-} \cdot c \cdot f \tag{6.29}$$

with I_{SI} the SI current, I_P the primary ion (PI) current, $S{\cdot}\beta^{+/-}$ the SI yield, S the sputter coefficient, $\beta^{+/-}$ the ionization state, c the ion concentration of a certain element, and f the transmission factor. The SI yield $S{\cdot}\beta^{+/-}$—generally $S{\cdot}\beta^{+}$—is influenced by both the target atoms and by the primary ions [82].

1. **Influence of target atoms:** For positively charged SI a high-SI yield is obtained for target atoms with low ionization energy. Especially elements of the main groups Ia, IIa, IIIa, and IVa in the periodic table of elements are characterized by a low ionization energy. The SI yield $S{\cdot}\beta^{+}$ approximately follows the relation

$$S \cdot \ \beta^{+} \sim \frac{1}{I - \Phi} \tag{6.30}$$

with I the ionization energy and Φ the work function.
For negatively charged SI the yield $S{\cdot}\beta^{-}$ depends on the electron affinity of target atoms, which can be expressed by the work function Φ in (6.30). Elements with high-electron affinity are, e.g., Ir, Pt, and Au having a high-yield $S{\cdot}\beta^{-}$.

2. **Influence of primary ions:** The SI yield $\beta^{+}{\cdot}S$ can be written as

$$\beta^{+} \cdot S = \frac{\text{SI}}{\text{sputter sum}} \times \frac{\text{sputter sum}}{\text{PI}} = \frac{\text{SI}}{\text{PI}} \tag{6.31}$$

that means the number of ejected secondary ions per impinging primary ion.
The diagram in Fig. 6.45 gives the dependence of both values, the sputter coefficient S, and the SI yield $\beta^{+}{\cdot}S$ of a Cu target, on the atomic number Z_1 of the bombarding ions.
The following results can be deduced from Fig. 6.45:

– The sputter coefficient S increases with growing Z_1
– The SI yield $\beta^{+}{\cdot}S$ remains nearly constant, that means the ionization state β^{+} decreases very strongly with growing Z_1
– β^{+} varies in a wide range from 10^{-5} to 1

Generally, the SI yield is a very sensitive value, depending also on the chemical composition of the sample matrix, its atom ionization energy and the surface state (cleanliness, native oxides, contaminants, etc.). Therefore, the SI yield is very sensitive to the presence of oxygen at the surface, as visible from Fig. 6.46. It presenting the SI yield $\beta^{+}{\cdot}S$ of different targets with atomic numbers Z_2 at 3 keV Ar^{+} ion bombardment. The open circles correspond to a clean target surface (10^{-8} Pa base pressure of the target chamber), and the full circles to values after oxygen adsorption. As can be seen an oxygen adsorption results in an enhancement

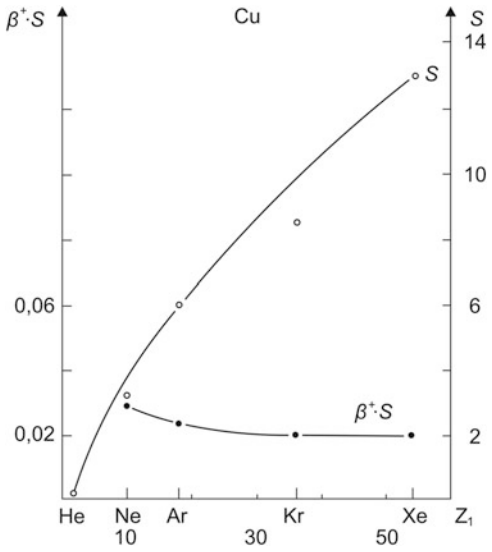

Fig. 6.45 Dependence of the sputter coefficient S and the secondary ions yield $\beta^+ \cdot S$ of a Cu target on the atomic number Z_1 of bombarding ions

of the SI yield by a factor 10^2–10^3. The usually high demand for surface cleanliness complicates a quantitative analysis of element concentrations by SIMS.

On the other hand, SIMS offers additional knowledge on the investigated sample:

- Element ions allow isotopes separation
- Molecule and cluster ions allow the investigation of chemical compounds
- By an additional "electron shower" insulators can be neutralized and therefore analyzed

In solid state analysis mainly three application fields of SIMS exist:

- Depth profile analysis with dynamic SIMS (see Sect. 6.7.1)
- Surface and thin film analysis with static SIMS (see Sect. 6.7.2)
- Two-dimensional and three-dimensional element distribution analysis with SI mapping or microscopy (see Sect. 6.8).

6.7.1 Dynamic Secondary Ion Mass Spectrometry (Dynamic SIMS)

For dynamic SIMS primary ions have two functions: they act as an analytical probe and simultaneously they give rise to sample sputtering, which means the sputtered part of the surface is immediately used for depth profile analysis. To produce depth profiles with sputter rates of typically 1 $nm \cdot s^{-1}$ a primary ion current density of about 10^{-4} A cm^{-2} is necessary. The depth resolution of a dynamic SIMS depth profile amounts to some nm.

The concentration-depth profile $c = f(z)$ must be evaluated from the measured intensity-time profile $I = f(t)$. Two steps are necessary to obtain the relation $c(z)$:

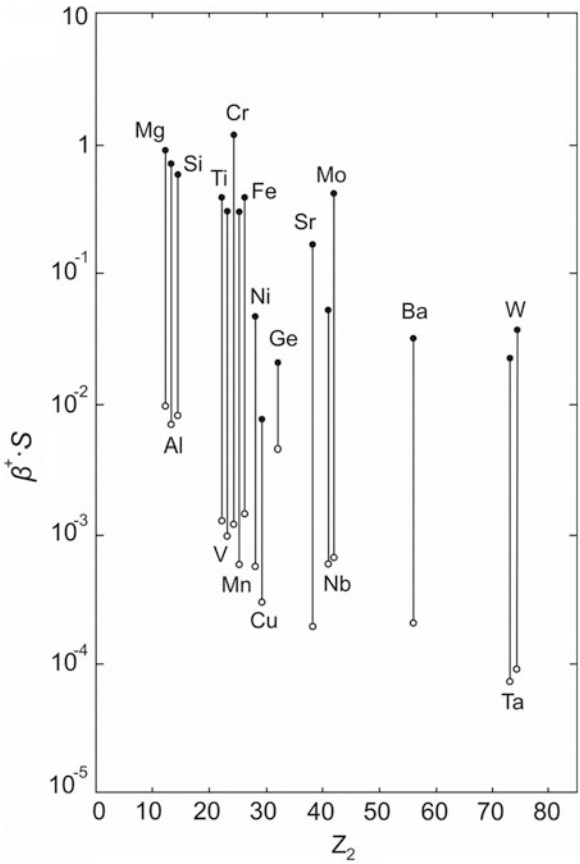

Fig. 6.46 Dependence of the secondary ion yield $\beta^+ \cdot S$ on the target atomic number Z_2 for different base pressures in the target vacuum chamber (Ar^+ ions used as primary ions)

1. Depth calibration $z = f(t)$
2. Element concentration calibration $c = f(I)$.

The sputter process itself results in a variation of composition and morphology of the uncovered target surface which must be taken into account to reveal the true profile $c = f(z)$ [83]. The eroded depth z is determined by the sputter rate $\dot{z}$ according to

$$z(t) = \int_0^t \dot{z}\ \mathrm{d}t. \tag{6.32}$$

Assuming a constant sputter rate (6.32) can be written as

$$\dot{z} = \frac{z_0}{t_0} = \text{const} \tag{6.33}$$

and the calibration is carried out by a crater depth measurement. The connection of the sputter rate $\dot{z}$ with physical parameters of the sputter process is given by (6.34):

$$\dot{z} = \frac{I_\mathrm{p}}{e \cdot A} \cdot A_\mathrm{Pa} \cdot d \cdot S = \frac{j_\mathrm{p}}{N_\mathrm{A} \cdot e} \cdot V_\mathrm{m} \cdot S = \frac{j_\mathrm{p}}{F} \cdot \frac{M}{\rho} \cdot S \tag{6.34}$$

with A_Pa—particle area on sample surface, d—thickness of a sample monolayer, V_m—molar volume ($\mathrm{m^3\ mol^{-1}}$), N_A—Avogadro's constant ($6.022 \times 10^{23}\ \mathrm{mol^{-1}}$), F—Faraday's constant ($9.648 \times 10^4\ \mathrm{As\ mol^{-1}}$), S—sputter coefficient, M—molar mass ($\mathrm{kg\ mol^{-1}}$), ρ—density ($\mathrm{kg\ m^{-3}}$), and j_P—$\mathrm{I_P/A}$ = PI current density.

With typical values for the sputter coefficient ($S \approx 3$) and the molar volume ($M/\rho = V \approx 10\ \mathrm{cm^3/mol}$) (6.34) can be written in a simple form as an approximated quantitative equation

$$\dot{z}(\mathrm{cm \cdot h^{-1}}) \approx j_\mathrm{P}(\mathrm{A \cdot cm^{-2}}). \tag{6.35}$$

A supposed primary ion current density of $j_\mathrm{P} = 10^{-4}\ \mathrm{A\ cm^{-2}}$ results in a sputter rate $\dot{z} = 1\ \mu\mathrm{m\ h^{-1}}$, which is typical for dynamic SIMS. The corresponding values for static SIMS are $j_\mathrm{P} = 10^{-9}\ \mathrm{A\ cm^{-2}}$ with a resulting sputter rate of $\dot{z} = 0.01\ \mathrm{nm\ h^{-1}}$, which means that static SIMS can be assumed as a nondestructive analytical method (see Sect. 6.7.2).

The experimental setup for dynamic SIMS is schematically shown in Fig. 6.47. Because of the surface sensitivity of SIMS the measuring equipment is placed in an UHV target chamber. The primary ions (PI) are generated in a PI source and pass through a magnetic sector field before bombarding the sample surface. The emitted secondary ions (SI) pass through an electrostatic lens system and subsequently they are mass selected in a quadrupole mass spectrometer and detected by a registration unit. SIMS measurement devices are well engineered and commercially available.

As an application of dynamic SIMS, Fig. 6.48 shows boron depth profiles after 140 keV (left) and 35 keV (right) boron implantations (fluence $10^{13}\ \mathrm{cm^{-2}}$) into a (100)Si target with and without crystal pre-damage [84]. The pre-damage defects were formed by 60 keV (left) and 200 keV (right) $\mathrm{Si^+}$ implantations at fluences of 10^{13} and $10^{14}\ \mathrm{cm^{-2}}$. The $\mathrm{B^+}$ ions incidence direction was nearly parallel to the [85] axial Si crystal channel. The boron range distributions obtained by implantation into an undamaged target are shown for comparison (black lines and symbols). As can be seen, without pre-damaging in both cases pronounced tails of the implanted profiles due to ion channeling were observed. The channeling tails can be suppressed by $\mathrm{Si^+}$ implantation with fluences $\geq 1 \times 10^{14}\ \mathrm{cm^{-2}}$. The SIMS data given by symbols were measured by Packan et al. [86]. The described experiment served as a process simulation for a n-MOS transistor structure.

As an example for diffusion depth profiles, Fig. 6.49 demonstrates the SI intensity distribution of $^{28}\mathrm{Si^+}$ after Si diffusion from a Si layer into an amorphous FeNbBCu-covering layer [87]. This layer got a thermal pretreatment at 400 °C for different annealing times between 1 and 16 h. According to Fick's laws progressive

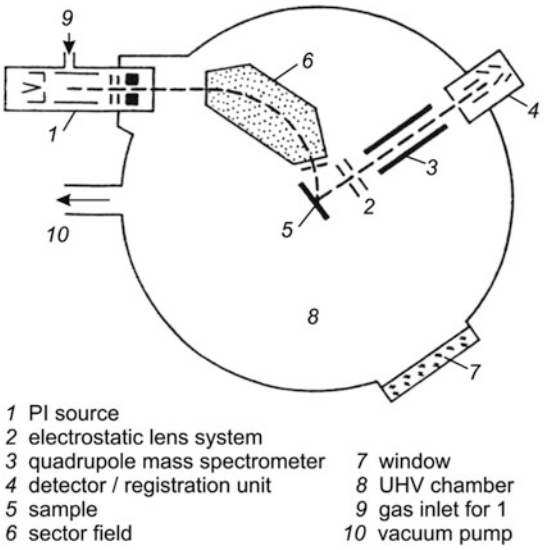

Fig. 6.47 Experimental setup of SIMS (schematically)

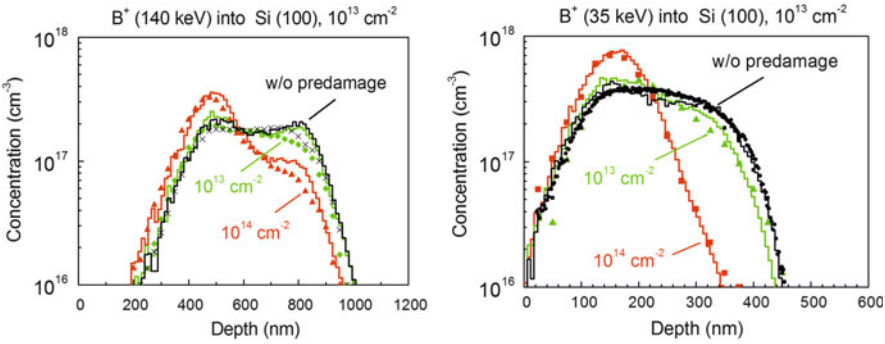

Fig. 6.48 SIMS depth profiles (*symbols*) for 140 keV (*left*) and 35 keV (*right*) boron implantations into a (100) Si target compared with theoretical profiles obtained by Crystal-TRIM simulations (*full lines*) [84]

Si diffusion into the direction of the surface takes place, as has been confirmed by the SIMS sputter profiles.

As mentioned above an important parameter for quantitative SIMS depth profile analysis is the depth resolution Δz. This resolution is limited not only by the penetration and escape depth of the interacting primary and secondary ions as well as neutrals, respectively but also by ion-induced surface roughening, atomic mixing, and preferential sputtering during surface removal. By an optimization of all these parameters a minimum value $\Delta z < 10$ nm can be obtained [88]. Because of the nondirected and low-energetic sputter process a narrow depth resolution

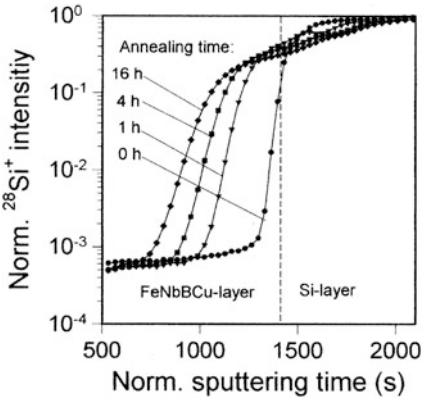

Fig. 6.49 SIMS depth profiles of Si diffusion into amorphous FeNbBCu after thermal treatment [87]

function down to few nm is available with plasma SNMS (see Sect. 6.7.3) [89]. In summary, the mean features of dynamic SIMS are drawn up in Table 6.10.

6.7.2 Static Secondary Ion Mass Spectrometry (Static SIMS)

Static SIMS is an established nondestructive surface analytical technique. It is characterized by a very low primary ion current density j_P, typically of $j_P \approx 10^{-9}$ A cm^{-2}. After the approximated quantity (6.34) discussed in Sect. 6.7.1, the resulting sputter rate can be estimated. For $j_P = 10^{-9}$ A cm^{-2} the corresponding sputter rate amounts to $\dot{z} = 0.01$ nm h^{-1}. Therefore, the removal of the first surface monolayer is a day-long procedure, and so the target surface can be analyzed with static SIMS in a quasi nondestructive manner. For static SIMS the detection limit is in the ppm range relating to about 10^{-6} monolayers which means a critical mass of ~10^{-14} g. Because of the low primary ion current density a large surface area must be bombarded for a sufficient confidence level. Therefore the resulting lateral resolution is only in the mm range. This is a significant disadvantage of static SIMS.

A typical static SIMS spectrum is demonstrated in Fig. 6.50. The SI^+ emission rate is plotted versus the atomic mass for an ion bombarded Ni–Cr layer on a glass substrate [90]. From the appearance of Si isotopes ($^{28}Si^+$, $^{29}Si^+$, $^{30}Si^+$) and alkaline ions one may conclude that no continuous Ni–Cr layer exists. Furthermore, the difficulty of quantification because of element dependence of the SI^+ yield is evident. Alkalis and alkaline earths are over-represented, e.g., the peaks of Al and of Na are higher than those of Ni. Therefore, static SIMS spectra need a calibration with standards to obtain (semi-) quantification. Nevertheless, the sensitive detection limit of about 10^{-6} monolayers is the outstanding advantage of static SIMS in comparison to other surface analytical methods.

Because the normally used quadrupole mass spectrometer is unsuitable for the analysis of heavy charged particles as large molecules or ions of heavy metals and

Table 6.10 Main features of dynamic SIMS

Elements	Be–U
Standard conditions	Primary ion density: ~10^{-4} A cm^{-2}
	Sputter rate: ~ 1–10 nm s^{-1}
Precision	Quantification only by calibration with standards
Sensitivity	Detection limit: ppm range
Depth resolution	1–10 nm
Remarks	Limitation: surface sensitivity of secondary ions yield

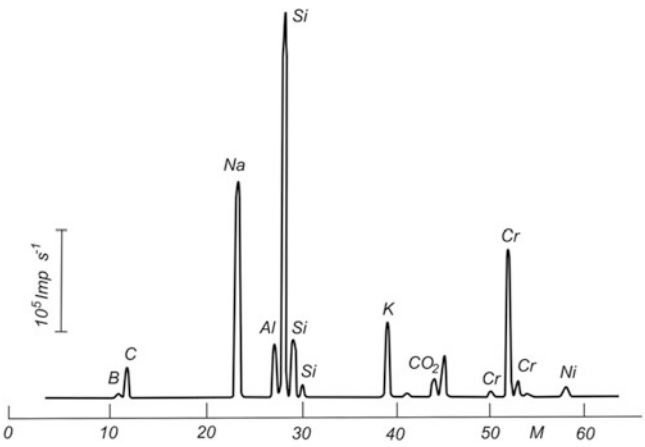

Fig. 6.50 Static SIMS spectrum (positive SI) from a Ni–Cr layer on a glass substrate [90]

alloys, a time-of-flight (ToF) mass spectrometer was developed for use in static SIMS by Benninghoven and Niehuis in 1985 [91, 92].

The mode of operation of such a ToF SIMS device is schematically illustrated in Fig. 6.51 [80]. The target c is bombarded by an electron impact ion source a or by a Ga^+ liquid metal ion source b, respectively. All sputtered ions are accelerated to a given potential of some kV, reaching the same kinetic energy. After passing secondary ion optics d the ions drift through a field-free path (length L) with gridless reflectrons e and then strike the detector f.

The measurement of the time-of-flight t of ions with a mass-to-charge ratio m/q provides their mass analysis by

$$t^2 = \frac{m \cdot L^2}{2q \cdot U_0}. \tag{6.36}$$

For an exact measurement of the start time the primary ion gun operates in a pulsed mode, and the flight path L must be sufficiently long for a demanded mass resolution of $m/\Delta m \approx 10{,}000$. An important advantage of ToF SIMS is its possibility of a simultaneous detection of all target masses of the same polarity.

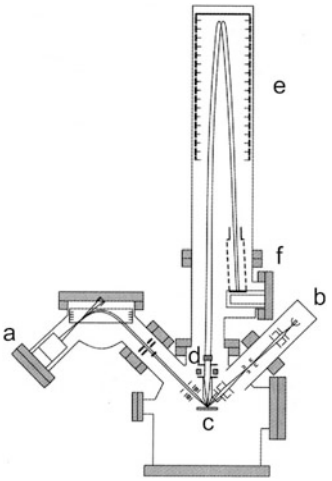

Fig. 6.51 Mode of operation of a ToF SIMS system (schematically, after [80]) with a an electron impact ion source, b a Ga^+ liquid metal ion source, c the target, d the SI optics, e the gridless reflectrons, and f the detector

ToF SIMS is meanwhile applied in many research and industrial laboratories because it allows not only spectroscopic information on elemental and molecular surfaces but also the lateral distribution of surface species can be obtained [93]. With a liquid metal ion gun, the lateral resolution of this so-called ToF SIMS imaging is better than 100 nm for elements and in the μm range for large molecules [94]. ToF SIMS has only a small information depth of the first 1–3 atomic layers, connected with a high-depth resolution of <1 nm. Furthermore, it is characterized by a high sensitivity in the range of some 10 ppb [95].

6.7.3 Sputtered Neutral Particle Mass Spectrometry

For SNMS the target is bombarded either with atomic primary ions (O^+, Cs^+, Ga^+, Ar^+) or with cluster ions (e.g., Au^{3+}, Bi^{3+}) in the low or medium-energy range (0.2–25 keV). The ion–target interaction predominantly results in the generation of not only neutral particles but also positively and negatively charged ions. Contrary to SIMS in SNMS the neutral particles are the subject of matter [80, 96]. In order to allow the spectrometry of their mass and concentration the sputtered neutral particles are post-ionized just in front of the emitting surface, either by electron impact in low-pressure HF plasma or by interaction with an intense laser beam or an accelerated electron beam. By this way the sputtering and the ionization process are decoupled.

The basic principle of an electron beam post-ionized SNMS is shown in Fig. 6.52 [85]. Sputtered neutral particles (SN) are generated by sample bombardment with primary ions PI and subsequently post-ionized using electrons accelerated to an energy of >50 eV which is higher than that of the first ionization energy for the SN (4–24 eV). The post-ionized emitted particles SN^+ are then

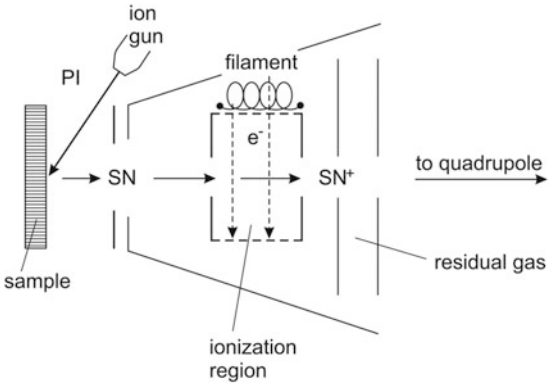

Fig. 6.52 Schematic setup of a SNMS apparatus with post-ionization by accelerated electrons [85]

analyzed in a quadrupole mass spectrometer. An other post-ionization technique was described by Oechsner [97]. Here an inductively coupled HF noble gas plasma, typically Ar, serves for sputtering and then for electron impact post-ionization using the Maxwellian electron gas.

In comparison with SIMS the Sputtered Neutral particle Mass Spectrometry has some essential advantages. Disturbing matrix effects can be neglected at SNMS because more than 90 % of sputtered material is used for analysis. Furthermore SNMS is suitable for a quantitative or at least semi-quantitative element analysis without standard calibration, because the ionization yield for different elements varies only marginally. This is evident in Fig. 6.53, which shows the element concentrations in a stainless steel, comparatively measured by wet chemistry analysis and by SNMS. Deviations from linearity caused by different ionization probabilities can be neglected.

An additional advantage of SNMS is the analysis of electrically insulating samples. SNMS measuring values comparable with SIMS exist for the detection limit (10^{-3}–10^{-4} at.%) and also for the information depth (0.2–2 nm). A disadvantage of SNMS with HF plasma is its poor lateral resolution in the 10 µm range because of the low post-ionization yield resulting in a serious sensitivity limitation. This handicap can be overcome by laser induced post-ionization of neutral secondary particles, allowing nano-analysis down to 50 nm lateral resolution [80].

In spite of the outstanding function parameters of SNMS there exist only few commercial developments, owing to the very complex and expensive equipment. A combined SIMS/SNMS system was developed by SPECS company, Berlin [98]. It bases on fundamental research activities of the group of Oechsner [97, 99–101]. This analytical instrument, called INA-X, offers outstanding features of the SNMS method with electron gas post-ionization. It allows a high sensitivity down to 1 ppm, a high-depth resolution in the nm region and a time efficient depth profile analysis.

The SNMS system INA-X was especially developed for element depth profile analysis with a depth resolution of only a few nm. For this reason it is outstandingly

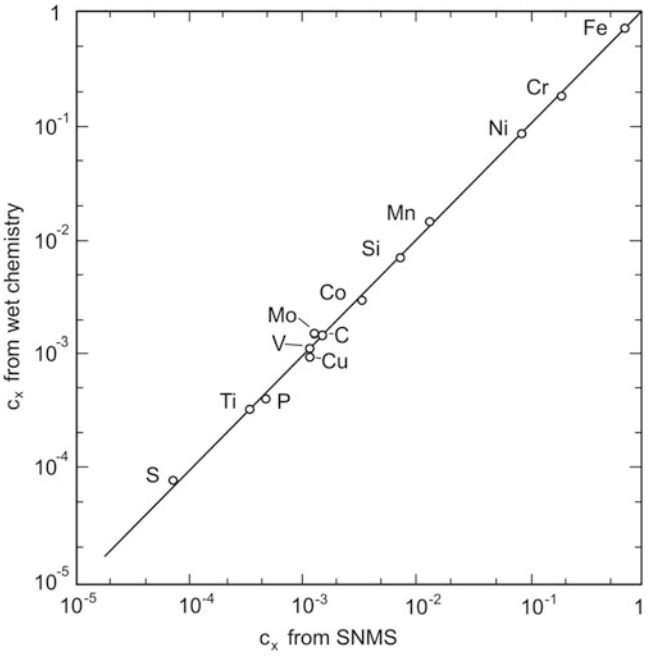

Fig. 6.53 Certificated element concentrations in a stainless steel related to SNMS signals

appropriate to thin film investigations. As an example, Fig. 6.54 shows the concentration depth profiles of $Fe^{56}Pt/Fe^{57}Pt/Pt$ multilayers on MgO, after 4 h annealing at 848 K (by courtesy of G. Langer and K. Vad (2006) Private communication, TU Dresden, unpublished). The multilayer preparation was realized by molecular beam epitaxy. Although the single layers have a nominal thickness of only few nm, they are clearly resolved, demonstrating the efficiency of the SNMS technique. In spite of the oscillating concentration of ^{56}Fe and ^{57}Fe the Pt concentration remains constant, and the sum of all element/isotope concentrations amounts to 100 % as an evidence for typical (semi-) quantitative SNMS depth profile analysis.

6.8 Ion Beam Imaging Techniques

A direct visualization of targets and their modification under ion irradiation is possible by different ion beam imaging techniques. One can distinguish between the following techniques:

- Field ion microscopy
- Ion microscopy with stationary beam
- Scanning ion microscopy

All these methods not only allow the acquisition of sample surface images, but also of element distribution patterns with ions. For this purpose, an advanced type

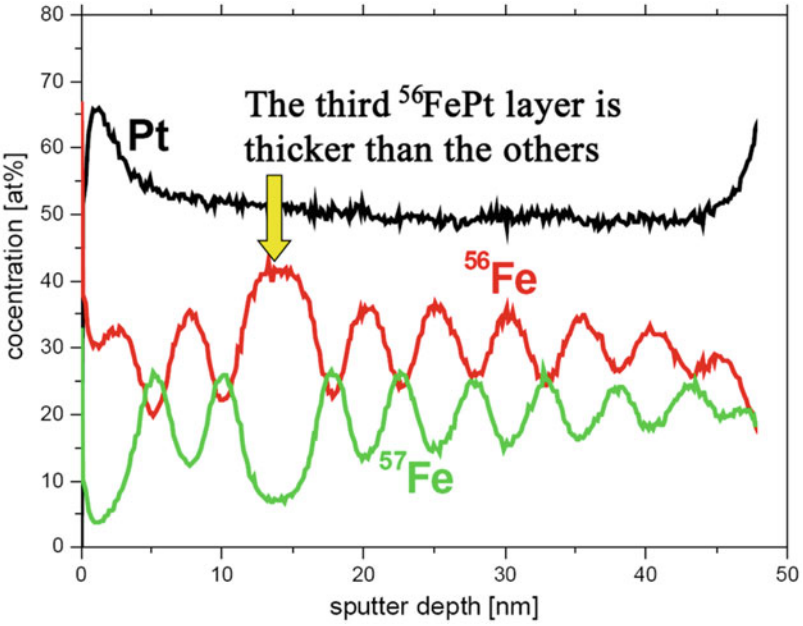

Fig. 6.54 SNMS concentration depth profiles of $Fe^{56}Pt/Fe^{57}Pt/Pt$ multilayers on MgO [Langer G, Vad K (2006) Private communication, TU Dresden, unpublished]

of the field ion microscope, the so-called field desorption microscope or atom probe, is utilized [102].

6.8.1 Field Ion Microscopy

The field ion microscope (FIM) represents a microscope that can be used to image the arrangement of single surface atoms on a sharp tip. It was developed by Müller et al. [103]. The physical principle is given in Fig. 6.55.

To the sharp tip (radius $r = 10$–100 nm) prepared from the specimen a positive high voltage $U_{tip} \approx 10$ kV is applied and the tip is cooled to a cryogenic temperature below 100 K. The specimen is placed in an ultrahigh vacuum chamber which is backfilled with He or Ne as an imaging gas. The gas atoms are firstly polarized and then ionized in front of the tip because of the strong electric field. The hopping and ionization process of the polarized residual gas atoms (here He) in the electric micro-field of the tip is illustrated in Fig. 6.56.

Unlike conventional microscopes where the spatial resolution is limited by the diffraction of imaging particles or waves, according to Abbe's equation the FIM is a projection type microscope with atomic resolution. Therefore, the useful magnification, which is the ratio of the screening radius to sample radius, amounts to more than 10^6. This is illustrated in Fig. 6.57, where the FIM image of a Pt

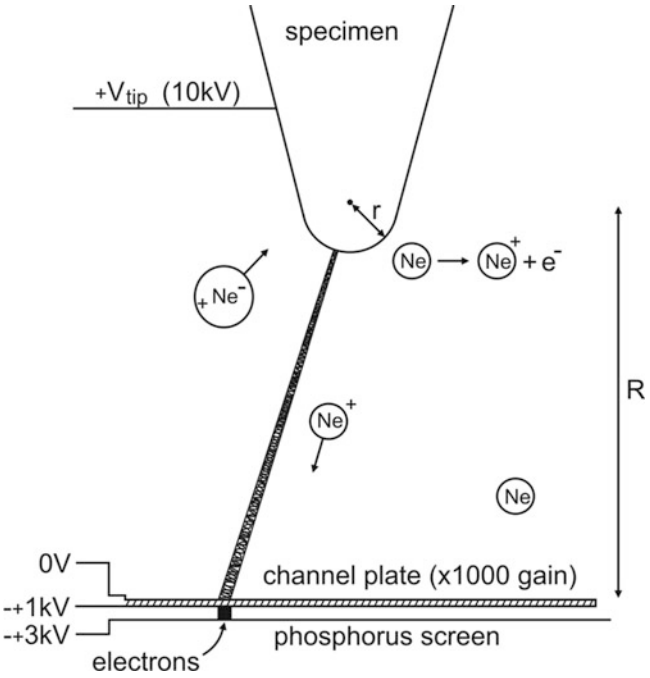

Fig. 6.55 Physical principle of field ion microscopy (FIM)

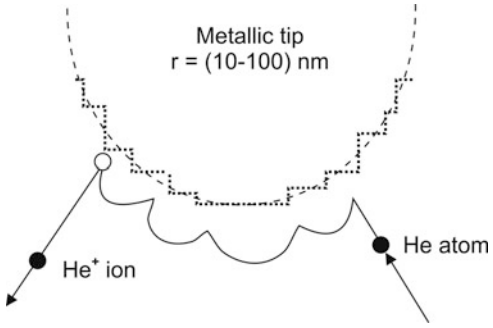

Fig. 6.56 The ionization process of a polarized He gas atom in front of the FIM tip

monocrystalline tip with a magnification of 700,000 is given [104]. The visible equipotential lines mark the positions of individual atoms.

A further actual development of the field ion microscope is the field desorption microscope, where atom desorption from the tip by high voltage impulses U_{imp} or by laser pulses takes place. In a combination with a time-of-flight (ToF) mass spectrometer this microscope is called atom probe. It was already developed by Müller et al. in 1967 [105]. The desorbed atoms fly through a drilled hole in the

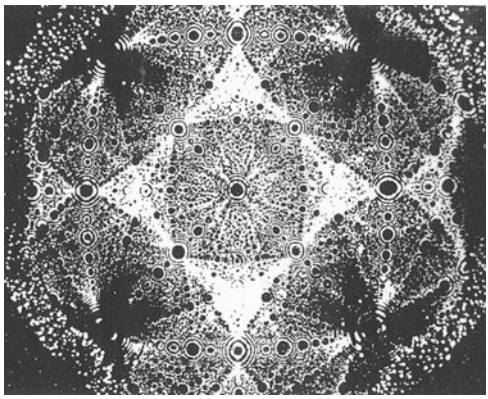

Fig. 6.57 FIM image of the tip of a Pt monocrystal (magnification ≈ 700.000:1) [104]

channel plate of the field desorption microscope into a ToF mass spectrometer (length L) and after it on a single atom detector. The mass m of each desorbed atom can be determined from the time-of-flight τ by

$$m = \frac{2e}{L^2} \cdot (U_{\text{tip}} + U_{\text{imp}}) \cdot \tau^2. \tag{6.37}$$

Per 100 pulses about 1 atom is field evaporated and the desorption of atom layers takes place with about 10 pulses per second. Desorption images can be taken as difference images before and after atom desorption via mass spectra of certain elements. As an example, Fig. 6.58 shows the 3D-visualization of individual desorbed atoms from a Cu/(Ni–Fe) multilayer system on a W substrate [106]. At closer inspection horizontal lattice planes in Cu are visible. Modern atom probe instruments with large detector areas allow the measurement of some millions of atoms. This relates to the detection and imaging of a volume of about 100 nm^3.

Chemical short range order can be determined by lateral preselection with a narrow diaphragm in the field desorption microscope. By this way an area of few nm^2 can be investigated. As an example, in Fig. 6.59, the element distribution analysis of two neighboring areas in a WC–Co hard metal tip is depicted. Figure 6.59a shows the element distribution at a grain boundary between WC and Co, whereas in Fig. 6.59b the element distribution in a WC grain in a distance of only 2 nm is demonstrated. Both spectra are similar, but in Fig. 6.59b the Co^{2+} peak is missing, which means there exist very sharp concentration profiles at grain boundaries.

An interesting application area of field desorption microscopy is the investigation of short range order by means of desorption spectroscopy, in order to study nucleation processes in amorphous metals. This shall be demonstrated for the metallic glass $Fe_{40}Ni_{40}B_{20}$. Its exact composition was determined to be
77.4 at.% metal atoms (Fe + Ni), called “A”
22.6 at.% metalloid atoms (boron), called “B”

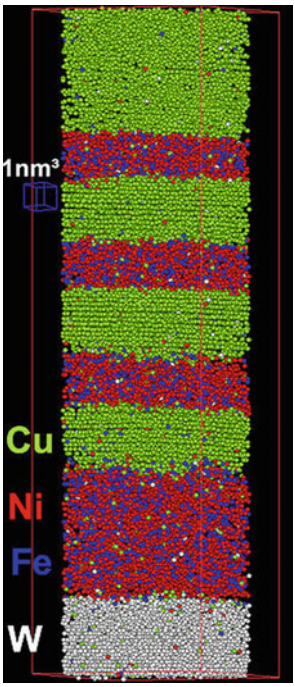

Fig. 6.58 Atom probe image of a Cu/(Ni–Fe) multilayer system on a W substrate with lateral resolution in the nm range [106]

The consecutive desorption of both "A" and "B" atoms was registered as a function of time by a data chain on the detector. For example, a part of this data chain is given here as:

AAABABBAAABAABAABABBAAAAABBABBAAAABAAAAAABBBA-BABBA... The relative frequency distribution of consecutive desorption of two metal atoms n_{A-A}, two metalloid atoms n_{B-B}, or a metal atom followed by a metalloid atom n_{A-B} or contrariwise n_{B-A} is calculated and then compared with the statistic values of a totally disordered amorphous state. The results are given in Table 6.11.

The excellent accordance between measured and statistic frequencies confirms a statistic disordered lateral distribution of metal and metalloid atoms in the amorphous metallic glass $Fe_{40}Ni_{40}B_{20}$. Therefore, nanocluster formation as an early nucleation state was not found.

6.8.2 Ion Microscopy with Stationary Ion Beam

A stationary microscopic image with secondary ions, emitted from a sample surface, can be received with ion imaging units combined with an ion–electron conversion system. Such stationary ion beam microscopes are manufactured by several companies. The schematic setup is shown in Fig. 6.60.

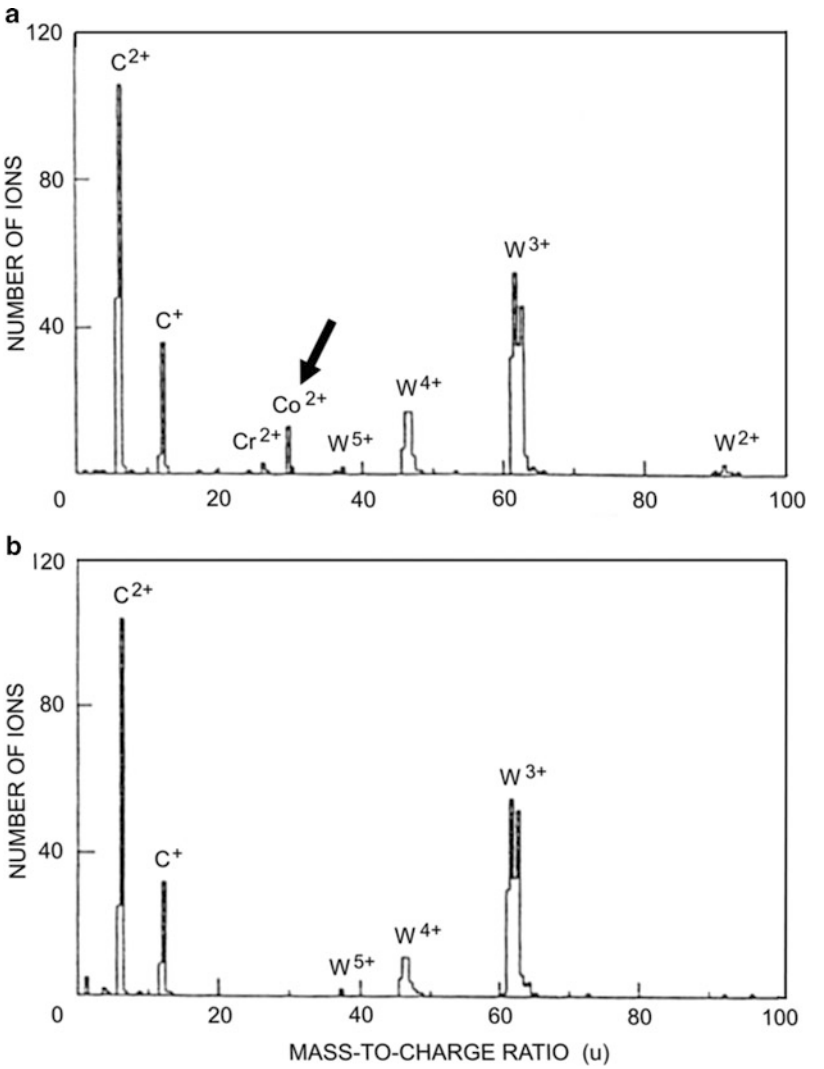

Fig. 6.59 Atom probe spectra of element distributions in a WC–Co hard metal tip; (**a**) at a grain boundary; (**b**) in a WC grain, 2 nm distant from (**a**)

Table 6.11 Relative frequency distribution of consecutive desorption of metal (A) and metalloid (B) atoms in an amorphous metallic glass with nominal composition $Fe_{40}Ni_{40}B_{20}$

Consecutive desorption	Measured frequency (%)	Statistic frequency (%)
$n_{A–A}$	59.0	59.8
$n_{A–B} + n_{B–A}$	36.5	35.1
$n_{B–B}$	4.5	5.1

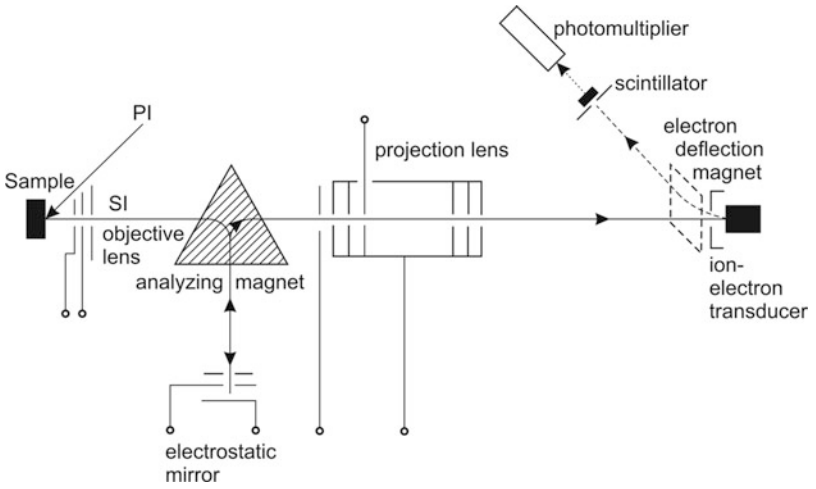

Fig. 6.60 Schematic setup of an ion microscope with a stationary ion beam

Secondary ions (SI) are emitted from a sample surface bombarded with primary ions (PI). The SI are deflected in an analyzing magnet and reflected by an electrostatic mirror, where ion energy selection takes place. After this the SI pass a projection lens and impinge on an ion–electron transducer. The generated electrons permit the imaging by means of a scintillator together with a photomultiplier. The lateral resolution of these ion microscope images is somewhat better than 1 μm.

An application example of this imaging technique is demonstrated in Fig. 6.61. It shows a three-dimensional (3D) imaging and retrospective depth profiling of layers on a substrate. The 3D-imaging is an exciting technique for the characterization of surfaces and thin layer structures. It is the result of composition of sequential lateral 2D-images. Figure 6.61 illustrates the lateral and depth distribution of 2 μm Al lines (blue) on a photoresist [107]. The vertical image is reconstructed from 64 sequential lateral images and is displayed in a rainbow color scale. The lateral image shown in Fig. 6.61 is the seventh one in sequence from the surface, corresponding to a depth of 2 nm.

6.8.3 Scanning Ion Microscopy

In the broadest sense, a scanning ion microscope (SIM) is an ion beam microprobe for the determination of lateral element distributions and/or depth profiles up to some μm by means of several ion beam analyzing methods, as PIXE, RBS, ERDA, NRA, or scanning microscopy with an incident ion beam, where the image is produced either with ions or with ion induced electrons. In this section the subject of matter shall be limited to the last-mentioned method of ion beam imaging techniques.

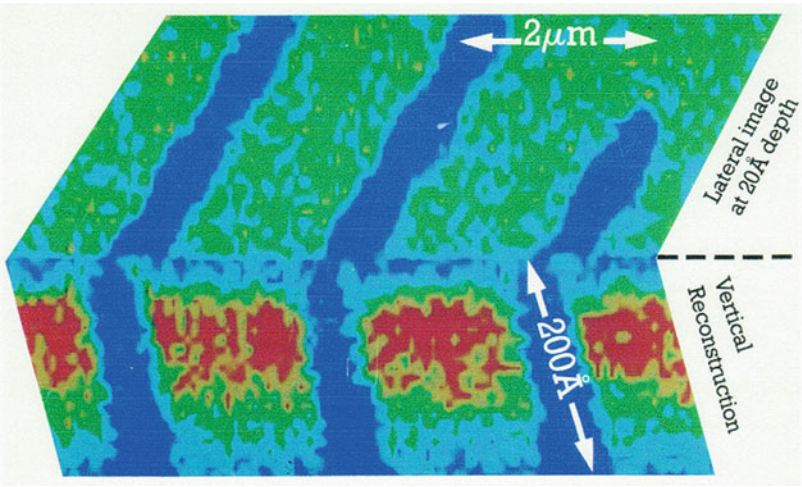

Fig. 6.61 Three dimensional ion microscopic imaging and retrospective depth profiling of 2 μm Al lines on a photoresist [107]

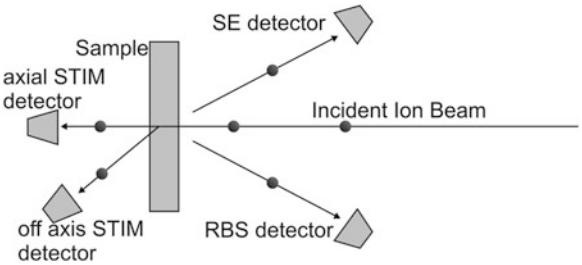

Fig. 6.62 Physical principle of a scanning transmission ion microscope (STIM)

A scanning ion microscope (SIM) has a similar setup as a scanning electron microscope (SEM) or—in the case of very thin samples—as a scanning transmission electron microscope (STEM). It was firstly described in 1974 by Levi-Setti [108]. The principle of such a scanning transmission ion microscope (STIM) is schematically illustrated in Fig. 6.62. The essential difference to SEM and STEM is the use of an incident high-energy ion beam instead of an electron beam, which is scanned across the sample pixel by pixel and focused on the sample down to the sub-nm range. In the backscattered mode two detectors are arranged: an ion detector for RBS and a SE detector for ion-induced secondary electrons. For very thin ion-transparent samples (transmission mode) STIM detectors are placed for the detection of transmitted ions in the axial mode and optionally for the detection of ions or ion-induced electrons in the off axis mode. In comparison with SEM with electrons as incident particles the incident focused ion beam produces a smaller interaction area at the sample surface resulting in a higher lateral resolution ($\delta < 1$ nm) and an improved material contrast imaging (see Fig. 6.2).

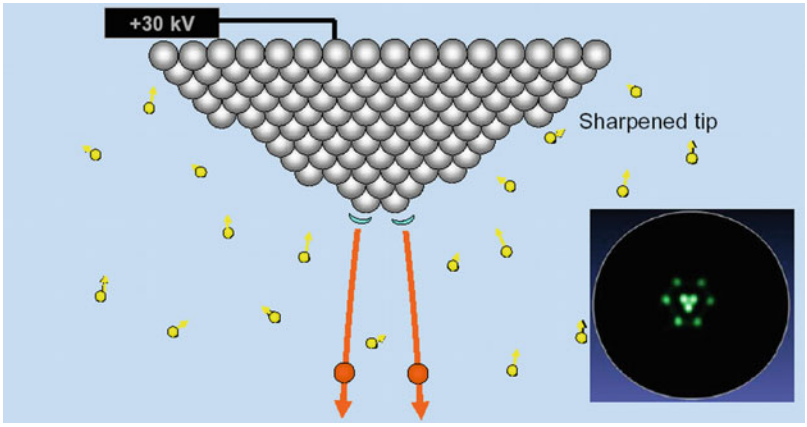

Fig. 6.63 Principle of an atomic-size He field ion source and the associated FIM image of the source tip [111]

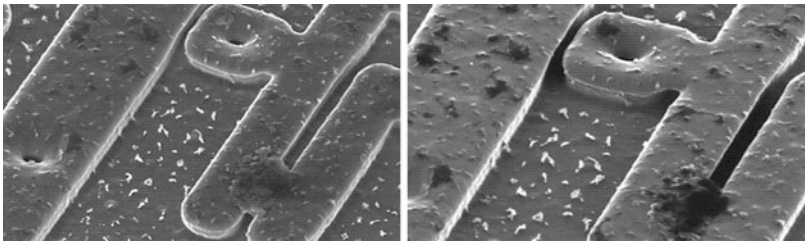

Fig. 6.64 Semiconductor circuit surface with contaminants causing short-circuit fault (*left*: SEM, *right*: SIM) [111]

Scanning ion microscopes work either with ion sources providing high-energy ions in the MeV range [109] or with ion sources supplying He^+ ions with energies in the 100 keV range [110]

Some key specifications of the world's first commercially available Helium scanning ion microscope ORION, manufactured by Carl Zeiss SMT [111, 112] are summarized as following:

- Probe size of incident ion beam 0.75 nm at 1 pA ion current
- Field of view down to 100 nm diameter
- Useful magnification up to 1,000,000
- He gas field ion source
- 2 electrostatic lenses column
- 5-axis motorized sample stage
- Everhart-Thornley and microchannel plate detectors

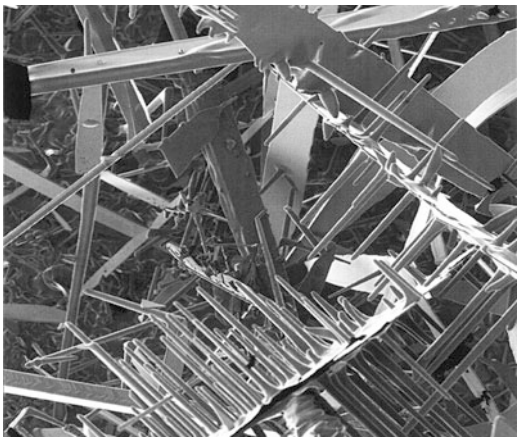

Fig. 6.65 Ion induced SE image of an eutectic alloy of Pb, Sn, In, and Bi [111]

The probe size of the incident ion beam is limited by the He ion source. The principle of an atomic field ion source is schematically shown in Fig. 6.63. By the sharpening process of a metallic needle, individual atoms are stripped away until an atomic pyramid is created just with three atoms at the tip. Under an extremely high electric field He gas atoms are attracted to the tip and ionized in the electric field of single atoms. The emerging ion beam has a very small size and a high brightness, producing a small probe size of <1 nm. This is evident from the FIM image of atoms at the end of the source tip emitting the He ions. Since each tip atom can be individually observed, the source size must be even much smaller [111].

The improved material contrast of SIM in comparison with SEM is evident in Fig. 6.64. The picture in the left shows the SEM image of metal interconnect lines in a silicon integrated circuit with contaminants causing short-circuit fault. In the SEM image it is hard to determine if the bridging material is the same or different from the substrate. The SIM image in the right picture clearly shows that the bridging material is different from the metal interconnecting lines because of its vastly different secondary electron yield as compared to the surrounding substrate material.

Furthermore, scanning ion microscope images show a superior depth of focus. It is inversely proportional to half angle of incident beam, which for SIM is typically 20 times smaller than for a SEM. As an example, Fig. 6.65 shows a SIM image of ion-induced SE emitted from an eutectic alloy of Pb, Sn, In, and Bi [111] impressively demonstrating the superior depth of focus of scanning ion microscopes.

References

1. Meijer J, Vogel T, Burchard B et al (2006) Concept of deterministic single ion doping with sub-nm spatial resolution. Appl Phys A 83:321–327
2. Hellborg J, Whitlow HJ, Zhang Y (2009) Ion beams in nanoscience and technology. Springer, Heidelberg

3. Verma HR (2007) Atomic and nuclear analytical methods. Springer, Berlin
4. Döbeli M (2001) Lecture materials analysis. CERN Accelerator School, Pruhonice
5. Winter HP, Aumayr F (2002) Slow multicharged ions hitting a solid surface. Europhys News 33:215–217
6. Winter HP, Burgdörfer J (2007) Slow heavy-particle induced electron emission from solid surfaces. Springer, Berlin
7. Burgdörfer J, Lerner P, Meyer FW (1991) Above-surface neutralization of highly charged ions. Phys Rev A 44:5674–5685
8. Tesmer JR, Nastasi M (1995) Handbook of modern ion beam materials analysis. MRS, Pittsburgh, PA
9. Breese M, Jamieson DN, King PJC (1996) Materials analysis using a nuclear microprobe. Wiley, Chichester
10. Breese M (2001) Lecture PC 4250 advanced analytical techniques. National University, Singapore
11. Rohmann D (2009) Mail Portal RUBION. Ruhr-Universität Bochum
12. Groleau R, Gujrathi S, Martin J (1983) Time-of-flight system for profiling recoiled light elements. Nucl Instrum Methods 218:11–15
13. Inouye A, Yamamoto S, Nagata S et al (2008) Hydrogen behaviour in gasochromic tungsten oxide films. Nucl Instrum Methods Phys Res B 266:301–307
14. Kimura K, Nakajima K, Suzuki M (2006) High resolution RBS for nano CMOS applications. Nano CMOS 2006:89–109
15. Lanford WA, Bedell S, Amadon S et al (2000) Characteristics of Albany's compact high resolution magnetic spectrometer. Nucl Instrum Methods Phys Res B 161–163:202–206
16. Nakajima K, Okura Y, Suzuki M et al (2004) Charge-state distribution of 400 keV He ions scattered from solids. Nucl Instrum Methods Phys Res B 219–220:514–518
17. Döbeli M et al (1990) Heavy ion backscattering analysis with a time-of-flight detector. Nucl Instrum Methods Phys Res B 47:148–154
18. Feldman LC (2006) Fundamentals of ion channeling. Script Lecture II, Pan-American Summer School "Ion Beams for the Nano Era", Buenos Aires (02/2006)
19. Grötzschel R, Klein C, Mäder M (2004) RBS with high depth resolution using small magnetic spectrometers. Nucl Instrum Methods Phys Res B 219–220:344–350
20. Kimura K, Joumori S, Oota Y et al (2004) High resolution RBS. Nucl Instrum Methods Phys Res B 219–220:351–357
21. Turkevich AL, Patterson JH, Franzgrote EJ (1968) Chemical analysis of the moon at the surveyor VI landing site. Science 160:1108–1110
22. Van der Veen JF (1985) Ion beam crystallography of surfaces and interfaces. Surf Sci Rep 5:199–288
23. Tromp RM, Copel M, Reuter MC et al (1991) A new two-dimensional particle detector for a toroidal electrostatic analyser. Rev Sci Instrum 62:2679–2683
24. Sortica MA et al (2009) Characterization of nanoparticles through medium-energy ion scattering. J Appl Phys 106:114320–114321
25. Matsumoto H et al (2010) Au/Pd structures analyzed by high-resolution medium energy ion scattering. Nucl Instrum Methods Phys Res B 268:2281–2286
26. Gustafson J, Haire AR, Baddeley CJ (2011) Depth-profiling the composition of bimetallic nanoparticles using medium energy ion scattering. Surf Sci 605:220
27. Goncharova L, Gustafsson T (2008) Preparation and characterization of CdSe semiconductor films. Lecture MRS meeting 2008, Section D
28. Brongersma HH, Buck TM (1978) Low energy ion scattering (LEIS) for composition and structure analysis of the outer surface. Nucl Instrum Methods 149:569
29. Brongersma HH et al (2007) Surface composition analysis by low energy ion scattering. Surf Sci Rep 62:63
30. Brongersma HH et al (1998) A round robin experiment of elemental sensitivity factors in LEIS. Nucl Instrum Methods Phys Res B 142:377–386

31. Rabalais JW (2003) In: Desiderio DM, Nibbering NMM (eds) Principles and applications of ion scattering spectrometry. Wiley, New York
32. Brongersma HH et al (1992) Developments in low energy ion scattering from surfaces. Nucl Instrum Methods Phys Res B 68:207
33. Brongersma HH, Groenen PAC, Jacobs JP (1994) Science of ceramic interfaces. Mater Sci Monogr 81:113
34. Brongersma HH (2011) Unique surface analysis symposium, Lehigh University, March 23 2011, Bethlehem, PA
35. L'Ecuyer J et al (1976) An accurate and sensitive method for the determination of the depth distribution of light elements in heavy materials. J Appl Phys 47:381–382
36. Hofsäß H (1996) Forward recoil spectrometry. Plenum, New York
37. Pretorius R, Peisach M, Mayer JW (1988) Use of absorber foils in front of a common Si particle detector to discriminate heavy scattered projectiles in conventional ERDA. Nucl Instrum Methods Phys Res B 35:478–483
38. Thomas JP et al (1983) High resolution depth profiling of light elements in high atomic mass materials. Nucl Instrum Methods 218:125–128
39. Arnold Bik WM, de Laat CTAM, Habraken FHPM (1992) On the use of a ΔE-E telescope in elastic recoil detection. Nucl Instrum Methods Phys Res B 64:832–835
40. Stoquert JP, Guillaume G, Hage- Ali M (1989) High resolution recoil spectrometry for separate characterization of Ga and As. Nucl Instrum Methods Phys Res 44:184–194
41. Assmann W (1992) Ionization chambers for materials analysis with heavy ion beams. Nucl Instrum Methods Phys Res B 64:267
42. Grigull S et al (1997) Element-dependent ERDA probing depths using different detection systems. Nucl Instrum Methods Phys Res B 132:709–717
43. Döbeli M et al (2005) ERDA at the low energy limit. Nucl Instrum Methods Phys Res B 241:428–435
44. Kottler C (2005) Dünnschichtanalyse mittels Vorwärtsstreuung bei tiefer Energie. PhD thesis, ETH Zürich, 16079
45. Abrasonis G et al (2008) Soft X-ray absorption and emission spectroscopic investigation of carbon and carbon: transition metal composite films. J Phys Chem C 112:17161–17170
46. Schietekatte F (2008) Fast Monte Carlo for ion beam analysis simulations. Nucl Instrum Methods Phys Res B 266:1880–1885
47. Arstila K, Sajavaara T, Keinonen J (2001) Monte Carlo simulation of multiple and plural scattering in elastic recoil detection. Nucl Instrum Methods Phys Res B 174:163–172
48. Mayer M (2002) Ion beam analysis of rough thin films. Nucl Instrum Methods Phys Res B 194:177–186
49. Barradas NP et al (1999) Unambiguous automatic evaluation of multiple ion beam analysis data with simulated annealing. Nucl Instrum Methods Phys Res B 149:233–237
50. Jeynes C et al (2003) Elemental thin film profiles by ion beam analysis using simulated annealing – a new tool. J Phys D Appl Phys 36:R97–R126
51. Donchev A, Richter E, Schuetze M et al (2006) Improvement of the oxidation behaviour of TiAl alloys by treatment with halogens. Intermetallics 14:1168–1174
52. Donchev A, Kolitsch A, Schuetze M et al (2009) Plasma-immersion-ion-implantation. Plasma Process Polym 6:434–439
53. Kimura K, Mannami M (1996) RBS single monolayer resolution. Nucl Instrum Methods Phys Res B 113:270–274
54. Vieluf M (2010) Hochauflösende RBS zur Untersuchung von ZrO_2-Schichtwachstum im Anfangsstadium. PhD thesis, Technical University Dresden
55. Dollinger D et al (1998) Elastic recoil detection with single atomic layer depth resolution. Nucl Instrum Methods Phys Res B 136–138:603–610
56. Johansson SAE, Campbell JL (1988) PIXE – a novel technique for elemental analysis. Wiley, Chichester

57. Ren M, van Kan JA, Bettiol AA et al (2007) Nanoimaging of single cells using STIM. Nucl Instrum Methods Phys Res B 260:124–129
58. Whitlow HJ, Ren M, van Kan JA et al (2007) Characterization of beam focus quality in biomedical nuclear microscopy. Nucl Instrum Methods Phys Res B 267:2149–2152
59. Mayer JW, Rimini E (1977) Ion beam handbook for material analysis. Academic, New York
60. Nastasi M, Clarke DR, Suresh S (1996) Ion-solid interactions: fundamentals and applications. Cambridge University Press, Cambridge
61. IAEA-TECDOC-1342 (2003) Intercomparison of PIXE spectrometry software packages
62. Kudejova P (2005) Two new installations for non-destructive sample analysis: PIXE and PGAA. Dissertation thesis, Universität zu Köln
63. Stoliar P, Kreiner AJ, Debray ME et al (2004) Microdistribution of BNCT-compound. Appl Radiat Isot 1:771–774
64. Ariola V, Campjola L, D'Alessandro A et al (2002) Aerosol characterization in Italian towns by IBA techniques. Nucl Instrum Methods Phys Res B 190:471–476
65. Schramm HP, Hering B (1989) Historische malmaterialien und ihre identifiifierung. Lecture ADVA, Berlin
66. Mando PA (2004) Particle accelerators in art and archaeology. Lecture International School on Written Records, 17 Apr 2004, Erice, Italy
67. Isobe Y, Sobue K, Ochiai K et al (2000) Analysis of deuterium and lithium on titanium surface by NRA method. Nucl Instrum Methods Phys Res B 170:171–179
68. Torri P, Keinonen J, Nordlund K (1994) A low-level detection system for hydrogen analysis. Nucl Instrum Methods Phys Res B 84:105–110
69. Amsel G, Lanford WA (1984) Nuclear reaction techniques in materials analysis. Ann Rev Nucl Part Sci 34:435–460
70. Lanford WA (1992) Analysis of hydrogen by nuclear reaction and energy recoil detection. Nucl Instrum Methods Phys Res B 66:65–82
71. Jarjis RA (1979) Nuclear cross section data for surface analysis. Department of Physics, Schuster Laboratory, University of Manchester
72. Mayer M (1996) SIMNRA: simulation of RBS, ERD and NRA spectra. http://www.rzg.mpg.de
73. Vizkelethy G (1990) SENRAS: simulation program for nuclear reaction analysis. Nucl Instrum Methods Phys Res B 45:1–5
74. Neelmeijer C, Grötzschel R, Hentschel E et al (1992) Ion beam analysis of steel surfaces modified by nitrogen ion implantation. Nucl Instrum Methods Phys Res B 66:242–249
75. Pellegrino S, Beck L, Trouslard PH (2004) Differential cross-sections for nuclear reactions 14 N (d, p)15 N. Nucl Instrum Methods Phys Res B 219–220:140–144
76. Laube M, Rauch F (1995) Ion beam analysis of temperature induced changes in the composition of float glass surfaces. Nucl Instrum Methods Phys Res B 99:436–439
77. Hagstrum HD, Becker GE (1967) Ion-neutralization spectroscopy of copper and nickel. Phys Rev 159:572–586
78. Wünsch G (1976) Optische Analysenverfahren zur Bestimmung anorganischer Stoffe. Sammlung Göschen, De Gruyter, Berlin
79. Düsterhöft H, Riedel M, Düsterhöft BK (2001) Einführung in die Sekundärionenmassenspektroskopie. Teubner, Leipzig
80. Bubert H, Jenett H (2002) Surface and thin film analysis. Wiley-VCH, Weinheim
81. Wetzig K, Schneider CM (2006) Metal based thin films for electronics. Wiley-VCH, Weinheim
82. Wilson RG, Stevie FA, Magee CW (1989) Secondary ion mass spectrometry: a practical handbook. Wiley, New York
83. Hofmann S (2004) Practical surface analysis. Surf Interface Anal 9:3–20
84. Posselt M, Schmidt B, Feudel T et al (2000) Atomistic simulation of ion implantation and its application in Si technology. Mater Sci Eng B 71:128–136

85. Bayly AR, Wolstenholme J, Petts CR (1993) E-beam SNMS: a complementary surface analysis technique. Surf Interface Anal 21:414–417
86. Packan P, Kennel H, Thompson S et al (1996) Understanding implant damage by implant channeling profile measurements. Proceedings of the 11th international conference on ion implantation technology, Austin, pp 539–542
87. Oswald S, Baunack S, Henninger G et al (2002) Model investigations on the effect of Si transport. Anal Bioanal Chem 374:736–741
88. Magee CW, Honig RE (1982) Depth profiling by SIMS. Surf Interface Anal 4:35–41
89. Wetzig K, Baunack S, Hoffmann V et al (1997) Quantitative depth profiling of thin layers. Fresenius J Anal Chem 358:25–31
90. Oswald S (1994) Internal Research Report, Leibniz-Institut IFW Dresden
91. Steffens P et al (1985) A time-of-flight mass spectrometer for static SIMS applications. J Vac Sci Technol A 3:1322–1325
92. Niehuis E et al (1987) High resolution surface analysis by ToF-SIMS. J Vac Sci Technol A 5:1243–1246
93. Grams J (2007) New trends and potentialities of ToF SIMS in surface studies. Nova Science, New York
94. Hagenhoff B (2000) High resolution surface analysis by ToF-SIMS. Microchim Acta 132:259–271
95. Vickerman JC, Gilmore I (2011) Surface analysis – the principal techniques. Wiley, New York
96. Jede R, Peters H et al (1986) Analyse dünner Schichten mittels Massenspektrometrie zerstäubter Neutralteilchen. Technisches Messen tm 11:407–413
97. Oechsner H (1970) Energy distribution in sputtering processes. Phys Rev Lett 24:583–584
98. INA-X system for SNMS and SIMS. http://www.specs.de
99. Jenett H (1997) Analytiker-Taschenbuch, vol 16. Springer, Berlin, pp 43–117
100. Oechsner H, Rühe W, Stumpe E (1979) Comparative SNMS and SIMS studies of oxidized Ce and Gd. Surf Sci 85:289–301
101. Oechsner H (2010) Plasma based secondary neutral mass spectrometry, vol 5. Elsevier, Oxford
102. Rühle M, Ernst F (2003) High resolution imaging and spectroscopy of materials, vol 50. Springer, Berlin, pp 271–320
103. Müller EW (1951) Das Feldionenmikroskop. Z Phys 131:136–142
104. Müller EW (1959) Beobachtung von nahezu fehlerfreien Metallkristallen und von Punktdefekten im FIM. Z Phys 156:399–410
105. Müller EW, Panitz JA, Mc Lane SB (1968) Seeing and catching atoms. Rev Sci Instrum 39:83–86
106. Ene CB (2005) http://en.wikipedia.org/wiki/File:Atomprobe_00_as-prepared_Cu-NiFe-W01.jpg
107. Gnaser H (1998) Spatially 3-dimensional SIMS analysis with MCs^+ ions. In: Gillen G et al (eds) Secondary Ion Mass Spectrometry XI. WILEY, Chichester, p 827
108. Levi-Setti R (1974) Proton scanning microscopy: feasibility and promise. In: Johari O, Corvin I (eds) Scanning electron microscopy/1974. IIT Research Institute, Chicago, pp 125–134
109. Lefevre HW et al (1987) Scanning transmission ion microscopy as it complements particle induced X-ray emission microanalysis. Scanning Microsc 1(3):879–889
110. Ward BW (2008) Scanning transmission ion microscope. US Patent: Nr. 7321118
111. Gnauck P (2008) New concepts in particle optics-. The helium ion microscope. Carl Zeiss SMT- Product Portfolio
112. Posteket MT et al (2007) Helium ion microscopy: a new technique for semiconductor metrology and nanotechnology. AIP Conference Proceedings 931: Frontiers of characterization and metrology for nanoelectronics

Special Ion Beam Applications in Materials Analysis Problems

7

7.1 Functional Thin Films and Layers

For the study of both the element composition and the microstructure of functional thin films and layers, the ion beam plays an important role. On the one hand, such thin layers can be produced by ion sputter deposition as DC-magnetron sputtering or by ion plating. Ions are also used for the cross-section preparation of thin solid films and layers. This can be either done with focused ion beams (FIB) or with the so called ion beam slope-cutting technique for larger cut areas. Furthermore, ion beams can be used for the actual near-surface or cross-section analysis of thin solid films and layers. Here the typical method of choice is secondary ion mass spectrometry (SIMS), which is a depth-profiling method with typical detection limits down to the ppm range.

In the following two examples for ion beam application in materials analysis the different mentioned possibilities shall be discussed.

7.1.1 Direct Study of Diffusion Processes in Amorphous Thin Layer Systems

The background for these experiments is the development of nanocrystalline materials for modern soft magnetic applications. One class of such materials is FeSiB-(Cu, Nb) alloys [1], which can be prepared as thin layers by physical vapor deposition [2, 3]. The soft magnetic properties of these layers are the result of nanocrystallization of the initially amorphous state by a well-defined thermal treatment. The redistribution of Si by this crystallization process seems to influence the soft magnetic properties in a decisive manner, and it is characterized by the formation of Fe_3Si nanocrystals embedded in a residual amorphous matrix [1].

In order to simulate and to characterize this residual amorphous phase both the Si diffusion and phase formation in a thin-layer system FeNbBCu/Si/FeNbBCu were studied by the two thin film characterization methods, secondary ion mass

B. Schmidt and K. Wetzig, *Ion Beams in Materials Processing and Analysis*,
DOI 10.1007/978-3-211-99356-9_7,

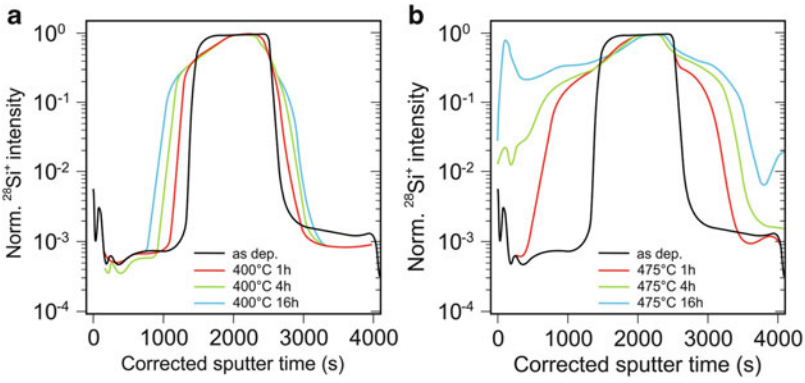

Fig. 7.1 SIMS depth profiles for the Si interlayer between two FeNbB(Cu) layers, as-deposited and after annealing for different times (**a**) at 400 °C and (**b**) at 475 °C [5]

spectrometry (SIMS, see Sect. 6.7) and transmission electron microscopy (TEM) [4, 5]. The multilayer samples were prepared by DC magnetron sputtering with Ar^+ ions. Two different targets—$Fe_{51}B_{31}Nb_{13}Cu_5$ alloy and pure Si—were used to produce a layer stack: FeNbBCu (80 nm)/Si (65 nm)/FeNbBCu (85 nm).

These thicknesses allow the assumption of an "unlimited source," which means that the FeNbBCu matrix and the embedded diffusive Si layer are connected by one interface. The total stack thickness was confirmed by TEM cross-section measurements [5].

The interdiffusion process occurred after thermal annealing which was performed under vacuum at 400 and 475 °C for 1 h, 4 h, and 16 h, respectively [5]. After the annealing process, element depth profiles were taken in a SIMS microanalyzer with bombarding O_2^+ ions at 8.5 and 18.5 keV under normal incidence. The ion current was about 40 nA, and positively charged secondary ions from a scanned area of 300 μm × 300 μm were analyzed in a magnetic mass analyzer with low mass resolution.

In Fig. 7.1 the Si interlayer concentration depth profiles are shown for the as-deposited state and after annealing (a) at 400 °C and (b) at 475 °C for different times [5]. The $^{28}Si^+$ ion intensity was normalized and the sputter time was corrected using the Nb depth profile, because it does not change remarkably by annealing. From Fig. 7.1, it is evident that a noticeable Si diffusion takes place even at 400 °C (Fig. 7.1a). However, the diffusion profiles of Fig. 7.1 are caused not only by the Si interlayer but also by reversionary diffusion processes from the outer FeBNbCu layers into the Si interlayer. Therefore both the matrix composition and the diffusion behavior in the interface region will change. This can be immediately shown from the concentration depth profiles of all constituents of the whole layer stack, which are given in Fig. 7.2 in the as-deposited state and after annealing at 475 °C for 1 h and for 16 h.

From Fig. 7.2, it is evident that a substantial interdiffusion of all elements, except Nb, takes place. Some of the depth profiles in Fig. 7.2 show an asymmetric

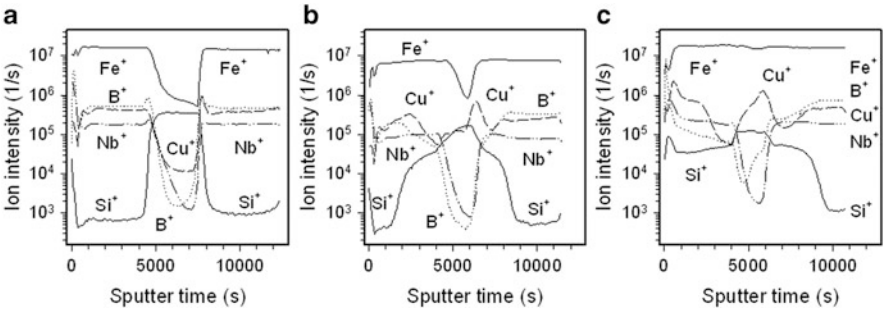

Fig. 7.2 SIMS concentration depth profiles of all main constituents of the layer stack FeNbBCu/Si/FeNbBCu in the as-deposited state (**a**) and after annealing at 475 °C for 1 h (**b**) and for 16 h respectively (**c**) [5]

course. This may be the result of changing diffusion coefficients or of the formation of new phases [5].

In the case of proportionality between ion intensities and element concentrations diffusion coefficients can be determined from the SIMS profiles. Yet, this presumes no new phases will develop.

Additional Auger electron spectroscopic (AES) depth profiles confirmed the occurrence of complete element intermixing, as already supposed from the SIMS experiments [5]. Furthermore, from a factor analysis procedure [6] the formation of a new phase Si (+Fe) as a result of interdiffusion of Si and Fe could be found.

This is illustrated in Fig. 7.3.

In Fig. 7.3a two-characteristic peak shapes of the Si (LVV) transition for the Si interlayer were found which are assumed to be pure Si (full line) and Si with Fe (dashed line). From the depth profiles of the loadings of these two phases (Fig. 7.3b–d), it is evident that the new phase Si (+Fe) at first appears at the interfaces (in the as-deposited state and after 4 h annealing at 475 °C) but after 16 h annealing it exists in the complete Si interlayer.

For a direct comparison of the interlayer thickness and of phase formation in the interface region TEM and electron diffraction experiments were carried out. The TEM cross-section specimens were prepared by conventional face-to-face technique with sticking, grinding, and ion milling. Figure 7.4 shows the cross-section micrograph (a) and typical electron diffraction patterns (b, c) of the layer stack FeNbBCu/Si/FeNbBCu after annealing at 475 °C for 1 h.

The Si interlayer thickness of 65 nm, measured by ion beam depth profiling, is in good agreement with the TEM cross-section thickness of Si (Fig. 7.4a). The microstructure of the layer stack was completely changed by the annealing process [5]. In Fig. 7.4a, taken after annealing at 475 °C for 1 h, crystalline interlayers, ~10 nm thick, are observed at both interfaces of FeNbBCu with Si. This can be explained by an interdiffusion of both Si and Fe, which is in good agreement with the SIMS concentration depth profiles of Fig. 7.2. Though most of the FeNbBCu layers remain in the amorphous state (Fig. 7.4b), the microdiffraction pattern of the

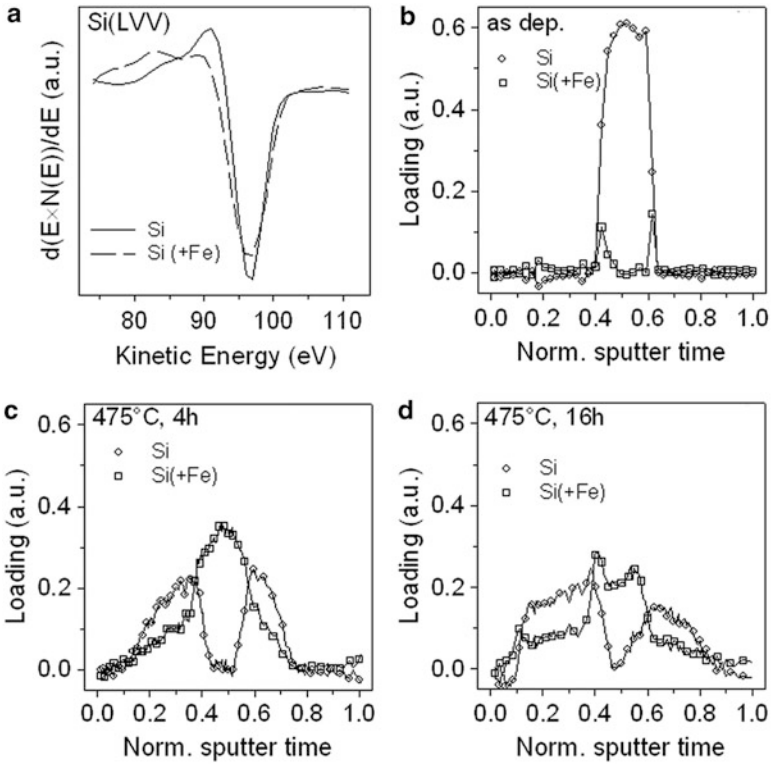

Fig. 7.3 Results from factor analysis of the (LVV) AES transition of the Si interlayer [5]. (**a**) Two characteristic peak shapes can be assigned to the two phases Si and Si (+Fe) (**b–d**) Normalized phase depth profiles: (**b**) in the as-deposited state, (**c**) after 4 h annealing at 475 °C, (**d**) after 16 h annealing at 475 °C

interface layer (Fig. 7.4c) could be best approximated in simulation calculations with FeSi (cubic, lattice constant $d = 0.449$ nm, structure type B 20, space group $P2_13$) as a newly formed phase. Although this phase identification is complicated by the small crystallite sizes and by the crystallographic similarity of possible iron silicide phases the TEM results are in good agreement with the SIMS and AES results discussed above.

By means of the combined application of following ion beam techniques:

- DC-magnetron sputtering
- SIMS depth profiling
- Ion milling and FIB cross section preparation

the effect of Si diffusion on the nanocrystallization of the layer system FeNbBCu/Si/FeNbBCu could be successfully investigated. This is a contribution for the development of nanocrystalline materials for modern soft magnetic applications in materials science.

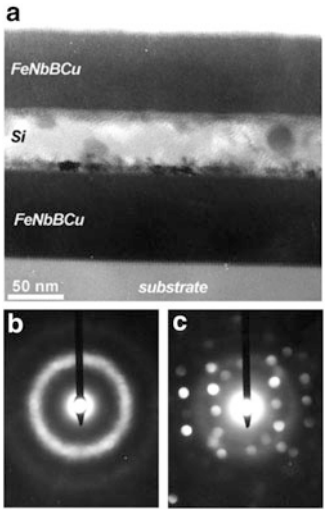

Fig. 7.4 TEM investigation of the layer stack FeNbBCu/Si/FeNbBCu after annealing at 475 °C for 1 h: (**a**) TEM cross-section micrograph, (**b**) microdiffraction pattern of amorphous FeNbBCu layer, (**c**) microdiffraction pattern of the interface layer (FeSi, zone axis [110])

7.1.2 Nanoanalytical Investigations of Tunnel Magnetoresistance Layers

In electronic technology the electron spin became an important fact by the discovery of interlayer exchange coupling in the 1980s [7, 8]. This new research field is named magnetoelectronics or spintronics [9]. One of the topics of magnetoelectronics is tunnel magnetoresistance (TMR). Application fields of TMR are magnetoresistance random access memory (MRAM) technique, reading heads of hard disc drives and also sensor applications as in modern cars anti-blocking systems (ABS).

The fundamental setup of a TMR device is illustrated in Fig. 7.5. An electrically insulating tunnel barrier layer, usually from Al oxide and about 1 nm thick, is situated between two ferromagnetic layers. The lower layer is hard magnetic with a pinned direction of magnetization. This pinning is realized by an additional antiferromagnetic layer directly deposited on the substrate. The upper ferromagnetic layer is soft magnetic, that means its magnetization is free and can follow an external magnetic field.

The tunnel current I and therefore the TMR depend on the magnetization direction of the free layer concerning the pinned layer. The TMR becomes maximal for antiparallel alignment and minimal for parallel alignment. This explains the represented switching behavior with increasing magnetic field: the soft magnetic layer switches first, causing an antiparallel alignment and therefore a high TMR. Further increase of the magnetic field results in switching of the hard magnetic layer. Because of the parallel magnetization the TMR decreases again.

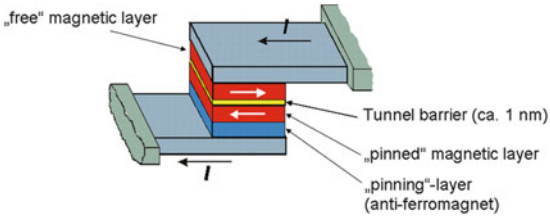

Fig. 7.5 Fundamental setup of a tunnel magnetoresistance device

Both the TMR ratio and the switching behavior strongly depend on the nanoscopic quality of the barrier layer and the magnetic layers [10]. Relevant questions for nanoanalytical investigations at TMR stacks are:

1. The uniformity of the tunnel barrier layer. Neither short circuits nor high-interface roughness are allowed.
2. The barrier quality on the edges of TMR dots, down to only some nanometers in size.
3. Element concentration profiles on a nanometer scale, influencing the magnetic behavior.
4. The morphology, nanostructure, and chemical composition of the pinning layer, which influence the switching characteristics.

The main characterization method to answer these questions is analytical transmission electron microscopy (ATEM) in combination with cross-section preparation by focused ion beam (FIB, see Sect. 5.4) technology. It combines the possibility of TEM imaging with chemical analysis at very high spatial resolution in the nanometer range [11].

The tunnel junction stacks were prepared by two different techniques [11]:

- Deposition onto cooled oxidized Si wavers by e-beam evaporation
- Deposition in an UHV sputter chamber with DC magnetron sources

Cross-section specimens were produced by TEM lamella preparation with focused ion beam (FIB) technique under 30 keV Ga^+ ion beam bombardment (Fig. 7.6).

The ion beam sputters material from both sides of a layer stack until a residual lamella of some 10 nm thickness remains. This lamella is shielded by a thin Pt film mask, and it can be transmitted perpendicularly by the TEM electron beam. That means a cross section of the layer stack is imaged.

Waviness and interface roughness of the layer stacks result in the formation of magnetic poles at the barrier interfaces, which lead to unwanted magnetic coupling between the two ferromagnetic electrodes [9]. High-resolution TEM micrographs allow the quantitative investigation of the interface roughness by the study of thickness fluctuations of the amorphous (Al–O) tunnel barrier layer, which is localized between the metallic layers from Co and from Permalloy [Py, i.e., Ni (80 wt%)–Fe(20 wt%)]. In Fig. 7.7, the uniformity of the tunnel barrier layer is demonstrated from mass thickness image contrast. Its mean thickness and standard deviation can be measured as width in the TEM micrograph. The mean thickness

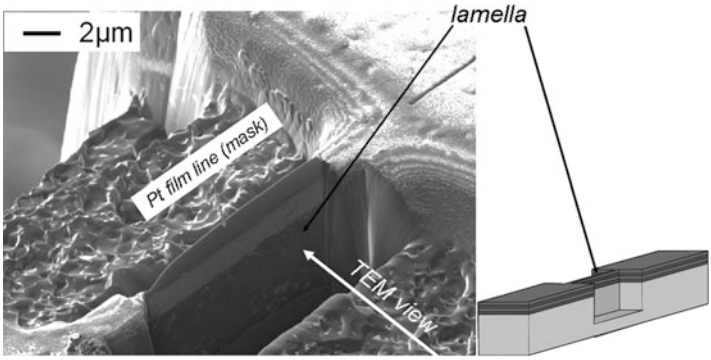

Fig. 7.6 Preparation of a TEM lamella with focused ion beam (FIB) technique

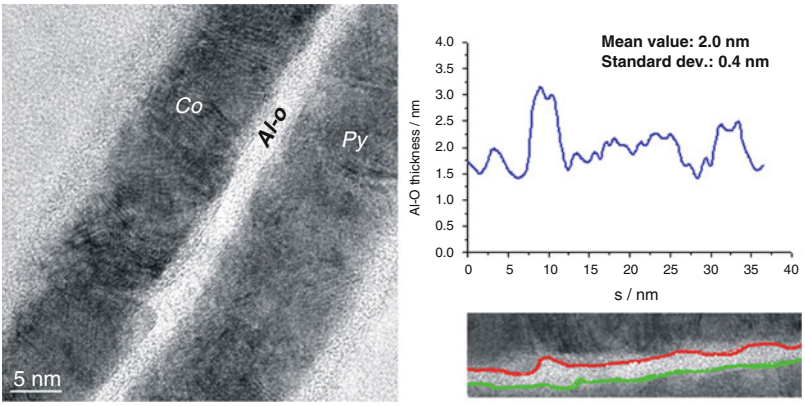

Fig. 7.7 Uniformity of a (Al–O) tunnel barrier between the two metallic layers Co and Permalloy respectively [11]; *left*: HRTEM micrograph, *right*: quantitative thickness fluctuations

amounts to 2.0 nm with a standard deviation of 0.4 nm. High-resolution TEM micrographs as in Fig. 7.7 need specimens thinner than 20 nm. This can be reached by a carefully focused ion beam preparation.

To reach a high-memory density in MRAM devices, the elements must be very small. Therefore MRAM devices are used in the form of dots down to only a few 100 nm in size [11]. The quality of tunnel barrier layers at the edges of these dots is a critical point, because short circuits at the edges may cause unwanted, uncontrollable tunnel currents and can therefore lead to a failure of the MRAM device. Figure 7.8 shows the TEM overview of a TMR in cross section, demonstrating the efficiency of focused ion beam cross section preparation. This gives the advantage of a constant film thickness [12]. To avoid mechanical curvature of the layers they are supported by special support bars in the FIB window, as can be seen in Fig. 7.8.

The quality of tunnel barrier layers at TMR dot edges was studied in detail by high-resolution TEM and analytical TEM (Fig. 7.9). Figure 7.9a gives an overview

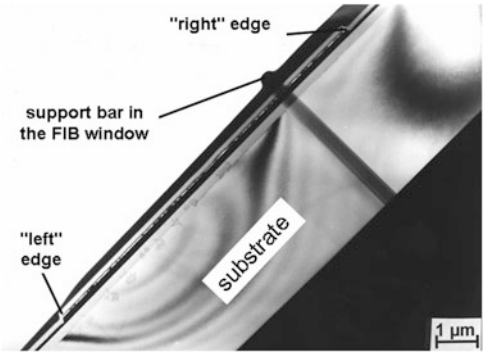

Fig. 7.8 Quality of the barrier layer at the edges of TMR dots, studied by a TEM brightfield micrograph [11]

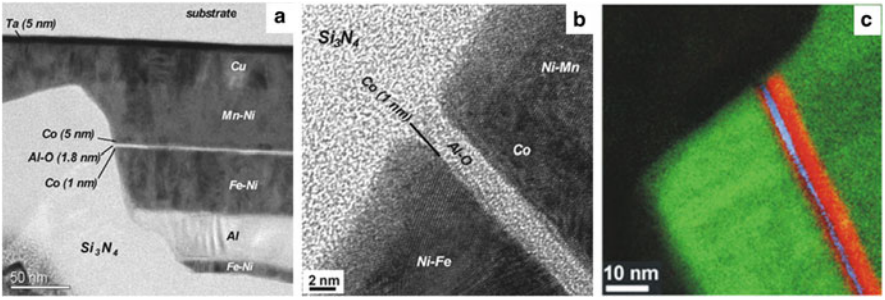

Fig. 7.9 Quality of the (Al–O) barrier layer at the edge of a TMR dot (**a**) TEM overview micrograph, (**b**) HRTEM image of the (Al–O) barrier, (**c**) energy filtered, colored and overlaid images of Ni (*green*), Co (*red*), O (*blue*)

of a typical layer stack with Mn–Ni as pinning and Co as pinned magnetic layer, followed by the Al oxide (Al–O) barrier layer. Permalloy (Fe–Ni) works as free magnetic layer. To stabilize the dot structure, the trenches have been filled with silicon nitride Si_3N_4.

Both the uniformity of the barrier layer and the absence of short circuits at the dot edge are demonstrated in the high-resolution TEM image of Fig. 7.9b. Unfortunately, the 1 nm thick Co cap layer between the barrier (Al–O) and the Permalloy layer cannot be distinguished. This Co cap could be uncovered by energy-filtered TEM imaging (Fig. 7.9c). This technique is based on energy losses of the imaging electrons by inelastic interaction with specimen atoms [13]. By filtering element-specific energy losses, the local element distribution can be imaged. The contrast of such energy-filtered images can be improved by a subtraction of the non-specific intensity background created by ionization losses and interband transitions [14]. By choosing to Co-L edge in the electron energy loss spectrum at 779 eV the only 1 nm thick pinned Co layer is clearly visible as a thin red bar (Fig. 7.9c).

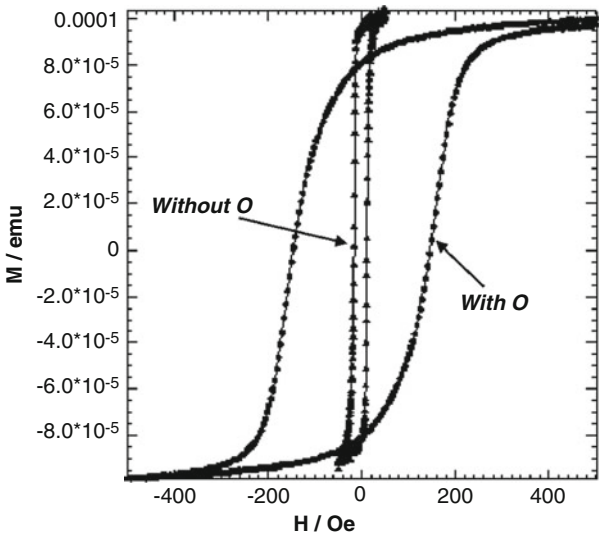

Fig. 7.10 Hysteresis curves of thin Co layers with and without oxygen content [11]

The magnetic behavior of TMR layer stacks is decisively influenced by the chemical purity of the individual layers. Especially the trilayer stack Co/(Al–O) barrier/Permalloy is of interest. One special problem is to avoid the possible oxygen content within the Co layer. The penetration of oxygen can be a consequence of the barrier formation, and it influences the TMR-switching behavior negatively, leading to unwanted, uncontrollable, harder magnetic properties. This is demonstrated in Fig. 7.10, showing the hysteresis curves of two samples with and without oxygen in the Co layer. The Co layer with oxygen is magnetically harder [11].

The local distribution of oxygen concentration can be controlled by energy-filtered TEM images (EFTEM). As an example, the result from such a TEM and EFTEM analysis of the magnetically harder Co layer is shown in Fig. 7.11. Even from the EFTEM oxygen distribution mapping (Fig. 7.11b), remarkable oxygen content within the Co layer is visible. More quantitatively this result follows from the oxygen intensity along the red line of the EFTEM map (Fig. 7.11c), averaged over the whole image width, as from the small oxygen peak within the Co layer.

These EFTEM results basing on electron energy losses (EELS) were confirmed by photoelectron spectroscopy (XPS) of AlO_x barrier layers on a Co support [11]. For depth profiling, the sample was sputtered with 3.5 keV Ar^+ ions under 30° incidences to the surface normal and under UHV conditions to avoid a layer oxidation. Between the sputter steps, XPS spectra were taken in the energy range from 55 to 80 eV, enclosing the Al 2p and the Co 3p care-level peaks (Fig. 7.12). The top of Fig. 7.12 shows a comparison of the XPS spectra of a partially oxidized (Al–O) barrier layer (broken line) and of a completely oxidized (Al–O) barrier as that from Fig. 7.11 (full line). In the broken line spectrum a small peak at 72.5 eV—characteristic for Al—can be seen, whereas the full line spectrum does not show

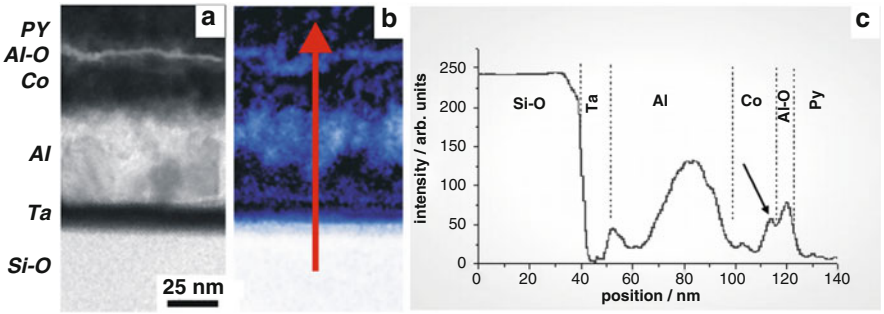

Fig. 7.11 TEM cross-section imaging and EFTEM of a TMR layer stack with the magnetically harder Co film, enriched with oxygen [11]. (**a**) TEM brightfield image, (**b**) oxygen map by EFTEM, (**c**) intensity profile of the oxygen map along the *red arrow* (averaged vertically over the total image height)

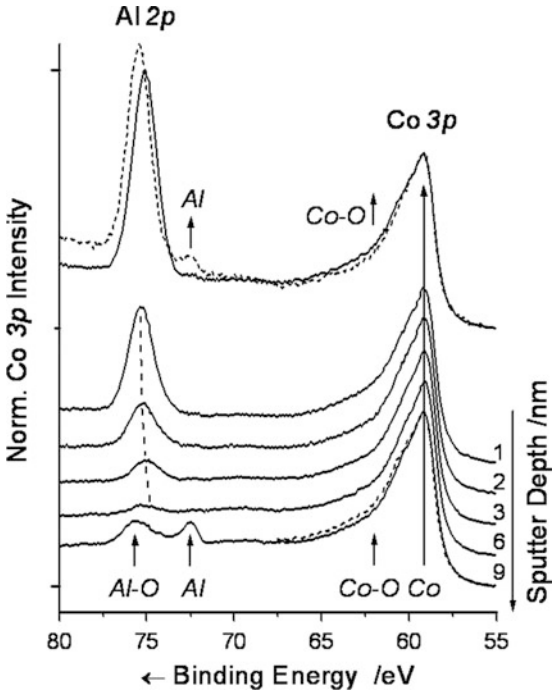

Fig. 7.12 Photoelectron (XPS) spectra of the TMR layer stack of Fig. 7.11 [11]. *Top*: comparison of (Al–O) barrier layers after different oxidation states; *bottom*: spectra in different sputter depths (3.5 keV Ar^+ ion sputtering)

elemental Al but a small shoulder at about 62 eV, typical for (Co–O) bonds. This signal comes from the partially oxidized supporting Co layer beneath the (Al–O) barrier, due to the information depth of some nanometers.

The lower part of Fig. 7.12 shows XPS spectra in different sputter depths. The Al 2p peak at 75 eV in the first spectrum shows (Al–O) within the barrier layer. Its intensity decreases with increasing sputter depth, and simultaneously the Al 2p peak shifts to lower bonding energies (broken line) because of the neighborhood of the metallic layer [15]. The Co 3p signal is present in all sputter steps because its information depth is high enough (about 4 nm). In the lowest spectrum of Fig. 7.12 the information depth reaches the lower Al layer, which is partially oxidized. The Co 3p peak of this spectrum shows less (Co–O) signal intensity than the spectrum from the Co/(Al–O) interface on the top. The Co 3p peak from the unsputtered sample is overlaid with a broken line. From these curves, it can be concluded that Co immediately below the (Al–O) barrier is more strongly oxidized than the remaining layer. This result is in good agreement with that of the analytical TEM investigations [11].

By the following ion beam techniques:

- DC magnetron sputtering for TMR stack deposition
- FIB cross-section preparation for TEM investigations
- Ar^+ ion depth profiling of TMR stacks for XPS concentration spectra

both the structural and compositional properties of TMR devices could be investigated on a nanometer scale. As an important result, it was found that an overdose of oxygen leads to oxygen diffusion in the TMR layers beneath the insulating (Al–O) barrier layer and to an uncontrollable magnetic hardness of the TMR device.

7.2 Ion Beam Analysis in Art and Archeometry

Ion beams provided by small particle accelerators with terminal voltages of several MV play an important role in the field of applications to cultural heritage (e.g., for material analysis and dating). Demands on analysis of historical objects are quantitative, multielement and nondestructive investigations with detection limits down to trace elements. The materials analysis in archeometry is mainly motivated to get insights into technological skills in the past and to find sources of supply of raw materials. Furthermore, questions of indirect "dating," attributions, authentications (or discovery of forgeries) have to be solved and prerequisites for compatible and reversible restoration techniques are often desired.

At present, for the nondestrucive analysis of the sample composition two radiation-induced analytical techniques have been established: X-ray fluorescence analysis (XRF) and ion beam analysis (IBA). In the case of XRF, the detected characteristic X-rays are excited by an appropriate X-ray source, whereas for IBA the emission of characteristic X-rays is excited by high-energy ions, in most cases by protons (1–4 MeV) and the corresponding analytical techniques are particle induced X-ray emission (PIXE) and particle induced γ-ray emission (PIGE). PIXE allows the simultaneous measurement of all elements above sodium ($Z > 14$). Due to the low background produced by the PIXE process, the sensitivity can reach the µg/g level. The emission of γ-rays resulting from nuclear reactions

between the incident protons and the nucleus of target atoms happen on light target nuclei, and the PIGE method usefully extends the PIXE bulk characterization to elements lighter than sodium ($Z \leq 14$), such as Be, B, or F. Simultaneous measurement of backscattered ions (RBS—Rutherford backscattering spectrometry) can clarify the near-surface composition, i.e., provide information on the uppermost paint layer, varnish film thickness, etc. The basics, techniques advantages, and drawbacks of these methods are described in detail, for example in [16–18]. Most important similarities and distinctions of both X-ray methods, XRF and PIXE, are described, for example, in [19, 20]. Recently, the XRF has been increasingly applied in archeometry and arts because at present, portable (hand-held) instruments for on-site composition analysis are available on the market.

Compared to XRF, IBA methods can be advantageously combined in one-measuring setup where PIGE extends the analytical possibilities for light elements and RBS the possibilities of depth-dependent information about materials composition. In spite of the difficulties encountered for analysis of cultural heritage and many archeological objects as fragile samples, IBA measuring setups with an external ion beam were developed enabling nondestructive analysis without sampling in air [21, 22]. The external beam can be considered as the cornerstone of the adaptation of IBA to this field since it perfectly matches the noninvasive and nondestructive character of analysis. The major benefits of the external beam are:

- It allows the analysis of objects with any size and shape
- It avoids the alteration due to vacuum (dehydration, outgassing, etc.)
- It reduces the risk of heating and beam-induced damage
- It eliminates the need of sample preparation such as the deposition of conductive coating
- It improves system efficiency by simplifying external sample positioning and changing

A detailed review of the advantages and limitations of external beams has been published by Mando [23]. In a typical IBA setup with an external proton (Fig. 7.13) used for analysis of paintings, paper, and other flat objects [24], the proton beam leaves the vacuum tube through a thin foil (e.g., 2 μm thick HARVAR foil) into a nozzle around which the different photon and particle detectors are arranged as close as possible to the beam spot on the sample surface. The nozzle is adjusted closely to the object and its inner volume is flooded by a helium atmosphere which:

- Reduces the energy loss and straggling of protons as well as the beam divergence from the foil to the object surface
- Reduces the attenuation of low-energy X-rays which are emitted from light elements
- Avoids X-ray emission from argon in air (Ar-K_α: 2.958 keV)
- Results in a better heat removal by the He stream protecting temperature-sensitive objects against damage

He gas may escape only from the end of nozzle, which is at a distance of 0.1–0.3 mm from the object during measurement. Graphitic linings inside the terminal vacuum tube and along the 11 mm-long proton path through the pipe prevent the beam halo from striking the stainless steel. X-rays from elements with

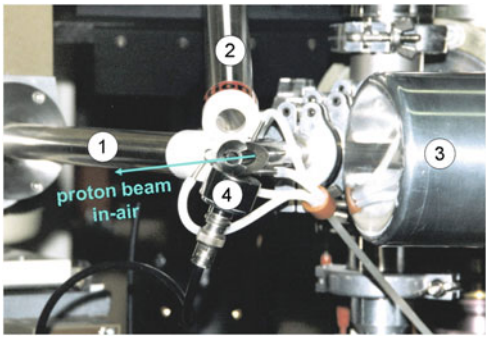

Fig. 7.13 External proton beam facility and detector arrangement at the HZDR 6 MV Tandetron accellerator with (1) first 12 mm^2 Si (Li) detector for registration of low energy X-radiation $E_x > 1.3$ keV and (2) second 80 mm^2 Si(Li) detector for detection of X-rays of higher energies $E_x > 5.9$ keV for PIXE analysis, (3) high-purity Ge-detector for light element ($Z < 14$) PIGE analysis and (4) silicon particle detector for RBS analysis. Objects are positioned in front of the nozzle exit (Photo HZDR)

$Z > 14$ are measured at 135° backward angle by means of a conventional Si(Li) detector (12.5 mm^2 active area, $\Delta E = 170$ eV at 5.9 keV, detector (1) in Fig. 7.13). On the non-vacuum side, the entrance window of this detector is coupled to the He flow for registration of low-energy X-radiation $E_X > 1.3$ keV. The second Si(Li) detector [detector (2) in Fig. 7.13] with a large active area of 80 mm^2 and a 12.5 μm Be entrance window records X-rays with higher energies $E_X > 5.9$ keV and is positioned at 148° backward angle. It detects X-rays passing through a 17 mm-distance of the He atmosphere, a thin adhesive tape, and an air gap of 26 mm. The PIXE detector (2) allows the efficient detection of K-radiation of heavier elements at low-proton beam currents $I_p \sim 200$ pA with 1 mm^2 spot size and therefore the examination of very delicate art objects.

The backscattered protons are detected also at 135° using a light protected and cleanable silicon particle detector (Canberra CAM PIPS, 100 mm^2 active area, 300 μm depletion depth, $\Delta E = 30$ keV at 5.4 MeV particle energy). Light element ($Z < 14$) analysis takes place by PIGE using a large volume HPGe detector of 60 % relative efficiency ($\Delta E = 1.9$ keV at 1.33 MeV). The characteristic γ-radiation can be detected from the rear of the object or, using another special exit pipe, at 128° backward direction which is used, for example, for analysis of historical glass objects [25, 26]. The choice of geometry depends on the type of material as well as the thickness and shape of the individual object. PIGE only works for some light elements (B, Mg, Na, Al, Si) which are of special interest for distinguishing different types of modern and historical glasses [27]. Light element analysis via PIXE has the advantage of high X-ray production cross sections. However, target self-absorption of the very low-energy X-radiation limits the applicability to small depth regions or to the object surface.

Typical measuring parameters using 4 MeV H^+ ions with an ion beam current $I = (0.2–2.0)$ nA and a beam spot size of $A = 1$ mm^2 under He flooding are an

Table 7.1 Usable proton-energy densities depending on art materials with resistances to damage at 4 MeV H^+ ion irradiation

Object	Beam spot area (mm^2)	Proton beam current (nA)	Beam current density (nA mm^{-2})	Acquisition time (s)	Energy density (mWs mm^{-2})
Metal*, ivory	1 × 1	20	20	120	10,000
Painting (varnish)	1.5 × 1.5	2	1	30	100
Water color (paper)	2 × 2	1	0.2	5	5

*Higher H^+ ion current densities and acquisition times do not affect metallic objects, however high counting rates are the limiting factors.

analyzing depth of (0–150) μm for PIXE/PIGE analysis and (0–20) μm for RBS depth profiling. In IBA tools with an external ion beam, the usually large objects can be positioned over a large area with high reproducibility and an accuracy of ±0.2 mm with respect to the location of the beam spot and the object. Typical measuring times are in the order of 30 s up to 5 min leading to relatively short exposure times without remarkable ion beam-induced changes of the sample. The exposure increases if the information depth is varied for depth-dependent studies which record a series of spectra at different proton energies on one and the same lateral surface position. As outlined in Table 7.1, the energy density which may be introduced during proton irradiation without any visible effects of damage varies by orders of magnitude depending on the material composition which has to be analyzed.

The combined PIXE/PIGE allows a sensitive high-resolution elemental analysis of main and secondary elements with comparable detection limits for all elements with atomic numbers in the range $5 < Z < 83$. The IBA analysis of art and archeological objects is limited due to examinations in laboratories at stationary ion accelerators. Yet, the method does not give information about chemical bond states and composition of organic materials, for which only their presence in the object can be detected.

Over the last 25 years, about 20–25 IBA setups with external beams were installed worldwide and used for characterization of painting matter and in the archeological domain. Most of these installations are equipped with PIXE and with simultaneous PIXE–PIGE and RBS detector arrangements. However, from the current literature, it can be seen that only a few of them have a regular activity in this field. The only one exclusively dedicated to works of art and archeology until now, is the IBA facility located in the Louvre with the most extended IBA setup AGLAE (an acronym for Accelerateur Grand Louvre d'Analyse Elementaire) at the Centre for Research and Restoration of the Museums of France located in the Louvre palace in Paris [28, 29]. External beam setups have reached a high level of sophistication, but still some progress is needed to render accelerator-based methods more systematically and routinely applied to the study of our cultural heritage. Typical applications of IBA with an external ion beam for the

determination of chemical elements in cultural heritage items are the analysis of painting, graphics, and pigment materials, of porcelains and ceramics, of paper documents and books, as well as of varity of different historical glasses and metals.

Paintings represent one of the most complicated and unique art objects. Cross sections always show pigmented multilayer structures, and typical layer thicknesses are in the order of some microns up to some 100 μm. The minimum lateral dimensions of structures amount to tenths of millimeters. On the one hand, paintings are highly vulnerable and a guaranteed nondestructive diagnosis is required for the sensitive ground materials such as paper materials and the surface-passivating organic varnishes. In the case of historical paintings, the substantial and structural analysis of details of paint layers, e.g., pigments and binding media, are helpful and necessary to:

- Distinguish between originals and forgeries
- Obtain information on the original and later additives
- Support statements on the age and the provenance
- Understanding aging phenomena
- Optimize conservation and restoration techniques

For this purpose necessary informations are related to (1) the identification of chromophoric constituents and additives in painting materials, (2) the determination of layer structures and thicknesses of varnishing glazes, and (3) the determination of chemical layer compositions. For example, the combination of external PIXE and PIGE has been applied to analyze oil paintings, taking advantage of the rapid analysis to study many spots on a Dutch altar piece dated ca. 1,500 A.D. to identify the different pigments, thus providing a good knowledge of the painting techniques [30, 31]. To get a good knowledge of the pigment palette of Caspar David Friedrich, two of his works have been examined: (1) "Zwei Männer in Betrachtung des Mondes" (1819/1820) and "Gebüsch im Schnee" (1828) [32]. As a typical example for investigation of pigment concentration and distribution in painting layers, Fig. 7.14 shows the analytical setup at the Rossendorf 5 MV tandem accelerator placed in front of the retable "14 Nothelfer" from Lucas Cranach the Elder (1472–1553) [24].

From detailed PIXE and RBS spectra shown in Fig. 7.15a–c, it was concluded that PIXE analysis of the painting "14 Nothelfer" of Lucas Cranach the Elder confirms the elements of a typical pigment pallet of the early sixteenth century and the results agree with those published earlier for two other paintings of Lucas Cranach, "Porträt einer jungen Frau" and "Lucretia" [33].

The PIXE spectra in Fig. 7.15a show the main elements Hg, Pb, and Ca, secondary elements K and Fe, as well as Cu and Zn impurities. The details of PIXE spectra in Fig. 7.15a taken from the red robe show, with increasing proton energy there is a strong increase of the Pb-L/Hg-L peak ratio. This has been interpreted that the element Pb must be attributed to an inner paint layer, and the element Hg must be located on the top layer, which means that Cinnobar (HgS) was painted on lead white ($PbCO_3 \cdot Pb(OH)_2$) or minimum (Pb_3O_4). The assignment of Pb to an inner lead white or minimum cannot be decided from the PIXE spectra. The RBS spectrum in Fig. 7.15b also taken from the red robe shows the heavy

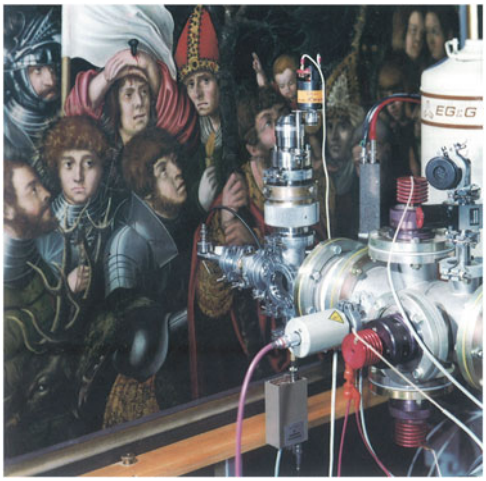

Fig. 7.14 Photograph of Lucas Cranach the Elder's painting "14 Nothelfer" positioned in front of the external proton beam facility. The beam nozzle excites points to the *red robe* of the holy Christophorus

element Hg plus the light elements O and C, superimposed by the He signal from the gas stream. The marked element surface energies were determined by calibration measurements. As can be seen, the Hg surface signal shifts towards lower energies due to proton energy loss within an uppermost varnish-coating layer. This shift allows to estimate the thickness of the varnish coating. From the technical point of view, it was of interest to clarify whether the lead white pigment ($PbCO_3$) of the flag and the adjacent dark background border in the upper part of Fig. 7.14 overlap each other. The result of proton energy-dependent PIXE analysis showed a layered arrangement of black pigment on lead white with the maximum concentration of Pb in the lead white of the flag. Furthermore, RBS spectra simultaneously measured on the white flag and on the adjacent black background (Fig. 7.15c) show that the black pigments consist mainly carbon. Again, the Pb surface signal shift indicated in Fig. 7.15c is caused by the uppermost varnish layer. With the same external beam setup several painting objects have been investigated, results of which were published elsewhere, for example, in [34, 35]. The analysis technique was also applied to study reverse painting on glasses regarding the knowledge of special painting techniques and the necessity of preventive conservation [36]. PIXE at different proton ion energies (differential PIXE) has been used for the analysis of paintings of great masters like Leonardo [37], Antonello da Messina [38], and Vasari [39]. These examples of IBA investigations allowed not only to reconstruct the color palette used by the artists but also to answer more difficult and detailed questions asked by the art historians and restorers.

Historical glass objects are another important art domain which has been intensively investigated because glass surfaces are sensitive to aging processes even under air conditioning in museums. Decomposed glass surfaces are the

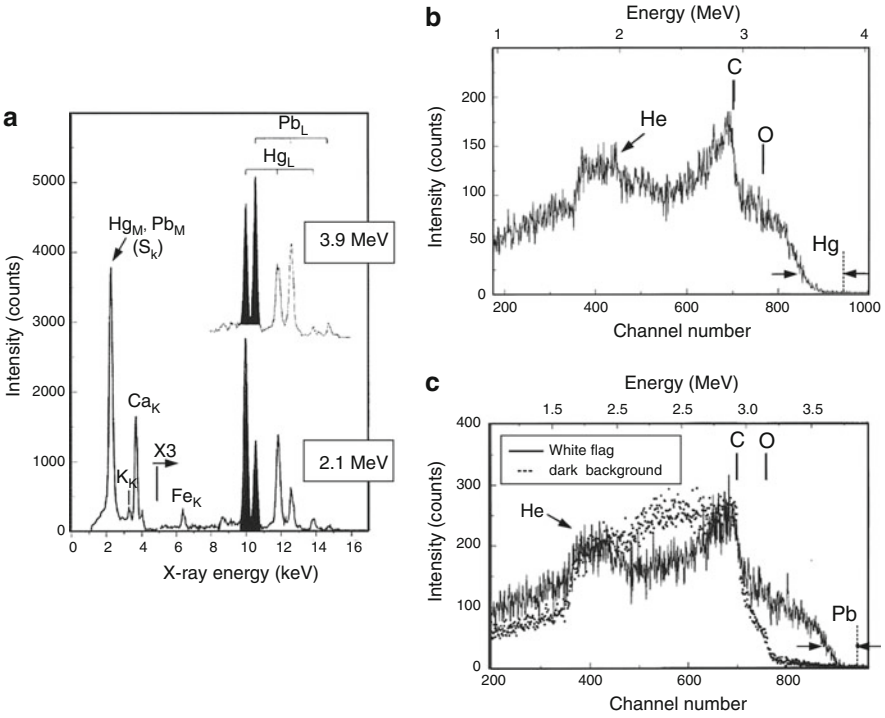

Fig. 7.15 (**a**) PIXE spectra obtained from the *red robe* of the holy Christophorus (see Fig. 7.14). The *dark peaks* represent the L_α lines of Hg and Pb for two proton energies 2.1 and 3.9 MeV. (**b**) RBS spectrum ($E_p = 3.9$ MeV) from the *red robe* of holy Christophorus (see Fig. 7.14). (**c**) RBS spectra ($E_p = 3.9$ MeV) obtained from the retable shown in Fig. 7.14. The *full line* represents the spectrum taken from the *white flag* and the *dotted line* the spectrum taken from the position of the adjacent *dark background*

consequence of chemical processes, which take place between the silicate network and the humidity of the ambient atmosphere. In particular, potassium–calcium–-silica glasses can significantly be affected, where the degradation takes place via ion exchange reactions, where potassium and calcium are leached out and hydrogen-bearing species are incorporated into the silica network structure. Typical layer thicknesses are in the range of a few nanometers up to some 100 µm. Simultaneous use of ion beam methods of PIXE, PIGE, and RBS were successfully used to determine both the glass corrosion state as well as the composition of the bulk glass [40, 41]. Investigations were done on test glasses, the composition of which was comparable with relevant historical glasses, for example, on a potassium–calcium–silica glass with 60 % SiO_2, 25 % CaO, and 15 % K_2O (concentration in weight%). The natural weathering of this glass was simulated by treating the freshly polished glass specimens in a 0.1 mol HCl-leaching solution at room temperature where the times varied between 90 min and 195 h. After 195 h chemical treatment drastic losses of K and Ca are visible from the reduction of the

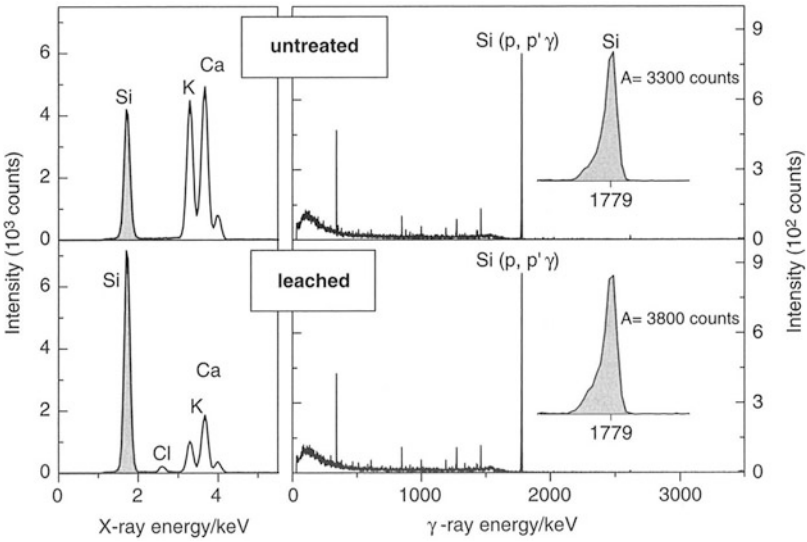

Fig. 7.16 PIXE (*left*) and PIGE (*right*) obtained from the potassium–calcium–silica glass at $E_p = 3.9$ MeV proton energy before and after chemical treatment, see text. The Si γ-lines are zoomed to compare and evaluate the peak areas [40]

corresponding X-ray peaks (see Fig. 7.16, left) whereas the intensity of the Si peak increases indicating the growing surface layer enriched with Si and depleted by K and Ca. The γ-ray intensity (see Fig. 7.16, right) shows only a slight increase by ~10 %. This confirms that the most PIGE information depth is large compared to the thickness of the leached surface layer.

The Si concentration values deduced from the PIXE and PIGE spectra as a function of the corrosion layer thickness are compared in Fig. 7.17. For PIXE, two regions can be distinguished: (1) a proportional region, $d < 6$ μm, where the leached layer plus the unaffected glass bulk contribute to the signal and (2) a saturation region in the case of thicker corrosion layers. The corresponding curve obtained by PIGE analysis imparts that corroded surface layers at $d < 3$ μm do not falsify the Si concentration value of the bulk glasses given by PIGE. From this kind of leached layer investigations the conclusion was done that the concentration ration $C_{PIXE}(Si)/C_{PIGE}(Si)$ is an informative indicator for the corrosion sate of aged glasses as found in museums. Using additional RBS measurements the depth-dependent material composition of the chemically modified surface layers can be obtained [41].

As can be seen from RBS spectra in Fig. 7.18, two effects appear if the thickness increases over a critical value of $d \sim 2$ μm. The highest energy edge shifts towards lower energies and the near surface O signal increases. With increasing corrosion layer thickness, both effects become more pronounced, and they origin from progressive leaching of K and Ca and growing concentration of SiO_2 giving rise to an increased RBS signal from O and Si, which is visible only for oxygen.

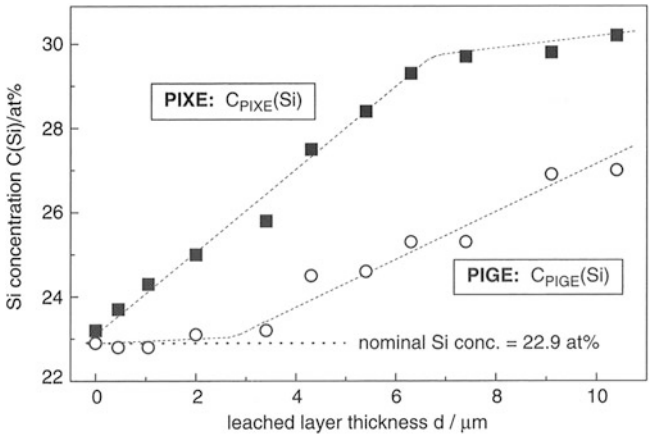

Fig. 7.17 Si concentration in at.% of a potassium–calcium–silica glass deduced from PIXE and PIGE measurements in dependence on the thickness of the surface modified by leaching, see text

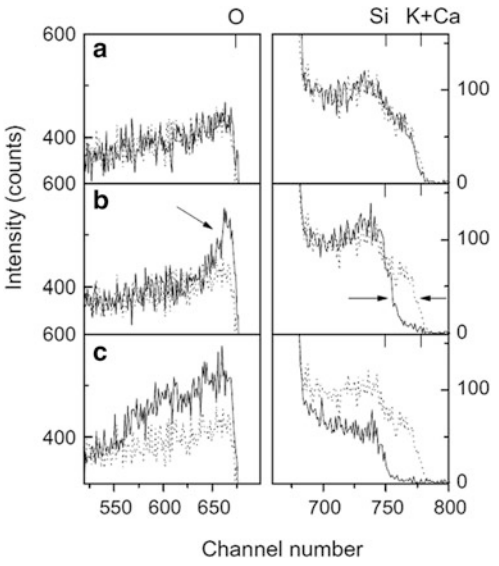

Fig. 7.18 RBS spectra (regions of interest) obtained from a potassium–calcium–silica glass before (*dotted lines*) and after (*full lines*) chemical treatments for different time durations: (**a**) 90 min, (**b**) 20 h, (**c**) 195 h which cause surface layer thickness of (**a**) 0.45 µm, (**b**) 3.4 µm, (**c**) 10.4 µm, respectively. The *arrows* in example (**b**) indicate an enhanced concentration of oxygen as well as a shift of the high energy K + Ca edge

The replacement of leached K and Ca by penetrating O (and H) atoms from the surrounding humidity amplifies the increase of the oxygen RBS signal. The presence of H with a concentration $C_H \sim 10$ at.% in the leached layer was confirmed by

independent NRA analysis [42]. From this, it has been generalized that modified glass surface regions consist of SiO_2 + 10 at.% H, where the glass network modifiers K and Ca are almost completely leached out. Based on the fundamental understanding of glass exposure to the ambient atmosphere and the chemical composition of the historical glass conclusions related to the endangerment of precious objects by corrosion can be given. Furthermore, from the measured composition of the glass indications concerning art historical classification (origin, age, glass recipe, and fabrication technique) can be attained. Historical glass objects were investigated and characterized, for example, iridescent art nouveau glasses in [25, 43, 44], stained glasses [26, 45], and archeological glasses [46].

Historical objects of *pottery, earthenware or stoneware*, *ceramics*, *and porcelain* are a part of cultural heritage, which has been also intensively investigated by IBA with an external ion beam. For example, historical objects made from stoneware by Johann Friedrich Böttger were analyzed in the last 15 years. In the early eighteenth century, on the track to the invention of famous European hard porcelain, J.F. Böttger succeeded first in the production of "red porcelain" or "Jaspis porcelain," the so-called Böttger stoneware. In comparison to other ceramics, Böttger stoneware is characterized by a high-material density, consequently high hardness, and the suitability for surface polishing. Böttger reached these excellent properties by using basic mass of very high quality and a special high-temperature burning procedure. His first red stoneware body (1706–1707) was similar to the wares produced in Yixing, China (Yixing stoneware). Recently, the authenticity of a number of "Böttger" objects in various museums and private collections in North America and Europe has been questioned. To aid in resolving these questions several nondestructive analytical techniques have been employed, the most important being PIXE [47, 48].

Concentration ratios of main and secondary elements in stoneware of different origin obtained by PIXE are suggested to show characteristic "fingerprints" for the different provenance of stoneware. In the present case for PIXE, analysis of "Böttger stoneware" objects (see Fig. 7.19) was performed using the external proton beam of the 5 MV Rossendorf Tandem accelerator. The ion energy on the object was $E_p = 3.85$ MeV and the ion current density $j_{ion} \approx 0.2$ nA mm^{-2}. For good statistics in the peak areas in the PIXE spectra for main elements of Al, Si, K, Ca, Ti, and Fe, an irradiation time of about 1–2 min is sufficient. However, even a measuring time of 5 min is insufficient for reasonable statistics in the signals of trace elements. This is demonstrated in Fig. 7.20, which gives typical X-ray spectra as obtained from a brown, unpolished Pilgrim bottle of Böttger stoneware. Therefore, in the present studies of PIXE, analysis for the evaluation of material characteristic "fingerprints" was restricted mainly to the main elements in the stoneware.

Figure 7.20a shows the low-energy (1–8 keV) spectrum of main elements Al, Si, K, Ca, Ti, and Fe, and Fig. 7.20b shows the spectrum at higher energies (8–18 keV) of trace elements of Cu, Zn, Pb, Rb, Sr, and Zr. As can be seen, the detection efficiency for the main elements in the low-energy range of X-rays is higher by a factor of about 10^3 compared to the detection efficiency of trace elements. For reliability of "fingerprints" it was necessary (1) to guarantee representative

Fig. 7.19 Tankard made from Böttger stoneware in front of the Rossendorf external proton beam setup

composition data for the given object and (2) to analyze a sufficient number of objects representative for the certain type of stoneware material. For the main material components, the concentration values were obtained from seven objects of authentic Böttger stoneware and were compared to those found in the case of single objects from China (Tea pot China) and The Netherlands (Tea pot, Ary de Milde). The results of all comparative PIXE measurements are summarized in Fig. 7.21.

The lengths of the bars reflect different concentrations measured for the seven objects of Böttger stoneware; the lowest and highest concentration values are given as numbers in Fig. 7.21a. Note that (1) the corresponding mean values are graphed in Fig. 7.21 at one and the same level of the ordinate and (2) the fluctuations are represented in percent of the mean values. As can be deduced from Fig. 7.21, there are characteristic deviations of the contents for several oxide components. Compared to Böttger stoneware both the tea pot and the tea caddy (provenance: China) show a factor of 1.3 higher Al_2O_3 concentrations and a lower level of SiO_2. Most significant is the strongly enhanced MnO concentration (a factor of 5) in the case of the tea pot. This statement, however, must be reproduced by higher statistics in the Mn K-line (see inset in Fig. 7.20a) making use of a selective chromium X-ray filter. The tea pot of Ary de Milde (The Netherlands) indicates a broader spectrum of deviating components in Fig. 7.21. Again, the MnO concentrations exceed

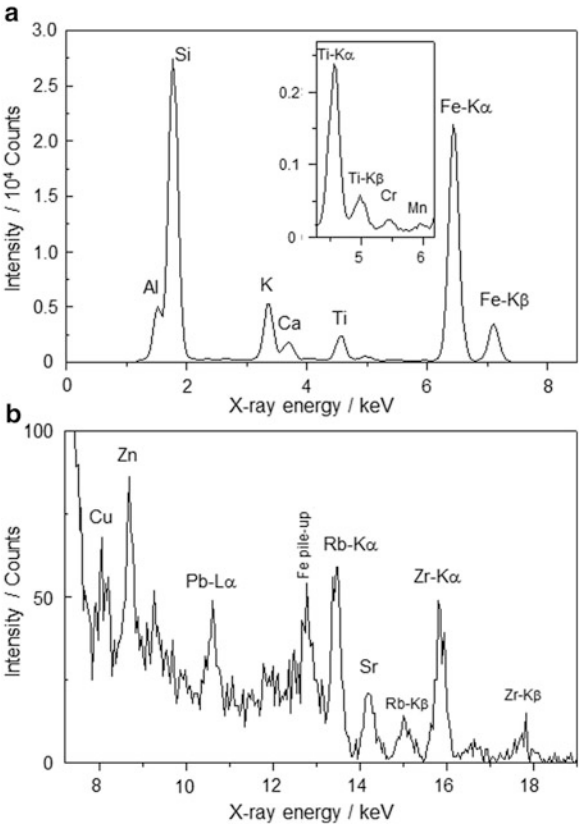

Fig. 7.20 PIXE spectra of Böttger stoneware obtained from the brown unpolished Pilgrim bottle PE 737 (porcelain collection in Zwinger Dresden). The measurements were taken with $E_p = 3.85$ MeV external proton beam: (**a**) main elements, (**b**) trace elements

those of Böttger stoneware by more than a factor of 4. But also the CaO content is a factor of 5 higher. For Al_2O_3 and SiO_2 the tea pot of Ary de Milde shows the same trend as in the case of China stoneware; in comparison to Böttger stoneware the concentrations of K_2O and TiO_2 are enhanced.

By PIXE "fingerprint" measurements, it was shown that for two private objects, a tankard and a tea pot of uncertain provenance, there was no contradiction between the PIXE analytical result and the attributed Böttger authenticity. For more reliable materials, composition data of stoneware further efforts are necessary (1) to minimize concentration fluctuations due to low statistics in the PIXE peak areas and (2) to improve the statistical accuracy for a given type of stoneware material by both examining a higher number of positions per object and including more authentic objects of given provenance.

Examining the applications of ion beam analysis in art and archeology we can conclude that PIXE is by far the most used IBA technique, sometimes coupled with PIGE. Its popularity stems from its easy implementation in air, due to the smooth energy dependence of the X-ray production rate and its high sensitivity.

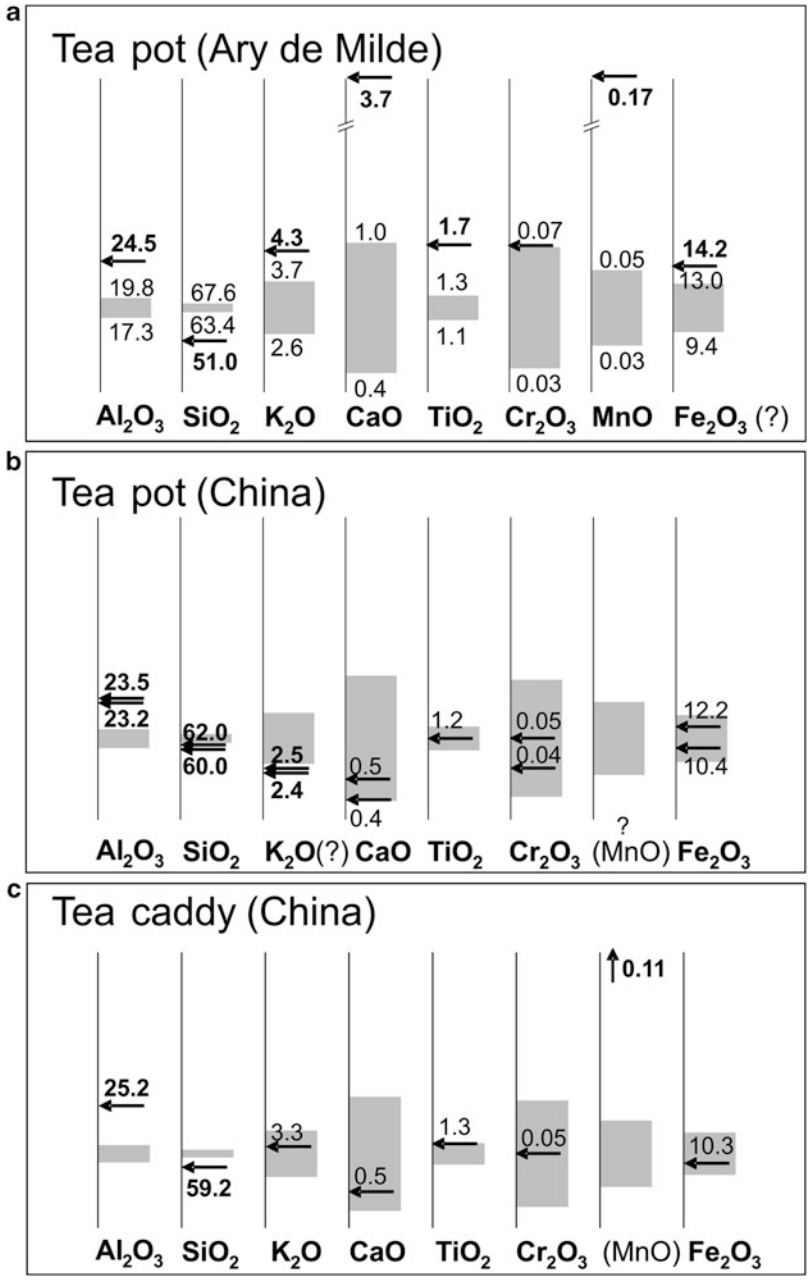

Fig. 7.21 Material compositions of main components (wt%), obtained for stoneware made in The Netherlands (**a**) and China (**b**, **c**), are graphed by *black arrows*. For comparison, the *gray bars* represent the results for seven different authentic objects of Böttger stoneware (see text). Mean concentration values for Böttger stoneware can be deduced by averaging the *upper* and *lower limits* of fluctuations given at the *bars* in Fig. 7.21a as numbers. Note that the *gray bars* are identical in Figs. 7.21a–c

IBA techniques based on the detection of charged particles (RBS, ERDA, or NRA) have been more recently applied because their more complicated implementation under air has been solved. With the ion beam techniques, identification is achieved by means of the chemical composition. Among the various ion beam analysis methods, PIXE and PIGE are the most efficient techniques for the determination of bulk target material constituents. For homogeneous samples like one thin layer on top of a substrate, such as manuscripts, drawings, or water colors in-air, PIXE represents an almost unrivaled technique for the analysis of these types of samples, e.g., the identification of papers and inks [49].

Despite its poor profiling capability, PIXE analysis has been applied to samples with depth-dependent composition such as paintings, glazed ceramics, or objects with metallic coatings by varying the energy of the incident proton beam [24], by comparing the relative intensity of different X-ray lines of the same element at a selected energy (e.g., K/L ratio or within the L series) [50], and by use of the comparative results delivered by PIXE and PIGE in the same run [41]. The best solution is to rely on RBS and NRA techniques that have intrinsic profiling abilities. RBS is even possible to distinguish between an alloy and a multilayer gilding and assign the layer ordering and thickness. RBS can be advantageously combined to PIXE for the determination of paint layer arrangement in paintings [24, 35]. As has been shown, RBS is used to evaluate the possible varnish thickness and confirms the layer thickness. NRA techniques, yielding the C, N, O depth profiles are particularly well suited, for example, for the study of patina [51].

The help of complementary techniques for the identification of art and archeological objects is sometimes needed to fully specify the material (chemical state and structure, organic materials). Portable XRF has appeared as a useful tool for direct in-museum analysis or in-museum preselection of paintings for further studies with PIXE [50]. Other techniques have been used like Raman spectrometry [52] as well as analytical SEM-EDX and LAICP-MS [53], with the disadvantage of the last two methods of taking samples from the objects and accomplishing analysis in vacuum.

7.3 Special Applications in Life Sciences

In recent years ion beams were increasingly applied in life sciences. On the one hand this is related to the nondestructive element analysis of tissues, as by ion beam-induced X-ray emission (PIXE, see Sect. 6.4.1). Furthermore, ion beams are used more and more for medical diagnostics and therapy, especially for the discreation of cancer cells.

As an example for the nondestructive element analysis of human tissue by PIXE technique, Fig. 7.22 shows microprobe element maps over a section of lung tissue from a patient suffering from hard metal lung disease [54]. Hard metals (Ti, Fe, W) and nonmetallic elements (P, S, Ca) are clearly visible with lateral resolution in the 10 μm range as well. Remarkably is the strong correlation between the lateral

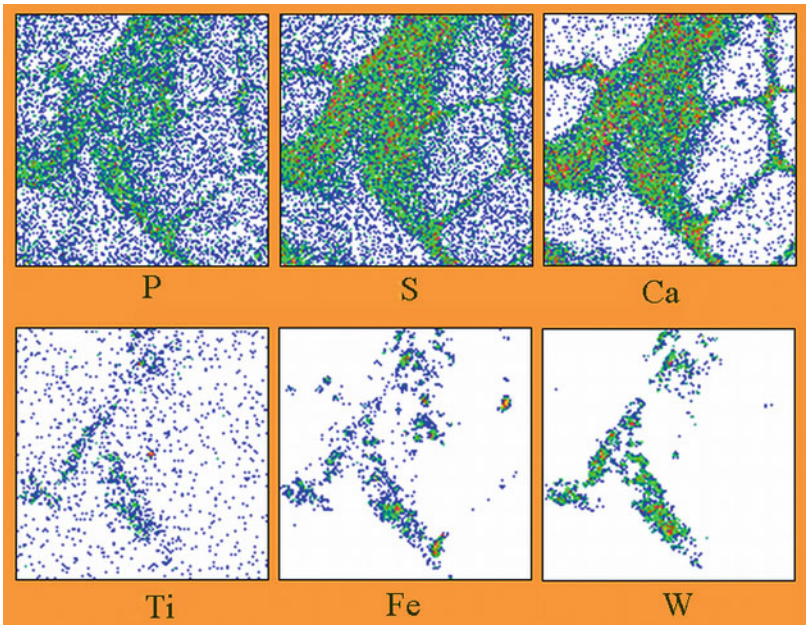

Fig. 7.22 Microprobe PIXE element maps over a section of a human lung. Scan area about 400 μm × 400 μm [54]

density distribution of the different nonmetals and also that of the discovered hard metals.

Ion beam-induced X-ray emission technique (PIXE) can be also used to determine the lateral or spatial distribution, respectively, of different elements in both healthy and tumor tissue sections, as e.g., for a hamster [55]. Copper carborane containing tetraphenylporphyrin (CuTCPH) was administered to hamsters in four doses, each of 32 μg/g, over 2 days, both to healthy and cancer-carrying animals. At day 3, the hamsters were sacrificed and tissue sections were prepared by cryomicrotome and freeze drying.

The integral PIXE element spectrum of a tumor hamster tissue is given in Fig. 7.23. It is identical with Fig. 6.33, but its content is discussed here in more detail. The tissue section bombardment was realized with heavy ^{16}O ions at an energy of 50 MeV, implemented with a Tandor accelerator. The data acquisition was carried out by scanning the beam over the sample and by writing on a list-mode hard disk file, the emitted X-ray energies along with the simultaneous x and y coordinates of the beam spot. These data can be projected onto the X-ray energy axis to produce a one-dimensional integral X-ray spectrum.

The electronic pulser peak in Fig. 7.23 is used to determine the dead-time corrections. The Cu K_α peak and those of many other elements (e.g., Fe $K_{\alpha,\beta}$, Zn

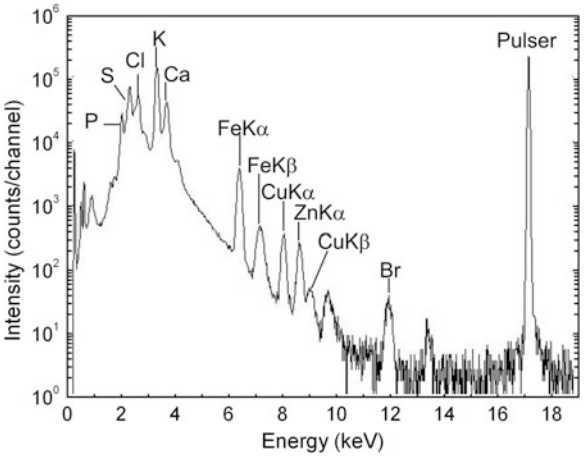

Fig. 7.23 PIXE spectrum of tumor tissue section of a hamster [55]

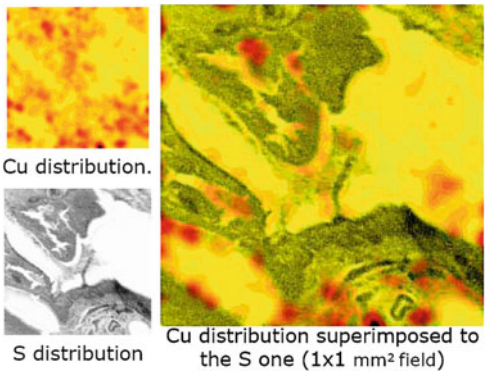

Fig. 7.24 Microdistribution of Cu and S in a hamster tissue. Area 1,000 μm × 1,000 μm [55]

K_α, K, S, Br,...) are clearly visible. By gating on discrete element lines, one can construct two-dimensional element maps which show the lateral drug distribution.

This is realized in Fig. 7.24, which gives the microdistribution of Cu and of S (left) and their superimposition (right) in a 1×1 mm^2-area of hamster cancer tissue (tumor A) [55]. The average Cu concentration in the section area imaged is about (15 ± 1) μg/g or (15 ± 1) ppm, respectively. Its lateral distribution is quite inhomogeneous and the average values vary for different tumors, as can be found from Table 7.2. As a remarkable result it follows that average Cu concentrations in tumor tissues are clearly increased compared to those in a healthy tissue section. From these results one may conclude that micro-PIXE is a powerful analytical tool

Table 7.2 PIXE measurement of average Cu concentrations in different hamster cheek pouch (HCP) tissue sections after CuTCPH drug injections [55]

Sample description	Scanned area (μm^2)	Average Cu concentration (ppm)
Healthy HCP tissue	1,000 × 1,000	5.2 ± 0.7
HCP tumor A	1,000 × 1,000	15 ± 1
HCP tumor B	1,000 × 1,000	27 ± 1
HCP tumor C	1,000 × 1,000	23 ± 1
HCP tumor D	1,000 × 1,000	10 ± 1

for the study of multielement distributions in histological sections at the few ppm level.

Some special advantages of heavy ions and also of protons result in their increasing application for tumor tissue irradiation [56, 57]. Because of the physical nature of bombarding ions, this kind of irradiation is also called particle therapy, contrary to the conventional photon radiotherapy with X-rays or γ-rays. An international research center that leads the way for ion beam irradiation of tumor tissue is Heidelberg Ion-Beam Therapy Centre (HIT) [58–60].

Ion beam irradiation is used when the conventional radiotherapy reaches its limits: either for tumors that are nearly insensitive to photons or for tumors located next to high sensitive healthy tissue that could be changed by the dangerous radiation. The special physical and biological advantages of proton and heavy ion radiation are obvious from Figs. 7.25 to 7.26.

Figure 7.25 illustrates the depth dose profiles of X-rays and ions in a biological tissue with a tumor that is located in a certain depth t. The following physical advantages of proton and of heavy ion beam radiation exist:

- High-accelerated ions can deeper penetrate into the tissue, up to some 10 cm. By this way, tumors which are located deep in the body will receive a sufficiently high radiation dose for their destruction. In contrast, the radiation dosage of X-rays that reaches deeper tumors is extenuated because of energy loss by scattering on the penetration way. Furthermore, the scattered part of energy affects healthy tissue. Contrariwise, if tumors are located near the surface the scattering process effects that the underlying tissue is damaged.
- Ions transfer their destructive energy to the tissue mainly in one "burst" just before they stop. This is the so-called Bragg peak which is visible in Fig. 7.25 as a sharp dose maximum. After that, the dosage drops quickly to almost zero, because the ions are completely stopped. Thus, the tumor is irradiated with the highest precision, sparing the surrounding healthy tissue.
- The high precision of proton and of heavy ion radiation allows the administration of a higher irradiation dosage, increasing the chances for healing. This applies especially to the case when the tissue surrounding the tumor is extremely sensitive to radiation, as for example brainmass, nerves, or eyes.

The biological advantages of protons and heavy ions—here carbon ions—compared to photons are illustrated in Fig. 7.26:

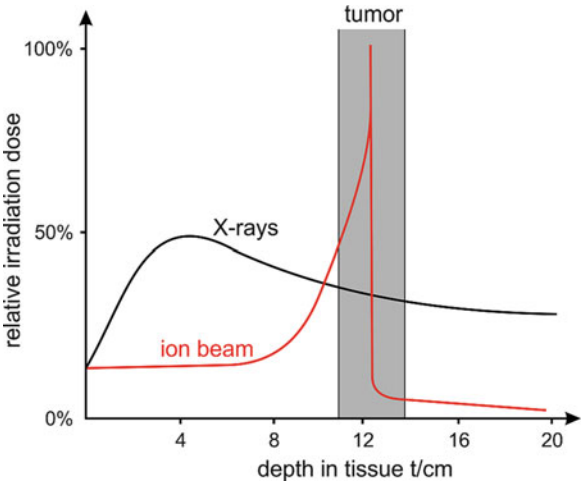

Fig. 7.25 Depth dose profiles of X-rays and ions in biological tissues

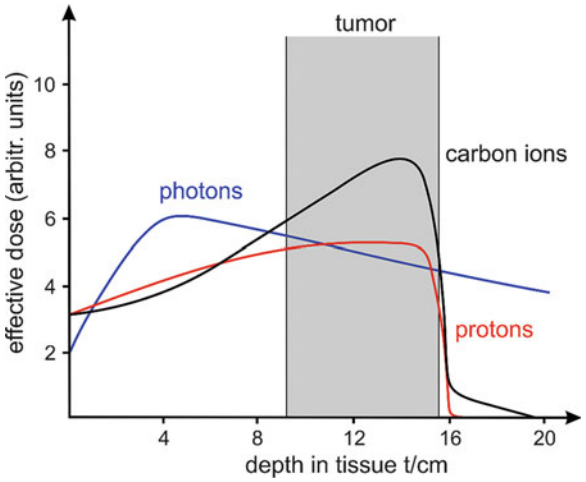

Fig. 7.26 Biologically effective dose for photons, protons, and carbon ions

- Both heavy ion and proton radiation can be arranged to have their maximum effective dose at the critical depth in tissue where the tumor is located.
- Heavy ion or proton radiation is biologically more effective, for it causes considerably more opposing breaks, so called double breaks, in the DNA. These double breaks can rarely be repaired by the tumor cell and therefore leads to its death.
- Photon radiation mainly damages cells in the cell division stage, whereas heavy ion radiation also attacks resting cancer cells or those that divide only rarely. Thus, ion beams destroy even slowly growing tumors which are almost

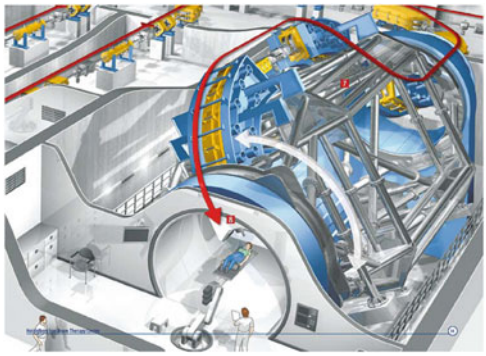

Fig. 7.27 View of the ion irradiation place in the Heidelberg Ion-Beam Therapy Centre (HIT) [58]

completely resistant to photon radiation. This biological effectiveness increases with the ion mass, and it reaches its maximum value in the Bragg peak area.

In the Heidelberg Ion-Beam Therapy Centre (HIT), world's first heavy ion therapy facility with a movable radiation source, the so called gantry, was developed [58]. It needs a very large and sophisticated device, and it works with carbon, oxygen, and helium ions and also with protons. First ion beam acceleration takes place in a 5 m-straight tube, leading in a "roundabout," the synchrotron. There occurs a further beam acceleration up to 75 % of light velocity. Thereby the ion beam can penetrate to about 30 cm into the patient's body, depth increasing with ion velocity.

Figure 7.27 gives a view of patient's exposure place. It consists of a gantry (7) for three-dimensional ion irradiation and an ion beam and X-ray path (8). The ion beam leaves the tubes, as a rule horizontally. An X-ray source and two detectors are located to check the position of the patient.

Figure 7.28 shows on its right partial image the three-dimensional ion beam control by a rotating gantry in Heidelberg Ion-Beam Therapy Centre, allowing radiation treatment from all directions. The left image illustrates a patient's horizontal ion beam irradiation. The beam travels through a vacuum tube out of the wall. The patient is placed on a mobile table adjusted by a high-tech robot. Then the tumor is hit by a precisely directed ion beam. This can be realized slice by slice with a special raster scanning technique [58].

A further center for heavy ion radiotherapy of tumors was the GSI Helmholtzzentrum für Schwerionenforschung, Darmstadt/Germany. Within its research framework investigations of moving targets, of dosimetry, of cell survival, and of DNA damage and repair are in the center of interest [61–63]. To date, ion beam radiotherapy at GSI Darmstadt had been successfully used to treat about 500 patients with tumors in sensible regions, as in the head, neck, pelvis, or prostate. Even heavy ion radiotherapy during pregnancy was successfully realized [64].

The success of cancer treatment at GSI Darmstadt is the result of many years of research in conjunction with GSI large ion beam accelerator system. This

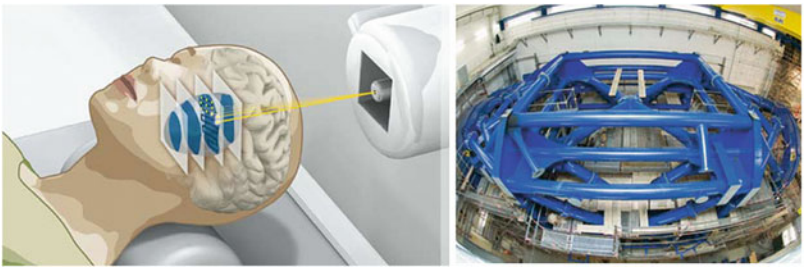

Fig. 7.28 Intensity-controlled raster scanning technique for ion beam tumor irradiation (*left*) and rotating gantry for three-dimensional ion beam control (*right*) [58]

accelerator system is similar to that of Heidelberg Ion-Beam Therapy Centre [58], consisting of a combination of linear and ring accelerators.

The biologically effective dose in the tumor can be optimized by selecting the appropriate kind of ions. Long lasting research at GSI Darmstadt has established that carbon ions are particularly favorable. For ^{12}C ion the maximum biological effect coincides exactly with the maximum physical dose. These effects intensify each other synergistically so that the carbon ions damage cells very effectively at their full penetration depth within the body. By contrast, protons and lighter ions show only a small increase in biological effectiveness. For heavier ions, it occurs too soon and tends to damage healthy tissue overlying the tumor.

Another advantage of using carbon ions is that lateral scattering in the body is much less than with protons and lighter ions. As a result, carbon ions are best suited for irradiating deep-seated tumors selectively [65–67].

A high precision radiotherapy treatment with ions requires efficient quality assurance techniques because small changes in the irradiated volume will lead to a mismatch of the deposited dose maximum and the tumor position. This causes missing dose in the tumor volume and potential damage to healthy tissue. The situation is illustrated in Fig. 7.29.

It shows the diagrammed relative dose distribution D/D_{max} for tissue irradiation with photons (left) or ions (right) as a function of the penetration depth. The frame with the dark solid line represents the beam path in the target volume, and the solid line itself shows the planned dose distribution on the basis of given density information. The maximum ion dose is placed at the tumor position (red). The example framed with a dotted line shows the situation in the patient if density changes occur compared to the situation during planning of the experiment (e.g., some cavity was filled with mucus or air). The dotted curve displays then the real dose distribution. For photons the dose deviation is negligible (see left picture), whereas for ion irradiation the dose deviation is larger, implying severe consequences. The orange color shows an area with a significant higher dose in the normal, healthy tissue compared to the planning, whereas in the light blue area the dose needed to destroy the tumor is missing.

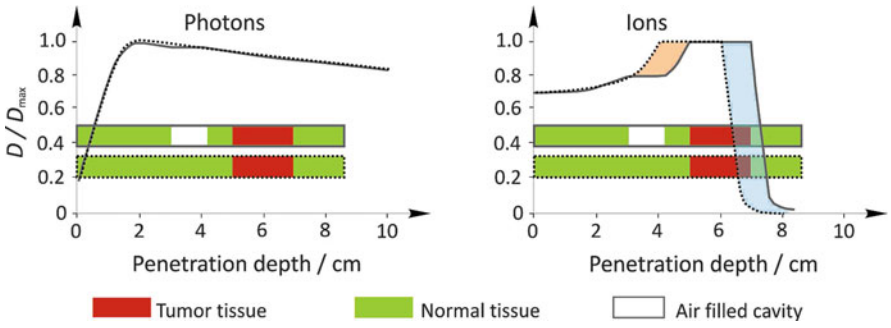

Fig. 7.29 Relative dose distribution D/D_{max} as a function of penetration depth for tissue irradiation with photons (*left*) and ions (*right*)

To avoid such discrepancies between local dose distribution of ion irradiation and the tumor position a dose monitoring system—the so-called Position Emission Tomography (PET)—was developed controlling the dose delivered by ^{12}C ion beams to cancer patients [68].

The spatial distribution of positron emitters (predominantly ^{15}O, ^{11}C, ^{10}C) generated via nuclear interactions between projectile ions and atomic nuclei of the tissue is measured during or shortly after the irradiation. Due to different physical processes for dose deposition and activity production a simulation of the expected activity is required. By means of a comparison between measured and simulated activity distribution, conclusions on the accuracy of the dose localization can be drawn [69]. Since ion therapy is usually applied as fractionated treatment over more than 2 weeks, any detected deviations can be corrected in the following fractions.

The operation mode of an in-beam double head PET scanner is visible in Fig. 7.30 [68]. It is part of the carbon ion therapy facility at GSI Darmstadt. The left picture shows the patient room with couch and mask for fixation. The horizontal ^{12}C beam leaves the beam line through a 20 × 20 cm^2 window in the center of the photograph. The right picture gives the scheme of the clinical implementation of in-beam PET. As seen from the dose distribution superimposed onto the CT the carbon ions must not reach the brain stem as an organ of risk. The comparison of the predicted with the measured β^+-activity distributions shows that the requirement has been fulfilled during the treatment. The isodose and isoactivity lines are decoded in rainbow colors. These colors denote levels of 5, 15, … 95 % of the maximum.

To date, in-beam PET, i.e., measuring the activity during the irradiation has been applied to a great number of patients, most of them with head and neck tumors [60, 70]. According to this experience, the method is capable of identifying deviations in the maximum particle ranges. Such deviations may be due to systematic errors like inaccuracies of the physical beam model in treatment planning, to random errors as minor positioning errors and to local modifications of the density distributions in comparison to the planning computed tomogram. Reasons for these modifications

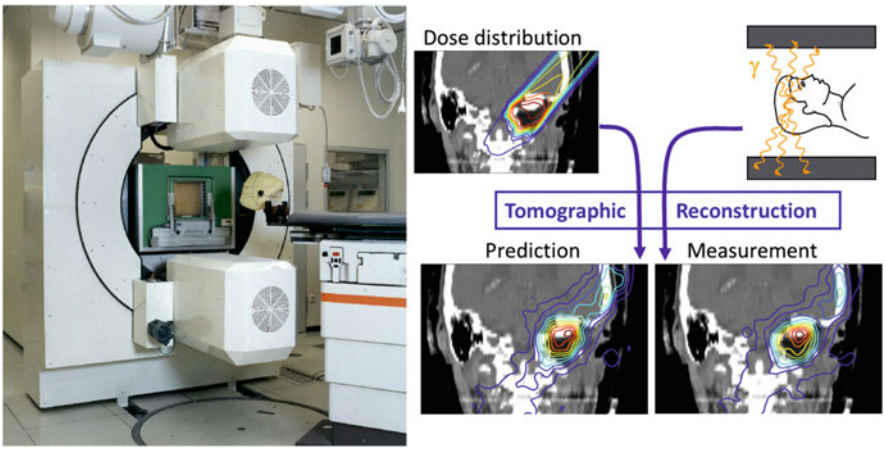

Fig. 7.30 *Left*: in-beam double head PET scanner as part of the carbon ion therapy facility at GSI Darmstadt [66]. *Right*: scheme of the clinical implementation of in-beam PET with tomographic reconstruction of dose distribution [67]

are, e.g., the filling of nasal or paranasal sinuses with mucus or tissue reduction during the healing process after previous surgery [67]. It has been shown that particle therapy PET can be applied in-beam as well as after the irradiation by means of a commercially available PET scanner [71, 72].

Due to inherent limitations of this method, a direct quantification of the delivered dose is not feasible by means of particle therapy PET since this is semiquantitative method. Therefore, another approach based on dose monitoring by detection of prompt γ-rays is currently under investigation. For this purpose, a Compton camera design was evaluated with respect to the special requirements and conditions that arise from ion beam therapy application [73]. Different concepts were compared by means of simulation, and a first prototype was tested under beam conditions [Fiedler F (2011) Private communication].

References

1. Yoshizawa Y, Oguma S, Yamauchi K (1988) New Fe-based soft magnetic alloys composed of ultrafine grain structure. J Appl Phys 64:6044–6046
2. Shima T, Kobayashi N, Kataoka N, Fujimori H (1992) Soft magnetic properties of nanocrystalline Fe-Cu-Nb-Si-B multilayers. Sci Rep Res Inst Tohoku Univ Ser A 36:224
3. Shima T, Takanashi K, Fujimori H (2001) Effect of Dy on spin-flop and magnetostri tion in exchange-coupled Tb-Dy-Fe/Fe-Cu-Nb-Si-B multilayers. IEEE Trans Magn 37:2684–2686
4. Henninger G, Teresiak A, Präßler F, Mattern N, Hofman D (1997) The influence of Cu addition on the structural properties of sputtered multilayers of the FeSiB-CuNb alloy system. J Magn Magn Mater 197:110–111
5. Oswald S, Baunack S, Henninger G, Hofman D (2002) Model investigations on the effect of Si transport on the nanocrystallization of amorphous FeSiB-(Cu, Nb). Anal Bioanal Chem 374:736–741

6. Wetzig K, Baunack S, Hoffmann V, Oswald S, Präßler F (1997) Quantitative depth profiling of thin layers. Fresenius J Anal Chem 358:25–31
7. Grünberg P, Schreiber R, Pang Y, Brodsky MB, Sowers H (1986) Layered magnetic structures: evidence for antiferromagnetic coupling of Fe layers across Cr interlayers. Phys Rev Lett 57:2442–2445
8. Baibich MN, Broto JM, Fert A, Van Dau Nguyen F, Petroff F (1988) Giant magnetoresistance of (001) Fe/(001) Cr magnetic superlattices. Phys Rev Lett 61:2472–2475
9. Wetzig K, Schneider CM (2006) Metal based thin films for electronics. Wiley-VCH, Weinheim
10. Moodera JS, Mathon GJ (1999) Spin polarized tunnelling in ferromagnetic junctions. J Magn Magn Mater 200:248–273
11. Thomas J, Reiche R, Vinzelberg H (2004) Analytical investigations of tunnel magnetoresistance layers. Anal Bioanal Chem 379:576–581
12. Nowak ER, Spradling P, Weissman MB, Parkin SSP (2000) Electron tunnelling and noise studies in ferromagnetic junctions. Thin Solid Films 377–378:699–704
13. Reimer L (1997) Transmission electron microscopy, 4th edn. Springer, Berlin
14. Thomas J, Gemming T (2013) Analytische Transmissionselektronenmikroskopie – eine Einführung für den Praktiker. Springer, Wien
15. Gonzalez-Elipe AR, Yubero F (2001) Spectroscopic characterization of oxide/oxide interfaces. In: Nalva HS (ed) Handbook of surfaces and interfaces of materials, vol 2. Academic, San Diego, CA
16. Tesmer JR, Nastasi M, Barbour IC, Maggiore CJ, Mayer JW (1995) Handbook of modern ion beam materials analysis. Materials Research Society, Pittsburgh, PA
17. Respaldiza MA, Gomez-Camacho J (1997) Applications of ion beam analysis techniques to arts and archaeometry. Universidad de Sevilla, Sevilla
18. Johansson SAE, Campell JL, Malmqvist KG (eds) (1995) Particle-induced X-ray emission spectrometry, vol 133, Chemical analysis series. Wiley, New York
19. Heitz C, Lagarde G, Pape A et al (1986) Radioisotope induced X-ray emission - a complementary method to PIXE Nucl. Instrum Methods Phys Res B 14:93–98
20. Malmqvist KG (1986) Comparison between PIXE and XRF for applications in art and archaeology. Nucl Instrum Methods Phys Res B 14:86–92
21. Demortier G, Morciaux Y (1994) PIXE gadgets. Nucl Instrum Methods Phys Res B 85:112–117
22. Wagner W, Neelmeijer C (1995) External proton beam analysis of layered objects. Fresenius J Anal Chem 353:297–302
23. Mando PA (1994) Advantages and limitations of external beams in applications to art and archeology. Nucl Instrum Methods Phys Res B 85:815–823
24. Neelmeijer C, Wagner W, Schramm HP (1996) Depth resolved ion beam analysis of objects of art. Nucl Instrum Methods Phys Res B 118:338–345
25. Jembrih D, Neelmeijer C, Schreiner M et al (2001) Iridescent Art Nouveau glass. Nucl Instrum Methods Phys Res B 181:698–702
26. Jembrih-Simbürger D, Neelmeijer C, Schalm O et al (2002) The colour of silver stained glass – analytical investigations. J Anal At Spectrom 17:321–328
27. Neelmeijer C, Wagner W, Schramm HP (1994) Depth resolved ion beam analysis of objects of art. In: Proceedings of the 4th international conference on non-destructive testing of works of art, DGZfP e.V., Berlin, p. 296
28. Menu M (1993) External beam applications to painting materials. Nucl Instrum Methods Phys Res B 75:469–475
29. Dran JC, Salomon J, Calligaro T et al (2004) Ion beam analysis of art works. Nucl Instrum Methods Phys Res B 219–220:7–15
30. Neelmeijer C, Matthes H, Pfestorf W et al (1990) External proton beam analysis of organic and inorganic art objects. Nucl Instr and Meth in Phys ResB 51:140–144

31. Schramm H, Neelmeijer C, Matthes H et al (1987/1988) Möglichkeiten und Grenzen der zerstörungsfreien Pigmentanalyse auf Gemäldeoberflächen mittels externem Protonenstrahl. In: Wiener Berichte über Naturwissenschaft in der Kunst 4–5:26
32. Neelmeijer C, Schramm HP, Matthes H et al (1990) Nondestructive multielement analysis of art objects. In: Proceedings of the 9th triennial meeting of ICOM committee for conservation, Dresden, Germany, pp 51–56
33. Tuurnula T, Hautojärvi A, Nurminen S (1991) A factory of beautiful pictures? A physical study of 3 paintings by Lucas Cranach the Elder. In: Revue des Archeologues et Historiens d'Art de Louvain 24:63
34. Neelmeijer C, Wagner W, Schramm HP et al (1995) De re metallica – IBA on air. Nucl Instrum Methods Phys Res B 99:390–393
35. Neelmeijer C, Mäder M (2002) The merits of particle induced X-ray emission in revealing painting techniques. Nucl Instrum Methods Phys Res B 189:293–302
36. Neelmeijer C, Mäder M (2004) Reverse painting on glassas seen by the proton beam. Nucl Instrum Methods Phys Res B 226:126
37. Grassi N, Migliori A, Mandò PA et al (2005) Differential PIXE measurements for the stratographic analysis. X-Ray Spectrom 34:306–309
38. Grassi N (2009) Differential and scanning mode external PIXE. Nucl Instrum Methods Phys Res B 267:825–831
39. Grassi N, Bonanni P, Mazzotta C et al (2009) PIXE analysis of a painting by Giorgio Vasari. X-Ray Spectrom 38:301–307
40. Mäder M, Grambole D, Herrmann F et al (1998) Non-destructive evaluation of glass corrosion states. Nucl Instrum Methods Phys Res B 136–138:863–868
41. Mäder M, Neelmeijer C (2004) Proton beam examination of glass. Nucl Instrum Methods Phys Res B 226:110–118
42. Mäder M (2002) Charakterisierung historischer Glasobjekte mittels Ionenstrahlen, PhD thesis, Technische Universität Dresden
43. Jembrih-Simbürger D, Neelmeijer C, Mäder M et al (2004) X-ray fluorescence and ion beam analysis of iridescent Art Nouveau glass. Nucl Instrum Methods Phys Res B 226:119–125
44. Mäder M, Jembrih-Simbürger D, Neelmeijer C et al (2005) IBA of iridescent Art Nouveau glass-comparative studies. Nucl Instrum Methods Phys Res B 239:107–113
45. Calligaro T (2008) PIXE in the study of archaeological and historical glass. X-Ray Spectrom 37:169–177
46. Zucchiatti A, Canonica L, Prati P et al (2007) Pixe analysis of V-XVI century glasses from the archaelogical site of San Martino di Ovaro. J Cult Herit 8:307–314
47. Neelmeijer C, Mäder M, Pietsch U et al (1998) Böttger Stoneware – authentic or not? Annual report, Institute of Ion Beam Physics and Materials Research, Research Center Rossendorf, FZR-253, pp 11–14
48. Swann CP, Nelson CH (2000) Böttger stoneware from North America and Europe. Nucl Instrum Methods Phys Res B 161–163:694–698
49. Reiche I, Berger A, Duval A et al (2003) Non-destructive investigations of Dürer's silver point drawings by PIXE and μ-SR-XRF. In: Proceedings of the 7th international conference on nondestructive testing and microanalysis for the diagnostics and conservation of the cultural and environmental heritage, ART 2002, June 2002, Antwerp Belgium, p 82
50. Neelmeijer C, Brissaud I, Calligaro T et al (2000) Paintings – a challenge for XRF and PIXE analysis. X-Ray Spectrom 29:101–110
51. Kalliabakos G, Kossionides S, Misialides P et al (2000) Determination of sulphur and copper depth distribution in patina layers. Nucl Instrum Methods Phys Res B 170:467–473
52. Calligaro T, Colinart S, Poirot JP et al (2002) Combined external beam PIXE and μ-Raman characterization of garnets. Nucl Instrum Methods Phys Res B 189:320–327
53. Smit Z, Pelicon P, Vidmar G et al (2000) Analysis of medieval glass by X-ray spectrometric methods. Nucl Instrum Methods Phys Res B 161–163:718–723

54. Tan KL, Lee HS, Poh WT, Ren MQ, Watt F, Tang SM, Eng P (2000) Hard metal lung disease – the first case in Singapore. Ann Acad Med Singapore 29(4):521–527
55. Stoliar P, Kreiner AJ, Debray ME et al (2004) Microdistributions of BNCT-compound. Appl Radiat Isot 61:771–774
56. Wonnemacher M, Debus J, Wenz F (2006) Strahlentherapie. Springer, Berlin
57. DeLaney TF, Kooy HM (2007) Proton and charged particle radiotherapy. Wolters Kluwer Health, Philadelphia, PA
58. Winkelmann T, Cee R, Haberer T et al (2008) Experience at the ion beam therapy center (HIT) with 2 years of continuous ECR ion source operation. In: Proceed. ECRIS 08, Chicago/USA p 86f
59. Combs SE, Ellerbrock M, Heberer T et al (2010) Initial clinic experience in the first 80 patients. Acta Oncol 49(7):1132–1140
60. Schulz-Ertner D, Nicoghosyan A, Hof H, Didinger B, Combs SE, Jäkel O, Karger CP, Edler L, Debus J (2007) Carbon ion radiotherapy of skull base chondrosarcomas. Int J Radiat Oncol Biol Phys 67(1):171–177
61. Ensminger M, Conrad S, Beucher A, Taucher-Scholz G, Löbrich M (2011) DNA damage after high LET-exposure. GSI Scientific Report 2010 – Health 04
62. Virsik P, Lee R, Gregus A, Hessel P, Ritter S (2011) Clonogenic survival of metastatic prostate cancer cells. GSI Scientific Report 2010 – Health 10
63. Eley J, Lüchtenberg R, Richter D, Durante M, Bert C (2011) Robustness of beam tracking for moving tumors. GSI Scientific Report 2010 – Health 35
64. Münter MW, Wengenroth M, Fehrenbacher G, Schardt D, Nikghosyan A, Durante M, Debus J (2010) Heavy ion radiotherapy during pregnancy. J Fertil Steril 94(6):2329.e5–2329.e7
65. La Tessa C, Schuy C, Schardt D, Durante M (2010) Bragg curve measurements of ^{12} C and ^{56}Fe in Al. GSI Scientific Report 2009 – Radiation/Biophysics 33
66. Kraft G (2000) Tumor therapy with heavy charged particles. Prog Part Nucl Phys 45 (2):473–544
67. Weyrather WK, Kraft G (2004) RBE of carbon ions: experimental data and the strategy of RBE calculation for treatment planning. Radiother Oncol 73(2):161–169
68. Enghardt W, Crespo P, Fiedler F, Hinz R, Parodi K, Pawelke J, Pönisch F (2004) Charged hadron tumour therapy monitoring by means of PET. Nucl Instrum Methods Phys Res A 525:284–286
69. Pönisch F, Parodi K, Hasch BG, Enghardt W (2004) The modelling of positron emitter production and PET imaging during carbon ion therapy. Phys Med Biol 49:5217–5232
70. Schulz-Ertner D, Karger CP, Feuerhake A, Nikoghosyan A, Combs SE, Jäkel O, Edler L, Scholz M, Debus J (2007) Effectiveness of carbon ion radiotherapy in the treatment ofskull-base chordomas. Int J Radiat Oncol Biol Phys 68(2):449–457
71. Nishio T, Miyatake A, Ogino T et al (2010) The development and clinical use of a beam on-line PET system mounted on a rotating gantry port in proton therapy. Int J Radiat Oncol Biol Phys 76:277–286
72. Shakirin G, Braess H, Fiedler F, Kunath D, Laube K, Parodi K, Priegnitz M, Enghardt W (2011) Implementation and workflow for PET monitoring of therapeutic ion irradiation: a comparison of in-beam, in-room and off-line techniques. Phys Med Biol 56:1281–1298
73. Kormoll T, Fiedler F, Schöne S, Wüstemann J, Zuber K, Enghardt W (2010) A comp-ton imager for in-vivo dosimetry of proton beams. Nucl Instrum Methods Res A 626–627:114–119

Index

B. Schmidt and K. Wetzig, *Ion Beams in Materials Processing and Analysis*,
DOI 10.1007/978-3-211-99356-9,